frontiers | Research Topics

Immune studies of SARS-CoV2 and vaccines using preclinical modeling

Edited by
William Murphy, Cordelia Dunai and Smita S. Iyer

Published in
Frontiers in Immunology

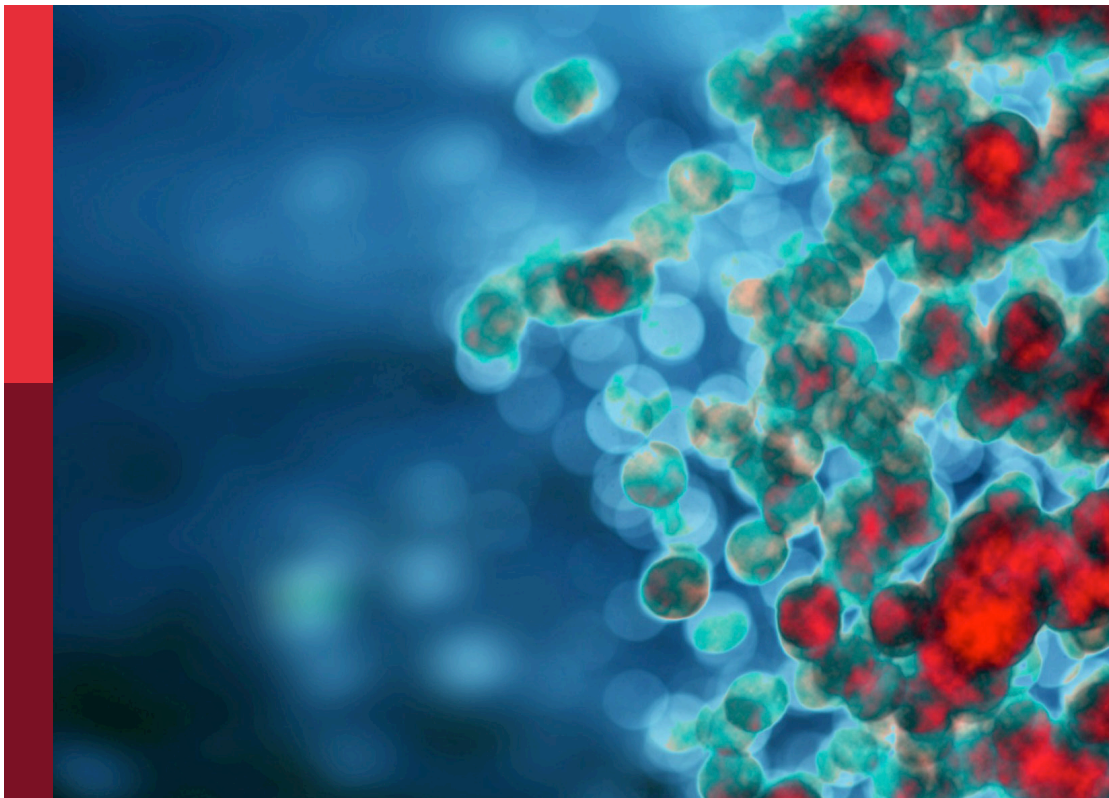

ISSN 1664-8714
ISBN 978-2-8325-5944-4
DOI 10.3389/978-2-8325-5944-4

About Frontiers

Frontiers is more than just an open access publisher of scholarly articles: it is a pioneering approach to the world of academia, radically improving the way scholarly research is managed. The grand vision of Frontiers is a world where all people have an equal opportunity to seek, share and generate knowledge. Frontiers provides immediate and permanent online open access to all its publications, but this alone is not enough to realize our grand goals.

Frontiers journal series

The Frontiers journal series is a multi-tier and interdisciplinary set of open-access, online journals, promising a paradigm shift from the current review, selection and dissemination processes in academic publishing. All Frontiers journals are driven by researchers for researchers; therefore, they constitute a service to the scholarly community. At the same time, the *Frontiers journal series* operates on a revolutionary invention, the tiered publishing system, initially addressing specific communities of scholars, and gradually climbing up to broader public understanding, thus serving the interests of the lay society, too.

Dedication to quality

Each Frontiers article is a landmark of the highest quality, thanks to genuinely collaborative interactions between authors and review editors, who include some of the world's best academicians. Research must be certified by peers before entering a stream of knowledge that may eventually reach the public - and shape society; therefore, Frontiers only applies the most rigorous and unbiased reviews. Frontiers revolutionizes research publishing by freely delivering the most outstanding research, evaluated with no bias from both the academic and social point of view. By applying the most advanced information technologies, Frontiers is catapulting scholarly publishing into a new generation.

What are Frontiers Research Topics?

Frontiers Research Topics are very popular trademarks of the *Frontiers journals series*: they are collections of at least ten articles, all centered on a particular subject. With their unique mix of varied contributions from Original Research to Review Articles, Frontiers Research Topics unify the most influential researchers, the latest key findings and historical advances in a hot research area.

Find out more on how to host your own Frontiers Research Topic or contribute to one as an author by contacting the Frontiers editorial office: frontiersin.org/about/contact

Immune studies of SARS-CoV2 and vaccines using preclinical modeling

Topic editors

William Murphy — University of California, Davis, United States
Cordelia Dunai — University of Liverpool, United Kingdom
Smita S. Iyer — University of California, Davis, United States

Citation

Murphy, W., Dunai, C., Iyer, S. S., eds. (2025). *Immune studies of SARS-CoV2 and vaccines using preclinical modeling*. Lausanne: Frontiers Media SA.
doi: 10.3389/978-2-8325-5944-4

Table of contents

frontiers | Frontiers in Immunology

TYPE Editorial
PUBLISHED 16 January 2025
DOI 10.3389/fimmu.2024.1548624

OPEN ACCESS

EDITED AND REVIEWED BY
Rita Carsetti,
Bambino Gesù Children's Hospital (IRCCS), Italy

*CORRESPONDENCE
Cordelia Dunai
cdunai@liverpool.ac.uk

RECEIVED 19 December 2024
ACCEPTED 30 December 2024
PUBLISHED 16 January 2025

CITATION
Dunai C, Iyer SS and Murphy WJ (2025) Editorial: Immune studies of SARS-CoV2 and vaccines using preclinical modeling. *Front. Immunol.* 15:1548624. doi: 10.3389/fimmu.2024.1548624

Editorial: Immune studies of SARS-CoV2 and vaccines using preclinical modeling

Cordelia Dunai[1,2]*, Smita S. Iyer[3,4] and William J. Murphy[1,5]

[1]Department of Dermatology, University of California, Davis, Davis, CA, United States, [2]Clinical Infection, Microbiology and Immunology (CIMI), Institute of Infection, Veterinary and Ecological Sciences (IVES), University of Liverpool, Liverpool, United Kingdom, [3]Department of Pathology, School of Medicine, University of Pittsburgh, Pittsburgh, PA, United States, [4]California National Primate Research Center, University of California, Davis (UC), Davis, CA, United States, [5]Department of Internal Medicine, University of California, Davis, Davis, CA, United States

KEYWORDS

immunology, virology, SARS-CoV-2, mouse models, preclinical models

Editorial on the Research Topic
Immune studies of SARS-CoV2 and vaccines using preclinical modeling

Introduction

Preclinical animal models remain essential for understanding viral pathogenesis as well as for the development and assessment of vaccines and therapeutic strategies. It is extremely important, particularly for immunological studies, to understand species differences and limitations both from the viral pathogenesis as well as immune standpoints (summarized in Table 1). Much has been learned about coronaviruses (including pivotal earlier studies on SARS-Co-V) from preclinical animal models which shed insights on both viral pathogenesis as well as immune responses underlying them (reviewed by Collins et al.).

It is difficult to estimate how many lives the vaccines saved globally during the COVID-19 pandemic, but approximately 1.5 million lives were saved in the WHO European Region by vaccines which were first developed and tested in preclinical models (1). SARS-CoV-2 virus pathology is complex and systemic, leading to challenges in how best to model it preclinically in different species. A lot of research has focused on the neutralizing antibodies in the immune response against SARS-CoV-2 and their apparent rapid diminution. Previous research has demonstrated aberrant inflammatory responses, particularly in the elderly and obese due to cytokine release syndrome [reviewed in Chegni et al. (2)]. Additionally, it was shown that inflammation can occur in the brain even during mild COVID-19 infection in non-human primate studies offering an initial insight into how other organs, not just the lungs, are affected (3).

Efforts continue to make preclinical models more similar to the human scenarios by modifying genes and the infection method and incorporating factors such as age, obesity, and multiple infections. This Research Topic on preclinical models of SARS-CoV-2 covers this concept of increased translatability as well as strategies to improve vaccines.

TABLE 1 Pros and cons of preclinical models.

Property of Preclinical Models	Pros	Cons
Mammalian Genetics	High genetic similarity to humans enables relevant insights	Differences in gene expression and immune response can limit applicability
Genetic homogeneity	Studying inbred strains allows replicates, reduces variability, and increases reproducibility	Studying a single strain does not model human genetic diversity
Ease of Genetic Manipulation	Can create transgenic, knockout, or humanized mice to model specific conditions	Human immune components in humanized mice may not function identically
Immune System Studies	Ability to study specific immune pathways in isolation	Mouse immune system differs significantly (e.g. cytokine profiles, T-cell responses) and they are Specific-Pathogen-Free (SPF) and more naïve (or lack diversity in antigen-experienced T and B cell repertoire) than humans
Pathogen Adaptation	SARS-CoV-2 can infect hamsters, ferrets, and non-human primates. SARS-CoV-2 has been adapted to mice for study	Adaptation may alter pathogen and relevance to human infection. Otherwise, K18-hACE2 transgenic mice are needed to study SARS-CoV-2
Vaccination Studies	Useful for preclinical testing of vaccine efficacy	Immune responses to vaccines may not predict human outcomes and the immune response in genetically identically SPF mice does not model human diversity and diverse immune memory responses
Rapid Life Cycle	Short lifespan allows studying disease progression over generations	Short lifespan limits study of chronic or long-term infections. Mostly young animals are studied
Ethics and Accessibility	Considered ethically acceptable with regulations; cost-effective	Ethical concerns still exist, especially with non-human primates
Cost and Maintenance	Low cost and simple housing requirements	Environment and social conditions not reflective of humans. Non-human primate studies are expensive
Drug Testing	Enables high-throughput testing of vaccines and therapeutics	Differences in drug metabolism and immune interactions can lead to poor translatability

Improving translatability of preclinical models

One of the limitations of the mouse model is the species difference of ACE2, a receptor that SARS-CoV-2 uses to enter cells. Initial studies using a transgenic mice expressing human ACE2 under the K18 promoter (K18-hACE2) transgenic mouse model enabled infection with SARS-CoV-2, however its broader expression is not representative of the clinical scenario and leads to more severe and wider-spread pathology (4–8). Fine-tuning this model, Liu et al. introduced human ACE2 and TMPRSS2 to replace the orthologous mouse gene loci but remain under control of their respective murine promoters. This model enabled investigation of mild infection (with peak viral load at dpi 4) and longer-term studies which are useful for understanding long-term effects of the virus and immune memory.

A novel low inoculum SARS-CoV-2 infection model also enabled study of mild infection and lacked active viral replication in the brain as is present in severe and neuroinvasive SARS-CoV-2 models (Dunai et al.). This is more representative of the majority of clinical cases because it is very rare to find viral protein in human brain parenchyma even in severe COVID-19 cases (9). Despite a lack of viral replication in the brains of SARS-CoV-2-infected K18-hACE2-tg mice, there were elevated pro-inflammatory cytokines and an increase in microglia reactivity indicating indirect immune activation in the brain during SARS-CoV-2 infection (Dunai et al.).

Intriguingly, quite early in the pandemic, an interesting phenomenon emerged—the BCG vaccine was associated with protection from COVID-19 (10). However, this was not replicated in randomized controlled clinical trials (11, 12). Due to the prevalence and health impact of tuberculosis, co-infection is an important issue. Williams et al. investigated co-infection of mice with *M. tuberculosis* and SARS-CoV-2. Counter-intuitively, mice with co-infection actually had a reduced mortality rate. The authors found that the protection was associated with high levels of cytokines including TNF and IFN-γ *in vivo* and *in vitro* with human PBMCs and epithelial cells suggesting that activated innate pathways can lead to broad protective antiviral effects (Williams et al.).

Strategies to improve SARS-CoV-2 vaccines

It is important to increase vaccine efficiency and optimize delivery, timing, targets, and adjuvants especially since periodic immunizations are now recommended due to persistent generation of new viral variants. While the emphasis in the literature has been on the generation of neutralizing antibodies, it has been shown that generating a strong T cell response is important for long-term immunity although the precise roles of T cells remain poorly understood and understudied (13, 14). Therefore, using multiple B and T cell epitopes for a vaccine is a promising strategy

investigated in this Research Topic by Prakash et al. Other promising strategies investigated include: intranasal delivery i.e. a needle-free method with all the advantages of stimulating mucosal immunity by Zhou et al.; coupling vaccine with cytokine stimulation (CCL20/MIP-3α) by Gordy et al.; and stabilizing the spike trimer for a more robust immune response by Avila-Nieto et al. Song et al. went a step beyond most studies which usually do not look at more than one vaccine administration or more than one regimen and found that a heterologous boost resulted in more B cell activation and antibody production. These types of studies are particularly important given the paucity of studies assessing effects of repeated vaccinations on different components of immune responses, as well as means to further optimize them.

Conclusion

It is important to note that preclinical models have the advantage of controlling for the numerous variables (outbred and diverse populations, sex, age, obesity, prior pathogen exposure, etc) associated with clinical studies (summary of pros and cons in Table 1). Added to these are the limitations of clinical studies regarding tissue assessment and assays available, particularly for immune studies. This is the advantage of robust preclinical modelling which offers the ability to control for many of these factors and allow for thorough mechanistic dissection of therapeutic and vaccine strategies as reviewed in this Research Topic (Collins et al.). The emergence of chronic symptoms well after SARS-CoV-2 infection, termed post-acute sequelae of COVID-19 (PASC), also highlight the importance of using preclinical models in long-term studies to determine immunological mechanisms involved. The marked immune changes that arise with normal aging further necessitate more robust preclinical modelling in this area given the populations most at risk for poor outcomes following viral infection (15). Given the tremendous heterogeneity of the human population along with the need for multiple vaccinations due to continuous SARS-CoV-2 exposure, consideration of these variables needs to be undertaken in preclinical modelling to determine effects of different vaccines and vaccine strategies that result in greatest efficacy with minimal adverse effects over time.

Author contributions

CD: Writing – original draft, Writing – review & editing. SI: Writing – original draft, Writing – review & editing. WM: Writing – original draft, Writing – review & editing.

Conflict of interest

The authors declare that the research was conducted in the absence of any commercial or financial relationships that could be construed as a potential conflict of interest.

Publisher's note

References

1. Meslé MMI, Brown J, Mook P, Katz MA, Hagan J, Pastore R, et al. Estimated number of lives directly saved by COVID-19 vaccination programmes in the WHO European Region from December, 2020, to March, 2023: a retrospective surveillance study. *Lancet Respir Med*. (2024) 12:714–27. doi: 10.1016/S2213-2600(24)00179-6

2. Chegni H, Babaii H, Hassan ZM, Pourshaban M. Immune response and cytokine storm in SARS-CoV-2 infection: Risk factors, ways of control and treatment. *Eur J Inflammation*. (2022) 20:1721727X221098970. doi: 10.1177/1721727X221098970

3. Choudhary S, Kanevsky I, Yildiz S, Sellers RS, Swanson KA, Franks T, et al. Modeling SARS-CoV-2: comparative pathology in rhesus macaque and golden Syrian hamster models. *Toxicol Pathol*. (2022) 50(3):280–93. doi: 10.1177/01926233211072767

4. Leist SR, Dinnon KH, Schäfer A, Tse LV, Okuda K, Hou YJ, et al. A mouse-adapted SARS-CoV-2 induces acute lung injury and mortality in standard laboratory mice. *Cell*. (2020) 183:1070–1085.e12. doi: 10.1016/j.cell.2020.09.050

5. Carossino M, Kenney D, O'Connell AK, Montanaro P, Tseng AE, Gertje HP, et al. Fatal neurodissemination and SARS-CoV-2 tropism in K18-hACE2 mice is only partially dependent on hACE2 expression. (2022) *Viruses*, 14(3):535. doi: 10.3390/v14030535

6. Golden JW, Cline CR, Zeng X, Garrison AR, Carey BD, Mucker EM, et al. Human angiotensin-converting enzyme 2 transgenic mice infected with SARS-CoV-2 develop severe and fatal respiratory disease. *JCI Insight*. (2020) 5(19). doi: 10.1172/jci.insight.142032

7. Kumari P, Rothan HA, Natekar JP, Stone S, Pathak H, Strate PG, et al. Neuroinvasion and encephalitis following intranasal inoculation of SARS-CoV-2 in K18-hACE2 mice. *Viruses*. (2021) 13:132. doi: 10.3390/v13010132

8. Ullah I, Prévost J, Ladinsky M, Stone H, Lu M, Anand SP, et al. *Live Imaging of SARS-CoV-2 Infection in Mice Reveals Neutralizing Antibodies Require Fc Function for Optimal Efficacy*. Rochester, NY: Social Science Research Network (2021). doi: 10.2139/ssrn.3817810

9. Meinhardt J, Radke J, Dittmayer C, Franz J, Thomas C, Mothes R, et al. Olfactory transmucosal SARS-CoV-2 invasion as a port of central nervous system entry in individuals with COVID-19. *Nat Neurosci*. (2021) 24:168–75. doi: 10.1038/s41593-020-00758-5

10. Escobar LE, Molina-Cruz A, Barillas-Mury C. BCG vaccine protection from severe coronavirus disease 2019 (COVID-19). *Proc Natl Acad Sci*. (2020) 117:17720–6. doi: 10.1073/pnas.2008410117

11. Pittet LF, Messina NL, Orsini F, Moore CL, Abruzzo V, Barry S, et al. Randomized trial of BCG vaccine to protect against Covid-19 in health care workers. *N Engl J Med*. (2023) 388:1582–96. doi: 10.1056/NEJMoa2212616

12. ten Doesschate T, van der Vaart TW, Debisarun PA, Taks E, Moorlag SJCFM, Paternotte N, et al. Bacillus Calmette-Guérin vaccine to reduce healthcare worker absenteeism in COVID-19 pandemic, a randomized controlled trial. *Clin Microbiol Infect*. (2022) 28:1278–85. doi: 10.1016/j.cmi.2022.04.009

13. Cankat S, Demael MU, Swadling L. In search of a pan-coronavirus vaccine: next-generation vaccine design and immune mechanisms. *Cell Mol Immunol*. (2024) 21:103–18. doi: 10.1038/s41423-023-01116-8

14. Moore SC, Kronsteiner B, Longet S, Adele S, Deeks AS, Liu C, et al. Evolution of long-term vaccine-induced and hybrid immunity in healthcare workers after different COVID-19 vaccine regimens. *Med*. (2023) 4:191–215.e9. doi: 10.1016/j.medj.2023.02.004

15. Murphy WJ, Longo DL. A possible role for anti-idiotype antibodies in SARS-CoV-2 infection and vaccination. *New Engl J Med*. (2022) 386(4):394–96. doi: 10.1056/NEJMcibr2113694

frontiers | Frontiers in Immunology

TYPE Original Research
PUBLISHED 04 December 2023
DOI 10.3389/fimmu.2023.1291972

OPEN ACCESS

EDITED BY
William Murphy,
University of California, Davis, United States

REVIEWED BY
David Nemazee,
The Scripps Research Institute, United States
Arta Monjazeb,
UC Davis Health, United States

*CORRESPONDENCE
Jorge Carrillo
jcarrillo@irsicaixa.es
Joaquim Segalés
joaquim.segales@irta.cat
Victor Guallar
victor.guallar@bsc.es

†PRESENT ADDRESSES
Marco Brustolin,
Department of Biomedical Sciences, Institute of Tropical Medicine, Antwerp, Belgium
Jordi Rodon,
Institute of Virology, Charité-Universitätsmedizin Berlin, Berlin, Germany
Ferran Tarrés-Freixas,
Unitat Mixta d'Investigació IRTA-UAB en Sanitat Animal, Centre de Recerca en Sanitat Animal (CReSA), Campus de la Universitat Autònoma de Barcelona (UAB), Barcelona, Spain; IRTA Programa de Sanitat Animal, Centre de Recerca en Sanitat Animal (CReSA), Campus de la Universitat Autònoma de Barcelona (UAB), Barcelona, Spain
Jordana Muñoz-Basagoiti,
Unitat Mixta d'Investigació IRTA-UAB en Sanitat Animal, Centre de Recerca en Sanitat Animal (CReSA), Campus de la Universitat Autònoma de Barcelona (UAB), Barcelona, Spain; IRTA Programa de Sanitat Animal, Centre de Recerca en Sanitat Animal (CReSA), Campus de la Universitat Autònoma de Barcelona (UAB), Barcelona, Spain

‡These authors have contributed equally to this work

RECEIVED 10 September 2023
ACCEPTED 20 November 2023
PUBLISHED 04 December 2023

Novel Spike-stabilized trimers with improved production protect K18-hACE2 mice and golden Syrian hamsters from the highly pathogenic SARS-CoV-2 Beta variant

Carlos Ávila-Nieto[1‡], Júlia Vergara-Alert[2,3‡], Pep Amengual-Rigo[4‡], Erola Ainsua-Enrich[1], Marco Brustolin[2,3†], María Luisa Rodríguez de la Concepción[1], Núria Pedreño-Lopez[1], Jordi Rodon[2,3†], Victor Urrea[1], Edwards Pradenas[1], Silvia Marfil[1], Ester Ballana[1,5,6], Eva Riveira-Muñoz[1], Mònica Pérez[2,3], Núria Roca[2,3], Ferran Tarrés-Freixas[1†], Julieta Carabelli[1], Guillermo Cantero[2,3], Anna Pons-Grífols[1], Carla Rovirosa[1], Carmen Aguilar-Gurrieri[1], Raquel Ortiz[1], Ana Barajas[1], Benjamin Trinité[1], Rosalba Lepore[4], Jordana Muñoz-Basagoiti[1†], Daniel Perez-Zsolt[1], Nuria Izquierdo-Useros[1,5,6], Alfonso Valencia[4,7], Julià Blanco[1,5,6,8], Bonaventura Clotet[1,5,6,8,9], Victor Guallar[4,7*], Joaquim Segalés[2,10*] and Jorge Carrillo[1,5,6*]

[1]IrsiCaixa AIDS Research Institute, Badalona, Spain, [2]Unitat Mixta d'Investigació IRTA-UAB en Sanitat Animal, Centre de Recerca en Sanitat Animal (CReSA), Campus de la Universitat Autònoma de Barcelona (UAB), Barcelona, Spain, [3]IRTA Programa de Sanitat Animal, Centre de Recerca en Sanitat Animal (CReSA), Campus de la Universitat Autònoma de Barcelona (UAB), Barcelona, Spain, [4]Life Sciences Department, Barcelona Supercomputing Center (BSC), Barcelona, Spain, [5]Germans Trias i Pujol Research Institute (IGTP), Badalona, Spain, [6]Centro de Investigación Biomédica en Red (CIBER) de Enfermedades Infecciosas, Instituto de Salud Carlos III (ISCIII), Madrid, Spain, [7]Catalan Institution for Research and Advanced Studies, Barcelona, Spain, [8]Centre for Health and Social Care Research (CESS), Faculty of Medicine, University of Vic – Central University of Catalonia (UVic – UCC), Vic, Spain, [9]Fundació Lluita contra les Infeccions, Hospital Germans Trias i Pujol, Badalona, Spain, [10]Departament de Sanitat i Anatomia Animals, Facultat de Veterinària, UAB, Cerdanyola del Vallès, Spain

Most COVID-19 vaccines are based on the SARS-CoV-2 Spike glycoprotein (S) or their subunits. However, S shows some structural instability that limits its immunogenicity and production, hampering the development of recombinant S-based vaccines. The introduction of the K986P and V987P (S-2P) mutations increases the production and immunogenicity of the recombinant S trimer, suggesting that these two parameters are related. Nevertheless, S-2P still shows some molecular instability and it is produced with low yield. Here we described a novel set of mutations identified by molecular modeling and located in the S2 region of the S-2P that increase its production up to five-fold. Besides their immunogenicity, the efficacy of two representative S-2P-based mutants, S-

29 and S-21, protecting from a heterologous SARS-CoV-2 Beta variant challenge was assayed in K18-hACE2 mice (an animal model of severe SARS-CoV-2 disease) and golden Syrian hamsters (GSH) (a moderate disease model). S-21 induced higher level of WH1 and Delta variants neutralizing antibodies than S-2P in K18-hACE2 mice three days after challenge. Viral load in nasal turbinate and oropharyngeal samples were reduced in S-21 and S-29 vaccinated mice. Despite that, only the S-29 protein protected 100% of K18-hACE2 mice from severe disease. When GSH were analyzed, all immunized animals were protected from disease development irrespectively of the immunogen they received. Therefore, the higher yield of S-29, as well as its improved immunogenicity and efficacy protecting from the highly pathogenic SARS-CoV-2 Beta variant, pinpoint the S-29 mutant as an alternative to the S-2P protein for future SARS-CoV-2 vaccine development.

KEYWORDS

COVID-19, SARS-CoV-2, vaccine, neutralizing antibodies, humoral response, Spike glycoprotein

1 Introduction

Vaccines have been extensively used to control infectious diseases. While smallpox is the only pathogen that has been eradicated in human, mass immunization programs have reduced the spread of other infectious diseases, including tetanus, polio, and measles (1, 2). In January 2020, the severe acute respiratory syndrome coronavirus 2 (SARS-CoV-2) was identified as the causal agent of the coronavirus disease 2019 (COVID-19), and many laboratories rapidly started programs to develop COVID-19 vaccines (3, 4). To date, several COVID-19 vaccines are available and have contributed to the reduction of COVID-19 impact on public health (5, 6). However, COVID-19 is still present in the world and new SARS-CoV-2 variants continue emerging with high transmissibility and/or resistance to the immune responses elicited after infection and/or vaccination (7).

Within the SARS-CoV-2 proteome, the Spike (S) mediates virus attachment by binding to the angiotensin-converting enzyme 2 receptor (ACE2) on the surface of target cells. After being primed by host proteases, S promotes viral entry and cell infection (8, 9). Therefore, most SARS-CoV-2 vaccines are based on this protein since it is the main target of neutralizing antibodies (NAbs) [particularly, the receptor binding domain (RBD)] (3, 4, 10). The S is a trimer, and each monomer has two subunits: the S1 extracellular, and the S2 membrane anchor subunits. While the S1 binds to ACE2 via the RBDs, the S2 domain participates in the membrane fusion process, which involves drastic conformational changes (8, 11, 12). Thus, the S glycoprotein shows a certain degree of structural instability that might hamper its production as recombinant protein and modulate its immunogenicity. This feature is shared with functional homologous surface proteins from other viruses, including the S of Middle East respiratory syndrome coronavirus (MERS-CoV), the Fusion protein of the respiratory syncytial virus (RSV), or the Envelope glycoprotein of the human immunodeficiency virus (HIV) (13). Several studies have shown that it is possible to stabilize these proteins in their prefusion state and improve their production and immunogenicity (13). In this sense, the introduction of two proline mutations in the S2 (S-2P) has been proposed as a common strategy for the stabilization of this glycoprotein from several coronaviruses, including the SARS-CoV-2 (11, 14). In fact, some of the most used SARS-CoV-2 vaccines, such as BNT162b2, mRNA-1273 or Ad26.COV2.S are based on the S-2P strategy (15–17).

Importantly, the S-2P protein still retains some structural instability and generates a poor yield when the protein is produced as recombinant protein (around 0.5 mg/L) (11, 18). Several studies have addressed these limitations by introducing additional stabilizing mutations. In this sense, the incorporation of four additional prolines (S-6P) improved the stability of the S trimer and increased its yield by ten-fold (18). In another approach, the incorporation of the mutations D614N, A892P, A942P, and V987P stabilized the S protein in a close-prefusion state and increased its yield by 6-fold (19). However, whereas the addition of disulfide bridges between different domains of the S glycoprotein reduced the motility of the RBD, it failed improving recombinant trimer production (20, 21). Alternatively, pre-fusion stabilizing mutations have also been identified by high-throughput methods. Thus, the addition of D994Q mutation to the S-2P backbone increased its production as soluble recombinant protein by three-fold (22). However, it remains poorly understood how all these mutations modify the S immunogenicity compared to S-2P.

Here, we describe a set of novel mutations that increase SARS-CoV-2 S yields by five-fold, while maintaining the immunogenicity and protection efficacy against the development of SARS-CoV-2-induced disease in K18-hACE2 transgenic mice and golden Syrian hamsters (GSH) previously observed with the S-2P prototype.

2 Materials and methods

2.1 Recombinant trimeric S glycoprotein design and modeling

Unsolved secondary structures of the trimer in closed (PDB: 6VXX) and open (PDB: 6VYB) conformations (8) were reconstructed using SwissModel (23). Then, all possible single mutations in both conformations were modeled using FoldX (24). For selecting potential variants, two different approaches were used. First, we computed the Gibbs free energy change ($\Delta\Delta G_{open}$) between the WT and the mutant using the open state as a reference. Negative values indicate introduction of stabilization. Second, comparison of the Gibbs free energy changes upon mutation between the closed ($\Delta\Delta G_{closed}$) and open ($\Delta\Delta G_{open}$) conformations ($\Delta\Delta G$) revealed a set of mutations predicted to strengthen the open conformation in combination with 2P (positive values indicate stabilization of the open state). For both approaches, all single mutations predicting beneficial energies (or just slightly neutral/worst values) were addressed by inspecting the three-dimensional models. In this regard, the final selection was based on: i) selection of mutations predicted to increase the stability of the open-conformation using FoldX; ii) selection of mutations predicted to increase the stability of the open-conformation over the closed one using FoldX, iii) selection of mutations creating well-defined intermolecular interactions between the RBD domains (including hydrophobic bonds, π-π interactions and cation-π interactions, ionic bonds, hydrophobic contacts or cavity filling mutations) that would exert a positive impact in the open state or a negative one on the closing motion of the trimer.

2.2 Recombinant protein production and purification

Recombinant trimeric S glycoproteins based on the Wuhan WH-1 sequence were designed as previously described by Wrapp (11). Briefly, the C-terminal end of the S, without the transmembrane and cytoplasmatic domains, was fused to a T4 foldon trimerization domain in tandem with an 8xhis tag and a strep tag II. The furin cleavage site was removed by mutating it to GSAS. All constructs include the K986P and V987P mutations. DNA constructs were supplied by GeneART (ThermoFisher scientific) as pcDNA3.4-based plasmids. Proteins were produced by transient transfection using the Expi293 expression system (ThermoFisher Scientific), following the manufacturer instructions. Five days after transfection, cell culture supernatants were harvested and clarified by centrifugation (3000xg for 20 minutes) or using Sartoclear Dynamics® Lab V (Sartorius). Supernatants were then filtered at 0.2 µm using Nalgene Rapid Flow sterile single using vacuum filter units (ThermoFisher Scientific) and were purified using Ni-Sepharose Excel histidine-tagged protein purification resin (Cytiva), concentrated, and buffer exchanged to phosphate buffer saline by ultrafiltration (Merck Millipore). Integrity and purity of purified proteins were analyzed by sodium dodecyl sulfate polyacrylamide gel electrophoresis and Coomassie G-250 staining (ThermoFisher Scientific). Purified proteins were stored at -80°C until use.

2.3 Recombinant S proteins quantification and RBD exposure

S variants production was determined in duplicate by an in-house developed ELISA. Nunc MaxiSorp ELISA plates were coated overnight at 4°C with the anti-6xHis antibody HIS.H8 (ThermoFisher Scientific) at 2 µg/mL in PBS. Then, plates were blocked with PBS/1% of bovine serum albumin (BSA, Miltenyi Biotech) for two hours at room temperature. The recombinant SARS-CoV-2 Spike S1+S2-His protein (Sino Biological) was used as standard at 1µg/mL followed by 3-fold dilutions. S variants samples (supernatant and purified proteins) were serially diluted so that they could be quantified. Standards and samples were diluted in blocking buffer. After blocking, 50 µL of each sample and standard were added to plates and incubated overnight at 4°C. Next day, the SARS-CoV-2 Spike S2 IgG rabbit antibody (Sino Biological) was diluted (1/1000) in blocking buffer and added to plates for 2 hours at room temperature. The HRP-donkey anti-rabbit IgG (H+L) (1/10.000) (Jackson ImmunoResearch) was used as detection antibody. Plates were revealed with o-Phenylenediamine (OPD) (Sigma Aldrich) and stopped using 4N of H_2SO_4 (Sigma-Aldrich). Signal was analyzed as the optical density (OD) at 492 nm with noise correction at 620 nm. S mutants quantification was done according to standard curve using Graphpad.

The RBD exposition was evaluated using an in-house ELISA. Nunc Maxisorp ELISA plates were coated with the HIS.H8 anti-6xHis tag monoclonal antibody (ThermoFisher Scientific) at 2 µg/mL in PBS and incubated overnight at 4°C. Then, plates were washed and blocked for two hours using PBS/1% of BSA (Miltenyi Biotech) at room temperature. After that, each sample was added in triplicate and incubated overnight (4°C) at 0.1 µg/ml. The next day, plates were washed and incubated with a purified ACE2-human IgG Fc-fusion protein at 0.1 µg/mL in blocking buffer for 2 hours at room temperature. Next, plates were incubated for 1 hour at room temperature with HRP conjugated- $(Fab)_2$ goat anti-human IgG (Fc specific) (1/10000) (Jackson ImmunoResearch). Plates were revealed with OPD (Sigma Aldrich) and stopped using 2N of H_2SO_4 (Sigma Aldrich). Signal was analyzed as the OD at 492 nm with noise correction at 620 nm. ACE2 binding was determined as the signal obtained with the ACE2-human Fc fusion protein, normalized according to protein concentration. Data are shown as fold change compared to S-2P.

2.4 Viral stock preparation

In vivo challenge experiments were performed using Cat24 SARS-CoV-2 B.1.531 (Beta) variant isolate (EPI_ISL_1663571) (25, 26). Cat24 was isolated from a nasopharyngeal swab from a COVID-19 affected patient, as previously described (25, 26) and subsequently grown and titrated in Vero E6 cells (ATCC CRL-1586). Vero E6 cells were cultured in Dulbecco's modified Eagle

medium (Invitrogen) supplemented with 10% fetal bovine serum (FBS, Invitrogen), 100 U/mL penicillin, and 100 µg/mL streptomycin, (all from Invitrogen).

2.5 *In vivo* immunization and challenge experiments

K18-hACE2 transgenic mice (B6.Cg-Tg(K18-ACE2)2Prlmn/J; stock #034860; Jackson Laboratories) were maintained by breeding K18-hACE2 hemizygous mice with C57BL/6J mice, following the instructions of Jackson Laboratory (https://www.jax.org/strain/034860). Offspring genotyping was performed according to the protocol 38170: Probe Assay - Tg (K18-ACE2) 2Prlmn QPCR version 2.0 (https://www.jax.org/Protocol?stockNumber=034860&protocolID=38170). GSH were purchased from Envigo and maintained by brother/sister mating. Both K18-hACE2 transgenic mice and GSH colonies were established at the Centre for Comparative Medicine and Bioimage (CMCiB). Animal studies were evaluated and approved in advance by the Committee on the Ethics of Animal Experimentation of the IGTP and count with the authorization of Generalitat de Catalunya (Code: 10965 and 11094).

Ninety-one K18-hACE2 mice (balanced female-male ratio, 7-9 weeks old) were distributed in five experimental groups: S-2P (n=21), S-21(n=22), S-29 (n=22), unvaccinated and challenged controls (n=16), and uninfected negative controls (n=10). In the case of GSHs, a total of forty-nine animals were used (balanced female-male ratio, 5-7 weeks old) and distributed in five experimental groups: S-2P (n=11), S-21 (n=11), S-29 (n=11), unvaccinated and challenged controls (n=11), and uninfected negative controls (n=5). Both mice and hamsters from S-2P, S-21, and S-29 groups were immunized with 15 µg of recombinant protein with AddaVax™ (Invivogen) as adjuvant in the hock (27). Three weeks later, immunized animals were boosted with a second dose of the same formulation. Control animals were primed and boosted with PBS and AddaVax™. Two weeks after boosting, mice were challenged with 1000 $TCID_{50}$ of SARS-CoV-2 (Cat24 isolate) and followed up for 14 days. GSHs were challenged three weeks after boosting with 10000 $TCID_{50}$ of SARS-CoV-2 (Cat24 isolate) and followed up for 7 days. After infection, body weight and clinical signs were monitored daily until the end of the experiment. Six mice for each experimental group, except the uninfected controls, were euthanized on days 3 and 6. The remaining mice were followed up until day 14 post-infection. Three and four hamsters from each experimental group, except the uninfected control group, were euthanized on days 2 and 4, respectively. The remaining GSHs were euthanized on day 7 post infection. In both challenge experiments, uninfected control group was euthanized at the end of the experiment. In addition, any animal showing weight loss higher than 20%, a drastic lack of motility, or a significant reduction of their response to stimuli were euthanized according to the humane endpoints defined in the supervision protocol. Biological samples were collected after euthanasia, including oropharyngeal swab, nasal turbinate, lung, and brain (only in the case of mice) to determine viral loads and perform histopathological analysis. Furthermore, blood samples were collected before each immunization, viral challenge, and under euthanasia. Blood was left at room temperature for two hours for clotting, and serum was collected after centrifugation (10 minutes at 5000xg) and stored at -80°C until use.

2.6 Quantification of anti-S and anti-RBD antibodies by ELISA

An in-house ELISA was developed to evaluate IgG antibodies elicited against the S and RBD glycoproteins in serum samples obtained as described before. Nunc MaxiSorp ELISA plates were coated overnight at 4°C. Half plate was coated with 50 ng/well of antigen diluted in PBS (S or RBD, Sino Biological) and the other half plate was incubated only with PBS. Next day, the whole plate was blocked for two hours at room temperature using blocking buffer [PBS with 1% of bovine serum albumin (BSA, Miltenyi Biotech)]. After that, 50 µL of the appropriate standard or diluted samples were added to each half plate in duplicates and incubated overnight at 4°C. All samples were prepared in blocking buffer. For the mouse standard curve, we used anti-6xHis antibody His.H8 (ThermoFisher Scientific) starting at 1 µg/mL followed by 3-fold dilutions. For GSH standard, a positive GSH serum was used. GSH standard was prepared as seven 1/3 dilution of a stating 1/100 dilution. To reduce inter-assay variability, plates were run in parallel, and each plate contained samples from all experimental groups. The following day, plates were incubated with detection antibodies for 1 hour at room temperature. HRP conjugated (Fab)2 Goat anti-mouse IgG (Fc specific (1/20,000 dilution), or Goat anti-hamster IgG (H-L) (1/20,000 dilution) (all from Jackson ImmunoResearch) were used as secondary antibodies in the mouse and GSH IgG ELISA, respectively. Finally, plates were revealed with o-phenylenediamine dihydrochloride (OPD) (Sigma Aldrich) and stopped using 2N of H_2SO_4 (Sigma Aldrich). Optical density (OD) was measured at 492 nm with noise correction at 620 nm. The background OD obtained from the half antigen-free plate was subtracted from the half antigen-coated plate to obtain the specific signal for each sample. Data are showed as arbitrary units (AU/ml) according to the standard used.

2.7 Neutralizing activity of serum samples

Sera neutralizing activity was evaluated as described by Pradenas et al. (28). HIV reporter pseudoviruses expressing SARS-CoV-2 S glycoprotein and carrying the luciferase gene were produced in Expi293F cells (ThermoFisher Scientific) by co-transfection of the pNL4-3. Luc.R-. E- plasmid (NIH AIDS Reagent Program (29)) and plasmids coding for the following SARS-CoV-2 S glycoproteins lacking the last 19 amino acid in C-terminal: Wuhan (WH1), Beta, Delta, or Omicron variants. VSV-G-pseudotyped pseudoviruses were used as negative controls. Transfections were performed with ExpiFectamine293 Reagent kit (ThermoFisher Scientific). Forty-eight hours later, cell supernatants were harvested, filtered at 0.45 µm and frozen at -80°C until use.

Pseudovirus titration was performed using HEK293T cells overexpressing WT human ACE-2 (HEK293T/hACE2) (Integral Molecular, USA).

Serum samples were inactivated at 56°C for 60 minutes before use. Once inactivated, serum samples were serially diluted 1/3 in cell culture medium (RPMI-1640, 10% fetal bovine sera) (range 1/60–1/14,580) and incubated with 200 $TCID_{50}$ of SARS-CoV-2-derived pseudoviruses for 1 hour at 37°C. Then, $1x10^4$ HEK293T/hACE2 cells treated with DEAE-Dextran (Sigma-Aldrich) were added. After 48 hours, plates were read using BriteLite Plus Luciferase reagent (PerkinElmer, USA) in an EnSight Multimode Plate Reader. Neutralizing activity was calculated using a four-parameter logistic equation in Prism 8.4.3 (GraphPad Software, USA) and visualized as normalized ID_{50} (reciprocal dilution inhibiting 50% of the infection).

2.8 Viral load quantification in oropharyngeal swab and tissue samples

After euthanasia, oropharyngeal swab and samples from nasal turbinate, lung, and brain were collected in 1.5 mL tubes with DMEM media supplemented with penicillin (100 U/mL) and streptomycin (100 µg/mL). Tissues were homogenized twice at 25 Hz for 30 seconds using a Tissue Lyser II, and a 1.5 mm Tungsten bead (QIAGEN). After that, samples were centrifuged for 2 minutes at 2000xg and supernatants were collected and processed using the Viral RNA/Pathogen Nucleic Acid Isolation kit and a KingFisher instrument (ThermoFisher Scientific), or an IndiMag pathogen kit (Indical Bioscience) on a Biosprint 96 workstation (QIAGEN), following manufacturer's instructions.

PCR amplification was based on the 2019-Novel Coronavirus Real-Time RT-PCR Diagnostic Panel guidelines, following the protocol developed by the American Center for Disease Control and Prevention (https://www.fda.gov/media/134922/download). Briefly, 20 µL PCR reaction was set up containing 5 µL of RNA, 1.5 µL of N2 primers and probe (2019-nCov CDC EUA Kit, Integrated DNA Technologies) and 10 µl of GoTaq 1-Step RT-qPCR (Promega, Madison, WI, USA). Thermal cycling was performed at 50°C for 15min for reverse transcription, followed by 95°C for 2 min and then 45 cycles of 95°C for 10 sec, 56°C for 15 sec and 72°C for 30 sec in the Applied Biosystems 7500 or QuantStudio5 Real-Time PCR instruments (ThermoFisher Scientific). For absolute quantification, a standard curve was built using 1/5 serial dilutions of a SARS-CoV2 plasmid (2019-nCoV_N_Positive Control, 200 copies/µL, Integrated DNA Technologies) and run in parallel in all PCR determinations. Triplicates were performed to determine viral load of each sample, which was extrapolated from the standard curve (in copies/mL) and corrected by the corresponding dilution factor. Alternatively, results are shown as Ct or 2-ΔCt.

SARS-CoV-2 subgenomic RNA was quantified as previously described (30) with the following primers (Forward; 5-CGATCTCTTGTAGATCTGTTCTC-3′; Reverse, 5′-ATATTG CAGCAGTACGCACACAA-3′) and probe (5′- FAM-ACACTAG CCATCCTTACTGCGCTTCG-TAMRA-3′). Mouse or GSH *gapdh* gene expression was measured in duplicate for each sample using TaqMan gene expression assay (ThermoFisher Scientific) as amplification control.

2.9 Pathology and immunohistochemistry

Nasal turbinate and lung from mice and GSHs, and additionally brain from mice, were collected after euthanasia and fixed by immersion in 10% buffered formalin and embedded into paraffin. Then, tissue slides were stained with hematoxylin/eosin and examined by optical microscopy to be analyzed histopathologically. Samples were scored semi-quantitatively based on the level of inflammation (0-No lesion; 1-Mild, 2-Moderate, or 3-Severe lesion) as described in (31, 32).

The levels of SARS-CoV-2 Nucleoprotein in tissue slides were determined by immunohistochemistry. A rabbit monoclonal antibody 40143-R019 (Sino Biological) at 1:15,000 dilution, and the EnVision®+ System linked to horseradish peroxidase (HRP, Agilent-Dako) and 3,3'-diaminobenzidine (DAB) were used. A semi-quantitative score was used to measure the amount of viral antigen in the analyzed tissues (0-No antigen detection, 1-low, 2-moderate and 3- high amount of antigen) according to previous classifications (31, 32).

2.10 Statistical analysis

Anti-S and anti-RBD IgG data, as well as neutralizing activity differences among groups at each time point were analyzed using Kruskal-Wallis and Conover's *post-hoc* tests with multiple comparison correction by using false discovery rate (FDR). Differences among animals within a particular group along time were analyzed using the Friedman test and Conover's *post-hoc* tests for paired data and corrected for multiple comparison by FDR. Krustal Wallis and Dunn's *post-hoc* test were used in weight variation in SARS-CoV-2 challenged animals. Severe disease incidence was represented by Kaplan Meier plots and Mantel-Cox test was implemented to calculated statistical differences against uninfected group. To analyze SARS-CoV-2 gRNA and sgRNA data, a Peto & Peto Left-censored k-sample test corrected by FDR was performed. Asymptotic Generalized Pearson Chi-Squared test with FDR correction was applied to histopathology analysis. P values are indicated as follows: * $p<0.05$, ** $p<0.01$, *** $p<0.001$, **** $p<0.0001$. Statistical analyses were conducted using the R software environment (version 4.1).

3 Results

3.1 Strategy for S glycoprotein stabilization

To increase the S glycoprotein stability and immunogenicity, we followed two different approaches: 1) introduction of point mutations into the S sequence to increase its stabilization (using the open state as a reference structure), and 2) increase of RBD

10.3389/fimmu.2023.1291972

exposure by forcing an open conformation. In this regard, we built a computational pipeline involving the three-dimensional modeling of all possible single mutations in both scenarios (see the Methods section for more details). Moreover, all single mutations that showed a preference for any of these two conditions were visually inspected. Mutations that clearly generated well-defined interactions (e.g. hydrogen bonds, ionic interactions for filling hydrophobic pockets) between different chains of the S trimer were prioritized (Figure 1A).

S mutants, based on the two prolines (K986P/V987P) stabilized Wuhan WH-1 sequence, (Figure 1B) were then produced, and yields evaluated (Figure 1C). Based on their production levels, these glycoproteins were classified into three different groups (Figures 1B, C). Group 1 included those constructs (i.e., S-29 and S-22) that were

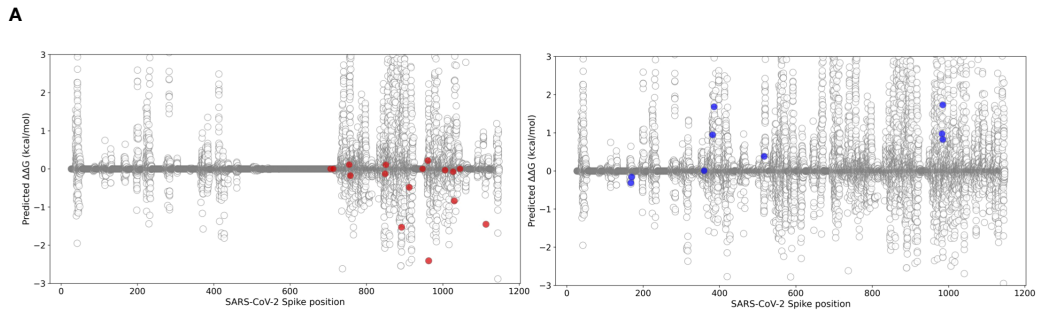

B

Group	Construct	Mutations
1	S-22	Q755K; L849K; A892N; K947R; K1045R
1	S-29	S758E; T912R; K947R
2	S-21	A706Q; S758E; L849K; V963E; S1030R; Q1113R
2	S-24	S758E; L849K; V963E
2	S-26	Q755K; C851Q; T961E
2	S-27	A706Q; S1030R; Q1113R
2	S-30	L849K
2	S-31	T961E
3	S-20	A713R; Q755K; C851Q; T912R; T961E; T1027E
3	S-23	A706Q; C851Q; T1006W; T1027E; Q1113R
3	S-25	A713R; T912R; T1027E
3	S-28	A706Q; C851Q; T1027E
3	S-32	T1027E
3	S-33	N360R; F168D; Y170D
3	S-34	K386A; D985A
3	S-35	D985A
3	S-36	D985W
3	S-37	L517A; V382A
3	S-38	L517A; V382A; R983A

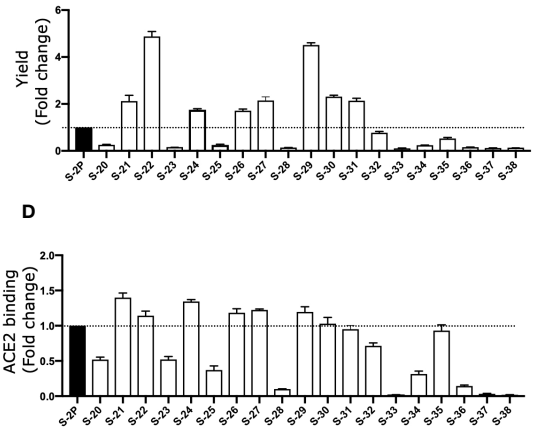

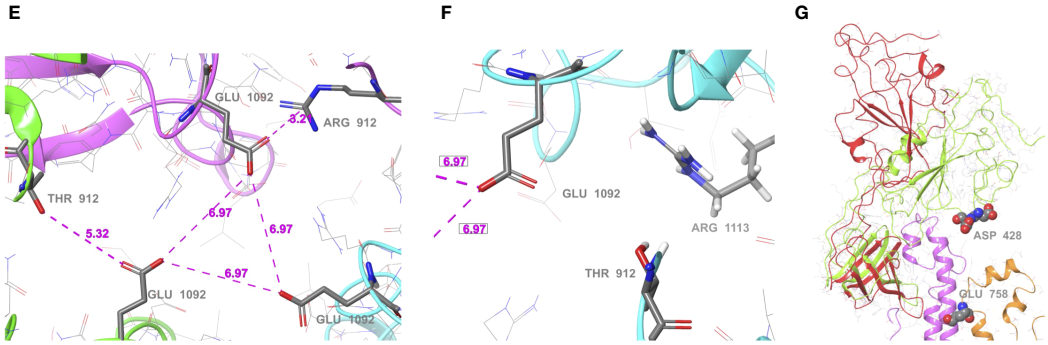

FIGURE 1
Selection of mutations that stabilized S glycoproteins. **(A)** S stabilizing mutations (red variants, left plot), or amino acids changes that increased RBD exposition (blue variants, right plot) were selected based on energetic filters and visual inspection. Positive energy values indicate stabilization of the open structure versus the closed one. Mutations with neutral (or slightly opposite) energetic trend were included. **(B)** List of S constructs that incorporate the selected mutations identified in **(A)**. **(C)** Yields of recombinant S mutants in a five-day cell culture supernatant. Mean plus standard deviation of three experiments are shown. **(D)** RBD exposure index in selected recombinant proteins. Data are shown as ratio between RBD binding and total protein. Mean plus standard deviation of three experiments are shown. **(E)** Presence of a cluster of three Glu residues (one Glu1092 from each chain) that are facing each other in close proximity, with no positive residues nearby. Location of Thr912 is underlined as well. Also notice that one of the three Thr has been mutated to Arg clearly showing a salt bridge interaction with the glutamic acid. **(F)** A detail of the proximity of the 1113 residue, already mutated to Arg, to the Glu1092 cluster. Thr912 is also showed. Structure models were based on 6VXX PDB structure. **(G)** Detail of the RBD opening process and location of some key residues. The red and green ribbons indicate the difference between the open and closed states, underlying the position of the two consecutive aspartic acid residues, Asp428 and Asp427, at the tip of the RBD domain. In orange ribbons the location of the S758E mutation is shown. Notice that the inserted glutamic residue collides with the neighbor helix (pink ribbons). Models generated from the 6VXX (closed) and 6VYB (open) PDB structures.

produced at the highest levels (five-fold compared to the S-2P protein). Group 2 contained S-21, S-24, S-26, S-27, S-30, and S-31, whose production was intermediate (two-fold higher than S-2P). Last, Group 3 included those S mutants with a protein yield lower than S-2P (S-20, S-23, S-25, S-28, S-32, S-33, S-34, S-35, S-36, S-37, and S-38). Remarkably, all constructs designed to increase RBD exposure were in Group 3, suggesting that those mutations drastically impacted the S stability and/or its production. However, most constructs with an improved production, also showed a better RBD exposure (Figures 1C, D).

Variants S-22 and S-29, with higher expression yield, introduced a positive charge per chain in a local area where the Glu1092 of each chain might cause destabilization. Figure 1E shows the presence of this cluster of Glutamic acid residues facing each other and how the T912R mutation in S-29 might introduce significant stabilization. Similarly, the Q1113R mutant in S-22 placed an arginine next to Glu1092 (Figure 1F). Analogous observations can be extracted of most mutants introducing a net charge. We also observed that most mutants increasing RBD exposure, such as S-21, S-24 and S-29, incorporated the S758E mutation. This mutation is in the vicinity of the tip of the closed RBD domain, where two consecutive Aspartic acid residues, Asp427 and Asp428 are located (Figure 1G). After modeling the possible positioning of Glu758 (with an initial significant clash with a helix backbone), we speculate that it would be displaced toward the tip of the RBD domain and destabilize the closed conformation by electrostatic repulsion.

Interestingly, S-22 and S-29 constructs share the conservative mutation K947R located in the middle of the heptad repeat 1 (HR1) helix, which could enhance the thermal stability of the protein (33).

3.2 S-21 and S-29 vaccination protects K18-hACE2 mice from SARS-CoV-2-induced disease

To investigate the impact of S mutations on its immunogenicity and capability to protect from SARS-CoV-2-induced disease, we selected two representative S mutants from group 1 (S-29) and 2 (S-21). Then, we performed an immunization study using K18-hACE2 transgenic mice that were subsequently challenged with SARS-CoV-2 B.1.351 (Beta) variant (Figure 2A). We used this experimental design for the following reasons: 1) K18-hACE2 transgenic mice develop a severe form of the disease that leads to death (34) unless animals are vaccine-protected; 2) the SARS-CoV-2 Beta variant is partially resistant to antibodies elicited by natural infection or vaccination with immunogens based on the original strain (Wuhan, WH1) (35); and 3) the SARS-CoV-2 Beta variant is one of the most pathogenic SARS-CoV-2 variants tested in K18-hACE2 transgenic mice (34). Thus, we established five experimental groups: S-2P (n=21), S-21 (n=22), S-29 (n=22), infected positive controls (n=16), and uninfected negative controls (n=10). Mice from S-2P, S-21, and S-29 groups were immunized twice, three weeks apart. Animals from both control groups received antigen-free doses. Two weeks after the boost, all animals (except the negative controls) were intranasally challenged with the SARS-CoV-2 Beta variant. Blood and tissue samples were collected after viral challenge on days 3 (n=6), 6 (n=6) and 14 (n=10 for S-21, S-29 and uninfected controls, and n=8 for S-2P) to analyze tissue damage and viral replication (Figure 2A). All mice that developed severe disease (one mouse in the S-2P and S-21 groups, and all mice from the positive control group) were euthanized before day 14 following humane endpoints and were analyzed separately.

Anti-RBD (Figure 2B) and anti-S (Supplementary Figure 1A) IgG humoral responses were evaluated prior to each immunization and viral challenge, and in euthanized animals after infection on days 3, 6, and 14, or due to humane endpoints. Regardless of the immunogen used, all vaccinated animals developed similar anti-RBD (Figure 2B) and anti-S IgG levels (Supplementary Figure 1A), which increased after each immunization and after viral challenge ($p<0.01$, Conover´s *post-hoc* test). Since we did not identify significant differences in the humoral responses among vaccinated groups after challenge (Supplementary Figures 1B, C), we pooled these mice in a single "post-challenge" group to simplify the analysis. Of note, unvaccinated but challenged positive controls elicited low levels of anti-RBD and anti-S IgG antibodies (Figure 2B and Supplementary Figure 1A) that were detected from day 6 after viral challenge (Supplementary Figures 1B, C).

Sera neutralizing activity against SARS-CoV-2 WH1, Beta, Delta, and Omicron variants was detected in all three vaccinated groups (Figures 2C–F). Interestingly, despite having similar levels of anti-RBD IgGs (Figure 2B), and a slightly higher levels of anti-S IgG antibodies (Supplementary Figure 1A), S-2P vaccinated mice showed lower sera neutralizing activity against WH1 and Delta variants on day 3 than those immunized with S-21 (Figures 2C, E) (WH1 $p<0.05$; Delta $p=0.052$, Conover´s *post-hoc* test). Sera neutralizing activity against Delta and Beta variants increased over time in the S-2P vaccinated group after viral challenge (Beta $p<0.05$; Delta $p=0.052$, Conover´s *post-hoc* test), suggesting that infection boosted the humoral response in these animals. In line, unvaccinated mice developed low sera neutralizing activity against the SARS-CoV-2 Beta variant (Figure 2D) with some cross-reactivity with WH1 but limited cross-neutralizing activity against other SARS-CoV-2 variants (Figures 2C, E, F) after viral challenge. No boost effect on sera neutralizing activity was detected in S-21- and S-29-immunized mice after challenge, suggesting that the humoral response reached a plateau in these groups.

To determine whether S-2P-, S-21-, and S-29-vaccinated mice were protected against SARS-CoV-2-induced severe disease, we measured body weight evolution (Figure 2G), clinical sings, and survival rate after viral challenge (Figure 2H). A progressive weight loss was observed in all unvaccinated but challenged mice starting on day 2 post-challenge. These mice developed a severe disease on days 5-9 post-infection and were euthanized following humane endpoints. Conversely, all vaccinated mice (except one S-2P- and one S-21-immunized mice), were disease-free (Figure 2H) and did not experience weight loss. All mice belonging to S-29 group were protected from severe disease development (Figures 2G, H).

The presence of SARS-CoV-2 in oropharyngeal swabs and tissue samples from nasal turbinate, lung, and brain was analyzed by RT-qPCR. All vaccinated mice had significantly lower levels of genomic viral RNA (gRNA) in lung on day 3 post-inoculation

10.3389/fimmu.2023.1291972

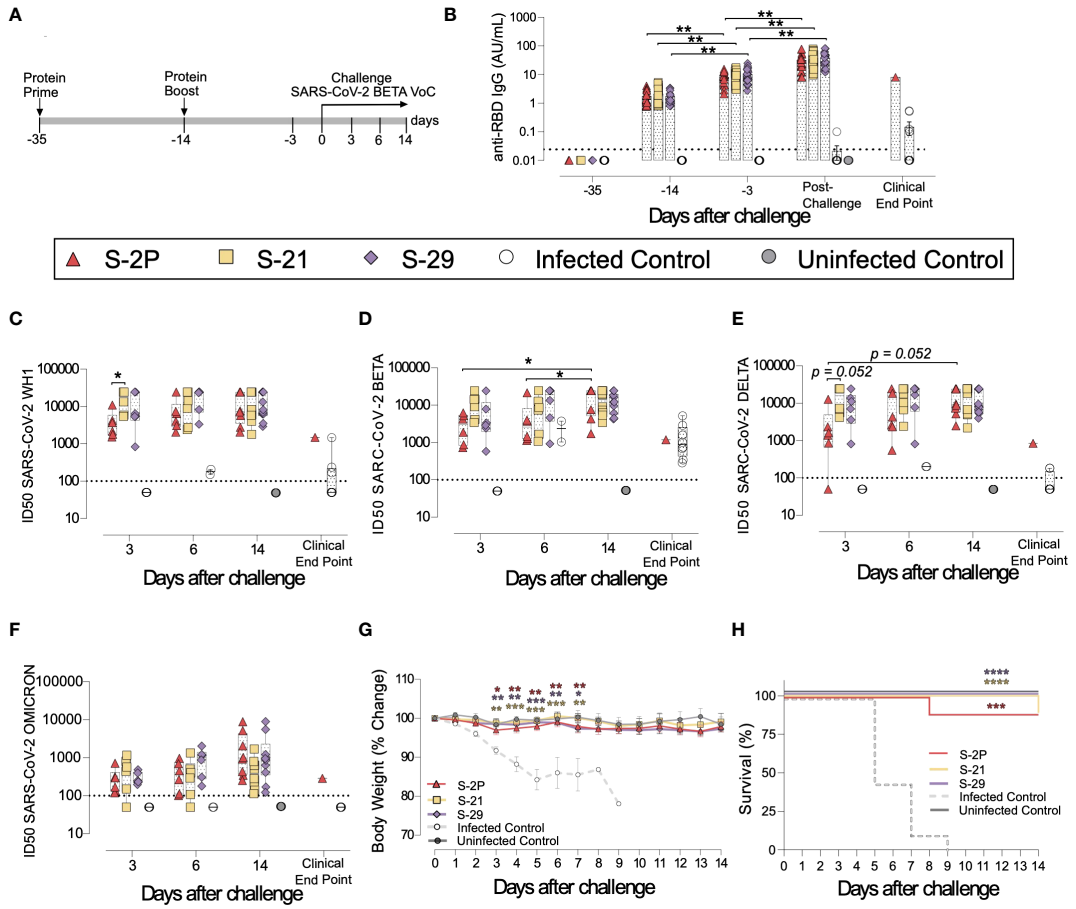

FIGURE 2
Prophylactic activity of S-21 and S-29 immunization and vaccine-induced humoral response elicited in K18-hACE2 transgenic mice challenged with SARS-CoV-2 B.1.351 (Beta) variant. K18-hACE2 transgenic mice were immunized following a prime/boost strategy with S-21, S-29, or S-2P, and challenged with SARS-CoV-2 Beta. The vaccine-induced humoral responses, weight changes, and survival of mice were evaluated after immunization and/or viral challenge. **(A)** Overview of immunization strategy and infection timeline. Biological samples were collected at indicated time points. **(B)** Kinetics of anti-RBD antibodies in serum samples. Red triangles: S-2P group (n=21). Yellow squares: S-21 (n=22). Purple diamond: S-29 (n=22). White circles: unvaccinated-challenge mice (n=16). Grey circles: unvaccinated-uninfected mice (n=10). Groups in each time point were analyzed using Kruskal-Wallis and Conover's *post-hoc* tests with multiple comparison correction by FDR. Differences among animals within a particular group along time were analyzed using Friedman and Conover's *post-hoc* test for paired data with FDR correction. Sera neutralizing activity against: **(C)** SARS-CoV-2 WH-1 variant, **(D)** B.1.351 (Beta) variant, **(E)** B.1.617.2 (Delta), and **(F)** B.1.1.529 (Omicron) variants after viral challenge. Neutralization data were analyzed as indicated in "b". **(G)** Percentage of weight variation in SARS-CoV-2 B.1.351 infected K18-ACE2 mice over time. Statistical analysis was performed against the unvaccinated and challenged group using Kruskal Wallis with Dunn´s *post-hoc* test. **(H)** Kaplan-Meier plot showing the percentage of SARS-CoV-2-infected animals that were disease-free at the end of the experiment. Statistical analysis was performed against unvaccinated group using Mantel-Cox test. * $p<0.05$, ** $p<0.01$, *** $p<0.001$, **** $p<0.0001$. Mean plus standard errors of the means (SEM) are shown.

compared to the positive control group ($p<0.05$, Peto & Peto Left-censored k-sample test) (Figure 3A). Most notably gRNA was scarcely detected in brain of vaccinated mice compared to unvaccinated animals (Figure 3A). Interestingly, S-21- and S-29-vaccinated mice showed lower viral load in nasal turbinate than S-2P and control groups on day 3, and S-2P vaccinated mice on day 6 ($p<0.05$, Peto & Peto Left-censored k-sample test) (Figure 3A). The lack of differences with the control group on day 6 could be explained due to the small number of unvaccinated mice that reached this timepoint, since the majority had been euthanized on day 5 post-infection (Figure 2H). Similarly, S-21 and S-29 groups exhibited lower viral loads in oropharyngeal swabs than unvaccinated mice (S-21 $p<0.05$; S-29 $p=0.066$; Peto & Peto Left-censored k-sample test) (Figure 3A). Generally, gRNA decreased over time in all immunized mice regardless of the analyzed sample, whereas the opposite outcome was observed in mice belonging to the challenged control group, and in those vaccinated mice that developed severe disease (Figure 3A). Similar results were observed when subgenomic viral RNA (sgRNA) was analyzed using the same biological samples (Supplementary Figure 1D).

To confirm active viral replication, nucleoprotein (NP) levels were analyzed by immunohistochemistry. NP was hardly detected in lung and brain samples from S-2P, S-21 and S-29 groups (Figure 3B). These data are in accordance with the viral loads detected in these samples. Despite that, some tissue damage was still detected in the lungs of all vaccinated groups. Remarkably, limited tissue damage was found in the brain of vaccinated mice, except in those animals euthanized due to humane endpoints (Figure 3C).

10.3389/fimmu.2023.1291972

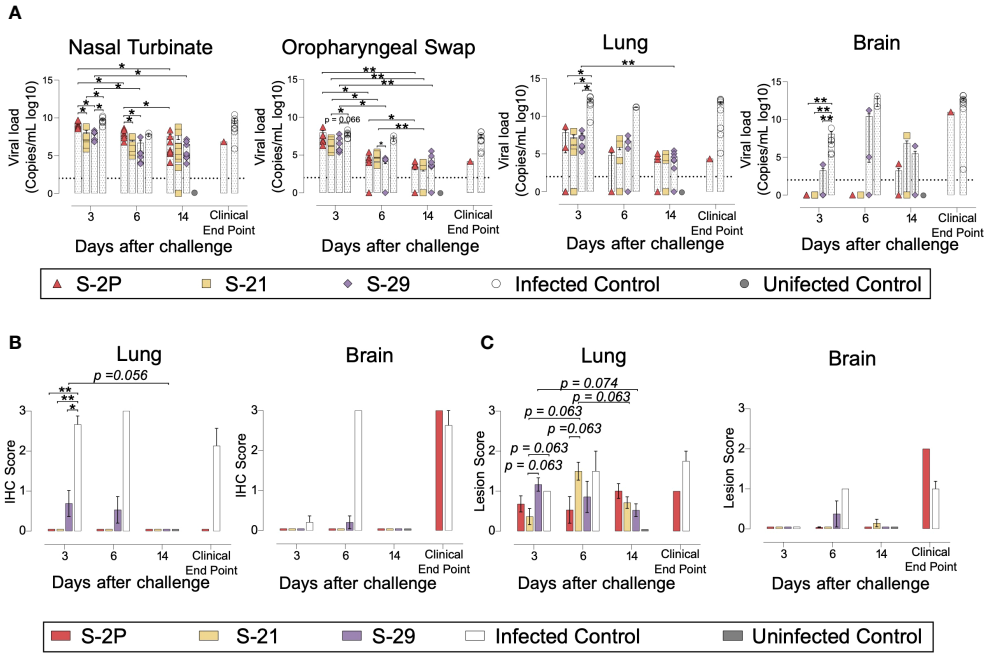

FIGURE 3
Viral load and histopathology analysis of biological samples from SARS-CoV-2 B.1.351 infected K18-hACE2 transgenic mice after vaccination. SARS-CoV-2 viral loads were analyzed in oropharyngeal swabs, and samples from nasal turbinate, lung, and brain of infected K18-hACE2 mice. Virus distribution and tissue damage were analyzed by immunohistochemistry and histopathology, respectively. **(A)** Levels of SARS-CoV-2 gRNA (expressed as logarithmic of copies/mL) in oropharyngeal swabs, nasal turbinate, lung, and brain during infection. Dotted line indicates limit of detection (100 copies/mL). Differences among groups were analyzed using Peto & Peto left-censored k-sample test with FDR correction. **(B)** Detection of SARS-CoV-2 Nucleocapsid protein in brain and lung by immunohistochemistry. Staining score: (0) no antigen, (1) low, (2) moderate, and (3) high viral antigen. **(C)** Histopathological analysis of brain and lung by hematoxylin and eosin staining. Lesion score: (0) no lesion, (1) mild lesion, (2) moderate lesion, and (3) severe lesion. Differences among groups were analyzed using Asymptotic Generalized Pearson Chi-Squared test with FDR correction. * $p<0.05$, ** $p<0.01$.

Overall, S-2P, S-21, and S-29 trimers displayed an equivalent immunogenicity in K18-hACE2 transgenic mice and protected these animals from developing severe disease after SARS-CoV-2 Beta variant challenge. Interestingly, S-21- and S-29-immunized animals had lower viral loads in nasal turbinate than S-2P and infected controls on days 3 and 6 after challenge. Viral loads were also reduced in oropharyngeal swabs of these mice on day 3 compared to infected control groups.

3.3 S-21 and S-29 trimer vaccination protects golden Syrian hamsters from COVID-19 development

To confirm the results obtained in K18-hACE2 mice, a second immunization and challenge experiment was performed using GSH with the same immunogens. Unlike K18-hACE2 mice, GSH develop a moderate form of SARS-CoV-2-induced disease, from which they spontaneously recover by day 14 after challenge (31, 36). GSH were immunized following a similar prime/boost strategy to the previously used for K18-hACE2 transgenic mice. Animals were intranasally challenged with the SARS-CoV-2 Beta variant and followed up until day 7 post-challenge (Figure 4A), since it has been described that GSH start recovering weight from this day (31, 36).

In accordance with K18-hACE2 transgenic mice data, the three vaccinated groups (S-2P, S-21 and S-29) developed similar levels of anti-RBD and anti-S binding IgG (Figure 4B and Supplementary Figures 2A, B). Interestingly, the second immunization did not boost vaccine-induced anti-S IgGs (Supplementary Figures 2A, B), but slightly increased anti-RBD IgG antibodies by 2 to 3-fold, ($p>0.05$) (Figure 4B). An increase in anti-S IgG levels was observed after viral challenge in both vaccinated and unvaccinated but challenged mice (Supplementary Figure 2A). Nonetheless, when anti-RBD IgG responses were analyzed, that boosting effect was less evident and only detected in the S-2P and in unvaccinated and challenged groups (Figure 2B and Supplementary Figure 2B). These results suggest that viral challenge elicited a rapid humoral response in naïve animals, boosting anti-S IgG responses, but had little effect in vaccinated GSH. Despite that, immunized GSH showed higher levels of anti-S and anti-RBD antibodies than challenged controls ($p<0.001$ for S-2P and S-29 group, and $p<0.01$ for S-21 group; Friedman test) (Figure 4B and Supplementary Figure 2A).

Sera neutralizing activity against SARS-CoV-2 WH1, Beta and Delta, and to a lesser extent, Omicron variants was detected in vaccinated animals at all post-challenge timepoints (Figures 4C–F). No differences were identified among immunized groups. Remarkably, and contrarily to K18-hACE2 transgenic mice data, sera neutralizing activity against all four SARS-CoV-2 variants were observed in some challenged positive control animals by day 4 after

10.3389/fimmu.2023.1291972

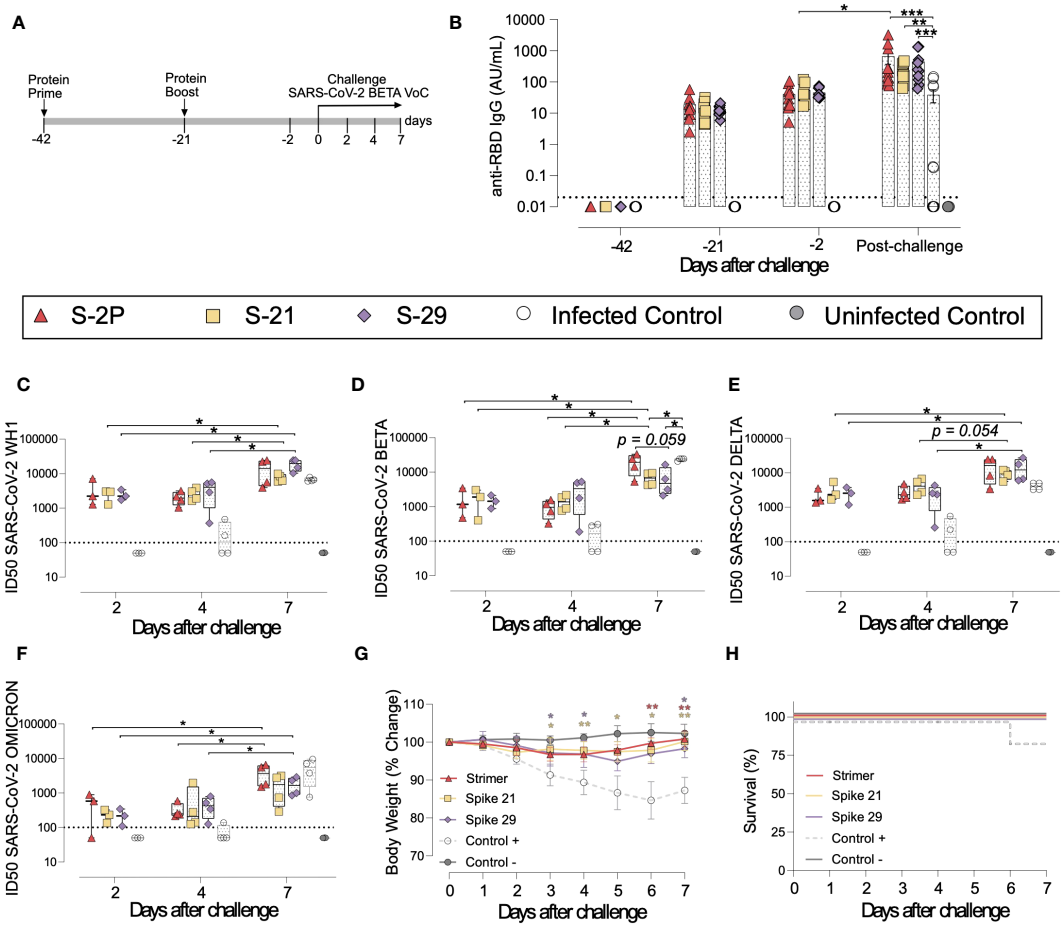

FIGURE 4
Vaccine-induced humoral responses and prophylactic activity of S-21 and S-29 in immunized GSH after challenge with the SARS-CoV-2 B.1.351 (Beta) variant. GSH were immunized twice with S-21, S-29 or S-2P, and subsequently challenged with SARS-CoV-2 B.1.351 variants. The humoral response, weight changes, and survival of mice were evaluated after immunization and/or viral challenge. **(A)** Outline of immunization schedule and infection timeline. Biological samples were collected at the indicated time points. **(B)** Kinetics of anti-RBD antibodies in serum samples. Red triangles: S-2P group (n= 11). Yellow squares: S-21 (n=11). Purple diamond: S-29 (n=11). White circles: unvaccinated-challenged mice (n=11). Grey circles: unvaccinated-uninfected mice (n=5). Groups in each time point were analyzed using Kruskal-Wallis and Conover's *post-hoc* tests with multiple comparison correction by FDR. Differences among animals within a particular group along time were analyzed using the Friedman and Conover's *post-hoc* tests for paired data with FDR correction. Sera neutralizing activity after viral challenge against: **(C)** SARS-CoV-2 WH-1, **(D)** B.1.351 (Beta), **(E)** B.1.617.2 (Delta), and **(F)** B.1.1.529 (Omicron) variants. Neutralization data were analyzed as indicated in **(B)**. **(G)** Percentage of weight variation in SARS-CoV-2 B.1.351-infected GSH over time. **(H)** Kaplan-Meier plot showing the frequency of disease-free SARS-CoV-2-infected animals at the end of the experiment. Statistical analysis was performed against the unvaccinated group using Kruskal Wallis and Dunn´s *post-hoc* tests. * p<0.05, ** p<0.01, *** p<0.001.

challenge (Figures 4C–F). These results indicate that cross-reactive neutralizing antibodies were generated in those individuals. Unexpectedly, the neutralizing activity against the SARS-CoV-2 Beta variant was higher in challenged control animals than in S-21- and S-29-vaccinated GSH by day 7 (Figure 4D). According to the binding ELISA data, neutralization titers also increased in immunized GSH by day 7 after viral challenge (p<0.05; Conover´s *post-hoc* test), indicating that infection boosts vaccine-induced humoral neutralizing responses (Figures 4C–F).

To determine whether vaccination protected GSHs from SARS-CoV-2-induced disease, we monitored animal weight over time after viral challenge (Figure 4G). Challenged control GSHs showed progressive weight reduction until day 6, which was indicative of disease progression. One animal from this group suffered a weight reduction greater than 20% by day 6 post-inoculation and was euthanized according to humane endpoints (Figure 4H). No significant weight loss was observed in vaccinated GSHs, indicating that these animals were protected from disease development (Figures 4G, H).

To evaluate viral replication in tissues, we determined the levels of gRNA and sgRNA by RT-qPCR. We did not identify any differences among study groups in the levels of gRNA and sgRNA in nasal turbinate, lung, in oropharyngeal samples were detected (Figure 5A and Supplementary Figure 2C). However, vaccinated animals exhibited a decreasing trend in their nasal turbinate levels of both gRNA and sgRNA over time after challenge (p=0.061; Peto & Peto Left-censored k-sample test) (Figure 5A and Supplementary Figure 2C). In addition, the analysis of nasal turbinate samples on day 7 post-challenge showed that vaccinated GSH displayed lower gRNA and sgRNA levels tendency compared with unvaccinated-challenged controls (gRNA: p=0.061; sgRNA: p=0.056; Peto & Peto

10.3389/fimmu.2023.1291972

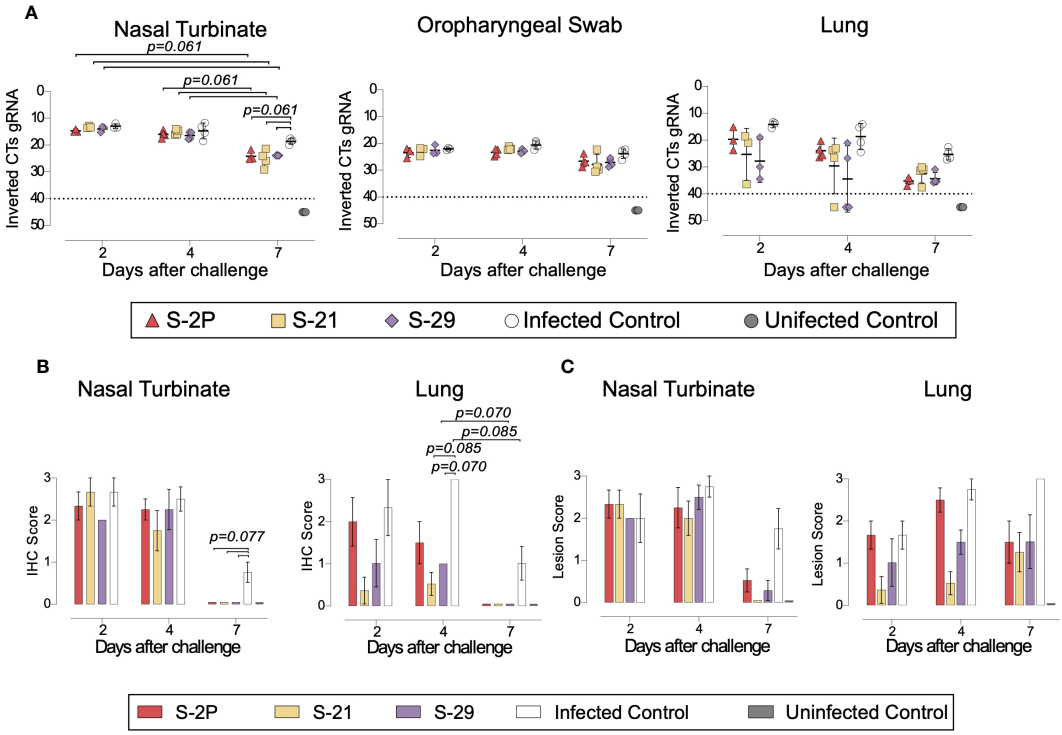

FIGURE 5
Histopathology and viral loads in tissues from vaccinated GSH after challenge with SARS-CoV-2 Beta variant. SARS-CoV-2 viral loads were analyzed in oropharyngeal swabs, and samples from nasal turbinate and lung of vaccinated and challenged GSH. Virus distribution and tissue damage was analyzed by immunohistochemistry and histopathology, respectively. **(A)** Levels of SARS-CoV-2 gRNA, expressed as cycles threshold (CTs), in oropharyngeal swabs, nasal turbinate, and lung during infection. Dotted line indicates limit of positivity (40 CTs). Differences among groups were analyzed using Peto & Peto left-censored k-sample test with FDR correction. **(B)** Detection of SARS-CoV-2 Nucleocapsid protein in lung and nasal turbinate by immunohistochemistry. Staining score: (0) no antigen, (1) low, (2) moderate, and (3) high viral antigen. **(C)** Histopathological analysis of lung and nasal turbinate by hematoxylin and eosin staining. Lesion score: (0) no lesion, (1) mild lesion, (2) moderate lesion, and (3) severe lesion. Differences among groups were analyzed using Asymptotic Generalized Pearson Chi-Squared test and FDR.

Left-censored k-sample test) (Figure 5A and Supplementary Figure 2C). To confirm RT-qPCR data, the presence of NP was analyzed in nasal turbinate and lung by IHC. NP was not detected in nasal turbinate samples from immunized animals on day 7 (Figure 5B). These results confirm the decreasing trend observed when gRNA and sgRNA were analyzed over time. Similarly, SARS-CoV-2 replication associated lesions were hardly detected in nasal turbinate samples on day 7 (Figure 5C). However, despite NP was not detected in lung of vaccinated GSHs on day 7, low levels of tissue lesions were still present (Figure 5C). No significant differences in tissue damage were observed in lung samples among study groups, probably due to the low number of animals per group.

Overall, these results confirm that all three S-2P, S-21 and S-29 immunogens showed an equivalent immunogenicity and prophylactic activity in GSHs, protecting these animals from the development of severe SARS-CoV-2-induced disease.

4 Discussion

The implementation of SARS-CoV-2 vaccines became an inflexion point on the course of the COVID-19 pandemic. However, new SARS-CoV-2 variants have shown partial resistance to the immunity generated by the first generation of COVID-19 vaccines, which were based on the ancestral WH1 sequence (37–39). Although additional immunizations proved to increase the protection level against new emerging SARS-CoV-2 variants (40, 41), this protection remains transient (42). Particularly, the levels of NAbs elicited against the newest variants (i.e. Omicron and subvariants) wane overtime (43, 44), pointing out the importance of developing novel vaccines that increase coverage and duration of immunity. Thus, the adaptation of vaccines to the new variants has shown encouraging results (45–47), and several studies performed in animal models indicate that intranasal immunization may also improve protection (48, 49). Besides these two complementary approaches, S immunogenicity can be enhanced by protein stabilization strategies. Studies performed with the S glycoprotein of MERS and with functional analogous of other viruses have shown that the introduction of mutations that stabilize these proteins in a prefusion state may increase its production and immunogenicity (13, 50). Accordingly, the introduction of two prolines (K986P and V987P) into the S2 subunit of SARS-CoV-2 S was promptly confirmed to enhance its stability and immunogenicity (50), and was successfully implemented in several widely used commercial vaccines (e.g. BNT162b2, mRNA-1273 and Ad26.COV2.S). However, it is still

possible to improve the current S-2P strategy since the target recombinant protein is produced with low yield and shows some degree of instability (18). Initial attempts to stabilize the S in its closed conformation yielded low production, suggesting that the open conformation of the RBD or its intrinsic motility might play a role in protein expression (20). Recently, Juraszek and colleagues showed that the incorporation of the D614N, A892P, A942P, and V987P mutations were able to stabilize the S glycoprotein in its closed conformation and increase its yield by six-fold compared to the original S-2P protein (19). Interestingly, Hsieh et al. improved the S stability and production by ten-fold, after introducing four additional proline mutations into the S-2P backbone (18).

Here, we designed and produced a set of S-2P mutated variants whose yield increased between two and five-fold using our new computational pipeline. Unlike proline substitutions, we selected mutations that generated hydrogen bonds, ionic interactions filling hydrophobic pockets, or other well-defined interaction between different chains of the S trimer. We selected two representative S mutants based on their production levels and RBD exposure. Thus, S-21 showed the highest RBD exposure and a moderate increased production, while S29 showed the highest production but a moderate increased RBD exposure compared to S-2P. S-21, S-29 and S-2P were then compared in terms of immunogenicity and capacity to protect against the SARS-CoV-2 Beta variant, one of the most virulent SARS-CoV-2 variants tested in the K18-hACE2 mouse model (34). To substantiate our results, we used two different animal models: K18-hACE2 transgenic mice and GSHs. The K18-hACE2 is a transgenic mouse model that develops severe disease after SARS-CoV-2 challenge (51, 52). Most mice succumb after viral challenge, mainly due to the infection of the central nervous system (32). On the other hand, GSHs develop a moderate disease, and animals spontaneously recover two weeks after challenge (31, 36). Our results showed that despite S-2P, S-21, and S-29 showed equivalent immunogenicity and protected both animal models against disease progression, they differed in the degree of protection. The S-29 protein induced an immune response that protected 100% of K18-hACE2 transgenic mice after challenge with the SARS-CoV-2 Beta variant. On the contrary, one mouse in both S-2P and S-21 groups developed severe disease and had to be euthanized on days 8 and 14 after challenge, respectively. Therefore, our results suggested that the S stabilization may impact on the capacity of this protein to induce a protective immune response, particularly against heterologous SARS-CoV-2 variants. According to the *in vivo* protection data, S-29- and S-21-immunized animals showed a faster viral clearance in nasal turbinate than S-2P immunized mice.

In summary, we described a novel set of mutations that stabilized the S glycoprotein, increasing its production *in vitro*, and improving its protective capacity against SARS-CoV-2-induced disease *in vivo*. Despite all these immunogens were based on the original WH1 S sequence, S-29 protein showed 100% protection against the SARS-CoV-2 Beta variant. The inclusion of these mutations on the next generation of variant-adapted S-based COVID-19 vaccines could enhance the degree of protection to new emerging variants. In addition to an improvement in mucosal vaccine delivery, these advances could significantly contribute to the generation of novel COVID-19 mucosal vaccines that prevent viral infection, irrespectively of the circulating variants. Our results, including our new computational pipeline, may also contribute to the development of novel vaccines for other pathogenic viruses.

Data availability statement

The original contributions presented in the study are included in the article/Supplementary Material. Further inquiries can be directed to the corresponding authors.

Ethics statement

The animal study was approved by Committee on the Ethics of Animal Experimentation of the IGTP and counted with the authorization of Generalitat de Catalunya (Code: 10965 and 11094). The study was conducted in accordance with the local legislation and institutional requirements.

Author contributions

CÁ-N: Data curation, Formal analysis, Investigation, Writing – original draft. JV-A: Conceptualization, Data curation, Funding acquisition, Investigation, Methodology, Supervision, Writing – review & editing. PA-R: Investigation, Software, Writing – review & editing. EA-E: Investigation, Methodology, Writing – review & editing. MB: Investigation, Writing – review & editing. MR: Investigation, Writing – review & editing. NP-L: Investigation, Writing – review & editing. JR: Investigation, Writing – review & editing. VU: Formal analysis, Writing – review & editing. EP: Investigation, Writing – review & editing. SM: Investigation, Writing – review & editing. EB: Data curation, Investigation, Writing – review & editing. ER-M: Investigation, Writing – review & editing. MP: Investigation, Writing – review & editing. NR: Investigation, Writing – review & editing. FT-F: Investigation, Writing – review & editing. JC: Investigation, Writing – review & editing. GC: Investigation, Writing – review & editing. AP-G: Investigation, Writing – review & editing. CR: Investigation, Writing – review & editing. CA-G: Investigation, Writing – review & editing. RO: Investigation, Writing – review & editing. AB: Investigation, Writing – review & editing. BT: Investigation, Writing – review & editing. RL: Investigation, Software, Writing – review & editing. JM-B: Investigation, Writing – review & editing. DP-Z: Investigation, Writing – review & editing. NI-U: Conceptualization, Writing – review & editing. AV: Conceptualization, Writing – review & editing. JB: Conceptualization, Data curation, Funding acquisition, Writing – review & editing. BC: Conceptualization, Funding acquisition, Writing – review & editing. VG: Conceptualization, Software, Writing – review & editing. JS: Conceptualization, Data curation, Investigation, Writing – review & editing. JC: Conceptualization, Data curation, Funding acquisition,

Investigation, Methodology, Writing – original draft, Writing – review & editing.

Funding

The author(s) declare financial support was received for the research, authorship, and/or publication of this article. This work was supported by Grifols pharmaceutical, the CERCA Program (2021 SGR 00452; Generalitat de Catalunya), Direcció General de Recerca i Innovació en Salut (Generalitat de Catalunya) (projects SLD0015 and SLD0016), the Carlos III Health Institute (PI17/01518 and PI18/01332), and the crowdfunding projects "YomeCorono", BonPreu/Esclat, and Correos. JB is supported by the Health Department of the Catalan Government (Generalitat de Catalunya). CÁ-N, AP-G, and PA-R were supported by predoctoral grants from Generalitat de Catalunya and Fons Social Europeu (2020 FI_B_0742; 2022 FI_B_00698 and 2020FI_B2_00138, respectively). EP was supported by a doctoral grant from National Agency for Research and Development of Chile (ANID: 72180406). NI-U is supported by the Spanish Ministry of Science and Innovation (grant PID2020-117145RB-I00), EU HORIZON-HLTH-2021-CORONA-01 (grant 101046118). This study was also supported by CIBER - Consorcio Centro de Investigación Biomédica en Red (CB 2021), Carlos III Health Institute, Ministerio de Ciencia e Innovación and Unión Europea – NextGenerationEU. The funder was not involved in the study design, collection, analysis, interpretation of data, the writing of this article, or the decision to submit it for publication.

Acknowledgments

We would like to thank Foundation Dormeur that support the acquisition of the QuantStudio-5 real time PCR system, an Eclipse Ts2R-FL Inverted Research Microscope, and an ÄKTA go protein purification system. We thank to the CMCiB´s staff (Sara Capdevila, Jordi Grifols, Rosa Maria Ampudia, Jorge Diaz, Yaiza Rosales and Sergi Sunyé) and the BSL3 IRTA-CReSA staff (Xavier Abad, Ivan Cordon, Anna Pou, Oscar García, Joanna Wiacek, Maria Angeles Osuna, Luís Ribas and Claudia Pereira Sunyé) for their technical assistance with *in vivo* animal studies.

Conflict of interest

Author PA-R is currently employed by the company Sanofi, which has no association with any content related to this work. Unrelated to the submitted work, JB and JC are founders and shareholders of AlbaJuna Therapeutics, S.L. BC is founder and shareholder of AlbaJuna Therapeutics, S.L. and AELIX Therapeutics, S.L, and VG is founder and shareholder of Nostrum Biodiscovery. Unrelated to the submitted work, NI-U is supported by institutional funding from Pharma Mar, HIPRA, Amassence and Palobiofarma.

The remaining authors declare that the research was conducted in the absence of any commercial or financial relationships that could be construed as a potential conflict of interest.

The author(s) declared that they were an editorial board member of Frontiers, at the time of submission. This had no impact on the peer review process and the final decision.

Publisher's note

Supplementary material

The Supplementary Material for this article can be found online at: https://www.frontiersin.org/articles/10.3389/fimmu.2023.1291972/full#supplementary-material

References

1. Greenwood B. The contribution of vaccination to global health: past, present and future. *Philos Trans R Soc Lond B Biol Sci* (2014) 369:20130433. doi: 10.1098/rstb.2013.0433

2. Strassburg MA. The global eradication of smallpox. *Am J Infect Control* (1982) 10:53–9. doi: 10.1016/0196-6553(82)90003-7

3. Krammer F. SARS-CoV-2 vaccines in development. *Nature* (2020) 586:516–27. doi: 10.1038/s41586-020-2798-3

4. Poland GA, Ovsyannikova IG, Kennedy RB. SARS-CoV-2 immunity: review and applications to phase 3 vaccine candidates. *Lancet* (2020) 6736: 1595-1606. doi: 10.1016/s0140-6736(20)32137-1

5. Watson OJ, Barnsley G, Toor J, Hogan AB, Winskill P, Ghani AC. Global impact of the first year of COVID-19 vaccination: a mathematical modelling study. *Lancet Infect Dis* (2022) 22:1293–302. doi: 10.1016/S1473-3099(22)00320-6

6. Chen X, Huang H, Ju J, Sun R, Zhang J. Impact of vaccination on the COVID-19 pandemic in U.S. states. *Sci Rep* (2022) 12:1554. doi: 10.1038/S41598-022-05498-Z

7. Alexandridi M, Mazej J, Palermo E, Hiscott J. The Coronavirus pandemic – 2022: Viruses, variants & vaccines. *Cytokine Growth Factor Rev* (2022) 63:1–9. doi: 10.1016/j.cytogfr.2022.02.002

8. Walls AC, Park Y-J, Tortorici MA, Wall A, McGuire AT, Veesler D. Structure, function, and antigenicity of the SARS-CoV-2 spike glycoprotein. *Cell* (2020) 181:281–92.e6. doi: 10.1016/j.cell.2020.02.058

9. Hoffmann M, Kleine-Weber H, Schroeder S, Krüger N, Herrler T, Erichsen S, et al. SARS-CoV-2 cell entry depends on ACE2 and TMPRSS2 and is blocked by a clinically proven protease inhibitor. *Cell* (2020) 181:271–80.e8. doi: 10.1016/j.cell.2020.02.052

10. Premkumar L, Segovia-Chumbez B, Jadi R, Martinez DR, Raut R, Markmann AJ, et al. The receptor-binding domain of the viral spike protein is an immunodominant and highly specific target of antibodies in SARS-CoV-2 patients. *Sci Immunol* (2020) 5:1–10. doi: 10.1126/SCIIMMUNOL.ABC8413

11. Wrapp D, Wang N, Corbett KS, Goldsmith JA, Hsieh C-L, Abiona O, et al. Cryo-EM structure of the 2019-nCoV spike in the prefusion conformation. *Science* (2020) 367:1260–3. doi: 10.1126/science.abb2507

12. Cai Y, Zhang J, Xiao T, Peng H, Sterling SM, Walsh RM, et al. Distinct conformational states of SARS-CoV-2 spike protein. *Science* (2020) 369:1586–92. doi: 10.1126/science.abd4251

13. Graham BS, Gilman MSA, McLellan JS. Structure-based vaccine antigen design. *Annu Rev Med* (2019) 70:91–104. doi: 10.1146/annurev-med-121217-094234

14. Pallesen J, Wang N, Corbett KS, Wrapp D, Kirchdoerfer RN, Turner HL, et al. Immunogenicity and structures of a rationally designed prefusion MERS-CoV spike antigen. *Proc Natl Acad Sci U S A* (2017) 114:E7348–57. doi: 10.1073/pnas.1707304114

15. Walsh EE, Frenck RW, Falsey AR, Kitchin N, Absalon J, Gurtman A, et al. Safety and immunogenicity of two RNA-based Covid-19 vaccine candidates. *New Engl J Med* (2020) 383:2439–50. doi: 10.1056/nejmoa2027906

16. Polack FP, Thomas SJ, Kitchin N, Absalon J, Gurtman A, Lockhart S, et al. Safety and efficacy of the BNT162b2 mRNA Covid-19 vaccine. *New Engl J Med* (2020) 383:2603–15. doi: 10.1056/nejmoa2034577

17. Sadoff J, le Gars M, Shukarev G, Heerwegh D, Truyers C, de Groot AM, et al. Interim results of a phase 1–2a trial of Ad26.COV2.S Covid-19 vaccine. *New Engl J Med* (2021) 384(19):1824–35. doi: 10.1056/nejmoa2034201

18. Hsieh C-L, Goldsmith JA, Schaub JM, DiVenere AM, Kuo H-C, Javanmardi K, et al. Structure-based design of prefusion-stabilized SARS-CoV-2 spikes. *Sci (1979)* (2020) 369:1501–5. doi: 10.1126/science.abd0826

19. Juraszek J, Rutten L, Blokland S, Bouchier P, Voorzaat R, Ritschel T, et al. Stabilizing the closed SARS-CoV-2 spike trimer. *Nat Commun* (2021) 12:1–8. doi: 10.1038/s41467-020-20321-x

20. Xiong X, Qu K, Ciazynska KA, Hosmillo M, Carter AP, Ebrahimi S, et al. A thermostable, closed SARS-CoV-2 spike protein trimer. *Nat Struct Mol Biol* (2020) 27:934–41. doi: 10.1038/s41594-020-0478-5

21. Riley TP, Chou HT, Hu R, Bzymek KP, Correia AR, Partin AC, et al. Enhancing the prefusion conformational stability of SARS-CoV-2 spike protein through structure-guided design. *Front Immunol* (2021) 12:660198. doi: 10.3389/fimmu.2021.660198

22. Tan TJC, Mou Z, Lei R, Ouyang WO, Yuan M, Song G, et al. High-throughput identification of prefusion-stabilizing mutations in SARS-CoV-2 spike. *Nat Commun* (2023) 14:2003. doi: 10.1038/s41467-023-37786-1

23. Waterhouse A, Bertoni M, Bienert S, Studer G, Tauriello G, Gumienny R, et al. SWISS-MODEL: homology modelling of protein structures and complexes. *Nucleic Acids Res* (2018) 46:W296–303. doi: 10.1093/nar/gky427

24. Schymkowitz J, Borg J, Stricher F, Nys R, Rousseau F, Serrano L. The FoldX web server: An online force field. *Nucleic Acids Res* (2005) 33: 382–8. doi: 10.1093/nar/gki387

25. Perez-Zsolt D, Muñoz-Basagoiti J, Rodon J, Elosua-Bayes M, Raïch-Regué D, Risco C, et al. SARS-CoV-2 interaction with Siglec-1 mediates trans-infection by dendritic cells. *Cell Mol Immunol* (2021) 18:2676–8. doi: 10.1038/s41423-021-00794-6

26. Rodon J, Muñoz-Basagoiti J, Perez-Zsolt D, Noguera-Julian M, Paredes R, Mateu L, et al. Identification of plitidepsin as potent inhibitor of SARS-CoV-2-induced cytopathic effect after a drug repurposing screen. *Front Pharmacol* (2021) 12:646676. doi: 10.3389/fphar.2021.646676

27. Kamala T. Hock immunization: A humane alternative to mouse footpad injections. *J Immunol Methods* (2007) 328:204–14. doi: 10.1016/j.jim.2007.08.004

28. Pradenas E, Trinité B, Urrea V, Marfil S, Ávila-Nieto C, Rodríguez de la Concepción ML, et al. Stable neutralizing antibody levels 6 months after mild and severe COVID-19 episodes. *Med* (2021) 2:313–20.e4. doi: 10.1016/j.medj.2021.01.005

29. Connor RI, Chen BK, Choe S, Landau NR. Vpr is required for efficient replication of human immunodeficiency virus type-1 in mononuclear phagocytes. *Virology* (1995) 206:935–44. doi: 10.1006/viro.1995.1016

30. Wölfel R, Corman VM, Guggemos W, Seilmaier M, Zange S, Müller MA, et al. Virological assessment of hospitalized patients with COVID-2019. *Nature* (2020) 581:465–9. doi: 10.1038/s41586-020-2196-x

31. Brustolin M, Rodon J, Rodríguez de la Concepción ML, Ávila-Nieto C, Cantero G, Pérez M, et al. Protection against reinfection with D614- or G614-SARS-CoV-2 isolates in golden Syrian hamster. *Emerg Microbes Infect* (2021) 12:1–36. doi: 10.1080/22221751.2021.1913974

32. Vidal E, López-Figueroa C, Rodon J, Pérez M, Brustolin M, Cantero G, et al. Chronological brain lesions after SARS-CoV-2 infection in hACE2-transgenic mice. *Vet Pathol* (2022) 59:613–26. doi: 10.1177/03009858211066841

33. Mrabet NT, van den Broeck A, van den Brande I, Stanssens P, Laroche Y, Lambeir AM, et al. Arginine residues as stabilizing elements in proteins. *Biochemistry* (1992) 31:2239–53. doi: 10.1021/bi00123a005

34. Tarrés-Freixas F, Trinité B, Pons-Grífols A, Romero-Durana M, Riveira-Muñoz E, Ávila-Nieto C, et al. Heterogeneous infectivity and pathogenesis of SARS-CoV-2 variants beta, delta and omicron in transgenic K18-hACE2 and wildtype mice. *Front Microbiol* (2022) 13:840757. doi: 10.3389/fmicb.2022.840757

35. Pradenas E, Trinité B, Urrea V, Marfil S, Tarrés-Freixas F, Ortiz R, et al. Clinical course impacts early kinetics,magnitude, and amplitude of SARS-CoV-2 neutralizing antibodies beyond 1 year after infection. *Cell Rep Med* (2022) 3:100523. doi: 10.1016/j.xcrm.2022.100523

36. Sia SF, Yan LM, Chin AWH, Fung K, Choy KT, Wong AYL, et al. Pathogenesis and transmission of SARS-CoV-2 in golden hamsters. *Nature* (2020) 583:834–8. doi: 10.1038/s41586-020-2342-5

37. Cele S, Jackson L, Khoury DS, Khan K, Moyo-Gwete T, Tegally H, et al. Omicron extensively but incompletely escapes Pfizer BNT162b2 neutralization. *Nature* (2022) 602:654–6. doi: 10.1038/s41586-021-04387-1

38. Hoffmann M, Krüger N, Schulz S, Cossmann A, Rocha C, Kempf A, et al. The Omicron variant is highly resistant against antibody-mediated neutralization: Implications for control of the COVID-19 pandemic. *Cell* (2022) 185:447–56.e11. doi: 10.1016/j.cell.2021.12.032

39. Pouwels KB, Pritchard E, Matthews PC, Stoesser N, Eyre DW, Vihta KD, et al. Effect of Delta variant on viral burden and vaccine effectiveness against new SARS-CoV-2 infections in the UK. *Nat Med* (2021) 27:2127–35. doi: 10.1038/s41591-021-01548-7

40. Choi A, Koch M, Wu K, Chu L, Ma LZ, Hill A, et al. Safety and immunogenicity of SARS-CoV-2 variant mRNA vaccine boosters in healthy adults: an interim analysis. *Nat Med* (2021) 27:2025–31. doi: 10.1038/s41591-021-01527-y

41. Atmar RL, Lyke KE, Deming ME, Jackson LA, Branche AR, el Sahly HM, et al. Homologous and heterologous Covid-19 booster vaccinations. *New Engl J Med* (2022) 386:1046–57. doi: 10.1056/nejmoa2116414

42. Patalon T, Saciuk Y, Peretz A, Perez G, Lurie Y, Maor Y, et al. Waning effectiveness of the third dose of the BNT162b2 mRNA COVID-19 vaccine. *Nat Commun* (2022) 13:3203. doi: 10.1038/s41467-022-30884-6

43. Pajon R, Doria-Rose NA, Shen X, Schmidt SD, O'Dell S, McDanal C, et al. SARS-CoV-2 Omicron Variant Neutralization after mRNA-1273 Booster Vaccination. *N Engl J Med* (2022) 386:1088–91. doi: 10.1056/NEJMc2119912

44. Lassaunière R, Polacek C, Frische A, Boding L, Sækmose SG, Rasmussen M, et al. Neutralizing antibodies against the SARS-CoV-2 omicron variant (BA.1) 1 to 18 weeks after the second and third doses of the BNT162b2 mRNA vaccine. *JAMA Netw Open* (2022) 5:e2212073. doi: 10.1001/jamanetworkopen.2022.12073

45. Chalkias S, Harper C, Vrbicky K, Walsh SR, Essink B, Brosz A, et al. A bivalent omicron-containing booster vaccine against Covid-19. *N Engl J Med* (2022) 387:1279–91. doi: 10.1056/NEJMoa2208343

46. Xu K, Gao P, Liu S, Lu S, Lei W, Zheng T, et al. Protective prototype-Beta and Delta-Omicron chimeric RBD-dimer vaccines against SARS-CoV-2. *Cell* (2022) 185:2265–78.e14. doi: 10.1016/j.cell.2022.04.029

47. Chalkias S, Eder F, Essink B, Khetan S, Nestorova B, Feng J, et al. Safety, immunogenicity and antibody persistence of a bivalent Beta-containing booster vaccine against COVID-19: a phase 2/3 trial. *Nat Med* (2022) 28:2388–97. doi: 10.1038/s41591-022-02031-7

48. Bricker TL, Darling TL, Hassan AO, Harastani HH, Soung A, Jiang X, et al. A single intranasal or intramuscular immunization with chimpanzee adenovirus-vectored SARS-CoV-2 vaccine protects against pneumonia in hamsters. *Cell Rep* (2021) 36:109400. doi: 10.1016/j.celrep.2021.109400

49. Hassan AO, Kafai NM, Dmitriev IP, Fox JM, Smith BK, Harvey IB, et al. A single-dose intranasal ChAd vaccine protects upper and lower respiratory tracts against SARS-CoV-2. *Cell* (2020) 183:169–84.e13. doi: 10.1016/j.cell.2020.08.026

50. Corbett KS, Edwards DK, Leist SR, Abiona OM, Boyoglu-Barnum S, Gillespie RA, et al. SARS-CoV-2 mRNA vaccine design enabled by prototype pathogen preparedness. *Nature* (2020) 586:567–71. doi: 10.1038/s41586-020-2622-0

51. McCray PB, Pewe L, Wohlford-Lenane C, Hickey M, Manzel L, Shi L, et al. Lethal infection of K18-hACE2 mice infected with severe acute respiratory syndrome coronavirus. *J Virol* (2007) 81:813–21. doi: 10.1128/jvi.02012-06

52. Dong W, Mead H, Tian L, Park J-G, Garcia JI, Jaramillo S, et al. The K18-human ACE2 transgenic mouse model recapitulates non-severe and severe COVID-19 in response to an infectious dose of the SARS-CoV-2 virus. *J Virol* (2022) 96:e0096421. doi: 10.1128/JVI.00964-21

CITATION

Ávila-Nieto C, Vergara-Alert J, Amengual-Rigo P, Ainsua-Enrich E, Brustolin M, Rodríguez de la Concepción ML, Pedreño-Lopez N, Rodon J, Urrea V, Pradenas E, Marfil S, Ballana E, Riveira-Muñoz E, Pérez M, Roca N, Tarrés-Freixas F, Carabelli J, Cantero G, Pons-Grífols A, Rovirosa C, Aguilar-Gurrieri C, Ortiz R, Barajas A, Trinité B, Lepore R, Muñoz-Basagoiti J, Perez-Zsolt D, Izquierdo-Useros N, Valencia A, Blanco J, Clotet B, Guallar V, Segalés J and Carrillo J (2023) Novel Spike-stabilized trimers with improved production protect K18-hACE2 mice and golden Syrian hamsters from the highly pathogenic SARS-CoV-2 Beta variant.
Front. Immunol. 14:1291972.
doi: 10.3389/fimmu.2023.1291972

frontiers | Frontiers in Immunology

TYPE Original Research
PUBLISHED 22 January 2024
DOI 10.3389/fimmu.2024.1328905

OPEN ACCESS

EDITED BY
Smita S Iyer,
University of California, Davis, United States

REVIEWED BY
Ebony Gary,
Wistar Institute, United States
Tanushree Dangi,
Northwestern University, United States

*CORRESPONDENCE
Lbachir BenMohamed
Lbenmoha@uci.edu

†These authors have contributed equally to this work

RECEIVED 27 October 2023
ACCEPTED 02 January 2024
PUBLISHED 22 January 2024

CITATION
Prakash S, Dhanushkodi NR, Zayou L, Ibraim IC, Quadiri A, Coulon PG, Tifrea DF, Suzer B, Shaik AM, Chilukuri A, Edwards RA, Singer M, Vahed H, Nesburn AB, Kuppermann BD, Ulmer JB, Gil D, Jones TM and BenMohamed L (2024) Cross-protection induced by highly conserved human B, CD4+, and CD8+ T-cell epitopes-based vaccine against severe infection, disease, and death caused by multiple SARS-CoV-2 variants of concern.
Front. Immunol. 15:1328905.
doi: 10.3389/fimmu.2024.1328905

Cross-protection induced by highly conserved human B, CD4$^+$, and CD8$^+$ T-cell epitopes-based vaccine against severe infection, disease, and death caused by multiple SARS-CoV-2 variants of concern

Swayam Prakash[1], Nisha R. Dhanushkodi[1], Latifa Zayou[1†], Izabela Coimbra Ibraim[2†], Afshana Quadiri[1], Pierre Gregoire Coulon[1], Delia F. Tifrea[3], Berfin Suzer[1], Amin Mohammed Shaik[1], Amruth Chilukuri[1], Robert A. Edwards[3], Mahmoud Singer[1], Hawa Vahed[4], Anthony B. Nesburn[1], Baruch D. Kuppermann[1], Jeffrey B. Ulmer[4], Daniel Gil[4], Trevor M. Jones[4] and Lbachir BenMohamed[1,4,5,6*]

[1]Laboratory of Cellular and Molecular Immunology, Gavin Herbert Eye Institute, University of California Irvine, School of Medicine, Irvine, CA, United States, [2]High Containment Facility, University of California Irvine, School of Medicine, Irvine, CA, United States, [3]Department of Pathology and Laboratory Medicine, School of Medicine, the University of California Irvine, Irvine, CA, United States, [4]Department of Vaccines and Immunotherapies, TechImmune, LLC, University Lab Partners, Irvine, CA, United States, [5]Division of Infectious Diseases and Hospitalist Program, Department of Medicine, School of Medicine, the University of California Irvine, Irvine, CA, United States, [6]Institute for Immunology; University of California Irvine, School of Medicine, Irvine, CA, United States

Background: The coronavirus disease 2019 (COVID-19) pandemic has created one of the largest global health crises in almost a century. Although the current rate of Severe acute respiratory syndrome coronavirus 2 (SARS-CoV-2) infections has decreased significantly, the long-term outlook of COVID-19 remains a serious cause of morbidity and mortality worldwide, with the mortality rate still substantially surpassing even that recorded for influenza viruses. The continued emergence of SARS-CoV-2 variants of concern (VOCs), including multiple heavily mutated Omicron sub-variants, has prolonged the COVID-19 pandemic and underscores the urgent need for a next-generation vaccine that will protect from multiple SARS-CoV-2 VOCs.

Methods: We designed a multi-epitope-based coronavirus vaccine that incorporated B, CD4$^+$, and CD8$^+$ T- cell epitopes conserved among all known SARS-CoV-2 VOCs and selectively recognized by CD8$^+$ and CD4$^+$ T-cells from asymptomatic COVID-19 patients irrespective of VOC infection. The safety, immunogenicity, and cross-protective immunity of this pan-variant SARS-CoV-2 vaccine were studied against six VOCs using an innovative triple transgenic h-ACE-2-HLA-A2/DR mouse model.

Results: The pan-variant SARS-CoV-2 vaccine (i) is safe , (ii) induces high frequencies of lung-resident functional $CD8^+$ and $CD4^+$ T_{EM} and T_{RM} cells , and (iii) provides robust protection against morbidity and virus replication. COVID-19-related lung pathology and death were caused by six SARS-CoV-2 VOCs: Alpha (B.1.1.7), Beta (B.1.351), Gamma or P1 (B.1.1.28.1), Delta (lineage B.1.617.2), and Omicron (B.1.1.529).

Conclusion: A multi-epitope pan-variant SARS-CoV-2 vaccine bearing conserved human B- and T- cell epitopes from structural and non-structural SARS-CoV-2 antigens induced cross-protective immunity that facilitated virus clearance, and reduced morbidity, COVID-19-related lung pathology, and death caused by multiple SARS-CoV-2 VOCs.

KEYWORDS

SARS-CoV-2, SL-CoVs, COVID-19, vaccine, epitopes, antibodies, T cells, immunity

Introduction

While the Wuhan Hu1 variant of SARS-CoV-2 is the ancestral reference virus, Alpha (lineage B.1.1.7), Beta (lineage B.1.351), Gamma (lineage B.1.1.28), and Delta (lineage B.1.617.2) variants of concern (VOCs) subsequently emerged in the United Kingdom, South Africa, Brazil, and India, respectively, between 2020 and 2022 (1). The most recent SARS CoV-2 variants, including multiple heavily mutated Omicron (B.1.1.529) sub-variants, have prolonged the COVID-19 pandemic (2–6). These new variants emerged beginning December 2020 at a much higher rate, with the accumulation of two mutations per month, and exerting strong selective pressure on the immunologically important SARS-CoV-2 genes (7). The Alpha, Beta, Gamma, Delta, and Omicron variants are defined as VOCs based on their high transmissibility associated with increased hospitalizations and deaths (8). This is a result of reduced neutralization by antibodies generated by previous variants and/or by the first-generation COVID-19 vaccines, together with failures of treatments and diagnostics (9, 10). Dr. Peter Marks, Director/CBER (Center for Biologics Evaluation and Research) for the FDA recently outlined the need for a superior next-generation vaccine that will protect from multiple SARS-CoV-2 VOCs (11, 12).

Besides SARS CoV-2 variants, two additional coronaviruses from the severe acute respiratory syndrome (SARS)-like betacoronavirus (sarbecovirus) lineage, SARS coronavirus (SARS-CoV-1) and MERS-CoV, have caused epidemics and pandemics in humans over the past 20 years (13). In addition, the discovery of diverse sarbecoviruses in bats together with the frequent "jumping" of these zoonotic viruses from bats to intermediate animal hosts raises the possibility of another COVID-19- like pandemic in the future (14–19). Hence, there is an urgency to develop a pre-emptive universal pan-variant SARS-CoV-2 vaccine to protect against all SARS-CoV-2 variants, SARS-CoV, MERS-CoV, and other zoonotic Sarbecoviruses with the potential to jump from animals into humans.

The SARS-CoV-2 genome comprises 29,903 bp. The Spike protein is a predominant surface antigen of SARS-CoV-2 involved in the docking and penetration of the virus into the target host cells (20–22). As such, the Spike protein is the main target of the first-generation COVID-19 subunit vaccines aiming mainly at inducing neutralizing antibodies (23, 24). Nearly 56% of the 10 billion doses of first-generation COVID-19 vaccines are based on the Spike antigen alone (25), while the remaining 44% were based on whole- virion- inactivated (WVI) vaccines (26, 27). Both the Spike-based COVID-19 sub-unit vaccines and the whole virion-inactivated vaccines were successful (20–22). However, because the Spike protein is the most mutated SARS-CoV-2 antigen, these first-generation vaccines lead to immune evasion by many new variants and sub-variants, such as Omicron XBB.1.5 sub-variant (25, 28, 29). Therefore, the next generation of COVID-19 vaccines should also target other highly conserved structural and non-structural SARS-CoV-2 antigens capable of inducing protection by cross-reactive $CD4^+$ and $CD8^+$ T cells (30–33).

Previously, we mapped and characterized the antigenicity and immunogenicity of genome-wide B cell, $CD4^+$ T cell, and $CD8^+$ T-cell epitopes that are highly conserved (33). We hypothesize that multi-epitope vaccine candidates that express these highly conserved, antigenic, and immunogenic B- and T- cell epitopes will provide broader global population coverage against multiple SARS-CoV-2 VOCs. The present study (1) identified seven B- cell epitopes, six $CD4^+$ T- cell epitopes, and 16 $CD8^+$ T- cell epitopes that are highly conserved within (i) 8.7 million genome sequences of SARS-CoV-2, (ii) all previous and current SARS-CoV-2 variants , (iii) SARS-CoV , (iv) MERS-CoV, (v) common cold coronaviruses (HKU, OC1), and (vi) in animal CoV (i.e., bats, civet cats, pangolin, and camels); (2) established that those epitopes were selectively recognized by B cells, $CD4^+$ T cells, and $CD8^+$ T cells from "naturally protected" asymptomatic COVID-19 patients; and (3) demonstrated that a multi-epitope pan-variant SARS-CoV-2

vaccine that includes the above B cell, $CD4^+$ T cell, and $CD8^+$ T- cell epitopes generated cross-protection against all the five SARS-CoV-2 VOCs, i.e., SARS-CoV-2 (USA-WA1/2020), Alpha (B.1.1.7), Beta (B.1.351), Gamma (P.1), Delta (B.1.617.2), and Omicron (B.1.1.529) in a novel triple transgenic HLA-A*02:01/HLA-DR hACE-2 mouse model of COVID-19.

Materials and methods

Viruses

SARS-CoV-2 viruses specific to six variants, namely, (i) SARS-CoV-2-USA/WA/2020 (Batch Number: G2027B), (ii) Alpha (B.1.1.7) (isolate England/204820464/2020, Batch Number: C2108K), (iii) Beta (B.1.351) (isolate South Africa/KRISP-EC-K005321/2020; Batch Number: C2108F), (iv) Gamma (P.1) (isolate hCoV-19/Japan/TY7-503/2021; Batch Number: G2126A), (v) Delta (B.1.617.2) (isolate h-CoV-19/USA/MA29189; Batch number: G87167), and Omicron (BA.1.529) (isolate h-CoV-19/USA/FL17829; Batch number: G76172) were procured from Microbiologics (St. Cloud, MN). The initial batches of viral stocks were propagated to generate high-titer virus stocks. Vero E6 (ATCC-CRL1586) cells were used for this purpose using an earlier published protocol (34). Procedures were completed only after appropriate safety training was obtained using an aseptic technique under BSL-3 containment.

Triple transgenic mice immunization with SARS-CoV-2 conserved peptides and infection

The University of California—Irvine conformed to the Guide for the Care and Use of Laboratory Animals published by the US National Institute of Health (IACUC protocol No. AUP-22-086). Seven- to eight-week-old triple transgenic HLA-A*02:01/HLA-DRB1*01:01-hACE-2 mice (n=60) were included in this experiment. Mice were subcutaneously immunized with a pool of conserved Pan-Coronavirus peptides. The peptide pool administered per mouse comprised 25 µg each of the 9-mer long 16 $CD8^+$ T-cell peptides ($ORF1ab_{2210–2218}$, $ORF1ab_{3013–3021}$, $ORF1ab_{4283–4291}$, $ORF1ab_{6749–6757}$, $ORF6_{3–11}$, $ORF7b_{26–34}$, $ORF8a_{73–81}$, $ORF10_{3–11}$, $ORF10_{5–13}$, $S_{958–966}$, $S_{1000–1008}$, $S_{1220–1228}$, $E_{20–28}$, $E_{26–34}$, $M_{52–60}$, and $M_{89–97}$), 15-mer long 6 $CD4^+$ T-cell epitopes ($ORF1a_{1350–1365}$, $ORF6_{12–26}$, $ORF8b_{1–15}$, $S_{1–13}$, $M_{176–190}$, and $N_{388–403}$), and 9 B-cell peptides. The pool of peptides was then mixed with 25 µg of CpG and 25 µg of alum to prepare the final composition. Mice were immunized with the peptide pool on Day 0 and Day 14 of the experiment. On Day 28, 14 days following the second immunization, mice were divided into six groups and intranasally infected with 1×10^5 pfu of SARS-CoV-2 (USA-WA1/2020) (n=10), 6×10^3 pfu of SARS-CoV-2-Alpha (B.1.1.7) (n=10), 6×10^3 pfu of SARS-CoV-2-Beta (B.1.351) (n=10), 5×10^2 pfu of SARS-CoV-2-Gamma (P.1) (n=10), 8×10^3 pfu of SARS-CoV-2-Delta (B.1.617.2) (n=10), and 6.9×10^4 pfu of SARS-CoV-2-Omicron (B.1.1.529) (n=10). The viruses were diluted, and each mouse was administered intranasally with 20 µl volume. Mice were monitored daily for weight loss and survival until Day 14 p.i. Throat swabs were collected for viral titration on Days 2, 4, 6, 8, 10, and 14 post-infection. The experiment was repeated twice to overcome data bias.

Before beginning the vaccine experiments, we performed a well-curated LD50 experiment in triple transgenic HLA-A*02:01/HLA-DRB1*01:01-hACE-2 mice, for each of the variants, namely, SARS-CoV-2 WA/USA, Alpha (B.1.1.7), Beta (B.1.351), Gamma (P.1), Delta (B.1.617.2), and Omicron (B.1.1.529) variant at 1×10^5 PFU, 8×10^4 PFU, 1×10^4 PFU, 5×10^3 PFU, and 5×10^2 PFU. Based on the LD50 results obtained, the triple transgenic HLA-A*02:01/HLA-DRB1*01:01-hACE-2 mice were challenged with 1×10^5 pfu for SARS-CoV-2 (USA-WA1/2020), 6×10^3 pfu for SARS-CoV-2-Alpha (B.1.1.7) and SARS-CoV-2-Beta (B.1.351), 5×10^2 pfu for SARS-CoV-2-Gamma (P.1), 8×10^3 pfu for SARS-CoV-2-Delta (B.1.617.2), and 6.9×10^4 pfu for SARS-CoV-2-Omicron (B.1.1.529) variants.

Human study population cohort and HLA genotyping

In this study, we have included 210 subjects from a pool of over 682 subjects. Written informed consent was obtained from participants before inclusion. The subjects were categorized as mild to severe COVID-19 groups and have undergone treatment at the University of California Irvine Medical Center between July 2020 and July 2022 (Institutional Review Board protocol no. 2020-5779). SARS-CoV-2 positivity was defined by a positive RT-PCR on nasopharyngeal swab samples. All the subjects were genotyped by PCR for class I HLA-A*02:01 and class II HLA-DRB1*01:01 among the 682 patients (and after excluding a few for which the given amount of blood was insufficient —i.e., <6ml), we ended up with 210 that were genotyped for HLA-$A^*02:01^+$ or/and HLA-$DRB1^*01:01^+$ (35, 36). Based on the severity of symptoms and ICU admission/intubation status, the subjects were divided into five broad severity categories, namely, Severity 5, patients who died from COVID-19 complications; Severity 4, infected COVID-19 patients with severe disease that were admitted to the intensive care unit (ICU) and required ventilation support; Severity 3, infected COVID-19 patients with severe disease that required enrollment in ICU, but without ventilation support; Severity 2, infected COVID-19 patients with moderate symptoms that involved a regular hospital admission; Severity 1, infected COVID-19 patients with mild symptoms; and Severity 0, infected individuals with no symptoms. Demographically, the 210 patients included were from mixed ethnicities [Hispanic (34%), Hispanic Latino (29%), Asian (19%), Caucasian (14%), Afro-American (3%), and Native Hawaiian and Other Pacific Islander descent (1%)].

Sequence comparison among variants of SARS-CoV-2 and animal CoV strains

We retrieved nearly 8.5 million human SARS-CoV-2 genome sequences from the GISAID database representing countries from

North America, South America, Central America, Europe, Asia, Oceania, Australia, and Africa. All the sequences included in this study were retrieved either from the NCBI GenBank (www.ncbi.nlm.nih.gov/nuccore) or GISAID (www.gisaid.org). Multiple sequence alignment was performed keeping SARS-CoV-2-Wuhan-Hu-1 (MN908947.3) protein sequence as a reference against all the SARS-CoV-2 VOCs, common cold, and animal CoV strains. The sequences were aligned using the high throughput alignment tool DIAMOND (37).This comprised of all the VOCs and VBMs of SARS-CoV-2 (B.1.177, B.1.160, B.1.1.7, B.1.351, P.1, B.1.427/B.1.429, B.1.258, B.1.221, B.1.367, B.1.1.277, B.1.1.302, B.1.525, B.1.526, S:677H.Robin1, S:677P.Pelican, B.1.617.1, B.1.617.2, and B,1,1,529) and common cold SARS-CoV strains (SARS-CoV-2-Wuhan-Hu-1 (MN908947.3), SARS-CoV-Urbani (AY278741.1), HKU1-Genotype B (AY884001), CoV-OC43 (KF923903), CoV-NL63 (NC_005831), CoV-229E (KY983587), and MERS (NC_019843)). In addition, for evaluating the evolutionary relationship among the SARS-CoV-2 variants and common cold CoV strains, we have included whole-genome sequences from the bat (RATG13 (MN996532.2), ZXC21 (MG772934.1), YN01 (EPI_ISL_412976), YN02(EPI_ISL_412977), WIV16 (KT444582.1), WIV1 (KF367457.1), YNLF_31C (KP886808.1), and Rs672 (FJ588686.1)), pangolin (GX-P2V (MT072864.1), GX-P5E (MT040336.1), GX-P5L (MT040335.1), GX-P1E (MT040334.1), GX-P4L (MT040333.1), GX-P3B (MT072865.1), MP789 (MT121216.1), and Guangdong-P2S (EPI_ISL_410544)), camel (KT368891.1, MN514967.1, KF917527.1, and NC_028752.1), and civet (Civet007, A022, and B039)).

SARS-CoV-2 $CD8^+$ and $CD4^+$ T-cell epitope prediction

Epitope prediction was performed considering the spike glycoprotein (YP_009724390.1) for the reference SARS-CoV-2 isolate, Omicron BA.2. The reference spike protein sequence was used to screen $CD8^+$ T cell and $CD4^+$ T- cell epitopes. The tools used for $CD8^+$ T- cell-based epitope prediction were SYFPEITHI, MHC-I binding predictions, and Class I Immunogenicity. Of these, the latter two were hosted on the IEDB platform. We used multiple databases and algorithms for the prediction of $CD4^+$ T- cell epitopes, namely, SYFPEITHI, MHC-II Binding Predictions, Tepitool, and TEPITOPEpan. For $CD8^+$ T cell epitope prediction, we selected the 5 most frequent HLA-A class I alleles (HLA-A*01:01, HLA-A*02:01, HLA-A*03:01, HLA-A*11:01, HLA-A*23:01) with nearly 80% coverage of the world population, regardless of race and ethnicity, using a phenotypic frequency cutoff ≥ 6%. Similarly, for $CD4^+$ T- cell epitope prediction, HLA-DRB1*01:01, HLA-DRB1*11:01, HLA-DRB1*15:01, HLA-DRB1*03:01, and HLA-DRB1*04:01 alleles with population coverage of 60% were selected. Subsequently, using NetMHC, we analyzed the SARS-CoV-2 protein sequence against all the MHC-I and MHC-II alleles. Epitopes with 9-mer lengths for MHC-I and 15-mer lengths for MHC-II were predicted. Subsequently, the peptides were analyzed for binding stability to the respective HLA allotype. Our stringent epitope selection criteria were based on picking the top 1% epitopes focused on prediction percentile scores. N and O glycosylation sites were screened using NetNGlyc 1.0 and NetOGlyc 4.0 prediction servers, respectively.

Population-coverage- based T- cell epitope selection

For a robust epitope screening, we evaluated the conservancy of $CD8^+$ T cell, $CD4^+$ T cell, and B- cell epitopes within spike glycoprotein of Human-SARS-CoV-2 genome sequences representing North America, South America, Africa, Europe, Asia, and Australia. As of 20 April 2022, the GISAID database extrapolated 8,559,210 human-SARS-CoV-2 genome sequences representing six continents. Population coverage calculation (PPC) was carried out using the Population Coverage software hosted on the IEDB platform. PPC was performed to evaluate the distribution of screened $CD8^+$ and $CD4^+$ T- cell epitopes in the world population at large in combination with HLA-I (HLA-A*01:01, HLA-A*02:01, HLA-A*03:01, HLA-A*11:01, and HLA-A*23:01) and HLA-II (HLA-DRB1*01:01, HLA-DRB1*11:01, HLA-DRB1*15:01, HLA-DRB1*03:01, and HLA-DRB1*04:01) alleles.

T- cell epitopes screening, selection, and peptide synthesis

Peptide-epitopes from 12 SARS-CoV-2 proteins, including 9-mer long 16 $CD8^+$ T- cell epitopes ($ORF1ab_{2210–2218}$, $ORF1ab_{3013–3021}$, $ORF1ab_{4283–4291}$, $ORF1ab_{6749–6757}$, $ORF6_{3-11}$, $ORF7b_{26–34}$, $ORF8a_{73–81}$, $ORF10_{3–11}$, $ORF10_{5–13}$, $S_{958–966}$, $S_{1000–1008}$, $S_{1220–1228}$, $E_{20–28}$, $E_{26–34}$, $M_{52–60}$, and $M_{89–97}$) and 15-mer long 6 $CD4^+$ T- cell epitopes ($ORF1a_{1350–1365}$, $ORF6_{12–26}$, $ORF8b_{1–15}$, $S_{1–13}$, $M_{176–190}$, and $N_{388–403}$) that we formerly identified were selected as described previously (33). The Epitope Conservancy Analysis tool was used to compute the degree of identity of $CD8^+$ T- cell and $CD4^+$ T- cell epitopes within a given protein sequence of SARS-CoV-2 set at 100% identity level (33). Peptides were synthesized as previously described (21st Century Biochemicals, Inc, Marlborough, MA). The purity of peptides determined by both reversed-phase high-performance liquid chromatography and mass spectroscopy was over 95%. Peptides were first diluted in DMSO and later in PBS (1 mg/mL concentration). The helper T-lymphocyte (HTL) epitopes for the selected SARS-CoV-2 proteins were predicted using the MHC-II epitope prediction tool from the Immune Epitope Database (IEDB, http://tools.iedb.org/mhcii/). Selected epitopes had the lowest percentile rank and IC_{50} values. Additionally, the selected epitopes were checked by the IFN epitope server (http://crdd.osdd.net/raghava/ifnepitope/) for the capability to induce Th1 type immune response accompanied by IFN-ϒ production. Cytotoxic T-lymphocyte (CTL) epitopes for the screened proteins were predicted using the NetCTL1.2 server (http://www.cbs.dtu.dk/services/NetCTL/).

SARS-CoV-2 B- cell epitope prediction

Linear B- cell epitope predictions were carried out on the spike glycoprotein (S), the primary target of B- cell immune responses for SARS-CoV. We used the BepiPred 2.0 algorithm embedded in the B- cell prediction analysis tool hosted on the IEDB platform. For each protein, the epitope probability score for each amino acid and the probability of exposure was retrieved. Potential B- cell epitopes were predicted using a cutoff of 0.55 (corresponding to a specificity >0.81 and sensitivity <0.3) and considering sequences having more than five amino acid residues. This screening process resulted in eight B-cell peptides. These epitopes represent all the major non-synonymous mutations reported among the SARS-CoV-2 variants. One B-cell epitope ($S_{439–482}$) was observed to possess the maximum number of variant-specific mutations. Structure-based antibody prediction was performed using Discotope 2.0, and a positivity cutoff greater than −2.5 was applied (corresponding to specificity ≥ 0.80 and sensitivity <0.39), using the SARS-CoV-2 spike glycoprotein structure (PDB ID: 6M1D).

TaqMan quantitative polymerase reaction assay for the screening of SARS-CoV-2 variants in COVID-19 patients

We utilized a laboratory-developed modification of the CDC SARS-CoV-2 RT-PCR assay, which received Emergency Use Authorization by the FDA on April 17th 2020. (https://www.fda.gov/media/137424/download [accessed 24 March 2021]).

Mutation screening assays

SARS-CoV-2-positive samples were screened by four multiplex RT-PCR assays. Through the qRT-PCR, we screened for 11 variants of SARS-CoV-2 in our patient cohort. The variants that were screened included B.1.1.7 (Alpha), B.1.351 (Beta), P.1 (Gamma), and B.1.427/B.1.429 (Epsilon), B.1.525 (Eta), R.1, P.2 (Zeta), B.1.526 (Iota), B.1.2/501Y or B.1.1.165, B.1.1.529 (BA.1) (Omicron), B.1.1.529 (BA.2) (Omicron), and B.1.617.2 (Delta). The sequences for the detection of Δ69–70 were adapted from a multiplex real-time RT-PCR assay for the detection of SARS-CoV-2 (38). The probe overlaps with the sequences that contain amino acids 69 –70; therefore, a negative result for this assay predicts the presence of deletion S-Δ69–70 in the sample. Using a similar strategy, a primer/probe set that targets the deletion S- Δ242–244 was designed and was run in the same reaction with S-Δ69–70. In addition, three separate assays were designed to detect spike mutations S-501Y, S-484K, and S-452R, and wild-type positions S-501N, S-484E, and S-452L.

Briefy, 5 µl of the total nucleic acid eluate was added to a 20- µl total volume reaction mixture (1× TaqPath 1-Step RT-qPCR Master Mix, CG [Thermo Fisher Scientific, Waltham, MA], with 0.9 mM each primer and 0.2 mM each probe). The RT-PCR was carried out using the ABI StepOnePlus thermocycler (Life Technologies, Grand Island, NY). The S-N501Y, S-E484K, and S-L452R assays were carried out under the following running conditions: 25°C for 2 min, then 50°C for 15 min, followed by 10 min at 95°C and 45 cycles of 95°C for 15 s and 65°C for 1 min. The Δ 69–70/Δ242–244 assays were run under the following conditions: 25°C for 2 min, then 50°C for 15 min, followed by 10 min at 95°C and 45 cycles of 95°C for 15 s and 60°C for 1 min. Samples displaying typical amplification curves above the threshold were considered positive. Samples that yielded a negative result or results in the S-Δ69–70/Δ242–244 assays or were positive for S-501Y P2, S-484K P2, and S-452R P2 were considered screen positive and assigned to a VOC.

Neutralizing antibody assays for SARS-CoV-2

Serially diluted heat-inactivated plasma (1:3) and 300 pfu of SARS-CoV-2 variants are combined in Dulbecco's modified Eagle's medium (DMEM) and incubated at 37°C 5% CO_2 for 30 min. After neutralization, the antibody–virus inoculum was transferred onto Vero E6 cells (ATCC C1008) and incubated at 34°C 5% CO_2 for 1 h. The cells were then fixed with 10% neutral buffered formalin and incubated at −20°C for 10 min followed by 20 min at room temperature. Plates were developed with True Blue HRP substrate and imaged on an ELISpot reader. The half maximum inhibitory concentration (IC50) was calculated using normalized counted foci.

Histology of animal lungs

Mouse lungs were preserved in 10% neutral buffered formalin for 48 h before transferring to 70% ethanol. The tissue sections were then embedded in paraffin blocks and sectioned at 8-µm thickness. Slides were deparaffinized and rehydrated before staining for hematoxylin and eosin for routine immunopathology. IHC was performed on mice lung tissues probed with SARS/SARS-CoV-2 Coronavirus NP Monoclonal Antibody (B46F) (Product No. MA1-7404) at a dilution of 1:100. The antibody showed significant staining in lung tissues of non-immunized, SARS-CoV-2- infected mice when compared to the tissues of the vaccinated group of mice. This method was meant to demonstrate the relative expression of the Nucleocapsid protein between non-immunized Mock and immunized samples. Further $CD8^+$ T- cell and $CD4^+$ T- cell-specific staining were performed to identify the T- cell infiltration among the immunized and Mock groups.

Peripheral blood mononuclear cells isolation and T cell stimulation

Peripheral blood mononuclear cells (PBMCs) from COVID-19 patients were isolated from the blood using Ficoll (GE Healthcare) density gradient media and transferred into 96-well plates at a concentration of 2.5×10^6 viable cells per ml in 200 µl (0.5×10^6 cells per well) of RPMI-1640 media (Hyclone) supplemented with 10% (v/v) FBS (HyClone), sodium pyruvate (Lonza), L-glutamine, non-essential amino acids, and antibiotics (Corning). A fraction of

the blood was kept separated to perform HLA genotyping of the patients and select only the HLA-A*02:01- and/or DRB1*01: 01-positive individuals. Subsequently, cells were then stimulated with 10 μg/ml of each one of the 22 individual T- cell peptide epitopes (16 $CD8^+$ T- cell peptides and 6 $CD4^+$ T- cell peptides) and incubated in humidified 5% CO_2 at 37°C. Post-incubation, cells were stained by flow cytometry analysis or transferred in IFN-γ ELISpot plates. The same isolation protocol was followed for healthy donor (HD) samples obtained in 2018. PBMC samples were kept frozen in liquid nitrogen in 10% FBS in DMSO. Upon thawing, HD PBMCs were stimulated in the same manner for the IFN-γ ELISpot technique.

ELISpot assay

COVID-19 patients were first screened for their HLA status (DRB1*01:01 positive = 108, HLA-A*02:01 positive = 83, DRB1*01:01 and HLA-A*02:01 positive = 19). PBMC samples from the 108 DRB1*01:01 positive individuals were used to assess the $CD4^+$ T-cell response against our SL-CoVs-conserved SARS-CoV-2-derived class-II restricted epitopes by IFN-γ ELISpot. Subsequently, we assessed the $CD8^+$ T- cell response against our SL-CoVs conserved SARS-CoV- 2-derived class-I restricted epitopes in the PBMC sample of 83 HLA-A*02:01- positive individuals representing different disease severity categories. Furthermore, to evaluate the immunogenicity of conserved SARS-CoV-2 $CD8^+$ and $CD4^+$ T- cell epitopes in triple transgenic HLA-A*02:01/HLA-DRB1*01:01-hACE-2 mice, mononuclear cells from lung tissues were collected 14 days post-infection. ELISpot assay was performed as described previously (33, 39).

Flow cytometry analysis

After 72 h of stimulation with each SARS-CoV-2 class I or class II restricted peptide, PBMCs (0.5×10^6 cells) from 147 patients were stained for the detection of surface markers and subsequently analyzed by flow cytometry. First, the cells were stained with a live/dead fixable dye (Zombie Red dye, 1/800 dilution —BioLegend, San Diego, CA) for 20 min at room temperature, to exclude dying/apoptotic cells. Cells were stained for 45 min at room temperature with five different HLA-A*02*01 restricted tetramers and/or five HLA-DRB1*01:01 restricted tetramers (PE labeled) specific toward the SARS-CoV-2 $CD8^+$ T- cell epitopes $Orf1ab_{2210–2218}$, $Orf1ab_{4283–4291}$, $S_{1220–1228}$, $ORF10_{3–11}$ and toward the $CD4^+$ T- cell epitopes $ORF1a_{1350–1365}$, $S_{1–13}$, $M_{176–190}$, $ORF6_{12\ 26}$, respectively. We have optimized our tetramer staining according to the instructions published by Dolton et al. (40) As a negative control aiming to assess tetramer staining specificity, we stained HLA-A*02*01-HLA-DRB1*01:01-negative patients with our four tetramers. Subsequently, we used anti-human antibodies for surface marker staining: anti-CD62L, anti-CD69, anti-CD4, anti-CD8, and anti-IFN-g. mAbs against these various cell markers were added to the cells in phosphate-buffered saline (PBS) containing 1% FBS and 0.1% sodium azide (fluorescence-activated cell sorter [FACS] buffer) and left for 30 min at 4°C. At the end of the incubation period, the cells were washed twice with FACS buffer and fixed with 4% paraformaldehyde (PFA, Affymetrix, Santa Clara, CA). A total of ~200,000 lymphocyte-gated PBMCs (140,000 alive $CD45^+$) were acquired by Fortessa X20 (Becton Dickinson, Mountain View, CA) and analyzed using FlowJo software (TreeStar, Ashland, OR).

Enzyme-linked immunosorbent assay

Serum antibodies specific for epitope peptides and SARS-CoV-2 proteins were detected by ELISA. The 96-well plates (Dynex Technologies, Chantilly, VA) were coated with 0.5 μg peptides and 100 ng S or N protein per well at 4°C overnight, respectively, and then washed three times with PBS and blocked with 3% BSA (in 0.1% PBST) for 2 h at 37°C. After blocking, the plates were incubated with serial dilutions of the sera (100 μl/well, in twofold dilution) for 2 h at 37°C. The bound serum antibodies were detected with HRP-conjugated goat anti-mouse IgG and chromogenic substrate TMB (Thermo Fisher, Waltham, MA). The cut-off for seropositivity was set as the mean value plus three standard deviations (3SD) in HBc-S control sera. The binding of the epitopes to the sera of SARS-CoV-2- infected samples was detected by ELISA using the same procedure; 96-well plates were coated with 0.5 μg peptides, and sera were diluted at 1:50. All ELISA studies were performed at least twice.

Data and code availability

The human-specific SARS-CoV-2 complete genome sequences were retrieved from the GISAID database, whereas the SARS-CoV-2 sequences for pangolin (*Manis javanica*) and bat (*Rhinolophus affinis*, *Rhinolophus malayanus*) were retrieved from NCBI. Genome sequences of previous strains of SARS-CoV for humans, bats, civet cats, and camels were retrieved from the NCBI GenBank.

Results

Highly conserved SARS-CoV-2 epitopes are selectively recognized by $CD8^+$ and $CD4^+$ T cells from asymptomatic COVID-19 patients irrespective of variants of concern infection

To identify "universal" SARS-CoV-2 epitopes to be included in a multi-epitope pan-coronavirus vaccine, we previously screened the degree of conservancy for human $CD8^+$ T cell, $CD4^+$ T cell, and B-cell epitopes that span the whole SARS-CoV-2 genome (33). $CD8^+$ T- cell epitopes were screened for their conservancy against variants, namely, h-CoV-2/Wuhan (MN908947.3), h-CoV-2/WA/USA2020 (OQ294668.1), h-CoV-2/Alpha(B1.1.7) (OL689430.1), h-CoV-2/Beta(B 1.351) (MZ314998), h-CoV-2/Gamma(P.1) (MZ427312.1), h-CoV-2/Delta(B.1.617.2) (OK091006.1), and h-CoV-2/Omicron (B.1.1.529) (OM570283.1) (33). We observed 100% conservancy in

all the SARS-CoV-2 variants of concern for 14 of our 16 predicted $CD8^+$ T- cell epitopes ($ORF1ab_{2210–2218}$, $ORF1ab_{3013–3021}$, $ORF1ab_{4283–4291}$, $ORF1ab_{6749–6757}$, $ORF6_{3–11}$, $ORF7b_{26–34}$, $ORF10_{3–11}$, $ORF10_{5–13}$, $S_{958–966}$, $S_{1000–1008}$, $S_{1220–1228}$, $E_{20–28}$, $M_{52–60}$, and $M_{89–97}$) (Supplementary Figure S1) and (33). The only exceptions were epitopes $E_{26–34}$ and $ORF8a_{73–81}$, which showed an 88.8% conservancy against Beta (B.1.351) and Alpha (B.1.1.7) variants, respectively (Supplementary Figure S1) and (33). All of the six highly immunodominant "universal" $CD4^+$ T- cell epitopes ($ORF1a_{1350–1365}$, $ORF6_{12–26}$, $ORF8b_{1–15}$, $S_{1–13}$, $M_{176–190}$, and $N_{388–403}$) that we previously reported (33) remained 100% conserved across all the SARS-CoV-2 VOCs (Supplementary Figure S2).

Next, we determined whether the highly conserved "universal" $CD8^+$ and $CD4^+$ T-cell epitopes were differentially recognized by T cells from asymptomatic (ASYMP) versus symptomatic (SYMP) COVID-19 patients. We recruited COVID-19 patients infected with SARS-CoV-2 Beta (B.1.351) and SARS-CoV-2 Omicron (B.1.1.529) spanning 2 years of the COVID-19 pandemic (Figure 1A). We compared the magnitude of $CD8^+$ and $CD4^+$ T- cell responses specific to each of the conserved epitopes from among 38 ASYMP and 172 SYMP COVID-19 patients. Fresh PBMCs were isolated from SYMP and ASYMP COVID-19 patients, on average, within 4 days after reporting their first symptoms. PBMCs were then stimulated *in vitro* for 72 h with each of the 16 $CD8^+$ T- cell epitopes or each of the 6 $CD4^+$ T cell epitopes. Numbers of responding IFN-γ-producing $CD8^+$ and $CD4^+$ T cells (quantified in ELISpot assay as the number of IFN-γ-spot forming cells, or "SFCs") were subsequently determined.

ASYMP COVID-19 patients showed significantly higher frequencies of SARS-CoV-2 epitope-specific IFN-γ-producing $CD8^+$ T cells (mean SFCs > 25 per 1×10^6 pulmonary immune cells), irrespective of infection with Beta ($p < 0.5$, Figure 1B, left panel) or Omicron ($p < 0.$, Figure 1B, right panel) variants. In contrast, severely ill or hospitalized symptomatic COVID-19 patients showed significantly lower frequencies of SARS-CoV-2 epitope-specific IFN-γ-producing $CD8^+$ T cells ($p < 0.5$,

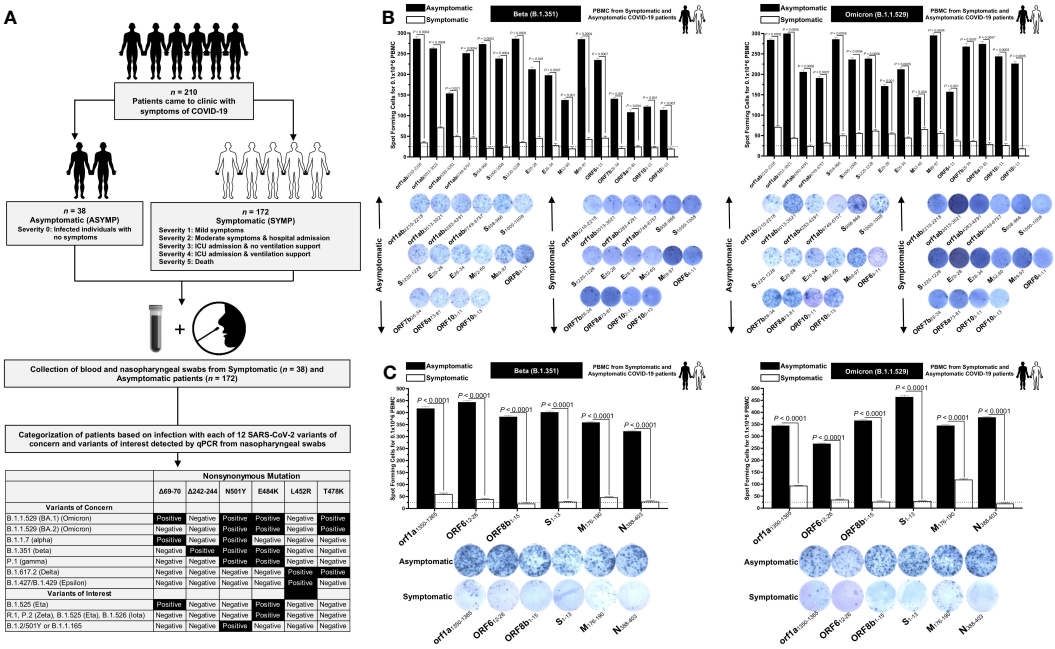

FIGURE 1
Screening of COVID-19 patients based on SARS-CoV-2 variants and subsequent evaluation of IFN-γ $CD8^+$ and $CD4^+$ T- cell responses for conserved $CD8^+$, and $CD4^+$ T-cell epitopes in asymptomatic vs. symptomatic COVID-19 patients: **(A)** experimental plan showing screening process of COVID-19 patients (n = 210) into asymptomatic and symptomatic categories based on clinical parameters. Blood and nasopharyngeal swabs were collected from all the subjects, and a qRT-PCR assay was performed. Six novel nonsynonymous mutations (Δ69–70, Δ242–244, N501Y, E484K, L452R, and T478K) were used to identify the haplotypes unique to different SARS-CoV-2 variants of concern (Omicron (B.1.1.529 (BA.1)), Omicron (B.1.1.529 (BA.2)), Alpha (B.1.1.7), Beta (B.1.351), Gamma (P.1), Delta (B.1.617.2), and Epsilon (B.1.427/B.1.429)) and variants of interest (Eta (B.1.525), R.1, Zeta (P.2), Iota (B.1.526), and B.1.2/501Y or B.1.1.165). **(B)** ELISpot images and bar diagrams showing average frequencies of IFN-γ- producing cell spots from immune cells from PBMCs (1×10^6 cells per well) of COVID-19 infected with highly pathogenic SARS-CoV-2 variants of concern Beta (B.1.351) (left panel) and Omicron (B.1.1.529) (right panel). Cells were stimulated for 48 h with 10 mM of 16 immunodominant $CD8^+$ T- cell peptides derived from SARS-CoV-2 structural (Spike, Envelope, and Membrane) and non-structural (orf1ab, ORF6, ORF7b, ORF8a, and ORF10) proteins. **(C)** ELISpot images and bar diagrams showing average frequencies of IFN-γ- producing cell spots from immune cells from PBMCs (1×10^6 cells per well) of COVID-19 infected with SARS-CoV-2 variants of concern Alpha (B.1.1.7) (left panel) and Omicron (B.1.1.529) (right panel). Cells were stimulated for 48 h with 10 mM of six immunodominant $CD4^+$ T- cell peptides derived from SARS-CoV-2 structural (Spike, Membrane, and Nucleocapsid) and non-structural (ORF1a, ORF6, and ORF8a) proteins. The bar diagrams show the average/mean numbers (± SD) of IFN-γ-spot forming cells (SFCs) after $CD8^+$ T- cell peptide-stimulation PBMCs of asymptomatic and symptomatic COVID-19 patients. Dotted lines represent an arbitrary threshold set to evaluate the relative magnitude of the response. A strong response is defined for mean SFCs > 25 per 1×10^6 stimulated PBMCs. Results were considered statistically significant at $p < 0.05$.

Figure 1B, left panel) or Omicron ($p < 0.$, Figure 1B, right panel) variants. This observation was consistent regardless of whether the $CD8^+$ T- cell targeted epitopes were from structural or non-structural SARS-CoV-2 protein antigens, suggesting that strong $CD8^+$ T- cell responses specific to selected "universal" SARS-CoV-2 epitopes were commonly associated with better COVID-19 outcomes. In contrast, low SARS-CoV-2-specific $CD8^+$ T- cell responses were more commonly associated with severe onset of disease.

Similarly, higher frequencies of functional IFN-γ-producing $CD4^+$ T cells ASYMP COVID-19 patients (mean SFCs > 25 per 1×10^6 pulmonary immune cells) were detected, irrespective of infection with Beta ($p < 0.5$, Figure 1C, left panel) or Omicron ($p < 0.$, Figure 1C, right panel) variants, whereas reduced frequencies of IFN-γ-producing $CD4^+$ T cells were detected in SYMP COVID-19 patients, irrespective of infection with Beta ($p < 0.5$, Figure 1C, left panel) or Omicron ($p < 0.$, Figure 1C, right panel) variants. This observation was consistent regardless of whether the $CD4^+$ T- cell targeted epitopes were from structural or non-structural SARS-CoV-2 protein antigens. Our results suggest that strong $CD4^+$ T- cell responses specific to selected "universal" SARS-CoV-2 epitopes were commonly associated with better COVID-19 outcomes. In contrast, low SARS-CoV-2-specific $CD4^+$ T- cell responses were more commonly associated with severe disease onset.

Taken together, these results (1) demonstrate an important role of SARS-CoV-2-specific $CD4^+$ and $CD8^+$ T cells directed against highly conserved structural and non-structural SARS-CoV-2 epitopes in protection from severe COVID-19 symptoms, (2) highlight the potential importance of these highly conserved "asymptomatic" epitopes in mounting protected $CD4^+$ and $CD8^+$ T cell responses against multiple SARS-CoV-2 VOCs, and (3) support targeting these conserved epitopes with a vaccine.

A pan-variant SARS-CoV-2 vaccine composed of a mixture of conserved "asymptomatic" $CD4^+$ and $CD8^+$ T cell epitopes provides robust protection against infection and disease caused by six SARS-CoV-2 variants of concern

We next used a prototype pan-variant SARS-CoV-2 vaccine composed of a mixture of 6 conserved "asymptomatic" $CD4^+$ T- cell epitopes and 16 conserved "asymptomatic" $CD4^+$ and $CD8^+$ T- cell epitopes that span the whole SARS-CoV-2 genome (33). We focused mainly on $CD4^+$ and $CD8^+$ T- cell epitopes that show immunodominance selectively in SYMP COVID-19 patients infected with various SARS-CoV-2 VOCs.

A pool of peptides comprising 25 μg each of 16 $CD8^+$ T- cell peptides ($ORF1ab_{2210-2218}$, $ORF1ab_{3013-3021}$, $ORF1ab_{4283-4291}$, $ORF1ab_{6749-6757}$, $ORF6_{3-11}$, $ORF7b_{26-34}$, $ORF8a_{73-81}$, $ORF10_{3-11}$, $ORF10_{5-13}$, $S_{958-966}$, $S_{1000-1008}$, $S_{1220-1228}$, E_{20-28}, E_{26-34}, M_{52-60}, and M_{89-97}), 6 $CD4^+$ T- cell epitopes ($ORF1a_{1350-1365}$, $ORF6_{12-26}$, $ORF8b_{1-15}$, S_{1-13}, $M_{176-190}$, and $N_{388-403}$), and 7 B-cell peptides selected from the Spike protein were mixed with cpG1826 adjuvant and administered subcutaneously on Day 0 and Day 14 to 7–8-week- old triple transgenic HLA-A*02:01/HLA-DR hACE-2 mice ($n = 30$). The remaining group (mock-immunized) received vehicle alone ($n = 30$) (Figure 2A). On day 28, 14 days after the second immunization, mice were divided into six groups and intranasally infected with 1×10^5 pfu of SARS-CoV-2 (USA-WA1/2020) ($n = 10$), 6×10^3 pfu of SARS-CoV-2-Alpha (B.1.1.7) ($n = 10$), 6×10^3 pfu of SARS-CoV-2-Beta (B.1.351) ($n = 10$), 5×10^2 pfu of SARS-CoV-2-Gamma (P.1) ($n = 10$), 8×10^3 pfu of SARS-CoV-2-Delta (B.1.617.2) ($n = 10$), and 6.9×10^4 pfu of SARS-CoV-2-Omicron (B.1.1.529) ($n = 10$) (Figure 2A).

Mice that received the pan-variant SARS-CoV-2 vaccine showed significant protection from weight loss (Figure 2B) and death (Figure 2C) following infection with each of the six SARS-CoV-2 variants of concern. In contrast, mock-immunized mice showed substantial mortality against infection with WA/USA2020 (60%), Alpha (B.1.1.7) (80%), Beta (B.1.351) (80%), Gamma (P.1) (40%), and Delta (B.1.617.2) (40%) (Figure 2C). Mortality was not observed for mock-immunized mice infected with the SARS-CoV-2 Omicron (B.1.1.529) variant (Figure 2C).

Throat swabs were collected from the vaccinated and mock-vaccinated groups of mice on days 2, 4, 6, 8, 10, and 14 post-infection (p.i.) and were processed to detect the viral RNA copy number by qRT-PCR (Figure 2D). Compared to the viral RNA copy number detected from the mock-vaccinated group of mice, we detected a statistically significant decrease in the viral RNA copy number among vaccinated groups of mice on day 4 p.i. for SARS-CoV-2 WA/USA2020 ($p = 0.04$), Delta (B.1.617.2) ($p = 0.00009$), and Omicron (B.1.1.529) ($p = 0.007$); on day 6 p.i. for SARS-CoV-2 WA/USA2020 ($p = 0.002$), Alpha (B.1.1.7) ($p = 0.002$), Delta (B.1.617.2) ($p = 0.001$), and Omicron (B.1.1.529) ($p = 0.001$); on day 8 p.i. for SARS-CoV-2 WA/USA2020 ($p = 0.006$), Alpha (B.1.1.7) ($p = 0.0002$), Beta (B.1.351) ($p = 0.002$), Gamma (P.1) ($p = 0.04$), and Omicron (B.1.1.529) ($p = 0.0001$); on day 10 p.i. for SARS-CoV-2 WA/USA2020 ($p = 0.005$), Gamma (P.1) ($p = 0.008$); and on day 14 p.i. for SARS-CoV-2 WA/USA2020 ($p = 0.02$) (Figure 2D). These results demonstrate that the pan-variant SARS-CoV-2 vaccine conferred significant protection from virus replication against SARS-CoV-2 variants and supports the hypothesis that a broad anti-viral effect following immunization with asymptomatic B and $CD4^+$ and $CD8^+$ T- cell epitopes carefully selected as being highly conserved from multiple SARS-CoV-2 variants.

Immunization with the pan-variant SARS-CoV-2 vaccine bearing conserved epitopes reduced COVID-19-related lung pathology and virus replication associated with increased infiltration of $CD8^+$ and $CD4^+$ T cells in the lungs

Hematoxylin and eosin staining of lung sections at day 14 p.i. showed a significant reduction in COVID-19-related lung pathology in the mice immunized with conserved pan-variant SARS-CoV-2 vaccine compared to mock-vaccinated mice (Figure 3A). This reduction in lung pathology was observed for all six SARS-CoV-2 variants: USA-WA1/2020, Alpha (B.1.1.7), Beta

10.3389/fimmu.2024.1328905

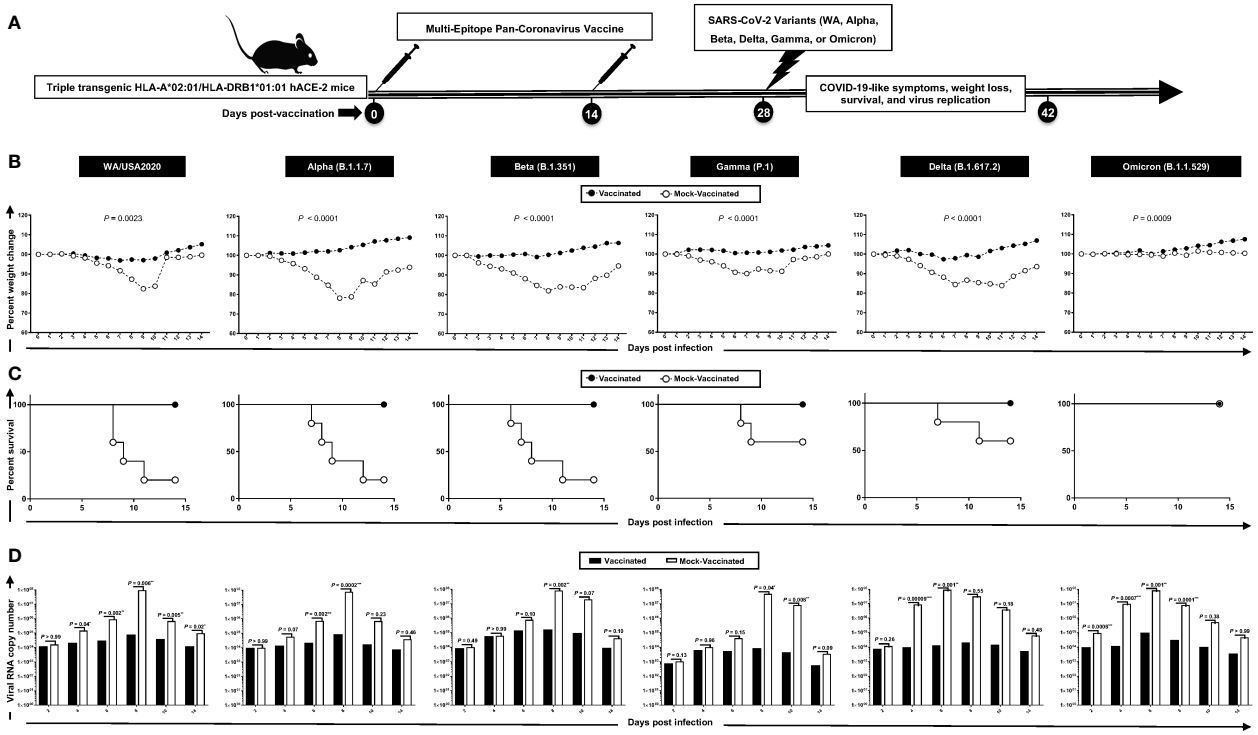

FIGURE 2
Protection induced against six SARS-CoV-2 variants of concern in triple transgenic HLA-A*02:01/HLA-DRB1*01:01-hACE-2 mice following immunization with a pan-variant SARS-CoV-2 vaccine incorporating conserved human B, $CD4^+$, and $CD8^+$ T- cell epitopes: **(A)** experimental scheme of vaccination and challenge triple transgenic HLA-A*02:01/HLA-DRB1*01:01-hACE-2 mice. Triple transgenic HLA-A*02:01/HLA-DRB1*01:01-hACE-2 mice (7–8 weeks old, n = 60) were immunized subcutaneously on Days 0 and 14 with a multi-epitope pan-variant SARS-CoV-2 vaccine consisting of a pool of conserved B, $CD4^+$ T-cell, and $CD8^+$ T-cell human epitope peptides. The pool of peptides comprised 25 µg of each of the 16 $CD8^+$ T- cell peptides, 6 $CD4^+$ T- cell peptides, and 7 B-cell peptides. The final composition of peptides was mixed with 25 µg of CpG and 25 µg of Alum. Mock-vaccinated mice were used as controls (*Mock*). Mice were intranasally challenged with each of the six different SARS-CoV-2 variants of concern (WA/USA2020, Alpha (B.1.1.7), Beta (B.1.351), Gamma (P.1), Delta (B.1.617.2), and Omicron (B.1.1.529)) 14 days following the second immunization. Vaccinated and mock-vaccinated mice were followed 14 days post-challenge for COVID-like symptoms, weight loss, survival, and virus replication. **(B)** Percent weight change recorded daily for 14 days p.i. in vaccinated and mock-vaccinated mice following the challenge with each of the six different SARS-CoV-2 variants. **(C)** Kaplan–Meir survival plots for vaccinated and mock-vaccinated mice following the challenge with each of the six different SARS-CoV-2 variants. **(D)** Virus replication in vaccinated and mock-vaccinated mice following the challenge with each of the six different SARS-CoV-2 variants detected in throat swabs on Days 2, 4, 6, 8, 10, and 14, The indicated p-values are calculated using the unpaired t-test, comparing results obtained in vaccinated VERSUS mock-vaccinated mice. Statistical significance was obtained when *: P < 0.05, **: P < 0.01, ***:P < 0.001, ****:P < 0.0001.

(B.1.351), Gamma (P.1), Delta (B.1.617.2), and Omicron (B.1.1.529) (Figure 3A). We further performed SARS-CoV-2 Nucleocapsid Antibody- Based Immunohistochemistry (IHC) staining on lung tissues obtained from vaccinated and mock-vaccinated groups of mice infected with SARS-CoV-2 variants. We detected significantly lower antibody staining in the lung tissues of the vaccinated compared mock-vaccinated group of mice following infection with each of the six SARS-CoV-2 variants of concern. This indicated higher expression of the target viral proteins in the lungs of the mock-vaccinated compared to the vaccinated group of mice (Figure 3B). Furthermore, IHC staining was performed to compare the infiltration $CD8^+$ and $CD4^+$ T cells into lung tissues of vaccinated and mock-vaccinated mice infected with various SARS-CoV-2 variants. We observed a significant increase in the infiltration of both $CD8^+$ T cells (Figure 3C) and $CD4^+$ T cells (Figure 3D) in the lungs of vaccinated mice compared to mock-vaccinated mice 14 days following infection with each of the six variants.

Taken together, these results indicate that immunization with the pan-variant SARS-CoV-2 vaccine bearing conserved epitopes induced cross-protective $CD8^+$ and $CD4^+$ T cells that infiltrated the lungs, faciltated clearance of virus, and reduced COVID-19-related lung pathology following infection with various multiple SARS-CoV-2 variants.

Increased frequencies of lung-resident functional $CD8^+$ and $CD4^+$ T_{EM} and T_{RM} cells induced by the pan-variant SARS-CoV-2 vaccine are associated with protection against multiple SARS-CoV-2 variants

To determine whether increased frequencies of lung-resident functional $CD8^+$ and $CD4^+$ T cells induced by the pan-variant SARS-CoV-2 vaccine are associated with protection against

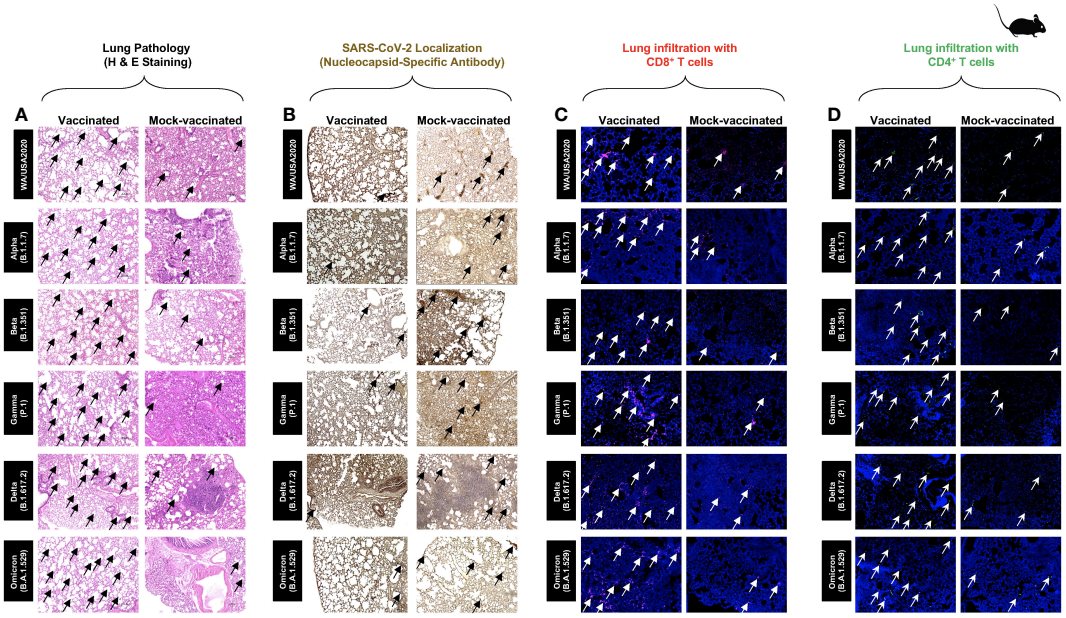

FIGURE 3
Histopathology and immunohistochemistry of the lungs from in triple transgenic HLA-A*02:01/HLA-DRB1*01:01-hACE-2 mice vaccinated and mock-vaccinated mice. **(A)** Representative images of hematoxylin and eosin (H & E) staining of the lungs harvested on day 14 p.i. from vaccinated (left panels) and mock-vaccinated (right panels) mice. **(B)** Representative immunohistochemistry (IHC) sections of the lungs were harvested on Day 14 p.i. from vaccinated (left panels) and mock-vaccinated (right panels) mice and stained with SARS-CoV-2 Nucleocapsid antibody. Black arrows point to the antibody staining. Fluorescence microscopy images showing infiltration of $CD8^+$ T cells **(C)** and of $CD4^+$ T cells **(D)** in the lungs from vaccinated (left panels) and mock-vaccinated (right panels) mice. Lung sections were co-stained using DAPI (*blue*) and mAb specific to $CD8^+$ T cells (pink) (magnification, ×20). The white arrows point to $CD8^+$ and $CD4^+$ T cells infiltrating the infected lungs.

multiple SARS-CoV-2 variants, we used flow cytometry to compared the frequencies of IFN-γ $CD8^+$ T cells and CD69 $CD8^+$ T cells (Figure 4A), IFN-γ $CD4^+$ T cells and CD69 $CD4^+$ T cells (Figure 4B) in cell suspensions from the lungs of vaccinated versus mock-vaccinated groups of mice.

Relatively higher frequencies of IFN-γ $CD8^+$ T cells were detected in the lungs of protected mice that received the pan-variant SARS-CoV-2 vaccine compared to non-protected mock-vaccinated mice following infections with various SARS-CoV-2 variants: USA-WA1/2020 (Vaccinated = 17.4% vs. Mock = 12.2%, $p = 0.5178$), Alpha (B.1.1.7) (Vaccinated = 9.2% vs. Mock = 4.4%, $p = 0.0076$), Beta (B.1.351) (Vaccinated = 7.5% vs. Mock = 2.1%, $p = 0.05$), Gamma (P.1) (Vaccinated = 12.9% vs. Mock = 8.1%, $p = 0.14$), Delta (B.1.617.2) (Vaccinated = 8.3% vs. Mock = 2.23%, $p < 0.0001$), and Omicron (B.1.1.529) (Vaccinated = 8.7% vs. Mock = 5.8%, $p = 0.02$) (Figure 4A, top row). Similarly, increased frequencies for $CD8^+CD69^+$ T cells were detected in the lungs of protected mice that received the pan-variant SARS-CoV-2 vaccine compared to non-protected mock-vaccinated mice following infections with various SARS-CoV-2 variants: Alpha (B.1.1.7) (Vaccinated = 6.9% vs. Mock = 3.4%, $p = 0.0033$), Beta (B.1.351) (Vaccinated = 7.4% vs. Mock = 2.9%, $p = 0.05$), Gamma (P.1) (Vaccinated = 12.3% vs. Mock = 10.4%, $p = 0.95$), Delta (B.1.617.2) (Vaccinated = 8.1% vs. Mock = 2.5%, $p < 0.0001$), and Omicron (B.1.1.529) (Vaccinated = 9.8% vs. Mock = 5.6%, $p = 0.01$) (Figure 4A, bottom row).

Moreover, higher frequencies of IFN-γ $CD4^+$ T cells were detected in the lungs of protected mice that received the pan-variant SARS-CoV-2 vaccine compared to non-protected mock-vaccinated mice following infections with some of the SARS-CoV-2 variants: USA-WA1/2020 (Vaccinated = 21.4% vs. Mock = 10.1%, $p = 0.5696$), Alpha (B.1.1.7) (Vaccinated = 5.6% vs. Mock = 4%, $p = 0.35$), Beta (B.1.351) (Vaccinated = 4.5% vs. Mock = 1.4%, $p = 0.01$), Gamma (P.1) (Vaccinated = 8.8% vs. Mock = 3%, $p = 0.02$), Delta (B.1.617.2) (Vaccinated = 3.7% vs. Mock = 1.2%, $p = 0.0002$), and Omicron (B.1.1.529) (Vaccinated = 4.5% vs. Mock = 2.4%, $p = 0.01$) (Figure 4B, top row). Similarly, increased frequencies for $CD4^+CD69^+$ T cells were detected in the lungs of protected mice that received the pan-variant SARS-CoV-2 vaccine compared to non-protected mock-vaccinated mice following infections with various SARS-CoV-2 variants: Alpha (B.1.1.7) (Vaccinated = 5.3% vs. Mock = 4.2%, $p = 0.1748$), Beta (B.1.351) (Vaccinated = 9.5% vs. Mock = 4%, $p = 0.009$), Gamma (P.1) (Vaccinated = 14.9% vs. Mock = 12.2%, $p = 0.7155$), Delta (B.1.617.2) (Vaccinated = 8.5% vs. Mock = 3.3%, $p < 0.0001$), and Omicron (B.1.1.529) (Vaccinated = 10.4% vs. Mock = 5%, $p = 0.003$) (Figure 4B, bottom row).

FACS-based immunophenotyping, confirmed higher frequencies of the memory $CD8^+$ T_{EM} ($CD44^+CD62L^-$) cell subset in immunized mice with a pool of pan- coronavirus peptides and subjected to infection against USA-WA1/2020 (Vaccinated = 12.2% vs. Mock = 5%, $p < 0.0001$), Alpha (B.1.1.7) (Vaccinated = 6.5% vs. Mock = 3.7%, $p = 0.0017$), Beta (B.1.351) (Vaccinated = 7.2% vs. Mock = 3.4%, $p = 0.0253$), and Omicron (B.1.1.529) (Vaccinated = 5.9% vs. Mock = 3%, $p = 0.9765$) (Figure 4C). Similarly, when the frequencies of the memory $CD8^+$ T_{RM} ($CD69^+CD103^+$) cell subset was evaluated, we found generally higher $CD8^+$ T_{RM} cell subset frequencies for immunized mice

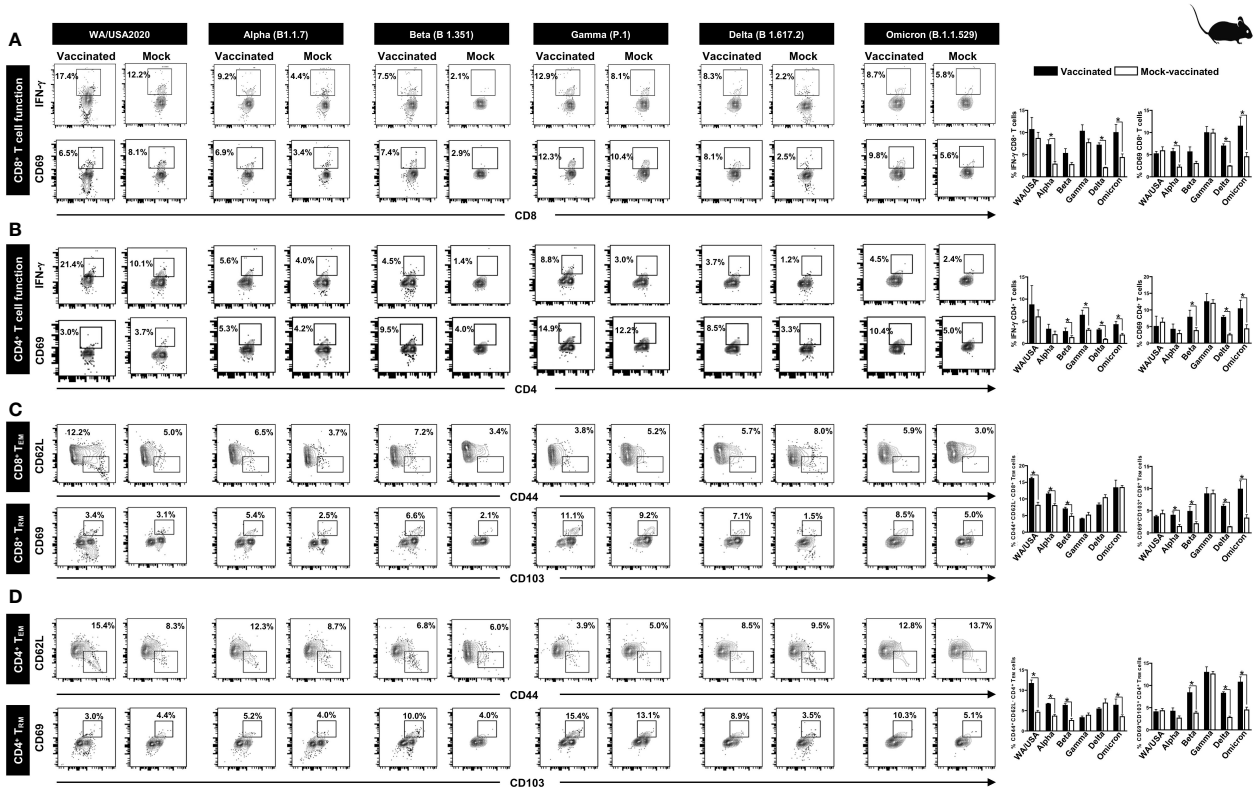

FIGURE 4
The effect of pan-coronavirus immunization on $CD8^+$ and $CD4^+$ T- cell function and memory response: FACS plots and bar graphs showing the **(A)** expression of $CD8^+$ T- cell function markers, **(B)** $CD4^+$ T- cell function associated markers, **(C)** $CD8^+$ T effector memory response ($CD44^+CD62L^-$), and $CD8^+$ T resident memory ($CD103^+CD69^+$) response, and **(D)** $CD4^+$ T effector memory response ($CD44^+CD62L^-$), and $CD4^+$ resident memory ($CD103^+CD69^+$) response in the lung of vaccinated and mock-vaccinated groups of mice infected with multiple SARS-CoV-2 variants. Mononuclear cells from lung tissue were collected 14 days post-infection. Bars represent means ± SEM. Data were analyzed by Student's *t*-test. Results were considered statistically significant at $p < 0.05$.

infected with USA-WA1/2020 (Vaccinated = 3.4% vs. Mock = 3.1%, $p = 0.4004$), Alpha (B.1.1.7) (Vaccinated = 5.4% vs. Mock = 2.5%, $p = 0.0160$), Beta (B.1.351) (Vaccinated = 6.6% vs. Mock = 2.1%, $p = 0.0420$), Gamma (P.1) (Vaccinated = 11.1% vs. Mock = 9.2%, $p = 0.9961$), Delta (B.1.617.2) (Vaccinated = 7.1% vs. Mock = 1.5%, $p < 0.0001$), and Omicron (B.1.1.529) (Vaccinated = 8.5% vs. Mock = 5%, $p = 0.0139$) (Figure 4C).

Moreover, in context to memory $CD4^+$ T_{EM} ($CD44^+CD62L^-$) cell subset, relatively higher frequencies were observed for immunized mice subjected to infection with SARS-CoV-2 variants USA-WA1/2020 (Vaccinated = 15.4% vs. Mock = 8.3%, $p = 0.0001$), Alpha (B.1.1.7) (Vaccinated = 12.3% vs. Mock = 8.7%, $p < 0.0001$), and Beta (B.1.351) (Vaccinated = 6.8% vs. Mock = 6%, $p < 0.0004$) (Figure 4D). Generally higher frequencies of the $CD4^+$ T_{RM} ($CD69^+CD103^+$) cell subset were found in immunized mice infected with SARS-CoV-2 variants Alpha (B.1.1.7) (Vaccinated = 5.2% vs. Mock = 4%, $p = 0.0828$), Beta (B.1.351) (Vaccinated = 10% vs. Mock = 4%, $p = 0.005$), Gamma (P.1) (Vaccinated = 15.4% vs. Mock = 13.1%, $p = 0.7860$), Delta (B.1.617.2) (Vaccinated = 8.9% vs. Mock = 3.5%, $p < 0.0001$), and Omicron (B.1.1.529) (Vaccinated = 10.3% vs. Mock = 5.1%, $p = 0.0021$) (Figure 4D).

These findings suggest that immunization with the pan-variant SARS-CoV-2 vaccine bearing conserved epitopes induced high frequencies of functional $CD8^+$ and $CD4^+$ T_{EM} and T_{RM} cells that infiltrated the lungs, and were associated with a significant decrease in virus replication and reduction in COVID-19-related lung pathology following infection with various multiple SARS-CoV-2 variants.

Increased SARS-CoV-2 epitopes-specific IFN-γ-producing $CD8^+$ T cells in the lungs of vaccinated mice in comparison to mock-vaccinated mice

To determine whether the functional lung-resident $CD8^+$ T cells are specific to SARS-CoV-2, we stimulated lung-cell suspension from vaccinated and mock-vaccinated mice with each of the 14 "universal" human $CD8^+$ T- cell epitopes ($ORF1ab_{2210-2218}$, $ORF1ab_{3013-3021}$, $ORF1ab_{4283-4291}$, $ORF1ab_{6749-6757}$, $ORF6_{3-11}$, $ORF7b_{26-34}$, $ORF10_{3-11}$, $ORF10_{5-13}$, $S_{958-966}$, $S_{1000-1008}$, $S_{1220-1228}$, E_{20-28}, M_{52-60}, and M_{89-97}) and quantified the number of IFN-γ-producing $CD8^+$ T cells using ELISpot, as detailed in *Materials and methods* (Figure 5). To determine whether cross-reactive IFN-γ-producing $CD8^+$ T- cell responses will be detected regardless of SARS-CoC-2 variant, the number IFN-γ-producing $CD8^+$ T cells

were determined in the lung tissues of vaccinated and mock-vaccinated mice after challenge with each of six different SARS-CoV-2 variants of concern.

Overall, a significant increase in the number of IFN-γ-producing $CD8^+$ T cells was detected in the lungs of protected mice that received the pan-variant SARS-CoV-2 vaccine compared to non-protected mock-vaccinated mice (mean SFCs > 25 per 0.5 × 10^6 pulmonary immune cells), irrespective of the SARS-CoV-2 variants of concern: WA/USA2020 (Figure 5A), Alpha (B.1.1.7) (Figure 5B), Beta (B.1.351) (Figure 5C), Gamma (P.1) (Figure 5D), Delta (B.1.617.2) (Figure 5E), or Omicron (B.1.1.529) (Figure 5F). All the comparisons among vaccinated and mock-vaccinated groups of mice, irrespective of SARS-CoV-2 variants of concern, were found to be statistically significant regardless of whether $CD8^+$ T-cell targeted epitopes were from structural (Spike, Envelope, and Membrane) or non-structural (ORF1ab, ORF6, ORF7b, and ORF10) SARS-CoV-2 protein antigens ($p < 0.5$).

Taken together, these results (1) confirm that immunization with the pan-variant SARS-CoV-2 vaccine bearing conserved epitopes induced high frequencies of functional $CD8^+$ T cells that infiltrated the lungs and were associated with cross-protection against multiple SARS-CoV-2 variants; (2) demonstrate that increased SARS-CoV-2 epitope-specific IFN-γ-producing $CD8^+$ T cells in the lungs of vaccinated triple transgenic HLA-A*02:01/HLA-DRB1*01:01-hACE-2 mice were associated with protection from multiple variants of concern. In contrast, low frequencies of lung-resident SARS-CoV-2-specific IFN-γ-producing $CD8^+$ T cells were associated with severe disease onset in mock-vaccinated triple transgenic HLA-A*02:01/HLA-DRB1*01:01-hACE-2 mice. In this report, we suggest an important role for functional lung-resident SARS-CoV-2-specific $CD8^+$ T cells specific to highly conserved "universal" epitopes from structural and non-structural antigens in cross-protection against SARS-CoV-2 VOCs.

Increased SARS-CoV-2 epitopes-specific IFN-γ-producing $CD4^+$ T cells in the lungs of vaccinated mice in comparison to mock-vaccinated mice

We stimulated lung-cell suspension from vaccinated and mock-vaccinated groups of mice with each of the six "universal" human $CD4^+$ T- cell epitopes ($ORF1a_{1350–1365}$, $ORF6_{12–26}$, $ORF8b_{1–15}$, $S_{1–13}$, $M_{176–190}$, and $N_{388–403}$) and quantified the number of IFN-γ-

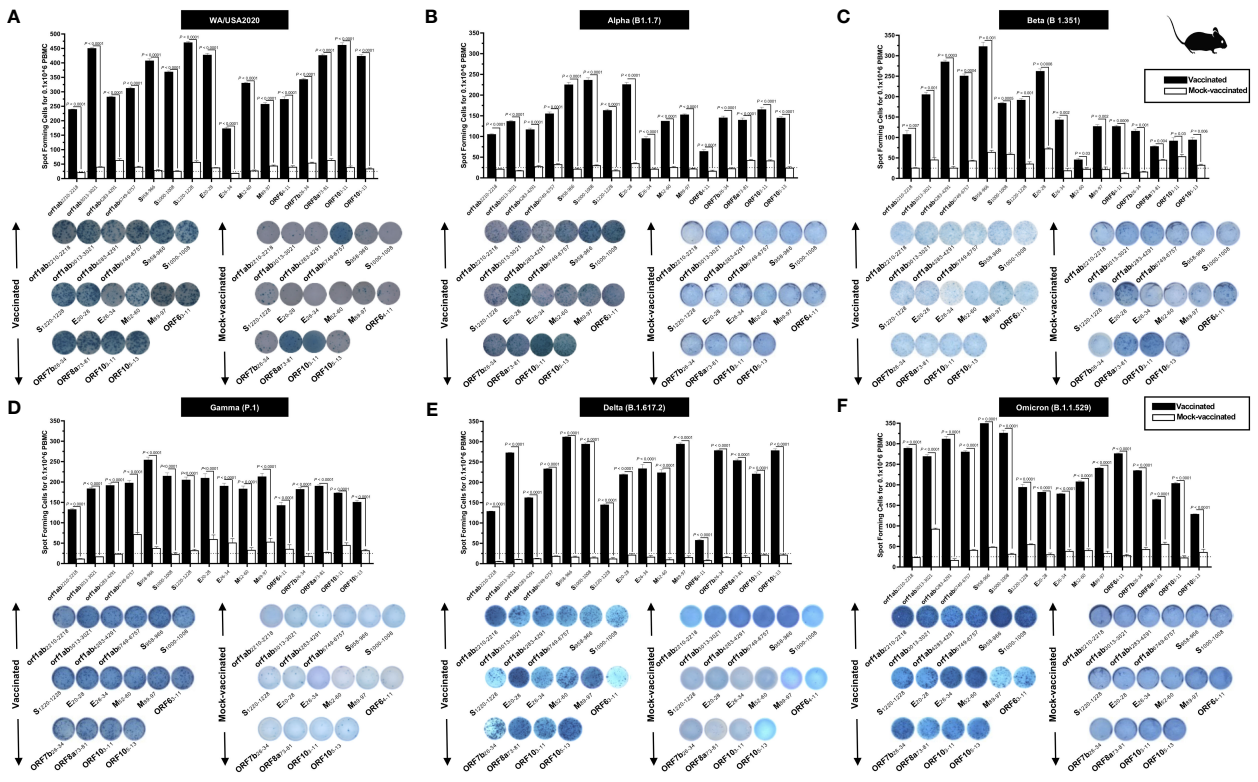

FIGURE 5
Immunogenicity of conserved SARS-CoV-2 $CD8^+$ T- cell epitopes in triple transgenic HLA-A*02:01/HLA-DRB1*01:01-hACE-2 mice: ELISpot images and bar diagrams showing average frequencies of IFN-γ- producing cell spots from mononuclear cells from lung tissue (1 × 10^6 cells per well) of vaccinated and mock-vaccinated mice challenged with **(A)** WA/USA2020, **(B)** Alpha (B.1.1.7), **(C)** Beta (B.1.351), **(D)** Gamma (P.1), **(E)** Delta (B.1.617.2), and **(F)** Omicron (B.1.1.529). Mononuclear cells from lung tissue were collected 14 days post- infection. The cells were stimulated for 48 h with 10 mM of 16 immunodominant $CD8^+$ T- cell peptides. The bar diagrams show the average/mean numbers (± SD) of IFN-γ-spot forming cells (SFCs) after $CD8^+$ T- cell peptide stimulation in lung tissues of vaccinated and mock-vaccinated mice. Dotted lines represent an arbitrary threshold set to evaluate the relative magnitude of the response. A strong response is defined for mean SFCs > 25 per 1 × 10^6 stimulated PBMCs. Results were considered statistically significant at $p < 0.05$.

producing CD4$^+$ T cells using ELISpot, to determine whether the functional lung-resident CD4$^+$ T cells are specific to SARS-CoV-2 (Figure 6).

Overall, we detected a significant increase in the number of IFN-γ-producing CD4$^+$ T cells in the lungs of protected mice that received the pan-variant SARS-CoV-2 vaccine compared to non-protected mock-vaccinated mice (mean SFCs > 25 per 0.5 × 10^6 pulmonary immune cells), irrespective of the SARS-CoV-2 VOCs: WA/USA2020 (Figure 6A), Alpha (B.1.1.7) (Figure 6B), Beta (B.1.351) (Figure 6C), Gamma (P.1) (Figure 6D), Delta (B.1.617.2) (Figure 6E), or Omicron (B.1.1.529) (Figure 6F). All the comparisons among vaccinated and mock-vaccinated groups of mice, irrespective of SARS-CoV-2 VOCs, were statistically significant regardless of whether CD4$^+$ T-cell targeted epitopes were from structural or non-structural SARS-CoV-2 protein antigens ($p < 0.5$).

Taken together, our findings demonstrate that increased SARS-CoV-2 epitopes-specific IFN-γ-producing CD4$^+$ T cells in the lungs of vaccinated triple transgenic HLA-A*02:01/HLA-DRB1*01:01-hACE-2 mice were associated with protection against multiple variants of concern. In contrast, low frequencies of lung-resident SARS-CoV-2-specific IFN-γ-producing CD4$^+$ T cells were associated with severe disease onset in mock-vaccinated triple transgenic HLA-A*02:01/HLA-DRB1*01:01-hACE-2 mice. The findings suggest an important role of functional lung-resident SARS-CoV-2-specific CD4$^+$ T cells specific to highly conserved "universal" epitopes from structural and non-structural antigens in cross-protection against SARS-CoV-2 VOCs.

Universal B- cell epitopes from SARS-CoV-2 Spike protein showed a high degree of immunogenicity across SARS-CoV-2 variants based on antibody response in COVID-19 patients and triple transgenic HLA-A*02:01/HLA-DRB1*01:01-hACE-2

We next determined whether the antibody responses were associated with protection, since the prototype pan-variant SARS-CoV-2 vaccine used herein also contains nine conserved B- cell epitopes selected from the Spike glycoprotein of SARS-CoV-2. The nine B-cell epitopes were screened for their conservancy against variants, namely, h-CoV-2/Wuhan (MN908947.3), h-CoV-2/WA/USA2020 (OQ294668.1), h-CoV-2/Alpha (B1.1.7) (OL689430.1), h-CoV-2/Beta (B 1.351) (MZ314998), h-CoV-2/Gamma (P.1) (MZ427312.1), h-CoV-2/Delta (B.1.617.2) (OK091006.1), and h-CoV-2/Omicron (B.1.1.529) (OM570283.1). We observed 100% conservancy in three of our earlier predicted B- cell epitopes, namely, $S_{287–317}$, $S_{524–558}$, and $S_{565–598}$ (Supplementary Figure S3).

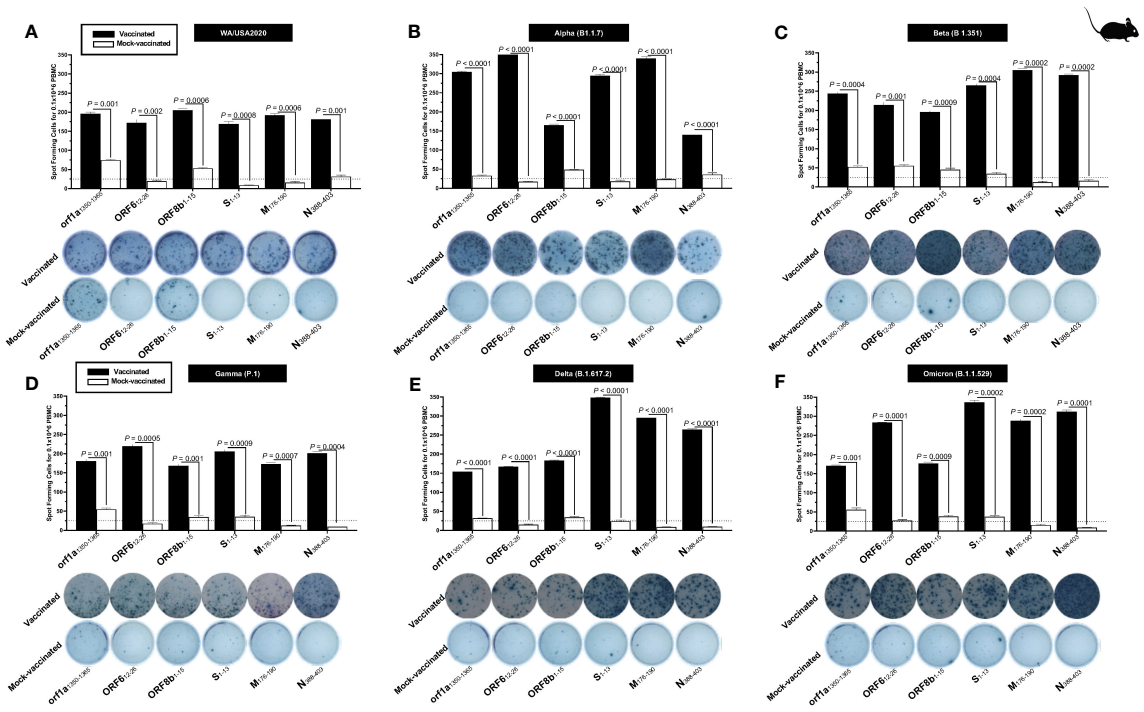

FIGURE 6
The magnitude of the IFN-γ CD4$^+$ T- cell responses for six conserved SARS-CoV-2 CD4$^+$ T- cell epitopes in triple transgenic HLA-A*02:01/HLA-DRB1*01:01-hACE-2 mice: ELISpot images and bar diagrams showing average frequencies of IFN-γ producing cell spots from mononuclear cells from lung tissue (1 × 10^6 cells per well) of vaccinated and mock-vaccinated mice challenged with **(A)** WA/USA2020, **(B)** Alpha (B.1.1.7), **(C)** Beta (B.1.351), **(D)** Gamma (P.1), **(E)** Delta (B.1.617.2), and **(F)** Omicron (B.1.1.529). Mononuclear cells from lung tissue were collected 14 days post-infection. Cells were stimulated for 48 h with 10 mM of six immunodominant CD4$^+$ T- cell peptides derived from SARS-CoV-2 structural (Spike, Envelope, and Membrane) and non-structural (orf1ab, ORF6, ORF7b, ORF8a, and ORF10) proteins. The bar diagrams show the average/mean numbers (± SD) of IFN-γ-spot forming cells (SFCs) after CD8$^+$ T- cell peptide stimulation in lung tissues of vaccinated and mock-vaccinated mice. The dotted lines represent an arbitrary threshold set to evaluate the relative magnitude of the response. A strong response is defined for mean SFCs > 25 per 1 × 10^6 stimulated PBMCs. Results were considered statistically significant at $p \leq 0.05$.

The antibody titer specific to each of the nine "universal" B-cell epitopes was determined by ELISA in COVID-19 patients infected with multiple SARS-CoV-2 variants of concern (Supplementary Figure S4, left panel) and in vaccinated and mock-vaccinated triple transgenic HLA-A*02:01/HLA-DRB1*01:01-hACE-2 mice challenged with same SARS-CoV-2 VOCs (Supplementary Figure S4, right panel). The peptide binding IgG level was significantly higher for all nine "universal" B cell epitopes in COVID-19 patients (Supplementary Figure S4, left panel) and in vaccinated triple transgenic mice (Supplementary Figure S4, right panel), irrespective of SARS-CoV-2 variant. Reduced peptide binding IgG level was observed for severely ill COVID-19 patients (Supplementary Figure S4, left panel) and in mock-vaccinated triple transgenic HLA-A*02:01/HLA-DRB1*01:01-hACE-2 mice (Supplementary Figure S4, right panel).

Altogether, these results indicate that immunization with the pan-variant SARS-CoV-2 vaccine bearing conserved "universal" B- and T- cell epitope induced cross-protective antibodies, $CD8^+$ and $CD4^+$ T cells that infiltrated the lungs, facilitate virus clearance, and reduced COVID-19-related lung pathology following infection with various multiple SARS-CoV-2 VOCs.

Discussion

COVID-19 remains a serious threat with continued high rates of morbidity and mortality worldwide. The ongoing emergence of SARS-CoV-2 variants and sub-variants of concern, including the recent heavily mutated and highly transmissible Omicron sub-variants, has led to vaccine breakthroughs that have contributed to prolonging the COVID-19 pandemic. Current Spike-based COVID-19 vaccines have made a substantial impact on the severity of the pandemic. Neutralizing antibody titers induced by current Spike-based vaccines are less effective against recent variants and sub-variants (41, 42), pointing to the urgent need to develop a next-generation B- and T-cell-based pan-variant SAS-CoV-2 vaccine–coronavirus vaccine that would be based not only on Spike protein but also on less-mutated non-Spike structural and non-structural antigens and epitopes. Such a universal CoV vaccine could induce broader and more durable protective immunity against infections and diseases caused by multiple emerging SARS-CoV-2 variants and sub-variants.

Much of the data on the efficacy of the current modified messenger RNA (mRNA) vaccines has shown that these vaccines elicited lower levels of neutralizing antibodies against newer SARS-CoV-2 variants than against the older variants (41). In the present report, we have identified "universal" $CD8^+$ and $CD4^+$ T- and B-cell epitopes conserved among all known SARS-CoV-2 variants, previous SARS and MERS coronavirus strains, and strains specific to different species that were reported to be hosts for SARS/MERS (bat, civet cat, pangolin, and camel). We used a combination of these highly conserved CD8+ and CD4+ T- and B- cell epitopes to design a multi-epitope pan-variant SARS-CoV-2 vaccine. The T- cell epitopes that constitute this pan-variant SARS-CoV-2 vaccine represent structural (Spike, Envelope, Membrane, and Nucleocapsid) and non-structural (orf1ab, ORF6, ORF7, ORF8, and ORF10) proteins.

We demonstrated that immunization of triple transgenic h-ACE-2-HLA-A2/DR mice with a pool of "universal" $CD8^+$ T-cell, $CD4^+$ T- cell, and B- cell peptides conferred protection against Washington, Alpha (B.1.1.7), Beta (B.1.351), Gamma (P.1), Delta (B.1.617.2), and Omicron (B.1.1.529) variants of SARS-CoV-2. The pan-variant SARS-CoV-2 vaccine was found to be safe, as no local or systemic side effects were observed in the vaccinated mice. Moreover, we found that the protection correlated with high frequencies of IFN-γ $CD4^+$ T cells, CD69 $CD4^+$ T cells, IFN-γ CD8+ T cells, and CD69 CD8+ T cells infuriating the lungs. We also found higher frequencies for the $CD8^+$ T_{EM} ($CD44^+CD62L^-$) cell population in the lungs of protected mice. High levels of peptide-specific IgG were also detected in protected animals, suggesting the contribution of Spike-specific antibodies in protection. A marked difference in the level of neutralizing viral titer was also observed between the vaccinated and mock-vaccinated groups of mice for all the studied variants. We observed no mortality in the vaccinated mice, irrespective of the SARS-CoV-2 variant. In contrast, high mortality was observed in the mock-vaccinated mice when challenged with six SARS-CoV-2 variants. The weight loss and survival shown in this study agree with previous reports in the context to Omicron B.1.1.529 infection in the mouse models (43). Limited weight loss and less virus replication were reported for Omicron B.1.1.529 in 129, C57BL/6, BALB/c, and K18-hACE2 transgenic mice models in comparison to other SARS-CoV-2 variants of concern, such as Alpha (B.1.1.7), Beta (B.1.351), and Delta (B.1.617.2) (43). Moreover, like mouse models, in both wild-type and hACE2 hamsters, a similar trend of milder lung infection, clinical disease, and pathology was observed using the B.1.1.519 variant of Omicron (43). Liu et al. have compared T- cell responses in subjects who received either mRNA or adenovirus-vectored vaccine (44). Both vaccines induced substantial spike-specific IFN-γ-producing $CD8^+$ and $CD4^+$ T cells, which showed similar reactivity against Wuhan, Delta, and Omicron variants (44). In addition, their findings showed that central and effector memory T-cell subsets cross-reacted with Delta and Omicron variants (44). Similarly, in the present study, we showed a significant increase in the frequency of IFN-γ-producing $CD8^+$ and $CD4^+$ T cells detected in the lungs of protected mice that received the pan-variant SARS-CoV-2 vaccine compared to non-protected mock-vaccinated mice. Overall, the vaccine was safe and immunogenic and provided cross-protection against multiple SARS-CoV-2 VOCs.

Interestingly, several earlier studies have performed epitope profiling in the existing COVID-19 mRNA vaccines (45, 46). One such study has mapped immunogenic amino acid motifs and linear epitopes of primary sequence of SARS-CoV-2 spike protein that induce IgG in recipients of PfizerBioNTech COVID-19 mRNA vaccine (45). The obtained data identified various distinctive amino acid motifs recognized by vaccine-elicited IgG, a subset of those recognized by IgG from natural infection (hospitalized COVID-19 patients), which can mimic three-dimensional conformation (mimotopes). The identified dominant linear epitopes in the C-terminal region of the spike protein are identical with those of SARS-CoV, bat coronavirus, and epitopes that trigger IgG during natural infection, but have limited homology to spike protein of non-pathogenic human coronavirus (45). In another study, high-

resolution linear epitope profiling of recipients of Pfizer-BioNTech COVID-19 mRNA vaccine and COVID-19 patients was performed and found that vaccine-induced antibodies targeting viral spike RBD have a broader distribution across RBD than natural infection-induced antibodies (46). Moreover, mutation panel assays targeting the viral variants of concern demonstrated that the epitope variety induced by mRNA vaccine is rich in breadth, thus can grant resistance against viral evolutionary escapes in the future, which represents an advantage of vaccine-induced immunity (46). The identified epitopes in COVID-19 mRNA vaccine may form the basis for further research of immune escape, viral variants, and design of vaccine and therapy.

The SARS-CoV-2 virus shares homology to some degree at the level of its sequence, structure, and function with that of SARS-CoV and MERS-CoV (47). Studies revealed that anti SARS-CoV spike antibodies possessed the ability to inhibit the binding of SARS-CoV-2 to ACE2 (48). Furthermore, unique features of the spike, including crucial functions in host receptor binding, conserved sequences, good immunogenicity for neutralizing antibody induction, and effective target for T- cell responses, promote the priority of the spike for COVID-19 vaccine development. As per the WHO, among the existing clinical COVID-19 vaccine candidates, 32% (55/172) were recombinant protein vaccines. RNA vaccines, viral vectored vaccines, and inactivated virus vaccines accounted for 23% (40/172), 13% (23/172), and 13% (22/172), respectively. Except for the inactivated vaccine, most vaccine candidates are constituted by variations in antigen fragments from the spike. In brief, the antigen fragments may contain full length spike, different lengths of RBD, or even synthesized peptides as engineered multiepitope to induce high neutralizing antibodies to neutralize viruses (49, 50). Therefore, mutations in the spike of several SARS-CoV-2 variants impaired the protective efficacy of COVID-19 vaccines that were developed based on the spike.

Several COVID-19 vaccines have been approved for use and exert adequate protection when wild- type SARS-CoV-2 was still prevalent. NVX-CoV2373 from Novavax is a protein subunit vaccine showing 89.3% efficacy against SARS-CoV-2 in a phase III trial operated in United Kingdom (51). BNT162b2 from Pfizer-BioNTech and mRNA-1273 from Moderna are messenger RNA (mRNA) vaccines, showing 95% and 93.2% efficacy in preventing COVID-19 (28, 52). The adenovirus vector vaccine ChAdOx1 (AZD1222) also shows 90% efficacy if vaccinated at a low dose followed by a standard dose (53). In addition, the viral vectored and inactivated virus vaccines also exhibited effective protection against COVID-19 (53–55). However, these vaccine candidates are designed based on wild- type SARS-CoV-2, and the vaccine effectiveness against SARS-CoV-2 variants is of particular concern.

The effectiveness of the COVID-19 vaccine against Delta and Omicron variant transmission is a great concern. The effectiveness of BNT162b2 or mRNA-1273 vaccines in preventing contact transmission of Delta is reportedly between 9% and 38%. Even if fully vaccinated, the effectiveness is 27%–65% (56). The effectiveness of the ChAdOx1 vaccine against Delta transmission is 36%–42% (57). Notably, the protection of full vaccination against Omicron infection of close contacts was significantly reduced compared to that of Delta. The effectiveness of vaccination with COVID-19 mRNA vaccines against contact transmission decreased to 22.5% (58). These results indicate that physical protection, such as wearing a mask, is still necessary.

While looking at the effectiveness of currently authorized COVID-19 vaccines against symptomatic infection, hospitalization, and death induced by SARS-CoV-2 Alpha, Beta, Gamma, Delta, and Omicron variants, a decline in vaccine effectiveness was observed. The vaccine efficacy decreased to a different degree for each COVID-19 vaccine, even after full vaccination, especially for the protection of documented infection (59–63). The protective efficacy of the Novavax NVX-CoV2373 subunit vaccine declined from 89.3% to 49.4% in the clinical studies carried out in South Africa, where the Beta variant is prevalent (64). The effectiveness of the inactivated vaccine CoronaVac produced by Sinovac decreased to approximately 50% against symptomatic infection with the Gamma variant (65). BNT162b2 was reported with 95% efficacy against wild type in the clinical trial. However, in Qatar, the effectiveness of the BNT162b2 vaccine was reduced by approximately 20% against the Beta variant as detected 14 days after the second dose of vaccination (66). This is consistent with the speculation that the E484K mutation affects the efficacy of the BNT162b2 vaccine (67). Similarly, the efficacy of the ChAdOx1 chimpanzee adenoviral vector vaccine decreased to 10.4% against Beta variant (68). Other studies reported that the efficacy of one dose of the BNT162b2 vaccine was 33.5% and 51.1% against the Delta and Alpha variants, respectively (69). The ChAdOx1 vaccine also showed significant differences after one- or two-dose vaccinations against the Delta and Alpha variants. After the second dose, the efficacy elevated from 51.4% to 66.1% against the Alpha variant, while the protective efficacy increased from 32.9% to 59.8% against the Delta variant (70). In case of the Omicron variant, a marked reduction in the efficacy of most approved vaccines was observed. The antibody- neutralizing titers against Omicron in the serum collected from individuals with two doses of BNT162b2 were decreased more than 22- fold compared with that of the ancestor (71, 72). In addition, the sera from individuals fully vaccinated with ChAdOx1 vaccines could barely neutralize the Omicron variant (71). Later, several Omicron spike-specific vaccines were constructed. The results showed that boosting with mRNA-1273 had higher neutralizing antibody titers against Omicron than boosting with mRNA-Omicron (73).

Meanwhile, the Omicron S1 recombinant protein vaccine elicited a significantly weaker T-cell response compared to the prototype S1-based recombinant protein vaccine candidate (74), which indicates that the Omicron S1 subunit may not be an appropriate selection for developing specific vaccines against Omicron- included SARS-CoV-2 variants. Some other studies found that mRNA vaccines containing several pivotal mutations of the Omicron and Delta spike could elicit high neutralizing antibodies against the Omicron variant (75), suggesting the consideration of the essential mutations of SARS-CoV-2 virus spike, not limited to the currently prevalent VOCs. Taken together, the ongoing pandemic of SARS-CoV-2 variants calls for continuous surveillance of vaccine efficacy against emerging mutations, which is an extremely important factor for vaccine optimization.

In this context, universal pan-variant vaccines generating T- and B- cell-mediated immunity like that of ours will be of crucial help. Such vaccines could induce strong humoral and cellular immunity against several viruses. On the one hand, B cells are activated upon recognizing antigens with B- cell receptors (BCRs) and further differentiate into memory B cells or plasma cells that can produce antigen-specific antibodies. Th2 cells help in B- cell activation by secreting cytokines such as IL 4 and IL-5. The induced neutralizing antibodies can block viral infection at the initial stage. On the other hand, antigens from the combined vaccine are taken up, processed, and presented to $CD4^+$ and $CD8^+$ T cells by antigen-presenting cells (APCs) through MHCII and MHCI antigen complexes, respectively. Then, $CD4^+$ T cells are activated and can differentiate toward Th1, Th2, and memory $CD4^+$ T cells. Th1 cells also promote the activation of $CD8^+$ T cells by generating cytokines such as IFN-γ, IFN-β, and IL-2. Activated $CD8^+$ T cells can differentiate into effector and memory $CD8^+$ T cells. The effector $CD8^+$ T cells could kill and lyse infected cells by releasing cytokines, including IFN-γ.

Furthermore, the cross-reactive SARS-CoV-2-specific memory $CD4^+$ and $CD8^+$ T cells are present in up to 50% of unexposed, pre-pandemic, healthy individuals (UPPHI). However, the characteristics of cross-reactive memory $CD4^+$ and $CD8^+$ T cells associated with subsequent protection of asymptomatic COVID-19 patients (i.e., unvaccinated individuals who never develop any COVID-19 symptoms despite being infected with SARS-CoV-2) remains to be fully elucidated. Studies from our group and others have detected cross-reactive $CD4^+$ and $CD8^+$ T cells, directed toward specific sets of conserved SARS-CoV-2 epitopes, not only from unvaccinated COVID-19 patients but also from a significant proportion of unexposed pre-pandemic healthy individuals (UPPHI) who were never exposed to SARS-CoV-2 (33, 50, 76, 77). Cross-reactive SARS-CoV-2-specific memory $CD4^+$ and $CD8^+$ T cells are not only present in COVID-19 patients but also in up to 50% of UPPHI (50, 77–83). Moreover, pre-existing common cold coronavirus (CCCs)/SARS-CoV-2 cross-reactive memory $CD4^+$ and $CD8^+$ T cells are present in unvaccinated UPPHI who were never exposed to SARS-CoV-2 (33, 50, 76, 77, 84–89). These data suggest the presence of clones of memory $CD4^+$ and $CD8^+$ T cells in UPPHI induced following previous exposures with seasonal CCCs that cross-recognize conserved SARS-CoV-2 and CCCs epitopes (77, 90, 91). However, it is not yet known whether these cross-reactive memory $CD4^+$ and $CD8^+$ T cells: (i) preferentially cross-recognize the alpha CCCs (i.e., α-CCC-229E and α-CCC-NL63) or the beta CCCs (i.e., β-CCC-HKU1 and β-CCC-OC43); and (ii) the antigen-specificity, frequency, phenotype, and function of the cross-reactive memory $CD4^+$ and $CD8^+$ T cells associated with protection against COVID-19 severity in unvaccinated asymptomatic patients. Compared with unvaccinated severely ill COVID-19 patients and unvaccinated patients with fatal COVID-19 outcomes, unvaccinated asymptomatic COVID-19 patients displayed significantly (i) higher rate of the α-CCC strain 229E (α-CCC-229E); (ii) higher frequencies of functional memory $CD134^+CD137^+CD4^+$ and $CD134^+CD137^+CD8^+$ T cells directed toward cross-reactive α-CCCs/SARS-CoV-2 epitopes from structural, non-structural, and regulatory proteins; and (iii) lower frequencies of cross-reactive exhausted $PD\text{-}1^+TIM3^+TIGIT^+CTLA4^+CD4^+$ and $PD\text{-}1^+TIM3^+TIGIT^+CTLA4^+CD8^+$ T cells. These findings (i) support a crucial role of functional, poly-antigenic α-CCCs/SARS-CoV-2 cross-reactive memory $CD4^+$ and $CD8^+$ T cells, induced following previous exposures to α-CCC strains, in protection against subsequent severe disease caused by SARS-CoV-2 infection; and (ii) provides a strong rationale for the development of broadly protective, T-cell-based, multi-antigen universal pan- coronavirus vaccines.

Since the B- and T- cell epitopes used in this study are highly conserved between SARS-CoV-1 and MERS-CoV, it is likely that protection will be observed against these strains as well. However, providing direct evidence of protection induced by our multi-epitope vaccine against SARS-CoV-1 and MERS-CoV would require (i) generating a new DPP4/HLA-DR0101/HLA-A*0201 triple transgenic mouse model that needs backcrossing the DPP4 transgenic mice with our HLA-DR0101/HLA-A*0201 double transgenic mice, a process that is time consumable, as it will take several months to establish; and (ii) extensive *in vivo* and *in vitro* studies. Hence, demonstration of the breadth of protection induced by our multi-epitope vaccine against SARS-CoV-1 and MERS-CoV will be the subject of future independent reports in continuation to the existing study.

In conclusion, we report that a CoV vaccine targeting conserved B- and T- cell epitopes was safe, immunogenic, and provided cross-protection against six SARS-CoV-2 variants of concern, supporting the next-generation vaccine strategy.

Data availability statement

The original contributions presented in the study are included in the article/Supplementary Material. Further inquiries can be directed to the corresponding author.

Ethics statement

The studies involving humans were approved by University of California Irvine IRB committee. The studies were conducted in accordance with the local legislation and institutional requirements. The participants provided their written informed consent to participate in this study. The animal study was approved by The University of California-Irvine conformed to the Guide for the Care and Use of Laboratory Animals published by the US National Institute of Health (IACUC protocol # AUP-22-086). The study was conducted in accordance with the local legislation and institutional requirements.

Author contributions

SP: Conceptualization, Data curation, Formal analysis, Investigation, Methodology, Project administration, Validation, Visualization, Writing – original draft, Writing – review & editing, Software. ND: Data curation, Formal analysis, Methodology, Project administration, Writing – original draft. LZ: Data curation, Formal analysis, Methodology, Project

administration, Writing – original draft. II: Data curation, Writing – original draft. AQ: Data curation, Methodology, Formal analysis, Writing – original draft. PC: Data curation, Formal analysis, Methodology, Conceptualization, Investigation, Software, Validation, Writing – original draft. DT: Data curation, Writing – original draft. BS: Data curation, Writing – original draft. AS: Data curation, Writing – original draft. AC: Data curation, Writing – original draft. RE: Data curation, Writing – original draft. MS: Data curation, Methodology, Writing – original draft. HV: Data curation, Methodology, Writing – original draft. AN: Writing – original draft. BK: Writing – original draft. JU: Conceptualization, Writing – original draft. DG: Conceptualization, Writing – original draft. TJ: Conceptualization, Writing – original draft. LB: Conceptualization, Data curation, Formal analysis, Funding acquisition, Investigation, Methodology, Project administration, Resources, Validation, Visualization, Writing – original draft, Writing – review & editing.

Funding

The author(s) declare financial support was received for the research, authorship, and/or publication of this article. This work is supported by the Fast-Grant PR12501 from Emergent Ventures, by a Gavin Herbert Eye Institute internal grant, by Public Health Service Research grants AI158060, AI174383, AI150091, AI143348, AI147499, AI143326, AI138764, AI124911, and AI110902 from the National Institutes of Allergy and Infectious Diseases (NIAID) to LB.

Conflict of interest

LB has an equity interest in TechImmune, LLC., a company that may potentially benefit from the research results and serves on the company's Scientific Advisory Board. LB's relationship with TechImmune, LLC., has been reviewed and approved by the University of California, Irvine by its conflict-of-interest policies. Authors, HV, JU, DG, TJ were employed by TechImmune, LLC.

The remaining authors declare that the research was conducted in the absence of any commercial or financial relationships that could be construed as a potential conflict of interest.

The author(s) declared that they were an editorial board member of Frontiers, at the time of submission. This had no impact on the peer review process and the final decision.

Publisher's note

Supplementary material

The Supplementary Material for this article can be found online at: https://www.frontiersin.org/articles/10.3389/fimmu.2024.1328905/full#supplementary-material

References

1. Zheng C, Shao W, Chen X, Zhang B, Wang G, Zhang W. Real-world effectiveness of COVID-19 vaccines: a literature review and meta-analysis. *Int J Infect Dis* (2022) 114:252–60. doi: 10.1016/j.ijid.2021.11.009

2. Planas D, Bruel T, Grzelak L, Guivel-Benhassine F, Staropoli I, Porrot F, et al. Sensitivity of infectious SARS-CoV-2 B.1.1.7 and B.1.351 variants to neutralizing antibodies. *Nat Med* (2021) 27(5):917–24.

3. Washington NL, Gangavarapu K, Zeller M, Bolze A, Cirulli ET, Schiabor Barrett KM, et al. Emergence and rapid transmission of SARS-CoV-2 B.1.1.7 in the United States. *Cell* (2021) 184(10):2587–94 e7. doi: 10.1016/j.cell.2021.03.052

4. Burki TK. Omicron variant and booster COVID-19 vaccines. *Lancet Respir Med* (2022) 10(2):e17. doi: 10.1016/S2213-2600(21)00559-2

5. Liu L, Iketani S, Guo Y, Chan JF, Wang M, Liu L, et al. Striking antibody evasion manifested by the Omicron variant of SARS-CoV-2. *Nature* (2022) 602(7898):676–81. doi: 10.1038/s41586-021-04388-0

6. Konings F, Perkins MD, Kuhn JH, Pallen MJ, Alm EJ, Archer BN, et al. SARS-CoV-2 Variants of Interest and Concern naming scheme conducive for global discourse. *Nat Microbiol* (2021) 6(7):821–3. doi: 10.1038/s41564-021-00932-w

7. Harvey WT, Carabelli AM, Jackson B, Gupta RK, Thomson EC, Harrison EM, et al. SARS-CoV-2 variants, spike mutations and immune escape. *Nat Rev Microbiol* (2021) 19(7):409–24. doi: 10.1038/s41579-021-00573-0

8. Focosi D, Quiroga R, McConnell S, Johnson MC, Casadevall A. Convergent evolution in SARS-CoV-2 spike creates a variant soup from which new COVID-19 waves emerge. *Int J Mol Sci* (2023) 24(3). doi: 10.3390/ijms24032264

9. Hvidt AK, Baerends EAM, Sogaard OS, Staerke NB, Raben D, Reekie J, et al. Comparison of vaccine-induced antibody neutralization against SARS-CoV-2 variants of concern following primary and booster doses of COVID-19 vaccines. *Front Med (Lausanne)* (2022) 9:994160. doi: 10.3389/fmed.2022.994160

10. Hawman DW, Meade-White K, Archer J, Leventhal SS, Wilson D, Shaia C, et al. SARS-CoV2 variant-specific replicating RNA vaccines protect from disease following challenge with heterologous variants of concern. *Elife* (2022) 11. doi: 10.7554/eLife.75537

11. Marks PW, Gruppuso PA, Adashi EY. Urgent need for next-generation COVID-19 vaccines. *JAMA* (2023) 329(1):19–20. doi: 10.1001/jama.2022.22759

12. Rubin EJ, Baden LR, Marks P, Morrissey S. Audio interview: the FDA and Covid-19 vaccines. *New Engl J Med* (2022) 387(20):e60. doi: 10.1056/NEJMe2209134

13. Tai W, Zhang X, Yang Y, Zhu J, Du L. Advances in mRNA and other vaccines against MERS-CoV. *Transl Res* (2022) 242:20–37. doi: 10.1016/j.trsl.2021.11.007

14. Alkhovsky S, Lenshin S, Romashin A, Vishnevskaya T, Vyshemirsky O, Bulycheva Y, et al. SARS-like coronaviruses in horseshoe bats (Rhinolophus spp.) in Russia, 2020. *Viruses* (2022) 14(1). doi: 10.3390/v14010113

15. Delaune D, Hul V, Karlsson EA, Hassanin A, Ou TP, Baidaliuk A, et al. A novel SARS-CoV-2 related coronavirus in bats from Cambodia. *Nat Commun* (2021) 12(1):6563. doi: 10.1038/s41467-021-26809-4

16. Zhou H, Ji J, Chen X, Bi Y, Li J, Wang Q, et al. Identification of novel bat coronaviruses sheds light on the evolutionary origins of SARS-CoV-2 and related viruses. *Cell* (2021) 184(17):4380–91 e14. doi: 10.1016/j.cell.2021.06.008

17. Wacharapluesadee S, Tan CW, Maneeorn P, Duengkae P, Zhu F, Joyjinda Y, et al. Evidence for SARS-CoV-2 related coronaviruses circulating in bats and pangolins in Southeast Asia. *Nat Commun* (2021) 12(1):972. doi: 10.1038/s41467-021-21240-1

18. Starr TN, Zepeda SK, Walls AC, Greaney AJ, Alkhovsky S, Veesler D, et al. ACE2 binding is an ancestral and evolvable trait of sarbecoviruses. *Nature* (2022) 603(7903):913–8. doi: 10.1038/s41586-022-04464-z

19. Letko M, Marzi A, Munster V. Functional assessment of cell entry and receptor usage for SARS-CoV-2 and other lineage B betacoronaviruses. *Nat Microbiol* (2020) 5(4):562–9. doi: 10.1038/s41564-020-0688-y

20. Abeywardhana S, Premathilaka M, Bandaranayake U, Perera D, Peiris LDC. In silico study of SARS-CoV-2 spike protein RBD and human ACE-2 affinity dynamics across variants and Omicron subvariants. *J Med Virol* (2023) 95(1):e28406. doi: 10.1002/jmv.28406

21. Solanki K, Rajpoot S, Kumar A, KY JZ, Ohishi T, Hirani N, et al. Structural analysis of spike proteins from SARS-CoV-2 variants of concern highlighting their functional alterations. *Future Virol* (2022). doi: 10.2217/fvl-2022-0003

22. Kumar S, Thambiraja TS, Karuppanan K, Subramaniam G. Omicron and Delta variant of SARS-CoV-2: A comparative computational study of spike protein. *J Med Virol* (2022) 94(4):1641–9. doi: 10.1002/jmv.27526

23. Sunagar R, Singh A, Kumar S. SARS-CoV-2: immunity, challenges with current vaccines, and a novel perspective on mucosal vaccines. *Vaccines (Basel)* (2023) 11(4). doi: 10.3390/vaccines11040849

24. Sharma S, Vercruysse T, Sanchez-Felipe L, Kerstens W, Rasulova M, Bervoets L, et al. Updated vaccine protects against SARS-CoV-2 variants including Omicron (B.1.1.529) and prevents transmission in hamsters. *Nat Commun* (2022) 13(1):6644.

25. Mallapaty S, Callaway E, Kozlov M, Ledford H, Pickrell J, Van Noorden R. How COVID vaccines shaped 2021 in eight powerful charts. *Nature* (2021) 600(7890):580–3. doi: 10.1038/d41586-021-03686-x

26. Tanriover MD, Doganay HL, Akova M, Guner HR, Azap A, Akhan S, et al. Efficacy and safety of an inactivated whole-virion SARS-CoV-2 vaccine (CoronaVac): interim results of a double-blind, randomised, placebo-controlled, phase 3 trial in Turkey. *Lancet* (2021) 398(10296):213–22. doi: 10.1016/S0140-6736(21)01429-X

27. Ella R, Reddy S, Blackwelder W, Potdar V, Yadav P, Sarangi V, et al. Efficacy, safety, and lot-to-lot immunogenicity of an inactivated SARS-CoV-2 vaccine (BBV152): interim results of a randomised, double-blind, controlled, phase 3 trial. *Lancet* (2021) 398(10317):2173–84. doi: 10.1016/S0140-6736(21)02000-6

28. Polack FP, Thomas SJ, Kitchin N, Absalon J, Gurtman A, Lockhart S, et al. Safety and efficacy of the BNT162b2 mRNA Covid-19 vaccine. *N Engl J Med* (2020) 383 (27):2603–15. doi: 10.1056/NEJMoa2034577

29. Baden LR, El Sahly HM, Essink B, Kotloff K, Frey S, Novak R, et al. Efficacy and safety of the mRNA-1273 SARS-CoV-2 vaccine. *N Engl J Med* (2021) 384(5):403–16. doi: 10.1056/NEJMoa2035389

30. Thiele T, Weisser K, Schonborn L, Funk MB, Weber G, Greinacher A, et al. Laboratory confirmed vaccine-induced immune thrombotic thrombocytopenia: Retrospective analysis of reported cases after vaccination with ChAdOx-1 nCoV-19 in Germany. *Lancet Reg Health Eur* (2022) 12:100270. doi: 10.1016/j.lanepe.2021.100270

31. Ghafouri F, Cohan RA, Noorbakhsh F, Samimi H, Haghpanah V. An in-silico approach to develop of a multi-epitope vaccine candidate against SARS-CoV-2 envelope (E) protein. *Res Sq* (2020). doi: 10.21203/rs.3.rs-30374/v1

32. Palatnik-de-Sousa CB. What would jenner and pasteur have done about COVID-19 coronavirus? The urges of a vaccinologist. *Front Immunol* (2020) 11:2173. doi: 10.3389/fimmu.2020.02173

33. Prakash S, Srivastava R, Coulon PG, Dhanushkodi NR, Chentoufi AA, Tifrea DF, et al. Genome-wide B cell, CD4(+), and CD8(+) T cell epitopes that are highly conserved between human and animal coronaviruses, identified from SARS-CoV-2 as targets for preemptive pan-coronavirus vaccines. *J Immunol* (2021) 206(11):2566–82. doi: 10.4049/jimmunol.2001438

34. Case JB, Bailey AL, Kim AS, Chen RE, Diamond MS. Growth, detection, quantification, and inactivation of SARS-CoV-2. *Virology* (2020) 548:39–48. doi: 10.1016/j.virol.2020.05.015

35. Gatz SA, Pohla H, Schendel DJ. A PCR-SSP method to specifically select HLA-A*0201 individuals for immunotherapeutic studies. *Tissue Antigens* (2000) 55(6):532–47. doi: 10.1034/j.1399-0039.2000.550604.x

36. Olerup O, Zetterquist H. HLA-DRB1*01 subtyping by allele-specific PCR amplification: a sensitive, specific and rapid technique. *Tissue Antigens* (1991) 37 (5):197–204. doi: 10.1111/j.1399-0039.1991.tb01872.x

37. Buchfink B, Reuter K, Drost HG. Sensitive protein alignments at tree-of-life scale using DIAMOND. *Nat Methods* (2021) 18(4):366–8. doi: 10.1038/s41592-021-01101-x

38. Wang H, Jean S, Eltringham R, Madison J, Snyder P, Tu H, et al. Mutation-specific SARS-CoV-2 PCR screen: rapid and accurate detection of variants of concern and the identification of a newly emerging variant with spike L452R mutation. *J Clin Microbiol* (2021) 59(8):e0092621. doi: 10.1128/JCM.00926-21

39. Coulon P-G, Prakash S, Dhanushkodi NR, Srivastava R, Zayou L, Tifrea DF, et al. High frequencies of PD-1+TIM3+TIGIT+CTLA4+ Functionally exhausted SARS-CoV-2-specific CD4+ and CD8+ T cells associated with severe disease in critically ill COVID-19 patients. *bioRxiv* (2022) 2022:01. doi: 10.1101/2022.01.30.478343

40. Dolton G, Tungatt K, Lloyd A, Bianchi V, Theaker SM, Trimby A, et al. More tricks with tetramers: a practical guide to staining T cells with peptide-MHC multimers. *Immunology* (2015) 146(1):11–22. doi: 10.1111/imm.12499

41. Duchene S, Featherstone L, Haritopoulou-Sinanidou M, Rambaut A, Lemey P, Baele G. Temporal signal and the phylodynamic threshold of SARS-CoV-2. *Virus Evol* (2020) 6(2):veaa061. doi: 10.1093/ve/veaa061

42. Rubin R. COVID-19 vaccines vs variants-determining how much immunity is enough. *JAMA* (2021) 325(13):1241–3. doi: 10.1001/jama.2021.3370

43. Halfmann PJ, Iida S, Iwatsuki-Horimoto K, Maemura T, Kiso M, Scheaffer SM, et al. SARS-CoV-2 Omicron virus causes attenuated disease in mice and hamsters. *Nature* (2022) 603(7902):687–92. doi: 10.1038/s41586-022-04441-6

44. Liu J, Chandrashekar A, Sellers D, Barrett J, Jacob-Dolan C, Lifton M, et al. Vaccines elicit highly conserved cellular immunity to SARS-CoV-2 Omicron. *Nature* (2022) 603(7901):493–6. doi: 10.1038/s41586-022-04465-y

45. Amanat F, Thapa M, Lei T, Ahmed SMS, Adelsberg DC, Carreno JM, et al. SARS-CoV-2 mRNA vaccination induces functionally diverse antibodies to NTD, RBD, and S2. *Cell* (2021) 184(15):3936–48.e10. doi: 10.1016/j.cell.2021.06.005

46. Nitahara Y, Nakagama Y, Kaku N, Candray K, Michimuko Y, Tshibangu-Kabamba E, et al. High-resolution linear epitope mapping of the receptor binding domain of SARS-CoV-2 spike protein in COVID-19 mRNA vaccine recipients. *Microbiol Spectr* (2021) 9(3):e0096521. doi: 10.1128/Spectrum.00965-21

47. Wu A, Peng Y, Huang B, Ding X, Wang X, Niu P, et al. Genome composition and divergence of the novel coronavirus (2019-nCoV) originating in China. *Cell Host Microbe* (2020) 27(3):325–8. doi: 10.1016/j.chom.2020.02.001

48. Salvatori G, Luberto L, Maffei M, Aurisicchio L, Roscilli G, Palombo F, et al. SARS-CoV-2 SPIKE PROTEIN: an optimal immunological target for vaccines. *J Transl Med* (2020) 18(1):222. doi: 10.1186/s12967-020-02392-y

49. Liang JG, Su D, Song TZ, Zeng Y, Huang W, Wu J, et al. S-Trimer, a COVID-19 subunit vaccine candidate, induces protective immunity in nonhuman primates. *Nat Commun* (2021) 12(1):1346. doi: 10.1038/s41467-021-21634-1

50. Nelde A, Bilich T, Heitmann JS, Maringer Y, Salih HR, Roerden M, et al. SARS-CoV-2-derived peptides define heterologous and COVID-19-induced T cell recognition. *Nat Immunol* (2021) 22(1):74–85. doi: 10.1038/s41590-020-00808-x

51. Cele S, Gazy I, Jackson L, Hwa SH, Tegally H, Lustig G, et al. Escape of SARS-CoV-2 501Y.V2 from neutralization by convalescent plasma. *Nature* (2021) 593(7857):142–6.

52. El Sahly HM, Baden LR, Essink B, Doblecki-Lewis S, Martin JM, Anderson EJ, et al. Efficacy of the mRNA-1273 SARS-CoV-2 Vaccine at Completion of Blinded Phase. *N Engl J Med* (2021) 385(19):1774–85. doi: 10.1056/NEJMoa2113017

53. Voysey M, Clemens SAC, Madhi SA, Weckx LY, Folegatti PM, Aley PK, et al. Safety and efficacy of the ChAdOx1 nCoV-19 vaccine (AZD1222) against SARS-CoV-2: an interim analysis of four randomised controlled trials in Brazil, South Africa, and the UK. *Lancet* (2021) 397(10269):99–111. doi: 10.1016/S0140-6736(20)32661-1

54. Ramasamy MN, Minassian AM, Ewer KJ, Flaxman AL, Folegatti PM, Owens DR, et al. Safety and immunogenicity of ChAdOx1 nCoV-19 vaccine administered in a prime-boost regimen in young and old adults (COV002): a single-blind, randomised, controlled, phase 2/3 trial. *Lancet* (2021) 396(10267):1979–93.

55. Logunov DY, Dolzhikova IV, Shcheblyakov DV, Tukhvatulin AI, Zubkova OV, Dzharullaeva AS, et al. Safety and efficacy of an rAd26 and rAd5 vector-based heterologous prime-boost COVID-19 vaccine: an interim analysis of a randomised controlled phase 3 trial in Russia. *Lancet* (2021) 397(10275):671–81. doi: 10.1016/S0140-6736(21)00234-8

56. Ng OT, Koh V, Chiew CJ, Marimuthu K, Thevasagayam NM, Mak TM, et al. Impact of delta variant and vaccination on SARS-CoV-2 secondary attack rate among household close contacts. *Lancet Reg Health West Pac* (2021) 17:100299. doi: 10.1016/j.lanwpc.2021.100299

57. de Gier B, Andeweg S, Backer JA, RIVM COVID-19 surveillance and epidemiology team, Hahne SJ, van den Hof S, et al. Vaccine effectiveness against SARS-CoV-2 transmission to household contacts during dominance of Delta variant (B.1.617.2), the Netherlands, August to September 2021. *Euro Surveill* (2021) 26(44). doi: 10.2807/1560-7917.ES.2021.26.44.2100977

58. Tan ST, Kwan AT, Rodriguez-Barraquer I, Singer BJ, Park HJ, Lewnard JA, et al. Infectiousness of SARS-CoV-2 breakthrough infections and reinfections during the Omicron wave. *Nat Med* (2023) 29(2):358–65. doi: 10.1038/s41591-022-02138-x

59. Martinez-Baz I, Trobajo-Sanmartin C, Miqueleiz A, Guevara M, Fernandez-Huerta M, Burgui C, et al. Product-specific COVID-19 vaccine effectiveness against secondary infection in close contacts, Navarre, Spain, April to August 2021. *Euro Surveill* (2021) 26(39). doi: 10.2807/1560-7917.ES.2021.26.39.2100894

60. Martinez-Baz I, Miqueleiz A, Casado I, Navascues A, Trobajo-Sanmartin C, Burgui C, et al. Effectiveness of COVID-19 vaccines in preventing SARS-CoV-2 infection and hospitalisation, Navarre, Spain, January to April 2021. *Euro Surveill* (2021) 26(21). doi: 10.2807/1560-7917.ES.2021.26.21.2100438

61. Pilishvili T, Gierke R, Fleming-Dutra KE, Farrar JL, Mohr NM, Talan DA, et al. Effectiveness of mRNA Covid-19 Vaccine among U.S. Health Care Personnel. *N Engl J Med* (2021) 385(25):e90.

62. Jalal K, Khan K, Basharat Z, Abbas MN, Uddin R, Ali F, et al. Reverse vaccinology approach for multi-epitope centered vaccine design against delta variant of the SARS-CoV-2. *Environ Sci pollut Res Int* (2022) 29(40):60035–53. doi: 10.1007/s11356-022-19979-1

63. Chemaitelly H, Tang P, Hasan MR, AlMukdad S, Yassine HM, Benslimane FM, et al. Waning of BNT162b2 vaccine protection against SARS-CoV-2 infection in Qatar. *N Engl J Med* (2021) 385(24):e83. doi: 10.1056/NEJMoa2114114

64. Abdool Karim SS, de Oliveira T. New SARS-CoV-2 variants - clinical, public health, and vaccine implications. *N Engl J Med* (2021) 384(19):1866–8. doi: 10.1056/NEJMc2100362

65. Gupta RK. Will SARS-CoV-2 variants of concern affect the promise of vaccines? *Nat Rev Immunol* (2021) 21(6):340–1. doi: 10.1038/s41577-021-00556-5

66. Abu-Raddad LJ, Chemaitelly H, Butt AA, National Study Group for C-V. Effectiveness of the BNT162b2 Covid-19 vaccine against the B.1.1.7 and B.1.351 variants. *N Engl J Med* (2021) 385(2):187–9.

67. Collier DA, De Marco A, Ferreira I, Meng B, Datir RP, Walls AC, et al. Sensitivity of SARS-CoV-2 B.1.1.7 to mRNA vaccine-elicited antibodies. *Nature* (2021) 593 (7857):136–41.

68. Madhi SA, Baillie V, Cutland CL, Voysey M, Koen AL, Fairlie L, et al. Efficacy of the ChAdOx1 nCoV-19 Covid-19 Vaccine against the B.1.351 Variant. *N Engl J Med* (2021) 384(20):1885–98.

69. Iacobucci G. Covid-19: Single vaccine dose is 33% effective against variant from India, data show. *BMJ* (2021) 373:n1346.

70. Lopez Bernal J, Andrews N, Gower C, Gallagher E, Simmons R, Thelwall S, et al. Effectiveness of Covid-19 vaccines against the B.1.617.2 (Delta) variant. *N Engl J Med* (2021) 385(7):585–94.

71. Planas D, Saunders N, Maes P, Guivel-Benhassine F, Planchais C, Buchrieser J, et al. Considerable escape of SARS-CoV-2 Omicron to antibody neutralization. *Nature* (2022) 602(7898):671–5. doi: 10.1038/s41586-021-04389-z

72. Muik A, Lui BG, Wallisch AK, Bacher M, Muhl J, Reinholz J, et al. Neutralization of SARS-CoV-2 Omicron by BNT162b2 mRNA vaccine-elicited human sera. *Science* (2022) 375(6581):678–80. doi: 10.1126/science.abn7591

73. Gagne M, Moliva JI, Foulds KE, Andrew SF, Flynn BJ, Werner AP, et al. mRNA-1273 or mRNA-Omicron boost in vaccinated macaques elicits similar B cell expansion, neutralizing responses, and protection from Omicron. *Cell* (2022) 185(9):1556–71 e18. doi: 10.1016/j.cell.2022.03.038

74. He C, He X, Yang J, Lei H, Hong W, Song X, et al. Spike protein of SARS-CoV-2 Omicron (B.1.1.529) variant have a reduced ability to induce the immune response. *Signal Transduct Target Ther* (2022) 7(1):119.

75. He C, Yang J, Hong W, Chen Z, Peng D, Lei H, et al. A self-assembled trimeric protein vaccine induces protective immunity against Omicron variant. *Nat Commun* (2022) 13(1):5459. doi: 10.1038/s41467-022-33209-9

76. Tan CCS, Owen CJ, Tham CYL, Bertoletti A, van Dorp L, Balloux F. Pre-existing T cell-mediated cross-reactivity to SARS-CoV-2 cannot solely be explained by prior exposure to endemic human coronaviruses. *Infect Genet Evol* (2021) 95:105075. doi: 10.1016/j.meegid.2021.105075

77. Grifoni A, Sidney J, Vita R, Peters B, Crotty S, Weiskopf D, et al. SARS-CoV-2 human T cell epitopes: Adaptive immune response against COVID-19. *Cell Host Microbe* (2021) 29(7):1076–92. doi: 10.1016/j.chom.2021.05.010

78. Sattler A, Angermair S, Stockmann H, Heim KM, Khadzhynov D, Treskatsch S, et al. SARS-CoV-2-specific T cell responses and correlations with COVID-19 patient predisposition. *J Clin Invest* (2020) 130(12):6477–89. doi: 10.1172/JCI140965

79. Brand I, Gilberg L, Bruger J, Gari M, Wieser A, Eser TM, et al. Broad T cell targeting of structural proteins after SARS-CoV-2 infection: high throughput assessment of T cell reactivity using an automated interferon gamma release assay. *Front Immunol* (2021) 12:688436. doi: 10.3389/fimmu.2021.688436

80. Tan AT, Linster M, Tan CW, Le Bert N, Chia WN, Kunasegaran K, et al. Early induction of functional SARS-CoV-2-specific T cells associates with rapid viral clearance and mild disease in COVID-19 patients. *Cell Rep* (2021) 34(6):108728. doi: 10.1016/j.celrep.2021.108728

81. Bange EM, Han NA, Wileyto P, Kim JY, Gouma S, Robinson J, et al. CD8(+) T cells contribute to survival in patients with COVID-19 and hematologic cancer. *Nat Med* (2021) 27(7):1280–9. doi: 10.1038/s41591-021-01386-7

82. Saini SK, Hersby DS, Tamhane T, Povlsen HR, Amaya Hernandez SP, Nielsen M, et al. SARS-CoV-2 genome-wide T cell epitope mapping reveals immunodominance and substantial CD8(+) T cell activation in COVID-19 patients. *Sci Immunol* (2021) 6 (58). doi: 10.1126/sciimmunol.abf7550

83. Thieme CJ, Anft M, Paniskaki K, Blazquez-Navarro A, Doevelaar A, Seibert FS, et al. Robust T cell response toward spike, membrane, and nucleocapsid SARS-CoV-2 proteins is not associated with recovery in critical COVID-19 patients. *Cell Rep Med* (2020) 1(6):100092. doi: 10.1016/j.xcrm.2020.100092

84. Diniz MO, Mitsi E, Swadling L, Rylance J, Johnson M, Goldblatt D, et al. Airway-resident T cells from unexposed individuals cross-recognize SARS-CoV-2. *Nat Immunol* (2022) 23(9):1324–9. doi: 10.1038/s41590-022-01292-1

85. Mateus J, Grifoni A, Tarke A, Sidney J, Ramirez SI, Dan JM, et al. Selective and cross-reactive SARS-CoV-2 T cell epitopes in unexposed humans. *Science* (2020) 370 (6512):89–94. doi: 10.1126/science.abd3871

86. Sekine T, Perez-Potti A, Rivera-Ballesteros O, Strålin K, Gorin JB, Olsson A, et al. Robust T cell immunity in convalescent individuals with asymptomatic or mild COVID-19. *Cell* (2020) 183(1):158–68.e14. doi: 10.1016/j.cell.2020.08.017

87. Le Bert N, Tan AT, Kunasegaran K, Tham CYL, Hafezi M, Chia A, et al. SARS-CoV-2-specific T cell immunity in cases of COVID-19 and SARS, and uninfected controls. *Nature* (2020) 584(7821):457–62. doi: 10.1038/s41586-020-2550-z

88. Bacher P, Rosati E, Esser D, Martini GR, Saggau C, Schiminsky E, et al. Low-avidity CD4(+) T cell responses to SARS-CoV-2 in unexposed individuals and humans with severe COVID-19. *Immunity* (2020) 53(6):1258–71 e5. doi: 10.1016/j.immuni.2020.11.016

89. Beretta A, Cranage M, Zipeto D. Is cross-reactive immunity triggering COVID-19 immunopathogenesis? *Front Immunol* (2020) 11:567710. doi: 10.3389/fimmu.2020.567710

90. Yu ED, Narowski TM, Wang E, Garrigan E, Mateus J, Frazier A, et al. Immunological memory to common cold coronaviruses assessed longitudinally over a three-year period pre-COVID19 pandemic. *Cell Host Microbe* (2022) 30(9):1269–78 e4. doi: 10.1016/j.chom.2022.07.012

91. An P, Song P, Wang Y, Liu B. Asymptomatic patients with novel coronavirus disease (COVID-19). *Balkan Med J* (2020). doi: 10.4274/balkanmedj.galenos.2020.2020.4.20

frontiers | Frontiers in Immunology

TYPE Original Research
PUBLISHED 02 February 2024
DOI 10.3389/fimmu.2024.1292059

OPEN ACCESS

EDITED BY
Cordelia Dunai,
University of Liverpool, United Kingdom

REVIEWED BY
Güliz Tuba Barut,
Institute of Virology and Immunology, Switzerland
Ravi Kant,
Nirma University, India
Fabio Fiorino,
LUM University Giuseppe Degennaro, Italy

*CORRESPONDENCE
Richard B. Markham
rmarkha1@jhu.edu

†These authors share first authorship

RECEIVED 10 September 2023
ACCEPTED 15 January 2024
PUBLISHED 02 February 2024

CITATION
Gordy JT, Hui Y, Schill C, Wang T, Chen F, Fessler K, Meza J, Li Y, Taylor AD, Bates RE, Karakousis PC, Pekosz A, Sachithanandham J, Li M, Karanika S and Markham RB (2024) A SARS-CoV-2 RBD vaccine fused to the chemokine MIP-3α elicits sustained murine antibody responses over 12 months and enhanced lung T-cell responses. *Front. Immunol.* 15:1292059. doi: 10.3389/fimmu.2024.1292059

A SARS-CoV-2 RBD vaccine fused to the chemokine MIP-3α elicits sustained murine antibody responses over 12 months and enhanced lung T-cell responses

James Tristan Gordy[1†], Yinan Hui[1†], Courtney Schill[1], Tianyin Wang[1], Fengyixin Chen[1], Kaitlyn Fessler[1], Jacob Meza[1], Yangchen Li[1], Alannah D. Taylor[1], Rowan E. Bates[1], Petros C. Karakousis[1,2], Andrew Pekosz[1], Jaiprasath Sachithanandham[1], Maggie Li[1], Styliani Karanika[2] and Richard B. Markham[1*]

[1]W. Harry Feinstone Department of Molecular Microbiology and Immunology, Bloomberg School of Public Health, Johns Hopkins University, Baltimore, MD, United States, [2]Division of Infectious Diseases, Department of Medicine, Johns Hopkins School of Medicine, Baltimore, MD, United States

Background: Previous studies have demonstrated enhanced efficacy of vaccine formulations that incorporate the chemokine macrophage inflammatory protein 3α (MIP-3α) to direct vaccine antigens to immature dendritic cells. To address the reduction in vaccine efficacy associated with a mutation in severe acute respiratory syndrome coronavirus 2 (SARS-CoV-2) mutants, we have examined the ability of receptor-binding domain vaccines incorporating MIP-3α to sustain higher concentrations of antibody when administered intramuscularly (IM) and to more effectively elicit lung T-cell responses when administered intranasally (IN).

Methods: BALB/c mice aged 6–8 weeks were immunized intramuscularly or intranasally with DNA vaccine constructs consisting of the SARS-CoV-2 receptor-binding domain alone or fused to the chemokine MIP-3α. In a small-scale (n = 3/group) experiment, mice immunized IM with electroporation were followed up for serum antibody concentrations over a period of 1 year and for bronchoalveolar antibody levels at the termination of the study. Following IN immunization with unencapsulated plasmid DNA (n = 6/group), mice were evaluated at 11 weeks for serum antibody concentrations, quantities of T cells in the lungs, and IFN-γ- and TNF-α-expressing antigen-specific T cells in the lungs and spleen.

Results: At 12 months postprimary vaccination, recipients of the IM vaccine incorporating MIP-3α had significantly, approximately threefold, higher serum antibody concentrations than recipients of the vaccine not incorporating MIP-3α. The area-under-the-curve analyses of the 12-month observation interval demonstrated significantly greater antibody concentrations over time in recipients of the MIP-3α vaccine formulation. At 12 months postprimary immunization, only recipients of the fusion vaccine had concentrations of serum-neutralizing activity deemed to be effective. After intranasal

immunization, only recipients of the MIP-3α vaccine formulations developed T-cell responses in the lungs significantly above those of PBS controls. Low levels of serum antibody responses were obtained following IN immunization.

Conclusion: Although requiring separate IM and IN immunizations for optimal immunization, incorporating MIP-3α in a SARS-CoV-2 vaccine construct demonstrated the potential of a stable and easily produced vaccine formulation to provide the extended antibody and T-cell responses that may be required for protection in the setting of emerging SARS-CoV-2 variants. Without electroporation, simple, uncoated plasmid DNA incorporating MIP-3α administered intranasally elicited lung T-cell responses.

KEYWORDS

SARS-CoV-2, vaccine, dendritic cell, MIP-3α, intranasal (IN), T-cell response, antibody, neutralizing antibody

Introduction

The severe acute respiratory syndrome coronavirus 2 (SARS-CoV-2) pandemic has provided yet one more example of how the mutability of RNA viruses hinders efforts to develop effective immunoprophylactic strategies. Emerging variants have been uniformly less susceptible to neutralizing antibodies elicited by exposure to earlier vaccines or prior infection (1–9). Resistance of new variants to pre-existing neutralizing antibodies is not absolute but varies with both the extent of mutation in vaccine-targeted proteins and the concentration of neutralizing antibodies targeting previous viral variants (4–6, 10). While repeated immunization targeting variants of the SARS-CoV-2 has proceeded as a strategy for addressing waning protective immunity, there has been sustained resistance to repeated immunization, as evidenced by surveys of current attitudes toward vaccination (11) and the small proportion of Americans who received the most recent vaccine booster (12).

Although declining antibody concentrations increase the risk of acquiring SARS-CoV-2 infection, evidence from clinical and non-human primate studies has indicated that the currently available vaccines may elicit T-cell-mediated immune responses that are less susceptible than neutralizing antibody responses to the immune escape associated with SARS-CoV-2 variants (12–15). These T-cell responses may at least partially explain how vaccines that elicit relatively short-lived neutralizing antibodies can still attenuate disease severity without preventing infection (16).

These findings indicate that vaccine development efforts to counter the ongoing emergence of variants should include the development of vaccines that elicit both more sustained antibody concentrations and T-cell responses with activity at the site of infection. Unlike the situation for circulating neutralizing antibodies elicited by immunization or previous infection that are readily accessible at the time of pathogen exposure, T-cell immunity is most effective if pathogen-specific T cells pre-exist within the targeted organ (16–19). To counter respiratory pathogens, multiple studies have indicated that intranasal (IN) immunization is more effective than systemic immunization at eliciting T-cell responses in the lungs (20–22).

In murine vaccine model systems analyzing protective or therapeutic efficacy against malaria, tuberculosis, and melanoma, we have studied the impact of fusing vaccine antigen to the chemokine macrophage inflammatory protein 3α (MIP-3α), also known as chemokine (C–C motif) ligand 20 (CCL20). Both human and mouse MIP-3α are able to bind mouse (23) C–C motif chemokine receptor 6 (CCR6), a member of the G protein-coupled receptor family found on immature but not mature dendritic cells (DC). Targeting immature DC (iDC) distinguishes this vaccine construct from other dendritic cell-targeting vaccines, which engage receptors expressed by more differentiated DC (24–29) to enhance vaccine efficacy. Employment of this vaccine platform has generated greater and, in some model systems, more sustained responses than those observed when the vaccine antigen is not fused to the chemokine (22, 23, 30–32). While MIP-3α serves as a chemoattractant for iDC (33–38), previous studies have demonstrated the requirement of fusing the vaccine antigen to chemokine to achieve maximum efficacy. In our recent study in a mouse challenge model using a therapeutic vaccine targeting the *Mycobacterium tuberculosis* stringent response, we found that IN immunization elicited significantly greater antibacterial activity than intramuscular (IM) immunization, and that IN vaccination with the MIP-3α-fused vaccine was also significantly more effective than immunization with vaccine antigen alone (22). Optimal immune responses were observed with a DNA vaccine construct that required no encapsulation of the DNA or use of adjuvant to achieve the observed therapeutic efficacy.

In the current study, we have examined in a mouse model the comparative immunogenicity of a DNA vaccine incorporating the receptor-binding domain (RBD) of the SARS-CoV-2 spike protein with or without fusion to human MIP-3α. Our results indicate that, over a year of observation, the fusion vaccine elicited and sustained significantly higher antibody concentrations compared to the vaccine incorporating RBD alone. Of particular note was the persistence in the recipients of the fusion vaccine of neutralizing antibody responses for at least 4 months after they were no longer detectable in the recipients of the vaccine only encoding RBD. Furthermore, we found that IN immunization yielded significantly greater T-cell responses in the lung than those elicited by IM immunization, but only when RBD was fused to MIP-3α.

Methods

Vaccine plasmid construction and verification

pUC57 plasmid containing DNA encoding codon-optimized RBD (spike amino acids 319–545 of Wuhan-Hu-1 isolate) was purchased from GenScript (Piscataway, NJ, USA). DNA was extracted and ligated into a previously generated pSecTag2b plasmid by *Hind*III and *Bam*HI to generate RBD alone and also by *Kas*I and *Bam*HI to generate MIP-3α-RBD (restriction enzymes from Thermo Fisher, Waltham, MA, USA) (22). Proper insertion was confirmed by agarose gel electrophoresis and sequencing, and the expression of target genes was confirmed by immunoblots probed by anti-C-myc (BioLegend, San Diego, CA, USA) of cell lysates and supernatants following transfection of HEK293T cells (American Type Culture Collection, Manassas, VA, USA) utilizing the Trans-IT 293 transfection system (Mirus Bio, Madison, WI, USA) (Supplementary Figure S1). In brief, lysates were prepped using 10× Cell Lysis Buffer (Cell Signaling Tech., Danvers, MA, USA) according to manufacturer protocol, protein amount was normalized utilizing Bradford Assay (Oz Biosciences, San Diego, CA, USA), separated on precast TGX Gels (Bio-Rad, Hercules, CA, USA), transferred to nitrocellulose membranes (Bio-Rad), blocked with milk solution, probed with anti-C-myc for 2 h to overnight at 1:1,000 dilution, washed, probed with AP-conjugated goat antimouse antibody (Jackson ImmunoResearch Laboratories, Inc., West Grove, PA, USA) at 1:1,000 dilution for 1 h, washed, and visualized with NBT-BCIP reagent (Sigma Aldrich, St. Louis, MO, USA). Vaccination plasmids were selected with ampicillin (100 mg/mL), and Qiagen® Endo-Free® Plasmid Series kits were used to extract the ligation product from DH5-α *Escherichia coli* (Invitrogen™, Thermo Fisher Scientific, Waltham, MA, USA). Plasmid DNA was diluted with endotoxin-free 1× PBS. Nanodrop spectrophotometry, agarose gel electrophoresis, and insert sequencing (JHSSF) were used to test the concentration, purity, and correctness of the extracted DNA.

Mice

BALB/c mice aged 6 to 8 weeks old were purchased from Charles River Laboratories Inc., Wilmington, MA, USA. The long-term experiment utilized all female mice. The intranasal experiment utilized a parallel distribution of male and female mice. All mice were kept in a pathogen-free micro-isolation facility at Johns Hopkins in accordance with the National Institutes of Health guidelines for the humane use of laboratory animals. All experimental procedures involving mice were approved by the Institutional Animal Care and Use Committee of Johns Hopkins University under protocol MO23H131. Johns Hopkins University has received Public Health Service-Approved Animal Welfare Assurance (No. D16-00173) from the National Institutes of Health Office of Laboratory Animal Welfare. Johns Hopkins University is also accredited by the Association for Assessment and Accreditation of Laboratory Animal Care International. Additionally, each mouse was monitored for at least 5 min after administration to ensure a lack of acute toxicity. Supplementary Figure S2 shows no change in weight gain over time across groups for either vaccine modality.

Intramuscular vaccination

For IM vaccination (Figure 1), the DNA vaccine construct was diluted in 1× endotoxin-free PBS, and each mouse received a volume of 50–70 µL by injection into the right gastrocnemius muscle. Immediately following injection, the muscle was pulsed using an ECM 830 Electro Square Porator with 2-Needle Array Electrode (BTX Harvard Apparatus, Holliston, MA, USA) under the following parameters: 106 V, 20 ms pulse length, 200 ms pulse interval, and eight total pulses. CpG type B (ODN1826) (InvivoGen, San Diego, CA, USA) was used as the adjuvant for IM immunization and was diluted in 1× endotoxin-free PBS at 1 mg/mL. The adjuvant was injected IM into the right gastrocnemius muscle at a volume of 50 µL. Three doses of the vaccine were given, each 2 weeks apart, and the adjuvant was given 1 day after every vaccination to allow for the expression of protein from the DNA vaccine. The long-term study utilized a 10-µg dose. The IM immunization used for comparison purposes in the IN immunization studies employed a dose of 50 µg (30).

Intranasal vaccination

The DNA vaccine construct was diluted in 1× endotoxin-free PBS to a concentration of 2 µg/µL for all groups. Mice were anesthetized before vaccination by inhalation of vaporized isoflurane. For each IN dose, 100 µg of vaccine was administered in each nostril in a volume of 50 µL. The IN vaccine was administered four times at 3-week intervals. IN adjuvant (CpG 25 µg in 50 µL of PBS in each nostril) was administered 1 day after the vaccine and only after the fourth IN vaccination. Each mouse was monitored in an upright position until complete recovery from anesthesia and vaccine absorption was confirmed by lack of nasal discharge.

Lymphocyte isolation

Under sterile conditions, mouse spleens and lungs were harvested and placed in 1× PBS on ice. Lungs were transferred to

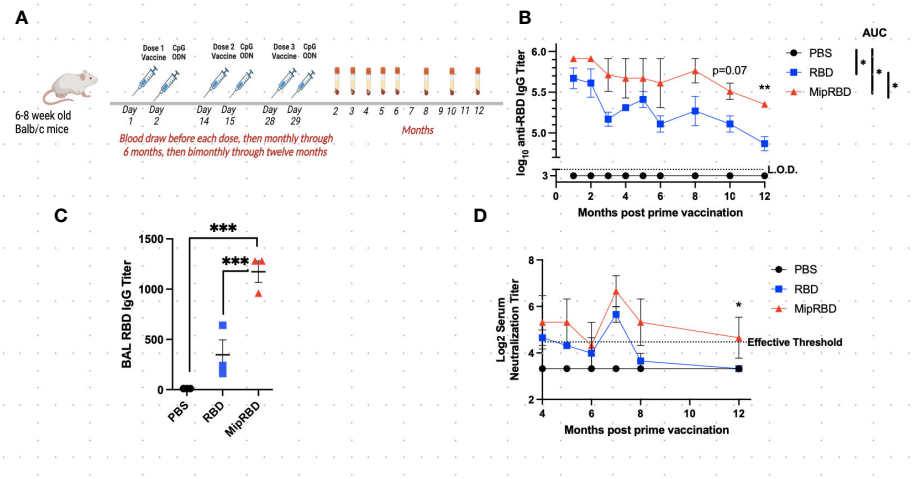

FIGURE 1
Effect of vaccine formulation on concentration of a specific antibody maintained over 12 months. **(A)** Vaccination and serum-sampling schedule for BALB/c mice, with primary vaccination initiated at 6–8 weeks of age. Mice were immunized IM with 10 µg of plasmid DNA encoding either MipRBD orRBD or with PBS. Immediately following vaccination, each mouse received electroporation, as described in Methods. At 24 h after immunization, each mouse received 50 µg of CpG at the immunization site. Tail vein bleeds were obtained at the indicated time points after the initial immunization. **(B)** Reciprocal antibody titers, determined by ELISA, indicate the highest dilution of serum at which the absorbance was twice the average value of the negative control wells (average of no serum, no secondary antibody, and no substrate wells in duplicate). The antibody titer was $\log_{10}$ transformed, and area under the curve (AUC) was conducted to compare differences and significance across the curves' entireties by nonoverlapping 95% confidence intervals (CI). Symbols represent group means nontransformed. Error bars represent the standard error of the mean (SEM). For AUC, 95% CI were PBS (33), RBD (56.40–58.87), and MipRBD (60.57–63.92). Comparison of MipRBD vs. RBD reciprocal antibody titers at individual time points using multiple unpaired *t*-tests demonstrated a significant difference at the 12-month time point ($p < 0.05$). **(C)** Reciprocal antibody titers in BAL fluid 12 months after the primary immunization, with significance determined by one-way ANOVA. Symbols represent individual mice. **(D)** Reciprocal titers of neutralizing antibodies at different points over the 12 months postprimary immunization. Symbols represent the group means. The significance of differences at individual time points was determined using the Kruskal–Wallis test to compare areas under the curve of the antibody titer dilutions. At the 12-month time point, the RBD and MipRBD differed significantly. Three female mice per group. *$p = 0.05$; **$p < 0.01$; ***$p < 0.001$.

wells containing 1 mL of digestion buffer (RPMI media, 167 µg/mL of Liberase, and 100 µg/mL of DNase), minced with scissors, and incubated at 37° for 30 min. Lungs and spleens were ground gently with a pestle over a 70-µM mesh filter into 50-mL conical tubes and immediately centrifuged at 300×*g* for 10 min at 4°. The supernatant was removed, and the pellet was then fully resuspended using 1 mL of ACK lysis buffer (Quality Biological, Gaithersburg, MD, USA) and incubated at room temperature (RT) for 3–4 min. To stop cell lysis, cells were diluted with 20–30 mL of cold 1× PBS and were then pelleted at 300×*g* for 10 min at 4°. After another resuspension in 10 mL of cold 1× PBS and centrifugation under the same conditions, the supernatant was removed and the pellet was resuspended in 1 mL (lungs) or 4 mL (spleens) freezing medium (90% FBS, 10% DMSO) and aliquoted into two (lungs) and four (spleens) tubes for cryostorage using isopropanol cooling containers (Mr. Frosty, ThermoFisher Scientific, Waltham, MA, USA) at −80° for at least 4 h and then moved to −150°.

Enzyme-linked immunosorbent assay

At the indicated time points postvaccination (Figure 1A), approximately 100 µL of mouse blood was collected in either heparin-coated (plasma) or heparin-uncoated (serum) 1.5 mL microcentrifuge tubes by tail vein nicking. Serum samples were allowed to coagulate at room temperature for 0.5–1 h and then spun at 2,200×*g* for 10 min at 4°C. For plasma, samples were spun at 300×*g* for 5 min at 4°C, the supernatant was transferred to a new tube, and the samples were spun at 1,500×*g* for 15 min at 4°C. The serum or plasma supernatant was frozen and stored at −20° until used. Humoral immune responses to RBD protein were measured using enzyme-linked immunosorbent assay (ELISA). The ELISA plates were coated overnight at 4° with 0.2 µg/microwell of S-RBD His-tag recombinant protein (Invitrogen, Rockford, IL, USA) diluted in 100 µL of sterile 1× PBS (2 ng/µL). Each well of the plate was washed three times using 250 µL of washing solution (0.05% Tween 20 diluted in 1× PBS). Plates were emptied, and the residual liquid was discarded before blocking each well with 250 µL of blocking solution (1% BSA in 1× PBS) for 30 min at RT. Following the addition of 100 µL of mouse serum samples serially diluted in triplicate in blocking solution to each well, the plate was incubated at RT for 2 h. After washing the plates six times with 250 µL/well of washing solution, 100 µL of 1:1,000 diluted HRP goat antimouse IgG (H+L) secondary antibody (Biotium, Fremont, CA, USA) was added to each well and incubated at RT for 1 h. The plates were washed six times using the same amount of washing solution again after the secondary antibody incubation, and 100 µL of KPL ABTS® Peroxidase Substrate (SeraCare Life Sciences Inc., Milford, MA, USA) was then added into each well, and the plates were incubated at RT in the dark for 1 h. Data were collected using the Synergy HT at O.D.405 nm (BioTek Instruments Inc., Winooski, VT, USA). Serum samples were diluted across the plate. Antibody titers were calculated as the highest serum dilution that registered absorbance values above (≥) the background threshold. The

threshold was defined as twice the average value of control wells. Control wells included in duplicate are (1) all but serum (2), all but secondary antibody, and (3) all but substrate.

SARS-CoV-2 virus and neutralization assay

SARS-CoV-2 infectious virus titers were determined via a 50% tissue culture infectious dose, as previously described (39). An early SARS-CoV-2 isolate containing the spike D614G mutation was used for all neutralization assays, as previously described (40, 41). All sera were diluted twofold (final dilutions of plasma ranging from 1:20 to 1:2,560), and infectious virus was added at a final concentration of 1×10^3 $TCID_{50}$/mL to the serial dilutions, and incubated for 1 h at room temperature. A 100 µL mixture of virus–serum (containing 100 TCID50 units) was transferred to a 96-well plate of VeroE6-TMPRSS2 cells in sextuplets and then incubated until a cytopathic effect was observed in the controls and the highest sera dilutions. The cells were fixed and stained, and the neutralization titers (NTs) were calculated as the highest serum dilutions that eliminated the cytopathic effect in 50% of the wells (NT50). A positive threshold was defined as NT ≥ 20. An area-under-the-curve analysis then converted the endpoint titer to a continuous variable, and the significance of differences at the different time points was determined using the Kruskal–Wallis test.

Bronchoalveolar lavage

Wash fluid {1× PBS, 100 µM EDTA from 0.5 M at pH 8 liquid stock (Corning, Glendale, AZ), protease inhibitors (1× PMSF from 200× stock, Cell Signaling Technology, Danvers, MA)} was prepared the day before bronchoalveolar lavage (BAL) and stored at 4°C. Following mouse euthanasia and cardiac puncture, the trachea was exposed, and a mouse endotracheal tube (20 G× 1 in., Kent Scientific Corp., Torrington, CT, USA) was inserted into the trachea to a point just above the carina. The guide needle was removed, and a syringe was attached to the endotracheal tube, which was manually held in place during syringe attachment. Next, 0.5 mL of the wash fluid was slowly injected into the lungs with visual confirmation that the lobes were inflated and that there was no leaking. The injected liquid was aspirated with mild pressure applied to the inflated lobes, as necessary. The aspirated fluid was transferred to a 1.5-mL vial on ice and then transferred to a new tube for centrifugation at 400×*g* for 7 min at 4°C. The supernatant was stored at either 20°C or −80°C, depending on subsequent plans for use.

Flow cytometry

Cryopreserved cells were recovered by thawing briefly in a water bath at 37° and diluted slowly to 10 mL with warm complete media (RPMI, 10% FBS, 1× antibiotics, 20 mM HEPES, 1% sodium pyruvate, 1% nonessential amino acids, and 1% L-glutamine). Cells were spun for 7 min at 250×*g* at RT and then resuspended in a smaller volume of warm media to obtain a final concentration of 5×10^5–1×10^6 viable cells/well in 200 µL of complete media. The cells were then rested in a 5%CO_2 incubator at 37° for 2–3 h prior to stimulation with 1 µg of SARS-CoV-2 S protein RBD (Invitrogen, Rockford, IL, USA) at 37° for 16 h. During the final four hours, the cells were incubated with Brefeldin-A at 1× dilution (5 µg/mL; 1 µg in the well) and costimulatory antibodies anti-CD28 and anti-CD49d at 1 µg each per well (BioLegend Cat. No. 420601, No. 102116, and No. 103629). Full-Minus-One (FMO) and positive control wells were stimulated for 4 h with Cell Activation Cocktail (with Brefeldin A) according to manufacturer protocol (BioLegend Cat. No. 423303). After stimulation, 20 µL of EDTA (20 mM of EDTA diluted in 1× PBS at pH 7.4) was added to each well to ensure cells were in suspension and then transferred to a 96-well V-bottom plate. After centrifugation at 300×*g* for 5 min at RT, cells were washed with 150 µL of FACS buffer (0.5% bovine serum albumin (Sigma-Aldrich, St. Louis, MO, USA) in 1× sterile PBS) and pelleted again. Cells were stained with 100 µL/well of live/dead (L/D) stain (1:1,000 dilution in 1× sterile PBS) for 30 min at RT in the dark (LIVE/DEAD Fixable Near-IR Dead Cell Stain Kit, Thermo Fisher Scientific). Cells were pelleted and resuspended in 150 µL of FACS buffer and washed. Following the L/D stain, 50 µL of 2% Fc block (TruStain FcX, BioLegend Cat. No. 101320) was added to each well and incubated in the dark for 15 min on ice. After centrifugation, cells were stained in the dark for 20 min with an antimouse monoclonal-antibody (mAb) cocktail (50 µL per well, diluted in FACS buffer), including 1:500 FITC-conjugated anti-CD4 (BioLegend Cat. No. 100405), 1:200 PercPCy5.5-conjugated anti-CD3 (BioLegend Cat. No. 100217), and 1:200 Alexa Fluor 700-conjugated anti-CD8 (BioLegend Cat. No. 155022). After centrifugation and resuspension in 50 µL of Fixation buffer (Cyto-Fast Fix/Perm Buffer Set, BioLegend Cat No. 426803), cells were then incubated in the dark either at RT for 30 min or at 4° overnight.

For intracellular cytokine staining, an intracellular antimouse mAb cocktail (50 µL per well, diluted in 1× Cyto-Fast Perm buffer) was used to stain the cells in the dark at RT for 20 min. The cocktail includes 1:500 PECy7-conjugated anti-TNF-α (BioLegend Cat. No. 506323) and 1:100 APC-conjugated anti-IFN-γ (BioLegend Cat. No. 505809). Each well received 100 µL of Cyto-Fast Perm buffer for centrifugation at 400×*g* at RT for 5 min. Cells were then washed and resuspended with 150 µL of FACS buffer and read on the Attune™ NxT flow cytometer (Thermo Fisher Scientific, Waltham, MA, USA). Flow data were analyzed using Flow Jo software (FlowJo 10.8.1, LLC, Ashland, OR, USA). FMO control stains utilizing positive control stimulations were used to guide the gating structure. Supplementary Figures S3, S4 provides the gating structure utilized for analyses as well as representative plots of the data presented in the Results section.

Statistics

Antibody titers were log transformed for graphical purposes. All statistics were performed on raw, nontransformed data. One-

way analysis of variance with Tukey correction was used for comparisons of multiple groups for flow analyses and BAL antibody titers, and multiple unpaired *t*-tests and area-under-the-curve analyses were used to test for the significance of differences in the long-term antibody studies. For neutralizing antibody studies, the areas under the curves of serum dilutions at a given time point were compared using the Kruskal–Wallis test. All experiments shown contained three to six mice per group, as noted. Females are represented by solid color symbols, and males are represented by open symbols. In longitudinal studies, each symbol represents the group mean, and in all other graphs, each symbol represents one mouse. All error bars represent the estimation of the standard error of the mean (SEM). For all tests, $p \leq 0.05$ was considered to be significant. Prism Graphpad 9 and 10 (San Diego, CA, USA) were used for all statistical analyses and figure generation.

Results

Effect of fusion of vaccine antigen with MIP-3α on sustaining IgG and neutralizing antibody concentrations

To evaluate the maintenance of antibody concentrations following vaccination, 6–8-week-old BALB/c mice were vaccinated IM three times at 2-week intervals with saline or with 10 μg of plasmid DNA encoding either codon-optimized MIP-3α-RBD or codon-optimized RBD using the electroporation procedure described in Methods. One day following plasmid inoculation, 50 μg of the adjuvant CpG was injected into the immunization site. Blood for serum IgG or neutralizing antibody concentrations was obtained before each vaccination, 2 weeks after the final vaccination, at monthly intervals through 6 months postvaccination, and at bimonthly intervals thereafter through 12 months (Figure 1A). Antibody titers at all time points evaluated were greater in recipients of the fusion vaccine compared to recipients of vaccine encoding only RBD (mean difference = 2.77 + 0.9-fold), with the difference assuming significance at the later time points postvaccination ($p = 0.07$ at 10 months, $p = 0.007$ at 12 months, Figure 1B). The area-under-the-curve-analysis of the antibody concentrations over time for the two vaccination protocols also showed nonoverlapping 95% confidence intervals for RBD (57.64; 56.40–58.87) and for MIP-3α-RBD (62.25; 60.57–63.92). Compared to IM immunization with the RBD construct alone, IM immunization with the MIP-3α-RBD vaccine construct yielded significantly higher IgG concentrations in BAL 12 months after the initiation of vaccination (Figure 1C, $p < 0.001$). The higher serum IgG antibody concentrations observed at the later time points assumed particular importance, as this resulted in the maintenance at the 12-month time point of neutralizing antibody titers at a critical efficacy threshold (42) (Figure 1D). The area-under-the-curve analysis of the antibody titer curves at the 12-month time point indicated a significant difference between recipients of the MIP-3α-RBD vaccine compared to those receiving the vaccine encoding RBD alone ($p = 0.05$).

Impact of the IN vaccination route and use of the fusion vaccine on the recruitment of T cells to the lungs

Because of the potentially important role of T-cell responses in attenuating the severity of SARS-CoV-2 disease, we examined the impact of the route of administration, as well as the role of MIP-3α fusion, in eliciting lung T-cell responses as well as serum antibody responses. These studies evaluated immunogenicity within a shorter time frame and did not analyze the duration of the observed immune responses (Figure 2A). The IN vaccination regimen employed was identical to that successfully employed in our previously described TB vaccine formulation (22), in which higher DNA plasmid doses were used to compensate for the lack of electroporation. Mice were immunized on four occasions at 3-week intervals and received either IN immunization with 200 μg of vaccine (100 μg in each nostril in 50 μL of PBS) or IM immunization with 50 μg of vaccine administered with electroporation and use of the CpG adjuvant, as described. For the first three IN immunizations, the plasmid DNA vaccine was administered without adjuvant or electroporation. Because interim antibody analyses indicated no serum antibody response after three IN immunizations, a fourth round of immunizations was undertaken, using the CpG adjuvant (25 μg in 50 μL of PBS in each nostril) for IN, as well as for IM, vaccination. The addition of CpG to the IN vaccine failed to elicit a significant serum antibody response (Figure 2B). As indicated (Figure 2B), despite receiving four immunizations, serum IgG concentrations remained significantly below those observed with a temporally identical IM immunization protocol ($p < 0.0001$). The MIP-3α fusion vaccine offered no advantage in eliciting systemic antibody responses following IN immunization. Similarly, IN immunization failed to elicit serum IgA antibody responses (data not shown).

The inclusion of MIP-3α in the vaccine formulation did, however, have a highly significant effect on the ability of IN immunization to recruit T cells to the lung (Figure 3A). At 12 weeks after initial vaccine administration (3 weeks after final vaccination), recipients of the MIP-3α fusion vaccine had an approximately fourfold increase in the number of $CD4^+$ T cells (Figure 3B) and $CD8^+$ T cells (Figure 3C) in the lungs compared to recipients of saline, RBD-only vaccine, or, importantly, IM immunization with the MIP-3α-fusion vaccine followed by electroporation and use of the CpG adjuvant. In fact, IM immunization or IN immunization with the RBD alone construct did not elicit T-cell responses in the lung that exceeded those of control mice receiving only PBS.

To examine antigen-specific T-cell responses elicited in the spleen (Figure 4) and lungs (Figure 5) after IM or IN immunization, we evaluated by flow cytometry at the 12-week time point the $CD4^+$ and $CD8^+$ T-cell expression patterns of activation cytokines IFN-γ and TNF-α following *ex vivo* stimulation with RBD. In the spleen, we see that IM administration of MIP-3α-RBD provides significant IFN-γ expression in $CD4^+$ T cells and trending levels in $CD8^+$ T cells. Meanwhile, the IN administration of MIP-3α-RBD showed trends of increased IFN-γ and TNF-α in $CD4^+$ T cells.

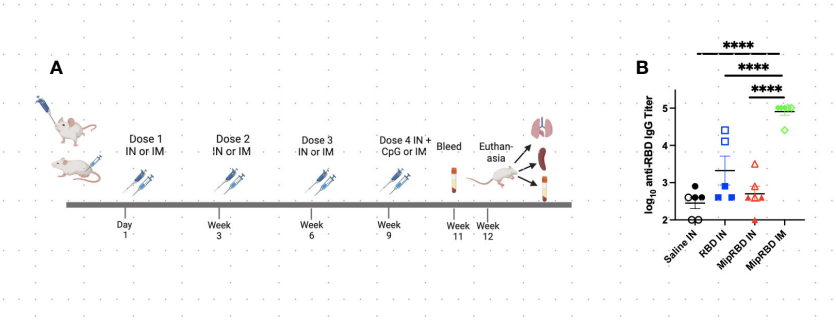

FIGURE 2
Effect of route of administration and vaccine formulation on serum antibody concentrations. **(A)** Vaccination and serum or tissue sampling schedule for 6–8-week-old BALB/c mice immunized with 50 µg of MipRBD IM followed by electroporation and CpG administration, as described in Figure 1B, or IN with 100 µg of plasmid DNA encoding either MipRBD or RBD in a volume of 50 µL of PBS in each nostril. In each nostril, 50 µL of PBS alone was used as a control IN immunization. Electroporation was not employed for IN immunization, and 50 µg of CpG (25 µg in each nostril in 50 µL of PBS) was administered once 1 day after the final immunization. **(B)** Serum antibody titers were determined by ELISA, as described in Figure 1B. The significance of differences in titer was determined using one-way ANOVA. Six mice per group, three males (open) and three females (filled), with each symbol representing one mouse. ****$p < 0.0001$.

At this sample size, RBD without fusion administered IN did not show statistical significance or trends in the spleen. TNF-α levels in $CD8^+$ T-cells were too low to provide robust data. Lung stimulation data showed a different picture than the spleen. In a pattern similar to that observed with T-cell recruitment to the lungs, only the MIP-3α fusion vaccine elicited a significantly increased number of IFN-γ- and TNF-α-expressing $CD4^+$ T cells post-RBD stimulation in the lungs compared to all other groups (Figure 5). The levels of $CD8^+$ T cells in the lungs were too low to provide robust data. Overall, the MIP-3α-RBD given IN provides relatively equivalent immunogenicity in the spleen compared to IM but superior immunogenicity in the lungs.

Discussion

The current preliminary studies have demonstrated that, compared to a DNA vaccine encoding only the SARS-CoV-2 RBD antigen, fusion of the chemokine MIP-3α gene to the RBD antigen gene in the vaccine construct resulted in persistently higher antibody concentrations in serum over a 12-month observation period (Figures 1B, D). One limitation of the long-term IM study is the small sample size of three mice per group. Despite this, statistical significance was consistently observed with several parameters over time. Therefore, we hypothesize the results of this preliminary long-term study to be valid. An area-under-the-curve analysis over that time frame indicated that the difference between the total IgG antibody responses to the two vaccine constructs was significant. At the final time point, 12 months following the initiation of vaccination, the concentrations of total IgG antibodies maintained were also significantly different between the two vaccine formulations, indicating the potential for a more extended period of protection against viral infection or severe disease provided by the fusion construct. This extended protection capability was further supported by the finding at the 12-month time point that the concentration of neutralizing antibodies was also significantly higher among recipients of the fusion vaccine, with only the fusion vaccine readily exceeding the threshold considered to be protective (42). Importantly,

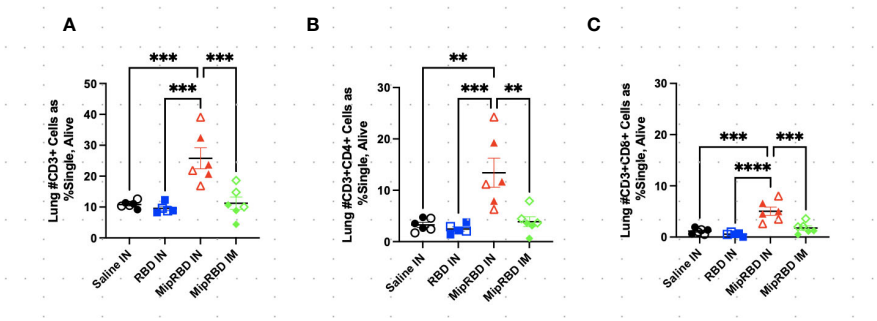

FIGURE 3
Effect of route of administration and vaccine formulation on T-cell recruitment to the lungs. The vaccination and tissue-harvesting schedule is described in Figure 2A. Three weeks after the final vaccination, the recruitment of T-cell subpopulations to the lungs elicited by the different immunization protocols was determined by flow cytometric analysis, as described in Methods. **(A)** All $CD3^+$ cells, as well as **(B)** $CD3^+CD8^+$ and **(C)** $CD3^+CD4^+$ cells, were analyzed by normalized cell counts. Differences between groups were analyzed using one-way ANOVA. Six mice per group, three males (open) and three females (filled), with each symbol representing one mouse. **$p < 0.01$; ***$p < 0.001$; ****$p < 0.0001$.

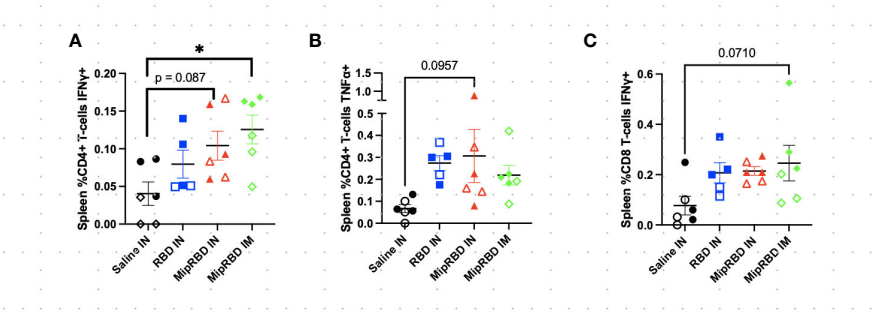

FIGURE 4
Effect of route of administration and vaccine formulation on IFN-γ and TNF-α responses by T cells in the spleen. The vaccination and tissue-harvesting schedule is described in Figure 2A. Harvested lymphocytes were incubated *in vitro* with 1 µg of RBD protein for 16 h, with the final 4 h accumulating intracellular cytokines. Flow cytometric analysis was then performed to evaluate T-cell IFN-γ and TNF-α expression associated with different immunization regimens in **(A)** %CD3$^+$CD4$^+$ T cells expressing IFN-γ; **(B)** %CD3$^+$CD4$^+$ T cells expressing TNF-α; and **(C)** %CD3$^+$CD8$^+$ T cells expressing IFN-γ. Six mice per group, three males (open) and three females (filled), with each symbol representing one mouse. *$p < 0.05$. Trends of $p < 0.1$ were noted on the graph.

significantly higher antibody concentrations among recipients of the MIP-3α fusion construct were also observed in BAL at the 12-month time point.

The results also indicate that the fusion of vaccine antigen with chemokine was critical to the recruitment of T cells to the lungs following IN immunization. Upon *in vitro* stimulation with the RBD protein, only mice immunized IN with the MIP-3α fusion vaccine construct elicited IFN-γ$^+$ and TNF-α T-cell responses that were significantly above control levels observed in unimmunized mice. IM immunization with the fusion vaccine construct failed to elicit a similar T-cell response in the lungs. The IN immunization experiment contained three mice of each sex per group. However, at this sample size, there were no clear trends of immunological differences between male and female mice.

Previous studies have indicated that, when the species-appropriate MIP-3α fusion product is used, no immune response is generated to the autologous MIP-3α component, even while markedly elevated responses are observed to the targeted antigen (32). While fusing vaccine antigens to DC-targeting ligands is not novel *per se*, studies using that approach have typically employed ligands for receptors found only on mature DC (25–28, 43), forgoing the opportunity to enhance antigen uptake in iDC and modify antigen processing during the earliest stages of the adaptive immune response.

Particularly relevant to the current work, studies by others examining IN immunization determined that MIP-3α played a unique role in eliciting immune responses at that site (44–46). Qin et al. demonstrated that MIP-3α drove DC recruitment to the nasal mucosa and further promoted the development of transepithelial dendrites in these cells. This effect resulted in enhanced antigen uptake and the rapid migration of DC into the draining cervical lymph nodes (46).

Our studies indicate that both the inclusion of MIP-3α in the vaccine construct and IN immunization were critical in the current model system for eliciting effector T-cell responses in the lungs. Multiple studies in the clinical setting have indicated that currently

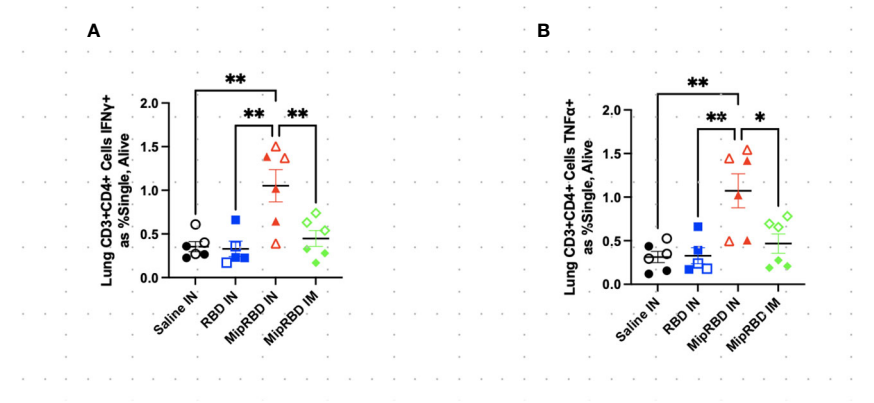

FIGURE 5
Effect of route of administration and vaccine formulation on IFN-γ and TNF-α responses by T cells in the lung. The vaccination and tissue-harvesting schedule is described in Figure 2A. Harvested lymphocytes were incubated *in vitro* with 1 µg of RBD protein for 16 h, with the final 4 h accumulating intracellular cytokines. Flow cytometric analysis was then performed to evaluate T-cell IFN-γ and TNF-α expression associated with different immunization regimens in **(A)** CD3$^+$CD4$^+$ T cells expressing IFN-γ as a percent of all cells and **(B)** CD3$^+$CD4$^+$ T cells expressing TNF-α as a percent of all cells. Six mice per group, three males (open) and three females (filled), with each symbol representing one mouse. *$p < 0.05$; **$p < 0.01$.

employed IM immunization regimens have not been effective in reducing nasal shedding of viruses in the setting of breakthrough infections [reviewed by Brussow (47)], and studies in nonhuman primates have indicated the importance of T-cell immunity in preventing nasal shedding (13). Le Nouen et al. (48) demonstrated in nonhuman primates the ability of intratracheal/IN immunization with a parainfluenza virus-vectored prefusion stabilized spike protein vaccine to elicit protective T-cell and antibody responses that included prevention of viral shedding in the upper and lower airways. They noted the dependence on T-cell immunity for the prevention of viral shedding. Lei et al. (49) demonstrated the ability of IN immunization with an experimental polyethyleneimine-adjuvanted SARS-CoV-2 spike protein to sustain systemic and BAL antibody levels, as well as lung T-cell responses. Potential disadvantages of these approaches are the reduced likelihood that a viral-vectored vaccine could be used for booster immunizations, the production issues associated with protein vaccines, and the untested clinical safety and efficacy associated with polyethyleneimine used as a vaccine adjuvant.

The current studies identify a novel approach for potentially eliciting both more durable antibody-mediated protection as well as enhancing T-cell responses within the lungs. Both of these outcomes offer the potential for more effective protection against emerging viral variants and for a reduction in viral shedding by vaccinated individuals with breakthrough infections. The results also provide an experimental system in which the individual protective contributions of humoral and cell-mediated immunity can be studied. While the current vaccine was studied as an easily constructed DNA formulation, the conclusions on the role of MIP-3α on the observed responses should be applicable across formulations that avoid issues around the use of viral-vectored or protein vaccines. Future studies can confirm that updated forms of this fusion vaccine will have similar efficacy to new SARS-CoV-2 variants of concern. The speed at which the vaccine could be updated is a strength in the constantly changing viral landscape. Our results suggest that a dual vaccination approach for this construct, IN and IM, would be most effective in providing optimal protection, warranting further study. While DNA vaccines have historically elicited poor responses in human studies, recent clinical studies demonstrating the efficacy of a DNA-formulated SARS-CoV-2 vaccine indicate the potential utility of stable, properly formulated DNA vaccines in the clinical setting (50, 51). These studies represent a preliminary analysis of an approach that will require currently planned future studies that define the duration of IN immunization-elicited T-cell-mediated protection, the roles of different T-cell subsets, the efficacy of this vaccine construct in murine and nonhuman primate challenge models, and the ability of mRNA formulations of this vaccine construct to elicit similar immune responses.

Data availability statement

The original contributions presented in the study are included in the article/Supplementary Material. Further inquiries can be directed to the corresponding author.

Ethics statement

The animal study was approved by The Animal Care and Use Committee of Johns Hopkins University. The study was conducted in accordance with the local legislation and institutional requirements.

Author contributions

JG: Conceptualization, Methodology, Supervision, Validation, Writing – review & editing, Formal analysis, Investigation. YH: Formal analysis, Investigation, Methodology, Writing – original draft, Writing – review & editing. CS: Investigation, Methodology, Writing – review & editing. TW: Investigation, Methodology, Writing – review & editing. FC: Investigation, Writing – review & editing. KF: Investigation, Writing – review & editing. JM: Writing – review & editing. YL: Writing – review & editing. AT: Writing – review & editing. RB: Writing – review & editing. PK: Writing – review & editing, Conceptualization, Formal analysis, Funding acquisition. AP: Data curation, Supervision, Writing – review & editing, Formal analysis, Investigation. JS: Investigation, Methodology, Writing – review & editing. ML: Investigation, Methodology, Writing – review & editing. SK: Investigation, Methodology, Writing – review & editing. RM: Conceptualization, Data curation, Funding acquisition, Methodology, Project administration, Supervision, Validation, Writing – original draft, Writing – review & editing.

Funding

The author(s) declare financial support was received for the research, authorship, and/or publication of this article. This work was supported by a grant from the Sea Grape Foundation to RBM and NIAID Grant 5R01AI148710 awarded to PK and RM.

Acknowledgments

We would like to acknowledge the staff at JHU Research Animal Resources for their assistance with animal care. The Attune Flow Cytometer was provided and supported by the Johns Hopkins Malaria Research Institute and the Department of Molecular Microbiology and Immunology (MMI). We thank Anne Jedlicka and Amanda Dziedzic in the JHSPH Genomic Analysis and Sequencing Core and Dr. Prakash Srinivasan (MMI) for core facility management, technological expertise, and instrument support.

Conflict of interest

Authors JG, PK, and RM are inventors on a pending patent application made by Johns Hopkins University for the vaccine constructs used in this manuscript.

The remaining authors declare that the research was conducted in the absence of any commercial or financial relationships that could be construed as a potential conflict of interest.

The author(s) declared that they were an editorial board member of Frontiers, at the time of submission. This had no impact on the peer review process and the final decision.

Publisher's note

All claims expressed in this article are solely those of the authors and do not necessarily represent those of their affiliated organizations, or those of the publisher, the editors and the reviewers. Any product that may be evaluated in this article, or claim that may be made by its manufacturer, is not guaranteed or endorsed by the publisher.

Supplementary material

The Supplementary Material for this article can be found online at: https://www.frontiersin.org/articles/10.3389/fimmu.2024.1292059/full#supplementary-material

SUPPLEMENTARY FIGURE 1
Plasmid Design and Construct Verification. **(A, B)** Map of the constructs within the pSecTag2b mammalian expression plasmid designed with Snap Gene software, with full length human Mip-3α fused to the receptor binding domain (RBD) of the Wuhan-Hu-1 isolate of SARS-CoV-2 **(A)** or with the RBD domain only **(B, C)** Single and Double digests of vaccine plasmid as further verification of construct purity and correctness. Each lane represents the digestion product of 500ng of purified DNA plasmid with specified enzymes as run on a 1% Agarose Gel embedded with ethidium bromide at 150V for 20 minutes and visualized by UV light. Relevant band sizes are labeled. **(D)** Expression of protein in mammalian HEK293T cells was verified by Western Blot against the C-myc tag in both cell lysate and supernatant.

SUPPLEMENTARY FIGURE 2
Mouse Mass Over Time. The percent increase of body mass was calculated over the time course of the IM vaccination series **(A)** and the IN vaccination series **(B)**. By Mixed Effects Models and Area Under the Curve analyses, no significant differences were found across groups.

SUPPLEMENTARY FIGURE 3
Spleen Gating Strategies and Representative Plots. **(A)** Gating strategy for splenocyte analysis. **(B)** Representative plots for cytokine expression in CD4+ and CD8+ T cells in the spleen. Numbers on plots are percent of parent gate.

SUPPLEMENTARY FIGURE 4
Lung Gating Strategies and Representative Plots. **(A)** Gating strategy for lung analysis. **(B)** Representative plots for lung T-cell infiltration. **(C)** Representative plots for cytokine expression in lung T cells. Numbers on plots are percent of parent for panel A and percent of Alive gate for panels B and C.

References

1. Abou-Saleh H, Abo-Halawa BY, Younes S, Younes N, Al-Sadeq DW, Shurrab FM, et al. Neutralizing antibodies against SARS-CoV-2 are higher but decline faster in mRNA vaccinees compared to individuals with natural infection. *J Travel Med* (2022) 29:1–7. doi: 10.1093/jtm/taac130

2. Abu-Raddad LJ, Chemaitelly H, Ayoub HH, AlMukdad S, Yassine HM, Al-Khatib HA, et al. Effect of mRNA Vaccine Boosters against SARS-CoV-2 Omicron Infection in Qatar. *N Engl J Med* (2022) 386(19):1804–16. doi: 10.1056/NEJMoa2200797

3. Abu-Raddad LJ, Chemaitelly H, Bertollini R, National Study Group for C-V. Waning mRNA-1273 Vaccine Effectiveness against SARS-CoV-2 Infection in Qatar. *N Engl J Med* (2022) 386(11):1091–3. doi: 10.1056/NEJMc2119432

4. Andrews N, Stowe J, Kirsebom F, Toffa S, Rickeard T, Gallagher E, et al. Covid-19 vaccine effectiveness against the omicron (B.1.1.529) variant. *N Engl J Med* (2022) 386 (16):1532–46. doi: 10.1056/NEJMoa2119451

5. Andrews N, Stowe J, Kirsebom F, Toffa S, Sachdeva R, Gower C, et al. Effectiveness of COVID-19 booster vaccines against COVID-19-related symptoms, hospitalization and death in England. *Nat Med* (2022) 28(4):831–7. doi: 10.1038/s41591-022-01699-1

6. Andrews N, Tessier E, Stowe J, Gower C, Kirsebom F, Simmons R, et al. Duration of protection against mild and severe disease by covid-19 vaccines. *N Engl J Med* (2022) 386(4):340–50. doi: 10.1056/NEJMoa2115481

7. Chemaitelly H, Abu-Raddad LJ. Waning effectiveness of COVID-19 vaccines. *Lancet* (2022) 399(10327):771–3. doi: 10.1016/S0140-6736(22)00277-X

8. Planas D, Saunders N, Maes P, Guivel-Benhassine F, Planchais C, Buchrieser J, et al. Considerable escape of SARS-CoV-2 Omicron to antibody neutralization. *Nature* (2022) 602(7898):671–5. doi: 10.1038/s41586-021-04389-z

9. Cele S, Jackson L, Khoury DS, Khan K, Moyo-Gwete T, Tegally H, et al. Omicron extensively but incompletely escapes Pfizer BNT162b2 neutralization. *Nature* (2022) 602(7898):654–6. doi: 10.1038/s41586-021-04387-1

10. Nordstrom P, Ballin M, Nordstrom A. Risk of infection, hospitalisation, and death up to 9 months after a second dose of COVID-19 vaccine: a retrospective, total population cohort study in Sweden. *Lancet* (2022) 399(10327):814–23. doi: 10.1016/S0140-6736(22)00089-7

11. El-Mohandes A, Wyka K, White TM, El-Sadr WM, Rauh L, Vasan A, et al. Comparison of current attitudes toward COVID-19 vaccination in new york city and the US nationally. *J Health Commun* (2023) 28(sup1):34–44. doi: 10.1080/10810730.2023.2208071

12. Link-Gelles R, Ciesla AA, Fleming-Dutra KE, Smith ZR, Britton A, Wiegand RE, et al. Effectiveness of bivalent mRNA vaccines in preventing symptomatic SARS-coV-2 infection - increasing community access to testing program, United States, september-november 2022. *MMWR Morb Mortal Wkly Rep* (2022) 71(48):1526–30. doi: 10.15585/mmwr.mm7148e1

13. Chandrashekar A, Yu J, McMahan K, Jacob-Dolan C, Liu J, He X, et al. Vaccine protection against the SARS-CoV-2 Omicron variant in macaques. *Cell* (2022) 185 (9):1549–55 e11. doi: 10.1016/j.cell.2022.03.024

14. Keeton R, Tincho MB, Ngomti A, Baguma R, Benede N, Suzuki A, et al. T cell responses to SARS-CoV-2 spike cross-recognize Omicron. *Nature* (2022) 603 (7901):488–92. doi: 10.1016/j.cell.2022.03.024

15. Geers D, Shamier MC, Bogers S, den Hartog G, Gommers L, Nieuwkoop NN, et al. SARS-CoV-2 variants of concern partially escape humoral but not T-cell responses in COVID-19 convalescent donors and vaccinees. *Sci Immunol* (2021) 6 (59):eabj1750. doi: 10.1126/sciimmunol.abj1750

16. Liu J, Chandrashekar A, Sellers D, Barrett J, Jacob-Dolan C, Lifton M, et al. Vaccines elicit highly conserved cellular immunity to SARS-CoV-2 Omicron. *Nature* (2022) 603(7901):493–6. doi: 10.1038/s41586-022-04465-y

17. Shin H, Iwasaki A. A vaccine strategy that protects against genital herpes by establishing local memory T cells. *Nature* (2012) 491(7424):463–7. doi: 10.1038/nature11522

18. McMahan K, Yu J, Mercado NB, Loos C, Tostanoski LH, Chandrashekar A, et al. Correlates of protection against SARS-CoV-2 in rhesus macaques. *Nature* (2021) 590 (7847):630–4. doi: 10.1038/s41586-020-03041-6

19. Poon MML, Rybkina K, Kato Y, Kubota M, Matsumoto R, Bloom NI, et al. SARS-CoV-2 infection generates tissue-localized immunological memory in humans. *Sci Immunol* (2021) 6(65):eabl9105. doi: 10.1126/sciimmunol.abl9105

20. Zens KD, Chen JK, Farber DL. Vaccine-generated lung tissue-resident memory T cells provide heterosubtypic protection to influenza infection. *JCI Insight* (2016) 1 (10):e172665. doi: 10.1172/jci.insight.85832

21. Van Dis E, Sogi KM, Rae CS, Sivick KE, Surh NH, Leong ML, et al. STING-Activating Adjuvants Elicit a Th17 Immune Response and Protect against Mycobacterium tuberculosis Infection. *Cell Rep* (2018) 23(5):1435–47. doi: 10.1016/j.celrep.2018.04.003

22. Karanika S, Gordy JT, Neupane P, Karantanos T, Ruelas Castillo J, Quijada D, et al. An intranasal stringent response vaccine targeting dendritic cells as a novel adjunctive therapy against tuberculosis. *Front Immunol* (2022) 13:972266. doi: 10.3389/fimmu.2022.972266

23. Luo K, Zavala F, Gordy J, Zhang H, Markham RB. Extended protection capabilities of an immature dendritic-cell targeting malaria sporozoite vaccine. *Vaccine* (2017) 35(18):2358–64. doi: 10.1016/j.vaccine.2017.03.052

24. Amorim KN, Rampazo EV, Antonialli R, Yamamoto MM, Rodrigues MM, Soares IS, et al. The presence of T cell epitopes is important for induction of antibody responses against antigens directed to DEC205(+) dendritic cells. *Sci Rep* (2016) 6:39250. doi: 10.1038/srep39250

25. Grossmann C, Tenbusch M, Nchinda G, Temchura V, Nabi G, Stone GW, et al. Enhancement of the priming efficacy of DNA vaccines encoding dendritic cell-targeted antigens by synergistic toll-like receptor ligands. *BMC Immunol* (2009) 10:43. doi: 10.1186/1471-2172-10-43

26. Hao S, Bai O, Li F, Yuan J, Laferte S, Xiang J. Mature dendritic cells pulsed with exosomes stimulate efficient cytotoxic T-lymphocyte responses and antitumour immunity. *Immunology* (2007) 120(1):90–102. doi: 10.1111/j.1365-2567.2006.02483.x

27. Idoyaga J, Lubkin A, Fiorese C, Lahoud MH, Caminschi I, Huang Y, et al. Comparable T helper 1 (Th1) and CD8 T-cell immunity by targeting HIV gag p24 to CD8 dendritic cells within antibodies to Langerin, DEC205, and Clec9A. *Proc Natl Acad Sci U S A*. (2011) 108(6):2384–9. doi: 10.1073/pnas.1019547108

28. Wang B, Zaidi N, He LZ, Zhang L, Kuroiwa JM, Keler T, et al. Targeting of the non-mutated tumor antigen HER2/neu to mature dendritic cells induces an integrated immune response that protects against breast cancer in mice. *Breast Cancer Res* (2012) 14(2):R39. doi: 10.1186/bcr3135

29. Mastelic-Gavillet B, Balint K, Boudousquie C, Gannon PO, Kandalaft LE. Personalized dendritic cell vaccines-recent breakthroughs and encouraging clinical results. *Front Immunol* (2019) 10:766. doi: 10.3389/fimmu.2019.00766

30. Gordy JT, Luo K, Kapoor A, Kim ES, Ayeh SK, Karakousis PC, et al. Treatment with an immature dendritic cell-targeting vaccine supplemented with IFN-alpha and an inhibitor of DNA methylation markedly enhances survival in a murine melanoma model. *Cancer Immunol Immunother* (2020) 69:569–80 doi: 10.1007/s00262-019-02471-0

31. Gordy JT, Luo K, Zhang H, Biragyn A, Markham RB. Fusion of the dendritic cell-targeting chemokine MIP3alpha to melanoma antigen Gp100 in a therapeutic DNA vaccine significantly enhances immunogenicity and survival in a mouse melanoma model. *J immunotherapy cancer*. (2016) 4:96. doi: 10.1186/s40425-016-0189-y

32. Luo K, Gordy JT, Zavala F, Markham RB. A chemokine-fusion vaccine targeting immature dendritic cells elicits elevated antibody responses to malaria sporozoites in infant macaques. *Sci Rep* (2021) 11(1):1220. doi: 10.1038/s41598-020-79427-3

33. Klein M, Brouwer MC, Angele B, Geldhoff M, Marquez G, Varona R, et al. Leukocyte attraction by CCL20 and its receptor CCR6 in humans and mice with pneumococcal meningitis. *PloS One* (2014) 9(4):e93057. doi: 10.1371/journal.pone.0093057

34. Zhao X, Jain S, Benjamin Larman H, Gonzalez S, Irvine DJ. Directed cell migration via chemoattractants released from degradable microspheres. *Biomaterials* (2005) 26(24):5048–63. doi: 10.1016/j.biomaterials.2004.12.003

35. He S, Cao Q, Yoneyama H, Ge H, Zhang Y, Zhang Y. MIP-3alpha and MIP-1alpha rapidly mobilize dendritic cell precursors into the peripheral blood. *J Leukoc Biol* (2008) 84(6):1549–56. doi: 10.1189/jlb.0708420

36. Schutyser E, Struyf S, Van Damme J. The CC chemokine CCL20 and its receptor CCR6. *Cytokine Growth Factor Rev* (2003) 14(5):409–26. doi: 10.1016/S1359-6101(03)00049-2

37. Biragyn A, Surenhu M, Yang D, Ruffini PA, Haines BA, Klyushnenkova E, et al. Mediators of innate immunity that target immature, but not mature, dendritic cells induce antitumor immunity when genetically fused with nonimmunogenic tumor antigens. *J Immunol* (2001) 167(11):6644–53. doi: 10.4049/jimmunol.167.11.6644

38. Fushimi T, Kojima A, Moore MA, Crystal RG. Macrophage inflammatory protein 3alpha transgene attracts dendritic cells to established murine tumors and suppresses tumor growth. *J Clin Invest*. (2000) 105(10):1383–93. doi: 10.1172/JCI7548

39. Klein SL, Pekosz A, Park HS, Ursin RL, Shapiro JR, Benner SE, et al. Sex, age, and hospitalization drive antibody responses in a COVID-19 convalescent plasma donor population. *J Clin Invest*. (2020) 130(11):6141–50. doi: 10.1172/JCI142004

40. Li M, Beck EJ, Laeyendecker O, Eby Y, Tobian AAR, Caturegli P, et al. Convalescent plasma with a high level of virus-specific antibody effectively neutralizes SARS-CoV-2 variants of concern. *Blood Adv* (2022) 6(12):3678–83. doi: 10.1182/bloodadvances.2022007410

41. Debes AK, Xiao S, Egbert ER, Caturegli P, Gadala A, Colantuoni E, et al. Neutralizing SARS-CoV-2 Spike Antibodies against Omicron in Paired Samples after Two or Three Doses of mRNA Vaccine. *Microbiol Spectr*. (2022) 10(5):e0204622. doi: 10.1128/spectrum.02046-22

42. Cromer D, Steain M, Reynaldi A, Schlub TE, Wheatley AK, Juno JA, et al. Neutralising antibody titres as predictors of protection against SARS-CoV-2 variants and the impact of boosting: a meta-analysis. *Lancet Microbe* (2022) 3(1):e52–61. doi: 10.1016/S2666-5247(21)00267-6

43. Li J, Ahmet F, Sullivan LC, Brooks AG, Kent SJ, De Rose R, et al. Antibodies targeting Clec9A promote strong humoral immunity without adjuvant in mice and non-human primates. *Eur J Immunol* (2015) 45(3):854–64. doi: 10.1002/eji.201445127

44. Kodama S, Abe N, Hirano T, Suzuki M. A single nasal dose of CCL20 chemokine induces dendritic cell recruitment and enhances nontypable Haemophilus influenzae-specific immune responses in the nasal mucosa. *Acta Otolaryngol* (2011) 131(9):989–96. doi: 10.3109/00016489.2011.576429

45. Kodama S, Hirano T, Noda K, Umemoto S, Suzuki M. Nasal immunization with plasmid DNA encoding P6 protein and immunostimulatory complexes elicits nontypeable Haemophilus influenzae-specific long-term mucosal immune responses in the nasopharynx. *Vaccine* (2011) 29(10):1881–90. doi: 10.1016/j.vaccine.2010.12.129

46. Qin T, Yin Y, Yu Q, Huang L, Wang X, Lin J, et al. CpG oligodeoxynucleotides facilitate delivery of whole inactivated H9N2 influenza virus via transepithelial dendrites of dendritic cells in nasal mucosa. *J Virol* (2015) 89(11):5904–18. doi: 10.1128/JVI.00296-15

47. Brussow H. Do we need nasal vaccines against COVID 19 to suppress the transmission of infections? *Microb Biotechnol* (2023) 16(1):3–14. doi: 10.1111/1751-7915.14181

48. Le Nouen C, Nelson CE, Liu X, Park HS, Matsuoka Y, Luongo C, et al. Intranasal pediatric parainfluenza virus-vectored SARS-CoV-2 vaccine is protective in monkeys. *Cell* (2022) 185(25):4811–25 e17. doi: 10.1016/j.cell.2022.11.006

49. Lei H, Alu A, Yang J, Ren W, He C, Lan T, et al. Intranasal administration of a recombinant RBD vaccine induces long-term immunity against Omicron-included SARS-CoV-2 variants. *Signal Transduct Target Ther* (2022) 7(1):159. doi: 10.1038/s41392-022-01002-1

50. Blakney AK, Bekker LG. DNA vaccines join the fight against COVID-19. *Lancet* (2022) 399(10332):1281–2. doi: 10.1016/S0140-6736(22)00524-4

51. Khobragade A, Bhate S, Ramaiah V, Deshpande S, Giri K, Phophle H, et al. Efficacy, safety, and immunogenicity of the DNA SARS-CoV-2 vaccine (ZyCoV-D): the interim efficacy results of a phase 3, randomised, double-blind, placebo-controlled study in India. *Lancet* (2022) 399(10332):1313–21. doi: 10.1016/S0140-6736(22)00151-9

frontiers | Frontiers in Immunology

TYPE Review
PUBLISHED 26 February 2024
DOI 10.3389/fimmu.2024.1345499

OPEN ACCESS

EDITED BY
Huan Huu Nguyen,
IGY Life Sciences, United States

REVIEWED BY
Sivaram Gunisetty,
Emory University, United States
Güliz Tuba Barut,
Institute of Virology and Immunology, Switzerland

*CORRESPONDENCE
William J. Murphy
wmjmurphy@ucdavis.edu

RECEIVED 27 November 2023
ACCEPTED 12 February 2024
PUBLISHED 26 February 2024

CITATION
Collins CP, Longo DL and Murphy WJ (2024) The immunobiology of SARS-CoV-2 infection and vaccine responses: potential influences of cross-reactive memory responses and aging on efficacy and off-target effects. *Front. Immunol.* 15:1345499. doi: 10.3389/fimmu.2024.1345499

The immunobiology of SARS-CoV-2 infection and vaccine responses: potential influences of cross-reactive memory responses and aging on efficacy and off-target effects

Craig P. Collins[1], Dan L. Longo[2] and William J. Murphy[3]*

[1]Graduate Program in Immunology, University of California (UC) Davis, Davis, CA, United States, [2]Harvard Medical School, Brigham and Women's Hospital, Boston, MA, United States, [3]Departments of Dermatology and Internal Medicine (Hematology/Oncology), University of California (UC) Davis School of Medicine, Sacramento, CA, United States

Immune responses to both SARS-CoV-2 infection and its associated vaccines have been highly variable within the general population. The increasing evidence of long-lasting symptoms after resolution of infection, called post-acute sequelae of COVID-19 (PASC) or "Long COVID," suggests that immune-mediated mechanisms are at play. Closely related endemic common human coronaviruses (hCoV) can induce pre-existing and potentially cross-reactive immunity, which can then affect primary SARS-CoV-2 infection, as well as vaccination responses. The influence of pre-existing immunity from these hCoVs, as well as responses generated from original CoV2 strains or vaccines on the development of new high-affinity responses to CoV2 antigenic viral variants, needs to be better understood given the need for continuous vaccine adaptation and application in the population. Due in part to thymic involution, normal aging is associated with reduced naïve T cell compartments and impaired primary antigen responsiveness, resulting in a reliance on the pre-existing cross-reactive memory cell pool which may be of lower affinity, restricted in diversity, or of shorter duration. These effects can also be mediated by the presence of down-regulatory anti-idiotype responses which also increase in aging. Given the tremendous heterogeneity of clinical data, utilization of preclinical models offers the greatest ability to assess immune responses under a controlled setting. These models should now involve prior antigen/viral exposure combined with incorporation of modifying factors such as age on immune responses and effects. This will also allow for mechanistic dissection and understanding of the different immune pathways involved in both SARS-CoV-2 pathogen and potential vaccine responses over time and how pre-existing memory responses, including potential anti-idiotype responses, can affect efficacy as well as potential off-target effects in different tissues as well as modeling PASC.

KEYWORDS

immunology, vaccination, SARS-CoV-2, anti-idiotype antibodies, aging

Introduction: the diverse immunology underlying SARS-CoV-2 and vaccine responses

The ongoing SARS-CoV-2 (CoV2) pandemic, with its devastating health and economic effects, has generated an urgent need to gain more in-depth understanding of the complex and interdependent immune mechanisms at work in response to both the virus and to the vaccines that have been developed to combat it. This has been particularly important given the continual emergence of new viral variants which increase in their immune evasive properties, resulting in the need for further vaccine optimization and periodic application. This need has also been highlighted by the extreme diversity of immunological effects observed within the population after CoV2 infection (and reinfection) or vaccination. At one end of the spectrum, some infected patients can have over-reactive immune responses resulting in a life-threatening pro-inflammatory cytokine storm, necessitating the need for immune suppression (1). Aging and obesity appear be risk modifying factors on pathogenesis and outcome. Conversely, many younger individuals can present with relatively asymptomatic infections with rapid viral clearance and spontaneous resolution (1, 2). Similarly, immediate adverse immune reactions to the various vaccines in otherwise healthy adults, while rarer, are also diverse, with some developing rapid allergic reactions and some, even less frequently, with potentially serious off-target effects such as myocarditis and thrombotic events (3). It is still unclear as to what effects are due to vaccine application versus possible past or concurrent CoV2 exposure, especially given recent data indicating that both CoV2 and S protein can be detected in some patients long after viral infection resolution (4, 5). Finally, a growing body of data accrued from patients has shown that various symptoms can persist for many months after infection, called post-acute sequelae of COVID-19 (PASC) or, more colloquially, "Long COVID," indicate that immune-mediated pathways are involved.

Regarding the potential of vaccine-mediated effects, some of these immune-mediated events may be intrinsic for the type and construct of vaccine applied (mRNA, adenovirus, inactivated virus, protein or protein fragment, use of carriers like polyethylene glycol, etc.), as well potential effects of the antigen targeted (i.e., the spike (S) protein in CoV2 which can have direct proinflammatory effects (6)). The immune responses induced to both the virus and vaccines likely play a driving role as well. The occurrence rate of these adverse effects are also notable and being increasingly appreciated as more data are generated. A recent report detailing that 70.79% of those that who were vaccinated and participated in a questionnaire had experienced side effects after the second dose of vaccine, while 46.76% of participants that had already experienced infection had adverse effects after the first injection (7). Another study observed that elderly patients experienced adverse events at a higher rate than other groups, with tachycardia, hypertension, and hypotension being commonly reported, though more serious events, like acute myocardial infarction and cardiac arrest, were also reported (8). Long-term effects of CoV2 infection have also been reported, with men being at an increased risk for cardiovascular complications after CoV2 infection (9, 10). Others have also reported similarly increased occurrence rates of adverse events, at elevated intensity, in the elderly population with repeated vaccination, with those having infection prior to vaccination typically having elevated rates of occurance (11). In comparison to adverse occurrence rates in the elderly with other common vaccinations (influenza, Td, Hepatitis B, etc.), adverse events have been reported to be lower than that observed with SARS-CoV-2 vaccination, though a direct comparison study has not yet been performed (12, 13). In addition, others have reported that mRNA SARS-CoV-2 vaccines have been associated with a higher occurrence of adverse events in comparison to adenoviral vector and inactivated virus vaccines (14, 15).

The diverse array of long-term and diverse effects defining PASC implicate multiple organ systems (cardiovascular, pulmonary, neurologic) being affected, similar to those reported with primary CoV2 infection itself (16). Data supporting the implication of the immune system mediating, at least in part, the development of PASC, is compelling, even considering the heterogeneity of immune responses reported. Primary infection has been demonstrated to cause apoptosis to hippocampal cells, as well as alteration of the neuronal landscape and cognitive impairment (17, 18), with preclinical studies also indicating neuronal inflammation even after clearance of the virus (19). Spike protein has been reported several months post-infection as well (5), with data demonstrating that the S protein has the ability to cross the blood brain barrier and cause inflammation through TLR triggering and inflammasome activation (20–22). While reports of possible long-term effects following vaccination have been shown (23), attributing these solely due to the vaccines is extremely problematic, given the reliance on clinical data and history. The presence of concurrent viral infections, such as asymptomatic CoV2, or common latent infections like Epstein-Barr virus (EBV) and cytomegalovirus (CMV), or continuous exposure to endemic hCoVs, can all be affecting immune responses and the symptoms reported. Additionally, the frequent emergence of CoV2 variants continuously alters immunologic epitopes targeted, which has further complicated the picture newer vaccine formulations are produced to combat them. Some of the initial data suggesting that pre-existing immune responses may affect CoV2 immunity revolved around the reported relatively rapid waning of protective antibody responses (within months), as well as reported reinfection rates (24, 25). More recent data has also demonstrated with both viral infection and vaccination that class switching of antibodies to IgG4 from IgG3 and IgG1 occurs, with IgG4 being a lower affinity subclass of IgG, compounding the issue of total antibody levels waning (26–28).

Given the tremendous heterogeneity of immune responses, pleiotropic pathologies reported, and the emergence of PASC, how can true mechanistic studies be performed to delineate not only causation but also treatment options? Unfortunately, most data regarding both CoV2 infection and vaccines have relied on imprecise measures of human immune function (primarily serum antibody levels or cytokines), variables known to be influenced by a number of clinical factors including underlying medical conditions, and to reflect *in vivo* immune function imperfectly as well as being

highly variable and affected by numerous factors. It is only through the use of preclinical studies that controlled situations and experimental conditions can occur that delineate these different questions.

Preclinical insights gained through SARS-CoV and SARS-CoV-2 virus and vaccine modeling

Mus musculus (Mouse)

Preclinical modeling has already provided significant insights into the mechanisms of SARS-CoV-2 infection and vaccination. Understanding the advantages and limitations of the different animal models is critical for determining relevance to the human condition, especially given species differences in not only immune biology, but also CoV2 susceptibility.

The inbred laboratory mouse continues to be the bedrock for biomedical research, particularly immune-based studies, due to cost, reagent availability, and extensive immune and genetic characterization that already exists. Mice do, however, have significant immune differences between strains that need to be taken into consideration before extrapolating to humans (29, 30). Laboratory mice are also housed under specific pathogen free conditions which severely restricts pathogen exposure and results in, for the most part, a naïve immune repertoire even as they age (31). Mice are inherently resistant to CoV2 infection due to differences between mouse vs human angiotensin converting enzyme 2 (ACE2) (mACE2 and hACE2, respectively) (32, 33). This has led to the generation and use of transgenic hACE2 and Cre-Lox induced mouse models, as well as mouse-adapted strains of CoV2 which produce robust and severe infection pathologies (34).

While mice are resistant to CoV2, they can be infected with SARS-CoV (CoV) which, while similarly utilizing a S protein that also binds ACE2, has the capacity to bind mACE2 due to differences in binding domains (35). Earlier studies with CoV showed that wild type (WT) young mice, such as BALB/c and C57BL/6, have minimal pathology following infection. However, it has been demonstrated that aged BALB/c mice experience pathology similar to that observed in severe human infection, such as pneumonia, pulmonary fibrosis, and large inflammatory cytokine responses, indicating the importance of involving age in preclinical modeling (36, 37). Vaccine efficacy, using mRNA-based vaccines to the CoV S protein, also was demonstrated in mice (38–40), with protective anti-viral antibody responses being produced. However, the mouse strain used appeared to be critical, as BALB/c mice following vaccination and then CoV viral challenge exhibited eosinophilia, lung pathology, and elevated inflammatory cytokines, events not observed in C57BL/6 (B6) mice (39, 41, 42). Another recent report supports this, as a group demonstrated that CoV2 mRNA vaccination of BALB/c mice induced significant weight loss and elevated inflammatory cytokines 1-2 days post injection, with histopathology revealing that myocarditis, as evidenced by apoptosis and necrosis, was observable as far as two weeks after initial infection, with further boosting amplifying myocarditis pathology (43). BALB/c strain mice are skewed towards producing Th2-mediated immune responses which likely contributes to these allergic-type effects, while B6 mice are more skewed towards Th1-mediated responses (44). The vaccine adjuvant was also shown to play a role, as TLR-triggering adjuvants skewing to Th1-type cytokines could ameliorate these allergic effects in the vaccinated mice, while some Th2 promoting adjuvants have been shown to promote such effects (39). A mouse adapted CoV2 has also been recently demonstrated these effects in BALB/c mice mirroring the CoV studies (45). Given that allergic reactions have been reported after vaccine administration in some people, with some only experiencing severe adverse events after boosting (46), this suggests that it is important to use multiple mouse strains to develop a more complete immunologic picture of both vaccine and infection effects to be reflective of an outbred population.

Keratin 18 (K18) hACE2 transgenic mice have the hACE2 gene put on the cytokeratin 18 promoter, allowing expression of hACE2 (47). K18 mice were originally utilized to study CoV, being used to study severe pathology that wasn't producible in young mice. K18 mice infected with CoV and CoV2 experience pathology similar to humans, such as elevated proinflammatory cytokines and cytokine storm with severe infection, innate immune infiltrates in the lungs, and lung and systemic tissue pathology (47–51). Neuropathology typical of CoV infection is also observable in K18 mice, with neuroinvasion via the nasal and central nervous system (CNS) occurring, followed by neuronal death and activation of immune cells such as microglia and T cells, consistent with human infection responses as well (52–55). While discussed at greater detail later, K18 mice have severe pathology that limits modeling of mild or asymptomatic infection.

Commonly used mRNA vaccines targeting the CoV2 S protein have been shown to be efficacious in K18 mice by generating robust antibody responses (56–60). Similarly, IgM (61–65), IgG (26–28, 66–69), and IgA (66, 70–72) mouse antibody kinetics mirroring those observed in humans have been demonstrated. While the vast majority of these vaccine studies have centered on antibody responses, T cell responses have also been characterized (72–74). While most preclinical studies have focused on vaccine efficacy, others have demonstrated adverse effects from mRNA and S1 protein vaccination. These adverse effects include weight loss, a proinflammatory response, acute lung injury, and presence of immune infiltrates (75, 76) suggesting these models may be appropriate in delineating immune-mediated effects due solely by the vaccine.

An issue in using transgenic K18 mice concerns the overexpression hACE2 due to use of the cytokeratin 18 promoter, which is present on all epithelial tissues, and can produce pathology not typical of humans (18, 77). Overexpression of hACE2 in the nasal passages and neuroepithelium has been shown to allow for aggressive SARS-CoV-2 neuroinvasion not observed with human infection (55), while neuropathology, such as neuronal death and immune infiltrates, has been shown by others to be more severe than typically seen in humans (52–54). This overexpression also can lead to more severe organ pathology in what would be considered

non-critical SARS-CoV-2 targets, such as the spleen and liver (47–51). These limitations should also be thought of when interpreting the adverse events that have been demonstrated in K18 SARS-CoV-2 vaccine models. It should also be noted that K18 mice still maintain expression of mACE2, which could further alter viral and vaccine kinetics, as well as the immune response to these challenges. While K18 mice have shown a dose dependent response to SARS-CoV-2 (78), studies are still limited and capturing nuances of human infection may prove to be a challenge in the future due to the severity of infection. While Cre-Lox and adenovirus hACE2 mouse models, which can be induced to express hACE2 on target tissues like the lungs unlike K18 mice, may be able to overcome some of the disadvantages of the K18 mouse model, these also limit mirroring of the systemic effects of CoV2 infection on tissues outside the lung (79–81).

Mouse adapted SARS-CoV and SARS-CoV-2 strains have been generated through reverse genetic engineering (82) and serial passaging in BALB/c mice (82–86). These compatible strains, such as MA10, HRB26M, MASCp6, and others, allow for the infection of young mice, particularly those of a C57BL/6 background, and tend to generate a Th1 skewed immune response with pathology similar to that seen in humans, with acute respiratory distress, lung tissue damage, pneumonia, and lung infiltrates being reported (84, 86). Both non-severe and severe infections can be modeled in a dose dependent manner, while mouse age has been shown to exacerbate pathology. Vaccine efficacy, in the form of antibody responses and resistance to the mouse adapted strains, has also been shown, using different vaccine formulations (84, 87, 88). Due to the novelty of these mouse adapted viruses, limitations have not been as extensively characterized, though it has been observed that they have a different tropism than that observed in humans, and that serially passaging induced mutations could alter viral pathology and the resulting altered immune responses (84). Further studies need to performed to establish the exact pathogenesis and immunobiology of this mouse adapted viruses, with hACE2 mouse models still primarily being used for vaccine assessment efficacy.

Other small animal SARS-CoV-2 models – *Mesocricetus auratus* and *Mustela putorius* (Syrian hamsters and ferrets)

While most preclinical small animal CoV2 models use mice, others have had success using Syrian hamsters and ferrets due to inherent CoV2 susceptibility. Syrian hamsters offer several advantages over WT and transgenic hACE2 mouse models, with hamsters having a structurally similar ACE2 amino acid sequence and S1 protein binding site to humans (89), allowing for natural susceptibility to CoV and CoV2 infection (90–92). Because of these structural similarities, and because Syrian hamsters express ACE2 in the same tissues as humans, viral pathology is fairly similar, with the virus targeting the respiratory tract and lungs for replication, while still generating a systemic immune response (93). Viral pathology severity is dose dependent, allowing for both lethal and non-lethal SARS-CoV-2 infection, while other variables that correlate with disease severity in humans, such as age (91) and sex (94), have been observed to have similar effects on hamster outcomes following infection.

Reports on neuropathology have been conflicting, with some reporting neuronal invasion and pathology, while other have reported a lack of viral mRNA in the CNS, although neuronal immune activation and tissue damage have been consistently reported (19, 91, 95, 96). This neuropathology is more representative of human infection than what has been observed in K18 mice, and given similar viral clearance patterns to humans, hamsters have been used to model PASC (19, 96, 97). A recent report detailed structural and transcriptional changes to the lungs, kidneys, olfactory bulb, and olfactory epithelium following CoV2 infection in Syrian hamsters, with an elevated inflammatory transcriptional profile being observed in the hamsters' brains 31 days after initial infection (19). This was accompanied by behavioral and cognitive changes. While not yet extensively performed, these models may be of particular use to also model PASC pathobiology.

While viral pathology in Syrian hamsters may more resemble humans, significant immune differences exist, although precise characterization of these differences has been hampered by limitations in validated reagents needed to delineate the complex immune responses occurring. The innate immune response is similar, with multiple groups reporting an increase in inflammatory cytokines such as TNF, IL-6, and IL-1B, as well as increase macrophage presence and activation in the lungs within the first 2-5 days of infection (91–93, 98). Adaptive immune characterization has been more difficult, however, due to limitations in hamster specific antibodies and reagents. While a robust virus specific T and B cell response has been observed, delineation and characterization of these adaptive immune responses beyond this has been limited (98). Infection also generates an antibody response similar to humans (98, 99). However, there has been acknowledgement on the limitations of hamsters in modeling human vaccine responses. Merkuleva, et al. demonstrated with a RBD-based vaccine that hamsters had a much smaller production of neutralizing antibodies in comparison to mice, rabbits, and ferrets when given the same vaccine formulation (100). Another group also demonstrated lower antibody titers in comparison to other animal models used (101), offering a potential explanation in Th2 skewing that could exist in hamsters, although this cannot be determined at this time due to the aforementioned lack of hamster specific antibodies for in-depth immune phenotyping.

Ferrets have also been extensively used in respiratory viral models, due to having a similar respiratory system to humans, as well as having similar clinical symptoms, such as coughing and sneezing (102). Ferret ACE2 is structurally similar to humans, and is also bound by the S1 protein, but actual disease severity has been shown to be mild, though severity has been shown to increase with age (not enough to be lethal however) (103–106). Neuropathology is also observable in ferrets, with viral RNA being detectable in the olfactory bulb and occipital lobe, though studies have been limited in regards to the neurological component of infection (107). PASC pathobiology has not been characterized in ferrets, and there are

contrasting opinions on whether they are suitable for modeling due to the lack of disease severity (108, 109).

Studies on ferret immune responses to SARS-CoV-2 infection are limited, as, similarly to hamsters, immune-specific reagents that are ferret specific are limited. Current studies have shown the development of virus specific antibodies, with one study showing a similar response between mice and ferrets (91, 100, 110). Another group showed that with infection, a lung transcriptome profile indicating strong enrichment of genes related type 1 interferons, T cell activation, and M1 macrophage polarization, was observable, which was further elevated with age (91). Another group similarly demonstrated type 1 and type 2 interferon gene upregulation with infection, noting that this response was delayed in male ferrets (111).

Non-human primates

Non-human primate (NPH) large animal models offer significant advantages over mouse models, being closer to humans on a genetic, physiological, immune, and even behavioral level. NHPs have similar ACE2 to humans, only differing by a few amino acids, though the amino acids that do differ are those that would be used in S1 protein binding. The major disadvantages of NHP models, in general, is the expensiveness per animal, which severely limits the numbers of animals that can be used in studies. This can also make reproducibility of data and statistics difficult due to limited animal numbers.

NHPs have pathology resembling mild human infection when inoculated with SARS-CoV-2, with clinical scoring of pneumonia, weight loss, malaise, and fever being comparable but the reduced severity of infection is problematic (112, 113). While viral replication occurs, less efficient S1 protein binding limits infectivity and pathology. One study did observed coagulation abnormalities in *Chlorocebus aethiops* (African Green Monkeys) that would be associated with more severe human infection, but this did not seem to impact long-term overall health (114). Vaccine efficacy has also been demonstrated in NHPs through antibody, immune, and antiviral responses, although studies are limited and often of a short duration, and thus adverse events have not been well documented or even assessed (115–117).

Effects of cross-reactive secondary viral memory responses on CoV2 responses

Although the CoV2 pathogen itself may be new to our species, other human coronaviruses (hCoVs) are not and provide critical common immunological links. Seven hCoVs exist, all of which use a spike (S) protein for cellular entry. CoV2 has been linked with the original CoV due to similarities in virulence, origin, and a high molecular/genetic homology (76%) in their S-proteins (118–120). Four other hCoVs (hCoV-229E, hCoV-NL63, hCoV-HKU1, and hCoV-OC43) are endemic within the population and responsible for common seasonal minor respiratory tract infections worldwide, with the entire population generating immune responses from an early age (121–123). Significant similarities exist between CoV2 and these other hCoVs, suggesting potential cross-reactive immune responses. As with SARS-CoV and CoV2, NL63 also targets the ACE2 receptor via its S- protein. Furthermore, even stronger homologies of CoV2 exist with HKU1 and OC43, which are also beta-coronaviruses, with cross-reactive immune responses having been reported with both antibody and T cell responses (124–126). Others have already demonstrated that in addition to having similar sequence homologies, conservation of epitopes exists between SARS-CoV-2 and a few of these seasonal coronaviruses (127–129), while others have shown the potential of cross reactivity through antibody responses (124, 130, 131), which, taken together with other epidemiological evidence of cross-protective immunity (132), illustrates the potential of cross-reactive mechanisms. Immunological cross-reactivity exists not only among the hCoVs but even with coronaviruses from other species, as antibodies capable of neutralizing both human and mouse CoVs have demonstrated (133). These point to the tremendous potential of pre-existing cross-reactive secondary responses which can then affect not only resistance but also primary antigen-specific response capabilities (119). Furthermore, the endemic nature of these hCoVs indicates that continuous antigen exposure regularly occurs, further amplifying this reshaping of immune repertoire.

The tendency of the immune system to preferentially use immunologic memory from a previous infection when encountering a different version of the original stimulus has been referred to as the "Original Antigenic Sin." This may represent a means to generate rapidly activated memory responses, even if not of high affinity, during acute infection, and provides a means to compensate in situations where optimal primary response induction is impaired. While not extensively characterized yet, the concept of original antigenic sin has been implicated in SARS-CoV-2 immunity, with recent publications supporting the impact this phenomenon could have on vaccine efficacy and disease outcome (134, 135). Other viruses, such as influenza, which have been published on more extensively in the context of antigenic sin, can potentially offer insight when extrapolated to CoV2. While cross-reactive antibody (xAb1) and T cell responses in CoV2 have been characterized, data on their overall role in efficacy of protection, either positive or negative, have been conflicting. However, many studies also illustrate the difficulty of relying on one readout especially with clinical data: use of antibody levels versus cell-mediated antigen- specific responses by T cells including an effector arm with CD8+ T cells and a helper arm with CD4+ T cells as surrogate predictors in ascertaining protection efficacy. The endemic nature of the hCoVs, with exposure occurring from a young age, combined with the presence of latent viral infections, such as CMV and EBV, add to T cell memory inflation over time, though the exact contribution of hCoVs to this memory inflation has not been well chracterized (136–139) (Figure 1). Preferential activation of these cross-reactive responses, even if of a lower affinity, is due to the tremendous speed advantage that memory responses have over generation of primary responses from naïve T cells. A critical question revolves around the effects of these cross-

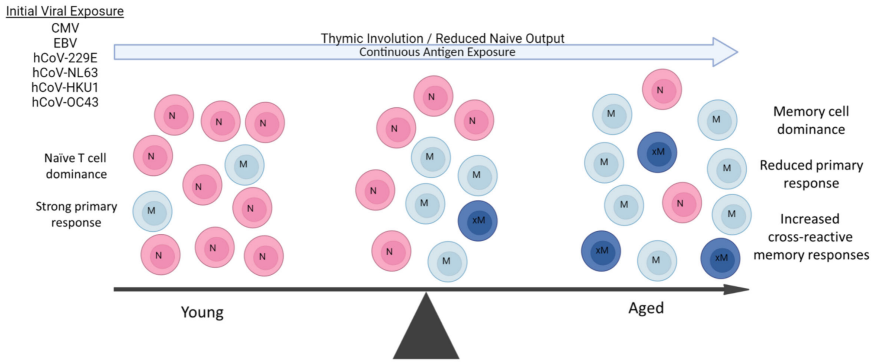

FIGURE 1
Aging Predisposes to Pre-existing Memory Responses. During aging, there is marked shift towards long-lived memory T cells due to both the massive reduction of naïve T cell output from thymic involution and constant antigenic exposure throughout life. Some viral pathogens are endemic and continuous (hCoVs), while others (CMV, EBV) are latent and a also continual source of antigen exposure. The resulting in contraction of the T cell repertoire due to naive T cell loss and predominance of memory T populations results in an increasingly impaired ability to mount primary immune responses with age. Some of these pre-existing memory cells can also be cross-reactive to new viral pathogens such as SARS-CoV-2 depending on extent of antigen similarities and affinity of original response., These cross-reactive responses can then be both of lower affinity and duration. A similar propensity for pre-existing memory B cell responses also occurs with aging, working in concert with long-lived memory CD4+ T cell help.

reactive pre-existing memory cells on overall efficacy towards the new pathogen, with the "net" effect highly contingent on host variables and degree of cross-reactivity. At one end, rapidly induced cross-reactive secondary immune responses, even though of lower affinity, may rapidly generate critically needed initial protection for the host and allow time for more specific primary responses to be generated, as has been suggested in CoV2 to be correlated with less severe disease (140), with a report that even prior responses to other vaccines such as to diphtheria, tetanus and pertussis (DPT), to be potential sources of protective cross-reactive responses to CoV2 (141). Another recent study demonstrated that CoV2 vaccination could induce long-lasting cross-reactive $CD4^+$ T cell responses, suggesting overall better immune effects (142). Conversely, recent reports examining antibody response data from patients and mouse models demonstrated these lower affinity cross-reactive secondary responses to other hCoVs are not only less efficacious, but actually compete and inhibit primary response generation (143, 144), with suggestions that these pre-existing cross-reactive responses are deleterious in protection (145–148). These cross-reactive responses also could have a significant effect on the therapeutic application of convalescent plasma as a source of protective antibodies, which by themselves are immunogenic and also affected by anti-idiotype responses (131). How can one reconcile these potentially opposing effects being observed?

Aging and immune responses: the increasing role of memory and cross-reactive secondary responses to overall immunity

Normal aging has been well-documented to result in significantly impaired primary antigen-specific immune responses, in part due to massive changes in the naive T-cell pool caused by thymic involution (149, 150), as well as other alterations that contribute to immunosenescence (151). Aging and obesity are also associated with a persistent pro-inflammatory state that contributes to increased naïve to memory T cell conversion (152–154). Combined with continuous pathogen exposure throughout life, this results in a marked skewing towards long-lived tissue resident memory T-cell numbers from prior antigen responses (Figure 1). Accordingly, the overall TCR repertoire of the aging host markedly contracts in part due to continuous expansion of long-lived memory T cells directed towards common latent viral infections such as CMV and EBV, further impacting the ability of the immune system to respond to acute viral infections (154–156). These memory T cells markedly outcompete the ever-reduced numbers of naive T cells due to their ability to rapidly respond to antigen recall, even if of lower affinity. Aging therefore increases reliance on pre-existing memory T-cell responses by the host when encountering a new pathogen. This reduced ability to mount new primary antigen-specific $CD4^+$ T-cell responses would then also impair the T-cell "help" needed for the generation of high-affinity B cell and antibody generation, also favoring pre-existing cross-reactive memory B-cell responses (157–159) (Figure 1). Thus, at both the B and T cell levels, activated cross-reactive memory responses can potentially suppress the primary CoV2 response in both specificity and duration while at the same time initially resulting in faster responses resulting in protective effects. However, even if activated, not all of these competitive cross-reactive responses may be efficacious, given a recent report of increased production of non-protective hCoV antibodies following CoV2 infection (160). Similarly, cross-reactive hCoV-specific T cells were observed in unexposed patients (125, 126), but it was observed that after infection, the $CD4^+$ T cells were weaker in response and detectable for shorter time periods (161, 162), indicative of lower functional avidity. Several of the studies also correlated the presence of these cross-reactive antibody responses

with increased disease severity, suggesting a net negative effect on protection (143, 144, 163).

While notable differences in antibody responses have been noted to occur in vaccinated vs naturally infected elderly patients, age as a factor has not been rigorously assessed in studies, although there was a report assessing T cell recall responses to OC43 and NL63, which showed an absence of T cell recall responses in elderly, but not younger individuals (164), with a caveat that one cannot rule out impaired function associated with aged T cell responses. Additionally, while reports on antibody responses and cross-reactive immune responses have centered on patients following CoV2 infection (165, 166), assessment of the potential effects of vaccines on cross-reactive activation have been lacking, although one study observed no effects of a vaccine on cross-reactive antibodies versus the virus itself (167). In contrast, activation of cross-reactive S-protein-specific $CD4^+$ T-cell responses following vaccination was observed, which notably did not occur in the $CD8^+$ T cell population (142), but the delineation of avidity and duration of these cells versus primed naïve T cell responses was assessed. More studies are needed to determine the effects of these, and potentially other, cross-reactive immune responses following different vaccination regimens. Outside of cross-reactive T memory or antibody responses directly competing with the induction of primary responses, these pre-existing immune responses can also potentially mediate effects through activation of cross-reactive anti-idiotype responses. Understanding immune system dynamics and regulation in the context of aging could be highly revealing, especially given the potential of therapeutics already being investigated for restoring immune function and attenuating dysregulated immune responses in the elderly (168).

Revisiting the network hypothesis: immunoregulatory effects of anti-idiotype and cross-reactive anti-idiotype responses and the role of aging

Both immunoglobulin and T-cell receptor (TCR) gene rearrangement results in the appearance of new antigenic determinants or idiotypes (Ab1 for antibody) to which the immune system has not been tolerized, which can then also induce immune responses. These anti-idiotype or Ab2 responses were postulated by Niels Jerne in the Network Theory as a means of immune-mediated regulation (169). This has been robustly demonstrated using inbred mouse models to defined antigens and monoclonal antibodies, with the bulk of research being performed in the 1980's and 1990's (170–173). The difficulty in demonstrating physiologically relevant Ab2 responses in humans partly stems from the tremendous heterogeneity of antigen responses in an outbred population and reliance on clinical data. Nonetheless, demonstration of anti-idiotype antibodies have been demonstrated validating the concept. The immunoregulatory effects of anti-idiotype response is due to the ability of Ab2 to bind Ab1 and neutralize it directly, or to act on the Ab1-producing B cells resulting in clearance or suppression (174–176). The cascade does not stop there however, as the Ab2 also induce down-regulatory "anti-anti-idiotype" or Ab3 responses (177). Some of the Ab3 are similar with the Ab1 idiotype response being also capable of binding the original antigen and possibly protective (178). Ab2 antibodies have even been explored to be surrogates to the original antigen as a vaccine approach. Furthermore, this Ab1>Ab2>Ab3 cascade would then allow for continuation of immune responses long after the antigen itself has disappeared which may also explain for long-lasting off-target effects of either infection or vaccination depending on the nature of the original antigen targeted.

Outside of directly affecting primary Ab1 efficacy, anti-idiotype (Ab2) responses could also potentially exert immune-mediated effects on the host which may account for longer-lasting pathologies following infection and possibly vaccination. A unique type of molecular mimicry attributed to Ab2 can mediate agonistic effects of the primary immunogen. It is important to note that Ab1 responses are polyclonal in nature, and not all Ab1 will induce the same Ab2 (which are also polyclonal), though some clones may predominate (Figure 2). The paratope or binding region of some, but not all, Ab2 can also represent a mirror image of the original antigenic epitope itself and as such, have the capability of binding to the cellular ligand targeted by the original antigen target. Diversity in the anti-idiotypic cascade may also partly explain the tremendous diversity of immune responses within the general population to both CoV2 infection and vaccines (179). Attempts to exploit this antigen-mimicry have included using Ab2 as surrogates for the antigen (180, 181). In the case of CoV2 or vaccines, the ACE2 receptor may be bound by Ab2 in a manner same as the CoV2 S protein (182). Detection of antibodies towards ACE2 following CoV2 infection in some patients supports this hypothesis (183). These Ab2 potentially could then mediate various off-target effects given the diverse expression of ACE2 in many tissues and cell-types, which, depending on the strength of Ab2 response, could possibly result in pathology (Figure 2) (182). Another receptor targeted by the CoV2 S protein, neuropilin-1 (NRP1), which is expressed in astrocytes and neurons, should also be considered in the context of Ab2 antibodies, especially given its roles in axon guidance and VEGF-A modulation. Studies have demonstrated that knockout of NRP1 can have detrimental effects, such as sympathetic nervous system dysregulated sinus bradycardia and neuronal abnormalities, such as poorly condensed ganglia and extended neurons (184). It has not yet been established if antibodies develop against NRP1 during CoV2 infection, however. Because of this, this review will focus on Ab2 responses in the context of ACE2, while noting that NRP1 should also be investigated as well.

The kinetics of Ab2 responses to both T-dependent and T-independent antigens have been extensively studied in mice, although rats and non-human primates also have been used. Initial responses to antigen demonstrated delayed Ab2 kinetics of lower magnitude (185). However, when boosting was applied,

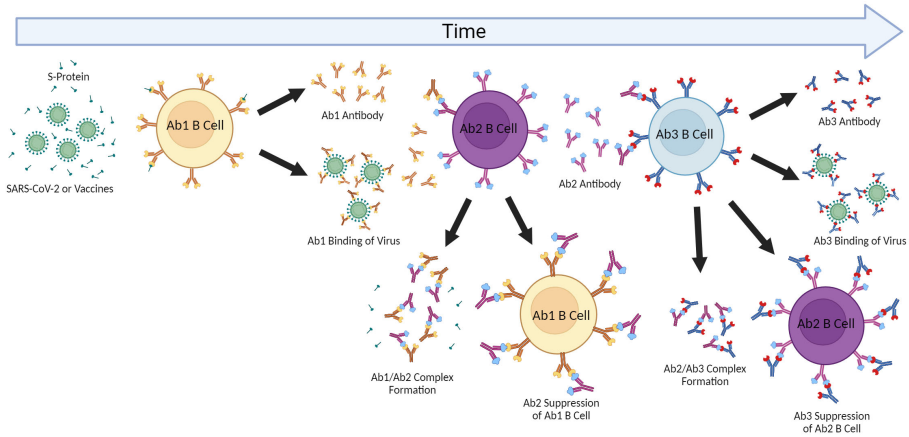

FIGURE 2
Anti-idiotype Response and the Network Cascade. The induction of antigen-specific antibody responses results in polyclonal antibodies (Ab1). The immunogenic nature of the paratope (antigen-binding region) of Ab1 then can result in polyclonal anti-idiotype (Ab2) antibodies capable of binding and inhibiting Ab1 by forming complexes resulting in Ab1 clearance. The paratope of some of these Ab2 antibodies may be a "mirror" to the original antigen and then induce anti-anti-idiotype antibody responses (Ab3) which can then regulate the down-regulatory Ab2 but also some of which may have similar binding as the Ab1 to the original antigen and be protective. This cascade and effects may be contingent on the extent of immunization or antigen exposure as repeated immunizations can result in greater Ab2 responses as well as effects on aging where cross-reactive Ab2 may also affect initial Ab1 responses.

robust and rapid Ab2 responses were observed, even comparable to Ab1, while also resulting in lessening Ab1 (185). This network would then have a major effect on Ab1 efficacy and duration upon repeated stimulation. Importantly, higher Ab2 responses were also observed in older mice suggesting aging predisposes to Ab2 suppression (186). Similarly, T cells from aged mice were observed to play major role in the increased production of Ab2 at the expense of Ab1 (187). These data would suggest that cross-reactive secondary responses are induced after pathogen exposure. It is possible that cross-reactive secondary anti-idiotype (xAb2) responses may also be induced following CoV2 infection or vaccination, although this needs to be definitively shown.

Just as cross-reactive idiotype antibodies (xAb1) or T cells can potentially directly interfere with primary immune response generation and efficacy, triggered secondary xAb2 responses, along with induced specific Ab2, could augment this down-regulatory cascade causing reduction of Ab1 responses. This may also account for the rapid waning of protective CoV2 immunity following infection or vaccination. Furthermore, repeated antigenic challenge (either by re-infection, vaccine boosting, or even continuous exposure to the original hCoV) may further amplify these inhibitory pathways (182). Aging may exacerbate these as well due to impaired primary immune response capabilities. It was reported that elderly patients following CoV2 infection had no detectable Cov2 antibodies despite having antigen-specific memory B cells, pointing to potential effects of Ab2-mediated clearance being higher in this population (188). It is also worth considering that autoantibodies to ACE2 have been previously reported in patients with connective tissue diseases (189). Antigen mimicry effects by Ab2 could also be affected by cross-reactive memory xAb2 responses based on the recognition of shared epitopes. Pre-existing xAb2 from prior NL63 infections could then also bind the ACE2 receptor and contribute to Ab2 effects. Furthermore, the continuous exposure to endemic CoVs as well as repeated administration of CoV2 vaccines could further stimulate and preferentially expand cross-reactive memory (both xAb1 and xAb2) responses, particularly with aging (Figure 3), possibly resulting in long-term effects that may contribute to PASC symptoms given the perpetuating cascades (Ab1, Ab2, Ab3) involved in the Network Theory. Studies are needed to ascertain if similar anti-idiotype responses are also induced after vaccinations as well as induction of comparable xAb2, which could contribute to effects given the continuous antigenic exposure to these endemic hCoVs. Determining whether increased Ab2 capable of binding ACE2 are induced following vaccination given the restricted antigen exposure versus actual CoV2 infection are also needed.

What are the implications of the anti-idiotype (either induced by Ab1 or cross-reactive) on viral protection and treatment? Other than contributing to loss of durability or down-regulation of the primary responses, they should be considered in immune-based therapies. As mentioned, therapeutic application of convalescent sera may be impacted. However, anti-idiotypic responses may have an even more profound down-regulatory effect when using monoclonal antibody-based therapeutics given the monoclonal nature of the therapeutic versus polyclonal Ab1 responses. Another issue centers on the vaccine formulation and schedule depending on the individual's ability to mount primary immune responses. This also can be important when using vaccines targeting the original CoV2 S protein due to the continuous emergence of viral variants which result in increasing selection and loss of antigenic determinants. This extensive mutation rate of the CoV2 resulting in dominance of viral variants (Delta, Omicron, as well as the continuing emergence of new variants/subvariants), particularly within the S-protein, poses another challenge. The continuous loss

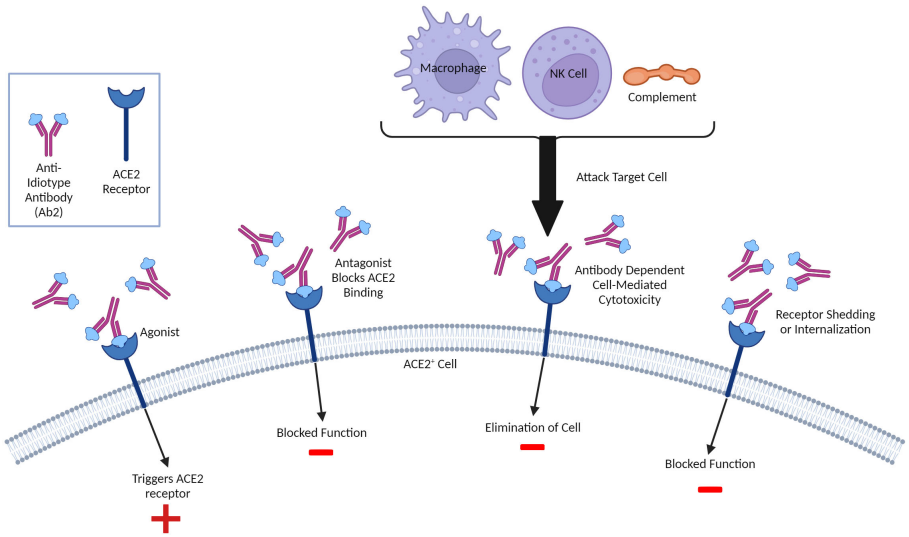

FIGURE 3
Molecular Mimicry and Potential Anti-Idiotype (Ab2)-Mediated Effects. Ab2 effects can be diverse and not limited to regulation of Ab1 responses. Ab2 are directed towards the Ab1 paratope or antigen- binding region and some can have their paratope be a mirror of the original antigen that is recognized. As such, these Ab2 can bind the same ligands the antigen which, in the case of SARS-CoV-2 infection or vaccination involving the Spike protein, can include the ACE2 receptor, resulting in multiple outcomes. If the Ab2 are antagonistic, they can competitively block ACE2 ligands from binding and inhibit function. The Ab2 upon binding can cause internalization thereby also being inhibitory. Some Ab2 could be agonistic and thereby stimulate ACE2 function. Finally, Ab2 binding ACE2+ cells can be targeted for attack by innate immune system due to ADCC (antibody-directed cell or complement-mediated cytotoxicity). A similar paradigm could exist with T cells, although this is much less characterized. Both inhibition and/or dysregulation of ACE2 function could result in potential pathology given critical role of ACE2 on multiple tissues/cells and in inflammation.

of antigenic epitopes in the S-protein to which immune responses were initially generated and then expanded with current vaccine boosting could further limit efficacy due more reliance on the increasingly lower affinity cross-reactive responses. Continuous exposure to endemic hCoVs further complicates the picture by restimulating these memory responses. This has been viewed as a potential issue given the failure to generate a successful vaccine to the endemic hCoV viruses over time.

These effects may be even more pronounced in the aged population with an already impaired priming capability. One group that focused on PASC in the context of the elderly showed that an approximated 30% of patients over the age of 65 developed it (190), while another study showed that Long COVID symptoms were more severe in elderly patients (191), supporting data gathered by the US Census Bureau, though it should be noted that the elderly do not have the highest reported incidence rate of post-COVID symptoms following infection (192). Within the context of vaccination alone, the development of Long COVID has not been extensively addressed, though neuropathic symptoms have been reported, albeit at a lesser occurrence rate than primary infection without vaccination (193–195). While evidence suggests that those vaccinated before infection have protection against Long COVID (196), symptom development after vaccination alone is a phenomenon that is not understood and warrants preclinical investigation, particularly in the context of the elderly. Thus, understanding the immunology of aging in pathogen resistance is a critical parameter that needs to be incorporated into not only clinical studies but more importantly, preclinical studies, given the susceptibility of this population to not only CoV2, but other viral pathogens as well.

Understanding the potential roles of cross-reactive secondary responses and idiotypic regulation: the importance of preclinical modeling

Fortunately, many of the issues raised are very testable hypotheses which can be mechanistically addressed using appropriate preclinical modeling. Preclinical modeling is essential for delineating the complex immunological pathways that arise following infection or vaccination at a mechanistic level, as well as ascertaining potential off-target effects over time under controlled settings. Cross-reactive immune responses, including anti-idiotype responses, on Cov2 and vaccine immunity need to be incorporated into preclinical modeling (119). It is crucial that these studies incorporate important variables such as aging, sex, obesity, and pregnancy, common conditions which all result in significant immune alterations (197–201). Immunological data involving preclinical models on CoV2 have been minimal, especially regarding long-term assessment or dissection of immune pathways under those different conditions. It is important to also recognize that while these models will provide answers, they also have significant limitations since most of these mice are housed under specific-pathogen free conditions and lack significant pathogen exposure, resulting in immature immune phenotypes. In addition, insights on off-target immune-mediated effects can also be gleaned, but choosing the appropriate model is pivotal.Long-term studies as well as effects of repeated vaccination are needed, particularly in aged mice where anti-idiotype responses may be

more dominant. It will also be important to use models in the context of prior immunization involving other hCoV viral antigens and repeated stimulation or with viral challenge to allow for accumulation of memory cells. These memory cells could potentially have cross-reactive responses, impacting the ability to later mount successful primary CoV2 antigen responses, which would require a monitoring of immunoregulatory anti-idiotype responses. As anti-idiotype responses are detected after CoV2 infection directed towards ACE2 and long-term effects associated with PASC can result, it is also important to understand the potential effects these antibodies can exert in such preclinical models. Publications have already shown that the spike protein itself can cross the blood brain barrier and cause acute pathology (202–204), particularly through activation of TLR-4 and NLRP3 inflammasome associated inflammatory pathways and mechanisms (21, 205). Direct administration of S protein to the hippocampus in mice has also been shown to induce cognitive defects, behavioral abnormalities, and neuronal death, acting primarily through glial activation and the upregulation of inflammatory cytokines like IL-1B (206). While publications investigating long term pathology in preclinical models have been limited, a recent preclinical model publication demonstrated that S protein administration intracranially produced long term synaptic damage and memory impairment, accompanied by upregulation of inflammatory cytokines, such as TNF and IL-6, complement proteins, most notably C1q, and increased microgliosis, which was also previously published on in relation to spike protein activation of the NLRP3 inflammasome (21, 22). Notably, this altered neurological landscape was associated with impaired cognitive and memory function, symptoms commonly associated with PASC (22). While elucidative, other potential immune mechanisms that could be related to PASC pathology must also be assessed preclinically.

ACE2 knock-out mice have been reported to develop cardiac dysfunction and pathology as they age, with predominantly male mice being affected (207), correlating to recent reports of increased susceptibility to cardiac disease in male patients recovering from CoV2 infection (10). Some tissues from ACE2 knock-out mice also can display increased inflammatory responses during certain stimuli (208) indicating that preclinical assessments should involve various immunostimulatory challenges in CoV2 models, although confounding issues may arise due to inappropriate expression of hACE2 in the tissues of these mice (209), as well as competition with mouse ACE2. Preclinical modeling using multiple approaches and conditions are needed, and it is crucial to take into consideration the limitations of each model before attempting to extrapolate results to the general population.

Preclinical studies on CoV2 responses are urgently needed to answer questions about potential effects of prior cross-reactive immunity on primary response generation and duration, tracking not only anti-idiotype responses but also other immunoregulatory pathways over time, as well as effects of heterologous and repeated vaccinations (Figure 4). It would also be pertinent to investigate these mechanisms in the context of viral infection as well, which is especially relevant given high reinfection rates reported with SARS-CoV-2. Such experiments would also allow for assessment of potential short- and long-term immune-mediated off-target effects on different tissues, a particularly pressing need given the complex biology and effects of ACE2 and other molecules by which the CoV2 S-protein can bind. The use of antibodies to ACE2 in mice as well as more complete characterization of the role of ACE2 on physiologic functions in various tissues may shed some light on issues surrounding PASC which is especially important given increased cardiac risks associated with infection after resolution.

Therefore, increasing basic science investigation on the potential effects of pre-existing immune responses underlying prior viral infections and their potential impact on CoV2, as well as vaccine immune responses in the context of aging, are critical next steps in the continuing fight against the current, and possibly future, viral pandemics. Moving forward, given the significant gaps in knowledge on the effects of both the virus and associated vaccines on immune responses and effects, preclinical studies should

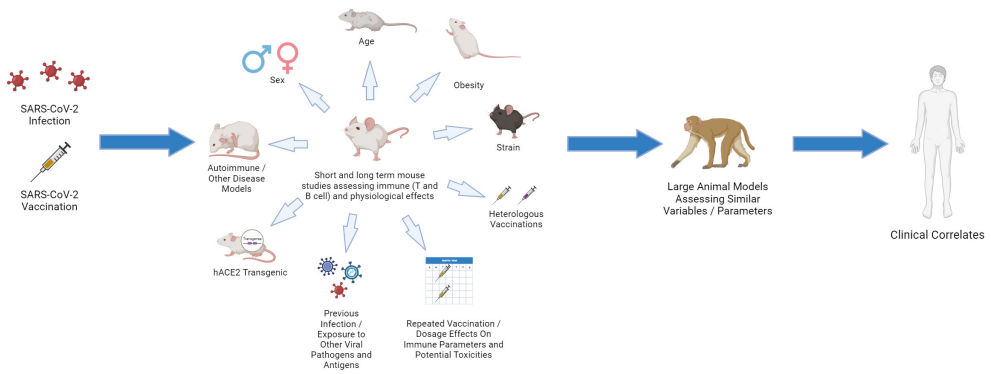

FIGURE 4
Choosing the Relevant Preclinical Models for CoV2: "Bench to Bedside Back to Bench". Using young, inbred laboratory mice under SPF conditions fails to mirror the human landscape. Use of aged and obese mice, different strains, pregnant mice, mice that are prone to various autoimmune and disease states, and mice that have been exposed to various pathogens (including HCoV antigens) can all provide important insights. Studies in which repeated vaccinations, including heterologous, are applied and dissection of immune responses, including in different tissues, are assessed. These preclinical studies can then be linked with large animal models, such as non-human primate (NHP) using similar parameters as aging and obesity, which more faithfully represent human immune dynamics. The data can then be linked and validated with clinical results which then can drive questions using the various preclinical models on immune response efficacy and maintenance.

emphasize human modifying variables such as obesity and aging combined with repeated stimulation on immune responses and possible off-target effects. It is only in preclinical models that control for exposure to the stimulus (virus or antigen) and incorporating these different variables can result in definitive data. The data observed with the original SARS-CoV vaccines and infection also point to potentially immunopathologic responses which were augmented in aged mice and in some cases, strain-dependent. Thus, it is perhaps not surprising that similar effects may occur with CoV2 and vaccines which need to be further delineated. The models should also be developed to better model PASC and the potential role of immune responses or the virus and associated antigens in perpetuating it these long-term effects. As the CoV2 virus continually changes, so do the vaccine formulations to combat it, and thus these variables also need to be incorporated in the preclinical models. Basic studies are still needed delineating the amount of protein being transcribed, by what cells and for how long as well as what variables affect it. The different components of the vaccine product need to also be more stringently studies regarding immune effects. In the case of the mRNA CoV2 vaccines, this involves understanding the immunogenicity of the NLP carrier, the mRNA itself, and finally the S protein made, both individually and as a composite on immune responses. Regarding anti-idiotype responses, studies in which transfer of anti-S antibodies to mice and assessing both longevity and generation of anti-idiotype responses will be revealing. This includes not only effects on adaptive (T and B cell) but also innate immune components. Finally, different dosing regimens need to be better assessed in determining boosting strategies also keeping in mind critical aspects such as age given the significant differences in immune status of young, adult, and advanced aged recipients towards any pathogen or antigenic challenge.

Author contributions

CC: Writing – original draft, Writing – review & editing. DL: Writing – original draft, Writing – review & editing. WM: Writing – original draft, Writing – review & editing.

Funding

The author(s) declare that no financial support was received for the research, authorship, and/or publication of this article.

Acknowledgments

Figures were made with BioRender.com.

Conflict of interest

The authors declare that the research was conducted in the absence of any commercial or financial relationships that could be construed as a potential conflict of interest.

Publisher's note

References

1. Harrison AG, Lin T, Wang P. Mechanisms of SARS-CoV-2 transmission and pathogenesis. *Trends Immunol.* (2020) 41:1100–15. doi: 10.1016/j.it.2020.10.004

2. Booth A, Reed AB, Ponzo S, Yassaee A, Aral M, Plans D, et al. Population risk factors for severe disease and mortality in COVID-19: A global systematic review and meta-analysis. *PloS One.* (2021) 16:e0247461. doi: 10.1371/journal.pone.0247461

3. Anand P, Stahel VP. Correction to: The safety of Covid-19 mRNA vaccines: a review. *Patient Saf Surg.* (2021) 15:22. doi: 10.1186/s13037-021-00296-4

4. Lai Y-C, Cheng Y-W, Chao C-H, Chang Y-Y, Chen C-D, Tsai W-J, et al. Antigenic cross-reactivity between SARS-CoV-2 S1-RBD and its receptor ACE2. *Front Immunol.* (2022) 13:868724. doi: 10.3389/fimmu.2022.868724

5. Swank Z, Senussi Y, Manickas-Hill Z, Yu XG, Li JZ, Alter G, et al. Persistent circulating severe acute respiratory syndrome coronavirus 2 spike is associated with post-acute coronavirus disease 2019 sequelae. *Clin Infect Dis.* (2023) 76:e487–90. doi: 10.1093/cid/ciac722

6. Haga S, Yamamoto N, Nakai-Murakami C, Osawa Y, Tokunaga K, Sata T, et al. Modulation of TNF-alpha-converting enzyme by the spike protein of SARS-CoV and ACE2 induces TNF-alpha production and facilitates viral entry. *Proc Natl Acad Sci U.S.A.* (2008) 105:7809–14. doi: 10.1073/pnas.0711241105

7. Ossato A, Tessari R, Trabucchi C, Zuppini T, Realdon N, Marchesini F. Comparison of medium-term adverse reactions induced by the first and second dose of mRNA BNT162b2 (Comirnaty, Pfizer-BioNTech) vaccine: a post-marketing Italian study conducted between 1 January and 28 February 2021. *Eur J Hosp Pharm.* (2023) 30:e15. doi: 10.1136/ejhpharm-2021-002933

8. Jeet Kaur R, Dutta S, Charan J, Bhardwaj P, Tandon A, Yadav D, et al. Cardiovascular adverse events reported from COVID-19 vaccines: A study based on WHO database. *Int J Gen Med.* (2021) 14:3909–27. doi: 10.2147/IJGM.S324349

9. Minhas AS, Shade JK, Cho S-M, Michos ED, Metkus T, Gilotra NA, et al. The role of sex and inflammation in cardiovascular outcomes and mortality in COVID-19. *Int J Cardiol.* (2021) 337:127–31. doi: 10.1016/j.ijcard.2021.05.011

10. Xie Y, Xu E, Bowe B, Al-Aly Z. Long-term cardiovascular outcomes of COVID-19. *Nat Med.* (2022) 28:583–90. doi: 10.1038/s41591-022-01689-3

11. Monami M, Gori D, Guaraldi F. COVID-19 vaccine hesitancy and early adverse events reported in a cohort of 7,881 italian physicians. *ANNALI DI IGIENE MED PREVENTIVA E DI COMUNITÀ.* (2021) 34(4):344–57. doi: 10.7416/ai.2021.2491

12. Govaert TM, Dinant GJ, Aretz K, Masurel N, Sprenger MJ, Knottnerus JA. Adverse reactions to influenza vaccine in elderly people: randomised double blind placebo controlled trial. *BMJ.* (1993) 307:988–90. doi: 10.1136/bmj.307.6910.988

13. Rodrigues D, de Cassia de Marchi Bacellos de Dalri R. Eventos adversos pós-vacinação contra influenza em idosos no Brasil/Adverse events following immunization against influenza the in elderly in Brazil. *Rev Salúd Publica.* (2019) 21:22–8. doi: 10.15446/rsap.v21n1.77308

14. Oudjedi A, Allali A, Bekli A, Lounis M, Ben Saad H, Boukoufa M. Reported COVID-19 vaccines side effects among Algerian athletes: a comparison between inactivated virus, adenoviral vector, and mRNA COVID-19 vaccines. *Phys Sportsmed.* (2023), 1–13. doi: 10.1080/00913847.2023.2186691

15. Kouhpayeh H, Ansari H. Adverse events following COVID-19 vaccination: A systematic review and meta-analysis. *Int Immunopharmacol.* (2022) 109:108906. doi: 10.1016/j.intimp.2022.108906

16. Nalbandian A, Sehgal K, Gupta A, Madhavan MV, McGroder C, Stevens JS, et al. Post-acute COVID-19 syndrome. *Nat Med.* (2021) 27:601–15. doi: 10.1038/s41591-021-01283-z

17. Borsini A, Merrick B, Edgeworth J, Mandal G, Srivastava DP, Vernon AC, et al. Neurogenesis is disrupted in human hippocampal progenitor cells upon exposure to serum samples from hospitalized COVID-19 patients with neurological symptoms. *Mol Psychiatry*. (2022) 27:5049–61. doi: 10.1038/s41380-022-01741-1

18. Yang J-H, Yang M-S, Kim D-M, Kim B, Tark D, Kang S-M, et al. Delta (B1.617.2) variant of SARS-CoV-2 induces severe neurotropic patterns in K18-hACE2 mice. *Sci Rep*. (2023) 13:3303. doi: 10.1038/s41598-023-29909-x

19. Frere JJ, Serafini RA, Pryce KD, Zazhytska M, Oishi K, Golynker I, et al. SARS-CoV-2 infection in hamsters and humans results in lasting and unique systemic perturbations after recovery. *Sci Trans Med*. (2022) 14:eabq3059. doi: 10.1126/scitranslmed.abq3059

20. Newell KL, Waickman AT. Inflammation, immunity, and antigen persistence in post-acute sequelae of SARS-CoV-2 infection. *Curr Opin Immunol*. (2022) 77:102228. doi: 10.1016/j.coi.2022.102228

21. Albornoz EA, Amarilla AA, Modhiran N, Parker S, Li XX, Wijesundara DK, et al. SARS-CoV-2 drives NLRP3 inflammasome activation in human microglia through spike protein. *Mol Psychiatry*. (2022) 28(7):2878–93. doi: 10.1038/s41380-022-01831-0

22. Fontes-Dantas FL, Fernandes GG, Gutman EG, De Lima EV, Antonio LS, Hammerle MB, et al. SARS-CoV-2 Spike protein induces TLR4-mediated long-term cognitive dysfunction recapitulating post-COVID-19 syndrome in mice. *Cell Rep*. (2023) 42:112189. doi: 10.1016/j.celrep.2023.112189

23. In rare cases, coronavirus vaccines may cause Long Covid–like symptoms . Available online at: https://www.science.org/content/article/rare-cases-coronavirus-vaccines-may-cause-long-covid-symptoms.

24. Choe PG, Kang CK, Suh HJ, Jung J, Song K-H, Bang JH, et al. Waning antibody responses in asymptomatic and symptomatic SARS-coV-2 infection. *Emerg Infect Dis*. (2021) 27:327–9. doi: 10.3201/eid2701.203515

25. Mao Y, Wang W, Ma J, Wu S, Sun F. Reinfection rates among patients previously infected by SARS-CoV-2: systematic review and meta-analysis. *Chin Med J (Engl)*. (2022) 135:145–52. doi: 10.1097/CM9.0000000000001892

26. Buhre JS, Pongracz T, Künsting I, Lixenfeld AS, Wang W, Nouta J, et al. mRNA vaccines against SARS-CoV-2 induce comparably low long-term IgG Fc galactosylation and sialylation levels but increasing long-term IgG4 responses compared to an adenovirus-based vaccine. *Front Immunol*. (2022) 13:1020844. doi: 10.3389/fimmu.2022.1020844

27. Juno JA, Tan H-X, Lee WS, Reynaldi A, Kelly HG, Wragg K, et al. Humoral and circulating follicular helper T cell responses in recovered patients with COVID-19. *Nat Med*. (2020) 26:1428–34. doi: 10.1038/s41591-020-0995-0

28. Kiszel P, Sík P, Miklós J, Kajdácsi E, Sinkovits G, Cervenak L, et al. Class switch towards spike protein-specific IgG4 antibodies after SARS-CoV-2 mRNA vaccination depends on prior infection history. *Sci Rep*. (2023) 13:13166. doi: 10.1038/s41598-023-40103-x

29. Mestas J, Hughes CCW. Of mice and not men: differences between mouse and human immunology. *J Immunol*. (2004) 172:2731–8. doi: 10.4049/jimmunol.172.5.2731

30. Sellers RS, Clifford CB, Treuting PM, Brayton C. Immunological variation between inbred laboratory mouse strains: points to consider in phenotyping genetically immunomodified mice. *Vet Pathol*. (2012) 49:32–43. doi: 10.1177/0300985811429314

31. Hamilton SE, Badovinac VP, Beura LK, Pierson M, Jameson SC, Masopust D, et al. New insights into the immune system using dirty mice. *J Immunol*. (2020) 205:3–11. doi: 10.4049/jimmunol.2000171

32. Shang J, Ye G, Shi K, Wan Y, Luo C, Aihara H, et al. Structural basis of receptor recognition by SARS-CoV-2. *Nature*. (2020) 581:221–4. doi: 10.1038/s41586-020-2179-y

33. Li F, Li W, Farzan M, Harrison SC. Structure of SARS coronavirus spike receptor-binding domain complexed with receptor. *Science*. (2005) 309:1864–8. doi: 10.1126/science.1116480

34. Corleis B, Bastian M, Hoffmann D, Beer M, Dorhoi A. Animal models for COVID-19 and tuberculosis. *Front Immunol*. (2023) 14:1223260. doi: 10.3389/fimmu.2023.1223260

35. Saravanan UB, Namachivayam M, Jeewon R, Huang J-D, Durairajan SSK. Animal models for SARS-CoV-2 and SARS-CoV-1 pathogenesis, transmission and therapeutic evaluation. *World J Virol*. (2022) 11:40–56. doi: 10.5501/wjv.v11.i1.40

36. Roberts A, Paddock C, Vogel L, Butler E, Zaki S, Subbarao K. Aged BALB/c mice as a model for increased severity of severe acute respiratory syndrome in elderly humans. *J Virol*. (2005) 79:5833–8. doi: 10.1128/jvi.79.9.5833-5838.2005

37. Rockx B, Baas T, Zornetzer GA, Haagmans B, Sheahan T, Frieman M, et al. Early upregulation of acute respiratory distress syndrome-associated cytokines promotes lethal disease in an aged-mouse model of severe acute respiratory syndrome coronavirus infection. *J Virol*. (2009) 83:7062–74. doi: 10.1128/JVI.00127-09

38. Honda-Okubo Y, Barnard D, Ong CH, Peng B-H, Tseng C-TK, Petrovsky N. Severe acute respiratory syndrome-associated coronavirus vaccines formulated with delta inulin adjuvants provide enhanced protection while ameliorating lung eosinophilic immunopathology. *J Virol*. (2015) 89:2995–3007. doi: 10.1128/JVI.02980-14

39. Tseng C-T, Sbrana E, Iwata-Yoshikawa N, Newman PC, Garron T, Atmar RL, et al. Immunization with SARS coronavirus vaccines leads to pulmonary immunopathology on challenge with the SARS virus. *PloS One*. (2012) 7:e35421. doi: 10.1371/journal.pone.0035421

40. Iwata-Yoshikawa N, Nagata N, Takaki H, Matsumoto M, Suzuki T, Hasegawa H, et al. Prophylactic vaccine targeting TLR3 on dendritic cells ameliorates eosinophilic pneumonia in a mouse SARS-coV infection model. *Immunohorizons*. (2022) 6:275–82. doi: 10.4049/immunohorizons.2200020

41. Iwata-Yoshikawa N, Uda A, Suzuki T, Tsunetsugu-Yokota Y, Sato Y, Morikawa S, et al. Effects of toll-like receptor stimulation on eosinophilic infiltration in lungs of BALB/c mice immunized with UV-inactivated severe acute respiratory syndrome-related coronavirus vaccine. *J Virol*. (2014) 88:8597–614. doi: 10.1128/JVI.00983-14

42. Bolles M, Deming D, Long K, Agnihothram S, Whitmore A, Ferris M, et al. A double-inactivated severe acute respiratory syndrome coronavirus vaccine provides incomplete protection in mice and induces increased eosinophilic proinflammatory pulmonary response upon challenge. *J Virol*. (2011) 85:12201–15. doi: 10.1128/JVI.06048-11

43. Li C, Chen Y, Zhao Y, Lung DC, Ye Z, Song W, et al. Intravenous injection of coronavirus disease 2019 (COVID-19) mRNA vaccine can induce acute myopericarditis in mouse model. *Clin Infect Dis*. (2021) 74:1933–50. doi: 10.1093/cid/ciab707

44. Hsieh CS, Macatonia SE, O'Garra A, Murphy KM. T cell genetic background determines default T helper phenotype development in *vitro*. *J Exp Med*. (1995) 181:713–21. doi: 10.1084/jem.181.2.713

45. Iwata-Yoshikawa N, Shiwa N, Sekizuka T, Sano K, Ainai A, Hemmi T, et al. A lethal mouse model for evaluating vaccine-associated enhanced respiratory disease during SARS-CoV-2 infection. *Sci Adv*. (2022) 8:eabh3827. doi: 10.1126/sciadv.abh3827

46. Patone M, Mei XW, Handunnetthi L, Dixon S, Zaccardi F, Shankar-Hari M, et al. Risk of myocarditis after sequential doses of COVID-19 vaccine and SARS-coV-2 infection by age and sex. *Circulation*. (2022) 146:743–54. doi: 10.1161/CIRCULATIONAHA.122.059970

47. McCray PB, Pewe L, Wohlford-Lenane C, Hickey M, Manzel L, Shi L, et al. Lethal infection of K18-hACE2 mice infected with severe acute respiratory syndrome coronavirus. *J Virol*. (2007) 81:813–21. doi: 10.1128/jvi.02012-06

48. Moreau GB, Burgess SL, Sturek JM, Donlan AN, Petri WA, Mann BJ. Evaluation of K18-hACE2 mice as a model of SARS-coV-2 infection. *Am J Trop Med Hyg*. (2020) 103:1215–9. doi: 10.4269/ajtmh.20-0762

49. Oladunni FS, Park J-G, Pino PA, Gonzalez O, Akhter A, Allué-Guardia A, et al. Lethality of SARS-CoV-2 infection in K18 human angiotensin-converting enzyme 2 transgenic mice. *Nat Commun*. (2020) 11:6122. doi: 10.1038/s41467-020-19891-7

50. Winkler ES, Bailey AL, Kafai NM, Nair S, McCune BT, Yu J, et al. SARS-CoV-2 infection of human ACE2-transgenic mice causes severe lung inflammation and impaired function. *Nat Immunol*. (2020) 21:1327–35. doi: 10.1038/s41590-020-0778-2

51. Bao L, Deng W, Huang B, Gao H, Liu J, Ren L, et al. The pathogenicity of SARS-CoV-2 in hACE2 transgenic mice. *Nature*. (2020) 583:830–3. doi: 10.1038/s41586-020-2312-y

52. Seehusen F, Clark JJ, Sharma P, Bentley EG, Kirby A, Subramaniam K, et al. Neuroinvasion and neurotropism by SARS-coV-2 variants in the K18-hACE2 mouse. *Viruses*. (2022) 14:1020. doi: 10.3390/v14051020

53. Kumari P, Rothan HA, Natekar JP, Stone S, Pathak H, Strate PG, et al. Neuroinvasion and encephalitis following intranasal inoculation of SARS-coV-2 in K18-hACE2 mice. *Viruses*. (2021) 13:132. doi: 10.3390/v13010132

54. Fumagalli V, Ravà M, Marotta D, Di Lucia P, Laura C, Sala E, et al. Administration of aerosolized SARS-CoV-2 to K18-hACE2 mice uncouples respiratory infection from fatal neuroinvasion. *Sci Immunol*. (2021) 7:eabl9929. doi: 10.1126/sciimmunol.abl9929

55. Carossino M, Montanaro P, O'Connell A, Kenney D, Gertje H, Grosz KA, et al. *Fatal neuroinvasion and SARS-CoV-2 tropism in K18-hACE2 mice is partially independent on hACE2 expression*. Cold Spring Harbor Laboratory, 1 Bungtown Rd, Cold Spring Harbor, NY 11724: Preprint at bioRxiv (2021). doi: 10.1101/2021.01.13.425144

56. Ying B, Whitener B, VanBlargan LA, Hassan AO, Shrihari S, Liang C-Y, et al. Protective activity of mRNA vaccines against ancestral and variant SARS-CoV-2 strains. *Sci Trans Med*. (2021) 14:eabm3302. doi: 10.1126/scitranslmed.abm3302

57. van Oosten L, Yan K, Rawle DJ, Le TT, Altenburg JJ, Fougeroux C, et al. An S1-nanoparticle vaccine protects against SARS-coV-2 challenge in K18-hACE2 mice. *J Virol*. (2022) 96:e00844–22. doi: 10.1128/jvi.00844-22

58. Arieta CM, Xie YJ, Rothenberg DA, Diao H, Harjanto D, Meda S, et al. The T-cell-directed vaccine BNT162b4 encoding conserved non-spike antigens protects animals from severe SARS-CoV-2 infection. *Cell*. (2023) 186:2392–2409.e21. doi: 10.1016/j.cell.2023.04.007

59. Ying B, Scheaffer SM, Whitener B, Liang C-Y, Dmytrenko O, Mackin S, et al. *Boosting with Omicron-matched or historical mRNA vaccines increases neutralizing antibody responses and protection against B.1.1.529 infection in mice*. Cold Spring Harbor Laboratory, 1 Bungtown Rd, Cold Spring Harbor, NY 11724: Preprint at bioRxiv (2022). doi: 10.1101/2022.02.07.479419

60. Scheaffer SM, Lee D, Whitener B, Ying B, Wu K, Liang C-Y, et al. Bivalent SARS-CoV-2 mRNA vaccines increase breadth of neutralization and protect against the BA.5 Omicron variant in mice. *Nat Med*. (2023) 29:247–57. doi: 10.1038/s41591-022-02092-8

61. Röltgen K, Nielsen SCA, Arunachalam PS, Yang F, Hoh RA, Wirz OF, et al. mRNA vaccination compared to infection elicits an IgG-predominant response with greater SARS-CoV-2 specificity and similar decrease in variant spike recognition. *medRxiv*. (2021). doi: 10.1101/2021.04.05.21254952

62. Prabhu M, Yang YJ, Johnston CD, Murphy EA, Ketas TJ, Diaz-Tapia R, et al. Longitudinal antibody response kinetics following SARS-CoV-2 messenger RNA vaccination in pregnant and nonpregnant persons. *Am J Obstet Gynecol MFM*. (2023) 5:100796. doi: 10.1016/j.ajogmf.2022.100796

63. Garcia-Dominguez D, Henry C, Ma L, Jani H, Amato NJ, Manning T, et al. Altering the mRNA-1273 dosing interval impacts the kinetics, quality, and magnitude of immune responses in mice. *Front Immunol*. (2022) 13. doi: 10.3389/fimmu.2022.948335

64. Huang H, Zhang C, Yang S, Xiao W, Zheng Q, Song X. The investigation of mRNA vaccines formulated in liposomes administrated in multiple routes against SARS-CoV-2. *J Controlled Release*. (2021) 335:449–56. doi: 10.1016/j.jconrel.2021.05.024

65. Gebre MS, Rauch S, Roth N, Gergen J, Yu J, Liu X, et al. mRNA vaccines induce rapid antibody responses in mice. *NPJ Vaccines*. (2022) 7:1–7. doi: 10.1038/s41541-022-00511-y

66. Wisnewski AV, Luna JC, Redlich CA. Human IgG and IgA responses to COVID-19 mRNA vaccines. *PloS One*. (2021) 16:e0249499. doi: 10.1371/journal.pone.0249499

67. Gil-Manso S, Alonso R, Catalán P, Sánchez-Arcilla I, Marzola M, Correa-Rocha R, et al. IgG anti-RBD levels during 8-month follow-up post-vaccination with BNT162b2 and mRNA-1273 vaccines in healthcare workers: A one-center study. *Front Cell Infect Microbiol*. (2022) 12:1035155. doi: 10.3389/fcimb.2022.1035155

68. Huang Q, Ji K, Tian S, Wang F, Huang B, Tong Z, et al. A single-dose mRNA vaccine provides a long-term protection for hACE2 transgenic mice from SARS-CoV-2. *Nat Commun*. (2021) 12:776. doi: 10.1038/s41467-021-21037-2

69. Li J-Q, Zhang Z-R, Zhang H-Q, Zhang Y-N, Zeng X-Y, Zhang Q-Y, et al. Intranasal delivery of replicating mRNA encoding neutralizing antibody against SARS-CoV-2 infection in mice. *Sig Transduct Target Ther*. (2021) 6:1–8. doi: 10.1038/s41392-021-00783-1

70. Denis J, Garnier A, Cheutin L, Ferrier A, Timera H, Jarjaval F, et al. Long-term systemic and mucosal SARS-CoV-2 IgA response and its association with persistent smell and taste disorders. *Front Immunol*. (2023) 14:1140714. doi: 10.3389/fimmu.2023.1140714

71. Americo JL, Cotter CA, Earl PL, Liu R, Moss B. Intranasal inoculation of an MVA-based vaccine induces IgA and protects the respiratory tract of hACE2 mice from SARS-CoV-2 infection. *Proc Natl Acad Sci U.S.A*. (2022) 119:e2202069119. doi: 10.1073/pnas.2202069119

72. Lapuente D, Fuchs J, Willar J, Vieira Antão A, Eberlein V, Uhlig N, et al. Protective mucosal immunity against SARS-CoV-2 after heterologous systemic prime-mucosal boost immunization. *Nat Commun*. (2021) 12:6871. doi: 10.1038/s41467-021-27063-4

73. Joag V, Wijeyesinghe S, Stolley JM, Quarnstrom CF, Dileepan T, Soerens AG, et al. Cutting edge: mouse SARS-coV-2 epitope reveals infection and vaccine-elicited CD8 T cell responses. *J Immunol*. (2021) 206:931–5. doi: 10.4049/jimmunol.2001400

74. Zhuang Z, Lai X, Sun J, Chen Z, Zhang Z, Dai J, et al. Mapping and role of T cell response in SARS-CoV-2-infected mice. *J Exp Med*. (2021) 218:e20202187. doi: 10.1084/jem.20202187

75. Colunga Biancatelli RML, Solopov PA, Sharlow ER, Lazo JS, Marik PE, Catravas JD. The SARS-CoV-2 spike protein subunit S1 induces COVID-19-like acute lung injury in K18-hACE2 transgenic mice and barrier dysfunction in human endothelial cells. *Am J Physiol Lung Cell Mol Physiol*. (2021) 321:L477–84. doi: 10.1152/ajplung.00223.2021

76. Syenina A, Gan ES, Toh JZN, Alwis R, Lin LZ, Tham CYL, et al. Adverse effects following anti–COVID-19 vaccination with mRNA-based BNT162b2 are alleviated by altering the route of administration and correlate with baseline enrichment of T and NK cell genes. *PloS Biol*. (2022) 20:e3001643. doi: 10.1371/journal.pbio.3001643

77. Weerasinghe SVW, Ku N-O, Altshuler PJ, Kwan R, Omary MB. Mutation of caspase-digestion sites in keratin 18 interferes with filament reorganization, and predisposes to hepatocyte necrosis and loss of membrane integrity. *J Cell Sci*. (2014) 127:1464–75. doi: 10.1242/jcs.138479

78. Dong W, Mead H, Tian L, Park J-G, Garcia JI, Jaramillo S, et al. The K18-human ACE2 transgenic mouse model recapitulates non-severe and severe COVID-19 in response to an infectious dose of the SARS-coV-2 virus. *J Virol*. (2022) 96:e0096421. doi: 10.1128/JVI.00964-21

79. Winkler ES, Chen RE, Alam F, Yildiz S, Case JB, Uccellini MB, et al. SARS-coV-2 causes lung infection without severe disease in human ACE2 knock-in mice. *J Virol*. (2022) 96:e01511–21. doi: 10.1128/JVI.01511-21

80. Bruter AV, Korshunova DS, Kubekina MV, Sergiev PV, Kalinina AA, Ilchuk LA, et al. Novel transgenic mice with Cre-dependent co-expression of GFP and human ACE2: a safe tool for study of COVID-19 pathogenesis. *Transgenic Res*. (2021) 30:289–301. doi: 10.1007/s11248-021-00249-8

81. Rathnasinghe R, Strohmeier S, Amanat F, Gillespie VL, Krammer F, García-Sastre A, et al. Comparison of transgenic and adenovirus hACE2 mouse models for SARS-CoV-2 infection. *Emerg Microbes Infect*. (2020) 9:2433–45. doi: 10.1080/22221751.2020.1838955

82. Roberts A, Deming D, Paddock CD, Cheng A, Yount B, Vogel L, et al. A mouse-adapted SARS-coronavirus causes disease and mortality in BALB/c mice. *PloS Pathog*. (2007) 3:e5. doi: 10.1371/journal.ppat.0030005

83. Wang J, Shuai L, Wang C, Liu R, He X, Zhang X, et al. Mouse-adapted SARS-CoV-2 replicates efficiently in the upper and lower respiratory tract of BALB/c and C57BL/6J mice. *Protein Cell*. (2020) 11:776–82. doi: 10.1007/s13238-020-00767-x

84. Leist SR, Dinnon KH, Schäfer A, Tse LV, Okuda K, Hou YJ, et al. A mouse-adapted SARS-coV-2 induces acute lung injury and mortality in standard laboratory mice. *Cell*. (2020) 183:1070–1085.e12. doi: 10.1016/j.cell.2020.09.050

85. Dinnon KH, Leist SR, Schäfer A, Edwards CE, Martinez DR, Montgomery SA, et al. A mouse-adapted model of SARS-CoV-2 to test COVID-19 countermeasures. *Nature*. (2020) 586:560–6. doi: 10.1038/s41586-020-2708-8

86. Gu H, Chen Q, Yang G, He L, Fan H, Deng Y-Q, et al. Adaptation of SARS-CoV-2 in BALB/c mice for testing vaccine efficacy. *Science*. (2020) 369:1603–7. doi: 10.1126/science.abc4730

87. Zhang N-N, Li X-F, Deng Y-Q, Zhao H, Huang Y-J, Yang G, et al. A Thermostable mRNA Vaccine against COVID-19. *Cell*. (2020) 182:1271–1283.e16. doi: 10.1016/j.cell.2020.07.024

88. DiPiazza AT, Leist SR, Abiona OM, Moliva JI, Werner A, Minai M, et al. COVID-19 vaccine mRNA-1273 elicits a protective immune profile in mice that is not associated with vaccine-enhanced disease upon SARS-CoV-2 challenge. *Immunity*. (2021) 54:1869–1882.e6. doi: 10.1016/j.immuni.2021.06.018

89. Liu Y, Hu G, Wang Y, Ren W, Zhao X, Ji F, et al. Functional and genetic analysis of viral receptor ACE2 orthologs reveals a broad potential host range of SARS-CoV-2. *Proc Natl Acad Sci U.S.A*. (2021) 118:e2025373118. doi: 10.1073/pnas.2025373118

90. Zhang Y-N, Zhang Z-R, Zhang H-Q, Li N, Zhang Q-Y, Li X-D, et al. Different pathogenesis of SARS-CoV-2 Omicron variant in wild-type laboratory mice and hamsters. *Sig Transduct Target Ther*. (2022) 7:1–3. doi: 10.1038/s41392-022-00930-2

91. Osterrieder N, Bertzbach LD, Dietert K, Abdelgawad A, Vladimirova D, Kunec D, et al. Age-dependent progression of SARS-coV-2 infection in Syrian hamsters. *Viruses*. (2020) 12:779. doi: 10.3390/v12070779

92. Imai M, Iwatsuki-Horimoto K, Hatta M, Loeber S, Halfmann PJ, Nakajima N, et al. Syrian hamsters as a small animal model for SARS-CoV-2 infection and countermeasure development. *Proc Natl Acad Sci U.S.A*. (2020) 117:16587–95. doi: 10.1073/pnas.2009799117

93. Kreye J, Reincke SM, Kornau H-C, Sánchez-Sendin E, Corman VM, Liu H, et al. A therapeutic non-self-reactive SARS-coV-2 antibody protects from lung pathology in a COVID-19 hamster model. *Cell*. (2020) 183:1058–1069.e19. doi: 10.1016/j.cell.2020.09.049

94. Lieber CM, Cox RM, Sourimant J, Wolf JD, Juergens K, Phung Q, et al. SARS-CoV-2 VOC type and biological sex affect molnupiravir efficacy in severe COVID-19 dwarf hamster model. *Nat Commun*. (2022) 13:4416. doi: 10.1038/s41467-022-32045-1

95. Zhang AJ, Lee AC-Y, Chu H, Chan JF-W, Fan Z, Li C, et al. SARS-CoV-2 infects and damages the mature and immature olfactory sensory neurons of hamsters. *Clin Infect Dis*. (2020) 73(2):e503–12. doi: 10.1093/cid/ciaa995

96. Serafini RA, Frere JJ, Zimering J, Giosan IM, Pryce KD, Golynker I, et al. SARS-CoV-2 airway infection results in the development of somatosensory abnormalities in a hamster model. *Sci Signaling*. (2023) 16:eade4984. doi: 10.1126/scisignal.ade4984

97. Heydemann L, Ciurkiewicz M, Beythien G, Becker K, Schughart K, Stanelle-Bertram S, et al. Hamster model for post-COVID-19 alveolar regeneration offers an opportunity to understand post-acute sequelae of SARS-CoV-2. *Nat Commun*. (2023) 14:3267. doi: 10.1038/s41467-023-39049-5

98. Horiuchi S, Oishi K, Carrau L, Frere J, Møller R, Panis M, et al. Immune memory from SARS-CoV-2 infection in hamsters provides variant-independent protection but still allows virus transmission. *Sci Immunol*. (2021) 6:eabm3131. doi: 10.1126/sciimmunol.abm3131

99. Field CJ, Heinly TA, Patel DR, Sim DG, Luley E, Gupta SL, et al. Immune durability and protection against SARS-CoV-2 re-infection in Syrian hamsters. *Emerg Microbes Infect*. (2022) 11:1103–14. doi: 10.1080/22221751.2022.2058419

100. Merkuleva IA, Shcherbakov DN, Borgoyakova MB, Isaeva AA, Nesmeyanova VS, Volkova NV, et al. Are hamsters a suitable model for evaluating the immunogenicity of RBD-based anti-COVID-19 subunit vaccines? *Viruses*. (2022) 14:1060. doi: 10.3390/v14051060

101. Sui Y, Andersen H, Li J, Hoang T, Bekele Y, Kar S, et al. Protection from COVID-19 disease in hamsters vaccinated with subunit SARS-CoV-2 S1 mucosal vaccines adjuvanted with different adjuvants. *Front Immunol*. (2023) 14:1154496. doi: 10.3389/fimmu.2023.1154496

102. Belser JA, Katz JM, Tumpey TM. The ferret as a model organism to study influenza A virus infection. *Dis Model Mech*. (2011) 4:575–9. doi: 10.1242/dmm.007823

103. Sun H, Wang A, Wang L, Wang B, Tian G, Yang J, et al. Systematic tracing of susceptible animals to SARS-coV-2 by a bioinformatics framework. *Front Microbiol*. (2022) 13:781770. doi: 10.3389/fmicb.2022.781770

104. Richard M, Kok A, de Meulder D, Bestebroer TM, Lamers MM, Okba NMA, et al. SARS-CoV-2 is transmitted via contact and via the air between ferrets. *Nat Commun*. (2020) 11:3496. doi: 10.1038/s41467-020-17367-2

105. Ryan KA, Bewley KR, Fotheringham SA, Slack GS, Brown P, Hall Y, et al. Dose-dependent response to infection with SARS-CoV-2 in the ferret model and evidence of protective immunity. *Nat Commun*. (2021) 12:81. doi: 10.1038/s41467-020-20439-y

106. Zamoto A, Taguchi F, Fukushi S, Morikawa S, Yamada YK. Identification of ferret ACE2 and its receptor Function for Sars-Coronavirus. In: Perlman S, Holmes KV, editors. *The Nidoviruses Advances in Experimental Medicine and Biology*. One New York Plaza, Suite 4600, New York, NY 10004-1562, USA: Springer US (2006). p. 519–22. doi: 10.1007/978-0-387-33012-9_93

107. Au GG, Marsh GA, McAuley AJ, Lowther S, Trinidad L, Edwards S, et al. Characterisation and natural progression of SARS-CoV-2 infection in ferrets. *Sci Rep*. (2022) 12:5680. doi: 10.1038/s41598-022-08431-6

108. Jansen EB, Orvold SN, Swan CL, Yourkowski A, Thivierge BM, Francis ME, et al. After the virus has cleared-Can preclinical models be employed for Long COVID research? *PloS Pathog*. (2022) 18:e1010741. doi: 10.1371/journal.ppat.1010741

109. van de Ven K, van Dijken H, Wijsman L, Gomersbach A, Schouten T, Kool J, et al. Pathology and immunity after SARS-coV-2 infection in male ferrets is affected by age and inoculation route. *Front Immunol*. (2021) 12:750229. doi: 10.3389/fimmu.2021.750229

110. Shi J, Wen Z, Zhong G, Yang H, Wang C, Huang B, et al. Susceptibility of ferrets, cats, dogs, and other domesticated animals to SARS-coronavirus 2. *Science*. (2020) 368:1016–20. doi: 10.1126/science.abb7015

111. Francis ME, Richardson B, Goncin U, McNeil M, Rioux M, Foley MK, et al. Sex and age bias viral burden and interferon responses during SARS-CoV-2 infection in ferrets. *Sci Rep*. (2021) 11:14536. doi: 10.1038/s41598-021-93855-9

112. Lu S, Zhao Y, Yu W, Yang Y, Gao J, Wang J, et al. Comparison of nonhuman primates identified the suitable model for COVID-19. *Sig Transduct Target Ther*. (2020) 5:1–9. doi: 10.1038/s41392-020-00269-6

113. Munster VJ, Feldmann F, Williamson BN, van Doremalen N, Pérez-Pérez L, Schulz J, et al. Respiratory disease in rhesus macaques inoculated with SARS-CoV-2. *Nature*. (2020) 585:268–72. doi: 10.1038/s41586-020-2324-7

114. Woolsey C, Borisevich V, Prasad AN, Agans KN, Deer DJ, Dobias NS, et al. Establishment of an African green monkey model for COVID-19 and protection against re-infection. *Nat Immunol*. (2021) 22:86–98. doi: 10.1038/s41590-020-00835-8

115. Corbett KS, Nason MC, Flach B, Gagne M, O'Connell S, Johnston TS, et al. Immune correlates of protection by mRNA-1273 vaccine against SARS-CoV-2 in nonhuman primates. *Science*. (2021) 373:eabj0299. doi: 10.1126/science.abj0299

116. Corbett KS, Gagne M, Wagner DA, O' Connell S, Narpala SR, Flebbe DR, et al. Protection against SARS-CoV-2 Beta variant in mRNA-1273 vaccine-boosted nonhuman primates. *Science*. (2021) 374:1343–53. doi: 10.1126/science.abl8912

117. Gagne M, Moliva JI, Foulds KE, Andrew SF, Flynn BJ, Werner AP, et al. mRNA-1273 or mRNA-Omicron boost in vaccinated macaques elicits similar B cell expansion, neutralizing responses, and protection from Omicron. *Cell*. (2022) 185:1556–1571.e18. doi: 10.1016/j.cell.2022.03.038

118. Kronvall G, Nordenfelt E. On the history of human coronaviruses. *APMIS*. (2021) 129(7):381–3. doi: 10.1111/apm.13109

119. Sealy RE, Hurwitz JL. Cross-reactive immune responses toward the common cold human coronaviruses and severe acute respiratory syndrome coronavirus 2 (SARS-coV-2): mini-review and a murine study. *Microorganisms*. (2021) 9:1643. doi: 10.3390/microorganisms9081643

120. Weiss SR. Forty years with coronaviruses. *J Exp Med*. (2020) 217:e20200537. doi: 10.1084/jem.20200537

121. Riski H, Hovi T. Coronavirus infections of man associated with diseases other than the common cold. *J Med Virol*. (1980) 6:259–65. doi: 10.1002/jmv.1890060309

122. Killerby ME, Biggs HM, Haynes A, Dahl RM, Mustaquim D, Gerber SI, et al. Human coronavirus circulation in the United States 2014-2017. *J Clin Virol*. (2018) 101:52–6. doi: 10.1016/j.jcv.2018.01.019

123. V'kovski P, Kratzel A, Steiner S, Stalder H, Thiel V. Coronavirus biology and replication: implications for SARS-CoV-2. *Nat Rev Microbiol*. (2021) 19:155–70. doi: 10.1038/s41579-020-00468-6

124. Ng KW, Faulkner N, Cornish GH, Rosa A, Harvey R, Hussain S, et al. Preexisting and *de novo* humoral immunity to SARS-CoV-2 in humans. *Science*. (2020) 370:1339–43. doi: 10.1126/science.abe1107

125. Mateus J, Grifoni A, Tarke A, Sidney J, Ramirez SI, Dan JM, et al. Selective and cross-reactive SARS-CoV-2 T cell epitopes in unexposed humans. *Science*. (2020) 370:89–94. doi: 10.1126/science.abd3871

126. Woldemeskel BA, Kwaa AK, Garliss CC, Laeyendecker O, Ray SC, Blankson JN. Healthy donor T cell responses to common cold coronaviruses and SARS-CoV-2. *J Clin Invest*. (2020) 130:6631–8. doi: 10.1172/JCI143120

127. Schulien I, Kemming J, Oberhardt V, Wild K, Seidel LM, Killmer S, et al. Characterization of pre-existing and induced SARS-CoV-2-specific CD8+ T cells. *Nat Med*. (2021) 27:78–85. doi: 10.1038/s41591-020-01143-2

128. Smit WL, van Tol S, Haas LEM, Limonard GJM, Bossink A, Reusken C, et al. Differential abundance of IgG antibodies against the spike protein of SARS-CoV-2 and seasonal coronaviruses in patients with fatal COVID-19. *Virol J*. (2023) 20:85. doi: 10.1186/s12985-023-02050-x

129. Simula ER, Manca MA, Jasemi S, Uzzau S, Rubino S, Manchia P, et al. HCoV-NL63 and SARS-coV-2 share recognized epitopes by the humoral response in sera of people collected pre- and during coV-2 pandemic. *Microorganisms*. (2020) 8:1993. doi: 10.3390/microorganisms8121993

130. Murray SM, Ansari AM, Frater J, Klenerman P, Dunachie S, Barnes E, et al. The impact of pre-existing cross-reactive immunity on SARS-CoV-2 infection and vaccine responses. *Nat Rev Immunol*. (2023) 23:304–16. doi: 10.1038/s41577-022-00809-x

131. Morgenlander WR, Henson SN, Monaco DR, Chen A, Littlefield K, Bloch EM, et al. Antibody responses to endemic coronaviruses modulate COVID-19 convalescent plasma functionality. *J Clin Invest*. (2021) 131:146927. doi: 10.1172/JCI146927

132. Nickbakhsh S, Ho A, Marques DFP, McMenamin J, Gunson RN, Murcia PR. Epidemiology of seasonal coronaviruses: establishing the context for the emergence of coronavirus disease 2019. *J Infect Dis*. (2020) 222:17–25. doi: 10.1093/infdis/jiaa185

133. Klompus S, Leviatan S, Vogl T, Mazor RD, Kalka IN, Stoler-Barak L, et al. Cross-reactive antibodies against human coronaviruses and the animal coronavirome suggest diagnostics for future zoonotic spillovers. *Sci Immunol*. (2021) 6:eabe9950. doi: 10.1126/sciimmunol.abe9950

134. Aguilar-Bretones M, Fouchier RA, Koopmans MP, van Nierop GP. Impact of antigenic evolution and original antigenic sin on SARS-CoV-2 immunity. *J Clin Invest*. (2023) 133:e162192. doi: 10.1172/JCI162192

135. Anderson EM, Li SH, Awofolaju M, Eilola T, Goodwin E, Bolton MJ, et al. SARS-CoV-2 infections elicit higher levels of original antigenic sin antibodies compared with SARS-CoV-2 mRNA vaccinations. *Cell Rep*. (2022) 41:111496. doi: 10.1016/j.celrep.2022.111496

136. Karrer U, Sierro S, Wagner M, Oxenius A, Hengel H, Koszinowski UH, et al. Memory inflation: continuous accumulation of antiviral CD8+ T cells over time. *J Immunol*. (2003) 170:2022–9. doi: 10.4049/jimmunol.170.4.2022

137. Shin HS, Kim Y, Kang J, Um J, Park JS, Park WB, et al. Longitudinal analysis of memory T-cell responses in survivors of middle east respiratory syndrome. *Clin Infect Dis*. (2022) 75:596–603. doi: 10.1093/cid/ciab1019

138. Taira N, Toguchi S, Miyagi M, Mori T, Tomori H, Oshiro K, et al. Altered pre-existing SARS-CoV-2-specific T cell responses in elderly individuals. *Clin Immunol Commun*. (2022) 2:6–11. doi: 10.1016/j.clicom.2021.12.001

139. Townsend JP, Hassler HB, Wang Z, Miura S, Singh J, Kumar S, et al. The durability of immunity against reinfection by SARS-CoV-2: a comparative evolutionary study. *Lancet Microbe*. (2021) 2:e666–75. doi: 10.1016/S2666-5247(21)00219-6

140. Sagar M, Reifler K, Rossi M, Miller NS, Sinha P, White LF, et al. Recent endemic coronavirus infection is associated with less-severe COVID-19. *J Clin Invest*. (2021) 131(1):e143380. doi: 10.1172/JCI143380

141. Reche PA. Potential cross-reactive immunity to SARS-coV-2 from common human pathogens and vaccines. *Front Immunol*. (2020) 11:586984. doi: 10.3389/fimmu.2020.586984

142. Mateus J, Dan JM, Zhang Z, Rydyznski Moderbacher C, Lammers M, Goodwin B, et al. Low-dose mRNA-1273 COVID-19 vaccine generates durable memory enhanced by cross-reactive T cells. *Science*. (2021) 374:eabj9853. doi: 10.1126/science.abj9853

143. Wratil PR, Schmacke NA, Karakoc B, Dulovic A, Junker D, Becker M, et al. Evidence for increased SARS-CoV-2 susceptibility and COVID-19 severity related to pre-existing immunity to seasonal coronaviruses. *Cell Rep*. (2021) 37:110169. doi: 10.1016/j.celrep.2021.110169

144. Lin C-Y, Wolf J, Brice DC, Sun Y, Locke M, Cherry S, et al. Pre-existing humoral immunity to human common cold coronaviruses negatively impacts the protective SARS-CoV-2 antibody response. *Cell Host Microbe*. (2022) 30:83–96.e4. doi: 10.1016/j.chom.2021.12.005

145. Beretta A, Cranage M, Zipeto D. Is cross-reactive immunity triggering COVID-19 immunopathogenesis? *Front Immunol*. (2020) 11:567710. doi: 10.3389/fimmu.2020.567710

146. Song G, He W-T, Callaghan S, Anzanello F, Huang D, Ricketts J, et al. Cross-reactive serum and memory B-cell responses to spike protein in SARS-CoV-2 and endemic coronavirus infection. *Nat Commun*. (2021) 12:2938. doi: 10.1038/s41467-021-23074-3

147. Chan KH, Cheng VCC, Woo PCY, Lau SKP, Poon LLM, Guan Y, et al. Serological responses in patients with severe acute respiratory syndrome coronavirus infection and cross-reactivity with human coronaviruses 229E, OC43, and NL63. *Clin Diagn Lab Immunol*. (2005) 12:1317–21. doi: 10.1128/CDLI.12.11.1317-1321.2005

148. de Assis RR, Jain A, Nakajima R, Jasinskas A, Felgner J, Obiero JM, et al. Analysis of SARS-CoV-2 antibodies in COVID-19 convalescent blood using a coronavirus antigen microarray. *Nat Commun*. (2021) 12:6. doi: 10.1038/s41467-020-20095-2

149. Aspinall R, Andrew D. Thymic involution in aging. *J Clin Immunol*. (2000) 20:250–6. doi: 10.1023/a:1006611518223

150. Liang Z, Dong X, Zhang Z, Zhang Q, Zhao Y. Age-related thymic involution: Mechanisms and functional impact. *Aging Cell*. (2022) 21:e13671. doi: 10.1111/acel.13671

151. Castelo-Branco C, Soveral I. The immune system and aging: a review. *Gynecol Endocrinol*. (2014) 30:16–22. doi: 10.3109/09513590.2013.852531

152. Wang Z, Aguilar EG, Luna JI, Dunai C, Khuat LT, Le CT, et al. Paradoxical effects of obesity on T cell function during tumor progression and PD-1 checkpoint blockade. *Nat Med*. (2019) 25:141–51. doi: 10.1038/s41591-018-0221-5

153. Jiang J, Fisher EM, Murasko DM. CD8 T cell responses to influenza virus infection in aged mice. *Ageing Res Rev*. (2011) 10:422–7. doi: 10.1016/j.arr.2011.02.001

154. Nikolich-Žugich J, Bradshaw CM, Uhrlaub JL, Watanabe M. Immunity to acute virus infections with advanced age. *Curr Opin Virol*. (2021) 46:45–58. doi: 10.1016/j.coviro.2020.09.007

155. Naylor K, Li G, Vallejo AN, Lee W-W, Koetz K, Bryl E, et al. The influence of age on T cell generation and TCR diversity. *J Immunol*. (2005) 174:7446–52. doi: 10.4049/jimmunol.174.11.7446

156. Yager EJ, Ahmed M, Lanzer K, Randall TD, Woodland DL, Blackman MA. Age-associated decline in T cell repertoire diversity leads to holes in the repertoire and impaired immunity to influenza virus. *J Exp Med*. (2008) 205:711–23. doi: 10.1084/jem.20071140

157. Eaton SM, Burns EM, Kusser K, Randall TD, Haynes L. Age-related defects in CD4 T cell cognate helper function lead to reductions in humoral responses. *J Exp Med*. (2004) 200:1613–22. doi: 10.1084/jem.20041395

158. Cancro MP, Hao Y, Scholz JL, Riley RL, Frasca D, Dunn-Walters DK, et al. B cells and aging: molecules and mechanisms. *Trends Immunol*. (2009) 30:313–8. doi: 10.1016/j.it.2009.04.005

159. Weksler ME, Russo C, Siskind GW. Peripheral T cells select the B-cell repertoire in old mice. *Immunol Rev*. (1989) 110:173–85. doi: 10.1111/j.1600-065x.1989.tb00033.x

160. Aguilar-Bretones M, Westerhuis BM, Raadsen MP, de Bruin E, Chandler FD, Okba NMA, et al. Seasonal coronavirus–specific B cells with limited SARS-CoV-2 cross-reactivity dominate the IgG response in severe COVID-19. *J Clin Invest*. (2021) 131(21):e150613. doi: 10.1172/JCI150613

161. Bacher P, Rosati E, Esser D, Martini GR, Saggau C, Schiminsky E, et al. Low-avidity CD4+ T cell responses to SARS-coV-2 in unexposed individuals and humans with severe COVID-19. *Immunity*. (2020) 53:1258–1271.e5. doi: 10.1016/j.immuni.2020.11.016

162. Dykema AG, Zhang B, Woldemeskel BA, Garliss CC, Cheung LS, Choudhury D, et al. Functional characterization of CD4+ T cell receptors crossreactive for SARS-CoV-2 and endemic coronaviruses. *J Clin Invest*. (2021) 131:146922. doi: 10.1172/JCI146922

163. Meyer-Arndt L, Schwarz T, Loyal L, Henze L, Kruse B, Dingeldey M, et al. Cutting Edge: Serum but Not Mucosal Antibody Responses Are Associated with Pre-Existing SARS-CoV-2 Spike Cross-Reactive CD4+ T Cells following BNT162b2 Vaccination in the Elderly. *J Immunol*. (2022) 208:1001–5. doi: 10.4049/jimmunol.2100990

164. Saletti G, Gerlach T, Jansen JM, Molle A, Elbahesh H, Ludlow M, et al. Older adults lack SARS CoV-2 cross-reactive T lymphocytes directed to human coronaviruses OC43 and NL63. *Sci Rep*. (2020) 10:21447. doi: 10.1038/s41598-020-78506-9

165. Müller L, Andrée M, Ostermann PN, Jazmati N, Flüh G, Fischer JC, et al. SARS-coV-2 infection in fully vaccinated individuals of old age strongly boosts the humoral immune response. *Front Med*. (2021) 8. doi: 10.3389/fmed.2021.746644

166. Bag Soytas R, Cengiz M, Islamoglu MS, Borku Uysal B, Yavuzer S, Yavuzer H. Antibody responses to COVID-19 vaccines in older adults. *J Med Virol*. (2022) 94:1650–4. doi: 10.1002/jmv.27531

167. Crowley AR, Natarajan H, Hederman AP, Bobak CA, Weiner JA, Wieland-Alter W, et al. Boosting of cross-reactive antibodies to endemic coronaviruses by SARS-CoV-2 infection but not vaccination with stabilized spike. *eLife*. (2022) 11:e75228. doi: 10.7554/eLife.75228

168. Aspinall R, Lang PO. Interventions to restore appropriate immune function in the elderly. *Immun Ageing*. (2018) 15:5. doi: 10.1186/s12979-017-0111-6

169. Jerne NK. Towards a network theory of the immune system. *Ann Immunol (Paris)*. (1974) 125C:373–89.

170. Kearney JF, Barletta R, Quan ZS, Quintáns J. Monoclonal vs. heterogeneous anti-H-8 antibodies in the analysis of the anti-phosphorylcholine response in BALB/c mice. *Eur J Immunol*. (1981) 11:877–83. doi: 10.1002/eji.1830111106

171. Wittner MK, Bach MA, Köhler H. Immune response to phosphorylcholine. IX. Characterization of hybridoma anti-TEPC15 antibodies. *J Immunol*. (1982) 128:595–9.

172. Cosenza H. Detection of anti-idiotype reactive cells in the response to phosphorylcholine. *Eur J Immunol*. (1976) 6:114–6. doi: 10.1002/eji.1830060208

173. Cosenza H, Köhler H. Specific inhibition of plaque formation to phosphorylcholine by antibody against antibody. *Science*. (1972) 176:1027–9. doi: 10.1126/science.176.4038.1027

174. Urbain J, Wikler M, Franssen JD, Collignon C. Idiotypic regulation of the immune system by the induction of antibodies against anti-idiotypic antibodies. *Proc Natl Acad Sci*. (1977) 74:5126–30. doi: 10.1073/pnas.74.11.5126

175. Cazenave PA. Idiotypic-anti-idiotypic regulation of antibody synthesis in rabbits. *Proc Natl Acad Sci*. (1977) 74:5122–5. doi: 10.1073/pnas.74.11.5122

176. Geha RS. Idiotypic–anti-idiotypic interactions in man. *Am J Dis Children*. (1985) 139:417–20. doi: 10.1001/archpedi.1985.02140060099041

177. Jerne NK. *The immune system: a web of V-domains. Harvey Lect 70 Series*. Harvey Society of New York - New York City, New York (1974). pp. 93–110.

178. Stanova AK, Ryabkova VA, Utekhin SV, Shoenfeld VJ, Churilov LP, Shoenfeld Y. Anti-idiotypic agonistic antibodies: candidates for the role of universal remedy. *Antibodies (Basel)*. (2020) 9:E19. doi: 10.3390/antib9020019

179. Murphy WJ, Longo DL. A possible role for anti-idiotype antibodies in SARS-coV-2 infection and vaccination. *New Engl J Med*. (2021) 386(4):394–6. doi: 10.1056/NEJMcibr2113694

180. Eichmann K, Rajewsky K. Induction of T and B cell immunity by anti-idiotypic antibody. *Eur J Immunol*. (1975) 5:661–6. doi: 10.1002/eji.1830051002

181. Jean-Francois MJ, Poskitt DC, MacDonald LM, Turnbull SJ, Yasmeen D. Production of monoclonal anti-idiotype antibodies which mimic an M-like protein of Streptococcus equi. *Microbiol Immunol*. (1993) 37:737–42. doi: 10.1111/j.1348-0421.1993.tb01699.x

182. Murphy WJ, Collins CP, Ashwood P. Potential role of anti-Idiotype responses on the neurological effects of post-acute sequelae of COVID-19 (PASC). *Brain Behav Immun*. (2023) 116:317–20. doi: 10.1016/j.bbi.2023.12.017

183. Arthur JM, Forrest JC, Boehme KW, Kennedy JL, Owens S, Herzog C, et al. Development of ACE2 autoantibodies after SARS-CoV-2 infection. *PloS One*. (2021) 16:e0257016. doi: 10.1371/journal.pone.0257016

184. Maden CH, Gomes J, Schwarz Q, Davidson K, Tinker A, Ruhrberg C. NRP1 and NRP2 cooperate to regulate gangliogenesis, axon guidance and target innervation in the sympathetic nervous system. *Dev Biol*. (2012) 369:277–85. doi: 10.1016/j.ydbio.2012.06.026

185. Schlueter AJ, Segre D, Kuhlenschmidt MS, Segre M. Behavior of the idiotypic network in conventional immune responses: I. Kinetics of idiotypic and anti-idiotypic antibodies following immunization with T-independent and T-dependent antigens. *Cell Immunol*. (1992) 144:311–23. doi: 10.1016/0008-8749(92)90247-M

186. Borghesi C, Nicoletti C. Increase of cross(auto)-reactive antibodies after immunization in aged mice: a cellular and molecular study. *Int J Exp Pathol*. (1994) 75:123–30.

187. Kim YT, Goidl EA, Samarut C, Weksler ME, Thorbecke GJ, Siskind GW. Bone marrow function. I. Peripheral T cells are responsible for the increased auto-antiidiotype response of older mice. *J Exp Med*. (1985) 161:1237–42. doi: 10.1084/jem.161.5.1237

188. Jeffery-Smith A, Burton AR, Lens S, Rees-Spear C, Davies J, Patel M, et al. SARS-CoV-2-specific memory B cells can persist in the elderly who have lost detectable neutralising antibodies. *J Clin Invest*. (2021) 132(2). doi: 10.1172/JCI152042

189. Takahashi Y, Haga S, Ishizaka Y, Mimori A. Autoantibodies to angiotensin-converting enzyme 2 in patients with connective tissue diseases. *Arthritis Res Ther*. (2010) 12:R85. doi: 10.1186/ar3012

190. Fung KW, Baye F, Baik SH, Zheng Z, McDonald CJ. Prevalence and characteristics of long COVID in elderly patients: An observational cohort study of over 2 million adults in the US. *PloS Med*. (2023) 20:e1004194. doi: 10.1371/journal.pmed.1004194

191. Sudre CH, Murray B, Varsavsky T, Graham MS, Penfold RS, Bowyer RC, et al. Attributes and predictors of long COVID. *Nat Med*. (2021) 27:626–31. doi: 10.1038/s41591-021-01292-y

192. Thaweethai T, Jolley SE, Karlson EW, Levitan EB, Levy B, McComsey GA, et al. Development of a definition of postacute sequelae of SARS-coV-2 infection. *JAMA*. (2023) 329:1934–46. doi: 10.1001/jama.2023.8823

193. Safavi F, Gustafson L, Walitt B, Lehky T, Dehbashi S, Wiebold A, et al. Neuropathic symptoms with SARS-CoV-2 vaccination. *medRxiv*. (2022). doi: 10.1101/2022.05.16.22274439

194. Finsterer J. Neurological adverse reactions to SARS-coV-2 vaccines. *Clin Psychopharmacol Neurosci*. (2023) 21:222–39. doi: 10.9758/cpn.2023.21.2.222

195. Yang Y, Huang L. Neurological disorders following COVID-19 vaccination. *Vaccines (Basel)*. (2023) 11:1114. doi: 10.3390/vaccines11061114

196. Zisis SN, Durieux JC, Mouchati C, Perez JA, McComsey GA. The protective effect of coronavirus disease 2019 (COVID-19) vaccination on postacute sequelae of COVID-19: A multicenter study from a large national health research network. *Open Forum Infect Dis*. (2022) 9:ofac228. doi: 10.1093/ofid/ofac228

197. Effros RB, Walford RL. The immune response of aged mice to influenza: diminished T-cell proliferation, interleukin 2 production and cytotoxicity. *Cell Immunol*. (1983) 81:298–305. doi: 10.1016/0008-8749(83)90237-x

198. Klein SL, Flanagan KL. Sex differences in immune responses. *Nat Rev Immunol*. (2016) 16:626–38. doi: 10.1038/nri.2016.90

199. Frasca D, Reidy L, Cray C, Diaz A, Romero M, Kahl K, et al. Influence of obesity on serum levels of SARS-CoV-2-specific antibodies in COVID-19 patients. *PloS One*. (2021) 16:e0245424. doi: 10.1371/journal.pone.0245424

200. Bouchlaka MN, Sckisel GD, Chen M, Mirsoian A, Zamora AE, Maverakis E, et al. Aging predisposes to acute inflammatory induced pathology after tumor immunotherapy. *J Exp Med*. (2013) 210:2223–37. doi: 10.1084/jem.20131219

201. Murphy WJ. The urgent need for more basic research on SARS-Cov2 infection and vaccines in assessing potential psychoneurological effects using maternal immune activation (MIA) and other preclinical modeling. *Brain Behav Immun*. (2021) 97:1–3. doi: 10.1016/j.bbi.2021.06.009

202. Rhea EM, Logsdon AF, Hansen KM, Williams LM, Reed MJ, Baumann KK, et al. The S1 protein of SARS-CoV-2 crosses the blood–brain barrier in mice. *Nat Neurosci*. (2021) 24:368–78. doi: 10.1038/s41593-020-00771-8

203. Buzhdygan TP, DeOre BJ, Baldwin-Leclair A, Bullock TA, McGary HM, Khan JA, et al. The SARS-CoV-2 spike protein alters barrier function in 2D static and 3D microfluidic *in-vitro* models of the human blood-brain barrier. *Neurobiol Dis*. (2020) 146:105131. doi: 10.1016/j.nbd.2020.105131

204. Yang AC, Kern F, Losada PM, Agam MR, Maat CA, Schmartz GP, et al. Dysregulation of brain and choroid plexus cell types in severe COVID-19. *Nature*. (2021) 595:565–71. doi: 10.1038/s41586-021-03710-0

205. Zhao Y, Kuang M, Li J, Zhu L, Jia Z, Guo X, et al. SARS-CoV-2 spike protein interacts with and activates TLR41. *Cell Res*. (2021) 31:818–20. doi: 10.1038/s41422-021-00495-9

206. Oh J, Cho W-H, Barcelon E, Kim KH, Hong J, Lee SJ. SARS-CoV-2 spike protein induces cognitive deficit and anxiety-like behavior in mouse via non-cell autonomous hippocampal neuronal death. *Sci Rep*. (2022) 12:5496. doi: 10.1038/s41598-022-09410-7

207. Crackower MA, Sarao R, Oudit GY, Yagil C, Kozieradzki I, Scanga SE, et al. Angiotensin-converting enzyme 2 is an essential regulator of heart function. *Nature*. (2002) 417:822–8. doi: 10.1038/nature00786

208. Wang J, Kaplan N, Wysocki J, Yang W, Lu K, Peng H, et al. The ACE2-deficient mouse: A model for a cytokine storm-driven inflammation. *FASEB J*. (2020) 34:10505–15. doi: 10.1096/fj.202001020R

209. Netland J, Meyerholz DK, Moore S, Cassell M, Perlman S. Severe acute respiratory syndrome coronavirus infection causes neuronal death in the absence of encephalitis in mice transgenic for human ACE2. *J Virol*. (2008) 82:7264–75. doi: 10.1128/JVI.00737-08

10.3389/fimmu.2024.1345499

Glossary

Idiotype: The antigenic part of the specific antigen-binding domain within the variable region of an immunoglobulin (Ab1) or TCR. With most antigens, these are polyclonal responses consisting of multiple idiotypes of different affinities.

Paratope: The region of an antibody that binds a specific antigen or epitope.

Anti-idiotype: Antibody or T-cell responses directed to idiotypes due to immunogenicity by being novel proteins arising from gene rearrangements of immunoglobulin or TCR. Anti-idiotype (Ab2) responses are also polyclonal and may not be induced to all Ab1 or to the same extent. Some Ab2 paratope regions may resemble the original antigen as a form of molecular mimicry and are capable of inducing immune responses similar to the antigen itself. Some of these Ab2 are therefore also of binding the ligand of the original antigen.

Anti-anti-idiotype: Immune responses (Ab3) targeting the idiotype of anti-idiotype (Ab2). Ab3 may resemble the Ab1 in specificity due to some Ab2 paratopes mirroring the original antigen.

hCoV: Human coronaviruses known for their characteristic spike (S) protein which facilitates entry into the target cell. There are seven hCoVs: hCoV-229E, hCoV-NL63, hCoV-OC43, hCoV-HKU1, MERS-CoV, SARS-CoV, and SARS-CoV-2 of which 229E, NL63, OC43, and HKU1 are endemic.

Original antigenic Sin: A phrase used to describe a phenomenon in which prior immune responses to other antigens/epitopes can cross-react (xAb1) and bind to a new antigen and possibly interfere with primary immune responses (Ab1) to the new antigen. These can also involve anti-idiotype (xAb2) responses.

Network hypothesis: A theory proposed by N Jerne to explain immunoregulatory pathways governing antigen-specific B and T cell responses over time in which immune responses are generated to initial adaptive immune cell products as a form of down-regulation.

Outstanding questions

Are cross-reactive memory responses beneficial or deleterious in CoV2 protection and does age or obesity influence these effects?

What are the differences between CoV2 infection versus vaccine application on activation of cross- reactive and anti-idiotype responses?

Do cross-reactive anti-idiotype responses occur after infection or vaccination and are anti-idiotype responses increased in aging playing a role in the diminution of protective responses or off-target or long-term pathology?

What preclinical model conditions can best mirror the human scenario and be used to assess potential roles of cross-reactive memory responses and anti-idiotype effects?

What vaccine regimens and types are needed in different clinical populations (age, obesity, comorbid illness as cofactors) to increase immune efficacy and maintain duration considering the CoV2 variants the arise?

Significance: Cross-reactive memory idiotype and anti-idiotype responses from prior pathogens may contribute and possibly interfere with the generation of primary antigen-specific responses to both SARS-CoV-2 infections and associated vaccines. Due to the predominance of memory T-cell and potentially anti-idiotypic responses, these effects may be heightened in aging and may also contribute to off-target effects. Preclinical modeling incorporating these variables are needed to follow immune responses over time and determine optimal regimens for vaccine application as well as potential therapeutic strategies to increase immune efficacy and durability.

frontiers | Frontiers in Immunology

TYPE Original Research
PUBLISHED 20 June 2024
DOI 10.3389/fimmu.2024.1424374

OPEN ACCESS

EDITED BY
William Murphy,
University of California, Davis, United States

REVIEWED BY
Tarek A. Ahmad,
Bibliotheca Alexandrina, Egypt
Delia Goletti,
Translational Research Unit National Institute for Infectious Diseases "Lazzaro Spallanzani" IRCCS, Italy

*CORRESPONDENCE
Rhea N. Coler
Rhea.Coler@seattlechildrens.org

RECEIVED 27 April 2024
ACCEPTED 06 June 2024
PUBLISHED 20 June 2024

CITATION
Williams BD, Ferede D, Abdelaal HFM, Berube BJ, Podell BK, Larsen SE, Baldwin SL and Coler RN (2024) Protective interplay: *Mycobacterium tuberculosis* diminishes SARS-CoV-2 severity through innate immune priming.
Front. Immunol. 15:1424374.
doi: 10.3389/fimmu.2024.1424374

Protective interplay: *Mycobacterium tuberculosis* diminishes SARS-CoV-2 severity through innate immune priming

Brittany D. Williams[1,2], Debora Ferede[2], Hazem F. M. Abdelaal[2], Bryan J. Berube[2,3], Brendan K. Podell[4], Sasha E. Larsen[2], Susan L. Baldwin[2] and Rhea N. Coler[1,2,5]*

[1]Department of Global Health, University of Washington, Seattle, WA, United States, [2]Seattle Children's Research Institute, Center for Global Infectious Disease Research, Seattle Children's, Seattle, WA, United States, [3]HDT Bio Corp, Seattle, WA, United States, [4]Mycobacteria Research Laboratories, Department of Microbiology, Immunology, and Pathology, Colorado State University, Fort Collins, CO, United States, [5]Department of Pediatrics, University of Washington School of Medicine, Seattle, WA, United States

At the beginning of the COVID-19 pandemic those with underlying chronic lung conditions, including tuberculosis (TB), were hypothesized to be at higher risk of severe COVID-19 disease. However, there is inconclusive clinical and preclinical data to confirm the specific risk SARS-CoV-2 poses for the millions of individuals infected with *Mycobacterium tuberculosis* (M.tb). We and others have found that compared to singly infected mice, mice co-infected with M.tb and SARS-CoV-2 leads to reduced SARS-CoV-2 severity compared to mice infected with SARS-CoV-2 alone. Consequently, there is a large interest in identifying the molecular mechanisms responsible for the reduced SARS-CoV-2 infection severity observed in M.tb and SARS-CoV-2 co-infection. To address this, we conducted a comprehensive characterization of a co-infection model and performed mechanistic *in vitro* modeling to dynamically assess how the innate immune response induced by M.tb restricts viral replication. Our study has successfully identified several cytokines that induce the upregulation of anti-viral genes in lung epithelial cells, thereby providing protection prior to challenge with SARS-CoV-2. In conclusion, our study offers a comprehensive understanding of the key pathways induced by an existing bacterial infection that effectively restricts SARS-CoV-2 activity and identifies candidate therapeutic targets for SARS-CoV-2 infection.

KEYWORDS

SARS-CoV-2, Mycobacterium tuberculosis, tuberculosis, co-infection, COVID-19

Introduction

The coronavirus disease 2019 (COVID-19), caused by severe acute respiratory syndrome coronavirus 2 (SARS-CoV-2), has resulted in a global pandemic that has claimed over 6.8 million lives as of March 2024 (1). Initially, individuals with underlying chronic lung conditions, including tuberculosis (TB), were thought to be at higher risk of severe COVID-19 and acute respiratory distress syndrome (ARDS) (2). This was a great concern for the 10 million individuals diagnosed with TB in 2019 (3). To speak to its detriment, TB was the long-standing number one infectious disease killer until the start of the COVID-19 pandemic (3). Although the prevalence of COVID-19 and TB co-infection has not been officially confirmed, a recent meta-analysis of 18 studies estimated that the prevalence of TB among COVID-19 positive patients was 1.1% in America, 1.5% in Asia and 3.6% in Africa (4). While TB was later removed as a significant risk factor, conclusive data on the specific risk SARS-CoV-2 poses for the millions infected with *Mycobacterium tuberculosis* (M.tb) remains elusive. Early clinical reports presented conflicting findings with some noting that TB was not a major determinant of mortality (2, 5, 6) and others suggesting co-infection led to worsened outcomes of COVID-19 (7, 8). Additionally, a longitudinal global cohort study which found survival was lower among co-infected individuals discovered certain risk factors, such as age, HIV co-infection, male sex, and invasive ventilation, influenced adverse TB and COVID-19 outcomes (9). Therefore, highlighting multiple factors that may contribute to an individual's response to SARS-CoV-2 and M.tb infection. While the characterization of the immune response within co-infected individuals has also been limited, studies have reported both overlapping and distinct immune responses (10–12). A clinical study characterizing plasma immune profiles of individuals with TB and COVID-19 versus singular TB or COVID-19 discovered an immune signature composed of TNF-α, MIP-1β, and IL-9 that discriminated co-infection from COVID-19 alone (11). In addition, a signature of TNF-α, IL-1β, IL-17A, IL-5, fibroblast growth factor-basic, and granulocyte macrophage colony-stimulating factor (GM-CSF), has discerned co-infected individuals from those with TB only (11). Indeed, there seems to be a nuanced relationship between M.tb infection and SARS-CoV-2 and multiple demographic and clinical factors may alter the immune response to both infections (2). Understanding how these two pulmonary pathogens interact starts with examining their individual induced innate immune responses, as these responses represent the first line of defense against pathogens.

Primary infection of angiotensin converting enzyme-2 (ACE2)-expressing airway and alveolar epithelial cells by SARS-CoV-2 initiates viral replication, pyroptosis of host cells, and activation of innate immune pathways (13). The innate immune response when properly activated is crucial in providing protection against early SARS-CoV-2 infection. Several pattern recognition receptors (PRRs) detect SARS-CoV-2 and initiate innate responses, including endosomal toll-like receptor 3 (TLR3) and toll-like receptor 7 (TLR7) signaling pathways, as well as cytoplasmic RNA sensor, melanoma differentiation-associated protein 5 (MDA5) (14–16). The cytoplasmic RNA sensor, retinoic acid-inducible gene I (RIG-I), acts more as a restriction factor in which RIG-I detection of the SARS-CoV-2 genome hinders the virus's first step of replication. Furthermore, knock out of RIG-I was shown to enhance viral activity and virus restriction was rescued with upregulation of RIG-I expression (17). Upon activation of the PRRs, downstream signaling results in the production of antiviral interferons (IFNs), and cytokines and chemokines which create an anti-viral environment and recruits innate cells to the site of infection (18). Type I, II, and III IFNs have been heavily focused on due to their ability to inhibit SARS-CoV-2 replication (19–23). IFN antiviral activity is driven by the upregulation of interferon-stimulated genes (ISGs), which have multiple mechanisms in restricting viral activity (24–26). Multiple ISGs which broadly act against SARS-CoV-2 by inhibiting viral entry, viral RNA synthesis, and virion assembly, have also been identified (26).

However, SARS-CoV-2 has evolved multiple strategies to evade initial innate immune responses, including blocking recognition by host sensors such as RIG-I, MDA5, and TLRs and inhibiting IFN signaling, thus promoting viral replication (27–29). This immune evasion is thought to delay immune responses, leading to unchecked viral replication, high viral load, and a subsequent dysregulated immune response. The resulting disproportionate response to SARS-CoV-2 infection is characterized by a robust release of proinflammatory cytokines and dysfunctional myeloid responses, including elevated levels of IL-2, IL-6, IL-7, IL-10, IL-12, and IL-1β, TNF-α, MCP-1α, IP-10, lymphopenia, and high lung infiltration of monocytes and T cells (13, 30–32).

In contrast to the acute hyperinflammatory profile associated with SARS-CoV-2, chronic M.tb infection is known to elicit a diverse array of proinflammatory and regulatory responses (33). Following initial infection, alveolar macrophages engulf M.tb bacilli, migrate to the lung parenchyma, and orchestrate the recruitment of various innate immune cells and effector T cells. While some infections resolve, others go on to result in granuloma formation, an attempt at prolonged containment by the host and persistent but quiescent latent infection (34–37). Major cell types involved in the control of M.tb are pro-inflammatory T helper 1 (Th1) and Th17 CD4+ T cells which are largely recruited to form a lymphocytic cuff around a core granuloma structure containing macrophages and bacteria. Th1 and Th17 CD4+ T cells express IL-2, IFN-γ, and TNF-a, or IL-17A, IL-21, and IL-23, respectively, which play critical roles in driving immune activation and inflammatory responses designed to control M.tb (33, 38). However certain hallmark stages of granuloma formation and persistent infection include the expression of anti-inflammatory cytokines IL-10, IL-27 and TGF-β to regulate T cell pro-inflammatory activity (33, 39). This balance of immune responses enables local containment of M.tb bacilli without more systemic inflammatory damage.

Further insights can be gleaned from other bacterial and viral co-infection studies. For instance, administering a live-attenuated mycobacteria, bacille Calmette-Guérin (BCG), intravenously, but not subcutaneously, significantly protected mice from SARS-CoV-2 challenge, characterized by reduced lung inflammation and viral burden (40). Similarly, aerosolized exposure to nontypeable *Haemophilus influenzae* (NTHi) bacterial lysate before influenza A infection conferred protection, as evidenced by heightened

inflammatory cytokines, decreased viral loads, and increased survival rates in treated mice (41). Notably, while both bacterial exposures provided protection against secondary viral infections, they triggered distinct immune responses, likely influenced by the route of administration, bacterial species and specific PRR pathways induced. These findings collectively underscore the role of nonspecific immune responses in defending against subsequent heterologous infections (42).

Given the global impact of the pandemic, delay of vaccine deployment in many TB endemic low- and middle-income countries (LMICs), and continuous emergence of hyper-transmissible variants, it is unknown how long the pandemic and its ramifications will last. This highlights the need to study co-infections to identify disease burdens, mechanisms of immunopathology, and heterologous protection to better inform susceptibility and population risk. With our work, we tested our hypothesis that acute M.tb infection induces a diffuse innate immune response within the lungs leading to a primed lung epithelium that limits viral replication, provides non-specific protection against SARS-CoV-2-induced lung viral burden, and host morbidity in a co-infection mouse model.

Recent M.tb and SARS-CoV-2 mouse co-infection studies (43–45) have similarly observed reduced SARS-CoV-2 infection severity in co-infected animals compared to those infected with SARS-CoV-2 alone. While these studies have offered model insights, the underlying mechanism(s) behind the protective phenotype in co-infected settings remains incompletely understood. In this study, by characterizing a discrete co-infection model using virulent M.tb and variant of high importance and incorporating *in vitro* studies we aimed to uncover the mechanism that could be leading to the observed protection.

Materials and methods

Preclinical animal model

Female and Male K18-hACE2 mice [strain: 2B6.Cg-Tg(K18-ACE2)2Prlmn/J], 6–8 weeks of age were purchased from Jackson Laboratory (Bar Harbor, ME). Mice were housed under pathogen-free conditions at Seattle Children's Research Institute (SCRI) biosafety level 3 animal facility and were handled in accordance with the specific guidelines of SCRI's Institutional Animal Care and Use Committee (IACUC). Mice were infected with a low dose (50–100 bacteria) aerosol (LDA) of M.tb HN878 using a Glas-Col whole-body exposure chamber (Glas-Col, Terre Haute, IN). Twenty-four hours post challenge the lungs of three mice were homogenized and plated on Mitchison 7H11 agar (Thermo Fisher Scientific, Waltham, MA) to confirm delivery of 50–100 CFU per mouse. For SARS-CoV-2 infection mice were first put under anesthesia with intraperitoneal (i.p.) administration of Ketamine (Patterson Veterinary, Loveland, CO) and Xylazine (Patterson Veterinary). SARS-CoV-2 clinical isolates were administered at 200 PFU via intranasal installation of 40μL per nare. Following SARS-CoV-2 infection mice were weighed daily. Animals that reached 20% weight loss and/or exhibited physical signs of morbidity were humanely euthanized.

Cells and pathogens

Vero TMPRSS2 (National Institute for Biological Standards and Control (NIBSC), Hertfordshire, England), Vero E6 (ATCC, Manassas, VA), and Calu-3 epithelial cells (ATCC) were maintained at 37 °C + 5% CO_2 in Dulbecco's modified Eagle's medium (DMEM) supplemented with 10% fetal bovine serum (FBS), 2 mM L-glutamine, and 1% penicillin/streptomycin (cDMEM). Cells were tested regularly for mycoplasma with Mycoplasma PCR detection kit (MilliporeSigma, Burlington, MA).

SARS-CoV-2 Beta (hCoV-19/SouthAfrica/KRISP-EC-K005321/2020) was obtained from BEI Resources and housed under standard BSL-3 laboratory conditions. SARS-CoV-2 virus was propagated and titered by plaque assay in Vero E6 cells. Cultured cells were infected with the original stock at a MOI of 0.1 and incubated at 37°C + 5% CO_2 for 72 h. Supernatants were harvested, centrifuged to remove debris, aliquoted and frozen at −80°C.

Bacterial counts

At the indicated time points harvested organs were homogenized in DMEM using gentleMACS Octo Tissue Dissociator (Miltenyi, Bergisch Gladbach, Germany). Serial dilutions of organ homogenates were made in PBS with 0.05% Tween80, and aliquots of dilutions were plated on Middlebrook 7H10 agar tri-plates (Molecular Toxicology, Boone, NC), as previously described (46, 47). After 3–4 weeks of incubation at 37°C + 5% CO_2, colony counts were recorded. Bacterial burden, in colony forming units (CFU) per organ, was calculated, and expressed as Log10.

Viral load measurements

Viral burden was measured with the plaque forming assay (PFA) using similar techniques described previously (48). Vero TMPRSS2 cells were plated in 6-well plates one day prior to titers at $4.8x10^5$ cells/mL in 2mL of cDMEM per well. Harvested organs were homogenized in DMEM containing 1% FBS (D1 media) using the gentleMACs Octo Dissociator. Organ homogenates were serially diluted ten-fold using D1 media and added dropwise to the plated Vero cells. Plates were incubated at 37 °C + 5% CO_2 for 60 minutes, with 15-minute intervals of rocking plates in all directions. After 60 minutes, 2mL of overlay media comprised of D1 media and 0.2% agarose was added to each well and incubated at 37°C + 5% CO_2 for 48 hours. Cells were then fixed with 2 mL of 10% Formaldehyde solution and incubated at room temperature for 30 minutes. The overlay was removed, and cells stained with 1mL of Crystal Violet (BD Biosciences, Franklin Lakes, NJ) per well for 20 minutes. Lastly, each well was washed with 1mL of PBS and the number of plaques in each well were recorded.

$$PFU/mL = \frac{\#\ of\ plaques}{(dilution\ factor\ x\ sample\ added)}$$

Histology

At the indicated time points, three whole lung and accessory lobes were collected per group and fixed in 10% Neutral Buffer Formalin (NBF) for 24 hours. The fixed lung samples were embedded in paraffin and sectioned by the University of Washington histology core. Blinded slides were sent to Colorado State University and stained with hematoxylin and eosin (H&E) then analyzed by veterinary pathologist Dr. Brendan Podell as previously published (46, 47). H&E stained sections were scanned at 20X magnification using an Olympus VS120 microscope, Hamamatsu ORCA-R2 camera, and Olympus VS-ASW 2.9 software. Visiopharm software was used for image analysis. For each tissue section, a region of interest (ROI) was generated at a low magnification with a custom tissue detecting algorithm using decision forest training and classification to differentiate tissue versus background based on color and area. Lesions were identified within tissue ROIs at a high magnification with an additional custom-made algorithm using decision forest training and classification based on staining intensity, color normalization and deconvolution, area, and morphological features. Percent lesion calculations were integrated into the same algorithm and calculated from tissue area and lesion area as designated by the ROI and lesions detected. Lesion identification and quantification were then reviewed by Dr. Podell (46, 47).

Flow cytometry

Cell populations within the lung were measured kinetically utilizing methods previously published (47). Briefly, lung homogenates were incubated in RBC lysis buffer (eBioscience/Thermo Fischer Scientific), washed and resuspended in RPMI 1640 + 10% FBS, and then evenly dispensed into 96-well round bottom plates. Cells were stained for surface markers with fluorochrome-conjugated monoclonal antibodies against mouse Ly6G (FITC, clone 1A8, Biolegend), Ly6C (PerCP-Cy5.5, clone HK1.4, eBioscience), MHCII I-A/I-E (eF450, clone M5/114.15.2, Invitrogen), CD11c (Bv510, clone N418, Biolegend), CD3 (Bv650, clone 17A2, Biolegend), CD19 (APC, clone 6D5, Biolegend), CD11b (Alexa700, clone M1/70, eBioscience), NK1.1 (PE, clone PK136, eBioscience), CD64 (PE-Cy7, clone X54–5/7.1, Biolegend) and 1 µg/mL of Fc receptor block anti-CD16/CD32 (clone 93, eBioscience) in PBS with 1% bovine serum albumin (BSA) for 15 minutes at room temperature. Samples were washed and before removing samples from the BSL3, samples were incubated in 4% paraformaldehyde for 30 minutes. After wash and resuspension in PBS + 1% BSA, cells were acquired on a BD Bioscience LSRII flow cytometer (BD Bioscience) and analyzed using FlowJo version 10.8.1 (BD Bioscience).

Cytokine measurement

Bronchoalveolar lavage fluid (BALF) was collected by flushing lungs with 1X PBS, then centrifuged at 400g for 7 minutes to remove cellular debris and filtered. The processed BALF was used in the Meso Scale Discovey (MSD) V-PLEX Proinflammatory Panel 1 Mouse kit (#K15048D), V-PLEX Cytokine Panel 1 Mouse Kit (#K15245D) and U-PLEX Interferon Combo 1 (#K15320K) to measure cytokine levels on the MESO QuickPlex SQ 120MM (Meso Scale Diagnostics, Rockville, MD). For similar *in vitro* endpoints from cultured Calu-3 supernatants, an MSD human U-PLEX Viral Combo 1 kit was used (#K15343K-1).

In vivo RT-qPCR

Accessory lung lobes from mice at specified time points post SARS-CoV-2 co-infection were harvested and homogenized in 900µL of Qiazol, followed by RNA extraction using the QIAGEN RNeasy Plus Universal mini kit according to the manufacturer's protocol (QIAGEN, Hilden, Germany). RNA was eluted into 30µl. RNA concentration and quality was determined using the NanoDrop 8000 (Thermo Fisher Scientific) and stored at -80°C until assayed. The obtained RNA was then utilized in the High-Capacity RNA-to-cDNA kit for cDNA synthesis using SuperScript™ IV Reverse Transcriptase (Thermo Fisher Scientific), containing a reverse transcriptase with a high-fidelity enzyme following manufacture protocol.

For Fluidigm Real-Time PCR and Dynamic Array IFC (Integrated Fluidic Circuit) Setup, specific target amplification (STA) was done as per the manufacturer's recommendations as the initial step (pre-amplification of cDNA) for the Biomark HD system (Standard BioTools, formerly Fluidigm) carried out on the Standard BioTools 48.48 Gene Expression (GE) Dynamic Array integrated fluidic circuit (IFC) (49). Assay-sets (primers only) were combined as a delta gene multiplex pool (see Supplementary Table 1). Preamplification was carried out for each cDNA sample against a reaction-set. Exonuclease I was then used to clean up the preamplification reactions.

Subsequently, the Biomark Chip was primed, and assay premix for each target was aspirated into the IFC assay inlets for a final concentration of 9 µM primers and 2.5 µM probe per reaction, and pre-amplified samples were aspirated into sample inlets. The IFC was then run in the Biomark HD thermocycler, using the manufacturer-supplied thermal cycling conditions. Results were analyzed using the Fluidigm Real-time PCR Analysis software, where thresholds were manually defined, the baseline was automatically assigned, and a Cycle of quantification (Cq) cut-off value of 38 was applied. The cycle threshold (Ct) values for the candidate housekeeping gene, *RPL13*, and target genes were obtained, and delta-delta CT values were calculated.

In vitro experiments

For the *in vitro* experiments, frozen human peripheral blood mononuclear cells (PBMCs) and whole blood were procured from Bloodworks Northwest (Seattle, WA). PBMCs were thawed, counted, and resuspended to a concentration of $2x10^6$ cells/mL, then rested overnight in RPMI media supplemented with 10% FBS

and 1% penicillin/streptomycin at 37°C + 5% CO_2. Cells were counted the next day and viability was assessed before being adjusted to a concentration of $1.5x10^6$ viable cells/mL. Subsequently, the cells were infected with M.tb HN878 at a multiplicity of infection (MOI) of 1 and incubated for 96 hours. Following infection, the cells were centrifuged at 700g for 3 minutes, and the supernatants were collected and filtered through a 0.22-micron filter. Vero or Calu-3 cells were plated and treated with supernatants for 24 hours at 37°C + 5% CO^2. Media-only treated cells were used as controls. Post-treatment, the cells were challenged with 75 PFU of SARS-CoV-2 Beta, and plaques were recorded 48 hours post-infection using the viral titer PFA described above.

To assess mRNA expression in cultured cells, RNA was extracted from cultured Calu-3 cells using the QIAGEN RNeasy Plus Universal mini kit. The cells were harvested using 900µL of Qiazol, followed by RNA isolation and cDNA synthesis employing the High-Capacity RNA-to-cDNA kit. RNA and cDNA concentration and quality was determined using the NanoDrop 8000 (Thermo Fisher Scientific) and stored at -80°C until assayed. Quantification of mRNA levels was performed using the GoTaq qPCR and RT-qPCR Systems kit from Promega, following the manufacturer's protocol, and the StepOne Plus Real-Time PCR System (Thermo Fisher Scientific). The mRNA expression levels of Calu-3 cells are presented as Log2 fold change (FC) compared to media-only treated cells and normalized to the housekeeping gene, *Beta Actin*. Primers used were selected from published sequences in PrimerBank (RRID: SCR_006898) (see Supplementary Table 2).

Neutralization assay

For neutralization studies, PBMCs were thawed and counted as described previously. PBMCs were plated in 12-well plates at $2.25x10^6$ cells/mL in one mL of RPMI media supplemented with 10% FBS and 1% penicillin/streptomycin. Neutralizing antibodies for human CD4 (BE0351, BioXcell), Lebanon, NH), CD8α (BE0004–2, BioXcell), CD314 (BE0288, BioXcell), and relevant isotype controls, mouse IgG1(BE0083, BioXcell), and mouse IgG2 (BE0085, BioXcell) were then administered at 10µg/mL, 20µg/mL and 100µg/mL in 1 mL. PBMCs and neutralizing antibodies were incubated for 1 hour at 37°C + 5% CO_2 prior to infection with M.tb HN878 at MOI of 1 for 96 hours. For IFNγ neutralization, the IFNγ antibody (BE0235, BioXcell) was added directly to the supernatant from PBMCs infected with M.tb HN878 at 10µg/mL, 20µg/mL and 100µg/mL escalating doses. After infection, supernatants were filtered through a 0.22-micron filter. Vero cells were treated with filtered PBMC supernatants for 24 hours, then challenged with 75 PFU of SARS-CoV-2 Beta, and plaques were recorded 48 hours post-infection using the viral titer PFA described above.

Statistical analysis

Survival analysis was based on the Mantel-Cox log-rank test with Bonferroni correction for multiple comparisons and carried out using GraphPad Prism 9.3.1 (GraphPad Software, San Diego, CA). Bacterial burden, viral titers, cytokine levels, and cell populations (percent frequency and counts) were assessed at a single time point using one-way ANOVA with Tukey's multiple comparison test to compare between infection groups. Flow cytometry data was assessed using FlowJo v10.8.1 (BD) and statistical analyses were performed using GraphPad Prism 9.3.1 software. The graphics were made with Biorender. Heat maps of *in vivo* mRNA expression were created with RStudio using 'pheatmap' function. P values < 0.05 were considered significant and labeled accordingly in each of the figures (* = P<0.05, **= P<0.01, ***=P<0.001, ****= P<0.0001). Outliers were identified using Grubbs' test at alpha 0.05.

Results

Active M.tb infection enhanced host survival and decreased viral burden after SARS-CoV-2 challenge

We hypothesized that infecting mice first with M.tb to induce an active infection and subsequent immune response, followed by co-infection with SARS-CoV-2, could potentially alter disease outcomes and affect survival endpoints. Highly virulent W-Beijing clinical strain, M.tb HN878, was delivered as a low dose aerosol challenge (LDA, 50–100 bacteria) to female and male K18-hACE2 mice. Three weeks post-M.tb infection, mice were challenged with 200 plaque forming units (PFU) of SARS-CoV-2 Beta. (Figure 1A). Male and Female mouse cohorts (n=10 per sex) were assessed for survival following infection with M.tb, SARS-CoV-2, or co-infection. Mice singularly infected with SARS-CoV-2 had significantly lower survival rates compared to those in the saline or M.tb infected groups. However, the M.tb and SARS-CoV-2 co-infected group showed a significantly higher survival rate than the group infected solely with SARS-CoV-2 (Figure 1B). The increased survival amongst the co-infection group versus the singular SARS-CoV-2 infection group suggests prior M.tb infection may provide partial protection from SARS-CoV-2 challenge, in alignment with our hypothesis.

Viral titers of SARS-CoV-2 were evaluated locally and systemically to determine if co-infected mice have differences in viral load magnitude or distribution. In alignment with prior work (43–45), the co-infected group exhibited decreased lung viral titers at day 1 post-co-infection and significantly decreased lung and lymph node viral titers at day 3 post-co-infection, the anticipated viral peak of our collection timeline, compared to SARS-CoV-2 alone cohorts (Figure 1C). There was no difference in viral burden in brain samples when comparing the two infection groups (Figure 1C). There was no difference in CFU between the groups for all organs and time points, suggesting the exhibited protection from morbidity was not due to a change in M.tb burden (Figure 1D).

We have previously seen that bacterial burden can be uncoupled from pulmonary pathology in mouse models of TB, where

10.3389/fimmu.2024.1424374

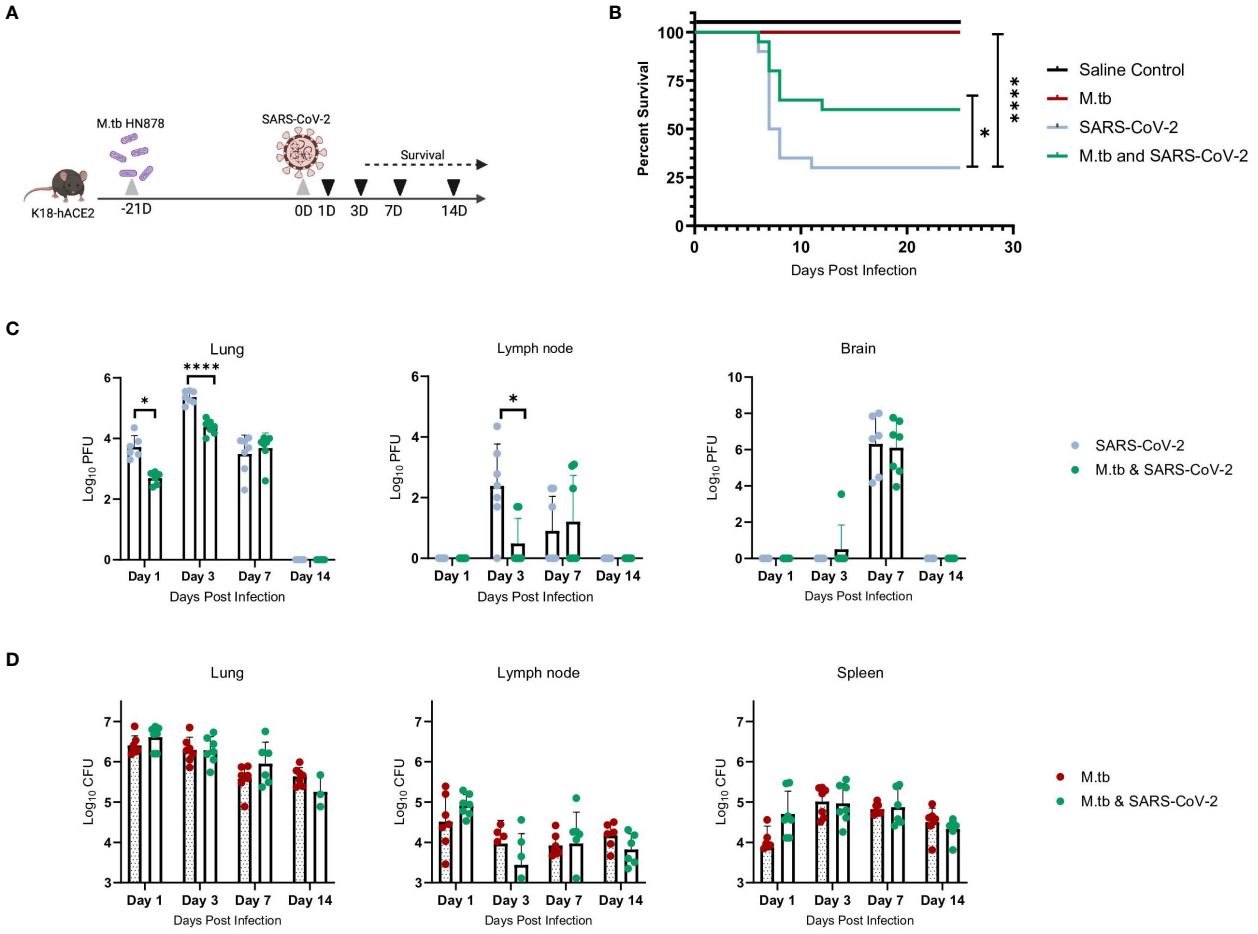

FIGURE 1
M.tb and SARS-CoV-2 co-infection animal model. **(A)** Experiment scheme for M.tb and SARS-CoV-2 co-infections including selected analysis time points. Image made with Biorender. **(B)** Survival analysis of male and female infection groups with 20 mice per group (10 mice per sex). Mouse weights (n=20/group) were recorded daily, and percent weight change calculated from the maximum recorded weight. (* = P<0.05 and **** = P<0.0001, Mantel-Cox and Wilcoxon). **(C)** Lung, lymph node and brain homogenates from seven female mice per group were used in a plaque formation assay (PFA) to measure viral titers. Each time point analyzed using unpaired T-Test with Welch's T Test and alpha of 0.05 (* = P<0.05 and **** = P<0.0001). **(D)** Lungs, lymph node and spleen homogenates from seven female mice per group were plated on 7H10 agar triplates to measure bacterial burden.

pulmonary disease and morbidity endpoints may be driven more by host factors (46). Interestingly, when assessing the lung pathology in these co-infection studies (Figure 2A) there was no significant difference in percent lesion area between co-infected animals and the SARS-CoV-2-only infected group at day 1 and 3 (Figures 2B, C). However, by day 7 there was a trend towards decreased lesion scores in the co-infected groups compared to the M.tb only infection group (Figure 2D), which became significant by day 14 (Figure 2E). This trend has been published previously (44) and speaks to the complexities of lung pathology in the context of co-infection. Conducting additional analysis which more clearly defines the differences between TB and COVID-19 pathology is worth further exploration. While these data suggest infection with SARS-CoV-2 may help resolve acute lesions from existing M.tb infection (Figure 2E), the primary focus of this work is to determine how infection with M.tb establishes an inhospitable pulmonary environment for SARS-CoV-2.

Established M.tb infection influences lung inflammation during acute SARS-CoV-2 infection

Given the partial protective phenotype displayed by the co-infection model, the immune profiles of M.tb-infected, SARS-CoV-2-infected and co-infected animals were evaluated. Using flow cytometry, the kinetic influx of immune cells to the lung following co-infection were compared to the other cohorts. Both M.tb-infected mice (21 days post infection) and M.tb-infected mice subsequently infected with SARS-CoV-2 (co-infected group) showed elevated levels of neutrophils and macrophages at the day 1 and 3 post-virus challenge time points, and increased influx of T cells and NK cells at day 3 compared to the group infected with SARS-CoV-2 only (Figure 3). Absolute cell counts mirroring these trends were also observed (Supplementary Figure 3). This showcases the influence chronic M.tb infection has on the

10.3389/fimmu.2024.1424374

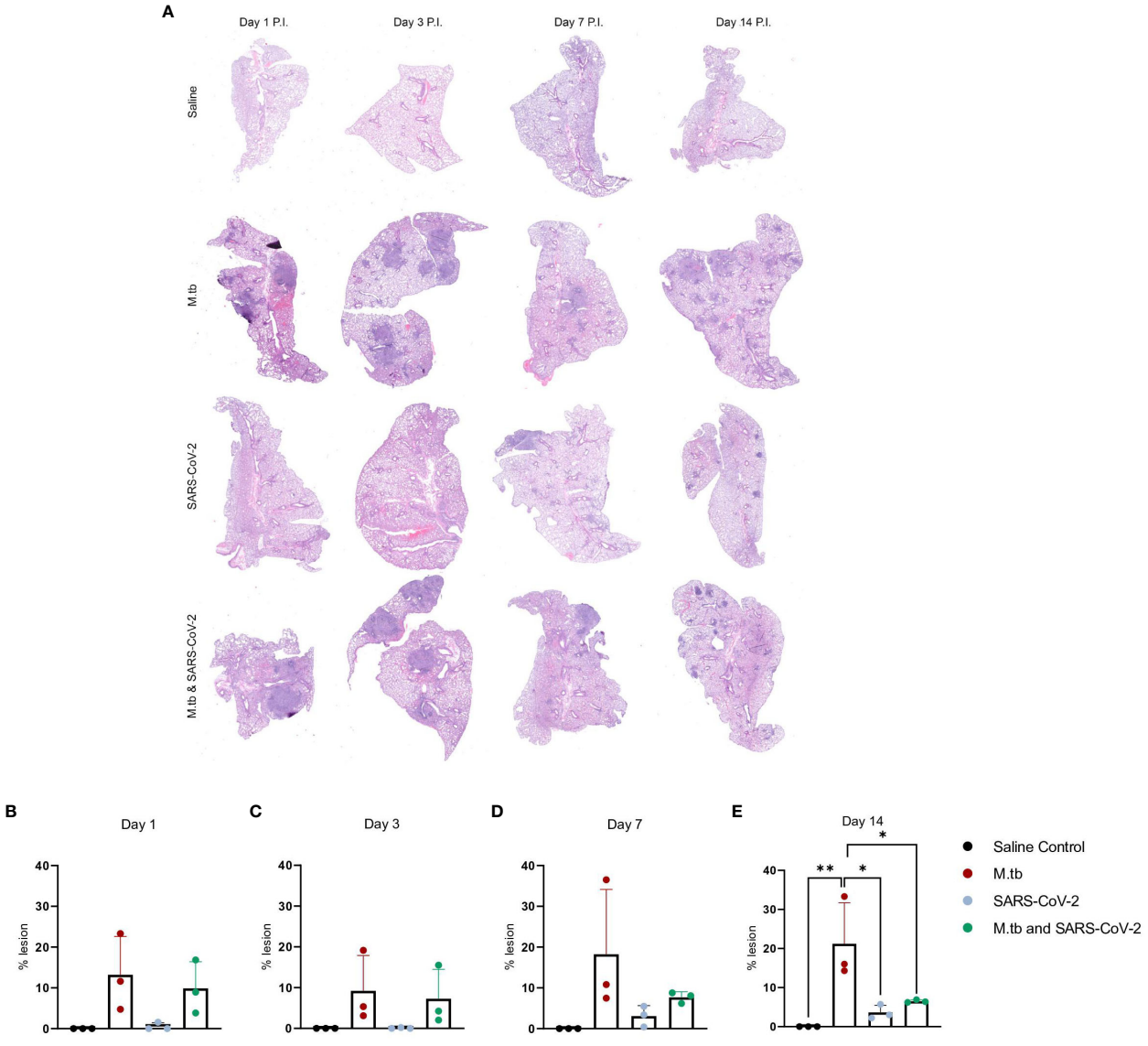

FIGURE 2
Kinetic quantitative lung histopathology among infection groups. **(A)** Representative H&E images of accessory lung lobe sections showing the presence of pulmonary lesions (dark purple). **(B)** Percent lesion was calculated by dividing the lesion area by the non-lesion area. Each time point was analyzed using one-way ANOVA alpha of 0.05 (* = P<0.05, **= P<0.01).

inflammatory environment of the lung. Bronchioalveolar lavage fluid (BALF) from M.tb-infected and co-infected mice contained significantly elevated IL-6, TNF-α, IFNγ, IP-10, MIP-1a, MCP-1, and KC-GRO at days 1 and 3 post-co-infection, while the SARS-CoV-2 infection group displayed delayed induction of these same effector molecules until day 7 (Figure 4). Interestingly, there was an absence of strong kinetic patterns of increases or persistent decreases in inflammatory gene expression within the lung across infection groups (Figures 5A-C). On day 3 there were trends of increased expression in certain ISGs, PRRs and inflammatory pathway genes in M.tb and co-infected groups (Figure 5B, Supplementary Figure 4).

The increased inflammatory response observed in the co-infected group was initially surprising since the robust pro-inflammatory response has been identified to be detrimental in SARS-CoV-2 infection (13). However, the timing and type of immune response induced may be important for priming the lung to combat SARS-CoV-2 infection. Mechanistic *in vitro* studies were next used to evaluate which innate immune response induced by the primary M.tb infection provide protection against subsequent SARS-CoV-2 infection.

Cytokines produced from M.tb infected PBMCs provide passive protection from SARS-CoV-2 challenge *in vitro*

To model co-infection *in vitro*, PBMCs were infected with M.tb, as they serve as niche host cells and are responsive to infection. Conversely, SARS-CoV-2 infection was modeled using permissive

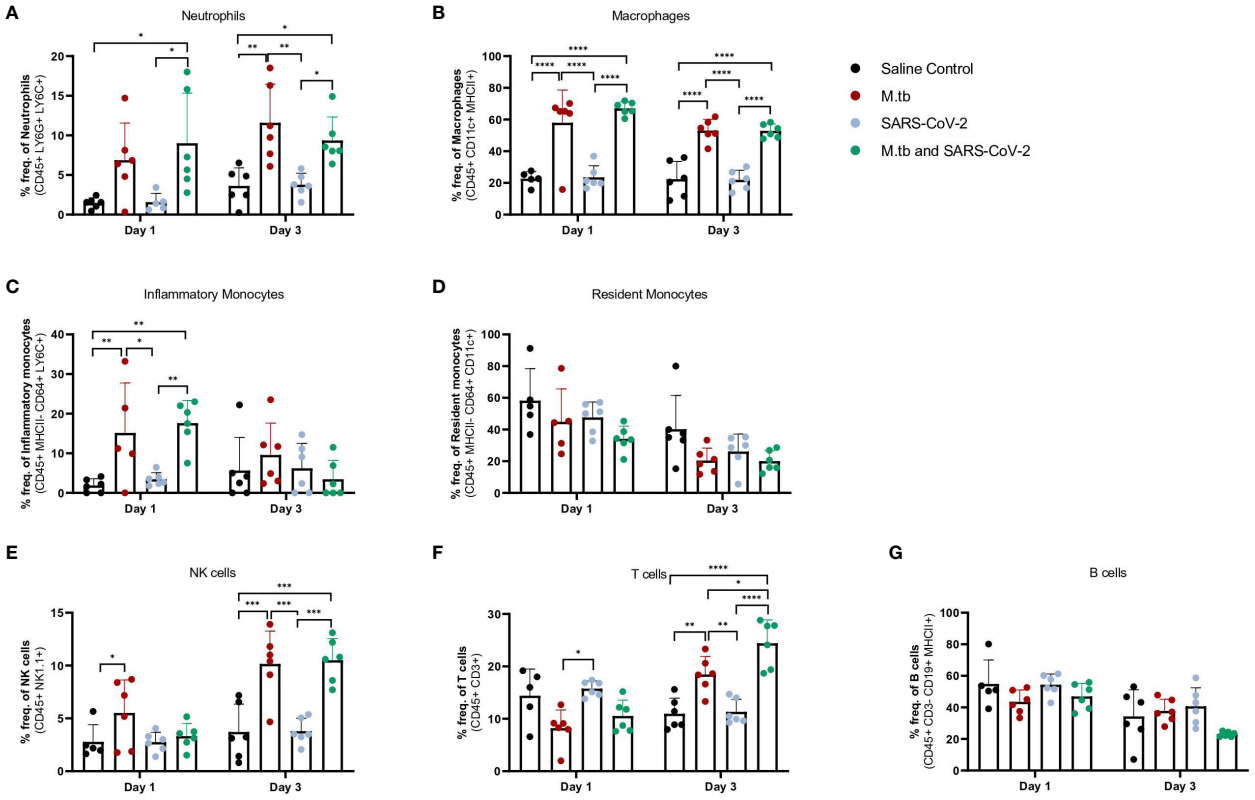

FIGURE 3
Measured cell populations in mouse lungs following singular infection with M.tb and SARS-CoV-2, and co-infection over time. **(A-G)** Whole lungs from six mice per group per time point were homogenized, processed, and stained for surface markers to measure percent frequency of immune cell populations at 1 day or 3 days following SARS-CoV-2 infection. Significant differences between cohorts at each time point were determined by One-way ANOVA, alpha of 0.05 (* = P<0.05, **= P<0.01, ***=P<0.001, ****=P<0.0001).

epithelial cells, which fulfill a similar role. While lung epithelial cells show limited direct responsiveness to M.tb, they exhibit heightened reactivity and transcriptional changes when exposed to M.tb-infected myeloid cells (50). Our investigation aimed to determine whether cytokines generated during initial M.tb infection of immune cells could confer protection against secondary SARS-CoV-2 infection in susceptible bystander epithelial cells.

We used PBMCs from healthy male and female donors, collected before and after 2019, as well as from Bacille Calmette-Guérin (BCG)-immunized donors (Supplementary Table 3), to investigate the effects of prior SARS-CoV-2 exposure or BCG immunization on immune responses. There was additional interest in investigating prior BCG immunizations given the attenuated *M. bovis* vaccine is currently the only licensed TB vaccine and regularly administered in TB endemic regions. While early in the pandemic there were hypotheses that prior BCG immunization may provide protection against SARS-CoV-2 (51), these claims were later dispelled in clinical studies (52, 53). Frozen PBMCs were thawed and either mock-infected or infected with M.tb HN878 at a MOI of 1 for 96 hours (Figure 6A). Supernatants were harvested, filtered, and applied to Vero cells, which are highly permissive to SARS-CoV-2 infection, to assess whether cytokines alone could confer protection against SARS-CoV-2 infection. Treatment of Vero cells with supernatants from M.tb-infected PBMCs resulted in significantly reduced viral titers, with no significant differences observed among PBMC groups defined by date or vaccination history (Figure 6B). These findings were confirmed using more physiologically relevant Calu-3 human airway epithelial cells (54–56) where diminished viral titers were observed in samples pre-treated with supernatants from M.tb-infected PBMCs (Figure 6C). To define the essential elements of protection, the cytokine levels within the supernatants were quantified, revealing increased production of several proinflammatory cytokines, including G-CSF, GM-CSF, TNF-α, IL-1β, IL-6, and IFNγ, following M.tb infection compared to mock-infected PBMCs (Figure 6D). Given the absence of significant differences between PBMC groups, subsequent experiments were conducted using PBMCs collected prior to 2019.

Supernatant-treated Calu-3 cells were then used in RT-qPCR analysis to determine if cells underwent transcriptional changes upon treatment with supernatants. Treated Calu-3 cells showed significantly increased expression of ISGs such as *OAS1*, *OAS3*, *MX2* and notably, *IFIH1*, the gene encoding MDA5, a primary PRR for SARS-CoV-2, compared to media-treated cells (Figure 7A). Subsequently, 24 hours post-SARS-CoV-2 infection, the expression of these ISGs increased in both control and M.tb-infected PBMC supernatant-treated cells, with a significant increase in expression sustained in the supernatant-treated cells (Figure 7B). These

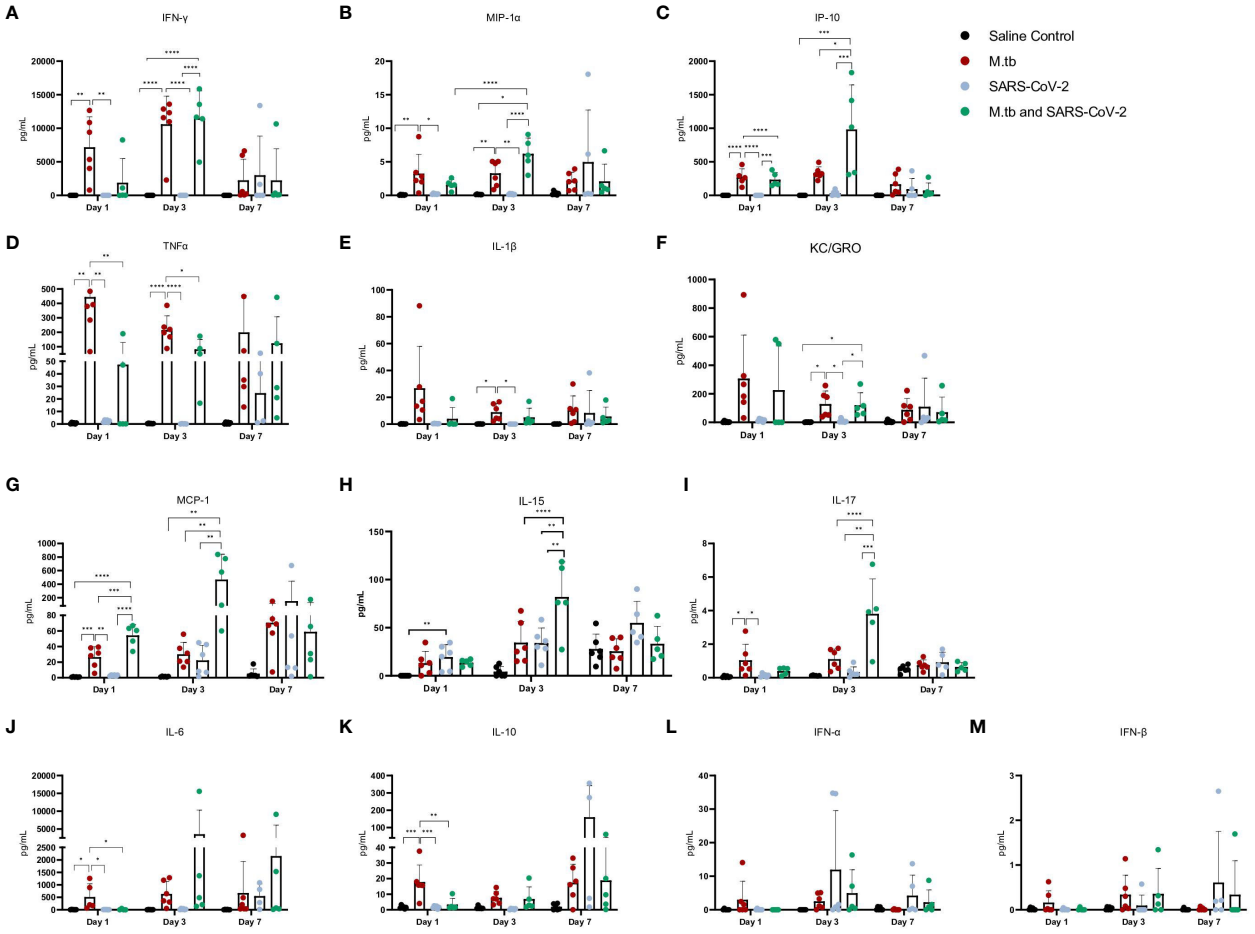

FIGURE 4
Cytokine and chemokine responses in the lung early after infection with SARS-CoV-2 or co-infection with M.tb. **(A-M)** Bronchoalveolar lavage fluid from seven female mice per group was collected 1, 3, and 7-days post-infection with SARS-CoV-2. Significant differences between cohorts at each time point was determined by one-way ANOVA, alpha of 0.05 (* = P<0.05, **= P<0.01, ***=P<0.001, ****=P<0.0001).

findings support our hypothesis that prior M.tb infection primes epithelial cells towards resisting viral infection by inducing ISG expression.

Passive protection from prior M.tb infection restricts viral replication

While pre-treatment led to transcriptional changes and protection from SARS-CoV-2 after 48 hours of infection, pinpointing the stage of the viral infection cycle that may be affected was of interest. To align with our transcriptional data, Calu-3 cells were treated with supernatants or media (positive control) and infected with SARS-CoV-2 for 1, 6, 24, and 48 hours, then assessed for viral load. Following 1 hour of infection, no significant differences in viral load were observed (Figure 8A), suggesting no influence or perturbations in viral entry pathways—a result consistent with the expected SARS-CoV-2 doubling time of around 6 hours (57). However, after 6 hours of infection, there was a noticeable trend toward decreased titers in treated Calu-3 cells (Figure 8B). By 24 hours, treated cells displayed no plaques likely reaching the limit of detection (Figure 8C), suggesting that treated cells were not permissive to replication and actively eliminated the virus, thereby conferring protection.

Neutralization of IFNγ attenuates protection against SARS-CoV-2

To explore the mechanism of protection, an investigation into the involvement of specific cell types and cytokines was conducted. While type I IFNs are normally associated as the predominant anti-viral response, we did not see significant levels within our measurements. However, we did detect significant levels of IFNγ in both *in vivo* and *in vitro* models, and wanted to determine if blocking IFNγ would attenuate the observed protection. Accordingly, major cell types known to induce IFNγ were targeted.

Human PBMCs were co-incubated with neutralizing antibodies against CD4+ T cells, CD8α+ T cells, CD314+ NK cells, and IFNγ at increasing concentrations, and then infected with M.tb for 96 hours.

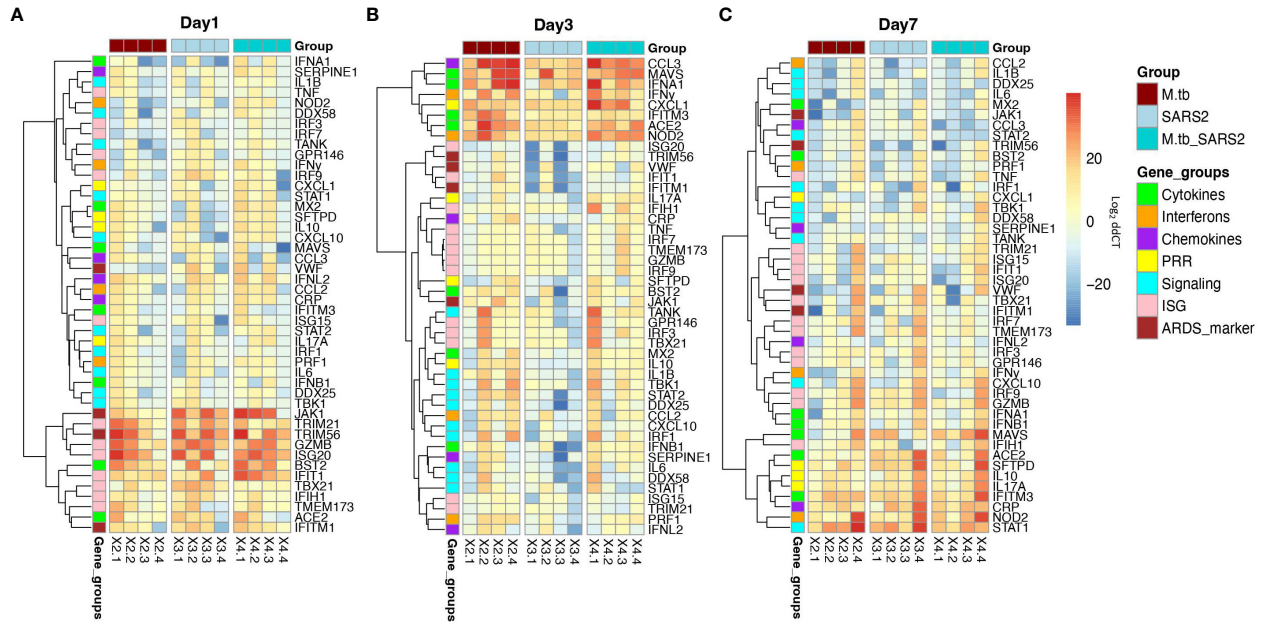

FIGURE 5
Lung mRNA expression of inflammatory-related genes early after infection with SARS-CoV-2 or co-infection with M.tb. Accessories lobes from four female mice per group were collected 1, 3, and 7-days post-SARS-CoV-2 infection used in RT-qPCR to measure the delta-delta CT values. Heat map depicts Log2 relative expression (delta-delta CT) of selected cytokines, chemokines, interferons, ISGs, and genes involved in inflammatory pathways and lung inflammation **(A)** 1-day post SARS-CoV-2 infection **(B)** 3-days post SARS-CoV-2 infection, and **(C)** 7-days post SARS-CoV-2 infection. Expression was normalized to non-infected saline control mice. Graphs were created using RStudio.

Mouse IgG1 and IgG2 antibodies were used as isotype negative controls, while media-only treated cells served as a control for viral replication. After the 96-hour incubation period, supernatants were collected, as previously described, and used to treat permissive Vero cells to measure PFU following SARS-CoV-2 infection. Blocking of CD314+ NK cells did not result in a significant increase in viral titer, and CD8α+ T cells reached significance only at the highest concentration (Figure 9). Neutralization of IFNγ led to diminished protection at 20 and 100 μg/mL, as evidenced by an increase in viral titer, highlighting its importance in conferring protection against SARS-CoV-2 (Figure 9).

Interestingly, neutralization of CD4+ T cells resulted in an increased viral load with escalating antibody concentrations, suggesting that protection could be dependent on IFNγ and CD4 + T cell activity.

Discussion

TB and COVID-19 remain leading infectious disease killers, with 1.3 million TB-related deaths reported by the World Health Organization (WHO) in 2022 (58) and a cumulative 6.8 million COVID-19-related deaths as of March 2024 (1). The lack of definitive clinical data on the risks associated with M.tb and SARS-CoV-2 co-infection has sparked significant interest in understanding the interplay between these pathogens. In this study, we contribute to the growing body of data on co-infection using a preclinical model, which allows for the investigation of specific interactions between infections while controlling for factors that influence disease outcomes. This is crucial given the challenges observed in many clinical studies on M.tb and SARS-CoV-2 co-infections, such as issues with study sizes, comorbidities, coinciding risk factors and unknown infection timelines. Consistent with previous findings, we observed a protective effect against SARS-CoV-2 following prior M.tb infection. This model is additive and unique given variations in pathogen strains, including clinical M.tb isolates and variants of interest. While the protective effects of M.tb and SARS-CoV-2 co-infection have been documented, the underlying mechanisms remain largely unknown (43–45). By pairing *in vivo* results with *in vitro* mechanistic studies, we were able to specifically examine the impact of M.tb-induced immune responses on epithelial cells, which are the primary targets of SARS-CoV-2. This focused approach addresses potential limitations of complex *in vivo* systems.

From our studies, we elucidated the importance of IFNγ and CD4+T cell activity in driving the protection seen *in vitro*. An early, and Th1-leaning CD4+ T cell response is deemed important for combatting SARS-CoV-2 (59). Additionally, a study has shown that pre-existing CD4+ T cells induced from previous infection provided protection against SARS-CoV-2 (60). Similarly, IFNγ has demonstrated driving vaccine-induced cellular immunity in K18-hACE2 transgenic B-cell deficient (μMT) mice (61) and recently confirmed to induce early control of SARS-CoV-2 infection when administered intranasally to wildtype C57BL/6 mice (62). Interestingly, clinical studies have reported on M.tb and SARS-CoV-2 co-infected individuals' limited cellular response to M.tb or

10.3389/fimmu.2024.1424374

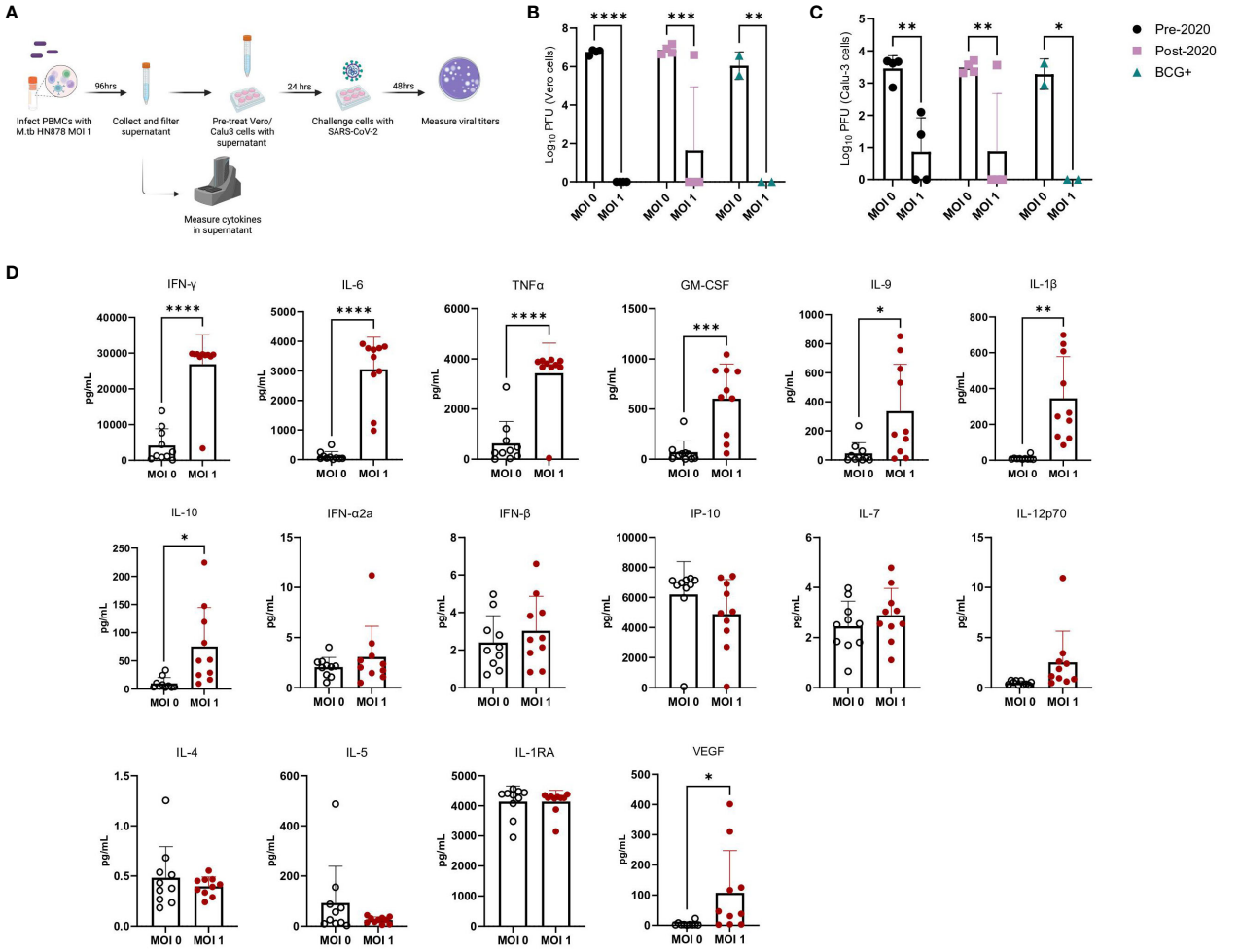

FIGURE 6
Cytokine levels from M.tb-infected PBMCs and the effect of M.tb infected PBMC supernatants on viral replication in cell culture. **(A)** Experimental scheme of *in vitro* PBMC M.tb infection, **(B)** Viral titers of SARS-CoV-2-challenged Vero cells treated with supernatants from mock-infected or M.tb-infected human PBMCs collected prior to 2020 (N=4), post-2020 (N=4), or from BCG-immunized patients (N=2), and **(C)** viral titers of SARS-CoV-2-challenged Calu-3 cells treated with supernatants from mock-infected or M.tb-infected human PBMCs collected prior to 2020 (N=4), post-2020 (N=4), or from BCG-immunized patients (N=2). Titers between mock-infected and M.tb-infected supernatant treatments for each PBMC group were analyzed using two-way ANOVA (* = P<0.05, **= P<0.01, ***=P<0.001, ****= P<0.0001). **(D)** Cytokine measurements of supernatants from mock-infected or PBMCs infected with M.tb HN878 at a MOI of 1. Measurements analyzed using unpaired T-Test with Welch's T Test and alpha of 0.05 (* = P<0.05, **= P<0.01, ***=P<0.001, ****= P<0.0001).

SARS-CoV-2 antigens potentially due to anergy or immune exhaustion (11, 63, 64). However, we hypothesize that while prior M.tb induced immune priming can be protective during acute SARS-CoV-2 infection, in certain individuals other factors may hinder this protection, allowing for co-infection to persist and worsening disease outcomes. While we were able to get a controlled look at M.tb and SARS-CoV-2 co-infection in a preclinical model there are many other conditions to consider that may affect co-infection in clinical contexts.

In turn, we remain curious about how our use of a low-dose M.tb infection model, which more closely mimics the chronic stage of human infection, may contribute to the observed protection. Exploring the ultra-low dose M.tb model (65), which delivers 1–3 CFU and strongly mirrors human pathology, may provide insight into whether the diffuse lung immune response exhibited with a low-dose model, or other factors drive protection in co-infection models. Interestingly, it has been reported that the magnitude of viral titers inversely correlated with increasing M.tb infectious dose (29), providing further evidence towards the need of a diffuse infection and accompanied response. Additionally, LMICs with large TB burden are heavily associated with comorbidities that affect TB and COVID-19 severity (66–68). In order to further understand and close the gap between preclinical and clinical studies investigating these additional factors such as sex, metabolic diseases, age, HIV co-infections, and antibiotic resistant M.tb strains in the pre-clinical model, will be vital for furthering knowledge on M.tb and SARS-COV-2 co-infections. Additionally, we acknowledge that differences based on the phase of M.tb infection, such as active versus latent infection, can impact the outcomes of co-infection with SARS-CoV-2, thus warranting further investigation.

10.3389/fimmu.2024.1424374

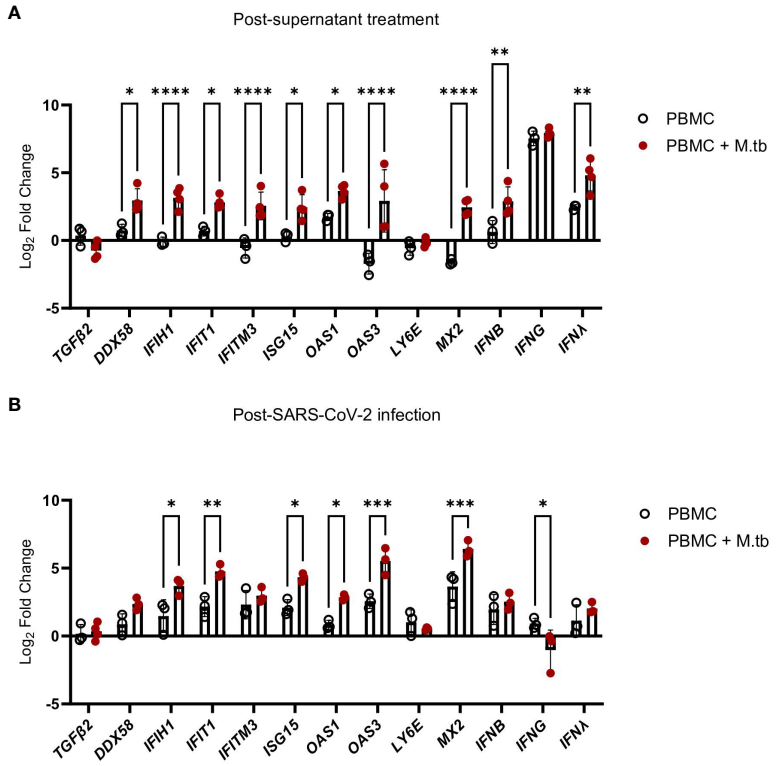

FIGURE 7
Gene expression changes in Calu-3 epithelial cells treated with supernatants from mock-infected or M.tb-infected human PBMCs and infected with SARS-CoV-2. Graphs depict fold-change expression of ISGs normalized to media-treated cells and the *Beta-Actin* house-keeping gene. **(A)** upregulation of genes 24 hours post-supernatant treatment and **(B)** upregulation of genes 24 hours post-SARS-CoV-2 infection. Expression of genes between mock-infected and M.tb-infected supernatant treatments was analyzed using two-way ANOVA (* = P<0.05, **= P<0.01, ***=P<0.001, ****=P<0.0001).

Moreover, our study underscores the importance of innate immune induction in protection against SARS-CoV-2. While increased global vaccination has significantly impacted the trajectory and harm of COVID-19, the emergence of humoral immune evasion by SARS-CoV-2 variants of concern highlighted the need for more comprehensive vaccine-induced responses. Our findings further emphasize the crucial role of innate immune responses in combating the earliest stages of viral infections.

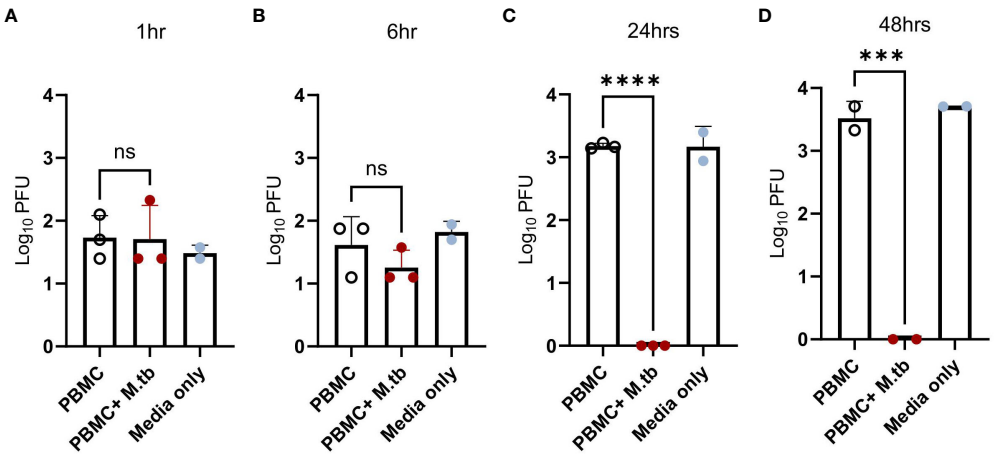

FIGURE 8
Viral load in Calu-3 cells treated with supernatants from mock-infected or M.tb-infected human PBMCs following infection with SARS-CoV-2. Calu-3 cells were treated with supernatants and infected with 75 PFU of SARS-CoV-2 for **(A)** 1 hour, **(B)** 6 hours, **(C)** 24 hours, and **(D)** 48 hours. Significant differences between groups at each time point was determined by one-way ANOVA, alpha of 0.05 (*** = P<0.001 and **** = P<0.0001).

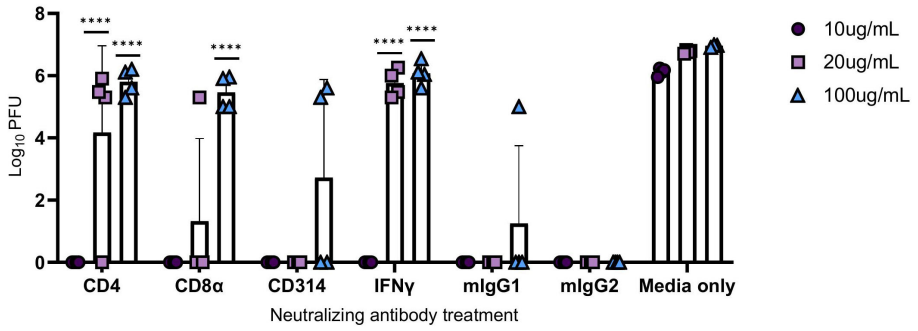

FIGURE 9
Viral titers following the administration of neutralizing antibodies against immune components. PBMCs were infected with M.tb in the presence of neutralizing antibodies against CD4, CD8α, CD314, and with isotype controls mouse IgG1 (mIgG1) and IgG2 (mIgG2). Some collected supernatants were treated with neutralizing antibodies against IFNγ. Vero cells were treated with the supernatants then challenged with SARS-CoV-2 and PFU recorded 48 hours post-infection. Significant differences of PFUs between neutralization treatments and relative isotype controls, mouse IgG1 (CD4, CD314, and IFNγ) and IgG2 (CD8α) were analyzed using two-way ANOVA (****=P<0.0001). Data are representative of two independent experiments.

Additionally, this highlights the need to fine-tune inflammatory responses to ensure they contribute to protection rather than exacerbate detrimental effects. These models help winnow down potential therapeutic targets and define features desirable for prophylactic vaccine strategies.

Data availability statement

The original contributions presented in the study are included in the article/Supplementary Material. Further inquiries can be directed to the corresponding author.

Ethics statement

Ethical approval was not required for the studies on humans in accordance with the local legislation and institutional requirements because only commercially available established cell lines were used. The animal study was approved by Seattle Children's Research Institute IACUC. The study was conducted in accordance with the local legislation and institutional requirements.

Author contributions

BW: Writing – review & editing, Writing – original draft, Visualization, Project administration, Methodology, Investigation, Formal analysis, Data curation, Conceptualization. DF: Writing – review & editing, Methodology, Investigation, Data curation. HA: Writing – review & editing, Methodology, Investigation, Formal analysis, Data curation. BB: Writing – review & editing, Supervision, Methodology, Investigation, Conceptualization. BP: Writing – review & editing, Formal analysis, Data curation. SL: Supervision, Methodology, Writing – review & editing, Project administration, Conceptualization. SB: Visualization, Supervision, Resources, Project administration, Funding acquisition, Conceptualization, Writing – review & editing. RC: Writing – review & editing, Supervision, Resources, Project administration, Funding acquisition, Conceptualization.

Funding

The author(s) declare financial support was received for the research, authorship, and/or publication of this article. This project has been funded in whole or in part with Federal funds from the National Institute of Allergy and Infectious Diseases, National Institutes of Health, Department of Health and Human Services, under Contract No. 75N93021C00029 (to RC), Grant R01AI125160 (to RC and SB) and additional funding from Seattle Tuberculosis Research Advancement Center under award P30 AI168034 (to RC). BW was supported through the National Institutes of Health Training grant to the University of Washington, Diseases of Public Health Importance No. AI00750922.

Acknowledgments

The authors express their gratitude to the committed vivarium personnel for their exceptional care of the animals throughout this study. The following reagents were obtained through BEI Resources by the Coler Lab, NIAID, NIH: Mycobacterium tuberculosis, Strain HN878, NR-13647.

Conflict of interest

Author BB was employed by HDT Bio Corp.

The remaining authors declare that the research was conducted in the absence of any commercial or financial relationships that could be construed as a potential conflict of interest.

The author(s) declared that they were an editorial board member of Frontiers, at the time of submission. This had no impact on the peer review process and the final decision.

Publisher's note

All claims expressed in this article are solely those of the authors and do not necessarily represent those of their affiliated organizations, or those of the publisher, the editors and the reviewers. Any product that may be evaluated in this article, or claim that may be made by its manufacturer, is not guaranteed or endorsed by the publisher.

Supplementary material

The Supplementary Material for this article can be found online at: https://www.frontiersin.org/articles/10.3389/fimmu.2024.1424374/full#supplementary-material

References

1. Dong E, Du H, Gardner L. An interactive web-based dashboard to track COVID-19 in real time. *Lancet Infect Dis.* (2020) 20:533–4. doi: 10.1016/S1473-3099(20)30120-1

2. Booysen P, Wilkinson KA, Sheerin D, Waters R, Coussens AK, Wilkinson RJ. Immune interaction between SARS-CoV-2 and Mycobacterium tuberculosis. *Front Immunol.* (2023) 14:1254206. doi: 10.3389/fimmu.2023.1254206

3. WHO. *Global tuberculosis report 2020*. Geneva: World Health Organization (2020).

4. Daneshvar P, Hajikhani B, Sameni F, Noorisepehr N, Zare F, Bostanshirin N, et al. COVID-19 and tuberculosis coinfection: An overview of case reports/case series and meta-analysis of prevalence studies. *Heliyon*. (2023) 9:e13637. doi: 10.1016/j.heliyon.2023.e13637

5. Motta I, Centis R, D'Ambrosio L, García-García JM, Goletti D, Gualano G, et al. Tuberculosis, COVID-19 and migrants: Preliminary analysis of deaths occurring in 69 patients from two cohorts. *Pulmonology*. (2020) 26:233–40. doi: 10.1016/j.pulmoe.2020.05.002

6. Stochino C, Villa S, Zucchi P, Parravicini P, Gori A, Raviglione MC. Clinical characteristics of COVID-19 and active tuberculosis co-infection in an Italian reference hospital. *Eur Respir J* (2020). 56(1):2001708. doi: 10.1183/13993003.01708-2020

7. Western Cape Department of Health in collaboration with the National Institute for Communicable Diseases, South Africa. Risk factors for coronavirus disease 2019 (COVID-19) death in a population cohort study from the Western Cape Province, South Africa. *Clin Infect Dis.* (2021) 73:e2005–e15. doi: 10.1093/cid/ciaa1198

8. du Bruyn E, Stek C, Daroowala R, Said-Hartley Q, Hsiao M, Schafer G, et al. Effects of tuberculosis and/or HIV-1 infection on COVID-19 presentation and immune response in Africa. *Nat Commun*. (2023) 14:188. doi: 10.1038/s41467-022-35689-1

9. Casco N, Jorge AL, Palmero DJ, Alffenaar JW, Fox GJ, Ezz W, et al. Long-term outcomes of the global tuberculosis and COVID-19 co-infection cohort. *Eur Respir J*. (2023) 62(5):2300925. doi: 10.1183/13993003.00925-2023

10. Aiello A, Najafi-Fard S, Goletti D. Initial immune response after exposure to Mycobacterium tuberculosis or to SARS-COV-2: similarities and differences. *Front Immunol.* (2023) 14. doi: 10.3389/fimmu.2023.1244556

11. Najafi-Fard S, Aiello A, Navarra A, Cuzzi G, Vanini V, Migliori GB, et al. Characterization of the immune impairment of patients with tuberculosis and COVID-19 coinfection. *Int J Infect Dis*. (2023) 130 Suppl 1:S34–s42. doi: 10.1016/j.ijid.2023.03.021

12. Sheerin D, Phan TK, Eriksson EM, Coussens AK. Distinct and synergistic immunological responses to SARS-CoV-2 and Mycobacterium tuberculosis during co-infection identified by single-cell-RNA-seq. *medRxiv*. (2023). doi: 10.1101/2023.05.24.23290499

13. Tay MZ, Poh CM, Rénia L, MacAry PA, Ng LFP. The trinity of COVID-19: immunity, inflammation and intervention. *Nat Rev Immunol.* (2020) 20:363–74. doi: 10.1038/s41577-020-0311-8

14. Bortolotti D, Gentili V, Rizzo S, Schiuma G, Beltrami S, Strazzabosco G, et al. TLR3 and TLR7 RNA sensor activation during SARS-coV-2 infection. *Microorganisms*. (2021) 9(9):1820. doi: 10.3390/microorganisms9091820

15. Salvi V, Nguyen HO, Sozio F, Schioppa T, Gaudenzi C, Laffranchi M, et al. SARS-CoV-2–associated ssRNAs activate inflammation and immunity via TLR7/8. *JCI Insight*. (2021) 6(18):e150542. doi: 10.1172/jci.insight.150542

16. Yin X, Riva L, Pu Y, Martin-Sancho L, Kanamune J, Yamamoto Y, et al. MDA5 governs the innate immune response to SARS-coV-2 in lung epithelial cells. *Cell Rep*. (2021) 34:108628. doi: 10.1016/j.celrep.2020.108628

17. Yamada T, Sato S, Sotoyama Y, Orba Y, Sawa H, Yamauchi H, et al. RIG-I triggers a signaling-abortive anti-SARS-CoV-2 defense in human lung cells. *Nat Immunol.* (2021) 22:820–8. doi: 10.1038/s41590-021-00942-0

18. Schiuma G, Beltrami S, Bortolotti D, Rizzo S, Rizzo R. Innate immune response in SARS-coV-2 infection. *Microorganisms*. (2022) 10(3):501. doi: 10.3390/microorganisms10030501

19. Hadjadj J, Yatim N, Barnabei L, Corneau A, Boussier J, Smith N, et al. Impaired type I interferon activity and inflammatory responses in severe COVID-19 patients. *Science*. (2020) 369:718–24. doi: 10.1126/science.abc6027

20. Felgenhauer U, Schoen A, Gad HH, Hartmann R, Schaubmar AR, Failing K, et al. Inhibition of SARS-CoV-2 by type I and type III interferons. *J Biol Chem*. (2020) 295:13958–64. doi: 10.1074/jbc.AC120.013788

21. Silva B, Krogstad PA, Teles RMB, Andrade PR, Rajfer J, Ferrini MG, et al. IFN-γ-mediated control of SARS-CoV-2 infection through nitric oxide. *Front Immunol.* (2023) 14. doi: 10.3389/fimmu.2023.1284148

22. Vanderheiden A, Ralfs P, Chirkova T, Upadhyay AA, Zimmerman MG, Bedoya S, et al. Type I and type III interferons restrict SARS-coV-2 infection of human airway epithelial cultures. *J Virol*. (2020) 94(19):e00985-20. doi: 10.1128/JVI.00985-20

23. Cremoni M, Allouche J, Graça D, Zorzi K, Fernandez C, Teisseyre M, et al. Low baseline IFN-γ response could predict hospitalization in COVID-19 patients. *Front Immunol.* (2022) 13. doi: 10.3389/fimmu.2022.953502

24. Lazear HM, Schoggins JW, Diamond MS. Shared and distinct functions of type I and type III interferons. *Immunity*. (2019) 50:907–23. doi: 10.1016/j.immuni.2019.03.025

25. Liu S-Y, Sanchez DJ, Aliyari R, Lu S, Cheng G. Systematic identification of type I and type II interferon-induced antiviral factors. *Proc Natl Acad Sci.* (2012) 109:4239–44. doi: 10.1073/pnas.1114981109

26. Samuel CE. Interferon at the crossroads of SARS-CoV-2 infection and COVID-19 disease. *J Biol Chem*. (2023) 299:104960. doi: 10.1016/j.jbc.2023.104960

27. Fung SY, Siu KL, Lin H, Yeung ML, Jin DY. SARS-CoV-2 main protease suppresses type I interferon production by preventing nuclear translocation of phosphorylated IRF3. *Int J Biol Sci*. (2021) 17:1547–54. doi: 10.7150/ijbs.59943

28. Minkoff JM, tenOever B. Innate immune evasion strategies of SARS-CoV-2. *Nat Rev Microbiol*. (2023) 21:178–94. doi: 10.1038/s41579-022-00839-1

29. Shemesh M, Aktepe TE, Deerain JM, McAuley JL, Audsley MD, David CT, et al. SARS-CoV-2 suppresses IFNβ production mediated by NSP1, 5, 6, 15, ORF6 and ORF7b but does not suppress the effects of added interferon. *PloS Pathog*. (2021) 17:e1009800. doi: 10.1371/journal.ppat.1009800

30. Merad M, Martin JC. Pathological inflammation in patients with COVID-19: a key role for monocytes and macrophages. *Nat Rev Immunol*. (2020) 20:355–62. doi: 10.1038/s41577-020-0331-4

31. Tan L, Wang Q, Zhang D, Ding J, Huang Q, Tang YQ, et al. Lymphopenia predicts disease severity of COVID-19: a descriptive and predictive study. *Signal Transduct Target Ther*. (2020) 5:33. doi: 10.1038/s41392-020-0148-4

32. Xiong Y, Liu Y, Cao L, Wang D, Guo M, Jiang A, et al. Transcriptomic characteristics of bronchoalveolar lavage fluid and peripheral blood mononuclear cells in COVID-19 patients. *Emerg Microbes Infect*. (2020) 9:761–70. doi: 10.1080/22221751.2020.1747363

33. Cicchese JM, Evans S, Hult C, Joslyn LR, Wessler T, Millar JA, et al. Dynamic balance of pro- and anti-inflammatory signals controls disease and limits pathology. *Immunol Rev*. (2018) 285:147–67. doi: 10.1111/imr.12671

34. Delogu G, Goletti D. The spectrum of tuberculosis infection: new perspectives in the era of biologics. *J Rheumatol Suppl*. (2014) 91:11–6. doi: 10.3899/jrheum.140097

35. Davis JM, Ramakrishnan L. The role of the granuloma in expansion and dissemination of early tuberculous infection. *Cell*. (2009) 136:37–49. doi: 10.1016/j.cell.2008.11.014

36. Joana Da Silva D, Laure D, Antonio P. Exploring the mechanisms of granuloma formation in *vivo* to prevent dissemination of a respiratory mycobacterium tuberculosis

infection: A live imaging approach. *Eur Respir J*. (2016) 48:PA2696. doi: 10.1183/13993003.congress-2016.PA2696

37. Ulrichs T, Kaufmann SHE. New insights into the function of granulomas in human tuberculosis. *J Pathology*. (2006) 208:261–9. doi: 10.1002/path.1906

38. Torrado E, Cooper AM. IL-17 and Th17 cells in tuberculosis. *Cytokine Growth Factor Rev*. (2010) 21:455–62. doi: 10.1016/j.cytogfr.2010.10.004

39. Zhang Y. Persistent and dormant tubercle bacilli and latent tuberculosis. *Front Biosci*. (2004) 9:1136–56. doi: 10.2741/1291

40. Hilligan KL, Namasivayam S, Clancy CS, O'Mard D, Oland SD, Robertson SJ, et al. Intravenous administration of BCG protects mice against lethal SARS-CoV-2 challenge. *J Exp Med*. (2022) 219(2):e20211862. doi: 10.1084/jem.20211862

41. Tuvim MJ, Evans SE, Clement CG, Dickey BF, Gilbert BE. Augmented lung inflammation protects against influenza A pneumonia. *PloS One*. (2009) 4:e4176. doi: 10.1371/journal.pone.0004176

42. Kolodny O, Berger M, Feldman MW, Ram Y. A new perspective for mitigation of SARS-CoV-2 infection: priming the innate immune system for viral attack. *Open Biol*. (2020) 10:200138. doi: 10.1098/rsob.200138

43. Baker PJ, Amaral EP, Castro E, Bohrer AC, Torres-Juárez F, Jordan CM, et al. Co-infection of mice with SARS-CoV-2 and Mycobacterium tuberculosis limits early viral replication but does not affect mycobacterial loads. *Front Immunol*. (2023) 14:1240419. doi: 10.3389/fimmu.2023.1240419

44. Hildebrand RE, Chandrasekar SS, Riel M, Touray BJB, Aschenbroich SA, Talaat AM. Superinfection with SARS-CoV-2 Has Deleterious Effects on Mycobacterium bovis BCG Immunity and Promotes Dissemination of Mycobacterium tuberculosis. *Microbiol Spectr*. (2022) 10:e0307522. doi: 10.1128/spectrum.03075-22

45. Rosas Mejia O, Gloag ES, Li J, Ruane-Foster M, Claeys TA, Farkas D, et al. Mice infected with Mycobacterium tuberculosis are resistant to acute disease caused by secondary infection with SARS-CoV-2. *PloS Pathog*. (2022) 18:e1010093. doi: 10.1371/journal.ppat.1010093

46. Larsen SE, Reese VA, Pecor T, Berube BJ, Cooper SK, Brewer G, et al. Subunit vaccine protects against a clinical isolate of Mycobacterium avium in wild type and immunocompromised mouse models. *Sci Rep*. (2021) 11(1):9040. doi: 10.1038/s41598-021-88291-8

47. Baldwin SL, Reese VA, Larsen SE, Pecor T, Brown BP, Granger B, et al. Therapeutic efficacy against Mycobacterium tuberculosis using ID93 and liposomal adjuvant formulations. *Front Microbiol*. (2022) 13:935444. doi: 10.3389/fmicb.2022.935444

48. Larsen SE, Berube BJ, Pecor T, Cross E, Brown BP, Williams BD, et al. Qualification of ELISA and neutralization methodologies to measure SARS-CoV-2 humoral immunity using human clinical samples. *J Immunol Methods*. (2021) 499:113160. doi: 10.1016/j.jim.2021.113160

49. Downs SL, Madhi SA, van der Merwe L, Nunes MC, Olwagen CP. High-throughput nanofluidic real-time PCR to discriminate Pneumococcal Conjugate Vaccine (PCV)-associated serogroups 6, 18, and 22 to serotypes using modified oligonucleotides. *Sci Rep*. (2021) 11:23728. doi: 10.1038/s41598-021-03127-9

50. Reuschl AK, Edwards MR, Parker R, Connell DW, Hoang L, Halliday A, et al. Innate activation of human primary epithelial cells broadens the host response to Mycobacterium tuberculosis in the airways. *PloS Pathog*. (2017) 13:e1006577. doi: 10.1371/journal.ppat.1006577

51. Escobar LE, Molina-Cruz A, Barillas-Mury C. BCG vaccine protection from severe coronavirus disease 2019 (COVID-19). *Proc Natl Acad Sci U S A*. (2020) 117:17720–6. doi: 10.1073/pnas.2008410117

52. Pittet LF, Messina NL, Orsini F, Moore CL, Abruzzo V, Barry S, et al. Randomized trial of BCG vaccine to protect against covid-19 in health care workers. *N Engl J Med*. (2023) 388:1582–96. doi: 10.1056/NEJMoa2212616

53. Ten Doesschate T, van der Vaart TW, Debisarun PA, Taks E, Moorlag S, Paternotte N, et al. Bacillus Calmette-Guérin vaccine to reduce healthcare worker absenteeism in COVID-19 pandemic, a randomized controlled trial. *Clin Microbiol Infect*. (2022) 28:1278–85. doi: 10.1016/j.cmi.2022.04.009

54. Chu H, Chan JF, Yuen TT, Shuai H, Yuan S, Wang Y, et al. Comparative tropism, replication kinetics, and cell damage profiling of SARS-CoV-2 and SARS-CoV with implications for clinical manifestations, transmissibility, and laboratory studies of COVID-19: an observational study. *Lancet Microbe*. (2020) 1:e14–23. doi: 10.1016/S2666-5247(20)30004-5

55. Fogh J, Fogh JM, Orfeo T. One hundred and twenty-seven cultured human tumor cell lines producing tumors in nude mice. *J Natl Cancer Inst*. (1977) 59:221–6. doi: 10.1093/jnci/59.1.221

56. Mautner L, Hoyos M, Dangel A, Berger C, Ehrhardt A, Baiker A. Replication kinetics and infectivity of SARS-CoV-2 variants of concern in common cell culture models. *Virology J*. (2022) 19(1):76. doi: 10.1186/s12985-022-01802-5

57. Cheemarla NR, Watkins TA, Mihaylova VT, Wang B, Zhao D, Wang G, et al. Dynamic innate immune response determines susceptibility to SARS-CoV-2 infection and early replication kinetics. *J Exp Med*. (2021) 218(8):e20210583. doi: 10.1084/jem.20210583

58. WHO. *Global tuberculosis report 2023*. Geneva: World Health Organization (2023).

59. Moss P. The T cell immune response against SARS-CoV-2. *Nat Immunol*. (2022) 23:186–93. doi: 10.1038/s41590-021-01122-w

60. dos Santos Alves RP, Timis J, Miller R, Valentine K, Pinto PBA, Gonzalez A, et al. Human coronavirus OC43-elicited CD4+ T cells protect against SARS-CoV-2 in HLA transgenic mice. *Nat Commun*. (2024) 15:787. doi: 10.1038/s41467-024-45043-2

61. Wang X, Yuen TT, Dou Y, Hu J, Li R, Zeng Z, et al. Vaccine-induced protection against SARS-CoV-2 requires IFN-γ-driven cellular immune response. *Nat Commun*. (2023) 14:3440. doi: 10.1038/s41467-023-39096-y

62. Hilligan KL, Namasivayam S, Clancy CS, Baker PJ, Old SI, Peluf V, et al. Bacterial-induced or passively administered interferon gamma conditions the lung for early control of SARS-CoV-2. *Nat Commun*. (2023) 14:8229. doi: 10.1038/s41467-023-43447-0

63. Petrone L, Petruccioli E, Vanini V, Cuzzi G, Gualano G, Vittozzi P, et al. Coinfection of tuberculosis and COVID-19 limits the ability to in vitro respond to SARS-CoV-2. *Int J Infect Dis*. (2021) 113 Suppl 1:S82–s7. doi: 10.1016/j.ijid.2021.02.090

64. Riou C, du Bruyn E, Stek C, Daroowala R, Goliath RT, Abrahams F, et al. Relationship of SARS-CoV-2-specific CD4 response to COVID-19 severity and impact of HIV-1 and tuberculosis coinfection. *J Clin Invest*. (2021) 131(12):e149125. doi: 10.1172/JCI149125

65. Plumlee CR, Barrett HW, Shao DE, Lien KA, Cross LM, Cohen SB, et al. Assessing vaccine-mediated protection in an ultra-low dose Mycobacterium tuberculosis murine model. *PloS Pathog*. (2023) 19:e1011825. doi: 10.1371/journal.ppat.1011825

66. Jarde A, Romano E, Afaq S, Elsony A, Lin Y, Huque R, et al. Prevalence and risks of tuberculosis multimorbidity in low-income and middle-income countries: a meta-review. *BMJ Open*. (2022) 12:e060906. doi: 10.1136/bmjopen-2022-060906

67. Jarde A, Siqueira N, Afaq S, Naz F, Irfan M, Tufail P, et al. Correction: Addressing TB multimorbidity in policy and practice: An exploratory survey of TB providers in 27 high-TB burden countries. *PloS Glob Public Health*. (2023) 3:e0002186. doi: 10.1371/journal.pgph.0002186

68. Hertz D, Dibbern J, Eggers L, von Borstel L, Schneider BE. Increased male susceptibility to Mycobacterium tuberculosis infection is associated with smaller B cell follicles in the lungs. *Sci Rep*. (2020) 10:5142. doi: 10.1038/s41598-020-61503-3

frontiers | Frontiers in Immunology

TYPE Original Research
PUBLISHED 21 June 2024
DOI 10.3389/fimmu.2024.1406138

OPEN ACCESS

EDITED BY
Cordelia Dunai,
University of Liverpool, United Kingdom

REVIEWED BY
Dhruv Desai,
University of Pennsylvania, United States
Akihiko Sakamoto,
Yamaguchi University, Japan

*CORRESPONDENCE
Huijie Yang
jieer6423@outlook.com
Changgui Li
changguili@aliyun.com

RECEIVED 24 March 2024
ACCEPTED 06 June 2024
PUBLISHED 21 June 2024

CITATION
Song Y, Wang J, Yang Z, He Q, Bao C, Xie Y, Sun Y, Li S, Quan Y, Yang H and Li C (2024) Heterologous booster vaccination enhances antibody responses to SARS-CoV-2 by improving Tfh function and increasing B-cell clonotype SHM frequency. *Front. Immunol.* 15:1406138. doi: 10.3389/fimmu.2024.1406138

Heterologous booster vaccination enhances antibody responses to SARS-CoV-2 by improving Tfh function and increasing B-cell clonotype SHM frequency

Yanli Song[1], Jiaolei Wang[2], Zhihui Yang[1], Qian He[2], Chunting Bao[2], Ying Xie[2], Yufang Sun[2], Shuyan Li[2], Yaru Quan[2], Huijie Yang[2]* and Changgui Li[2]*

[1]Division of the Second Vaccines, Wuhan Institute of Biological Products Co. Ltd., Wuhan, China, [2]Divsion of Respiratory Virus Vaccines, National Institutes for Food and Drug Control, Beijing, China

Heterologous prime-boost has broken the protective immune response bottleneck of the COVID-19 vaccines. however, the underlying mechanisms have not been fully elucidated. Here, we investigated antibody responses and explored the response of germinal center (GC) to priming with inactivated vaccines and boosting with heterologous adenoviral-vectored vaccines or homologous inactivated vaccines in mice. Antibody responses were dramatically enhanced by both boosting regimens. Heterologous immunization induced more robust GC activation, characterized by increased Tfh cell populations and enhanced helper function. Additionally, increased B-cell activation and antibody production were observed in a heterologous regimen. Libra-seq was used to compare the differences of S1-, S2- and NTD-specific B cells between homologous and heterologous vaccination, respectively. S2-specific CD19+ B cells presented increased somatic hypermutations (SHMs), which were mainly enriched in plasma cells. Moreover, a heterologous booster dose promoted the clonal expansion of B cells specific to S2 and NTD regions. In conclusion, the functional role of Tfh and B cells following SARS-CoV-2 heterologous vaccination may be important for modulating antibody responses. These findings provide new insights for the development of SARS-CoV-2 vaccines that induce more robust antibody response.

KEYWORDS

homologous, heterologous, SARS-CoV-2, Libra-seq, SHM, germinal center, Tfh cells

1 Introduction

SARS-CoV-2 vaccination has effectively reduced the prevalence of coronavirus disease 2019 (COVID-19). Several different kinds of vaccines were used during the pandemic, and these vaccines exhibited variations in immunogenicity, safety, protection efficacy and effectiveness. Interestingly, a heterologous prime-boost vaccine strategy may offer advantages over a homologous approach according to numerous recent studies across inactivated, adenoviral vector and mRNA vaccine platforms (1–4). Immunization with inactivated vaccines followed by mRNA or nonreplicative viral vector vaccines has increased the effectiveness of treatment to 87%~96.5% against symptomatic COVID-19 and 95.94%~97.67% against hospitalization (5–7). In animals, heterologous prime-boosting with an adenoviral vector or a mRNA vaccine induced a 12.8- to 51.2-fold increase in protective antibodies compared to those induced by homologous inactivated vaccination (8, 9). Heterologous boosters have appeared to exert greater vaccine protection effects than homologous boosters in both preclinical and clinical trials.

In fact, Hu and his coworkers in 1992 were among the first to employ the heterologous prime-boost immunization regimes. In their study, neutralizing antibody (NAb) titers against HIV were observed in mice primed with recombinant viral vector vaccines and boosted with subunit vaccines, but not in homologous immunized with vectored or subunit vaccines (10). Lu found that heterologous prime-boost with influenza virus vaccines could improve antibody titers 4- to 19-fold change, which may provide cross-protection against seasonal influenza virus. Also, heterologous vaccination displayed increased antibody titers in polio, malaria, tuberculosis and HSV-2 vaccines (11). It may provide a new way for those antigens that are easy to mutate, difficult to develop candidate vaccines, or induce poor immune responses with homologous vaccination. However, the mechanism that heterologous prime-boost is more effective than the "homologous" prime-boost has not been fully demonstrated, which may also limit the development of this strategy in the real world.

Studies have shown that heterologous prime-boosted with COVID-19 inactivated vaccines and adenovirus vector vaccines improve higher NAb titers. The inactivated vaccines are whole virus particles, and adenovirus vector vaccines are nonreplicated vectored vaccines expressing full-length S protein, which may induce different processes of T and B cell responses (12, 13). Immune responses may complement each other to produce higher antibody responses when prime-boosted with both. However, the mechanism remains poorly understood. When repeatedly stimulated with the same COVID-19 vaccines, T cells upregulated the expression of inhibitory signals PD-1 and LAG-3 and decreased its activity (14, 15). Also, B cells activity may decline due to low activity of T cells, which may exhaust immune cells, produce immune tolerance and decrease antibody responses (14, 15). Heterologous SARS-CoV-2 vaccination stimulates more antibody-secreting cells (ASC), T cells and cytokines to enhance humoral and cellular responses, which contribute to more cross-protection to variant strains (16). Although these studies have found some discrepancies in immune responses between heterologous and homologous vaccination, they still cannot fully explain why heterologous vaccination is more effective.

Innate immune cells activate at early stage to participate in immune defense when antigen stimulation, and then APCs present antigens to T and B cells to initiate adaptive immune response. Among them, B cells and T cells play key roles in immune response sites by secreting antibodies and adjusting immune responses. During this process, follicular helper T cells (Tfh) provide cytokines and co-stimulatory signals to promote the activation, proliferation and differentiation of B cells. Subsequently, B cells differentiate into plasma cells or memory B cells (17, 18). This intricate process occurs in germinal center (GC). Understanding the differences in GC responses between heterologous and homologous prime-boosts could potentially elucidate the mechanism behind the enhanced immune responses observed with a heterologous booster dose. In our study, the differences in antibody responses, the populations and function of B cells between heterologous and homologous regimes were analyzed. Also, B-cell specific to different subunit of spike protein was analyzed to investigate the mechanism of increased antibody responses in heterologous vaccination. The study of the mechanism will provide theoretical guidance for optimizing the existing and future vaccination strategies.

2 Materials and methods

2.1 Mice and vaccination

BALB/c mice were purchased from SPF (Beijing) Biotechnology Co., Ltd. All studies were performed in accordance with protocols approved by the Institutional Animal Care and Use Committee (IACUC) at the Beijing Institute of Biological Products Co., Ltd., Beijing, China (No. BSYYF20230130002). All mice in this paper were six- to eight-week-old female mice on a BALB/c background.

For the vaccination regimens, 0.5 μg prototyped SARS-CoV-2 inactivated vaccines (BBIBP-corv) combined with 22.5 μg aluminum hydroxide adjuvant (Croda) or 0.5×10^{10} viral particles (VP) of adenovirus 5 vector vaccines (Ad) encoding full-length prototyped SARS-CoV-2 spike (Convidecia) were injected intraperitoneally in 500 μL 0.01 M PBS. The control mice were vaccinated with 0.01 M PBS containing an equal concentration of aluminum hydroxide adjuvant. The first two doses were administered at D0/D21, and the subsequent booster doses were administered every 14 days (Figure 1A). Blood from each vaccination and spleen samples from 4In and 3InAd were collected on day 10 after vaccination (Figure 1A).

2.2 Determination of antigen-specific IgG titers in serum and culture supernatants

IgG titers specific to spike, S1 (a variable region in spike), S2 (a conserved region in spike) or NTD (a conserved region in S1) in serum and spike- or S2-specific IgG titers in supernatants were

10.3389/fimmu.2024.1406138

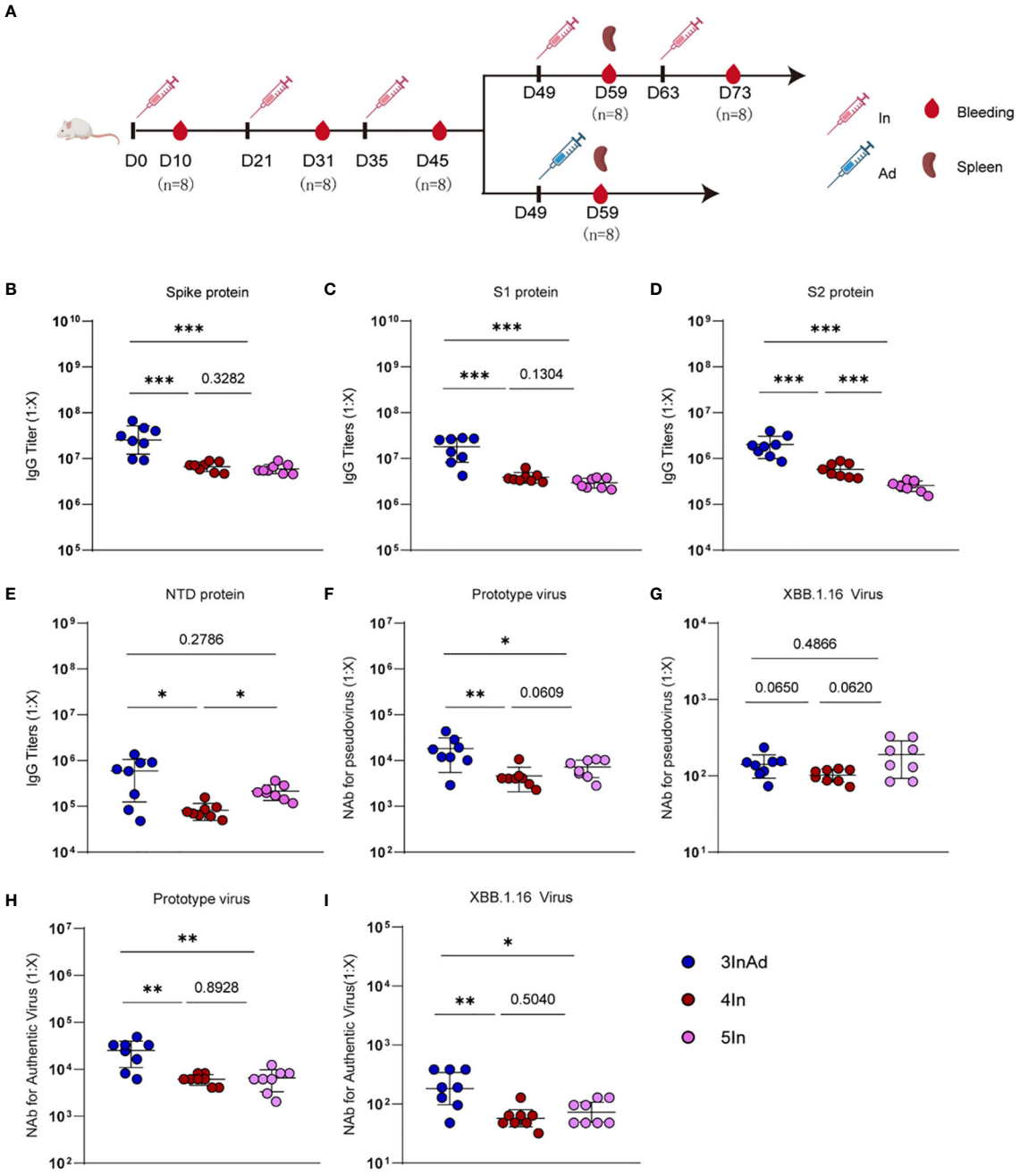

FIGURE 1
Antibody responses induced by homologous or heterologous SARS-CoV-2 vaccination in mice. **(A)** Timeline of vaccination and blood sampling. IgG titers specific to **(B)** spike, **(C)** S1, **(D)** S2, **(E)** NTD, and NAb titers against **(F)** the prototype pseudovirus, **(G)** the XBB.1.16 pseudovirus, **(H)** the prototype authentic virus, **(I)** and the XBB.1.16 authentic virus. In and Ad show inactivated vaccines and adenovirus vector vaccines, respectively. 3InAd represents mice immunized with 3 doses of In followed by one dose of Ad. 4In and 5In represent mice vaccinated with 4 or 5 identical doses of In, respectively. For **(A–I)**, n=8 per SARS-CoV-2 vaccination group, n=6 in control group. Each symbol represents one sample. The data are presented as the geometric mean ± standard error of the mean (SEM). The Mann–Whitney U test was used to analyze the differences between the indicated groups. *p < 0.05, **p < 0.01, and ***p < 0.001 were considered to indicate two-tailed significant differences. The numbers on the graph represent the p values between the indicated groups.

determined. 96-well plates (Costar, cat 42594) were coated with 100 µL of SARS-CoV-2 spike (Sino, cat 40589-V08H4) or S1 (Sino, cat 40591-V08B1), S2 (Sino, cat 40590-V08H1), or NTD (Sino, cat 40591-V49H) at 0.5 µg/mL overnight at 4°C. After 2 h of blocking with 3% BSA in PBS, 100 µL of each diluted serum sample or culture supernatant was incubated for 2 h at room temperature. The serum dilutions used were 1:10000 and 1:40000 (for spike, S1 and S2) and 1:1000 and 1:4000 (for NTD). The supernatants were not diluted. Standard curves were obtained by serial dilution of standard serums via titration, as previously described (19). The secondary antibody, anti-mouse IgG conjugated to HRP (Cytiva, cat. NA931V), was diluted 1:4000 in PBS-3% BSA and incubated for

1 h at room temperature. The reactions were developed with HRP substrate, and the absorbance was measured at 405 nm and 630 nm.

2.3 Determination of NAb against authentic and pseudo-viruses

NAb were determined using authentic and pseudo-SARS-CoV-2 virus, and the 50% inhibitory dilution (ID50) was defined as the serum dilution. NAb against authentic viruses (prototype and XBB.1.16 virus) were determined via a microcytopathogenic effect assay with a minimum eight-fold dilution and 2-fold serial dilutions, as previously described (20). NAb against pseudoviruses (prototype and XBB.1.16 virus) were determined with a minimum twenty-fold dilution and 3-fold serial dilutions, as previously described (12).

2.4 RNA sequencing

Spleens from the 3InAd, 4In and control groups were separated and stored in liquid nitrogen. All RNA extraction, library preparation, and sequencing were performed by BGI Genomics (Wuhan) Co., Ltd. DEGs were analyzed using DESeq2 (v1.4.5). KEGG and GO enrichment analyses were carried out as previously described (21, 22).

2.5 Antibodies and flow cytometry

The fixable viability dye eFluor™ 506 (eBioscience, cat 65–0866-14) was used to exclude dead cells according to the manufacturer's instructions. The following antibodies were used for surface staining at 4°C for 30 min: α-TCR (BioLegend, clone H57–597), α-CD4 (BioLegend, clone RM4–5), α-PD-1 (eBioscience, clone J43), α-CXCR5 (BioLegend, clone L138D7), α-B220 (BioLegend, clone RA3–6B2), α-Gl7 (BioLegend, clone GL7), and α-CD95 (BioLegend, clone SA367H8). The data were analyzed using FlowJo v10.8 or CytExpert.

2.6 Magnetic isolation of B cells and CD4+ T cells

B cells and CD4+ T cells were separated from splenetic cell suspensions using magnetic isolation kits (Stemcell, cat. 19854 for B cells, cat. 19852 for CD4+ T cells) according to the manufacturer's instructions. B and CD4+T cells were sorted to 90% purity and utilized in the subsequent experiment.

2.7 Sorting

CD4+CXCR5+PD-1+ Tfh cells or B220+CD95+Gl7+ GC B cells were sorted via the following steps. In brief, magnetically isolated CD4+ T or total B cells were stained with viability dye (eBioscience, cat 65–0866-14) and antibodies as above for 30 min at 4°C. Then, the cell suspensions were passed through 70-micron filters and resuspended in RPMI 1640 (Gibco, cat 11875093) supplemented with 10% FBS, 1 mM EDTA, 100 U penicillin, and 100 mg/ml streptomycin. Cell sorting was performed on an Aria III instrument.

2.8 Tfh and B-cell coculture *in vitro*

Isolated B cells and Tfh cells were cocultured as previously described with minor modifications (23, 24). 3×10^5/well B cells were cultured with or without 1.5×10^5/well Tfh cells in the presence of 5μg/ml spike peptide pools (GenScript, cat RP30020) in RPMI 1640 (Gibco, cat 11875093) supplemented with 10% heat-inactivated fetal bovine serum (Gibco, 16140071), 2 mM L-glutamine, 1 mM sodium pyruvate, 50 mM 2-mercaptoethanol, 100 U penicillin, and 100 mg/ml streptomycin. Round-bottom tissue culture plates were precultured with 2μg/ml anti-CD3 antibody (BD Biosciences, cat 553057) and 5μg/ml anti-IgM (Invitrogen, cat 16–5092-85) in PBS at 4°C overnight. Six days after coculture, the cells were stained with α-IgG1 (BioLegend, clone RMG1–1), α-IgG2b (BioLegend, clone RMG2b-1), and α-Gl7 (BioLegend, clone GL7). The supernatants were harvested, and the anti-spike IgG titers were assessed via ELISA.

2.9 Real-time PCR

CD4+T or B cells were magnetically sorted to 90% purity and used for RNA extraction. Total RNA was extracted from isolated cells using TRIzol reagent (Invitrogen, 15596026). First-strand cDNA was transcribed (Vazyme, cat R312–3), and real-time PCR was performed using universal qPCR SYBR Green Master Mix (Vazyme, cat Q711–03) according to the manufacturer's protocols. The experiment was performed on a CFX96 instrument (Roche). The data were normalized to the housekeeping gene Gapdh and analyzed by the 2^(−△△CT) method.

The primers used for cDNA amplification were obtained from previous methods (25–28) and are listed as follows:

Gapdh, (forward) 5'-GTGAAGGTCGGTGTGAACGGATT-3' and (reverse) 5'-GGAGATGATGACCCTTTTGGCTC-3'; Il21, (forward) 5'-GCCAGATCGCCTCCTGATTA-3' and (reverse) 5'-CATGCTCACAGTGCCCCTTT-3'; *Bcl6*, (forward) 5'-CCGGCTCAATAATCTCGTGAA-3' and (reverse) 5'-GGTGCATGTAGAGTGGTGAGTGA-3'; *Cxcr5*, (forward) 5'-ACTCCTTACCACAGTGCACCTT-3' and (reverse) 5'-GGAAACGGGAGGTGAACCA-3'; *Cxcr4*, (forward) 5'-TCCAACAAGGAACCCTGCTTC-3' and (reverse) 5'-TTGCCGACTATGCCAGTCAAG-3'; *Aicda*, (forward) 5'-GGCATGAGACCTACCTCTGC-3' and (reverse) 5'-CAGGAGGTGAACCAGGTGAC-3'.

2.10 Libra-seq

Antigen-specific B cells were labeled and sorted as previously described with minor modifications (29, 30). In brief, biotinylated S1 (Acro, cat S1N-C82E8), S2 (Acro, cat S2N-C52E8) and NTD

(Acro, cat S1D-C52E2) proteins were conjugated to two different streptavidin-fluorochrome conjugates, streptavidin-APC (BioLegend, cat 405207) and streptavidin-PE (BioLegend, cat 405203), in equimolar ratios. The cells were incubated with S1, S2, NTD, viability dye (eBioscience, cat. 65–0866-14) or α-CD19 (BioLegend, clone 1D3/CD19) at 4°C for 30 minutes. Then, the cells were sorted as above. Sorted cells were captured in droplets to generate nanoliter-scale gel beads in EMulsions (GEMs). The 5' gene expression library and BCR library were prepared, and sequencing was performed by Abiosciences (Beijing) Co., Ltd. The mRNA sequencing data were processed using CellRanger version 7.0. R version 4.3.1 and the Seurat package (v5.0.0) were used for downstream analysis. The following marker genes were examined: Bcl2 and Itgax (CD11c) for memory B cells (31, 32); Fas and Mki67 for GC B cells; Xbp1 and Mzb1 for plasma cells, while other non-B cells were removed. The SHM frequency was calculated for each heavy chain sequence in the variable segment leading up to the CDR3.

2.11 Statistical analysis

Statistical analysis was performed utilizing GraphPad 8.0. The Mann–Whitney test was used and is explicitly described in the figure legends.

3 Results

3.1 Heterologous vaccination induced more robust antibody responses in mice

To compare the antibody responses induced by heterologous and homologous vaccination, we designed different immunization strategies (Figure 1A). Mice were vaccinated intraperitoneally with SARS-CoV-2 inactivated vaccines (In) or adenovirus 5 vector vaccines (Ad) encoding the full-length SARS-CoV-2 spike protein. The homologous vaccination regimen was 1 to 5 In doses (marked as In, 2In, 3In, 4In and 5In), and the heterologous immunization regimen was 3 doses of In followed by one dose of Ad (3InAd). Blood was collected on day 10 after the last homologous or heterologous booster dose. IgG titers specific to spike, S1 (a variable region in spike), S2 (a conserved region in spike), the N-terminal domain (NTD, a conserved region in S1), and neutralizing antibodies (NAb) against spike pseudovirus, as well as the authentic virus, were determined to explore the antibody dynamics after heterologous and homologous vaccination.

To assess the antibody responses in the homologous group, IgG and NAb titers were measured after each vaccination (Supplementary Figure 1). For SARS-CoV-2 vaccination groups, the spike-specific IgG titer peaked after the 3rd dose of the vaccine and remained at this level even after the following doses (Supplementary Figure 1A). The S1-specific antibody showed similar changes (Supplementary Figure 1A). Interestingly, S2-specific IgG levels peaked after the 4th dose and decreased after the 5th dose (Supplementary Figure 1A), and NTD-specific IgG levels consistently increased (Supplementary Figure 1A). These results indicate that more than 3 doses of homologous prime-boosts with In may induce higher titers of IgG specific to the conserved spike protein regions (Supplementary Figure 1A). Moreover, the titers of NAb against the prototype spike pseudovirus slightly increased after the 5th dose (Figure 1F and Supplementary Figure 1B), while the titers of NAb against the prototype authentic virus peaked after the 4th dose (Figure 1H and Supplementary Figure 1C). Additionally, we found that every dose can induce antibody responses to the XBB.1.16 virus (Supplementary Figures 1B, C).

We next compared antibody responses between heterologous and homologous vaccination (Figure 1). Compared with those in the 4In group, the spike-, S1-, S2-, and NTD-specific IgG levels were significantly higher in the 3InAd group (Figures 1B-E). Similar results were obtained for the titers of NAb against the prototype spike pseudovirus and the prototype authentic virus (Figures 1F, H). Compared with those in the 5In group, the spike-, S1-, and S2-specific IgG titers were also higher in the 3InAd group (Figures 1B-D), but there was no difference in the NTD-specific antibody titers (Figure 1E). Moreover, we found that the titers of NAb against the prototype pseudovirus or authentic virus were significantly higher in 3InAd (Figures 1F, H). Heterologous immunization showed stronger neutralizing effects on authentic XBB.1.16 virus (Figure 1I), although no differences were found on XBB.1.16 pseudovirus (Figure 1G). These data suggest that heterologous vaccination induced more robust IgG and NAb responses than homologous vaccination, and even the 5In homologous vaccination regimen could not induce the same antibody response as that induced by heterologous vaccination. In the following study, we further compared the 4In and 3InAd groups.

3.2 Heterologous vaccination induced a more robust GC response according to global transcriptomic analysis

To explore the heterogeneity of homologous and heterologous immunization strategies, RNA-seq was performed on the spleens from the heterologous and homologous group mice to compare discrepancies in the GC response according to gene expression profiling.

One hundred fifty-two differentially expressed genes (DEGs) were screened between the 3InAd and 4In groups (Figure 2A). Among these DEGs, 38 immune-related genes were found using the GP_CFP and Kyoto Encyclopedia of Genes and Genomes (KEGG) pathway classification methods (Figure 2B). Then, through GO biological process (BP) and KEGG pathway enrichment analyses, we found that these immune-related DEGs were enriched in somatic hypermutation and production of immunoglobulin (*Nuggc*, *Aicda*, *Il21*, *Il6*), Tfh differentiation (*Il21*, *Il6*), germinal center B cell differentiation (*Il6*, *Il21*), cellular response to virus (*Gli2*, *Il6*, *Il21*) (Figures 2A, C, D). To further explore signaling changes in the 3InAd group, we next performed gene set enrichment analysis (GSEA) using

10.3389/fimmu.2024.1406138

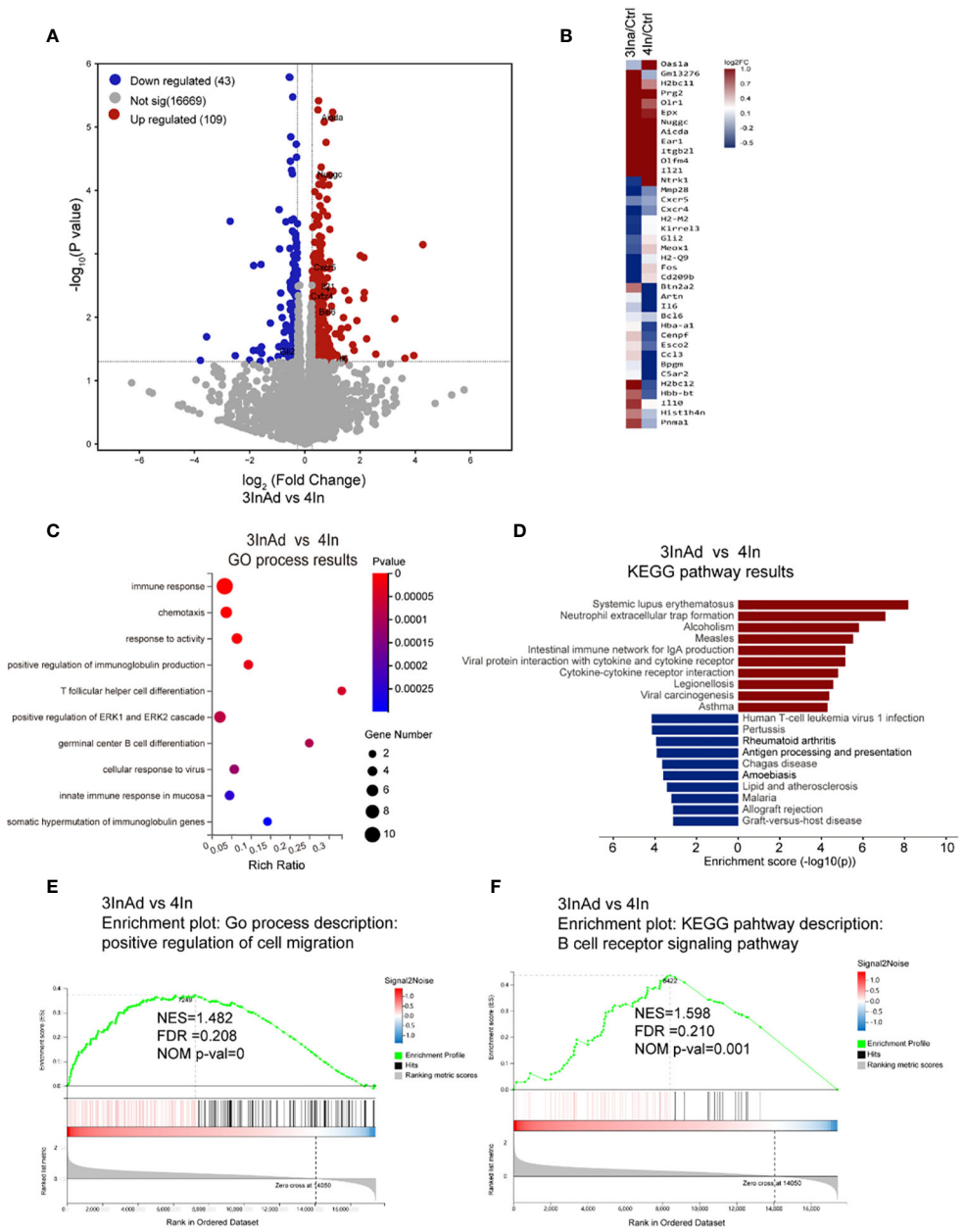

FIGURE 2
Transcriptional heterogeneity in homologous and heterologous vaccination groups. **(A)** DEGs among spleens from 3InAd *vs.* 4In. Genes with a $|\log_2$ (fold change [FC])|>0.6 and p<0.05 were annotated as DEGs. Red dots represented upregulated genes and blue dots showed downregulated genes. **(B)** Heatmap showing the immune-related DEGs between the 3InAd and 4In groups. Four-dose control mice (Ctrl) were used to exclude background effects. **(C)** Bubble plot showing the significantly enriched BPs between the 3InAd and 4In groups, as measured by the Rich Ratio factor and q value. **(D)** Bar graph showing the significantly enriched KEGG pathways evaluated by $-\log_{10}$ (p value) in the 3InAd group compared with the 4In group. Using gene set enrichment analysis (GSEA) to analyze the expressed genes, 2 gene sets related to **(E)** cell migration and **(F)** the B-cell antigen receptor (BCR) signaling pathway were found to be significantly upregulated in the 3InAd group. NES, normalized ES; FDR, false discovery rate; NOM p-val, normalized p value. Each sample was composed of spleen samples from 3 animals. Three samples per group were used.

transcripts per million (TPM) values. We found that genes associated with the positive regulation of cell migration, the immunoglobulin-mediated immune response, and the positive regulation of the B-cell receptor signaling pathway were upregulated in the 3InAd group compared to the 4In group (Figures 2E, F). These gene expression profiling results suggest that heterologous vaccination enhances B-cell and Tfh cell responses and GC activation.

3.3 Heterologous immunization increased Tfh cell populations and function in GC

Tfh cells are specialized B helper cells that enable the proliferation, survival, and differentiation of GC B cells through the delivery of cytokines and costimulatory signals (12). To further investigate the changes in Tfh cells and GC responses after SARS-

CoV-2 heterologous and homologous vaccination, the number and function of Tfh cells were analyzed.

We found that the 3InAd group showed higher Tfh cell populations than the 4In group (Figures 3A, B), indicating that heterologous vaccination induced more robust Tfh cell expansion. Moreover, to evaluate Tfh cell function in the heterologous group, PD1+CXCR5+ Tfh cells sorted from 3InAd or 4In group mice were cocultured with mature splenic B cells from 2In group mice (mice vaccinated with 2 doses of In), and B-cell activation defined by expression of Gl7 marker and isotype switching were detected. The coculture strategy is shown in Figure 3C. When B cells cocultured with 3InAd Tfh cells, we only found a slight increase of activation in the Gl7+IgG1+B group (Figures 3D, E), but both groups exhibit no statistical differences to the 4In Tfh cells, showing no discernible differences in Tfh helper function between heterologous and homologous groups. However, when antibodies in the coculture supernatants were further detected, a significant increase in spike-specific IgG titers was identified in B cells cocultured with 3InAd Tfh cells (Figure 3G), indicating an increase in IgG titers in the absence of significant B-cell activation. This discrepancy may be attributed to the different sensitivity between antibody detection and other immunologic parameters examination during the *in vitro* experiment (33). Additionally, in our study, Tfh cells were repeatedly activated by 3 doses of inactivated vaccination before the 4th-dose vaccination, therefore, the distinction of Tfh function between two groups may not be optimized.

It has been reported that IL-21, BCL-6 and CXCR5 play key roles in regulating Tfh cell differentiation and function. To compare Tfh cell proliferation and function at the gene level, we measured the mRNA expression of *Il21*, *Bcl6* and *Cxcr5* in the 3InAd and 4In groups on day 10 after vaccination. *Il21*, *Bcl6* and *Cxcr5* expression was significantly higher in the 3InAd group than that in the 4In group (Figures 3H-J), suggesting that enhanced Tfh cells populations and function in the heterologous group may be related to upregulating the expression of *Il21*, *Bcl6* and *Cxcr5*.

3.4 B-cell activation and antibody production were increased by the heterologous immunization regimen

We have proven that Tfh cell function is enhanced by heterologous vaccination. Tfh cells provide stimulatory signals to B cells, which promote their survival and ongoing proliferation (34). To compare B cells between the heterologous and homologous groups, we analyzed their proliferation and function.

Compared to those in the 4In group, the populations of GC B cells in the 3InAd group significantly increased (Figures 4A, B), indicating that a heterologous boost dose promote GC B-cell expansion. Then, we further compared the activation of B-cell from these two groups. CD19+ B cells separated from the 3InAd and 4In groups were cocultured with mature splenic Tfh cells sorted from the 2In group for 6 days *in vitro* (Figure 4C). We found that frequencies of Gl7+IgG1+B and Gl7+IgG2b+B cells was significantly greater in the 3InAd B cells cocultured with Tfh cells than in the 4In B cell coculture (Figures 4D-F). Next, antibody titers in the collected coculture supernatants were measured by ELISA. We found significantly increased anti-spike IgG titers in 3InAd B cells (Figure 4G). These results suggest that a heterologous booster dose induces more robust B-cell activation and greater antibody production.

To assess the relationship between GC B cells and antibody responses in both the heterologous and homologous groups, Spearman correlation analysis was used. We found a strong positive correlation between spike-specific IgG titers and the percentage of GC B cells in the 3InAd and 4In groups (Supplementary Figure 2A). This correlation was also observed between NAb titers against authentic virus and the frequencies of GC B cells in both the heterologous and homologous groups (Supplementary Figure 2B). These results suggest that heterologous vaccine induced more SARS-CoV-2-specific B cells, which led to higher antibody titers.

3.5 A heterologous booster dose promoted higher somatic hypermutation and B-cell clonal expansion specific to conserved regions

We have demonstrated that heterologous vaccination increases B-cell activation and antibody production in mice. B cells play a vital role in immune responses by generating NAb that defend SARS-CoV-2 infection and prevent reinfection (35). To compare the differences of antigen specific B-cell responses in heterologous and homologous vaccination, Libra-seq (linking B-cell receptor to antigen specificity through sequencing) was used to map spike-, S1-, S2- and NTD-specific BCR sequences. The number of SHMs and the expansion of antigen-specific B cells were evaluated.

Compared to those in the 4In group, the SHMs in the 3InAds group were increased in spike-, S1-, S2- and NTD-specific B cells (Figure 5A). S2-specific B cells exhibited 1.95-fold increases, respectively (Figure 5A). The 3InAd group exhibited increased SHMs in highly expanded clones (found more than 4 times), moderately expanded clones (found 2 to 3 times) and singleton clones (Figures 5B, C, Supplementary Figure 3A). These results suggest that a heterologous booster dose promoted higher SHM of B cells specific to conversed regions. We next assessed the SHM in phenotypes of the B cells above in heterologous and homologous groups. There was a slight change in the SHM of GC B cells in the 3InAd group compared to the 4In group (Figure 5D). The SHMs in the spike-, S1-, S2- and NTD-specific plasma cells from the 3InAds group exhibited 4.90-, 4.45-, 6.06- and 1.15-fold increases, respectively (Figure 5E). Additionally, we observed 1.98- and 1.34-fold SHM increases in spike- and S1-specific memory B cells, respectively (Figure 5F). These results suggest that the increased SHM of the heterologous group was mainly enriched in S2-specific plasma cells, which may contribute to high-affinity antibodies.

SHMs are regulated by activation-induced cytidine deaminase (AID), an enzyme that induces point mutations in CDR3 and leads to B-cell expansion (36–38). It is predominantly expressed in CXCR4^{hi}GC B cells[43]. To further assess the source of SHMs in the B cells of heterologous and homologous groups, we measured

10.3389/fimmu.2024.1406138

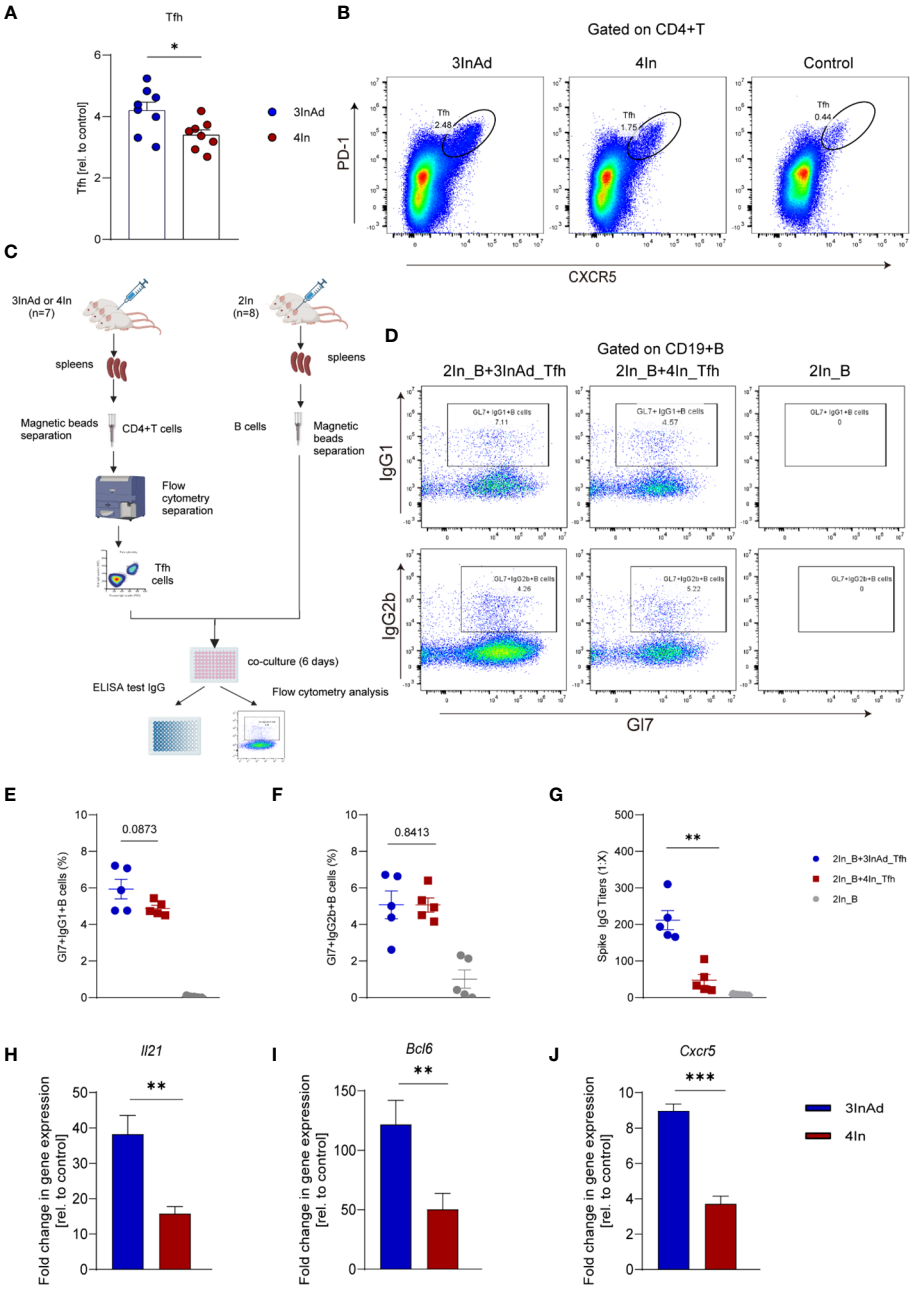

FIGURE 3
The Tfh response was enhanced in the heterologous group compared with homologous group. **(A)** Ratios of CD4+PD-1+CXCR5+ T cells (Tfh cells). Ratio = proportion of Tfh cells in the vaccine group/proportion of Tfh cells in the control group. **(B)** Representative flow plots of Tfh cells in the 3InAd and 4In groups. **(C)** Diagram of Tfh cells from heterologously vaccinated or homologously vaccinated mice cocultured with B cells isolated from mice injected with two doses of inactivated vaccine (2In). **(D–H)** Results of B-cell activation and antibody production in coculture experiments. **(D)** Representative flow plots of Gl7/IgG1 and Gl7/IgG2b gated on CD19+ B cells are shown. No plots were shown in the right panels(2In_B)because the B cells had died after being cultured *in vitro* for 6 days. **(E)** Gl7/IgG1 **(F)** and Gl7/IgG2b double-positive CD19+ B cells are shown. **(G)** Culture supernatants were harvested, and IgG titers specific to spike. **(H)** *Il21*, **(I)** *Bcl6*, **(J)** and *Cxcr5* mRNA expression were measured by qPCR. 2In_B represents B cells separated from the 2In group. 3InAd_Tfh and 4In_Tfh cells represent Tfh cells sorted from the 3InAd and 4In groups, respectively. **(A, E-J)** The data are presented as the mean ± SEM. The Mann–Whitney U test was used to analyze the differences between the indicated groups. *p < 0.05, **p < 0.01, and ***p < 0.001 were considered to indicate two-tailed significant differences. The numbers on the graph are the p values for the indicated groups. Each symbol represents one **(A)** individual animal or **(E-G)** coculture well. **(A, H-J)** n=8 in SARS-CoV-2 vaccination group, n=6 in control group. **(E-G)** n=7 mice in the 3InAd and 4In groups or n=8 mice in the 2In group.

the mRNA expression of *Aicda* (encoded AID) and *Cxcr4* in GC B cells. We found that *Aicda* and *Cxcr4* were significantly upregulated in the 3InAds group compared to the 4Ins group (Figure 5G and Supplementary Figure 3B), indicating that heterologous vaccination upregulated higher AID expression to increased SHMs in B cells than homologous group.

To measure the expansion and proliferation of B cells, we calculated the cell number ratio of each BCR clonotype to each

10.3389/fimmu.2024.1406138

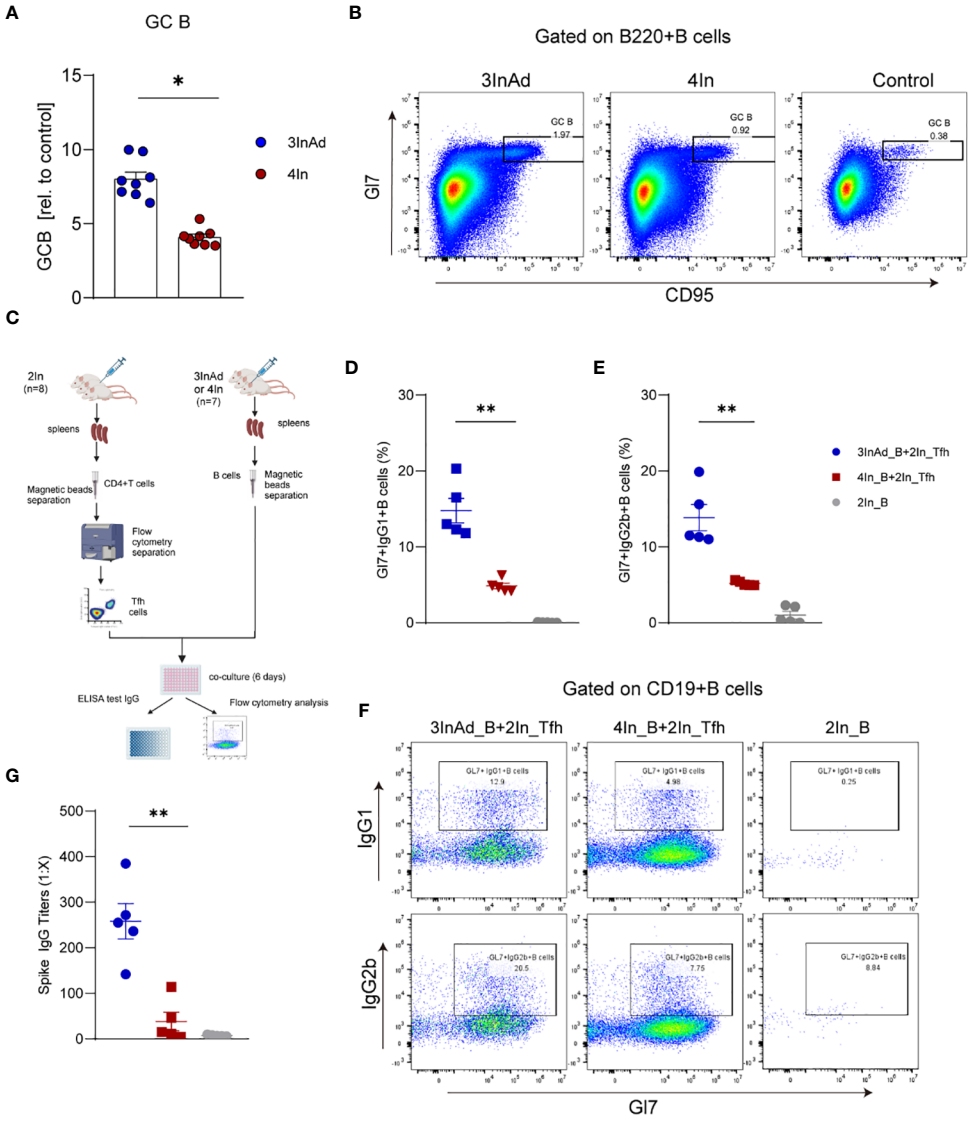

FIGURE 4
The number and function of B cells were increased in the heterologous group. **(A)** Ratios of CD95+Gl7+ B cells (GC B). Ratio = proportion of GC-B cells in the vaccine group/proportion of GC-B cells in the control group. **(B)** Representative flow plots of GC B cells gated on B220+ B cells. **(C)** Diagram of B cells from heterologously vaccinated or homologously vaccinated mice cocultured with Tfh cells isolated from the 2In group. **(D-G)** Results of B-cell activation and antibody titers via *in vitro* coculture experiments. **(D)** Gl7/IgG1 and **(E)** Gl7/IgG2b double-positive CD19+ B cells are shown. **(F)** Representative flow plots of Gl7/IgG1 and Gl7/IgG2b gated on CD19+ B cells are shown. **(G)** The culture supernatant was harvested, and IgG titers specific to spike were measured via ELISA. 3InAd_B and 4In_B represent B cells sorted from 3InAd and 4In group mice. 2In_Tfh cells represent Tfh cells sorted from the 2In group. **(A)** The data are presented as the mean ± SEM. The Mann–Whitney U test was used to analyze the differences between the indicated groups. *p < 0.05 and **p < 0.01 were considered to indicate two-tailed significant differences. The numbers in the graph represent p values. Each symbol represents **(A)** an individual animal or **(D, E, G)** one coculture well. **(A)** n=8 in SARS-CoV-2 vaccination group, n=6 in control group. **(D-G)** n=7 mice in the 3InAd and 4In groups or n=8 mice in the 2In group.

antigen-specific B-cell number. There was a greater percentage of spike-specific top 2 BCR clones in the 3InAd group (Figure 5H). Similarly, the proportions of the top 10 BCR clones specific to S1 exhibited similar tendencies in the 3InAd and 4In groups (Supplementary Figure 3C), whereas the proportions of the S2- and NTD-specific clones in the 3InAd group were greater than those in homologous group (Figures 5I, J). These data demonstrated that heterologous vaccination induced greater expansion of BCRs enriched in the conserved regions in the spike protein.

4 Discussion

In our study, to assess the mechanism by which heterologous booster vaccination enhances antibody responses, Tfh and B-cell responses in mice were compared. We found that the frequencies and helper function of Tfh cells were enhanced after a heterologous booster dose according to the *in vitro* coculture experiment. The expression of genes such as *Il21*, *Bcl6* and *Cxcr5*, which regulate the function and proliferation of Tfh cells, was upregulated. Moreover,

10.3389/fimmu.2024.1406138

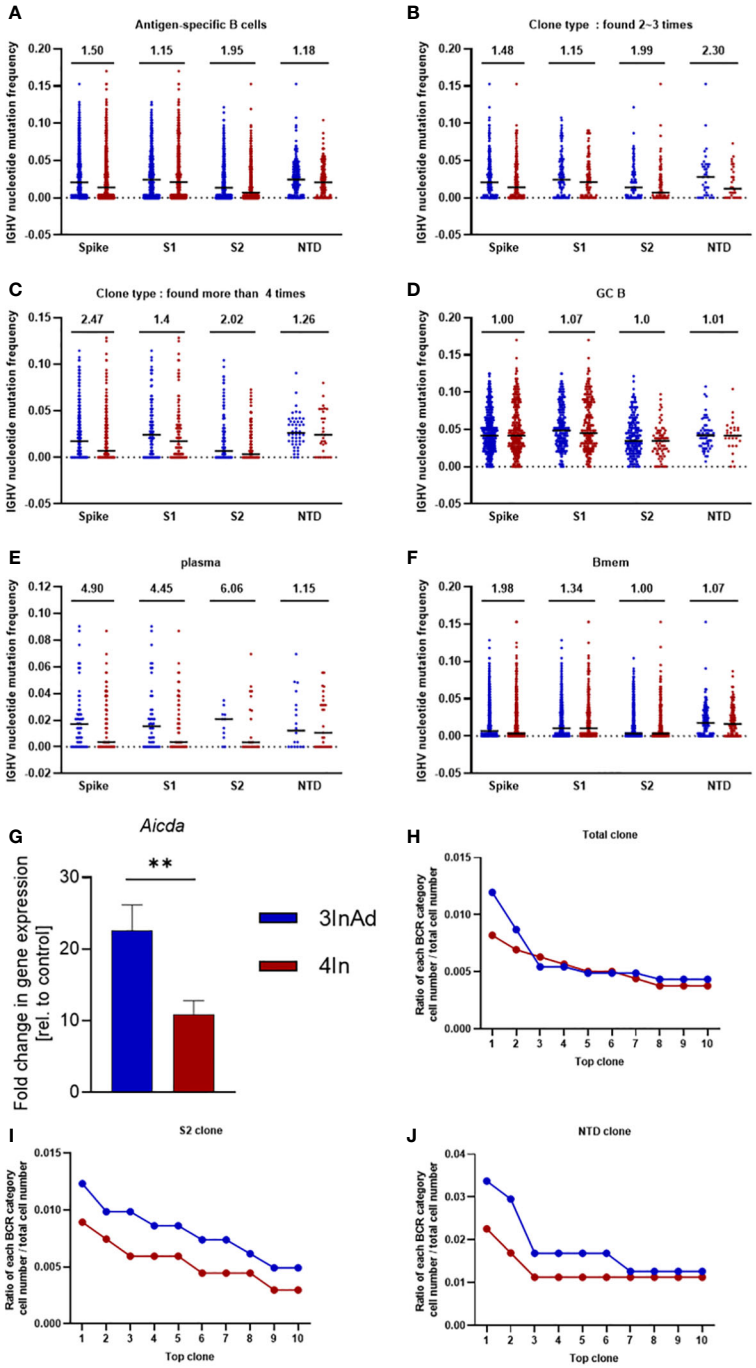

FIGURE 5
Somatic hypermutation (SHM) and clonal expansion in the heterologous vaccine group. Mutation frequency for spike-, S1-, S2- and NTD-specific **(A)** CD19+ clones; **(B)** moderately expanded clones (found 2~3 times); **(C)** highly expanded clones (found more than four times); **(D)** GC B cells; **(E)** plasma cells; and **(G)** memory B cells. **(G)** *Aicda* mRNA expression in B cells was measured by qPCR. The ratio of the top 10 BCR classifications to **(H)** spike-, **(I)** S2-, and **(J)** NTD-specific B-cell numbers. Ratio=cell count of each BCR classification/antigen-specific B-cell count. **(F)** n=8 for the SARS-CoV-2 vaccination group and n=6 for control group. The data are presented as the mean ± SEM. The Mann–Whitney U test was used to analyze the differences between the indicated groups. **$p < 0.01$ was considered to indicate a two-tailed significant difference. **(A–G)** The numbers in the graph represent the mutation ratio. Ratio=3InAd mutation ratio/4In mutation ratio. Each dot represents the hypermutation frequency of one B cell. One sequenced sample was formed by mixing 10 mouse spleen cells in each group to eliminate individual variances.

we found that the heterologous treatment increased the frequencies, activation and antibody production ability of B cells. These B cells showed increased expression of *Aicda*. Libra-seq showed that a heterologous booster dose induced increased SHMs in S1-, S2- and NTD-specific B cells, which were mainly enriched in S1- and S2-specific plasma cells. Additionally, clonal expansion of B cells specific to conserved regions in the spike protein was found in the heterologous group. In summary, the percentages and functions

of Tfh and B cells improved after heterologous immunization, which may induce more robust antibody responses (Figure 6).

Tfh cells provide cytokines and costimulation signals to B cells in the process of GC activation (17, 18, 39, 40). The ability of Tfh cells to activate B cells depends on the population and function of the cells (41–43). We found that Tfh cells expanded after a heterologous booster dose, indicating that a heterologous strategy may promote additional Tfh cells to provide costimulation signals for B cells. The transcription factor BCL-6 promotes the expression of CXCR5 in CD4+ T cells, and CXCR5 promotes the migration of differentiating Tfh cells to the T-B border by binding to CXCL13 (40, 44). Interlink 21 (IL-21) regulates Tfh cell proliferation and differentiation, and Tfh cells can in turn stimulate the proliferation of surrounding Tfh cells through the paracrine cytokine IL-21 (45). We assessed *Il21* and *Bcl6* mRNA expression and found that they were increased two- to three-fold after immunization with the adenovirus vector. These findings suggest that increased expression of these genes in heterologous strategies may promote Tfh differentiation and increase Tfh cell populations.

In vitro coculture experiments revealed that the Tfh cells derived from heterologously vaccinated mice were able to activate more B cells to secrete higher antibody titers. These results suggest that a heterologous vaccination strategy may enhance Tfh cell helper function. It has been shown that BCL-6 expressed by Tfh cells enhances B-cell activation by upregulating CD40L expression, an activation signal that provides a costimulation signal for B cells in the GC (46). In our study, we found that *Bcl6* expression in Tfh cells was elevated after a heterologous booster dose, which may provide additional activation signals for B cells. Although Il21 and Bcl6 were upregulated in the heterologous group, their detailed regulatory process deserves further study.

GCs are considered highly competitive environments where B cells initially encoding polyreactive, low-affinity antibodies evolve via iterative rounds of SHM and selection into clones expressing high-affinity BCRs (34, 43, 47–50). The highest affinity BCRs differentiate into plasma cells, which are the main cells that secrete antibodies (51). Cells expressing low-affinity BCRs differentiate into memory B cells, thereby supporting diversity (48–50). To assess SHM in the heterologous group, spike-, S1-, S2- and NTD-specific B cells were analyzed. The heterologous group exhibited more SHMs than the homologous group in terms of CD19+ B cells. Interestingly, the number of spike-, S1- and S2-specific plasma cells increased 4- to 6-fold in response to the heterologous strategy, which may be beneficial for obtaining high-affinity plasma cells and elevated antibody titers. Moreover, it has been shown that memory B-cell SHMs play an important role in the long-term protection ability of SARS-CoV-2 vaccines (52). According to our results, the number of SHMs in the memory B cells of the heterologous group was higher than that in the homologous group, suggesting that a heterologous booster dose may have a better long-term protective effect.

SHM and proliferation occur in the CXCR4^{hi} B cells sited in the DZ (53). To locate in this area, B cells increase the expression of CXCR4, which can interact with CXCL12 on reticular cells, facilitating B cell migration from LZ to DZ. Our study revealed a significant upregulation of genes associated with cell migration, such as *Cxcr4* and *Cxcl12*, following a heterologous booster dose as determined by RNA-seq analysis. The migration to DZ and the SHM process can further boost the screening B cells clones producing higher affinity antibodies. SHM is induced by AID, which is expressed predominantly in activated mature B cells and targets all transcriptionally active genes to catalyze the mismatch of

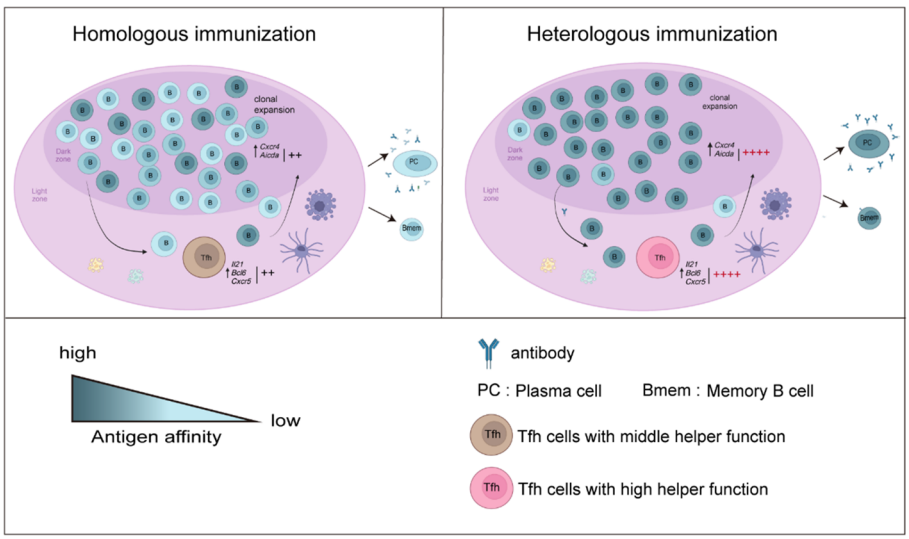

FIGURE 6
Overview of the results in this study. B-cell responses and Tfh cell function increased after a heterologous booster dose. The proliferation and helper function of Tfh cells in the heterologous group were improved. The expression of *Il21*, *Bcl6* and *Cxcr5* was elevated. A heterologous booster dose promoted B-cell activation and a robust antibody response. These B cells displayed increased SHMs, which were enriched mainly in S1- and S2-specific plasma cells. Additionally, heterologous vaccination increased the expansion of B cells specific to the conserved regions in the spike protein.

U:G variable regions (54–56). In our study, we found elevated expression of *Aicda* (encoded AID) at the gene level. Additionally, SHMs in antigen-specific B cells were observed via Libra-seq in the heterologous vaccination group. Moreover, AID induces point mutations in conserved regions of immunoglobulin DNA, base excision repair (BER) initiates, and a DNA double-strand break occurs. The C region of IgM/IgD is replaced by the C gene downstream of the gene chain to produce the IgG, IgE and IgA subtypes (55).

SARS-CoV-2 S protein is present on the surface of virions in the trimeric form, which consists of S1 subunit encompassing the NTD and the receptor-binding domain (RBD); and a membrane-proximal S2 subunit which is responsible for fusion of viral and cellular membranes (57). Effective NAb against SARS-CoV-2 primarily target the RBD, which is responsible for binding to the angiotensin-converting enzyme 2 (ACE2) on host (57). However, Chi et al. reported that the NTD-specific monoclonal antibody 4A8, isolated from COVID-19 recovered patients, exhibited a high neutralizing ability against authentic SARS-CoV-2 (51). In addition to S1, Kim and his co-workers demonstrated that mice immunized with the S2 protein could induce NAb against pseudoviral SARS-CoV-2 (58). In our homologous vaccination group, although the S1-specific antibody titer did not increase after the 4th or 5th dose, the IgG titers specific to S2 and NTD continuously increased, which is similar to that of other studies (59). Moreover, we observed an increase in IgG titers and expansion of B-cell clones specific to S2 and NTD in heterologous group, suggesting that a heterologous booster dose may enhance immune responses against these proteins and contribute to the overall production of NAb.

In our study, differences in Tfh and B-cell responses after homologous and heterologous booster vaccinations were compared, and the mechanism of increased antibody responses after a heterologous booster dose was elucidated. Adenovirus (Ad) is a nonenveloped virus with a linear double-stranded DNA (dsDNA) genome, which is recognized by TLR9 in plasmacytoid DCs and promotes type I interferon production (60). Then, the innate immune responses initiate (60, 61). In inactivated vaccines, aluminum adjuvants promote IL-1β production and the formation of the NLRP3/ASC1/NLR complex, which can activate the NF-kB signaling pathway. Through this process, TLR-independent and CD4+ T-cell-dependent responses are initiated (61–63). Additionally, the processes of uptake, processing and presentation of targeted antigens also differ between these two types of vaccines. For example, spike protein coded by dsDNA is primarily produced and presented to CD8+T cells by MHC-I through the endogenous pathway. In contrast, responses to inactivated vaccines result in antigens being mainly presented to CD4+T cells via MHC-II through the exogenous presentation pathway. The activated CD4 +T and CD8+T cells secrete different cytokines, potentially leading to the discrepancies of Th biases and B-cell responses. Therefore, we believe that the prime immunization with inactivated vaccines followed by adenovirus vaccines boost may initiate comprehensive or complementary immune responses, leading to higher antibody production (64, 65). Therefore, we believe that the prime immunization with inactivated vaccines followed by adenovirus vaccines boost may initiate comprehensive or complementary immune responses, leading to higher antibody production. However, whether other types of heterologous vaccination regimes can induce similar results deserves further study, since antibody induction is a complex process regulated by multiple types of cells, cytokines, and signaling pathways when antigens encounter immune system. In addition to germinal center Tfh and B-cell responses focused in this study, other crucial elements, such as antigen concentration and distribution routes can also affect the immune system to different extents.

In summary, Tfh and B-cell responses to heterologous and homologous vaccination were compared to explore the mechanism of increased antibody responses to heterologous booster doses. This study may provide a reference for optimizing vaccine strategies.

5 Conclusion

In our study, Tfh and B-cell responses in GC after homologous inactivated vaccination and heterologous prime boosting vaccination with adenoviral vaccines were analyzed to investigate how these two strategies regulate antibody responses. The results showed that populations and the helper function of Tfh cells were enhanced with the heterologous strategy. This improvement may be induced by increased gene expression of *Il21, Bcl6* and *Cxcr5* in Tfh cells. In the heterologous group, B cells exhibited more robust activation and a higher ability to produce antibodies, along with increased SHMs in S2- and NTD-specific plasma cells. Additionally, heterologous vaccination led to an expansion of B cell specific to conserved regions in the spike protein. These may contribute to increased antibody titers by a heterologous booster dose.

Data availability statement

The datasets presented in this study can be found in online repositories. The names of the repository/repositories and accession number(s) can be found below: NCBI via accession ID PRJNA1111280.

Ethics statement

The animal study was approved by Institutional Animal Care and Use Committee (IACUC) at the Beijing Institute of Biological Products Co., Ltd. The study was conducted in accordance with the local legislation and institutional requirements.

Author contributions

YaS: Writing – original draft. JW: Writing – original draft. ZY: Writing – original draft. QH: Writing – original draft, Funding acquisition. CB: Writing – original draft. YX: Writing – original draft. YuS: Writing –

original draft. SL: Writing – original draft. YQ: Writing – original draft. HY: Writing – review & editing. CL: Writing – review & editing.

Funding

The author(s) declare financial support was received for the research, authorship, and/or publication of this article. This work was supported by the Non-profit Central Research Institute Fund of Chinese Academy of Medica Sciences (grant number 2023-PT-350-01) and State Key Laboratory of Drug Regulatory Science (grant number 2024SKLDRS0205).

Acknowledgments

We acknowledge the support of the study participants in this study. All vaccines used in this study were also kindly donated by the manufacturers. We thank all these vaccine developers for providing COVID-19 vaccines. We thank the Beijing Institute of Biological Products Co., Ltd. for providing us with the animal experimental facilities.

Conflict of interest

Authors YS and ZY were employed by the company Wuhan Institute of Biological Products Co. Ltd.

The remaining authors declare that the research was conducted in the absence of any commercial or financial relationships that could be construed as a potential conflict of interest.

Publisher's note

Supplementary material

The Supplementary Material for this article can be found online at: https://www.frontiersin.org/articles/10.3389/fimmu.2024.1406138/full#supplementary-material

References

1. Atmar RL, Lyke KE, Deming ME, Jackson LA, Branche AR, El Sahly HM, et al. Homologous and heterologous Covid-19 booster vaccinations. *N Engl J Med*. (2022) 386:NEJMoa2116414. doi: 10.1056/NEJMoa2116414

2. Mallah SI, Alawadhi A, Jawad J, Wasif P, Alsaffar B, Alalawi E, et al. Safety and efficacy of COVID-19 prime-boost vaccinations: Homologous BBIBP-CorV versus heterologous BNT162b2 boosters in BBIBP-CorV-primed individuals. *Vaccine*. (2023) 41:1925–33. doi: 10.1016/j.vaccine.2023.01.032

3. Nordström P, Ballin M, Nordström A. Effectiveness of heterologous ChAdOx1 nCoV-19 and mRNA prime-boost vaccination against symptomatic Covid-19 infection in Sweden: A nationwide cohort study. *Lancet Reg Health Eur*. (2021) 11:100249. doi: 10.1016/j.lanepe.2021.100249

4. Pozzetto B, Legros V, Djebali S, Barateau V, Guibert N, Villard M, et al. Immunogenicity and efficacy of heterologous ChAdOx1-BNT162b2 vaccination. *Nature*. (2021) 600:701–6. doi: 10.1038/s41586-021-04120-y

5. Zhang X, Xia J, Jin L, Wu Y, Zheng X, Cao X, et al. Effectiveness of homologous or heterologous immunization regimens against SARS-CoV-2 after two doses of inactivated COVID-19 vaccine: A systematic review and meta-analysis. *Hum Vaccin Immunother*. (2023) 19:2221146. doi: 10.1080/21645515.2023.2221146

6. Jara A, Undurraga EA, Zubizarreta JR, González C, Pizarro A, Acevedo J, et al. Effectiveness of homologous and heterologous booster doses for an inactivated SARS-CoV-2 vaccine: a large-scale prospective cohort study. *Lancet Global Health*. (2022) 10: e798–806. doi: 10.1016/S2214–109X(22)00112–7

7. Li J-X, Wu S-P, Guo X-L, Tang R, Huang B-Y, Chen X-Q, et al. Safety and immunogenicity of heterologous boost immunisation with an orally administered aerosolised Ad5-nCoV after two-dose priming with an inactivated SARS-CoV-2 vaccine in Chinese adults: a randomised, open-label, single-centre trial. *Lancet Respir Med*. (2022) 10:739–48. doi: 10.1016/S2213-2600(22)00087-X

8. He Q, Mao Q, An C, Zhang J, Gao F, Bian L, et al. Heterologous prime-boost: breaking the protective immune response bottleneck of COVID-19 vaccine candidates. *Emerging Microbes Infections*. (2021) 10:629–37. doi: 10.1080/22221751.2021.1902245

9. Spencer AJ, McKay PF, Belij-Rammerstorfer S, Ulaszewska M, Bissett CD, Hu K, et al. Heterologous vaccination regimens with self-amplifying RNA and adenoviral COVID vaccines induce robust immune responses in mice. *Nat Commun*. (2021) 12:2893. doi: 10.1038/s41467–021-23173–1

10. Hu SL, Abrams K, Barber GN, Moran P, Zarling JM, Langlois AJ, et al. Protection of macaques against SIV infection by subunit vaccines of SIV envelope glycoprotein gp160. *Science*. (1992) 255:456–9. doi: 10.1126/science.1531159

11. Liu Z, Lu L, Jiang S. Application of "B+1" heterologous boosting strategy for preventing infection of SARS-CoV-2 variants with resistance to broad-spectrum coronavirus vaccines. *Emerg Microbes Infect*. (2023) 12:2192817. doi: 10.1080/22221751.2023.2192817

12. He R, Zheng X, Zhang J, Liu B, Wang Q, Wu Q, et al. SARS-CoV-2 spike-specific TFH cells exhibit unique responses in infected and vaccinated individuals. *Signal Transduct Target Ther*. (2023) 8:393. doi: 10.1038/s41392-023-01650-x

13. Zou P, Zhang P, Deng Q, Wang C, Luo S, Zhang L, et al. Two novel adenovirus vectors mediated differential antibody responses via interferon-α and natural killer cells. *Microbiol Spectr*. (2023) 11:e0088023. doi: 10.1128/spectrum.00880–23

14. Gao F-X, Wu R-X, Shen M-Y, Huang J-J, Li T-T, Hu C, et al. Extended SARS-CoV-2 RBD booster vaccination induces humoral and cellular immune tolerance in mice. *iScience*. (2022) 25:105479. doi: 10.1016/j.isci.2022.105479

15. Tani Y, Takita M, Wakui M, Saito H, Nishiuchi T, Zhao T, et al. Five doses of the mRNA vaccination potentially suppress ancestral-strain stimulated SARS-CoV2-specific cellular immunity: a cohort study from the Fukushima vaccination community survey, Japan. *Front Immunol*. (2023) 14:1240425. doi: 10.3389/fimmu.2023.1240425

16. Li X, Zeng F, Yue R, Ma D, Meng Z, Li Q, et al. Heterologous booster immunization based on inactivated SARS-CoV-2 vaccine enhances humoral immunity and promotes BCR repertoire development. *Vaccines*. (2024) 12:120. doi: 10.3390/vaccines12020120

17. Sheikh AA, Groom JR. Transcription tipping points for T follicular helper cell and T-helper 1 cell fate commitment. *Cell Mol Immunol*. (2021) 18:528–38. doi: 10.1038/s41423-020-00554-y

18. Cui D, Tang Y, Jiang Q, Jiang D, Zhang Y, Lv Y, et al. Follicular helper T cells in the immunopathogenesis of SARS-CoV-2 infection. *Front Immunol*. (2021) 12:731100. doi: 10.3389/fimmu.2021.731100

19. Yang H, Xie Y, Lu S, Sun Y, Wang K, Li S, et al. Independent protection and influence of the spike-specific antibody response of SARS-CoV-2 nucleocapsid protein (N) in whole-virion vaccines. *Vaccines (Basel)*. (2023) 11:1681. doi: 10.3390/vaccines11111681

20. Zhang Y, Zeng G, Pan H, Li C, Hu Y, Chu K, et al. Safety, tolerability, and immunogenicity of an inactivated SARS-CoV-2 vaccine in healthy adults aged 18–59 years: a randomised, double-blind, placebo-controlled, phase 1/2 clinical trial. *Lancet Infect Dis*. (2021) 21:181–92. doi: 10.1016/S1473–3099(20)30843–4

21. Wang W, Li Y, Hao J, He Y, Dong X, Fu Y-X, et al. The interaction between lymphoid tissue inducer-like cells and T cells in the mesenteric lymph node restrains intestinal humoral immunity. *Cell Rep*. (2020) 32:107936. doi: 10.1016/j.celrep.2020.107936

22. Song I-W, Nagamani SCS, Nguyen D, Grafe I, Sutton VR, Gannon FH, et al. Targeting TGF-β for treatment of osteogenesis imperfecta. *J Clin Invest*. (2022) 132: e152571. doi: 10.1172/JCI152571

23. Zhao Z, Xu B, Wang S, Zhou M, Huang Y, Guo C, et al. Tfh cells with NLRP3 inflammasome activation are essential for high-affinity antibody generation, germinal

centre formation and autoimmunity. *Ann Rheum Dis*. (2022) 81:1006–12. doi: 10.1136/annrheumdis-2021–221985

24. Coquery CM, Loo WM, Wade NS, Bederman AG, Tung KS, Lewis JE, et al. BAFF regulates T follicular helper cells and affects accumulation and IFNγ production in autoimmunity. *Arthritis Rheumatol*. (2015) 67:773–84. doi: 10.1002/art.38950

25. Nurieva RI, Chung Y, Hwang D, Yang XO, Kang HS, Ma L, et al. Generation of T follicular helper cells is mediated by interleukin-21 but independent of T helper 1, 2, or 17 cell lineages. *Immunity*. (2008) 29:138–49. doi: 10.1016/j.immuni.2008.05.009

26. Zhao H, Yang J, Qian Q, Wu M, Li M, Xu W. Mesenteric CD103+DCs initiate switched coxsackievirus B3 VP1-specific IgA response to intranasal chitosan-DNA vaccine through secreting BAFF/IL-6 and promoting Th17/Tfh differentiation. *Front Immunol*. (2018) 9:2986. doi: 10.3389/fimmu.2018.02986

27. Garg R, Theaker M, Martinez EC, Drunen Little Hurk S. A single intranasal immunization with a subunit vaccine formulation induces higher mucosal IgA production than live respiratory syncytial virus. *Virology*. (2016) 499:288–97. doi: 10.1016/j.virol.2016.09.023

28. Dominguez-Sola D, Kung J, Holmes AB, Wells VA, Mo T, Basso K, et al. The FOXO1 transcription factor instructs the germinal center dark zone program. *Immunity*. (2015) 43:1064–74. doi: 10.1016/j.immuni.2015.10.015

29. Weskamm LM, Dahlke C, Addo MM. Flow cytometric protocol to characterize human memory B cells directed against SARS-CoV-2 spike protein antigens. *STAR Protoc*. (2022) 3:101902. doi: 10.1016/j.xpro.2022.101902

30. Pušnik J, Richter E, Schulte B, Dolscheid-Pommerich R, Bode C, Putensen C, et al. Memory B cells targeting SARS-CoV-2 spike protein and their dependence on CD4+ T cell help. *Cell Rep*. (2021) 35:109320. doi: 10.1016/j.celrep.2021.109320

31. Nuñez G, Hockenbery D, McDonnell TJ, Sorensen CM, Korsmeyer SJ. Bcl-2 maintains B cell memory. *Nature*. (1991) 353:71–3. doi: 10.1038/353071a0

32. Yu S-C, Chen K-C, Huang RY-J. Nodal reactive proliferation of monocytoid B-cells may represent atypical memory B-cells. *J Microbiol Immunol Infect*. (2023) 56:729–38. doi: 10.1016/j.jmii.2023.03.010

33. Ansari A, Sachan S, Jit BP, Sharma A, Coshic P, Sette A, et al. An efficient immunoassay for the B cell help function of SARS-CoV-2-specific memory CD4+ T cells. *Cell Rep Methods*. (2022) 2:100224. doi: 10.1016/j.crmeth.2022.100224

34. Young C, Brink R. The unique biology of germinal center B cells. *Immunity*. (2021) 54:1652–64. doi: 10.1016/j.immuni.2021.07.015

35. Buckner CM, Kardava L, El Merhebi O, Narpala SR, Serebryannyy L, Lin BC, et al. Interval between prior SARS-CoV-2 infection and booster vaccination impacts magnitude and quality of antibody and B cell responses. *Cell*. (2022) 185:4333–46.e14. doi: 10.1016/j.cell.2022.09.032

36. Park S-R. Activation-induced cytidine deaminase in B cell immunity and cancers. *Immune Netw*. (2012) 12:230–9. doi: 10.4110/in.2012.12.6.230

37. Khurana S, Frasca D, Blomberg B, Golding H. AID activity in B cells strongly correlates with polyclonal antibody affinity maturation *in-vivo* following pandemic 2009-H1N1 vaccination in humans. *PloS Pathog*. (2012) 8:e1002920. doi: 10.1371/journal.ppat.1002920

38. Yewdell WT, Kim Y, Chowdhury P, Lau CM, Smolkin RM, Belcheva KT, et al. A hyper-IgM syndrome mutation in activation-induced cytidine deaminase disrupts G-quadruplex binding and genome-wide chromatin localization. *Immunity*. (2020) 53:952–70.e11. doi: 10.1016/j.immuni.2020.10.003

39. Karnowski A, Chevrier S, Belz GT, Mount A, Emslie D, D'Costa K, et al. B and T cells collaborate in antiviral responses via IL-6, IL-21, and transcriptional activator and coactivator, Oct2 and OBF-1. *J Exp Med*. (2012) 209:2049–64. doi: 10.1084/jem.20111504

40. Crotty S. T follicular helper cell biology: A decade of discovery and diseases. *Immunity*. (2019) 50:1132–48. doi: 10.1016/j.immuni.2019.04.011

41. Shlomchik MJ, Weisel F. Germinal center selection and the development of memory B and plasma cells: Germinal center differentiation and selection. *Immunol Rev*. (2012) 247:52–63. doi: 10.1111/j.1600-065X.2012.01124.x

42. Allen CDC, Okada T, Cyster JG. Germinal-center organization and cellular dynamics. *Immunity*. (2007) 27:190–202. doi: 10.1016/j.immuni.2007.07.009

43. Cavazzoni CB, Hanson BL, Podestà MA, Bechu ED, Clement RL, Zhang H, et al. Follicular T cells optimize the germinal center response to SARS-CoV-2 protein vaccination in mice. *Cell Rep*. (2022) 38:110399. doi: 10.1016/j.celrep.2022.110399

44. Kaneko N, Kuo H-H, Boucau J, Farmer JR, Allard-Chamard H, Mahajan VS, et al. Loss of Bcl-6-expressing T follicular helper cells and germinal centers in COVID-19. *Cell*. (2020) 183:143–57.e13. doi: 10.1016/j.cell.2020.08.025

45. Fallet B, Hao Y, Florova M, Cornille K, de Los Aires AV, Girelli Zubani G, et al. Chronic viral infection promotes efficient germinal center B cell responses. *Cell Rep*. (2020) 30:1013–26.e7. doi: 10.1016/j.celrep.2019.12.023

46. Liu D, Yan J, Sun J, Liu B, Ma W, Li Y, et al. BCL6 controls contact-dependent help delivery during follicular T-B cell interactions. *Immunity*. (2021) 54:2245–55.e4. doi: 10.1016/j.immuni.2021.08.003

47. Nutt SL, Hodgkin PD, Tarlinton DM, Corcoran LM. The generation of antibody-secreting plasma cells. *Nat Rev Immunol*. (2015) 15:160–71. doi: 10.1038/nri3795

48. Zhang Y, Garcia-Ibanez L, Ulbricht C, Lok LSC, Pike JA, Mueller-Winkler J, et al. Recycling of memory B cells between germinal center and lymph node subcapsular sinus supports affinity maturation to antigenic drift. *Nat Commun*. (2022) 13:2460. doi: 10.1038/s41467-022-29978-y

49. Viant C, Wirthmiller T, ElTanbouly MA, Chen ST, Cipolla M, Ramos V, et al. Germinal center–dependent and –independent memory B cells produced throughout the immune response. *J Exp Med*. (2021) 218:e20202489. doi: 10.1084/jem.20202489

50. Sprumont A, Rodrigues A, McGowan SJ, Bannard C, Bannard O. Germinal centers output clonally diverse plasma cell populations expressing high- and low-affinity antibodies. *Cell*. (2023) 186:5486–99.e13. doi: 10.1016/j.cell.2023.10.022

51. Chi X, Yan R, Zhang J, Zhang G, Zhang Y, Hao M, et al. A neutralizing human antibody binds to the N-terminal domain of the Spike protein of SARS-CoV-2. *Science*. (2020) 369:650–5. doi: 10.1126/science.abc6952

52. Ai J, Guo J, Zhang H, Zhang Y, Yang H, Lin K, et al. Cellular basis of enhanced humoral immunity to SARS-CoV-2 upon homologous or heterologous booster vaccination analyzed by single-cell immune profiling. *Cell Discovery*. (2022) 8:114. doi: 10.1038/s41421–022-00480–5

53. Sander S, Chu VT, Yasuda T, Franklin A, Graf R, Calado DP, et al. PI3 kinase and FOXO1 transcription factor activity differentially control B cells in the germinal center light and dark zones. *Immunity*. (2015) 43:1075–86. doi: 10.1016/j.immuni.2015.10.021

54. Xie X, Gan T, Rao B, Zhang W, Panchakshari RA, Yang D, et al. C-terminal deletion-induced condensation sequesters AID from IgH targets in immunodeficiency. *EMBO J*. (2022) 41:e109324. doi: 10.15252/embj.2021109324

55. Delgado P, Álvarez-Prado ÁF, Marina-Zárate E, Sernandez IV, Mur SM, de la Barrera J, et al. Interplay between UNG and AID governs intratumoral heterogeneity in mature B cell lymphoma. *PloS Genet*. (2020) 16:e1008960. doi: 10.1371/journal.pgen.1008960

56. Yu K. AID function in somatic hypermutation and class switch recombination. *Acta Biochim Biophys Sin (Shanghai)*. (2022) 54:759–66. doi: 10.3724/abbs.2022070

57. Hajizadeh F, Khanizadeh S, Khodadadi H, Mokhayeri Y, Ajorloo M, Malekshahi A, et al. SARS-COV-2 RBD (Receptor binding domain) mutations and variants (A sectional-analytical study). *Microbial Pathogenesis*. (2022) 168:105595. doi: 10.1016/j.micpath.2022.105595

58. Kim K-H, Bhatnagar N, Jeeva S, Oh J, Park BR, Shin CH, et al. Immunogenicity and neutralizing activity comparison of SARS-CoV-2 spike full-length and subunit domain proteins in young adult and old-aged mice. *Vaccines*. (2021) 9:316. doi: 10.3390/vaccines9040316

59. Wang J, Deng C, Liu M, Liu Y, Li L, Huang Z, et al. A fourth dose of the inactivated SARS-CoV-2 vaccine redistributes humoral immunity to the N-terminal domain. *Nat Commun*. (2022) 13:6866. doi: 10.1038/s41467–022-34633–7

60. Di Paolo NC, Miao EA, Iwakura Y, Murali-Krishna K, Aderem A, Flavell RA, et al. Virus binding to a plasma membrane receptor triggers interleukin-1 alpha-mediated proinflammatory macrophage response in *vivo*. *Immunity*. (2009) 31:110–21. doi: 10.1016/j.immuni.2009.04.015

61. Teijaro JR, Farber DL. COVID-19 vaccines: modes of immune activation and future challenges. *Nat Rev Immunol*. (2021) 21:195–7. doi: 10.1038/s41577-021-00526-x

62. Sprent J, King C. COVID-19 vaccine side effects: The positives about feeling bad. *Sci Immunol*. (2021) 6:eabj9256. doi: 10.1126/sciimmunol.abj9256

63. Mettelman RC, Allen EK, Thomas PG. Mucosal immune responses to infection and vaccination in the respiratory tract. *Immunity*. (2022) 55:749–80. doi: 10.1016/j.immuni.2022.04.013

64. Strawbridge AB, Blum JS. Autophagy in MHC class II antigen processing. *Curr Opin Immunol*. (2007) 19:87–92. doi: 10.1016/j.coi.2006.11.009

65. English L, Chemali M, Duron J, Rondeau C, Laplante A, Gingras D, et al. Autophagy enhances the presentation of endogenous viral antigens on MHC class I molecules during HSV-1 infection. *Nat Immunol*. (2009) 10:480–7. doi: 10.1038/ni.1720

frontiers | Frontiers in Immunology

TYPE Original Research
PUBLISHED 10 July 2024
DOI 10.3389/fimmu.2024.1428711

OPEN ACCESS

EDITED BY
Cordelia Dunai,
University of Liverpool, United Kingdom

REVIEWED BY
Nicolas Tchitchek,
Sorbonne Universités, France
Ebony Gary,
Wistar Institute, United States

*CORRESPONDENCE
Lark L. Coffey
lcoffey@ucdavis.edu

RECEIVED 06 May 2024
ACCEPTED 25 June 2024
PUBLISHED 10 July 2024

CITATION
Liu H, Brostoff T, Ramirez A, Wong T, Rowland DJ, Heffner M, Flores A, Willis B, Evans JJ, Lanoue L, Lloyd KCK and Coffey LL (2024) Establishment and characterization of an h*ACE2*/hTMPRSS2 knock-in mouse model to study SARS-CoV-2.
Front. Immunol. 15:1428711.
doi: 10.3389/fimmu.2024.1428711

Establishment and characterization of an h*ACE2*/ hTMPRSS2 knock-in mouse model to study SARS-CoV-2

Hongwei Liu[1], Terza Brostoff[1], Ana Ramirez[1], Talia Wong[1], Douglas J. Rowland[2], Mollie Heffner[3], Arturo Flores[1], Brandon Willis[3], Jeffrey J. Evans[3], Louise Lanoue[3], K. C. Kent Lloyd[3,4] and Lark L. Coffey[1*]

[1]Department of Pathology, Microbiology, and Immunology, School of Veterinary Medicine, University of California, Davis, CA, United States, [2]Center for Molecular and Genomic Imaging, College of Engineering, University of California, Davis, Davis, CA, United States, [3]Mouse Biology Program, University of California, Davis, Davis, CA, United States, [4]Department of Surgery, School of Medicine, University of California, Davis, Davis, CA, United States

Despite a substantial body of research, we lack fundamental understanding of the pathophysiology of COVID-19 caused by severe acute respiratory syndrome coronavirus 2 (SARS-CoV-2) including pulmonary and cardiovascular outcomes, in part due to limitations of murine models. Most models use transgenic mice (K18) that express the human (h) angiotensin converting enzyme 2 (*ACE2*), *ACE2* knock-in (KI) mice, or mouse-adapted strains of SARS-CoV-2. Further, many SARS-CoV-2 variants produce fatal neurologic disease in K18 mice and most murine studies focus only on acute disease in the first 14 days post inoculation (dpi). To better enable understanding of both acute (<14 dpi) and post-acute (>14 dpi) infection phases, we describe the development and characterization of a novel non-lethal KI mouse that expresses both the *ACE2* and transmembrane serine protease 2 (*TMPRSS2*) genes (h*ACE2*/h*TMPRSS2*). The human genes were engineered to replace the orthologous mouse gene loci but remain under control of their respective murine promoters, resulting in expression of *ACE2* and *TMPRSS2* instead of their murine counterparts. After intranasal inoculation with an omicron strain of SARS-CoV-2, h*ACE2*/h*TMPRSS2* KI mice transiently lost weight but recovered by 7 dpi. Infectious SARS-CoV-2 was detected in nasopharyngeal swabs 1-2 dpi and in lung tissues 2-6 dpi, peaking 4 dpi. These outcomes were similar to those in K18 mice that were inoculated in parallel. To determine the extent to which h*ACE2*/h*TMPRSS2* KI mice are suitable to model pulmonary and cardiovascular outcomes, physiological assessments measuring locomotion, behavior and reflexes, biomonitoring to measure cardiac activity and respiration, and micro computed tomography to assess lung function were conducted frequently to 6 months post inoculation. Male but not female SARS-CoV-2 inoculated h*ACE2*/h*TMPRSS2* KI mice showed a transient reduction in locomotion compared to control saline treated mice. No significant changes in respiration, oxygen saturation, heart rate variability, or conductivity were detected in SARS-CoV-2 inoculated mice of either sex. When re-inoculated

6 months after the first inoculation, h*ACE2*/h*TMPRSS2* KI became re-infected with disease signs similar to after the first inoculation. Together these data show that a newly generated h*ACE2*/h*TMPRSS2* KI mouse can be used to study mild COVID-19.

KEYWORDS

SARS-CoV-2, mouse ACE2, mouse TMPRSS2, knock-in mouse, COVID-19, virus, pathogenesis, pulmonary function

1 Introduction

The coronavirus disease 2019 (COVID-19) pandemic caused by severe acute respiratory syndrome coronavirus 2 (SARS-CoV-2) continues to cause a massive global burden with excess mortality and disruptions to social, economic, and healthcare systems. COVID-19 produces diverse manifestations that can affect respiratory, cardiovascular, neurological, immunological, and gastrointestinal systems (reviewed in (1, 2)). Many infected people report shortness of breath, fatigue, and exercise intolerance (1, 2) which are likely due to cardiovascular and pulmonary involvement. After SARS-CoV-2 infects the respiratory tract, inflammation can lead to irreversible pulmonary fibrosis and bronchiectasis that ultimately compromise respiratory function (3–8). Chest pain, dyspnea and heart palpitations, as well as more severe cardiovascular disease may result in inflammation, myocardial infarction, and other cardiac manifestations (reviewed in (2)). The underlying pathophysiological mechanisms for both respiratory and cardiovascular COVID-19 manifestations are still poorly understood. This lack of understanding in part stems from limitations inherent to human studies, where invasive assessments, repeated sampling, and human tissues are often not available. To circumvent these limitations, animal models of COVID-19 represent a valuable complement to information learned from human studies.

Animal models have been extensively used to study pathogenesis of acute SARS-CoV-2 infection and for evaluating COVID-19 countermeasures including vaccines and therapeutics (reviewed in (9)). Syrian hamsters typically recover from weight loss and interstitial pneumonia after SARS-CoV-2 infection, but are not widely used because of their size, aggressiveness, cost to maintain, and unfamiliar biology and husbandry requirements (9–12). Mice are especially valuable as COVID-19 models due to their rapid breeding, gestation, growth rates, highly characterized immune systems, and ease of genetic manipulation. Common murine models of acute COVID-19 include wildtype mice inoculated with serial mouse passaged SARS-CoV-2, engineered mice that express the human angiotensin converting enzyme 2 (*ACE2*) receptor under control of the cytokeratin-18 (Krt18 (K18)) promoter for epithelial cell expression, or mice that transiently express *ACE2* via adenovirus or adeno-associated virus (AAV) expression systems (reviewed in (9)). Depending on the murine model, virus variant, and dose employed, SARS-CoV-2 inoculated mice variously develop weight loss, detectable viral RNA and infectious virus in the respiratory tract, lung inflammation and injury, and death. Some models also show extrapulmonary SARS-CoV-2 detection in selected tissues including the brain which corresponds with neurologic signs of disease, likely due to non-physiological expression of h*ACE2* in the brain. While these models collectively serve as an extremely valuable resource for development of therapies and prophylactic measures, further improvements to murine models can enable understanding of the pathophysiological consequences of acute infection relevant to humans. Further, most experimental endpoints for murine studies using extant models do not exceed 2 weeks, which occurs before the onset of long COVID-19.

To model human expression of *ACE2* and thereby avoid neuroinvasive SARS-CoV-2 and neurologic or lethal disease characteristic of pre-omicron variants in the K18 model, we sought to develop a new mouse model. We reasoned that mice expressing human orthologous genes known to be involved in virus binding, entry, and activation similar to those in humans would better represent COVID-19. Our approach involves incorporating the human coding sequence directly into the endogenous mouse locus, thus replacing the orthologous mouse genes while recapitulating the expression level, pattern, and timing of the human gene under the control of specific neighboring gene regulators. This dual humanized (h) knockin/mouse knockout approach overcomes inherent genetic discrepancies between mouse and human genes, is highly relevant to human biology and disease compared to random genomic integration of multiple copies of coding sequence as seen in transgenic mice and can be used to generate murine models that are more efficiently managed and more cost effective than hamsters. Our approach is also predicated on the success of related *ACE2* knock-in (KI) models (13–16) in which the *Ace2* gene was substituted with *ACE2*. For example, in Winkler et al. (14), h*ACE2* KI mice express *ACE2* in lung, nasal turbinate, kidney, duodenum, and olfactory bulb, but not in colon, ileum, heart, spleen, or liver. After challenge with an early 2020 SARS-CoV-2 strain, viral infection was mainly restricted to the murine respiratory tract but not extrapulmonary tissues (including brain), implying an absence of *ACE2* expression in the brain (which

was not shown). Mice experienced no weight loss and limited histopathologic changes in the lung 3 days post-inoculation (dpi). These data demonstrate susceptibility of *hACE2* KI mice to SARS-CoV-2. Building on these established *hACE2* KI models, we also predicted that expression of an additional human gene involved in SARS-CoV-2 infection may more closely recapitulate human COVID-19. We therefore generated KI mice expressing both *ACE2* and human transmembrane serine protease 2 (*TMPRSS2*), where *TMPRSS2* encodes a protease that cleaves the SARS-CoV-2 spike protein after binding to *ACE2* to facilitate virus invasion and activation (17). After generating and validating expression of the human genes in these novel h*ACE2*/h*TMPRSS2* KI mice, we characterized acute SARS-CoV-2 infection dynamics and long-term changes in physiology, behavior, cardiac and respiratory activity, and lung function to evaluate suitability of the model for COVID-19. Our data show that h*ACE2*/h*TMPRSS2* KI survive SARS-CoV-2 infection, and male but not female mice develop transient reductions in locomotion like COVID-19 affected humans. New polygenic humanized models like the h*ACE2*/h*TMPRSS2* KI mouse developed here can provide new knowledge regarding SARS-CoV-2 infection and COVID-19 in humans and enable experiments to observe, monitor, and assess COVID-19 outcomes with current and emerging variants.

2 Materials and methods

2.1 Ethics statement

All mouse work was conducted on protocol #23489 approved by the institutional animal care and use committee (IACUC) at the University of California, Davis. Infectious virus was handled in certified animal biosafety level 3 laboratory (ABSL-3) spaces in compliance with approved institutional biological use authorization #R2813. The University of California, Davis, is accredited by the Association for Assessment and Accreditation of Laboratory Animal Care (AAALAC). All mouse work adhered to the NIH Guide for the Care and Use of Laboratory Animals.

2.2 Generation of humanized *ACE2*, *TMPRSS2*, and *ACE2/TMPRSS2* knock in mice

Human *ACE2* and *TMPRSS2* KI alleles were designed to replace expression of the endogenous mouse *Ace2* and *Tmprss2* genes with the corresponding full length human coding sequence (CDS) under transcriptional control by mouse regulatory elements. CRISPR Cas9 was used to target murine embryonic stem (ES) cells using a single guide RNA (gRNA) complexed with Cas9 nuclease as a ribonucleic protein (RNP) in the presence of a plasmid repair template harboring the coding sequence for both h*ACE2* and h*TMPRSS2* and mouse 3' untranslated region (UTR) flanked by 1 kilobase (kb) homology arms. Guide RNAs were screened with an established approach (18) and selected using the publicly available tool http://crispor.tefor.net/crispor.py.

TMPRSS2 plasmid repair template was synthesized as a gene product (IDT, Coralville, IA) and *ACE2* was constructed using Gibson assembly with synthesized G-block fragments (19). Once genetically verified by sequencing, plasmids were propagated and purified using an EndoFree Plasmid Maxi Kit following manufacturer's instruction (Qiagen, Germantown, MD) and subsequently validated by restriction fragment analysis followed by full sequencing of critical regions. RNP assembly included pairing of trans-acting CRISPR RNA (tracrRNA) with CRISPR RNA (crRNA) with a 2 minute denaturation at 95°C followed by room temperature incubation for 5 minutes to produce the guide RNA (gRNA) and then complexed with s.p. Cas9 Nuclease V3 for 10 minutes at 37°C at a 1.2:1 molar ratio (IDT). Constructed circular repair template plasmids along with a PGK-neomycin containing plasmid PGKneoF2L2DTA (Addgene, Watertown, MA, #13445) for transient selection were added for a final concentration of 2.4ug/uL RNP, 0.4ug/uL repair template plasmid, and 0.2ug/uL of neomycin plasmid. CRISPR targeting reagents were electroporated into JM8A3 C57BL/6N Agouti ES cells (20) on a BTX ECM 630 Pulse Generator set at 700V, 400Ω, 25μF and selected for 2 to 3 days with 400 ug/uL G418 following standard culture protocols (21). Individual ES cell colonies were picked and submitted for genetic analysis with KI copy number, 5' and 3' long range PCR, sequence confirmation, and pathogen free status confirmed prior to blastocyst injection. Genetically confirmed clones containing a single copy of the expected KI alleles were expanded for injection into C57BL/6N blastocysts to obtain high percentage chimeric F0 mice. Genetically-confirmed chimeras were backcrossed to C57BL/6N to produce first generation N1 progeny which were genetically screened by PCR for germline transmission of the KI allele (20). PCR positive N1 animals were then verified for correct targeting and copy number of the allele (Supplementary Figure S1). h*ACE2* and h*TMPRSS2* KI mice were then intercrossed to create a true breeding bi-genic h*ACE2*/h*TMPRSS2* KI line for propagation and experimental virus inoculation and analyses.

2.3 Characterization of gene expression in *hACE2/hTMPRSS2* knock-in mice

Approximately 10 mg of lung, upper respiratory tract (URT), brain, and lower intestine were collected from 2 females and 2 males of h*ACE2*/h*TMPRSS2* KI, as well as age- and sex- matched control (Wildtype) mice. Tissues were placed into RNAlater and stored at 4°C overnight. RNA was subsequently extracted using the RNeasy Mini Kit with on column DNase treatment following manufactures protocol (Qiagen). Purified RNA was analyzed by NanoDrop for concentration and purity and visualized on an agarose gel for confirmation of integrity. Each RNA sample was normalized for concentration and then converted to cDNA using the High-Capacity cDNA Reverse Transcription Kit according to the manufacturer's protocol (ThermoFisher). cDNA samples were processed in triplicate using the TaqMan™ Gene Expression Master Mix (ThermoFisher) for each target with sequence specific oligos (Supplementary Table 1) and multiplexed with a stable housekeeping gene (*Actb*) using TaqMan assays with 6FAM

reporter per target and VIC reporter for endogenous reference (IDT, ThermoFisher). 384 well plates were processed on a QuantStudio7 and analyzed with QuantStudio™ software using the relative Ct method (ΔΔCt) (22). Data shown represent values measured from all animals.

2.4 K18 human ACE2 transgenic mice

Transgenic mice (B6.Cg-Tg(K18-ACE2)2Prlmn/J; RRID : IMSR_JAX:034860) expressing the human ACE2 gene (K18) were obtained from The Jackson Laboratory (Strain #034860, Bar Harbor, ME) and maintained under identical vivarium conditions as h*ACE2*/h*TMPRSS2* KI mice.

2.5 Cell lines, SARS-CoV-2 isolates, and heat inactivation of SARS-CoV-2

African Green monkey kidney epithelial cells (Vero-E6, NR-53728), Vero E6 expressing *ACE2* and *TMPRSS2* (Vero-E6-TMPRSS2-T2A-ACE2, NR-54970) for culturing omicron, and Vero CCL-81 were obtained from ATCC/BEI (Manassas, VA). Vero-E6 and Vero CCL-81 cells were cultured at 37°C with 5% CO_2 in Dulbecco's modified Eagle medium (DMEM; Gibco, ThermoFisher Scientific, Emeryville, CA) supplemented with 5% fetal bovine serum (FBS; Genesee Scientific, San Diego, CA) and 1x antibiotic-antimycotic (Fisher Scientific, Waltham, MA). Vero-E6-TMPRSS2-T2A-ACE2 cells were cultured under the same conditions as the other Vero cell lines with the addition of 10 µg per mL puromycin (Fisher Scientific, Waltham, MA). SARS-CoV-2 strains were propagated one additional time after procurement in Vero CCL-81 cells to achieve titers of 6-7 $\log_{10}$ Vero plaque forming units (PFU)/mL, respectively. Single use virus aliquots were stored at -80°C until thaw for use in murine experiments. For studies with heat inactivated SARS-CoV-2, 5 $\log_{10}$ PFU of SARS-CoV-2 B.1.1.529 (omicron) diluted in Dulbecco's phosphate buffered saline (DPBS) was split into 2 tubes, one of which was subjected to heat treatment in a water bath at 56°C for 30 minutes. The other tube was held at 4°C during heat inactivation. The absence of detectable infectivity in the heat inactivated tube was verified by titration. Both tubes were used for inoculation into mice.

2.6 SARS-CoV-2 mouse inoculation and re-inoculation

h*ACE2*/h*TMPRSS2* KI mice aged 12 weeks and 7-12 week old K18 mice of both sexes were weighed and anesthetized with isoflurane, then inoculated intranasally (i.n.) via hanging drop over both nares with 30 µl DPBS, 5 $\log_{10}$ PFU of SARS-CoV-2 B.1.1.529 (omicron) diluted in DPBS, or 5 $\log_{10}$ PFU of heat inactivated SARS-CoV-2 B.1.1.59 diluted in DPBS. Before settling on omicron, we inoculated 4 $\log_{10}$ PFU of different strains (Table 1) of SARS-CoV-2 into K18 mice. These included B.1, alpha, beta, delta, and 2 doses (4 $\log_{10}$ and 5 $\log_{10}$ PFU) of the omicron B.1.1.529 strain. To evaluate susceptibility and disease signs after a second infection, a subset of h*ACE2*/h*TMPRSS2* KI mice of both sexes that had been inoculated first at 12 weeks of age with 5 $\log_{10}$ PFU omicron were re-inoculated 182 days (6 months) later, at 38 weeks of age, with 5 $\log_{10}$ PFU of the same omicron strain. Inocula were back-titrated to confirm the target dose. Mice were monitored once daily for changes in weight, ruffled fur, ataxia, and labored breathing for up to 15 days. On days 1 and 2 post-inoculation (dpi), mice were anesthetized with isoflurane and oropharyngeal samples were obtained by swabbing with rayon-tipped swabs (Puritan, Fisher

TABLE 1 SARS-CoV-2 strains used in mouse experiments.

Strain	Variant	Lineage	Location of Provider	Source	Passage	Viral titer Vero PFU/ml
hu/USA/CA-CZB-59X002/2020. (MT394529)	WA1-like	B.1	CA, USA	UC Davis Center for Immunology and Infectious Diseases	p2	$2.2x10^7$
hu/USA/CA_CDC_5574/2020	Alpha	B.1.1.7	CA, USA (UK origin)	BEI, NR-54011, batch: 70041598	p1	$7.7x10^6$
hCoV-19/USA/MD-HP01542/2021	Beta	B.1.351	USA (African origin)	BEI, NR-55282, batch: 70043066	p1	$2x10^7$
hCoV-19/USA/PHC658/2021	Delta	B.1.617.2	USA (India origin)	BEI, NR-55611, batch: 70045238	p1	$1.1x10^7$
hCoV-19/USA/HI-CDC-4359259-001/2021	Omicron	B.1.1.529	USA	BEI, NR-56475, Batch: 70049691	p1	$2.1x10^7$
hCoV-19/USA/MD-HP40900/2022 (XBB.1.5),	Omicron	XBB.1.5	USA	BEI, NR-59104, batch: 70057837	p1	$7.2x10^7$

Scientific, Fisher Scientific, Waltham, MA). Swabs were vortexed briefly in 500 µL of DMEM containing 1% FBS and frozen at -80°C. A subset of mice were euthanized on 2, 4, or 6 dpi and the remaining animals were euthanized at experiment end. At 17, 67, or 199 dpi or prior to euthanasia, blood was collected by submandibular vein puncture under isoflurane anesthesia. Whole blood was clotted for >10 minutes at room temperature then centrifuged for 5 minutes at 8,000 x g and cleared serum was stored at -80°C. Mice were euthanized by isoflurane overdose and cervical dislocation then perfused with sterile DPBS. The right inferior lung lobe and the left hemisphere of the brain were weighed and homogenized in 500 µL DMEM with a sterile glass bead at 30 Hz for 4 minutes using a TissueLyser (Qiagen, Germantown, MD). Homogenates were cleared by centrifugation at 10,000 x *g* for 4 minutes and the cleared fraction was stored at -80°C.

2.7 SARS-CoV-2 titrations

Fluid collected from oropharyngeal swabs, residual inocula, and lung and brain homogenates were thawed and assayed to quantify infectious SARS-CoV-2. Undiluted (125 µl) and serial 10-fold diluted samples in DMEM with 1% FBS were inoculated into confluent Vero-E6 or Vero-E6-TMPRSS2-T2A-ACE2 (used for omicron only) cells in 12-well plates with cell culture media decanted. Cells were incubated for 1 hour at 5% CO_2 in a humidified 37°C chamber. After the incubation, cell monolayers were overlaid with 0.5% agarose dissolved in DMEM with 5% FBS and 1x antibiotic-antimycotic and held for 2 (for omicron only) or 3 (all other viruses) days at 5% CO_2 and 37°C in a humidified incubator. After 2 or 3 days, cells were fixed for >30 minutes with 4% formaldehyde then agarose plugs were removed. Cells were stained with 0.05% crystal violet in 20% ethanol for 10 minutes then rinsed 3 times with water. Plates were inverted to dry completely and the number of plaques in each well was counted. Viral titers were recorded as the reciprocal of the highest dilution where plaques were noted and are represented as PFU per mL inoculum, swab, or mg of tissue. Each value reported represents a titer calculated from 1 replicate titration of serial dilutions. The lower limit of detection (LOD) of the assay was 8 PFU/ml. Samples with no detectable plaques are reported at the LOD.

2.8 Neutralizing antibody assessments

For plaque reduction neutralization test 50% ($PRNT_{50}$) to quantify neutralizing antibody titers, serum from blood collected on 17, 67 or 199 dpi (where the last time is 18 days after the second inoculation) was thawed at 37°C and 40 µL was heated to 56°C in a water bath for 30 minutes to inactivate complement proteins. Serum was diluted 5-fold in PBS and 1% FBS, then samples were serially 2-fold diluted 10 times for a dynamic range of 1:5 to 1:2560. An equal volume of virus diluent containing 80 PFU of SARS-CoV-2 homologous to the inoculum strain was added to each antibody dilution and a no-antibody control consisting of virus diluent only, resulting in a final dynamic range of 1:10 to 1:5126. Antibody-virus dilution series were incubated for 1 hour at 37°C after which they were applied to confluent Vero-E6 cells in single replicates and incubated for 1 hour at 5% CO_2 and 37°C in a humidified incubator. Cells were overlaid, incubated, fixed, and stained as described above for plaque assays. The neutralization titer was defined as the reciprocal of the dilution for which fewer than 50% of plaques were detected versus the no-antibody control (>50% neutralization). Each value reported represents a titer calculated from 1 replicate $PRNT_{50}$ assay.

2.9 Behavioral, respiratory, and cardiac assessments

Mice inoculated with SARS-CoV-2 or DPBS were assessed for locomotion, behavior, reflexes, cardiac activity, respiration, and lung morphology and function 5 days prior to inoculation and again 3 or 4, 15 or 16, and 30 or 31 dpi, then monthly thereafter within a 2 day window ending on 150 or 151 dpi. Phenotyping was performed on consecutive days, where the order, time of day, environment, and experimenters throughout the testing period were consistent. Experimenters were not blinded to SARS-CoV-2 or DPBS treatment for biosafety reasons, although all mice were housed in the ABSL-3 and handled identically. Assessments of morphology and gross motor and sensory functions were performed using a modified SmithKline Beecham, Harwell, Imperial College, Royal London Hospital, phenotype assessment (SHIRPA) primary screen test that includes a battery of observational measures of behaviors and functional assessments, implemented according to an International Mouse Phenotyping Consortium protocol (23). After a 15 minute acclimation period to testing room environmental conditions, mice were placed in a viewing jar to observe general appearance (e.g., coat, whiskers, teeth, and eyes), and behaviors (e.g., body position, tremor, head bobbing). Afterwards, mice were placed into an arena from a height of approximately 30 cm to assess transfer arousal, locomotor activity, gait, tail elevation, touch escape and startle response. Transfer arousal was measured as the delay (in seconds) before the mouse began to explore the arena. Locomotor activity was measured by tallying the number of squares crossed by the mouse in the first 30 seconds. Gait and tail elevation were observed during ambulation of the mouse in the arena. Touch escape was evaluated by the fleet response to an extended index finger; mouse should flee prior physical contact. Startle was evaluated using a click box activated behind the mouse. Finally, mice were manipulated to evaluate positional passivity, trunk curl, limb grasping, and contact righting reflex, and given a complete physical exam. Mice were placed in either a viewing jar or a larger arena. Observations included muscle, cerebellar, sensory, and autonomic functions as well as morphology. Overall, more than 40 specific behaviors and morphological parameters were assessed by observation and scored as present/absent or as expected/abnormal. Cardiac electrophysiology was evaluated by electrocardiogram (ECG) on anesthetized mice. Mice were anesthetized with 5% isoflurane and transferred to a warm

rodent surgical monitor platform (Scintica, London, Canada) in a prone position with a nose cone set a 2.5% isoflurane and a rectal probe to monitor body temperature. Hindlimb feet were secured to surface electrodes on the platform and ECG signals were recorded for 2 minutes. A section of the ECG tracing was selected and analyzed using the LabScribe software (iWorx, Dover, NH). P, Q, R, S and T peaks in ECG were automatically detected by the software and peak intervals and amplitudes were averaged over several cardiac cycles. Heart rate and heart rate variability were averaged over the entire length of the ECG tracing. Respiration rates and arterial blood oxygen saturation were recorded over 2 minutes using a pulse oximeter sensor (Scintica) secured to the right leg of mice and are reported as the mean from all mice in the cohort. All cardiorespiratory parameters were analyzed, and respiration rates (respiration per minute, rpm), QT interval corrected for heart rate (QTc) and heart rate variability (dRR) are reported herein. Data are boxplots with means and standard deviation, where each dot shows data from 1 measurement from 1 mouse.

2.10 Micro computed tomography and lung function assessments

Respiratory gated lung imaging by micro (μ)CT was performed under inhalation anesthesia. Male and female mice that were SARS-CoV-2 or DPBS inoculated were anesthetized with 5% isoflurane and transferred to a μCT imager. To maintain primary biosafety containment of animals upon transfer to the μCT, a custom imaging chamber was designed and built (UC Davis TEAM Facility) to provide HEPA air filtration of delivered anesthetic gas during imaging. Animals were maintained on 1-1.5% isoflurane during imaging with the Quantum GX2 μCT (Revvity, Waltham, MA). Images were acquired in respiratory gating mode using a Cu/Al filter, 90 kV, and 88 μA. Images were reconstructed into end inspiration and end expiration volumes at 72 micrometer voxel size. Imaging was performed multiple times on each mouse at -6, 5, 17, 33, 58, 94, 128 and 158 dpi. For the re-inoculation study, mice were imaged 6 days before and 5 and 17 days after the second inoculation. Pulmonary changes consistent with SARS-CoV-2 infection were evaluated by visual inspection and by segmenting aerated lung tissue. Whole lung segmentation was performed using a Sensor 3D deep learning model (24). The model was trained on an AMD Ryzen Threadripper Pro 3955WX workstation with a GeForce RTX 3090 Ti graphics card. The model was implemented in Dragonfly 2022.2 and had 15 time distributed convolutions (activation function = Conv2D), four time-distributed max pooling, and 2 bidirectional convolution long-short term memory steps. The model was trained with a patch size of 64, stride ratio 0.5, batch size 32, a loss function looking at the categorical cross entropy, and optimized with the Adadelta function with a linear learning rate set to 1. Data augmentation x10 was implemented with flip, rotation, scaling, brightness and gaussian noise. An image mask (347 x 347 x 277) was applied to 6 training sets (3 end inspiration and 3 end expiration scans) to minimize training time, which took approximately 82 hours. The model was applied to 6 additional test datasets. The model computation time for additional scans is under 2 minutes and requires minimal processing. The segmented lung was further split into aerated lung and connective/vessel tissues by Otsu's method (25).

2.11 Histopathologic assessments

For necropsy, a lungs from 4 SARS-CoV-2 and 4 DPBS-inoculated h*ACE2*/h*TMPRSS2* KI and K18 mice were inflated with 10% buffered formalin (Fisher Scientific, Waltham, MA) followed by fixation for 48 hours at room temperature in an approximate 10-fold volume of formalin. Lungs were then embedded in paraffin, thin-sectioned, and stained with hematoxylin and eosin (H&E). H&E-stained slides were scanned by a whole-slide image technique using an Aperio slide scanner (Leica, Buffalo Grove, IL) with a resolution of 0.24 μm/pixel. Image files were uploaded on a Leica hosted web-based site and a board certified veterinary anatomic pathologist without knowledge of treatment conditions evaluated sections for SARS-CoV-2 induced histologic lesions. A first round of scoring was conducted while the pathologist was masked to phenotype, and a second round was conducted after unmasking to allow comparison between DPBS- and SARS-CoV-2 inoculated mice, as well as between *hACE2/TMPRSS2* KI and K18 mice. The histopathologic grading scheme was developed with the goal of establishing a comprehensive scoring rubric that could accurately and reproducibly characterize the severity of pulmonary lesions specific to SARS-CoV-2. Each lung was scored using a rubric we previously described (26). Scores reported are a single composite measurement from evaluation of the entire lung for each mouse. Scores range from 0 (no significant findings) to 4 (severe lesions involving >25% of the pulmonary parenchyma), with an additional point possible for >25% neutrophilic inflammation, necrotizing vasculitis, and/or microthrombi.

2.12 Statistical analyses

Statistical assessments for were performed using SAS (SAS, version 9.4, SAS Institute, Cary, NC) or GraphPad Prism version 10 (Boston, MA). Repeated measures two-way ANOVA tests were performed on $\log_{10}$ transformed SARS-CoV2 titers and multiple comparisons were computed according to Tukey method. Main effect two-way ANOVA tests were performed on mouse weights normalized to 0 day values at the time of virus inoculation and on $\log_{10}$ transformed viral titers in tissues and multiple comparisons were computed with Tukey's method. Differences in locomotion and lung function parameters in males or females over time were analyzed using a 2-way analysis of variance (ANOVA) with time, treatment and the interaction of time and treatment as main effects. Differences in respiration, heart rates and ECG markers over time and across the SARS-CoV-2 or DPBS inoculated h*ACE2*/h*TMPRSS2* KI mice were analyzed by analysis of variance using a linear mixed model for each sex. Histopathologic lung scores were compared using two-way ANOVA with multiple comparisons.

3 Results

3.1 Generation of and characterization of gene expression in h*ACE2*/h*TMPRSS2* knock-in mice

ACE2 and *TMPRSS2* expression were measured in tissues collected from h*ACE2*/h*TMPRSS2* KI mice and compared to levels in tissues harvested from control Wildtype mice (Figure 1A). *ACE2* transcript expression, represented as $\log^2$ of $2^{-(\Delta\Delta Ct)}$ above Wildtype background, was detected in lung, upper respiratory tract (URT), brain, and intestine of h*ACE2*/h*TMPRSS2* KI mice, but not in Wildtype mice (Figure 1B). Similarly, *TMPRSS2* transcript was detected in all tissues tested in h*ACE2*/h*TMPRSS2* KI mice but not in Wildtype mice. As expected, neither *Ace2* (Figure 1B) or *Tmprss2* (Figure 1D) orthologs were expressed in h*ACE2*/h*TMPRSS2* KI mice, confirming that genomic insertion of *ACE2* and *TMPRSS2* coding sequences into the cognate mouse loci effectively interrupted and blocked expression of the corresponding mouse gene orthologs. To further assess relative expression of human and mouse genes, *ACE2* and *TMPRSS2* ΔCt in h*ACE2*/h*TMPRSS2* KI mice were compared to *Ace2* and *Tmprss2* ΔCt in Wildtype mice, respectively. There was no statistically significant difference in levels of expression between *ACE2* and *Ace2* in lung, URT, or brain, although *ACE2* expression was significantly less than *Ace2* in the intestine (Figure 1C). Similarly, there was no statistically significant difference in level of expression between *TMPRSS2* and *Tmprss2* in lung, URT, or lower intestine, although *TMPRSS2* expression was significantly higher than *Tmprss2* in brain (Figure 1E).

3.2 SARS-CoV-2 kinetics and tropism in knock-in mice

To understand SARS-CoV-2 infection and tropism in the KI mice, twelve-week-old male and female h*ACE2*/h*TMPRSS2* KI were inoculated intranasally (i.n.) with DPBS or 5 $\log_{10}$ PFU of SARS-CoV-2 B.1.1.529, which is an omicron variant (Figure 2A). Transgenic B6.Cg-Tg(K18-*ACE2*)2Prlmn/J mice expressing h*ACE2*, hereafter termed K18 mice, were used as a comparator. Weight compared to day 0 was measured once daily post-inoculation for each mouse and is represented as the mean of all animals. Starting 1 dpi, K18 mice inoculated with SARS-CoV-2

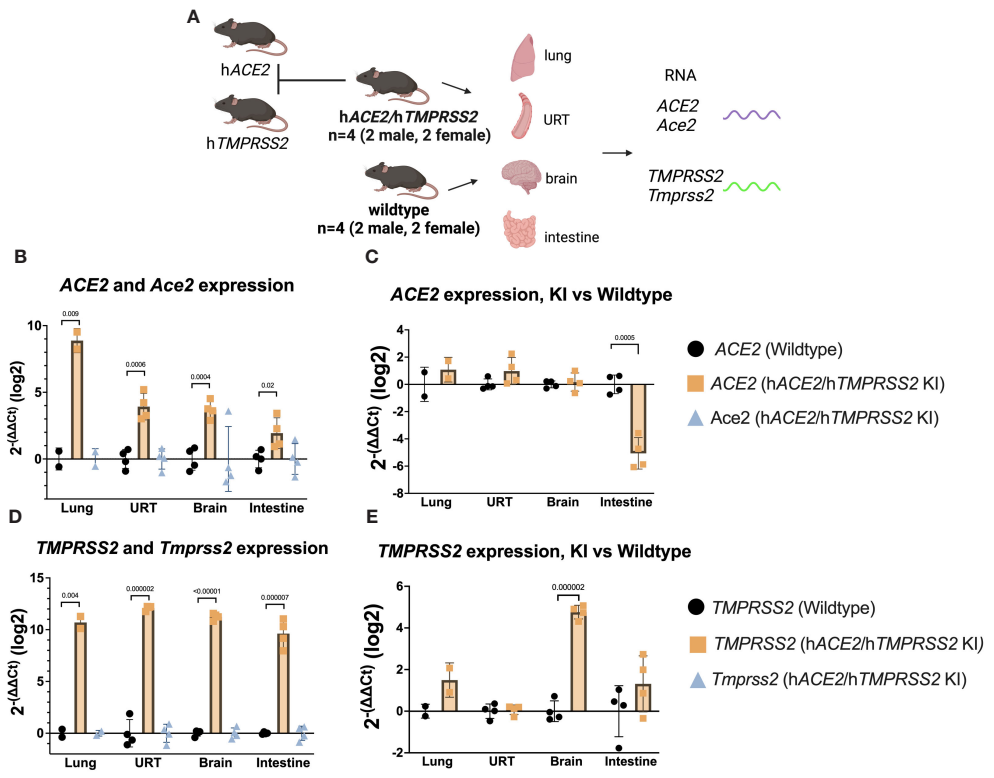

FIGURE 1
Transcript expression levels of *ACE2* and *TMPRSS2* in comparison to endogenous mouse orthologs *Ace2* and *Tmprss2*. **(A)** Schematic of mice and tissues for gene expression to validate mouse models. **(B-E)** Upper respiratory tract (URT), brain, and intestine were harvested from 4 (2M/2F) h*ACE2*/h*TMPRSS2* KI mice and lung harvested from 2 (1M/1F) h*ACE2*/h*TMPRSS2* KI mice as well as from the same number of age- and sex- matched Wildtype mice. qPCR using TaqMan probes from RNA derived cDNA for each human and mouse target was performed and values were compared to an *Actb* reference using the relative Ct method (ΔCt) in triplicate. Averaged ΔCt per sample and human or mouse assay were used to generate $2^{-(\Delta\Delta Ct)}$ for each sample as compared to the averaged Wildtype control group and transformed to $\log_2$. Each dot shows the measurement from one animal and bars show group means. P values were generated using t-tests and shown above bars; groups lacking p values were not significantly different at $p<0.05$.

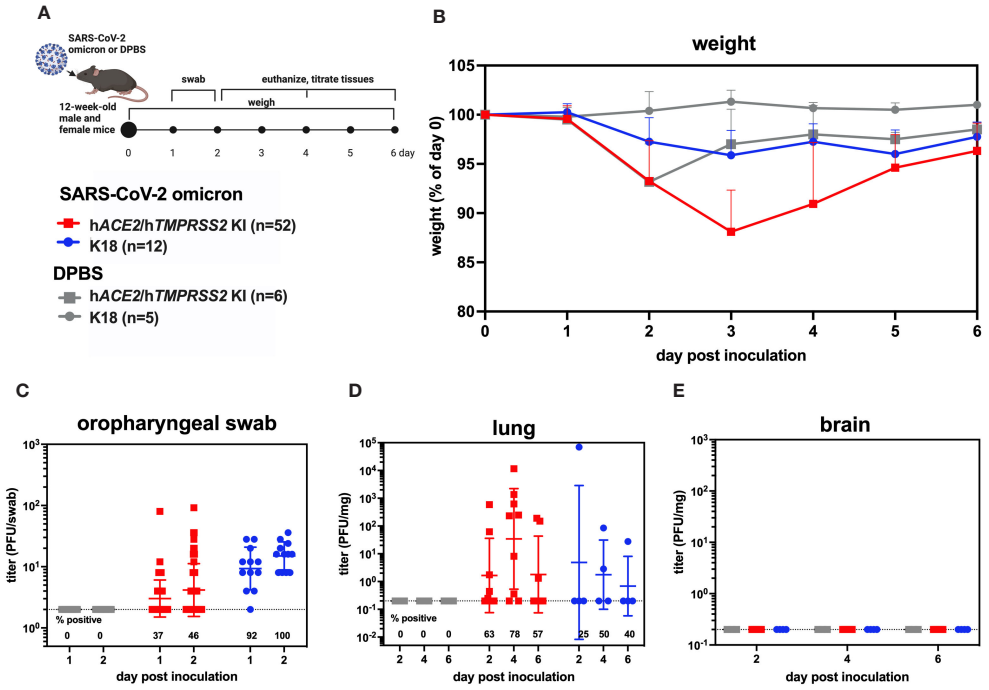

FIGURE 2
SARS-CoV-2 B.1.1529 (omicron) infection kinetics in h*ACE2*/h*TMPRSS2* KI and K18 mice. **(A)** Twelve-week-old male and female KI or K18 mice were inoculated intranasally with DPBS or 5 $\log_{10}$ PFU SARS-CoV-2 B.1.1.529 (omicron). Mice were monitored and weighed daily and the oropharynx was swabbed on 1 and 2 dpi. A subset of mice were euthanized at 2, 4, and 6 dpi. **(B)** Mean body weight change represented as a percentage of weight at the time of inoculation. Each timepoint represents mean with standard deviation. A main effect only model two-way ANOVA with Tukey corrected multiple comparisons yielded p<0.0001. Infectious SARS-CoV-2 titrated from **(C)** oropharyngeal swabs collected 1 and 2 dpi, and from necropsy samples in **(D)** lung and **(E)** brain on 2, 4, and 6 dpi, as quantified by plaque assay. Symbols represent individual animals, horizontal lines represent geometric mean, and error bars represent geometric standard deviation. Numbers below the dotted limit of detection lines indicate the percentage of mice with a detectable SARS-CoV-2 titer. Mean titers between groups of mice sampled on the same day were not significantly different from each other (paired T-tests on log-transformed PFU titers, p>0.05). Data shown are combined from three replicate experiments.

developed and sustained mean weight loss of about 5%, which contrasts with K18 mice administered DPBS, who maintained near 100% of 0 day weights (Figure 2B). By contrast, h*ACE2*/h*TMPRSS2* KI mice inoculated with DPBS or SARS-CoV-2 experienced a transient mean weight loss of about 7% beginning 2 dpi. Since both groups of h*ACE2*/h*TMPRSS2* KI mice were anesthetized to enable oropharyngeal swabbing 1 and 2 dpi, we attribute this weight loss to anesthesia or swabbing and infer that the h*ACE2*/h*TMPRSS2* KI mice are more susceptible to these effects compared to DPBS treated K18 mice, which did not show weight loss after the same procedures. Even with these treatment related changes in weight, mean weight loss in SARS-CoV-2 inoculated h*ACE2*/h*TMPRSS2* KI mice was significantly more than in DPBS treated h*ACE2*/h*TMPRSS2* KI (two-way ANOVA with multiple comparisons, p<0.0001), suggesting that some weight loss we observed was virus induced. At 2 dpi, infectious SARS-CoV-2 was detected in oropharyngeal swabs from 46% of h*ACE2*/h*TMPRSS2* KI mice, compared to 100% of K18 mice (Figure 2C). The mean swab titer in SARS-CoV-2 inoculated h*ACE2*/h*TMPRSS2* KI mice 1 or 2 dpi did not significantly differ; similarly, K18 mice showed no difference in mean swab titer on 1 or 2 dpi (paired t-tests, p>0.05). Infectious SARS-CoV-2 was detected in lungs of most SARS-CoV-2 inoculated h*ACE2*/h*TMPRSS2* KI mice on 2, 4, or 6 dpi, with titers ranging from the limit of detection of 0.2 PFU/mg to more than 4 $\log_{10}$ PFU/mg lung (Figure 2D). The mean lung titer on each day or between h*ACE2*/h*TMPRSS2* KI and K18 was not significantly different (paired t-test, p>0.05). Infectious virus was detected in at least 1 swab or the lungs for most of h*ACE2*/h*TMPRSS2* KI mice euthanized 2, 4, or 6 dpi, which was our criteria for demonstrating infection. However, given that not all mice met this metric, to ensure that titrated virus in murine samples did not reflect non-replicating residual inoculum, we also performed an experiment wherein cohorts of h*ACE2*/h*TMPRSS2* KI mice were inoculated with 5 $\log_{10}$ PFU SARS-CoV-2 omicron that had been heat inactivated to ablate infectivity (Supplementary Figure S2A). The same dose of virus and strain that was not heat inactivated was used as a comparator. No mouse inoculated with heat-inactivated SARS-CoV-2 omicron had detectable infectious virus in oropharyngeal swabs at 2 or 3 dpi (Supplementary Figure S2B), or in trachea (Supplementary Figure S2C) or lung (Supplementary Figure S2D) at 3 dpi, contrasting with mice that received non-heat inactivated SARS-CoV-2, where most animals had detectable infectious virus at all sites. These data support true SARS-CoV-2 infection of these KI cohorts and not detection of residual inoculum. No infectious SARS-CoV-2 was detected in the brain from any h*ACE2*/h*TMPRSS2* KI or K18 mouse on 2, 4, or 6 dpi (Figure 2E). This contrasts with our prior observations of high rates of SARS-CoV-2 neuroinvasion in K18 mice (Supplementary

Figure S3), where all pre-omicron strains we studied (B.1, alpha, beta, and delta) produce high brain titers in the majority of K18 inoculated mice. Together, these data show that h*ACE2*/h*TMPRSS2* KI mice are susceptible to infection with SARS-CoV-2 omicron and exhibit oropharyngeal and lung tropism and lack of brain infection, similar to K18 mice. The absence of virus detection in the brain of h*ACE2*/h*TMPRSS2* KI is likely due to reduced neuroinvasive capacity of omicron, which shows the same phenotype in K18 mice.

3.3 Pulmonary function assessments in SARS-CoV-2 inoculated mice

To evaluate whether SARS-CoV-2 infection of h*ACE2*/h*TMPRSS2* KI mice produces changes in pulmonary function, we used micro computed tomography (µCT). µCT produces cross-sectional anatomical images enabling detailed internal imaging of the mouse lung. These images can reveal evidence of pulmonary inflammation or changes in functional residual volume, tidal volume, and volume at end inspiration. End inspiration and expiration images from µCT scans were generated over a period of 156 dpi and compared to values 5 days prior to inoculation of SARS-CoV-2 or DPBS (Figure 3A). Changes in µCT intensity were detected in some of the male SARS-CoV-2 but not DPBS inoculated h*ACE2*/h*TMPRSS2* mice 5 dpi and resolved by 17 dpi (Figure 3B). Female and male mice showed differences in lung function metrics (Figures 3C-E). Beginning at -5 dpi and persisting over most times assessed, female SARS-CoV-2 inoculated mice showed significantly higher mean tidal and end inspiration volumes compared with DPBS inoculated mice (ANOVA); functional residual volume was not different most days. Since these differences were detected between treatment groups before SARS-CoV-2 administration, it

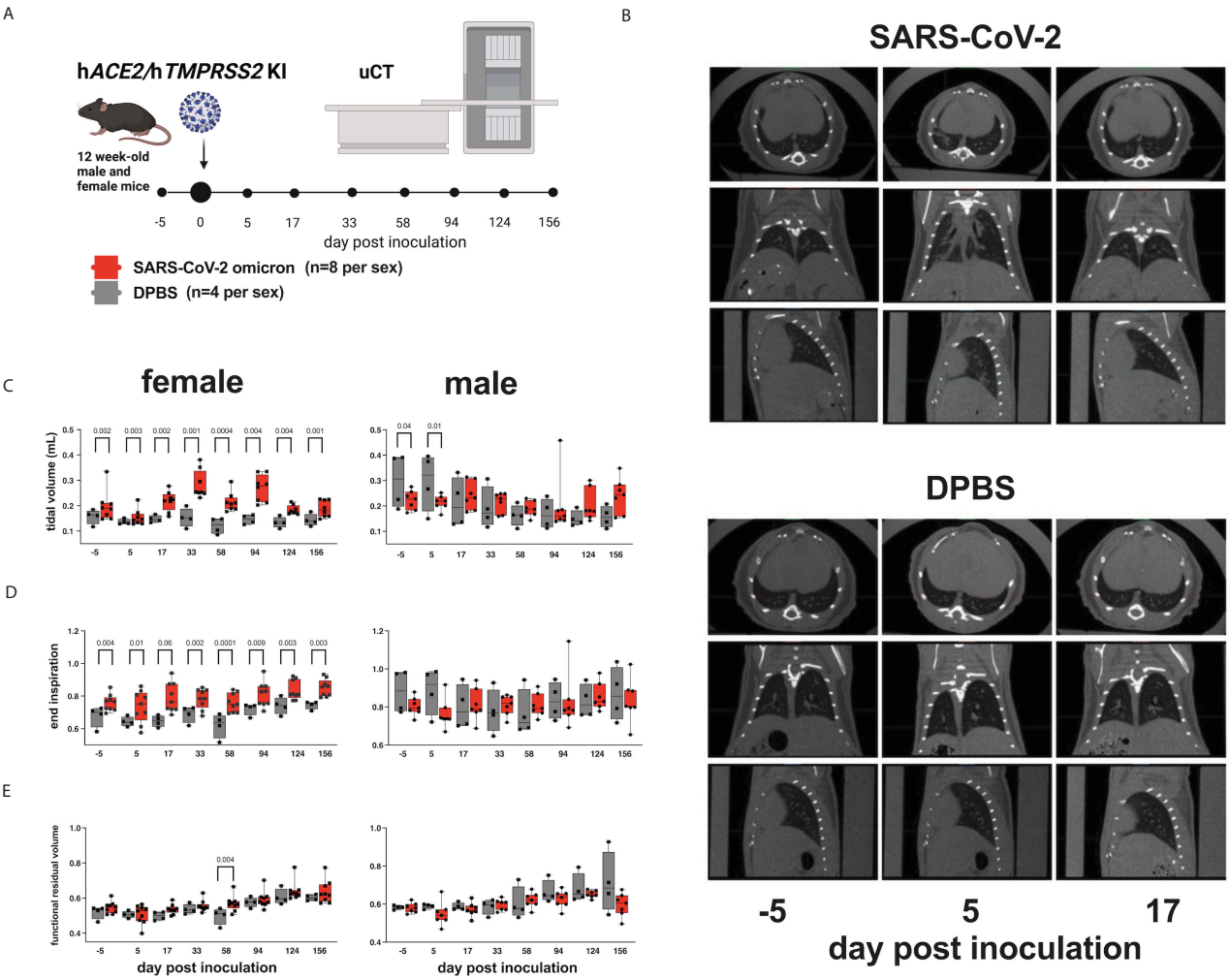

FIGURE 3
Lung function assessments in h*ACE2*/h*TMPRSS2* KI mice. **(A)** Twelve-week-old male and female h*ACE2*/h*TMPRSS2* KI mice inoculated intranasally with DPBS or 5 $\log_{10}$ PFU SARS-CoV-2 B.1.1.529 (omicron) were subjected to µCT to evaluate lung function at -5 (baseline), 5, and 17 dpi and then monthly thereafter to 156 dpi (~6 months). **(B)** Lung µCT images from 2 representative male mice inoculated with SARS-CoV-2 (upper) or DPBS (lower). **(C)** Tidal volume, **(D)** end inspiration, and **(E)** functional residual volume in female or male mice. Statistical designations are based on ANOVA analyses. Each symbol shows a measurement from one mouse, boxes show minimum and maximum measures, lines show means, and error bars show standard deviations. The absence of statistical designations across groups at matched times shows that no statistically significant ($p<0.05$) differences were measured. Data shown are from one experiment.

is not clear whether they are related to viral infection. Male SARS-CoV-2 inoculated mice showed significantly reduced tidal volume compared to DPBS inoculated mice at -5 and 5 dpi (ANOVA); since the -5 dpi differences were detected before virus administration reduced tidal volume was not related to virus infection.

3.4 SHIRPA and cardiovascular characteristics in h*ACE2/hTMPRSS2* KI mice

A subset of h*ACE2*/h*TMPRSS2* KI mice inoculated with SARS-CoV-2 or DPBS were evaluated for changes in behavioral and cardiac activity at monthly intervals for up to 151 dpi using SHIRPA and ECG assessment tests (Figure 4A). SHIRPA is a standardized set of procedures used to characterize muscle, cerebellar, sensory, and neuropsychiatric function in genetically modified mice. h*ACE2*/h*TMPRSS2* KI mice inoculated with SARS-CoV-2 exhibited no significant differences in reflex responses, gross morphology, or cardiac and respiratory parameters compared to DPBS inoculated mice (Supplementary Tables S2, 3). By contrast, a significant (ANOVA, $p<0.01$) reduction in locomotion 16 dpi was observed in SARS-CoV-2 inoculated male (Figure 4B) but not female (Figure 4C) h*ACE2*/h*TMPRSS2* KI mice compared to DPBS inoculated animals. This difference was significant despite the overall decreased ambulation in the test due to habituation to the repetitive nature of the assay. In SARS-CoV-2 inoculated mice of both sexes, no significant changes were detected in cardiorespiratory functions. We measured mild non-significant decreases in respiration rates (Figure 4D) and increases in markers of heart rate variability (dRR, Figure 4E) and conductivity (QTc Figure 4F), compared to DPBS treated animals (male data shown, repeated measures ANOVA, $p>0.05$; female data was similar). Together these data show that male h*ACE2*/h*TMPRSS2* KI mice experience transient reductions in locomotion after SARS-CoV-2 infection, but that neither sex experiences persistent changes in markers of cardiorespiratory function.

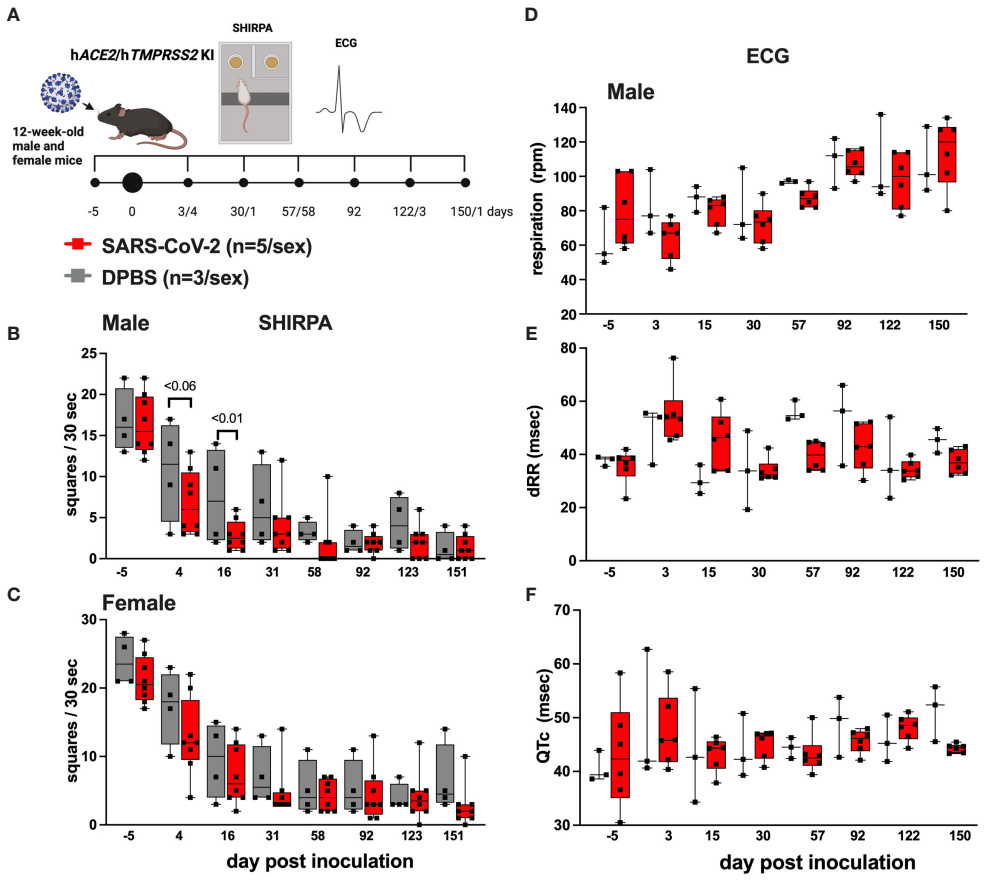

FIGURE 4
Behavioral and cardiac changes in h*ACE2*/h*TMPRSS2* KI mice as assessed by SHIRPA and ECG. **(A)** Twelve-week-old male and female hACE2/hTMPRSS2 KI mice were inoculated intranasally with DPBS or 5 $\log_{10}$ PFU SARS-CoV-2 B.1.1.529 (omicron), and a subset were swabbed and euthanized on or before 6 dpi for virology endpoints (Figure 2). The remaining animals were used for behavioral and cardiac assessments. Locomotion was assessed in **(B)** male and **(C)** female mice as the number of squares in a grid that mice occupied in a 30 second period. **(D)** Respiration rates and **(E, F)** cardiac activity markers measured in individual mice. dRR is difference between consecutive R peaks, a marker of heart rate variability, and QTc is QT interval adjusted for heart rate, a marker of ventricular repolarization. Each symbol shows a measurement from one mouse, boxes show minimum and maximum measures, lines show means, and error bars show standard deviations. Statistical designations are based on ANOVA analyses. The absence of statistical designations across groups at other times and in female groups at all times indicates no statistically significant differences were detected. Data shown are from one experiment.

3.5 Pulmonary histopathologic changes in h*ACE2*/h*TMPRSS2 KI* mice

Lung histopathologic lesions were evaluated in a subset of h*ACE2*/h*TMPRSS2* KI (Figures 5A-C) and K18 (Figures 5D-F) mice inoculated with SARS-CoV-2 omicron or DPBS and euthanized 6 dpi. Pulmonary histopathology was largely unremarkable for all groups of mice, with most mice scoring 0 (Figure 5G). Two DPBS-inoculated mice scored 1 (Supplementary Figure S4), indicative of a mild irritating effect due to DPBS. Histopathology scores across any groups were not statistically different (2 way ANOVA with multiple comparisons, $p>0.05$). These results suggest that infection with SARS-CoV-2 omicron produces similar, negligible histopathologic pulmonary changes 6 dpi in h*ACE2*/h*TMPRSS2* KI and K18 mouse models, with rare individual animal variation.

3.6 Re-inoculation of h*ACE2*/h*TMPRSS2* KI mice with SARS-CoV-2

To simulate repeated SARS-CoV-2 exposure as occurs in humans, we next evaluated SARS-CoV-2 susceptibility and disease manifestations after a second infection. We re-inoculated a subset of SARS-CoV-2 inoculated h*ACE2*/h*TMPRSS2* KI mice with the same strain and dose of omicron used in the first inoculation 6 months after the first inoculation, at 182 dpi, when the mice were 38-weeks-old (Figure 6A). Before the second inoculation, 65% (18/28) of serum samples from blood collected 67 dpi from SARS-CoV-2 inoculated mice had detectable $PRNT_{50}$ titers that ranged from 10 to 80 (Figure 6B). Re-inoculation of SARS-CoV-2 produced significantly more weight loss to 6 dpi than in DPBS inoculated mice (two-way ANOVA with multiple comparisons, $p<0.0001$) (Figure 6C). Infectious SARS-CoV-2 was detected in oropharyngeal swabs from some mice at 1 and 2 dpi (Figure 6D) and in the lungs of some mice 2, 4, and 6 dpi (Figure 6E), indicating re-infection. Counterintuitively, seropositivity rates decreased from 65% at 67 dpi to 21% at 199 dpi, where the latter time was 18 days after the second inoculation (Figure 6B). Three days after the second inoculation, male mice showed significant reductions in respiration rates (Figure 6F, ANOVA, $p<0.05$), and a trend toward increased heart rate variability (dRR, Figure 6G, ANOVA $p>0.05$), and an increased adjusted QT interval, a marker of ventricular repolarization time (QTc, Figure 6H, ANOVA, $p<0.003$). As observed after the first infection, female mouse respiratory and ECG parameters were not affected (Supplementary Tables S4, S5). Lung function assessments from µCT showed no significant changes in tidal volume (Figure 6I) or end inspiration (Figure 6J) for either sex, nor functional residual volume in male SARS-CoV-2 inoculated mice 6 days before compared to 5 or 17 days after the second inoculation (Figure 6K).

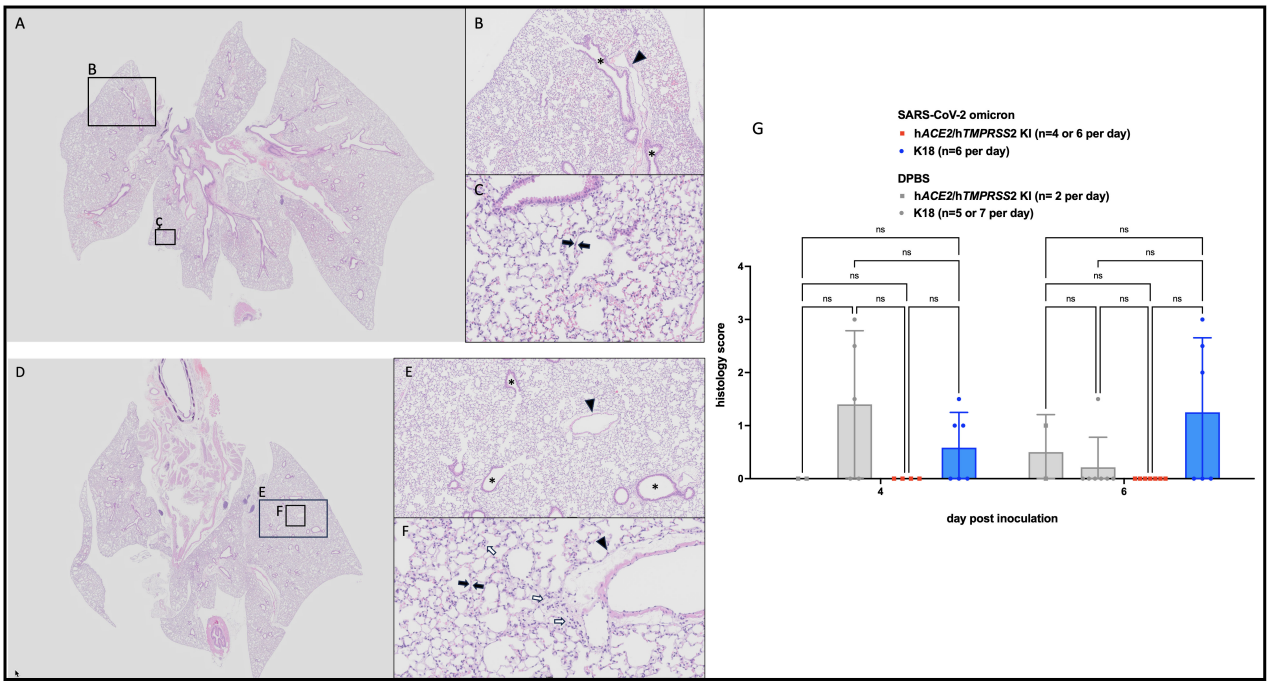

FIGURE 5
Histopathologic changes in SARS-CoV-2 B.1.1529 (omicron) inoculated h*ACE2*/h*TMPRSS2 KI* and K18 mice. Animals euthanized 6 dpi showed no to minimal histopathologic changes in lungs, mostly having scores of 0. **(A, D)** Low magnification (0.63x) of typical h*ACE2*/h*TMPRSS2 KI* **(A)** and K18 **(D)** lung with homogeneous, aerated parenchyma. **(B, E)** Medium (5x) magnification of indicated regions in A and D, respectively. Alveolar and bronchiolar (*) spaces are clear and free of cellular debris. **(C, F)** High (20x) magnification of the indicated regions in A and D, respectively. Alveolar septa (black arrows) are thin and parenchymal vessels are quiescent (arrowheads). Cellularity is minimally increased but within normal range (white arrows). **(G)** Lung histologic scores. Each symbol shows a measurement from one mouse, boxes show minimum and maximum measures, lines show means, and error bars show standard deviations. Statistical designations are based on ANOVA analyses, ns is not significant at $p<0.05$.

10.3389/fimmu.2024.1428711

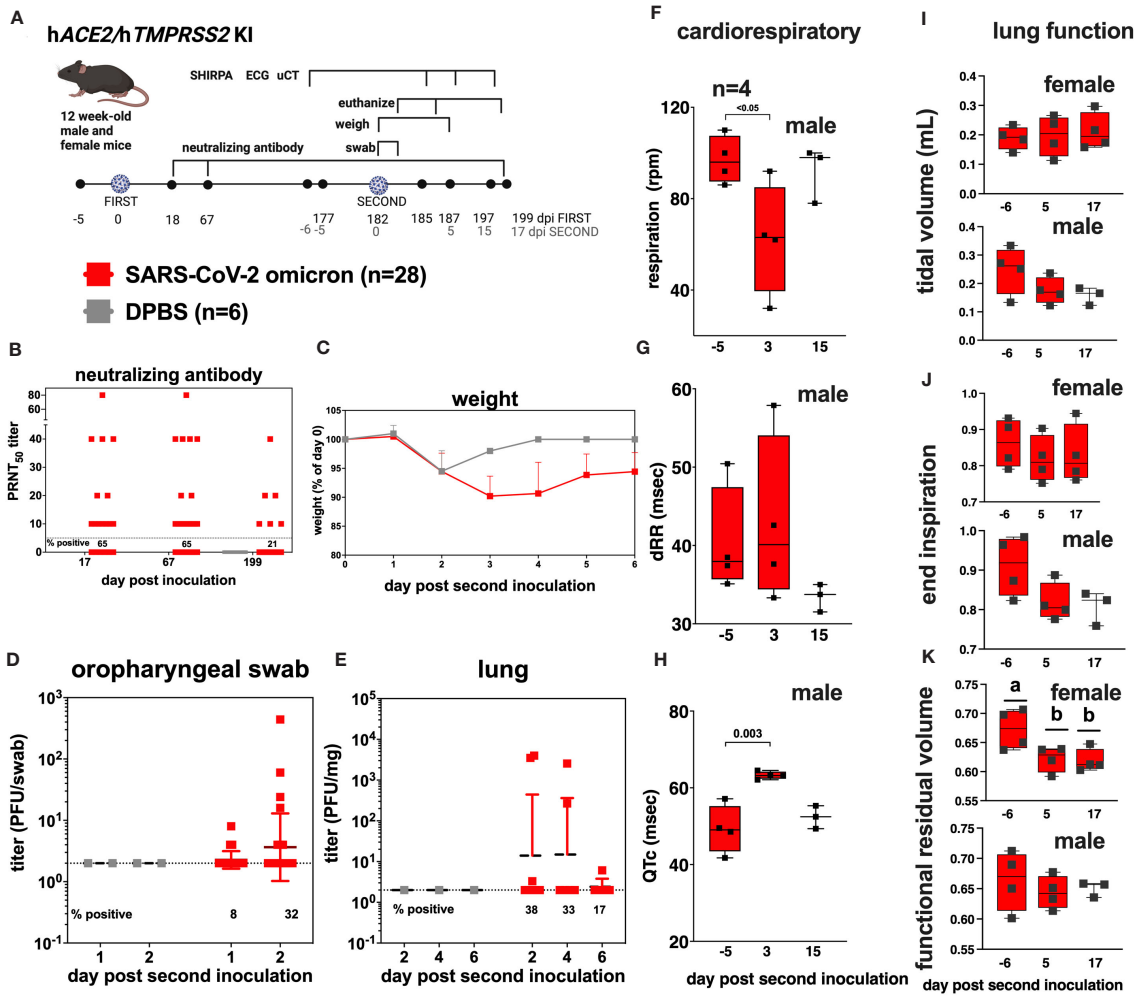

FIGURE 6
SARS-CoV-2 B.1.1529 (omicron) re-infection kinetics in h*ACE2*/h*TMPRSS2* KI mice. **(A)** Twelve-week-old male and female h*ACE2*/h*TMPRSS2 KI* mice inoculated intranasally with DPBS or 5 $\log_{10}$ PFU SARS-CoV-2 B.1.1.529 (omicron) were re-inoculated 182 days later (~6 months) with the same dose and strain of omicron used in the first inoculation. Blood was collected at 18, 67, and 199 dpi, and used for neutralizing antibody assays. Mice were monitored daily and weighed for 6 days, and the oropharyngeal cavity was swabbed 1 and 2 dpi after the second inoculation. A subset of mice were euthanized 2, 4, and 6 dpi after the second inoculation. **(B)** $PRNT_{50}$ titers from mouse serum showing neutralizing antibody titers in SARS-CoV-2 inoculated mice at 3 times post inoculation. Each dot represents the measurement from one mouse. The numbers below the dotted limit of detection lines show the percentage of mice with a detectable $PRNT_{50}$ titer. **(C)** Mean body weight change represented as a percentage of weight at the time of inoculation. Dots represent means and error bars represent standard deviations. A main effect only model two-way ANOVA yielded $p<0.0001$. Infectious SARS-CoV-2 measured in **(D)** oropharyngeal swabs collected 1 and 2 dpi, and in the **(E)** lung on 2, 4, and 6 dpi, quantified by plaque assay. Symbols represent individual animals, horizontal lines represent geometric mean, and error bars represent geometric standard deviation. The numbers below the dotted limit of detection lines show the percentage of mice with a detectable SARS-CoV-2 titer. A subset of 4 mice of each sex was used for cardiac and lung function assessments. Respiration rates **(F)** and **(G, H)** cardiac activity markers were measured in individual mice, where dRR is heart rate variability and QTc is heart rate. Lung function based on µCT showing **(I)** tidal volume, **(J)** end inspiration, and **(K)** functional residual volume in female and male mice. Statistical designations are based on ANOVA analyses; a versus b indicates $p<0.03$. The absence of statistical designations across groups indicates no statistically significant differences were detected. Each symbol shows a measurement from one mouse, boxes show minimum and maximum measures, lines show means, and error bars show standard deviations. Data shown are from one experiment.

Functional residual volume in female mice was significantly lower at 5 and 17 compared to -6 days post re-inoculation (Figure 6K, ANOVA, $p<0.03$). Together these data show that h*ACE2*/h*TMPRSS2* KI mice are susceptible to a second homologous infection with SARS-CoV-2 6 months after the first infection, characterized by weight loss, respiratory tissue tropism, transient acute changes in cardiac function in male mice, and reduced lung volume in female mice, but that reinoculation does not result in increased neutralizing antibody responses in all mice.

4 Discussion

In this study, we generated and characterized a novel mouse model of COVID-19. We expressed both *ACE2* and *TMPRSS2* in dual gene knock-in mice by incorporating the human coding sequence directly into the endogenous mouse loci to create h*ACE2*/h*TMPRSS2* KI mice. These mice express both human genes in respiratory tissues and are susceptible to infection with an omicron strain of SARS-CoV-2. Infection produced transient

weight loss and infectious virus detectable in the oropharynx at 1-2 dpi and in the lungs at 2, 4 and 6 dpi. Our data in h*ACE2*/h*TMPRSS2* KI mice are similar to observations from h*ACE2* KI mice (14, 15), although Sun et al. detected interstitial pneumonia, whereas we observed no significant pulmonary histopathologic changes. However, we used omicron whereas both other studies used pre-omicron variants, WA.1, B.1.1.7 (alpha) or B.1.351 (beta). The absence of neuroinvasion by omicron in both h*ACE2*/h*TMPRSS2* KI and K18 mice observed here is consistent with other reports of lower virulence of this variant compared to preceding variants, possibly due to less efficient TMPRSS2 use resulting in lower replication competence as was observed in *ex vivo* human lung explants (27) and reduced fusogenicity in nasal epithelial cell cultures (28). The mild weight loss and near absence of lung histopathologic changes in the h*ACE2*/h*TMPRSS2* KI mice evaluated here contrasts with murine models that transiently express h*ACE2* in the lung via adeno-associated vectors (29, 30), where weight loss was more severe and bronchopneumonia was noted 7 dpi, however, both of those studies were with pre-omicron strains that are generally more virulent than omicron in mouse and hamster models (31–33). Although we were initially surprised that not all h*ACE2*/h*TMPRSS2* KI mice developed detectable neutralizing antibody responses, our studies with heat-inactivated SARS-CoV-2 show that this model and the virus strain and dose used reproducibly establishes a productive infection, despite the lack of seroconversion in all mice. Unfortunately, neither of the other h*ACE2* KI studies (14, 15) evaluated antibody development to allow for a comparison with our results. The absence of neutralizing antibody in all h*ACE2*/h*TMPRSS2* KI mice parallels recent work in K18 mice showing that SARS-CoV-2 infection and vaccine mediated protection can be antibody independent, instead relying on T cell responses (34), which were not a subject of focus in our studies.

To our knowledge, although CT scan is commonly used for defining lung changes in COVID-19 patients (35), no studies to date have used μCT to evaluate lung function in small animal models of COVID-19. One study measured a drug mediated reduction in alveolar damage using μCT in outbred ICR inoculated SARS-CoV-2 mice (36). With uCT and the other cardiovascular metrics used here, we observed that SARS-CoV-2 infection produced visual changes in uCT intensity but no quantitative changes in total lung capacity or other measures of lung function or markers of cardiovascular function in the ensuing 6 months or after a second virus inoculation administered 6 months after the first inoculation. Our observations of reduced ambulation in male but not female mice mirror post-COVID-19 outcomes in people where females experience lower rates of cardiovascular-related hospitalizations after COVID-19 (37). When subjected to a six minute walking exercise followed by pulmonary function tests, males humans also experience higher post-stress respiratory outcomes compared to females (38).

Our study has limitations. The anesthesia and swabbing approach produced weight loss even in DPBS inoculated h*ACE2*/h*TMPRSS2* KI mice, limiting our ability to ascribe weight change to virus treatment. Many of the published studies using similar murine models used pre-omicron strains, limiting direct comparison of outcomes observed in these studies with omicron given that virus strain can impact phenotype. Our studies with h*ACE2*/h*TMPRSS2* KI mice only used omicron and not other SARS-CoV-2 variants. Although we performed power analyses to inform group sizes based on virology metrics prior to starting the project, it is possible the group sizes used were underpowered to detect small differences in lung function or cardiovascular metrics, if they occurred. Our immunology analyses were limited to assessment of neutralizing antibody responses. Future studies should further address immune responses to SARS-CoV-2 infection using the h*ACE2*/h*TMPRSS2* KI model.

Continued development of small animal models of COVID-19 can aid in more fully understanding the pathogenesis of disease caused by SARS-CoV-2. Given that the h*ACE2*/h*TMPRSS2* KI mice were developed on a C57BL/6N genetic background, they can further be employed in cross-breeding experiments with other transgenic mice to enable studies on other COVID-19-associated traits, including diabetes, Alzheimer's disease, and obesity.

Data availability statement

The datasets generated and analyzed for this study can be found at https://ucdavis.box.com/s/na5n0mvlhgp4zfx569n5duqmouyo9mo2. Newly generated mouse strains presented in this report (hACE2 KI [RRID:MMRRC_068346-UCD], hTMPRSS2 KI [RRID:MMRRC_032678-UCD], and hACE2/hTMPRSS2 KI [RRID:MMRRC_069727-UCD]) are available from the Mutant Mouse Resource and Research Center (MMRRC) at www.mmrrc.org.

Ethics statement

The animal study was approved by University of California, Davis Institutional Animal Care and Use Committee. The study was conducted in accordance with the local legislation and institutional requirements.

Author contributions

HL: Conceptualization, Data curation, Formal analysis, Investigation, Methodology, Visualization, Writing – original draft, Writing – review & editing. TB: Writing – review & editing. AR: Writing – review & editing, Investigation. TW: Investigation, Writing – review & editing. DR: Investigation, Writing – review & editing, Data curation, Formal analysis. MH: Data curation, Investigation, Writing – review & editing, Methodology. AF: Investigation, Writing – review & editing. BW: Investigation, Writing – review & editing, Data curation, Formal analysis, Methodology. JE: Investigation, Writing – review & editing. LL: Investigation, Writing – review & editing, Conceptualization, Data curation, Formal analysis, Methodology, Supervision, Visualization. KL: Conceptualization, Investigation, Supervision, Writing – review & editing, Funding acquisition, Project administration, Resources. LC: Conceptualization, Funding

acquisition, Project administration, Resources, Supervision, Writing – review & editing, Data curation, Methodology, Visualization, Writing – original draft.

Funding

The author(s) declare financial support was received for the research, authorship, and/or publication of this article. This work was supported by the University of California Davis Schools of Veterinary Medicine and Medicine and the US National Institute of Health Office of the Director DCM/ORIP/Division of Program Coordination, Planning, and Strategic Initiatives under U42OD012210.

Acknowledgments

Sarah Hazeltine supported mouse breeding efforts.

Conflict of interest

The authors declare that the research was conducted in the absence of any commercial or financial relationships that could be construed as a potential conflict of interest.

Publisher's note

Supplementary material

The Supplementary Material for this article can be found online at: https://www.frontiersin.org/articles/10.3389/fimmu.2024.1428711/full#supplementary-material

SUPPLEMENTARY FIGURE 1
Mouse design and production.

SUPPLEMENTARY FIGURE 2
Heat-inactivated SARS-CoV-2 in *hACE2/hTMPRSS2*.

SUPPLEMENTARY FIGURE 3
Multiple variant SARS-CoV-2 infection kinetics in K18 mice.

SUPPLEMENTARY FIGURE 4
Lung histopathology in DPBS-inoculated hACE2/hTMPRSS2 KI mice 6 dpi.

SUPPLEMENTARY TABLE 1
Primers used to generate KI mice.

SUPPLEMENTARY TABLE 2
SHIRPA measurements for each mouse.

SUPPLEMENTARY TABLE 3
ECG measurements for each mouse.

SUPPLEMENTARY TABLE 4
SHIRPA measurements for each mouse after re-inoculation.

SUPPLEMENTARY TABLE 5
ECG measurements for each mouse after re-inoculation.

References

1. Bohmwald K, Diethelm-Varela B, Rodríguez-Guilarte L, Rivera T, Riedel CA, González PA, et al. Pathophysiological, immunological, and inflammatory features of long COVID. *Front Immunol.* (2024) 15:1341600/full. doi: 10.3389/fimmu.2024.1341600/full

2. Sherif ZA, Gomez CR, Connors TJ, Henrich TJ, Reeves WB. RECOVER Mechanistic Pathway Task Force. Pathogenic mechanisms of post-acute sequelae of SARS-CoV-2 infection (PASC). *eLife*. (2023) 12:e86002. doi: 10.7554/eLife.86002

3. Tanni SE, Fabro AT, de Albuquerque A, Ferreira EVM, Verrastro CGY, Sawamura MVY, et al. Pulmonary fibrosis secondary to COVID-19: a narrative review. *Expert Rev Respir Med.* (2021) 15:791–803. doi: 10.1080/17476348.2021.1916472

4. Grosse C, Grosse A, Salzer HJF, Dünser MW, Motz R, Langer R. Analysis of cardiopulmonary findings in COVID-19 fatalities: High incidence of pulmonary artery thrombi and acute suppurative bronchopneumonia. *Cardiovasc Pathol.* (2020) 49:107263. doi: 10.1016/j.carpath.2020.107263

5. Piazza G, Campia U, Hurwitz S, Snyder JE, Rizzo SM, Pfeferman MB, et al. Registry of arterial and venous thromboembolic complications in patients with COVID-19. *J Am Coll Cardiol.* (2020) 76:2060–72. doi: 10.1016/j.jacc.2020.08.070

6. Eizaguirre S, Sabater G, Belda S, Calderón JC, Pineda V, Comas-Cufí M, et al. Long-term respiratory consequences of COVID-19 related pneumonia: a cohort study. *BMC Pulm Med.* (2023) 23:439. doi: 10.1186/s12890-023-02627-w

7. Babar M, Jamil H, Mehta N, Moutwakil A, Duong TQ. Short- and long-term chest-CT findings after recovery from COVID-19: A systematic review and meta-analysis. *Diagnostics (Basel).* (2024) 14:621. doi: 10.3390/diagnostics14060621

8. Cha MJ, Solomon JJ, Lee JE, Choi H, Chae KJ, Lee KS, et al. Chronic lung injury after COVID-19 pneumonia: clinical, radiologic, and histopathologic perspectives. *Radiology*. (2024) 310:e231643. doi: 10.1148/radiol.231643

9. Jansen EB, Orvold SN, Swan CL, Yourkowski A, Thivierge BM, Francis ME, et al. After the virus has cleared—Can preclinical models be employed for Long COVID research? *PLoS Pathog.* (2022) 18:e1010741. doi: 10.1371/journal.ppat.1010741

10. Sia SF, Yan LM, Chin AWH, Fung K, Choy KT, Wong AYL, et al. Pathogenesis and transmission of SARS-CoV-2 in golden hamsters. *Nature.* (2020) 583:834–8. doi: 10.1038/s41586-020-2342-5

11. Pinto MA, da Silva ADS, Rodrigues DDRF, Müller R, de Vasconcelos GALBM, Neves PC da C, et al. Animal models and SARS-CoV-2-induced pulmonary and neurological injuries. *Mem Inst Oswaldo Cruz.* (2023) 117:e220239. doi: 10.1590/0074-02760220239

12. Dillard JA, Martinez SA, Dearing JJ, Montgomery SA, Baxter VK. Animal models for the study of SARS-CoV-2-induced respiratory disease and pathology. *Comp Med.* (2023) 73:72–90. doi: 10.30802/AALAS-CM-22-000089

13. Song IW, Washington M, Leynes C, Hsu J, Rayavara K, Bae Y, et al. Generation of a humanized mAce2 and a conditional hACE2 mouse models permissive to SARS-COV-2 infection. *Mamm Genome*. (2024) 35:113–21. doi: 10.1007/s00335-024-10033-8

14. Winkler ES, Chen RE, Alam F, Yildiz S, Case JB, Uccellini MB, et al. SARS-CoV-2 causes lung infection without severe disease in human ACE2 knock-in mice. *J Virol.* (2022) 96:e01511–21. doi: 10.1128/JVI.01511-21

15. Sun SH, Chen Q, Gu HJ, Yang G, Wang YX, Huang XY, et al. A mouse model of SARS-CoV-2 infection and pathogenesis. *Cell Host Microbe*. (2020) 28:124–33.e4. doi: 10.1016/j.chom.2020.05.020

16. Zhou X, Sun W, Zhang Y, Gu H, Wang R, Xie P, et al. A novel hACE2 knock-in mouse model recapitulates pulmonary and intestinal SARS-CoV-2 infection. *Front Microbiol.* (2023) 14:1175188/full. doi: 10.3389/fmicb.2023.1175188/full

17. Sungnak W, Huang N, Bécavin C, Berg M, Queen R, Litvinukova M, et al. SARS-CoV-2 entry factors are highly expressed in nasal epithelial cells together with innate immune genes. *Nat Med.* (2020) 26:681–7. doi: 10.1038/s41591-020-0868-6

18. Concordet JP, Haeussler M. CRISPOR: intuitive guide selection for CRISPR/Cas9 genome editing experiments and screens. *Nucleic Acids Res*. (2018) 46:W242–5. doi: 10.1093/nar/gky354

19. Gibson DG, Young L, Chuang RY, Venter JC, Hutchison CA, Smith HO. Enzymatic assembly of DNA molecules up to several hundred kilobases. *Nat Methods*. (2009) 6:343–5. doi: 10.1038/nmeth.1318

20. Pettitt SJ, Liang Q, Rairdan XY, Moran JL, Prosser HM, Beier DR, et al. Agouti C57BL/6N embryonic stem cells for mouse genetic resources. *Nat Methods*. (2009) 6:493–5. doi: 10.1038/nmeth.1342

21. Moore K, Martin J. Electroporation of human pluripotent or embryonic stem cells with CRISPR reagents (2024). Available online at: https://www.idtdna.com/pages/education/decoded/article/protocols-for-crispr-genome-editing-in-your-model-system.

22. Livak KJ, Schmittgen TD. Analysis of relative gene expression data using real-time quantitative PCR and the 2(-Delta Delta C(T)) Method. *Methods*. (2001) 25:402–8. doi: 10.1006/meth.2001.1262

23. Groza T, Lopez Gomez F, Haseli Mashhadi H, Muñoz-Fuentes V, Gunes O, Wilson R, et al. The international mouse phenotyping consortium: comprehensive knockout phenotyping underpinning the study of human disease. *Nucleic Acids Res*. (2023) 51(D1):D1038–45. doi: 10.1093/nar/gkac972

24. Novikov AA, Major D, Wimmer M, Lenis D, Buhler K. Deep sequential segmentation of organs in volumetric medical scans. *IEEE Trans Med Imaging*. (2019) 38:1207–15. doi: 10.1109/TMI.42

25. Wikipedia. Otsu's method. Available online at: https://en.wikipedia.org/wiki/Otsu's_method.

26. Weiss CM, Liu H, Ball EE, Lam S, Hode T, Keel MK, et al. N-dihydrogalactochitosan reduces mortality in a lethal mouse model of SARS-CoV-2. *PLoS One*. (2023) 18(8):e0289139. doi: 10.1371/journal.pone.0289139

27. Hui KPY, Ho JCW, Cheung MC, Ng KC, Ching RHH, Lai KL, et al. SARS-CoV-2 Omicron variant replication in human bronchus and lung ex vivo. *Nature*. (2022) 603:715–20. doi: 10.1038/s41586-022-04479-6

28. Meng B, Abdullahi A, Ferreira IATM, Goonawardane N, Saito A, Kimura I, et al. Altered TMPRSS2 usage by SARS-CoV-2 Omicron impacts infectivity and fusogenicity. *Nature*. (2022) 603:706–14. doi: 10.1038/s41586-022-04474-x

29. Glazkova DV, Bogoslovskaya EV, Urusov FA, Kartashova NP, Glubokova EA, Gracheva AV, et al. Generation of SARS-CoV-2 mouse model by transient expression of the human ACE2 gene mediated by intranasal administration of AAV-hACE2. *Mol Biol*. (2022) 56:705–12. doi: 10.1134/S0026893322050065

30. Sun CP, Jan JT, Wang IH, Ma HH, Ko HY, Wu PY, et al. Rapid generation of mouse model for emerging infectious disease with the case of severe COVID-19. *PLoS Pathog*. (2021) 17:e1009758. doi: 10.1371/journal.ppat.1009758

31. Shuai H, Chan JFW, Hu B, Chai Y, Yoon C, Liu H, et al. The viral fitness and intrinsic pathogenicity of dominant SARS-CoV-2 Omicron sublineages BA.1, BA.2, and BA.5. *EBioMedicine*. (2023) 95:104753. doi: 10.1016/j.ebiom.2023.104753

32. Uraki R, Kiso M, Iida S, Imai M, Takashita E, Kuroda M, et al. Characterization and antiviral susceptibility of SARS-CoV-2 Omicron BA.2. *Nature*. (2022) 607:119–27. doi: 10.1038/s41586-022-04856-1

33. Wang E, Yang QJ, Xu XX, Zou QC, Long Y, Ma G, et al. Differential pathogenic and molecular features in neurological infection of SARS-CoV-2 Omicron BA.5.2 and BA.2.75 and Delta. *J Med Virol*. (2024) 96:e29357. doi: 10.1002/jmv.29357

34. Fumagalli V, Ravà M, Marotta D, Di Lucia P, Bono EB, Giustini L, et al. Antibody-independent protection against heterologous SARS-CoV-2 challenge conferred by prior infection or vaccination. *Nat Immunol*. (2024) 25:633–43. doi: 10.1038/s41590-024-01787-z

35. Arian A, Gity M, Kolahi S, Khani S, Ahmadi MA, Salehi M, et al. Evaluation of chest CT-scan appearances of COVID-19 according to RSNA classification system. *J Family Med Prim Care*. (2022) 11:4410–6. doi: 10.4103/jfmpc.jfmpc_8_22

36. Chernov AS, Rodionov MV, Kazakov VA, Ivanova KA, Meshcheryakov FA, Kudriaeva AA, et al. CCR5/CXCR3 antagonist TAK-779 prevents diffuse alveolar damage of the lung in the murine model of the acute respiratory distress syndrome. *Front Pharmacol*. (2024) 15:1351655. doi: 10.3389/fphar.2024.1351655

37. Mangion K, Morrow AJ, Sykes R, Kamdar A, Bagot C, Bruce G, et al. Post-COVID-19 illness and associations with sex and gender. *BMC Cardiovasc Disord*. (2023) 23:389. doi: 10.1186/s12872-023-03412-7

38. Raza SS, Zafar U, Shehwar DE, Zafar H, Ullah F, Wazir M, et al. Sex-linked differences in pulmonary functions of COVID-19 patients after a six-minute walk test. *Cureus*. (2023) 15:e50071. doi: 10.7759/cureus.50071

frontiers | Frontiers in Immunology

TYPE Original Research
PUBLISHED 30 August 2024
DOI 10.3389/fimmu.2024.1430928

OPEN ACCESS

EDITED BY
William Murphy,
University of California, Davis, United States

REVIEWED BY
Awadalkareem Adam,
University of Texas Medical Branch at Galveston, United States
Tamarand Lee Darling,
Washington University in St. Louis, United States

*CORRESPONDENCE
James M. Rini
james.rini@utoronto.ca
Jim Hu
jim.hu@sickkids.ca
Jun Liu
jun.liu@utoronto.ca

†These authors have contributed equally to this work

RECEIVED 10 May 2024
ACCEPTED 08 August 2024
PUBLISHED 30 August 2024

CITATION
Zhou P, Watt J, Mai J, Cao H, Li Z, Chen Z, Duan R, Quan Y, Gingras A-C, Rini JM, Hu J and Liu J (2024) Intranasal HD-Ad-FS vaccine induces systemic and airway mucosal immunities against SARS-CoV-2 and systemic immunity against SARS-CoV-2 variants in mice and hamsters.
Front. Immunol. 15:1430928.
doi: 10.3389/fimmu.2024.1430928

Intranasal HD-Ad-FS vaccine induces systemic and airway mucosal immunities against SARS-CoV-2 and systemic immunity against SARS-CoV-2 variants in mice and hamsters

Peter Zhou[1†], Jacqueline Watt[1†], Juntao Mai[1], Huibi Cao[2], Zhijie Li[1], Ziyan Chen[2,3], Rongqi Duan[2], Ying Quan[1], Anne-Claude Gingras[1,4], James M. Rini[1,5*], Jim Hu[2,3*] and Jun Liu[1*]

[1]Department of Molecular Genetics, Faculty of Medicine, University of Toronto, Toronto, ON, Canada, [2]Translational Medicine Program, Hospital for Sick Children Research Institute, Toronto, ON, Canada, [3]Department of Laboratory Medicine and Pathobiology, University of Toronto, Toronto, ON, Canada, [4]Lunenfeld-Tanenbaum Research Institute, Mount Sinai Hospital, Toronto, ON, Canada, [5]Department of Biochemistry, Faculty of Medicine, University of Toronto, Toronto, ON, Canada

The outbreak of coronavirus disease 19 (COVID-19) has highlighted the demand for vaccines that are safe and effective in inducing systemic and airway mucosal immunity against the aerosol transmission of severe acute respiratory syndrome coronavirus 2 (SARS-CoV-2). In this study, we developed a novel helper-dependent adenoviral vector-based COVID-19 mucosal vaccine encoding a full-length SARS-CoV-2 spike protein (HD-Ad-FS). Through intranasal immunization (single-dose and prime-boost regimens), we demonstrated that the HD-Ad-FS was immunogenic and elicited potent systemic and airway mucosal protection in BALB/c mice, transgenic ACE2 (hACE2) mice, and hamsters. We detected high titers of neutralizing antibodies (NAbs) in sera and bronchoalveolar lavages (BALs) in the vaccinated animals. High levels of spike-specific secretory IgA (sIgA) and IgG were induced in the airway of the vaccinated animals. The single-dose HD-Ad-FS elicited a strong immune response and protected animals from SARS-CoV-2 infection. In addition, the prime-boost vaccination induced cross-reactive serum NAbs against variants of concern (VOCs; Beta, Delta, and Omicron). After challenge, VOC infectious viral particles were at undetectable or minimal levels in the lower airway. Our findings highlight the potential of airway delivery of HD-Ad-FS as a safe and effective vaccine platform for generating mucosal protection against SARS-CoV-2 and its VOCs.

KEYWORDS

COVID-19, HD-Ad, adenoviral vector, intranasal delivery, SARS-CoV-2, vaccine

Introduction

Coronavirus disease 2019 (COVID-19) is caused by severe acute respiratory syndrome coronavirus 2 (SARS-CoV-2) and led to more than 670 million confirmed cases and 6.8 million deaths worldwide by 2022. SARS-CoV-2 is an airborne-transmitted disease that infects the mucosal surface of the respiratory tract (1, 2). Tremendous efforts and major progress have been made to develop effective vaccines to control the spread of SARS-CoV-2 and its variants. Approved COVID-19 vaccines include those that are based on nucleic acid (3, 4) subunit protein (5), inactivated whole-virus (6), and non-replicating virus (7, 8). These vaccines are administered intramuscularly (IM) and are effective at preventing severe disease and curbing the hospitalization rate (9, 10). The IM vaccines induce robust systemic immunity; however, they only elicit limited immunity on airway mucosal surfaces which are the primary site of viral entry, shedding, and transmission (11). Therefore, the development of vaccines that can induce airway mucosal immunity as well as systemic immunity is in need.

Mucosal vaccines can induce potent airway immune memory through intranasal or oral immunization (12, 13). Intranasal vaccination mimics a natural route of viral entry where the antigen is directly introduced at the epithelium to elicit a mucosal immune response. Mucosal vaccines prime airway resident memory T cells which respond stronger and faster than circulating memory T cells during viral infection (14). They also induce antibodies, especially secretory IgA (sIgA), on the mucosal surface which blocks viral entry (8). Moreover, mucosal vaccination generates systemic immunity through the production of serum neutralizing antibodies (NAbs) (15). To date, around twelve intranasal COVID-19 vaccines are in clinical trials. Among these are live-attenuated virus, non-replicating virus, and subunit protein vaccines (16).

The helper-dependent adenoviral (HD-Ad) vector is a non-replicating third generation adenoviral vector that can be used for developing intranasal vaccines. HD-Ad leads to robust antigen delivery in the airway (17), which allows for effective antigen presentation by antigen-presenting cells (APCs) during T cell priming. Additionally, HD-Ad is devoid of all viral genes except for the packaging signals and inverted terminal repeats (ITRs), thereby minimizing inflammation compared to the first and second generations adenoviral vectors (18). This reduces the anti-vector immune response, enabling prolonged antigen expression in the airway mucosa (19). Antigen expression can be sustained for more than 3 weeks in the mouse airway (17). Sustained antigen expression continuously primes T follicular helper cells and B cells in the geminal center and induces long-term immunity with NAb production (20). Intranasal delivery of HD-Ad has been demonstrated to be safe in different animal models (19, 21), as well as in clinical trials (22). Previously, we developed an HD-Ad intranasal vaccine expressing the receptor-binding domain (RBD) of SARS-CoV-2. We demonstrated that intranasal delivery of HD-Ad-RBD elicited strong immunity and protected mice from SARS-CoV-2 infection (23).

Here, we describe an intranasal COVID-19 vaccine based on an HD-Ad vector that encodes the full-length spike protein (FS) of SARS-CoV-2 (HD-Ad-FS). The spike protein binds to the host cell receptor, ACE2, through its RBD domain and mediates virus-cell fusion. The spike protein was chosen as the immunogen because it contains multiple epitopes, including those on the RBD, which can elicit NAb production (24). We examine the efficacy of single-dose HD-Ad-FS against the SARS-CoV-2 ancestral strain (SARS-CoV-2 hereafter). Since the Beta, Delta, and Omicron strains are the main variants of concern (VOC) (25–27), we also test the efficacy of prime-boost HD-Ad-FS against these VOCs. We find that intranasal vaccination with single-dose HD-Ad-FS induces robust systemic, and upper and lower airway mucosal immunity against SARS-CoV-2 in hACE2 mice and hamsters. Furthermore, the prime-boost HD-Ad-FS elicits systemic and lower airway mucosal immunity against SARS-CoV-2 VOCs in these animal models.

Results

Construction and expression of the HD-Ad-FS vaccine

The sequence of the full-length spike glycoprotein (FS) was codon-optimized, and two proline substitutions were introduced at positions 986 and 987 to stabilize the prefusion conformation (28). The expression of FS was driven by a chicken beta actin (CBA) promoter, and the first intron of human ubiquitin C (UbC) was included to increase the stability of the FS mRNA (Figure 1A). The transcription was terminated by a bovine growth hormone (bGH) polyadenylation tail.

To examine FS protein expression, human airway epithelial cells (IB3-1) were transduced with HD-Ad-FS at 10, 20, and 40 multiplicity of infection (MOI). Dose-dependent expression of the FS protein was detected from cell lysates by Western blot analysis at day 3 post-transduction, indicating that the FS protein was efficiently expressed (Figure 1B).

HD-Ad-FS elicits robust systemic and airway mucosal immunity in BALB/c mice

To study the immunogenicity of HD-Ad-FS, we immunized BALB/c mice (n=5/group) with HD-Ad-FS via the intranasal route using single-dose (single-FS) and prime-boost (boost-FS) regimens (Figure 1C). For the single-FS group, mice were immunized with one dose of $5x10^9$ viral particles (vp). For the boost-FS group, mice received two doses of $5x10^9$ vp at a three-week interval. For the sham control mice, an HD-Ad empty vector (HD-Ad-control; single-control and boost-control) was used at the same doses and time points. Three weeks after the last vaccination, mice were euthanized, and bronchoalveolar lavages (BALs) and sera were collected. We chose $5x10^9$ vp for both single-dose and prime-boost regimens because this dosage had been shown to induce robust immune protection against SARS-CoV-2 infection with a HD-Ad vector expressing RBD in our previous study (23).

We measured the FS-specific secretory IgA (sIgA) level in BAL by enzyme-linked immunosorbent assay (ELISA). High levels of sIgA were detected in BALs of the mice vaccinated with single-FS,

10.3389/fimmu.2024.1430928

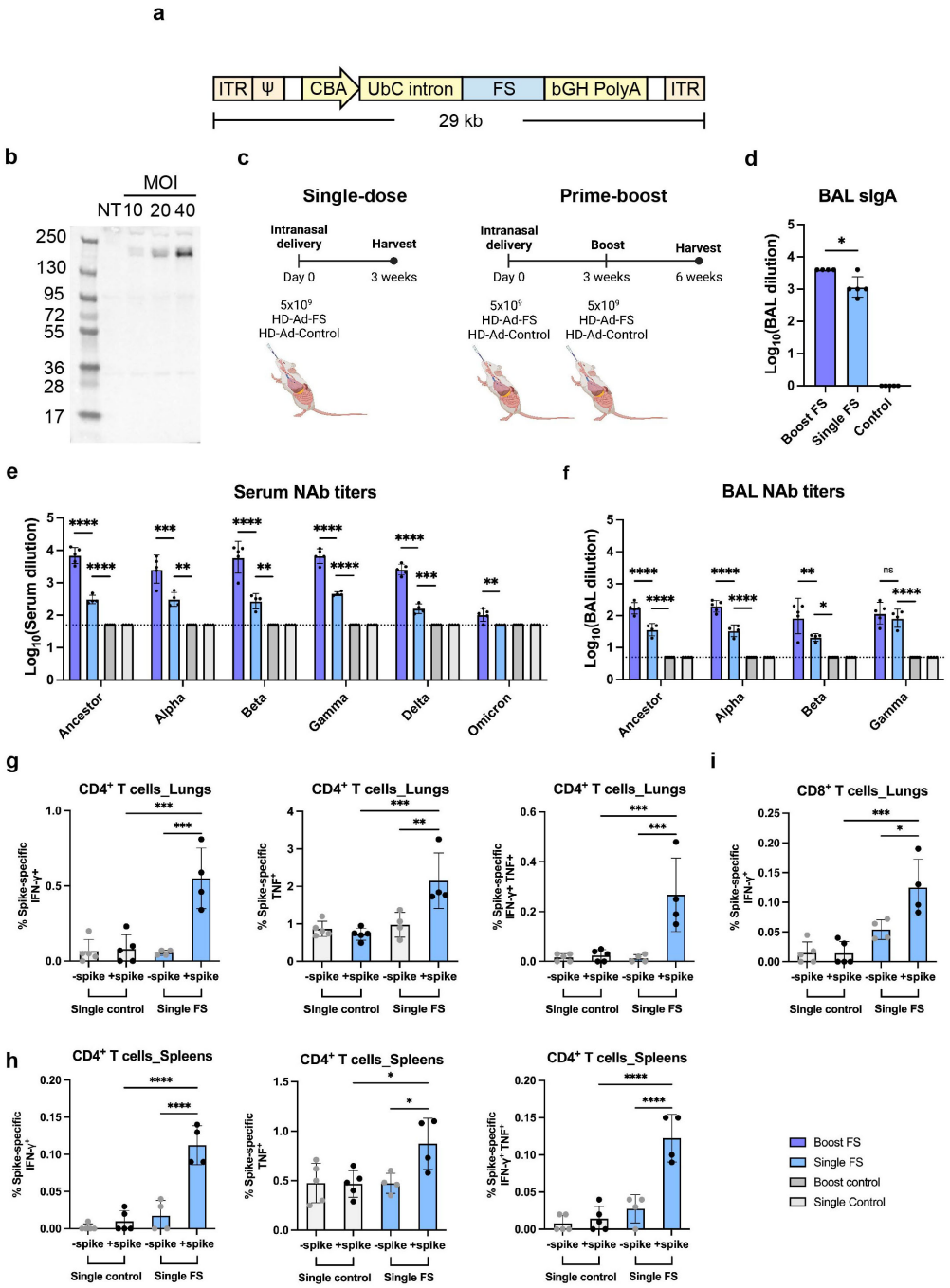

FIGURE 1
HD-Ad-FS induced efficient systemic and mucosal immunities in BALB/c mice. **(A)** Schematic of HD-Ad-FS vaccine. ITR, inverted terminal repeats; Ψ, adenoviral packaging signal; CBA, promoter of chicken beta-actin gene; UbC intron, first intron of ubiquitin C gene; FS, full-length spike gene of SARS-CoV-2 ancestral strain; bGH PolyA, polyadenylation tail of bovine growth hormone gene. **(B)** Western blot analysis of FS protein expression. IB3-1 cells were transduced with HD-Ad-FS at the indicated MOI, and proteins were harvested at day 3 post-transduction. **(C)** Schematic timelines of BALB/c mouse experiments. BALB/c mice were intranasally administered with HD-Ad-FS or HD-Ad-control at single-dose ($5x10^9$ vp) and prime-boost regimens ($5x10^9$ + $5x10^9$ vp, three weeks interval). Three weeks after the last administration, animal samples were harvested. **(D)** Levels of FS-specific sIgA responses in BALs were determined with Enzyme-linked immunosorbent assay (ELISA). The starting dilution factor was 1:1. **(E, F)** Neutralization of live SARS-CoV-2 and VOCs infection by sera **(E)** and BALs **(F)**. The Omicron used in this study was BA.1.18. The starting dilution factors were 1:50 and 1:5 for sera and BALs, respectively. **(G)** $CD4^+$ T cell responses in the lungs of single-dose mice were measured by the production of IFN-γ (left), TNF (middle), and double-positive IFN-γ and TNF (right) at 3 weeks post-immunization, following *ex vivo* stimulation with spike antigen. **(H)** The production of IFN-γ (left), TNF (middle), and double-positive IFN-γ and TNF (right) in $CD4^+$ T cells in the spleens of single-dose mice were measured at 3 weeks post-immunization, following *ex vivo* stimulation with spike antigen. **(I)** IFN-γ producing $CD8^+$ T cells in the lungs of single-dose mice were measured by *ex vivo* stimulation with spike antigen. In all figures, dots represent individual mice (n=4 or 5). The dotted lines represent the limit of detection (LOD) of the assays. Statistical analyses were performed by one-way ANOVA. Bars and errors represent the geometric mean with geometric SD. *p<0.05, **p<0.01, ***p<0.001, ****p<0.0001, and ns, not significant. Data represent one independent animal experiment with indicated biological replicates.

with a further increase observed after the booster dose (Figure 1D), indicating that both regimens induced sIgA in the airway. The reciprocal geometric mean titers (GMTs) of sIgA were 1148.7 and 3981 in single-FS and boost-FS mice, respectively (Figure 1D). FS-specific sIgA was not detectable in BALs from HD-Ad-control treated mice (Figure 1D).

The levels of NAbs against SARS-CoV-2 and the VOCs in sera and BALs were measured with a 50% tissue culture infectious dose ($TCID_{50}$) neutralization assay. We observed that the single-FS induced NAbs against SARS-CoV-2 in both sera and BALs, and that the boost-FS significantly enhanced the effect (Figures 1E, F). Moreover, we found that both HD-Ad-FS regimens induced cross-reactive NAbs against the variants. In single-FS mice, the reciprocal GMTs for the serum NAbs against SARS-CoV-2, Alpha, Beta, Gamma, and Delta were 303.9, 306.5, 268.9, 456.6, and 158.5, respectively, while the titer of the NAb against Omicron (BA.1.18 used in this study) was undetectable (Figure 1E). Boost-FS mice had ~1.5 log-fold increase in serum NAb titers against SARS-CoV-2 and all the variants (Figure 1E). In BALs of single-FS mice, the NAb titers were 36.6 (SARS-CoV-2), 33.5 (Alpha), 20.8 (Beta), and 82.9 (Gamma, Figure 1F). The NAb titers in BALs of boost-FS mice were similarly increased by ~1 log-fold compared to single-FS mice against SARS-CoV-2 and the variants (Figure 1F). There were not enough BAL samples to test NAb levels against Delta and Omicron. Both sera and BALs from HD-Ad-control treated mice showed undetectable NAb levels. These results suggest that intranasal vaccination with HD-Ad-FS can elicit a robust NAb response in both sera and the airway.

We examined spike-specific T cell responses in the lungs and spleens of single-dose BALB/C mice three weeks post-immunization. In the lungs, single-FS induced significantly increased numbers of IFN-γ^+ $CD4^+$ and TNF^+ (formerly known as TNF-α) $CD4^+$ T cells compared to the control (Figure 1G). Spike-specific IFN-γ^+ TNF^+ double-positive $CD4^+$ T cells were also identified in the lungs of single-FS mice (Figure 1G). In addition, in the spleens, single-FS significantly increased the populations of IFN-γ^+ $CD4^+$ and TNF^+ $CD4^+$ T cells (Figure 1H). Spike-specific IFN-γ^+ TNF^+ double-positive $CD4^+$ T cells were also detected in the spleens of single-FS mice (Figure 1H). Moreover, we identified a significantly elevated number of IFN-γ^+ $CD8^+$ T cells (Figure 1I). These results indicated that in single-FS mice, Th1-type responses were induced in the lungs and spleens, and a cytotoxic $CD8^+$ T cell response was elicited in the lungs.

Single-dose HD-Ad-FS protects hACE2 mice from SARS-CoV-2 infection

The hACE2 mice express human angiotensin I-converting enzyme 2 (hACE2) under the cytokeratin 18 (K18) gene promoter, and they develop severe disease upon SARS-CoV-2 infection (29). To examine the protective efficacy of single-dose HD-Ad-FS, we intranasally immunized hACE2 mice (n=12) with HD-Ad-FS (single-FS) or sham HD-Ad-control (single-control) at a dose of $5x10^9$ vp. At day 21 post-vaccination, the immunized hACE2 mice were intranasally challenged with SARS-CoV-2 at $1x10^5$ $TCID_{50}$. At day 3 post-infection (dpi), the hACE2 mice were euthanized, and serum, lung, spleen, and heart samples were harvested for analysis (Figure 2A).

The levels of viral RNA and infectious virus in the airway were measured with real-time quantitative PCR (RT-qPCR) and $TCID_{50}$ assays, respectively. In single-FS hACE2 mice, the viral RNA was undetectable in oropharyngeal swabs (Figure 2B). In contrast, the viral RNA was at high levels ($\geq 10^6$ copies/swab) in single-control hACE2 mice (Figure 2B). Moreover, the levels of viral RNA in the lungs were significantly lower in single-FS hACE2 mice ($2.3x10^3$ copies/mg tissue) than in single-control mice ($2.0x10^8$ copies/mg tissue, Figure 2C). Notably, the titers of infectious virus were undetectable in the lungs of single-FS hACE2 mice, while the titers were very high ($2.6x10^9$ $TCID_{50}$/g lung) in the lungs of single-control hACE2 mice (Figure 2D). These results show that SARS-CoV-2 could not replicate in the airway of single-FS vaccinated hACE2 mice. Additionally, there was no significant difference in the levels of viral RNA in the spleens of single-FS and single-control hACE2 mice, and the viral RNA in the hearts of single-FS hACE2 mice were undetectable or very low at 3 dpi (Figure 2E).

The titers of FS-specific IgG and NAb in serum were measured by ELISA and $TCID_{50}$ assays, respectively. Significantly higher titers of IgG (reciprocal GMT $2.0x10^6$) were detected in single-FS hACE2 mice compared to single-control hACE2 mice (79.4, Figure 2F). In addition, the NAb titers were 480.9 (SARS-CoV-2), 182.6 (Alpha), 182.3 (Beta), 165.5 (Gamma), and 228.6 (Delta) in single-FS hACE2 mice, whereas the NAb titers were undetectable or very low in single-control hACE2 mice (Figure 2G). The titer of NAb against Omicron was undetectable in single-FS hACE2 mice. These findings suggests that intranasal HD-Ad-FS vaccination could elicit NAbs in the sera, effectively protecting hACE2 mice from SARS-CoV-2 infection.

Prime-boost HD-Ad-FS protects the lungs of hACE2 mice from SARS-CoV-2 VOCs

The antibody-escape mutations and deletions in VOCs, particularly in the Beta, Delta, and Omicron strains, has resulted in reduced sensitivity to the neutralizing antibody elicited by COVID-19 vaccines (25, 30, 31). Therefore, we aimed to investigate whether intranasal administration of HD-Ad-FS could confer protection against these variants. hACE2 mice (n=36, equal ratio of sex) were intranasally immunized with a prime-boost regimen ($5x10^9$ + $5x10^9$ vp) of HD-Ad-FS (boost-FS) or HD-Ad-control (boost-control) at a three-week interval. Three weeks after the boost dose, the hACE2 mice were divided into three groups (n=12/group) and intranasally challenged with SARS-CoV-2 VOCs Beta, Delta, or Omicron at $1x10^5$ $TCID_{50}$. At 4 dpi, the hACE2 mice were euthanized, and lung, serum, and BAL samples were harvested (Figure 3A). Due to anesthetic issues, some hACE2 mice (n=3 in Beta, n=1 in Delta, and n=2 in Omicron group) died immediately after challenging with the variants. Although, disease signs typically occur in hACE2 mice at 5 dpi we harvested tissues at 4 dpi. This allowed us to investigate the ability of HD-Ad-FS to control the viral

10.3389/fimmu.2024.1430928

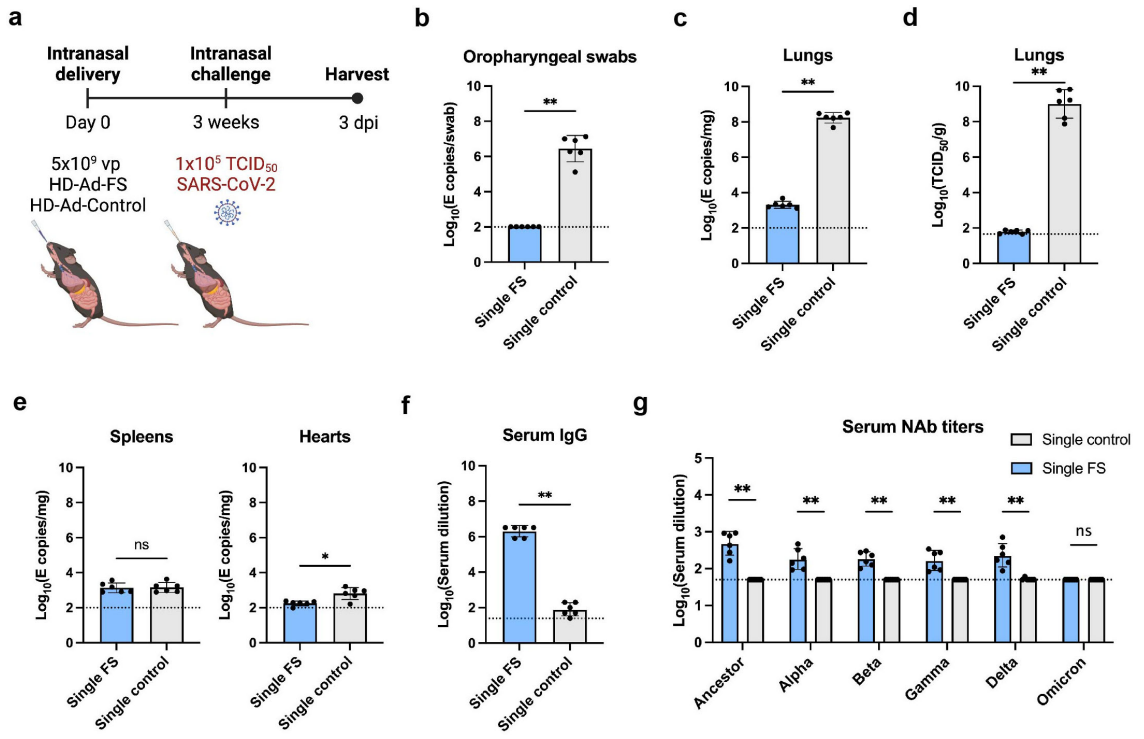

FIGURE 2
Vaccination of single-dose HD-Ad-FS protected hACE2 mice from SARS-Cov2 in the upper airway and lungs. **(A)** Schematic timeline of single-dose hACE2 experiment. The hACE2 mice were immunized with a single-dose of HD-Ad-FS (single-FS) or HD-Ad-control (single-control) at $5x10^9$ vp via intranasal delivery. Three weeks after immunization, the hACE2 mice were intranasally challenged with SARS-CoV-2 at $1x10^5$ $TCID_{50}$. Animal samples were harvested at day 3 post-infection (dpi). **(B)** RNA levels of SARS-CoV-2 in oropharyngeal swabs were determined with RT-qPCR. **(C)** RNA levels of SARS-CoV-2 in the lungs were determined with RT-qPCR. **(D)** The titers of infectious SARS-CoV-2 in the lungs were measured with $TCID_{50}$ assay. **(E)** RNA levels of SARS-CoV-2 in the spleens (left) and hearts (right) were measured with RT-qPCR. **(F)** FS-specific IgG response in serum were determined with ELISA. The starting dilution was 1:25. **(G)** Serum neutralizing activities against SARS-CoV-2 and VOCs were measured with neutralization assays. Dots represent individual mice (n=6). The dotted lines represent the LOD of the assays. For RT-qPCR, the LOD was set to 100 E copies/sample. Statistical analyses were performed by Mann-Whitney test, two-tailed. Bars and errors represent geometric mean with geometric SD. *p<0.05, **p<0.01, and ns, not significant. Data represent one independent animal experiment with indicated biological replicates.

replication during the initial stages of infection, before the onset of disease symptoms.

The body weights of hACE2 mice were recorded at 0 (pre-infection) and 4 dpi. In boost-FS hACE2 mice, they all gained weight from 0 to 4 dpi: 1.8% (Beta), 2.6% (Delta), and 1.3% (Omicron, Figure 3B). However, the weight difference was not statistically significant between boost-FS and boost-control hACE2 mice in each variant group (Figure 3B). Additionally, there was no significant difference in weight change between male and female hACE2 mice in each group (Supplementary Figure 1).

The levels of viral RNA and infectious virus in the lungs were measured with RT-qPCR and $TCID_{50}$ assays, respectively, at 4 dpi. The viral RNA level was undetectable (3/4 in Beta, 4/6 in Delta, and 3/5 in Omicron group) or very low in the lungs of boost-FS hACE2 mice. In contrast, high levels of viral RNA ($6.1x10^5$ in Beta, $1.1x10^5$ in Delta, and $2.5x10^6$ copies/mg in Omicron) were detected in the lungs of boost-control hACE2 mice (Figure 3C). In addition, the infectious virus was at very low levels in the lungs of boost-FS hACE2 mice, whereas high levels ($2.5x10^4$ in Beta, $1.4x10^6$ in Delta, and $6.0x10^3$ $TCID_{50}$/g lung in Omicron group) were detected in the lungs of boost-control hACE2 mice (Figure 3D). There was no significant difference in viral RNA levels in the lung between male and female mice in each VOC group (Supplementary Figure 2A). Furthermore, there was no difference in the levels of viral RNA from oropharyngeal swabs between boost-FS and boost-control hACE2 mice at 4 dpi (Supplementary Figure 3). These results suggest that prime-boost HD-Ad-FS protects against VOC infection in the lungs but not in the upper airway.

The levels of FS-specific IgG and sIgA were measured with ELISA at 4 dpi. In boost-FS hACE2 mice, the IgG titers were significantly elevated in sera and BALs, compared to boost-control hACE2 mice (Figures 3E, F). Specifically, in boost-FS hACE2 mice, the IgG reciprocal GMTs in sera were $1.9x10^7$ (Beta), $2.9x10^7$ (Delta), and $1.2x10^7$ (Omicron), and those in the BALs were $1.7x10^4$ (Beta), $1.1x10^4$ (Delta), and $4.6x10^4$ (Omicron). Notably, sIgA was also induced in the BALs of boost-FS hACE2 mice, with reciprocal GMTs of 141.4 (Beta), 126.0 (Delta), and 174.1 (Omicron, Figure 3G). There was no significant difference in the levels of sIgA between male and female mice in each variant group (Supplementary Figure 4A).

The titers of NAbs in sera and BALs were measured with the $TCID_{50}$ neutralization assay at 4 dpi. Compared to boost-control hACE2 mice, serum NAbs were only significantly increased in Delta-challenged boost-FS hACE2 mice (Figure 3H). However, in

10.3389/fimmu.2024.1430928

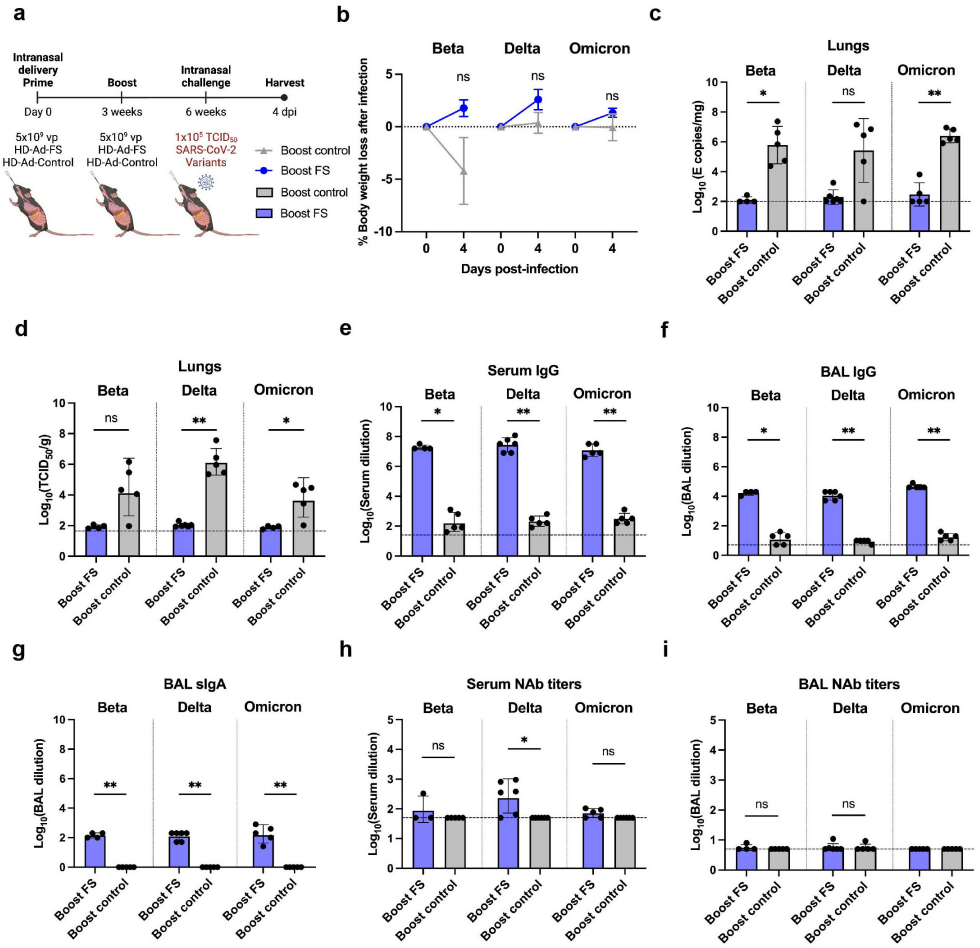

FIGURE 3
Prime-boost vaccination of HD-Ad-FS protected hACE2 mice from SARS-CoV-2 VOCs in the lungs. **(A)** Schematic timeline of prime-boost hACE2 experiment. The mice were intranasally administered with a prime-boost regimen of HD-Ad-FS or HD-Ad-control ($5x10^9$ + $5x10^9$ vp, three-week interval). Three weeks after the boost dose, the mice were intranasally challenged with a SARS-CoV-2 variant (Beta, Delta, or Omicron) at $1x10^5$ $TCID_{50}$. Animal samples were harvested at 4 dpi. **(B)** Body weight was recorded at 0 (pre-challenge) and 4 dpi after challenge. **(C)** SARS-CoV-2 variant RNA levels in the lungs were measured with RT-qPCR. **(D)** The titers of infectious SARS-CoV-2 variant in the lungs were determined with $TCID_{50}$ assays. **(E, F)** The titers of FS-specific IgG in sera **(E)** and BALs **(F)** were determined with ELISA. The starting dilution factors were 1:25 and 1:5 for sera and BALs, respectively **(G)** The titers of FS-specific sIgA in BALs were measured with ELISA. The starting dilution factor was 1:1. **(H, I)** Neutralizing activities in sera **(H)** and BALs **(I)** against SARS-CoV-2 variants were determined with neutralization assays. Dots represent individual mice (n=4, 5, or 6). For **(C-F, H, I)**, the horizontal dotted lines represent the LOD of the assays. For **(B)**, statistical analyses were performed by two-way ANOVA. Error bars represent mean ± s.e.m. For **(C-I)**, statistical analyses were performed by Mann-Whitney test, two-tailed. Error bars represent geometric mean with geometric SD. *p<0.05, **p<0.01, and ns, not significant. Data represent one independent animal experiment with indicated biological replicates.

all the VOC groups, the BAL NAbs were not increased significantly in boost-FS hACE2 mice compared to boost-control hACE2 mice (Figure 3I). There was no significant difference in either serum or BAL NAbs between male and female mice in each VOC group (Supplementary Figures 4B, C).

Single-dose HD-Ad-FS protects hamsters from SARS-CoV-2 infection

The protective efficacy of HD-Ad-FS was further examined in hamsters, which are susceptible to SARS-CoV-2 infection and can develop pathology similar to that of COVID-19 patients (32). The hamsters (n=32, equal ratio of sex) were intranasally immunized with a single dose of HD-Ad-FS (single-FS) or HD-Ad-control (single-control) at $5x10^9$ vp. At day 21 post-vaccination, the hamsters were intranasally challenged with SARS-CoV-2 at $1x10^5$ $TCID_{50}$. Hamsters were euthanized at 4 (n=12) and 14 (n=20) dpi, and oropharyngeal swab, serum, lung, spleen, and heart samples were collected and analyzed (Figure 4A).

The body weight of hamsters was monitored for 14 days following SARS-CoV-2 infection and compared to their pre-infection weight. In single-FS hamsters, the average weight mildly decreased between 1 and 3 dpi but then increased and exceeded the pre-infection levels between 4 and 14 dpi (Figure 4B). However, single-control hamsters had sustained weight loss between 1 and 9

10.3389/fimmu.2024.1430928

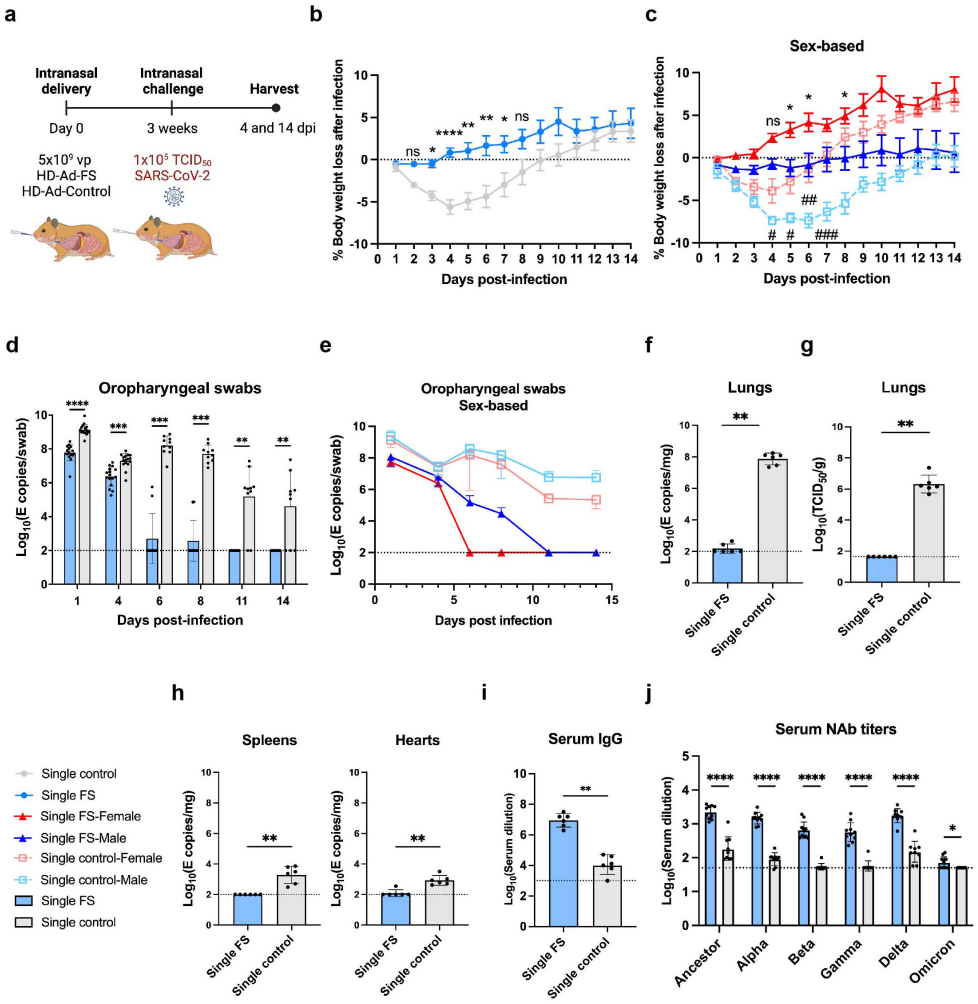

FIGURE 4
Single-dose vaccination of HD-Ad-FS protected hamsters against SARS-CoV-2 in the upper airway and lungs. **(A)** Schematic timeline of single-dose hamster experiment. Hamsters were immunized with a single-dose of HD-Ad-FS or HD-Ad-control at $5x10^9$ vp via intranasal route. Three weeks after immunization, hamsters were intranasally challenged with SARS-CoV-2 at $1x10^5$ $TCID_{50}$. Animal samples were harvested at 4 and 14 dpi. **(B, C)** Body weight was monitored at the indicated days after challenging with SARS-CoV-2. For **(C)**, the change of weight in male and female hamsters were analyzed separately. **(D, E)** RNA levels of SARS-CoV-2 from oropharyngeal swabs were determined with RT-qPCR. Swabs were collected at the indicated time points. For **(E)**, the levels of viral RNA in male and female hamsters were analyzed separately. **(F)** RNA levels of SARS-CoV-2 in lungs were determined with RT-qPCR at 4 dpi. **(G)** The titers of infectious SARS-CoV-2 in lungs were determined with $TCID_{50}$ assays at 4 dpi. **(H)** RNA levels of SARS-CoV-2 in spleens (left) and hearts (right) were measured with RT-qPCR at 4 dpi. **(I)** The titers of FS-specific IgG in sera were measured with ELISA at 4 dpi. The starting dilution factor was 1:1000. **(J)** Serum NAb activities against SARS-CoV-2 and variants were determined with neutralization assays at 14 dpi. Dots represent individual hamsters (4 dpi, n=6; 14 dpi, n=9 or 10). For **(D-J)**, the horizontal dotted lines represent the LOD of the assays. For **(B, C)**, statistical analyses were performed by two-way ANOVA; error bars represent mean ± s.e.m. For **(D, E)**, statistical analyses were performed by two-way ANOVA; error bars represent geometric mean with geometric SD. For **(F-J)**, statistical analyses were performed by Mann-Whitney test, two-tailed. Error bars represent geometric mean with geometric SD. For **(C)**, the asterisk signs represent statistical analyses in single-FS hamsters, and the pound signs represent statistical analyses in single-control hamsters. */# p<0.05, **/## p<0.01, ***<0.001, ****/####p<0.0001, and ns, not significant. Data represent one independent animal experiment with indicated biological replicates.

dpi (Figure 4B). Specifically, the most severe weight loss was 0.5% in single-FS hamsters at 3 dpi, as compared to 5.6% in single-control hamsters at 4 dpi (Figure 4B). The weight change observed in single-FS hamsters indicates the potential efficacy of HD-Ad-FS in preventing severe disease and promoting recovery following SARS-CoV-2 infection. Sex-based analysis showed that male hamsters in both single-FS and single-control groups had significantly more severe weight loss than female hamsters (Figure 4C).

Viral RNA levels in oropharyngeal swabs were measured with RT-qPCR. In single-FS hamsters, viral RNA was undetectable in 8 out of 10 swabs at 6 dpi and in all swabs at 11 dpi (Figure 4D). In contrast, in single-control hamsters, high levels of viral RNA ($2.7x10^7$ copies/swab) were detected in all swabs at 6 dpi and the levels remained elevated in 8 out of 10 swabs at 11 dpi (Figure 4D). These findings indicated that single-FS could reduce SARS-CoV-2 infection and replication in the upper airway. In addition, sex-based

analysis indicated that in female HD-Ad-FS hamsters viral RNA levels decreased more rapidly and became undetectable earlier than those in male hamsters (Figure 4E). In the single-control group, viral RNA levels were high in both male and female hamsters after infection, with male hamsters having slightly higher levels than female hamsters (Figure 4E).

The levels of viral RNA and infectious virus in the lungs were determined with RT-qPCR and $TCID_{50}$ assays, respectively, at 4 dpi. The viral RNA was either undetectable (4/6) or very low ($3.6x10^2$ copies/mg) in single-FS hamsters, whereas the viral RNA levels were high ($9.5x10^7$ copies/mg) in all single-control hamsters (Figure 4F). Furthermore, infectious virus was undetectable in single-FS hamsters, whereas substantial levels of infectious virus were detected in all single-control hamsters (Figure 4G). These findings indicate that single-FS could effectively prevent SARS-CoV-2 infection and replication in the lungs. Sex-based analysis showed no significant difference in viral RNA (Supplementary Figure 5A) or infectious virus levels (Supplementary Figure 5B) between male and female hamsters.

The levels of viral RNA in the spleens and hearts were also measured with RT-qPCR at 4 dpi. Viral RNA was undetectable in the spleens and hearts of single-FS hamsters (5/6), but it was detectable in all single-control hamsters (Figure 4H). These findings indicate that single-FS could prevent systemic spread of SARS-CoV-2. Furthermore, sex-based analysis showed that male single-control hamsters had significantly higher levels of viral RNA in the spleens compared to female hamsters. However, there was no significant difference in the levels of viral RNA in the hearts between male and female hamsters in each treatment (Supplementary Figure 5C).

The levels of FS-specific IgG and NAbs in serum were measured with ELISA at 4 dpi and by $TCID_{50}$ neutralization assays at 14 dpi, respectively. The level of serum IgG was increased significantly in single-FS hamsters (reciprocal GMTs $9.0x10^6$) compared to single-control hamsters (Figure 4I). Additionally, the NAb levels against SARS-CoV-2 were significantly higher in single-FS hamsters (ID_{50}: 2184.3) compared to single-control hamsters (Figure 4J). Notably, in single-FS hamsters, the serum NAbs cross-reacted with the Alpha (1463.4), Beta (647.2), Gamma (562), Delta (1731.9), and Omicron VOCs (71.3, Figure 4J). The presence of serum IgG and NAbs indicate that intranasally delivered single-FS could elicit a systemic antibody response. There were no significant differences in the serum NAb levels between male and female hamsters in each treatment, except that the titers of female hamsters were significantly higher than those of male hamsters in the single-control group after SARS-CoV-2 infection (Supplementary Figure 5D). We did not measure sIgA levels in hamsters as there were no commercially available antibodies for hamster IgA at the time of the experiment.

The presence and distribution of SARS-CoV-2 in the lungs after challenge was investigated with RNA *in situ* hybridization at 4 and 14 dpi. With the antisense probe, a positive signal was nearly absent in the lungs of single-FS hamsters at 4 dpi, whereas a strong signal was observed in the lungs of single-control hamsters, particularly in bronchial and bronchiolar epithelial cells, alveoli, and interalveolar

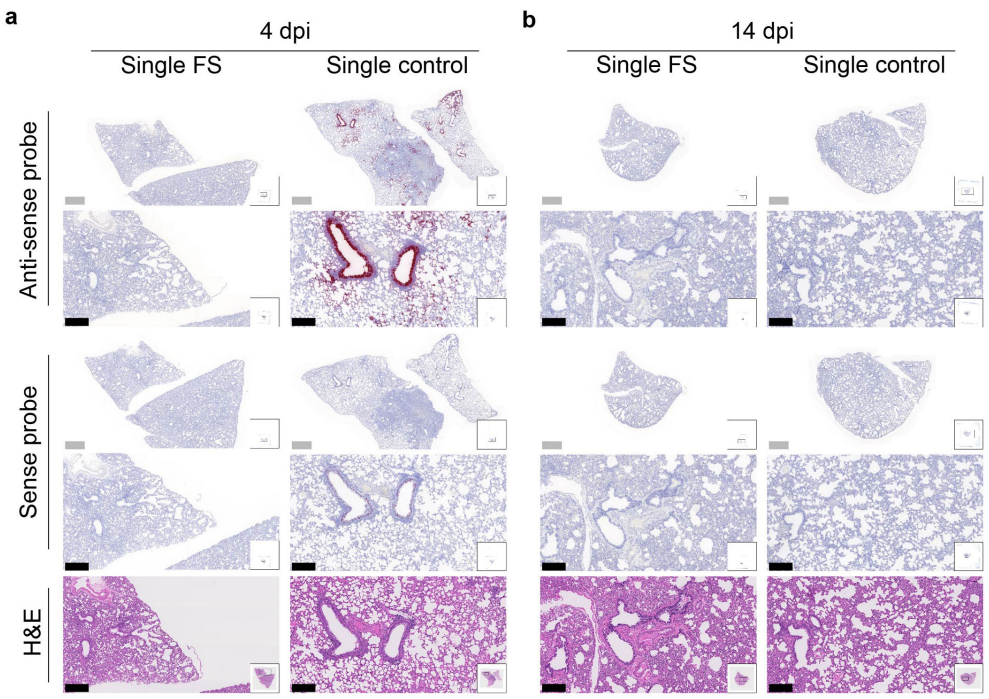

FIGURE 5
Histopathology of SARS-CoV-2 infection in the lungs of single-dose HD-Ad-FS immunized hamsters. **(A, B)** The presence of SARS-CoV-2 RNA in lung sections was detected with RNAscope *in situ* hybridization at 4 **(A)** and 14 dpi **(B)**. Hematoxylin and eosin staining (H&E, 5th row) was performed with lung sections of the indicated conditions. Continuous lung sections were used for staining. Scale bars = 200 (grey bar) or 1000 (black bar) μm. Images are representatives of n=2 per group. Data represent one independent animal experiment with indicated biological replicates.

septa (Figure 5A). With the sense probe, the signal was almost undetectable in single-FS hamsters at 4 dpi, but a moderate signal level was observed in single-control hamsters, especially in bronchial epithelial cells (Figure 5A). There was no obvious signal observed in the lungs of single-FS and single-control hamsters at 14 dpi (Figure 5B). These findings show that single-FS could protect hamsters from SARS-CoV-2 infection and replication in the lung.

Prime-boost HD-Ad-FS protects the lungs of hamsters from SARS-CoV-2 VOC infection

After evaluating the protective efficacy of single-dose HD-Ad-FS, we further investigated the efficacy of prime-boost HD-Ad-FS against the SARS-CoV-2 VOCs Beta, Delta, and Omicron. Hamsters (n=96, equal ratio of sex) were intranasally immunized with a prime-boost dose ($5x10^9$ + $5x10^9$ vp) of HD-Ad-FS (boost-FS) or HD-Ad-control (boost-control) at a three-week interval (Figure 6A). Three weeks after the boost dose, the hamsters were divided into three groups (n=32/group) and intranasally challenged with Beta, Delta, or Omicron at $1x10^5$ $TCID_{50}$. Due to a housing issue, one hamster (from the Omicron group) died prior to the challenge. At 4 (n=12/group) and 14 (n=19 or 20/group) dpi, the hamsters were euthanized, and serum, BAL, and lung samples were collected and analyzed.

The body weight of hamsters was monitored daily after infection and compared to their pre-infection weight. Both boost-FS and boost-control hamsters experienced weight loss after VOC challenge (Figures 6B, C, D). However, the boost-FS hamsters had significantly less weight loss compared to the boost-control hamsters in each group (Figures 6B–D). These findings suggest that the HD-Ad-FS could alleviate the morbidity caused by VOC infection in hamsters. Sex-based analysis showed that hamsters of the same sex in the boost-FS group had significantly less weight loss than hamsters in the boost-control group after challenge (Supplementary Figure 6).

The levels of viral RNA in the upper airway were measured from oropharyngeal swabs with RT-qPCR. At 4 dpi, the viral RNA levels in the swabs from boost-FS hamsters were significantly lower than those of the boost-control hamsters in each group (Supplementary Figure 7). However, viral RNA remained at high levels from 4 to 14 dpi in boost-FS hamsters (Supplementary Figure 7).

The levels of viral RNA and infectious virus in the lungs were measured with RT-qPCR and $TCID_{50}$ assays, respectively, at 4 and 14 dpi. At 4 dpi, viral RNA was either undetectable or at very low levels ($<10^2$ copies/mg) in boost-FS hamsters, while it was at high levels ($>10^4$ copies/mg) in boost-control hamsters in each group (Figure 6E). Notably, at 14 dpi, viral RNA was still undetectable or at very low levels ($<10^2$ copies/mg) in boost-FS hamsters (Figure 6E). Moreover, the infectious virus was undetectable or at very low levels in boost-FS hamsters at 4 and 14 dpi (Figure 6F). In contrast, the titers of infectious virus were high in boost-control hamsters at 4 dpi (Figure 6F). There were no significant differences in the levels of infectious virus between male and female hamsters in each group (Supplementary Figure 8A). These results, combined with the results of viral mRNA levels from oropharyngeal swabs, indicate that the boost-FS could protect hamsters from VOC infection and replication in the lungs, although it may not completely prevent infection in the upper airway.

The levels of FS-specific IgG in sera and BALs were measured with ELISA at 4 dpi. The IgG titers were significantly higher in sera and BALs of all the boost-FS hamsters compared to the boost-control hamsters in each group (Figures 6G, H). Specially, in boost-FS hamsters, the reciprocal serum IgG GMTs were $1.1x10^6$ (Beta), $2.4x10^7$ (Delta), and $1.6x10^7$ (Omicron, Figure 6G). The reciprocal BAL IgG GMTs were $1.4x10^4$ (Beta), $1.3x10^4$ (Delta), and $1.1x10^4$ (Omicron) in boost-FS hamsters (Figure 6H).

The titers of NAbs in sera and BALs were measured with $TCID_{50}$ neutralization assays at 4 and 14 dpi. For the serum NAbs, at 4 dpi, elevated titers were only detected in boost-FS hamsters (Figure 6J). Specifically, in boost-FS hamsters, the serum NAb titers were 448.4 (Beta), 785.2 (Delta), and 97.4 (Omicron, Figure 6I). At 14 dpi, elevated serum NAb titers were detected in both boost-FS and boost-control hamsters, but the NAb titers were significantly higher in boost-FS hamsters than in boost-control hamsters (Figure 6I). For BAL NAbs, at 4 dpi, a significantly increased titer was detected only in the Delta group (3/6) of boost-FS hamsters (Figure 6J). The levels of serum (Supplementary Figure 8B) and BAL (Supplementary Figure 8C) NAbs were significantly higher in female hamsters than male hamsters in the Delta group of boost-FS hamsters at 4 dpi.

RNA *in situ* hybridization was conducted to assess the presence of VOCs in the lungs of hamsters at 4 and 14 dpi. With the antisense probe, the signal was nearly absent in the lungs of boost-FS hamsters in each group at 4 dpi (Figures 7A-C). Conversely, strong and abundant signal was detected in the lungs of boost-control hamsters at 4 dpi, particularly in bronchial and bronchiolar epithelial cells, alveoli, and interalveolar septa (Figures 7A-C). We did not observe obvious signal in the lungs of boost-FS or boost-control hamsters at 14 dpi (Figures 7D-F). These findings suggest that boost-FS could inhibit VOC infection and replication in the lungs of hamsters.

Discussion

The present study evaluates the efficacy of a HD-Ad-based COVID-19 vaccine candidate (HD-Ad-FS) through intranasal administration in mice and hamsters. The HD-Ad-FS encodes the full-length spike protein of SARS-CoV-2. Following a single-dose of HD-Ad-FS, immunity against the ancestral SARS-CoV-2 strain was induced systemically as well as in the upper and lower airways. We detected potent NAb levels in sera, as well as robust levels of NAb and sIgA on the airway mucosal surface, the first line of defense against viral entry. Notably, minimal or undetectable levels of infectious virus were found in the upper and lower airways after SARS-CoV-2 challenge. In addition, the prime-boost elicited systemic and lower airway protection against SARS-CoV-2 VOCs in hamsters. Compared to our previous HD-Ad-RBD vaccine (23), the HD-Ad-FS vaccine demonstrates superior humoral and cellular immune responses. In particular, HD-Ad-FS generated higher levels of NAb in the airways and elicited

10.3389/fimmu.2024.1430928

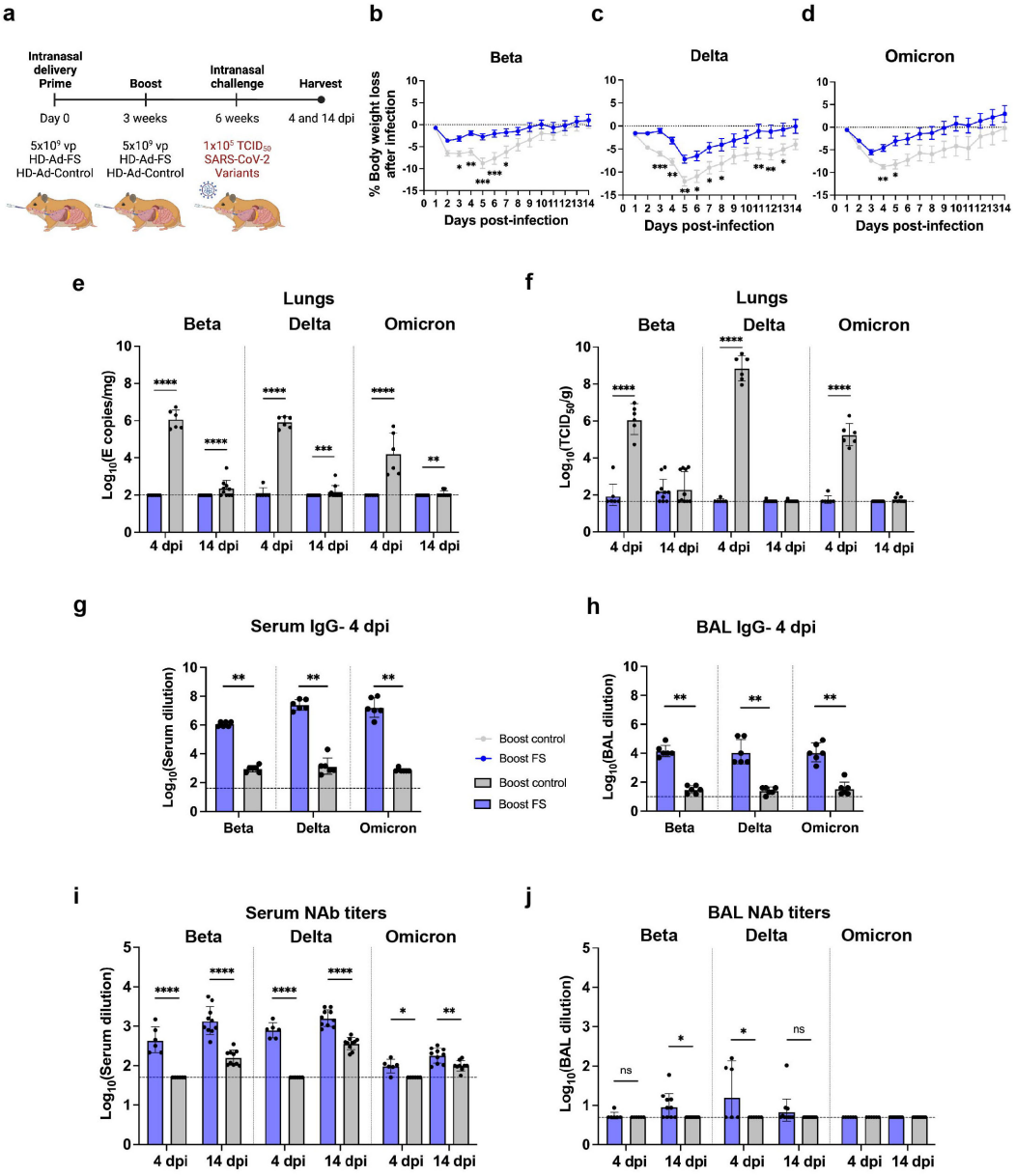

FIGURE 6
Prime-boost vaccination of HD-Ad-FS protected hamster against SARS-CoV-2 VOCs in the lungs. **(A)** Schematic timeline of the hamster experiment. Hamsters were intranasally immunized with a prime-boost regimen of HD-Ad-FS or HD-Ad-control ($5x10^9$ + $5x10^9$ vp, three-week interval). Three weeks after the second dose, the hamsters were intranasally challenged with SARS-CoV-2 variants (Beta, Delta, or Omicron) at $1x10^5$ $TCID_{50}$. **(B-D)** Hamster body weight was monitored at the indicated days after challenging with SARS-CoV-2 variant Beta **(B)**, Delta **(C)**, or Omicron **(D)**. **(E)** RNA levels of SARS-CoV-2 variants in the lungs were determined with RT-qPCR at 4 and 14 dpi. **(F)** Levels of infectious SARS-CoV-2 variants in the lungs were measured with $TCID_{50}$ assay at 4 and 14 dpi. **(G)** The titers of FS-specific IgG in sera were measured with ELISA at 4 dpi. The starting dilution factor was 1:40. **(H)** The titers of FS-specific IgG in BALs were measured with ELISA at 4 dpi. The starting dilution factor was 1:10. **(I)** Serum NAbs against SARS-CoV-2 variants were measured with neutralization assays at 4 and 14 dpi. **(J)** BAL NAbs against the SARS-CoV-2 variants were determined with neutralization assay at 4 and 14 dpi. Dots represent individual hamsters (4 dpi, n=6; 14 dpi, n=9 or 10). For **(E-J)**, the horizontal dotted lines represent the LOD of the assays. For **(B-D)**, statistical analyses were performed by two-way ANOVA; error bars represent mean ± s.e.m. For **(E, F)**, statistical analyses were performed by two-way ANOVA; error bars represent geometric mean with geometric SD. For **(G-J)**, statistical analyses were performed by Mann-Whitney test, two-tailed; error bars represent geometric mean with geometric SD. *p<0.05, **p<0.01, ***p<0.001, ****p<0.0001, and ns, not significant. Data represent one independent animal experiment with indicated biological replicates.

an increased number of spike-specific IFN-γ^+ $CD4^+$ and IFN-γ^+ $CD8^+$ T cells in the lungs.

The expression and distribution of vaccine-induced NAbs can be affected by immunization routes (11). Given that SARS-CoV-2 is primarily airborne, airway mucosal NAbs are crucial for blocking viral entry and transmission. However, current COVID-19 IM vaccines mainly induce serum neutralizing activity, with limited mucosal activity (11). In contrast, intranasal vaccination has the potential to induce both serum and mucosal NAbs. The induction of mucosal NAbs is likely achieved by providing antigen to lung-

10.3389/fimmu.2024.1430928

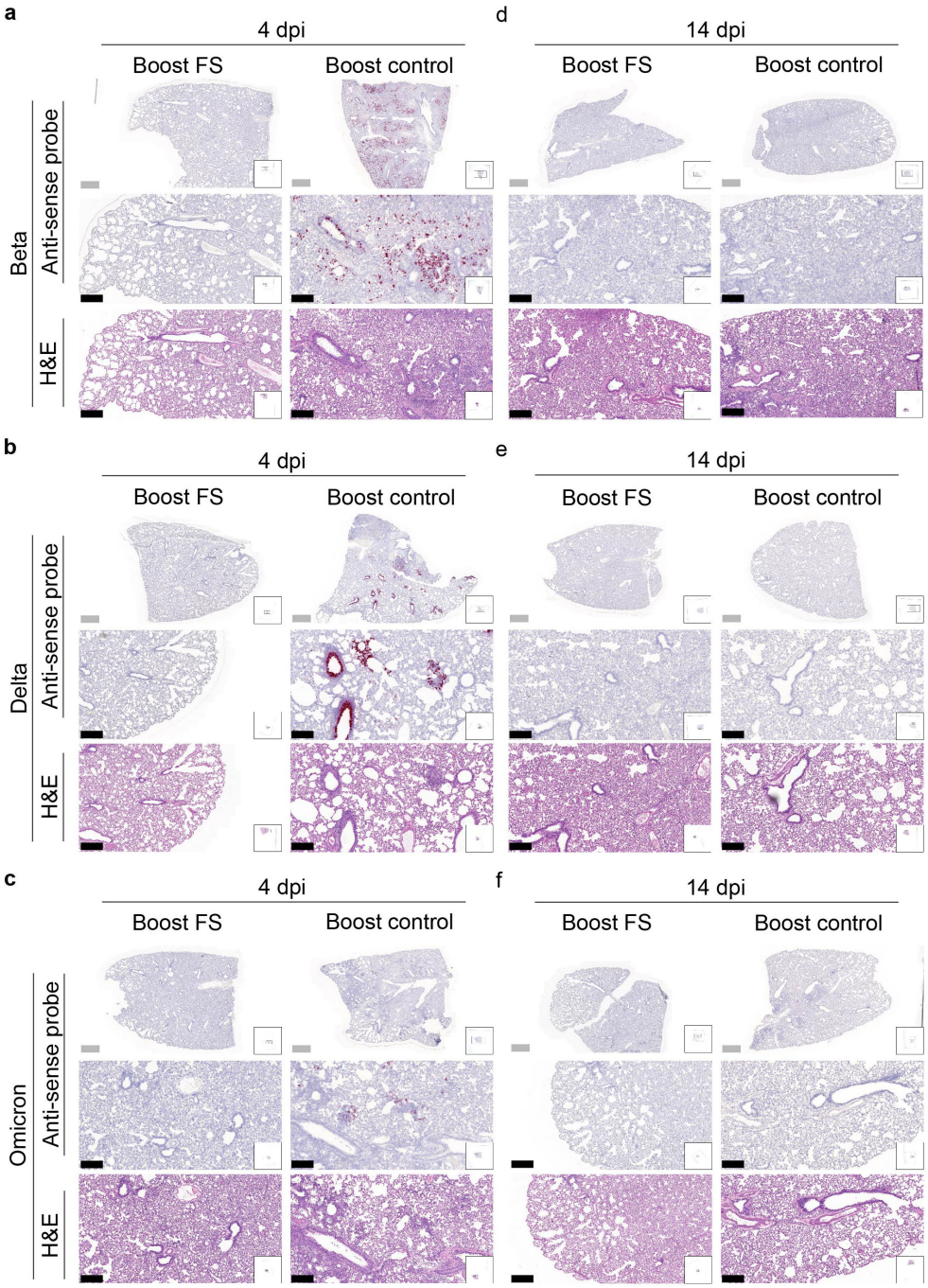

FIGURE 7
Histopathological analysis of SARS-CoV-2 VOC infection in the lungs of prime-boost HD-Ad-FS vaccinated hamsters. **(A-C)** Detection of SARS-CoV-2 variant RNA (Beta, **A**; Delta, **B**; Omicron, **C**) in lung sections with RNA *in situ* hybridization at 4 dpi. **(D-F)** The presence of SARS-CoV-2 variant RNA (Beta, d; Delta, e; Omicron, f) in lung sections with RNA *in situ* hybridization at 14 dpi. Continuous lung sections were used for H&E staining (3rd, 6th, and 9th rows). Scale bars = 200 (grey bar) or 1000 (black bar) μm. Images are representatives of n=2 per group. Data represent one independent animal experiment with indicated biological replicates.

resident T and B cells (15, 33). Indeed, intranasal COVID-19 vaccines have shown promising mucosal immunogenicity in animal models (34–36). For example, a mouse study using an Ad-based vaccine encoding the Omicron BA.1 spike showed that intranasal immunization induced NAbs against BA.1 in both BALs and sera, while IM immunization only induced NAbs in sera (36). Another study using a chimpanzee Ad-based vaccine demonstrated that intranasal immunization elicited serum NAbs and reduced SARS-CoV-2 infection in the upper airway and lungs compared to IM immunization in hamsters (34).

As mentioned above, intranasal administration of HD-Ad-FS induced FS-specific sIgA in the airway. Indeed, airway mucosal sIgA confers protection against respiratory viruses, such as influenza (37) and SARS-CoV-2 (38). In two human studies, the level of sIgA

correlates more strongly with protection against SARS-CoV-2 than the level of serum IgG (39, 40). However, we found that, in prime-boost hamsters and hACE2 mice challenged with VOCs, the levels of VOC mRNA in the upper airways did not differ significantly between vaccinated and unvaccinated animals, whereas the levels of infectious VOCs were undetectable in the lungs of vaccinated animals. These findings indicate that HD-Ad-FS can induce immune protection against VOCs in the lungs but not in the upper airway. The mechanism underlying the varied vaccine efficacies in different parts of the airway is not fully understood. Based on our results, since NAbs were only elicited in the sera of prime-boost vaccinated hamsters, it is likely that serum NAbs are more effective at protecting the lung than the upper airway. Alternately, the T cell response mounted in the lung may be more effective against VOCs than the B cell response in the lung. Supporting this suggestion, the VOC epitopes recognized by $CD4^+$ and $CD8^+$ T cells are better conserved than are the B cell epitopes (41).

We found that HD-Ad-FS vaccinated hamsters had less weight loss and recovered to the pre-infection weight sooner than unvaccinated hamsters. Interestingly, we also observed that male hamsters experienced more weight loss compared to female hamsters, independent of vaccination status, suggesting that sex differences play a role in the severity of the disease. The impact of sex differences on the severity of COVID-19-related disease has been observed in animal studies (42, 43) as well as in clinical studies (44, 45). Males have a higher percentage of severe disease (45) and a higher fatality rate compared to females (44). Although the exact mechanism determining the sex differences is still unknown, studies indicate that sex differences in the immune responses could be important (42, 45). For example, a study showed that activated $CD4^+$ and $CD8^+$ T cells were more abundant in the sera of female patients, while male patients had lower levels of these T cells (45). In a study using hACE2 mice, male mice had a higher fatality rate than female mice, with inflammatory cytokines and chemokines significantly increased in the lungs of the male mice (42).

The weight loss caused by the Omicron variant in other hamster studies is significantly less than that observed for the sublineage (Supplementary Table 1) used in our work (46–48). Given that the challenge dose used in our study was lower than those used in the aforementioned studies, we speculate that the difference in Omicron induced weight loss could be attributed to the varying infectivity of different Omicron sublineages.

Clinical studies have provided evidence supporting the safety of intranasal delivery of Ad-based vaccines (49, 50). For instance, a study demonstrated that intranasal delivery of the prime-boost Ad5-based COVID-19 vaccine was well-tolerated in adults (50). Another vaccine, Ad5-nCoV, using the same Ad5 capsid as used in this study, has been approved for use in the COVID-19 pandemic from the World Health Organization (51, 52). Recently, an Ad-based intranasal vaccine, iNCOVACC (phase III trial), has demonstrated promising mucosal immunogenicity, particularly in inducing an sIgA response, and has been granted emergency use authorization in India (53).

The safety of the HD-Ad vector has been established in clinical trials (54). Our group has demonstrated the safety of delivering an HD-Ad vector into the airways using a porcine model (21). We have also demonstrated that a HD-Ad vaccine encoding the RBD of SARS-CoV-2 was safe in mice (23). Here, we extended this finding and demonstrated the safety of HD-Ad-FS in mice and hamsters. Studies have indicated that the SARS-CoV-2 spike protein could potentially cause tissue damage and adverse effects (55, 56). We recognize the importance of comprehensively evaluating the safety profile of HD-Ad-FS vaccines in future studies.

There are limitations in this study. Firstly, the unexpected mortality during anesthesia limited the sample size for the prime-boost hACE2 mice, thereby reducing the statistical power. Secondly, BAL samples from the single-dose hACE2 mice and hamsters were not collected, which precluded a comprehensive assessment of vaccine-induced mucosal immune responses. Thirdly, we did not measure $CD4^+$ and $CD8^+$ tissue-resident memory T cells, which are important in providing rapid response and long-term immunity (57). Additionally, while BALB/c, hACE2, and hamsters were used to assess vaccine efficacy, we appreciate that the immune systems of animals do not precisely represent those of humans. Future research should incorporate nonhuman primates that closely mimic humans. Furthermore, we did not determine the profile of the proinflammatory cytokines and chemokines in lung samples. However, we do not expect high levels of vector-induced proinflammatory cytokines and chemokines since the vector dosage used in this study is 3 to10-fold lower than that used for gene delivery (58). Lastly, this study was conducted over a relatively short duration. A long-term study is needed to monitor vaccine-induced immunity over time.

In conclusion, our study demonstrates the safety and efficacy of an intranasal HD-Ad-FS vaccine in eliciting protective systemic and mucosal immunity against SARS-CoV-2 and VOCs. SARS-CoV-2 is continuously evolving to generate new variants and multivalent vaccines are one approach to addressing this issue (59, 60). With the large capacity (36kb) of the HD-Ad vector, multivalent HD-Ad can be engineered to express multiple variant-specific spike antigens simultaneously. Such multivalent HD-Ad vaccines have the potential to induce broadly neutralizing activities and provide protection in regions where multiple variants are circulating. In addition to SARS-CoV-2, other pathogens, including influenza virus, respiratory syncytial virus, human immunodeficiency virus, and rotavirus, rely on penetrating mucosal barriers for infection. Considering the ability of HD-Ad-FS to generate mucosal immunity, HD-Ad is a promising vaccine platform for these transmitted pathogens. Further research is needed to evaluate the efficacy of HD-Ad as vaccines against evolving SARS-CoV-2 variants and other mucosal pathogens.

Materials and methods

Tissue culture

Vero E6 and Vero-TMPRSS2 cells were cultured in Dulbecco's Modified Eagle's Medium (DMEM, Sigma-Aldrich, D5796) supplemented with 10% heat-inactivated fetal bovine serum (FBS,

Gibco, 12483-020) and 1% penicillin/streptomycin (Sigma-Aldrich, P4333). For the Vero-TMPRSS2 cells, blasticidin (A11139-03, Gibco) was added into DMEM at a final concentration of 5 μg/mL. The cells were maintained in T175 tissue culture flasks (Sarstedt, 83.3912.002) at 37°C with 5% CO_2.

SARS-CoV-2 strains

The SARS-CoV-2 ancestral (NR-53565), Alpha (B.1.1.7, NR-54011), Beta (B.1.351, NR-54009), Gamma (P.1, NR-54982), Delta (B.1.617.2, NR-55672), and Omicron (BA.1, NR-56461) strains were obtained from BEI resources. The Omicron strain was later confirmed as BA.1.18 by whole-genome sequencing. The ancestral, Alpha, Beta, and Gamma strains were cultured using Vero E6 cells, and the Gamma and Omicron strains were cultured using Vero-TMPRSS2 cells. The full sequences of all strains were confirmed by next-generation sequencing at the Lunenfeld-Tanenbaum Research Institute. All SARS-CoV-2-related experiments were approved by the Institutional Biosafety Committee and performed in Containment Level 3 facilities at EPIC (Emerging & Pandemic Infections Consortium) center of the University of Toronto.

Animals

BALB/c mice, K18-hACE2 C57BL/6 mice, and hamsters were purchased from the Jackson Laboratory. Mice and hamsters aged between 8-12 weeks were used in the study. Mice were housed in groups. Female hamsters were housed individually, and male hamsters were housed in pairs. All animals were acclimated for at least one week before experiments. The mouse and hamster models were randomly assigned into groups. All animal experiments were approved by the University of Toronto Animal Care Committee or the Hospital for Sick Children Animal Care Committee. Efforts were made to minimize animal suffering. All procedures were performed under anesthesia with isoflurane. The sample size was selected based on our previous study and other relevant studies (23, 32, 61). Ethical guideline on the numbers of animals were followed in designing this study. The sample size represents the minimum number of animals required to address our research question.

Construction of HD-Ad-FS vaccine and HD-Ad-C4 control

The pC4HSU-NM was used as the backbone for cloning HD-Ad-FS vector. The pPBCMV-sipke-1-1273-S-2P-WPRE contained the FS of SARS-CoV-2. A Bluescript plasmid containing chicken beta actin (CBA) promoter-Ubiquitin C (UbC) intron-bovine growth hormone (bGH) polyadenylation tail was used as a shuttle plasmid. The FS gene was first inserted between the UbC intron and bGH poly(A) tail in the shuttle plasmid by using the Rapid DNA Ligation kit (Thermo Scientific, K1422). Then, the cassette of CBA promoter-UbC intron-FS-bGH poly(A) was cut out from the shuttle plasmid by AscI restriction enzyme and ligated with AscI-digested pC4HSU-NM. The final HD-Ad-FS vector was constructed as inverted terminal repeats (ITR)-CBA promoter-UbC intron-FS-bGH poly(A)-ITR. The pC4HSU-NM was used for constructing HD-Ad-control.

HD-Ad production

The HD-Ad vectors were produced as previously described by Ng et al. (62). Briefly, the HD-Ad vectors were amplified in producer 116 cells with NG163 helper virus. The NG163 helper virus provided all the essential genes for HD-Ad production, and its package signal was flanked by two loxP sites. The 116 cells expressed Cre recombinase which cleaved off the package signal of NG163 helper virus. As a result, only HD-Ad vector could be packaged. After serial passages, the HD-Ad vectors were harvested from cell lysates and purified by 3 rounds of CsCl density gradient centrifugation. The number of HD-Ad particles were calculated by measuring the absorbance at 260nm.

Immunization of BALB/c mice

Female BALB/c mice were intranasally immunized with $5x10^9$ vp of either HD-Ad-FS or HD-Ad-control in 20 μl of PBS with 40 μg/mL of diethylaminoethyl (DEAE)-Dextran (Sigma-Aldrich, 30461) and 0.1% L-α–lysophosphatidylcholine (Sigma-Aldrich, L1381). For the single-dose group, mice only received one dose of HD-Ad-FS or HD-Ad-control and were euthanized at day 21 post-vaccination (dpv). For the prime-boost group, mice received two doses of HD-Ad-FS or HD-Ad-control (three-week interval) at the same viral particle dose and were euthanized at 21 dpv after the second dose. Lung, blood, and bronchoalveolar lavage (BAL) samples were collected and stored at -80°C.

Immunization and viral challenge of K18-hACE2 C57BL/6 mice

K18-hACE2 C57BL/6 mice (24 males and 24 females) were intranasally immunized with $5x10^9$ vp of either HD-Ad-FS or HD-Ad-control in 20 μl of PBS with 40 μg/mL of DEAE-Dextran and 0.1% LPC. For the single-dose group, K18-hACE2 mice (6 males and 6 females) received one dose of HD-Ad-FS or HD-Ad-control. For the prime-boost group, K18-hACE2 mice (18 males and 18 females) received two doses of HD-Ad-FS or HD-Ad-control (three-week interval) at the same viral particle dose. Three weeks after the last vaccination, all K18-hACE2 mice were intranasally challenged with $1x10^5$ $TCID_{50}$ of virus in 50 μl of DMEM. The single-dose group was infected with the ancestral strain, and the prime-boost group was infected with Beta, Delta, or Omicron variants. Body weights were monitored and recorded daily at 0 (before infection) and 4 dpi. The K18-hACE2 mice were euthanized at 4 dpi. Lung, BAL, blood, spleen, and heart samples were collected and stored at -80°C.

Immunization and viral challenge of hamsters

Hamsters (64 males and 64 females) were intranasally immunized with $5x10^9$ vp of either HD-Ad-FS or HD-Ad-control in 100 µl of PBS with 40 µg/mL of DEAE-Dextran and 0.1% LPC. For the single-dose group, hamsters (16 males and 16 females) received one dose of HD-Ad-FS or HD-Ad-control. For prime-boost group, hamsters (48 males and 48 females) were immunized with two doses of either HD-Ad-FS or HD-Ad-control (three-week interval). Three weeks after the last vaccination, the single-dose hamsters (16 males and 16 females) were intranasally infected with $1x10^5$ $TCID_{50}$ of the ancestral strain, and the prime-boost hamsters (16 males and 16 females for each strain) were intranasally infected with $1x10^5$ $TCID_{50}$ of either Beta, Delta, or Omicron variants in 100 µl of DMEM. Body weights were monitored and recorded daily from 0 (before infection) to 14 dpi. Hamsters were euthanized at 4 (12 hamsters per strain, equal sex ratio) and 14 (20 hamsters per strain, equal sex ratio) dpi. Lung, BAL, blood, spleen, and heart samples were collected and stored at -80°C.

Protein isolation and Western blot analysis

Proteins were isolated from cell lysates using RIPA buffer (1% Triton X-100, 0.1% SDS, 150mM NaCl, 20mM Tris-HCl, 0.5% Deoxycholate) and 10% proteinase inhibitor (Roche, 11836145001). Protein concentrations were measured by BCA assay (Thermo Fisher Scientific, 23225). The proteins were mixed with 4X Laemmli sample buffer (Bio-Rad, 1610747) and 2.5% beta-mercaptoethanol. 30 ug of protein was incubated at 95°C for 5 minutes before loading onto mini-PROTEAN TGX Stain-Free Gels (Bio-Rad, 4568086). Protein bands were transferred to Amersham Protran Premium 0.45 µm nitrocellulose membranes (GE Healthcare Life Science, 10600003), which were then probed with the SARS Spike protein antibody (Novus Biologicals, NB-56578) at 1:500, and the goat anti-rabbit IgG (H+L)-HRP conjugate antibody (Bio-Rad, 170-6515) at 1:10000. The antibodies were prepared in a blocking solution containing 2.5% albumin (BioShop, ALB001.500) and 2.5% non-fat dry milk (Bio-Rad, 1706404XTU) in TBST (1X TBS + 0.5M Tween-20). A purified recombinant FS protein was used as a positive control.

Neutralization assay

Vero E6 or Vero-TMPRSS2 cells were seeded into 96-well tissue culture microplates (Corning, 3997) at 20,000 to 30,000 cells/well. Serum and BAL samples were heat-inactivated at 56°C for 30 minutes. The starting dilution ratios for serum and BAL samples were 50-fold and 5-fold, respectively. Subsequently, the samples were serially diluted in DMEM at a 2-fold ratio. Each dilution was performed in 6 technical replicates. The diluted samples were mixed and incubated with 200 $TCID_{50}$ of SARS-CoV-2 or its variants at 37°C for 1 hour. After incubation, the sample-virus mixtures were added into Vero E6 or Vero-TMPRSSII cells. The final DMEM medium contained 2% FBS. Cytopathic effect (CPE) was monitored on day 4 and day 7 using a light microscope (EVOS FLoid Imaging system). The neutralization titer was determined as the highest dilution that protected 50% of cells from infection by SARS-CoV-2 and its variants.

Measurement of infectious SARS-CoV-2 and variant titers from lung homogenates

The infectious viral titers were determined by $TCID_{50}$ assay. Vero-E6 or Vero-TMPRSS2 cells were seeded into 96-well tissue culture microplates at 20,000 to 30,000 cells/well, 16 hours before inoculation. One lobe of lung tissue was weighted and placed in 1 mL of DMEM. The lobes were homogenized using 5 mm stainless steel beads (Qiagen, 69989) in a homogenizer (Bead Ruptor 4, Omni). Debris was removed by centrifuging the homogenates at 3,000 g for 5 minutes. The supernatants were serially diluted at a 10-fold ratio in DMEM and added to either Vero-E6 or Vero-TMPRSS2 cells in 6 technical replicates. The final DMEM medium contained 1% FBS. The CPE was monitored on day 4 and day 7. The $TCID_{50}$ was calculated by Karber method (63) and normalized to tissue weight.

Measurement of SARS-CoV-2 and variant viral RNA from lung homogenates and oropharyngeal swabs

For lung homogenates, one lobe of lung tissue was weighted and homogenized with 5 mm stainless steel beads (Qiagen, 69989) in buffer RLT (Qiagen, 79216) using a homogenizer. The RNA was extracted with the RNeasy Mini kit (Qiagen, 74106) following the manufacturer's instruction, and eluted in 35 µl of water.

For oropharyngeal swabs, samples were collected by oropharyngeal swabbing. In K18-hACE2 mice, swab samples were collected at 0 (post-infection) and 4 dpi. In single-dose hamsters, samples were collected at 1, 4, 6, 8, 11, and 14 dpi. In prime-boosted hamsters, swab samples were collected on 1, 2, 4, 10, and 14 dpi. All samples were stored in 500 µl of PBS at -80°C. Swabs were vortexed and centrifuged before RNA extraction. For each swab sample, 140 µl of eluted PBS was used for RNA extraction by the QIAamp Viral RNA Mini Kit (Qiagen, 52906), as per manufacturer's instruction. The RNA was eluted in 60 µl of buffer AVE.

The viral RNA (envelop gene) was reverse transcribed and amplified with the Luna Universal One-Step RT-qPCR kit (NEB, E3005). 1 µl of lung RNA and 5 µl of swab RNA were used for the RT-qPCR. Primers (E_Sarbeco_F1 Forward Primer, 10006889; E_Sarbeco_R2 Reverse Primer, 10006891; Integrated DNA Technologies) targeting the envelope (E) gene were used to detect genomic/subgenomic viral RNA. A standard curve was generated by serially diluting the E gene plasmid (2019-nCoV_E_Positive Control, 10006896, Integrated DNA Technologies) at a 10-fold ratio. The viral RNA copies were calculated by converting the Ct values based on the standard curve. The RT-qPCR stages were as follows: 55°C for 10 minutes; 95°C for 1 minute; 95°C for 10 seconds, 58°C for 30 seconds, read plate, 44 cycles; 95°C for 5

seconds; 65°C, 30 seconds; 65°C, 5 seconds, + 0.5°C/cycle, ramp 0.5° C/seconds, read plate, 60 cycles.

Enzyme-linked immunosorbent assay

96-well microplates (Nunc MaxiSorp flat-bottom, Invitrogen, 44-24-4-21) were coated with purified recombinant FS protein at 1 μg/mL in 50 mM carbonate coating buffer (Thermo Scientific, 28382) at 4°C overnight. Plates were washed with PBST (Phosphate-buffered saline with 0.1% Tween 20) and blocked with blocking buffer (1% BSA in PBST) for 1 hour at room temperature. Serial diluted serum or BAL samples were added to the plates and incubated for 1 hour at 37°C. After washing with PBST, the plates were incubated with goat anti-mouse IgG conjugated with horseradish peroxidase (1:5000, Invitrogen, 31430), goat anti-mouse IgA conjugated with horseradish peroxidase (1:2000, Invitrogen, 62-6720), or goat anti-hamster IgG conjugated with horseradish peroxidase (1:4000, Thermo Scientific, PA1-29626) in blocking solution for 1 hour at room temperature. Signal was developed with 3,3',5,5',-tetramethylbenzidine (TMB, Thermo Scientific, 34028) for 1 hour at room temperature. The reaction was stopped by adding 1 M H_2SO_4. Plates were read at OD_{450} (Cytation 5, BioTek).

Flow cytometry analysis

Left lung lobes and spleens from single-FS and single-control immunized BALB/c mice were used for flow cytometry analysis. Lung lobes were digested with a digestion buffer containing 2 ug/mL of Liberase (Roche Diagnostics, 1988433) and 25 unites/mL of type IV DNase I (Sigma-Aldrich, D5025) at 37°C for 45 minutes. Following digestion, lung tissues were dispersed with 18-gauged needles and filtered through 100 nm cell strainers (Falcon, 352360). Spleenocytes were isolated by straining spleens through 70 nm cell strainers (Falcon, 352350). Red blood cells (RBC) were lysed by resuspending filtered cells in 1X RBC Lysis Buffer (eBioscience, 00-4333-57). Subsequently, each cell sample was split into two replicates. One replicate was incubated with purified FS protein at 10 μg/mL at 37°C for 12 hours, while the other replicate was not incubated with FS protein. After incubation, GolgiPlug (Fixation/Permeabilization Solution Kit with BD GolgiPlug, 555028) was added for 6 hours. Cells were stained with the Live/Dead Fixable Violate Dead Cell kit (Invitrogen, L34955) and blocked with CD16 and CD32 antibodies (Mouse BD Fc Block, 553142). Next, cells were stained with surface markers: BV711 rat anti-mouse CD4 (BD Biosciences, 563726), APC-Cy7 rat anti-mouse CD8a (BD Biosciences, 557654), PE-Cy7 rat anti-mouse CD19 (BD Biosciences, 552854), and BV510 rat anti-mouse CD44 (BD Biosciences, 563114). The cells were then fixed and permeabilized with Fixation/Permeabilization Solution Kit (BD Biosciences, 555028). Finally, cells were stained with intracellular markers: FITC rat anti-mouse IFN-γ (BD Biosciences, 554411), and PE rat anti-mouse TNF-α (BD Biosciences, 554419). Flow cytometry was performed on a Becton Dickinson LSR II CF I and analyzed with Flowjo v10 software.

Histopathology and RNA *in situ* hybridization

Lung tissues were fixed directly in 10% neutral phosphate buffered formalin (Sigma-Aldrich, HT501128) without inflation for a minimum of 2 weeks prior to paraffin embedding. The paraffin blocks were continuously sectioned into 4 μm-thick slices and mounted onto slides (Fisherbrand, 12-550-15). The hematoxylin and eosin (H&E) staining was performed at the Centre for Phenogenomics in Toronto. The RNA *in situ* hybridization was performed using the RNAscope 2.5 High Definition-RED Assay (Advanced Cell Diagnostic, 322350), according to manufacturer's instruction. The Probe-V-nCoV2019-S (Advanced Cell Diagnostic, 848561) was an anti-sense probe for spike RNA. The Probe-V-nCoV2019-S-sense was a sense probe for spike RNA.

Briefly, formalin-fixed, paraffin-embedded tissues were baked at 60°C for 1 hour and then deparaffinized using xylene and ethanol. Subsequently, samples were treated with hydrogen peroxide for 10 minutes at room temperature, followed by target retrieval using RNAscope Target Retrieval Solution. Samples were incubated with Protease Plus solution at 40°C for 30 minutes. After hybridizing with the probes, signals were detected using a mixture of RED-B and RED-A. A counterstain was performed using 50% hematoxylin and 0.02% ammonia water. The slides were mounted with VectaMount Permanent Mounting Medium (Vector Laboratories, H-5000-60) and cover clips (VWR, 48366-067), and scanned with a 3DHistech Slide Scanner at the Imaging Facility at the Hospital for Sick Children.

Data analysis

The results and graphs were generated with GraphPad Prism version 8 (GraphPad Software). Statistical analyses were performed using analysis of variance (ANOVA) with multiple comparison test or unpaired t-test (two-tailed) with Mann-Whitney test. ChatGPT (OpenAI, GPT-3, 2023) was employed for grammar checking during the preparation of this manuscript. All AI-assisted revisions were reviewed and approved by the authors to ensure the accuracy and quality of the final manuscript.

Data availability statement

The original contributions presented in the study are included in the article/Supplementary Materials. Further inquiries can be directed to the corresponding authors.

Ethics statement

Ethical approval was not required for the studies on humans in accordance with the local legislation and institutional requirements because only commercially available established cell lines were used. The animal study was approved by University of Toronto Animal

Care Committee and the Hospital for Sick Children Animal Care Committee. The study was conducted in accordance with the local legislation and institutional requirements.

Author contributions

PZ: Writing – review & editing, Writing – original draft, Visualization, Validation, Software, Resources, Project administration, Methodology, Investigation, Formal analysis, Data curation, Conceptualization. JW: Investigation, Methodology, Writing – review & editing. JM: Investigation, Methodology, Writing – review & editing. HC: Investigation, Methodology, Writing – review & editing. ZL: Resources, Writing – review & editing. ZC: Investigation, Writing – review & editing. RD: Resources, Writing – review & editing. YQ: Resources, Writing – review & editing. A-CG: Conceptualization, Writing – review & editing. JR: Writing – review & editing, Conceptualization, Supervision. JH: Writing – review & editing, Conceptualization, Supervision. JL: Writing – review & editing, Conceptualization, Supervision, Funding acquisition.

Funding

The author(s) declare financial support was received for the research, authorship, and/or publication of this article. This work was supported by Canadian Institutes of Health Research (CIHR) grants, VR1-172771, VS-1-175531, GA-2-177717, and Covid-19 Immunity Task Force (CITF).

Acknowledgments

Animal figures were created with BioRender.com. ChatGPT (OpenAI, GPT-3, 2023) was used for grammar checking. We acknowledge the assistance of this tool in refining the grammar used in the text.

Conflict of interest

The authors declare that the research was conducted in the absence of any commercial or financial relationships that could be construed as a potential conflict of interest.

Publisher's note

Supplementary material

The Supplementary Material for this article can be found online at: https://www.frontiersin.org/articles/10.3389/fimmu.2024.1430928/full#supplementary-material

References

1. Van Doremalen, Bushmaker N, Morris T, Holbrook DH, Gamble MG, Williamson A, et al. Aerosol and surface stability of SARS-CoV-2 as compared with SARS-CoV-1. *New Engl J Med*. (2020) 382:1564–7. doi: 10.1056/NEJMc2004973

2. Azimi P, Keshavarz Z, Cedeno Laurent JG, Stephens B, Allen JG. Mechanistic transmission modeling of COVID-19 on the Diamond Princess cruise ship demonstrates the importance of aerosol transmission. *Proc Natl Acad Sci*. (2021) 118:e2015482118. doi: 10.1073/pnas.2015482118

3. Sahin U, Muik A, Derhovanessian E, Vogler I, Kranz LM, Vormehr M, et al. COVID-19 vaccine BNT162b1 elicits human antibody and TH1 T cell responses. *Nature*. (2020) 586:594–9. doi: 10.1038/s41586-020-2814-7

4. Walsh EE, Frenck RW Jr, Falsey AR, Kitchin N, Absalon J, Gurtman A, et al. Safety and immunogenicity of two RNA-based Covid-19 vaccine candidates. *New Engl J Med*. (2020) 383:2439–50. doi: 10.1056/NEJMoa2027906

5. Heath PT, Galiza EP, Baxter DN, Boffito M, Browne D, Burns F, et al. Safety and efficacy of NVX-CoV2373 Covid-19 vaccine. *New Engl J Med*. (2021) 385:1172–83. doi: 10.1056/NEJMoa2107659

6. Tanriover MD, Doğanay HL, Akova M, Güner HR, Azap A, Akhan S, et al. Efficacy and safety of an inactivated whole-virion SARS-CoV-2 vaccine (CoronaVac): interim results of a double-blind, randomised, placebo-controlled, phase 3 trial in Turkey. *Lancet*. (2021) 398:213–22. doi: 10.1016/S0140-6736(21)01429-X

7. Weisblum Y, Schmidt F, Zhang F, DaSilva J, Poston D, Lorenzi JC, et al. Escape from neutralizing antibodies by SARS-CoV-2 spike protein variants. *elife*. (2020) 9: e61312. doi: 10.7554/eLife.61312

8. Folegatti PM, Ewer KJ, Aley PK, Angus B, Becker S, Belij-Rammerstorfer S, et al. Safety and immunogenicity of the ChAdOx1 nCoV-19 vaccine against SARS-CoV-2: a preliminary report of a phase 1/2, single-blind, randomised controlled trial. *Lancet*. (2020) 396:467–78. doi: 10.1016/S0140-6736(20)31604-4

9. Abu-Raddad LJ, Chemaitelly H, Butt AA. Effectiveness of the BNT162b2 covid-19 vaccine against the B. 1.1. 7 and B. 1.351 variants. *New Engl J Med*. (2021) 385:187–9. doi: 10.1056/NEJMc2104974

10. Voysey M, Clemens SAC, Madhi SA, Weckx LY, Folegatti PM, Aley PK, et al. Single-dose administration and the influence of the timing of the booster dose on immunogenicity and efficacy of ChAdOx1 nCoV-19 (AZD1222) vaccine: a pooled analysis of four randomised trials. *Lancet*. (2021) 397:881–91. doi: 10.1016/S0140-6736(21)00432-3

11. Tang J, Zeng C, Cox TM, Li C, Son YM, Cheon IS, et al. Respiratory mucosal immunity against SARS-CoV-2 after mRNA vaccination. *Sci Immunol*. (2022) 7: eadd4853. doi: 10.1126/sciimmunol.add4853

12. Buchan SA, Booth S, Scott AN, Simmonds KA, Svenson LW, Drews SJ, et al. Effectiveness of live attenuated vs inactivated influenza vaccines in children during the 2012-2013 through 2015-2016 influenza seasons in Alberta, Canada: a Canadian Immunization Research Network (CIRN) study. *JAMA Pediatr*. (2018) 172:e181514–e181514. doi: 10.1001/jamapediatrics.2018.1514

13. Park H-S, Matsuoka Y, Luongo C, Yang L, Santos C, Liu X, et al. Intranasal immunization with avian paramyxovirus type 3 expressing SARS-CoV-2 spike protein protects hamsters against SARS-CoV-2. *NPJ Vaccines*. (2022) 7:72. doi: 10.1038/s41541-022-00493-x

14. Le Nouën C, Nelson CE, Liu X, Park H-S, Matsuoka Y, Luongo C, et al. Intranasal pediatric parainfluenza virus-vectored SARS-CoV-2 vaccine is protective in monkeys. *Cell*. (2022) 185:4811–4825. e4817. doi: 10.1016/j.cell.2022.11.006

15. Hassan AO, Kafai NM, Dmitriev IP, Fox JM, Smith BK, Harvey IB, et al. A single-dose intranasal ChAd vaccine protects upper and lower respiratory tracts against SARS-CoV-2. *Cell*. (2020) 183:169–184. e113. doi: 10.1016/j.cell.2020.08.026

16. Draft landscape of COVID-19 candidate vaccines (2023). Available online at: https://www.who.int/publications/m/item/draft-landscape-of-covid-19-candidate-vaccines (Accessed on November 5, 2022).

17. Toietta G, Koehler DR, Finegold MJ, Lee B, Hu J, Beaudet AL, et al. Reduced inflammation and improved airway expression using helper-dependent adenoviral vectors with a K18 promoter. *Mol Ther*. (2003) 7:649–58. doi: 10.1016/S1525-0016(03)00059-5

18. Muruve DA, Cotter MJ, Zaiss AK, White LR, Liu Q, Chan T, et al. Helper-dependent adenovirus vectors elicit intact innate but attenuated adaptive host immune responses *in vivo*. *J Virol*. (2004) 78:5966–72. doi: 10.1128/JVI.78.11.5966-5972.2004

19. Cao H, Wu J, Duan C, Du K, Lee CM, Yeger H, et al. Long-term expression of the human cftr gene in mouse airway via helper-dependent adenoviral vector delivery and transient immunosuppression. *Hum Gene Ther*. (2016) 27:83–91. doi: 10.1089/hum.2015.108

20. Tam HH, Melo MB, Kang M, Pelet JM, Ruda VM, Foley MH, et al. Sustained antigen availability during germinal center initiation enhances antibody responses to vaccination. *Proc Natl Acad Sci*. (2016) 113:E6639–48. doi: 10.1073/pnas.1606050113

21. Cao H, Machuca TN, Yeung JC, Wu J, Du K, Duan C, et al. Efficient gene delivery to pig airway epithelia and submucosal glands using helper-dependent adenoviral vectors. *Mol Therapy-Nucleic Acids*. (2013) 2:e127. doi: 10.1038/mtna.2013.55

22. Mitrani E, Pearlman A, Stern B, Miari R, Goltsman H, Kunicher N, et al. Biopump: Autologous skin-derived micro-organ genetically engineered to provide sustained continuous secretion of therapeutic proteins. *Dermatol Ther*. (2011) 24:489–97. doi: 10.1111/dth.2011.24.issue-5

23. Cao H, Mai J, Zhou Z, Li Z, Duan R, Watt J, et al. Intranasal HD-Ad vaccine protects the upper and lower respiratory tracts of hACE2 mice against SARS-CoV-2. *Cell Biosci*. (2021) 11:1–13. doi: 10.1186/s13578-021-00723-0

24. Ravichandran S, Coyle EM, Klenow L, Tang J, Grubbs G, Liu S, et al. Antibody signature induced by SARS-CoV-2 spike protein immunogens in rabbits. *Sci Trans Med*. (2020) 12:eabc3539. doi: 10.1126/scitranslmed.abc3539

25. Planas D, Bruel T, Grzelak L, Guivel-Benhassine F, Staropoli I, Porrot F, et al. Sensitivity of infectious SARS-CoV-2 B. 1.1. 7 and B. 1.351 variants to neutralizing antibodies. *Nat Med*. (2021) 27:917–24. doi: 10.1038/s41591-021-01318-5

26. Planas D, Veyer D, Baidaliuk A, Staropoli I, Guivel-Benhassine F, Rajah MM, et al. Reduced sensitivity of SARS-CoV-2 variant Delta to antibody neutralization. *Nature*. (2021) 596:276–80. doi: 10.1038/s41586-021-03777-9

27. Planas D, Saunders N, Maes P, Guivel-Benhassine F, Planchais C, Buchrieser J, et al. Considerable escape of SARS-CoV-2 Omicron to antibody neutralization. *Nature*. (2022) 602:671–5. doi: 10.1038/s41586-021-04389-z

28. Wrapp D, Wang N, Corbett KS, Goldsmith JA, Hsieh C-L, Abiona O, et al. Cryo-EM structure of the 2019-nCoV spike in the prefusion conformation. *Science*. (2020) 367:1260–3. doi: 10.1126/science.abb2507

29. Bao L, Deng W, Huang B, Gao H, Liu J, Ren L, et al. The pathogenicity of SARS-CoV-2 in hACE2 transgenic mice. *Nature*. (2020) 583:830–3. doi: 10.1038/s41586-020-2312-y

30. Tseng HF, Ackerson BK, Luo Y, Sy LS, Talarico CA, Tian Y, et al. Effectiveness of mRNA-1273 against SARS-CoV-2 Omicron and Delta variants. *Nat Med*. (2022) 28:1063–71. doi: 10.1038/s41591-022-01753-y

31. Lopez Bernal J, Andrews N, Gower C, Gallagher E, Simmons R, Thelwall S, et al. Effectiveness of Covid-19 vaccines against the B. 1.617. 2 (Delta) variant. *New Engl J Med*. (2021) 385:585–94. doi: 10.1056/NEJMoa2108891

32. Imai M, Iwatsuki-Horimoto K, Hatta M, Loeber S, Halfmann PJ, Nakajima N, et al. Syrian hamsters as a small animal model for SARS-CoV-2 infection and countermeasure development. *Proc Natl Acad Sci*. (2020) 117:16587–95. doi: 10.1073/pnas.2009799117

33. Allie SR, Bradley JE, Mudunuru U, Schultz MD, Graf BA, Lund FE, et al. The establishment of resident memory B cells in the lung requires local antigen encounter. *Nat Immunol*. (2019) 20:97–108. doi: 10.1038/s41590-018-0260-6

34. Bricker TL, Darling TL, Hassan AO, Harastani HH, Soung A, Jiang X, et al. A single intranasal or intramuscular immunization with chimpanzee adenovirus-vectored SARS-CoV-2 vaccine protects against pneumonia in hamsters. *Cell Rep*. (2021) 36:109400. doi: 10.1016/j.celrep.2021.109400

35. Hassan AO, Shrihari S, Gorman MJ, Ying B, Yaun D, Raju S, et al. An intranasal vaccine durably protects against SARS-CoV-2 variants in mice. *Cell Rep*. (2021) 36. doi: 10.1016/j.celrep.2021.109452

36. Wang Q, Yang C, Yin L, Sun J, Wang W, Li H, et al. Intranasal booster using an Omicron vaccine confers broad mucosal and systemic immunity against SARS-CoV-2 variants. *Signal Transduction Targeted Ther*. (2023) 8:167. doi: 10.1038/s41392-023-01423-6

37. Asahi-Ozaki Y, Yoshikawa T, Iwakura Y, Suzuki Y, Tamura S, Kurata T, et al. Secretory IgA antibodies provide cross-protection against infection with different strains of influenza B virus. *J Med Virol*. (2004) 74:328–35. doi: 10.1002/jmv.20173

38. Havervall S, Marking U, Svensson J, Greilert-Norin N, Bacchus P, Nilsson P, et al. Anti-spike mucosal IgA protection against SARS-CoV-2 omicron infection. *New Engl J Med*. (2022) 387:1333–6. doi: 10.1056/NEJMc2209651

39. Zuo F, Marcotte H, Hammarström L, Pan-Hammarström Q. Mucosal igA against SARS-coV-2 omicron infection. *New Engl J Med*. (2022) 387:e55–5. doi: 10.1056/NEJMc2213153

40. Azzi L, Dalla Gasperina D, Veronesi G, Shallak M, Ietto G, Iovino D, et al. Mucosal immune response in BNT162b2 COVID-19 vaccine recipients. *EBioMedicine*. (2022) 75:103788. doi: 10.1016/j.ebiom.2021.103788

41. Tarke A, Coelho CH, Zhang Z, Dan JM, Yu ED, Methot N, et al. SARS-CoV-2 vaccination induces immunological T cell memory able to cross-recognize variants from Alpha to Omicron. *Cell*. (2022) 185:847–859. e811. doi: 10.1016/j.cell.2022.01.015

42. Golden JW, Cline CR, Zeng X, Garrison AR, Carey BD, Mucker EM, et al. Human angiotensin-converting enzyme 2 transgenic mice infected with SARS-CoV-2 develop severe and fatal respiratory disease. *JCI Insight*. (2020) 5. doi: 10.1172/jci.insight.142032

43. Channappanavar R, Fett C, Mack M, Ten Eyck PP, Meyerholz DK, Perlman S. Sex-based differences in susceptibility to severe acute respiratory syndrome coronavirus infection. *J Immunol*. (2017) 198:4046–53. doi: 10.4049/jimmunol.1601896

44. Williamson EJ, Walker AJ, Bhaskaran K, Bacon S, Bates C, Morton CE, et al. OpenSAFELY: factors associated with COVID-19 death in 17 million patients. *Nature*. (2020) 584:430. doi: 10.1038/s41586-020-2521-4

45. Takahashi T, Ellingson MK, Wong P, Israelow B, Lucas C, Klein J, et al. Sex differences in immune responses that underlie COVID-19 disease outcomes. *Nature*. (2020) 588:315–20. doi: 10.1038/s41586-020-2700-3

46. McMahan K, Giffin V, Tostanoski LH, Chung B, Siamatu M, Suthar MS, et al. Reduced pathogenicity of the SARS-CoV-2 omicron variant in hamsters. *Med*. (2022) 3:262–268. e264. doi: 10.1016/j.medj.2022.03.004

47. Halfmann PJ, Iida S, Iwatsuki-Horimoto K, Maemura T, Kiso M, Scheaffer SM, et al. SARS-CoV-2 Omicron virus causes attenuated disease in mice and hamsters. *Nature*. (2022) 603:687–92. doi: 10.1038/s41586-022-04441-6

48. Yuan S, Ye Z-W, Liang R, Tang K, Zhang AJ, Lu G, et al. Pathogenicity, transmissibility, and fitness of SARS-CoV-2 Omicron in Syrian hamsters. *Science*. (2022) 377:428–33. doi: 10.1126/science.abn8939

49. Wu S, Huang J, Zhang Z, Wu J, Zhang J, Hu H, et al. Safety, tolerability, and immunogenicity of an aerosolised adenovirus type-5 vector-based COVID-19 vaccine (Ad5-nCoV) in adults: preliminary report of an open-label and randomised phase 1 clinical trial. *Lancet Infect Dis*. (2021) 21:1654–64. doi: 10.1016/S1473-3099(21)00396-0

50. Madhavan M, Ritchie AJ, Aboagye J, Jenkin D, Provstgaad-Morys S, Tarbet I, et al. Tolerability and immunogenicity of an intranasally-administered adenovirus-vectored COVID-19 vaccine: An open-label partially-randomised ascending dose phase I trial. *EBioMedicine*. (2022) 85:104298. doi: 10.1016/j.ebiom.2022.104298

51. Halperin SA, Ye L, MacKinnon-Cameron D, Smith B, Cahn PE, Ruiz-Palacios GM, et al. Final efficacy analysis, interim safety analysis, and immunogenicity of a single dose of recombinant novel coronavirus vaccine (adenovirus type 5 vector) in adults 18 years and older: an international, multicentre, randomised, double-blinded, placebo-controlled phase 3 trial. *Lancet*. (2022) 399:237–48. doi: 10.1016/S0140-6736(21)02753-7

52. Zhu F-C, Guan X-H, Li Y-H, Huang J-Y, Jiang T, Hou L-H, et al. Immunogenicity and safety of a recombinant adenovirus type-5-vectored COVID-19 vaccine in healthy adults aged 18 years or older: a randomised, double-blind, placebo-controlled, phase 2 trial. *Lancet*. (2020) 396:479–88. doi: 10.1016/S0140-6736(20)31605-6

53. Singh C, Verma S, Reddy P, Diamond MS, Curiel DT, Patel C, et al. Phase III Pivotal comparative clinical trial of intranasal (iNCOVACC) and intramuscular COVID 19 vaccine (Covaxin®). *NPJ Vaccines*. (2023) 8:125. doi: 10.1038/s41541-023-00717-8

54. Brunetti-Pierri N, Ng P. Helper-dependent adenoviral vectors for liver-directed gene therapy. *Hum Mol Genet*. (2011) 20:R7–R13. doi: 10.1093/hmg/ddr143

55. Biancatelli RMC, Solopov PA, Sharlow ER, Lazo JS, Marik PE, Catravas JD. The SARS-CoV-2 spike protein subunit S1 induces COVID-19-like acute lung injury in K18-hACE2 transgenic mice and barrier dysfunction in human endothelial cells. *Am J Physiology-Lung Cell Mol Physiol*. (2021) 321:L477–84. doi: 10.1152/ajplung.00223.2021

56. Lei Y, Zhang J, Schiavon CR, He M, Chen L, Shen H, et al. SARS-CoV-2 spike protein impairs endothelial function via downregulation of ACE 2. *Circ Res*. (2021) 128:1323–6. doi: 10.1161/CIRCRESAHA.121.318902

57. Poon MM, Rybkina K, Kato Y, Kubota M, Matsumoto R, Bloom NI, et al. SARS-CoV-2 infection generates tissue-localized immunological memory in humans. *Sci Immunol*. (2021) 6:eabl9105. doi: 10.1126/sciimmunol.abl9105

58. Cao H, Yang T, Li X, Wu J, Duan C, Coates A, et al. Readministration of helper-dependent adenoviral vectors to mouse airway mediated via transient immunosuppression. *Gene Ther*. (2011) 18:173–81. doi: 10.1038/gt.2010.125

59. Arbel R, Peretz A, Sergienko R, Friger M, Beckenstein T, Duskin-Bitan H, et al. Effectiveness of a bivalent mRNA vaccine booster dose to prevent severe COVID-19 outcomes: a retrospective cohort study. *Lancet Infect Dis*. (2023) 23:914–24. doi: 10.1016/S1473-3099(23)00122-6

60. Lin D-Y, Xu Y, Gu Y, Zeng D, Wheeler B, Young H, et al. Effectiveness of bivalent boosters against severe omicron infection. *New Engl J Med*. (2023) 388:764–6. doi: 10.1056/NEJMc2215471

61. Frere JJ, Serafini RA, Pryce KD, Zazhytska M, Oishi K, Golynker I, et al. SARS-CoV-2 infection in hamsters and humans results in lasting and unique systemic perturbations after recovery. *Sci Trans Med*. (2022) 14:eabq3059. doi: 10.1126/scitranslmed.abq3059

62. Doux JML, Palmer DJ, Ng P. Methods for the production of helper-dependent adenoviral vectors. *Gene Ther Protocols: Production In Vivo Appl Gene Transfer Vectors*. (2008) 1:33–54. doi: 10.1007/978-1-59745-237-3_3

63. Hierholzer J, Killington R. Virus isolation and quantitation. In *Virology methods manual*. Academic Press (1996) p. 25–46.

frontiers | Frontiers in Immunology

TYPE Original Research
PUBLISHED 14 October 2024
DOI 10.3389/fimmu.2024.1440324

OPEN ACCESS

EDITED BY
Frédéric Frézard,
Federal University of Minas Gerais, Brazil

REVIEWED BY
Zhen Zhao,
University of Southern California, United States
Mark Endsley,
University of Texas Medical Branch at Galveston, United States

*CORRESPONDENCE
Cordelia Dunai
cdunai@liverpool.ac.uk
Benedict D. Michael
benmic@liverpool.ac.uk

†PRESENT ADDRESSES
Jordan J. Clark,
Department of Microbiology, Icahn School of Medicine at Mount Sinai, New York, New York, NY, United States;
Center for Vaccine Research and Pandemic Preparedness, Icahn School of Medicine at Mount Sinai, New York, NY, United States
Sarosh R. Irani,
Department of Neurology, Mayo Clinic Florida, Jacksonville, FL, United States;
Department of Neurosciences, Mayo Clinic Florida, Jacksonville, FL, United States
Robyn Williams,
Department of Neurology, Mayo Clinic Florida, Jacksonville, FL, United States;
Department of Neurosciences, Mayo Clinic Florida, Jacksonville, FL, United States

‡These authors have contributed equally to this work

RECEIVED 29 May 2024
ACCEPTED 04 September 2024
PUBLISHED 14 October 2024

CITATION
Dunai C, Hetherington C, Boardman SA, Clark JJ, Sharma P, Subramaniam K, Tharmaratnam K, Needham EJ, Williams R, Huang Y, Wood GK, Collie C, Fower A, Fox H, Ellul MA, Held M, Egbe FN, Griffiths M, Solomon T, Breen G, Kipar A, Cavanagh J, Irani SR, Vincent A, Stewart JP, Taams LS, Menon DK and Michael BD (2024) Pulmonary SARS-CoV-2 infection leads to para-infectious immune activation in the brain. *Front. Immunol.* 15:1440324. doi: 10.3389/fimmu.2024.1440324

Pulmonary SARS-CoV-2 infection leads to para-infectious immune activation in the brain

Cordelia Dunai[1,2*], Claire Hetherington[2], Sarah A. Boardman[2], Jordan J. Clark[3†], Parul Sharma[3], Krishanthi Subramaniam[3], Kukatharmini Tharmaratnam[4], Edward J. Needham[5], Robyn Williams[6†], Yun Huang[2], Greta K. Wood[2], Ceryce Collie[2], Andrew Fower[6], Hannah Fox[6], Mark A. Ellul[2], Marie Held[7], Franklyn N. Egbe[2], Michael Griffiths[2], Tom Solomon[1,2,8], Gerome Breen[9,10], Anja Kipar[3,11], Jonathan Cavanagh[12], Sarosh R. Irani[8†], Angela Vincent[6], James P. Stewart[3], Leonie S. Taams[13‡], David K. Menon[14‡] and Benedict D. Michael[1,2,8*‡]

[1]NIHR Health Protection Research Unit in Emerging and Zoonotic Infections, Liverpool, United Kingdom, [2]Clinical Infection Microbiology and Immunology, Institute of Infection Ecology and Veterinary Sciences, University of Liverpool, Liverpool, United Kingdom, [3]Department of Infection Biology and Microbiomes, Institute of Infection, Veterinary and Ecological Sciences, University of Liverpool, Liverpool, United Kingdom, [4]Department of Health Data Science, Institute of Population Health, Faculty of Health and Life Sciences, University of Liverpool, Liverpool, United Kingdom, [5]Department of Clinical Neurosciences, University of Cambridge, Cambridge, United Kingdom, [6]Nuffield Department of Clinical Neurosciences, Medical Sciences Division, University of Oxford, Oxford, United Kingdom, [7]Centre for Cell Imaging, Faculty of Health and Life Sciences, University of Liverpool, Liverpool, United Kingdom, [8]Department of Neurology, The Walton Centre NHS Foundation Trust, Liverpool, United Kingdom, [9]Department of Social, Genetic & Developmental Psychiatry Centre, School of Mental Health & Psychological Sciences, King's College London, London, United Kingdom, [10]NIHR Maudsley Biomedical Research Centre, King's College London, London, United Kingdom, [11]Laboratory for Animal Model Pathology, Institute of Veterinary Pathology, Vetsuisse Faculty, University of Zurich, Zurich, Switzerland, [12]College of Medical, Veterinary and Life Sciences, University of Glasgow, Glasgow, United Kingdom, [13]Centre for Inflammation Biology and Cancer Immunology, Department of Inflammation Biology, School of Immunology & Microbial Sciences, Faculty of Life Sciences & Medicine, King's College London, London, United Kingdom, [14]Division of Anaesthesia, Addenbrooke's Hospital, Cambridge University Hospitals, Cambridge, United Kingdom

Neurological complications, including encephalopathy and stroke, occur in a significant proportion of COVID-19 cases but viral protein is seldom detected in the brain parenchyma. To model this situation, we developed a novel low-inoculum K18-hACE2 mouse model of SARS-CoV-2 infection during which active viral replication was consistently seen in mouse lungs but not in the brain. We found that several mediators previously associated with encephalopathy in clinical samples were upregulated in the lung, including CCL2, and IL-6. In addition, several inflammatory mediations, including CCL4, IFNγ, IL-17A, were upregulated in the brain, associated with microglial reactivity. Parallel *in vitro* experiments demonstrated that the filtered supernatant from SARS-CoV-2 virion exposed brain endothelial cells induced activation of uninfected microglia. This model successfully recreates SARS-CoV-2 virus-associated para-infectious brain inflammation which can be used to study the pathophysiology of the neurological complications and the identification of potential immune targets for treatment.

KEYWORDS

virology, immunology, SARS-CoV-2, neurology, microglia

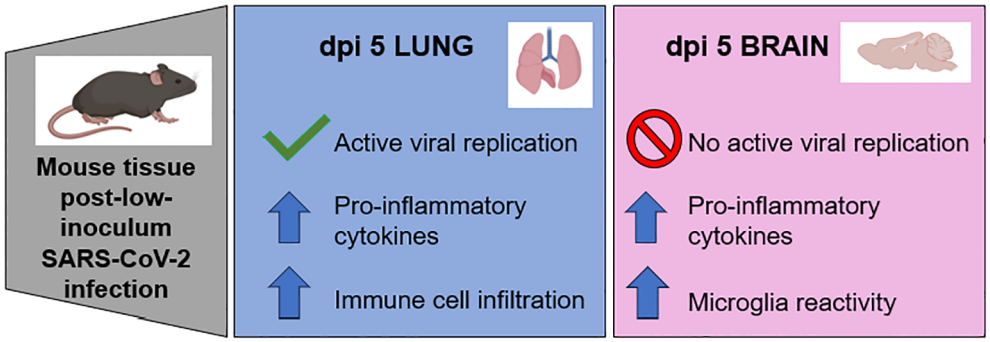

GRAPHICAL ABSTRACT
The low inoculum SARS-CoV-2 mouse model of para-infectious brain effects in the absence of active viral replication had increased cytokines (CCL4, IFNγ and IL-17A) and microglia reactivity (increased Iba1 expression and ramification index).

Introduction

SARS-CoV-2 infection has been associated with a range of neurological complications. Although their incidence has decreased with widespread vaccination and effective anti-viral and anti-inflammatory treatments, they remain a significant clinical issue (1). A large retrospective study with contemporary controls found neurological complications were more common in people who had experienced COVID-19 but were also found in non-hospitalised/mild cases of COVID-19, revealing a large healthcare burden left in the wake of the pandemic (2). The different neurological complications, ranging from loss of smell to encephalitis, caused by SARS-CoV-2 infection most likely have very different aetiologies, but viral protein is seldom found in the brain parenchyma strongly suggesting that indirect effects of the virus, such as immune-mediated pathologies, are a likely potential cause (3–6). Indeed, we and others previously found that COVID-19 patients with neurological complications had elevated serum immune mediators and cytokines (IL-6, IL-12p40, IL1-RA, M-CSF, CCL2, and HGF) which correlated with serum brain injury markers (7–10).

Mouse models are important to systematically study early changes in disease and disease progression, but most models of SARS-CoV-2 have involved systemic dissemination with brain pathology that may not reflect the clinical scenarios (11–14). We established a mouse model using an inoculum of virus ten times lower than that which earlier studies have used, and looked for evidence of brain immune activation in the absence of viral replication in the brain. We also developed an *in vitro* assay to investigate how exposure of endothelial cells to viral protein can lead to cytokine-mediated indirect effects on microglia, which we hypothesize is the most common clinical scenario for how SARS-CoV-2 affects the brain (15).

Methods

Mouse studies of infection with SARS-CoV-2

An AWERB-approved protocol was followed for the mouse studies (University of Liverpool Animal Welfare and Ethical Review Body, UK Home Office Project Licence PP4715265). Mice were maintained under SPF barrier conditions in individually ventilated cages. Male and female 2-4 month old heterozygote hACE2-transgenic C57BL/6 mice (Charles River Laboratory) were infected intranasally with $1x10^3$ or $1x10^4$ plaque-forming units (PFU) of a human isolate of SARS-CoV-2 (Pango B lineage hCoV-2/human/Liverpool/REMRQ0001/2020) under isoflurane anaesthesia. Mice were euthanized on day 5 post infection. Brains were perfused with 30mL PBS w/1mM EDTA, then one hemisphere fixed in formaldehyde-containing PLP buffer overnight at 4°C. Brains were then subjected to a sucrose gradient– 10 and 20% sucrose for 1hr each and then 30% sucrose O/N at 4°C. Brains were then frozen in OCT by submerging moulds in a beaker of 2-methylbutane on dry ice. The other hemisphere was divided in two sagittal sections and half preserved in 4%PFA for histology and half in trizol for RNA and protein extraction. Sera was collected and frozen and then heat-inactivated at 56°C for 30 mins prior to be moved from CL3 to CL2 lab. Lung tissue was preserved in 4%PFA for histology, in trizol for RNA and protein extraction, and in PLP for cryosectioning. Cytokines were measured from tissue protein extract with Bio-rad reagents on a Bio-plex 200 following the manufacturer's protocol.

qPCR of SARS-CoV-2 genes and mouse cytokines

Gene expression was measured from trizol isolated RNA (Invitrogen cat# 15596018, manufacturer's protocol) using Promega's GoTaq Probe 1-Step RT-qPCR system (cat#A6120, manufacturer's protocol) on an Agilent AriaMx. Primers and FAM probes for SARS-CoV-2, cytokines, and housekeeping genes were purchased from IDT (Tables 1, 2) with standard IDT qPCR primer/probe sets for the mouse cytokines.

The thermal cycle for N1 and the mouse cytokines was: 45°C for 15min 1x, 95°C for 2 min, then 45 cycles of 95°C for 3 secs followed by 55°C for 30 sec.

For subgenomic E: 45°C for 15 min 1x, 95°C for 2 min, then 45 cycles of 95°C for 15 secs followed by 58°C for 30 sec.

TABLE 1 Primers and probes for viral genes and normalization.

Gene	Reagent	IDT Cat#	Sequence (5′–3′)
N1	Forward primer:	10006830	GACCCCAAAATCAGCGAAAT
	Reverse primer:	10006831	TCTGGTTACTGCCAGTTGAATCTG
	FAM probe:	10006832	ACCCCGCATTACGTTTGGTGGACC
subgE	Forward primer:	10006889	CGATCTCTTGTAGATCTGTTCTC
	Reverse primer:	10006891	ATATTGCAGCAGTACGCACACA
	FAM probe:	10006893	ACACTAGCCATCCTTACTGCGCTTCG
18S	Forward primer:	Custom	ACCTGGTTGATCCTGCCAGTAG
	Reverse primer:	Custom	AGCCATTCGCAGTTTCACTGTAC
	FAM probe:	Custom	TCAAAGATTAAGCCATGCATGTCTAAGTACGCAC

For 18S it was: 45°C for 15 min, 95°C for 2 min and 40 cycles of 95°C for 15s, 60°C for 1 min.

Histology and confocal microscopy

Paraffin-embedded formalin-fixed tissue was sectioned to 4 um sections. Slides were baked at 60°C for 30 minutes and then stained with H&E in an autostainer. H&E slides were imaged on a Leica microscope. For immunofluorescent staining and confocal microscopy, OCT-embedded frozen tissue was sectioned to 12 um or 30 um sections (thicker sections needed for the Z-stack imaging and microglia ramification/reactivation quantification). 100% acetone was used for antigen retrieval (10 mins at room temperature). After air-drying, then PBS washing, tissue sections were permeabilized with 0.1% Triton X-100/PBS (20 mins at room temperature). After rinsing with PBS, tissue sections were blocked with Dako block (5 minutes at room temperature). After another PBS wash, primary antibodies were added at dilutions listed in table for an overnight incubation at 4°C in a humidified chamber. Tissue sections were washed twice with PBS for 5 minutes each wash. Secondary antibody (as described in Table 3) was added for a 2 hr room temperature incubation, followed by two 5-minute PBS washes. DAPI-mounting medium was used for coverslipping. Imaging was performed with Andor Dragonfly spinning disk confocal microscope. Marker fluorescence and microglia counts, intensity, and reactivation indices [method based on previous work (16, 17)] were quantified with Fiji (confocal microscope set up in Table 4 and macros downloadable from the public Github repository). The reactivation index is the area of the cell divided by the projection area (the whole polygon covered by the cell). Reactivation indices of 0-1 of objects with a threshold size of 19 mm^2 were quantified from three Z-stack images/mouse and two mice/group.

TABLE 2 Primers and probes for mouse cytokines.

Gene	IDT Primetime Cat#
IL-1RN	Mm.PT.58.43781580
IL-6	Mm.PT.58.10005566
IL-12p40	Mm.PT.58.12409997
M-CSF	Mm.PT.58.11661276
CCL2	Mm.PT.58.42151692
HGF	Mm.PT.58.9088506
CCL4	Mm.PT.58.5219433
IFNG	Mm.PT.58.41769240
IL-17A	Mm.PT.58.6531092

For mouse cytokines, the primer/probe sets listed in Table 2 were used and the cycle was: 45°C for 15 min; 95°C for 2 min; 45 cycles of 95°C for 3 sec and 55°C for 30 sec.

In vitro cell culture assays

The investigated cell lines were cultured according to the manufacturer's recommendations. The mouse brain endothelial cell line, bEnd.3 (ECACC 96091929) was used between passage 22 and 29. The cells were cultured in Dulbecco's Modified Eagle Medium (DMEM) supplemented with 2mM Glutamine, 5µM 2-Mercaptoethanol (2ME), 1mM Sodium Pyruvate (NaP), 1% Non Essential Amino Acids (NEAA), 10% Foetal Bovine Serum (FBS) and 1X penicillin/streptomycin (P/S). Primary mouse microglia (ScienCell, SC-M1900-57) were cultured on poly-L-lysine (ScienCell 0413) coated flasks in Microglia medium (ScienCell 1901) supplemented with 1% FBS, 1x microglia growth supplement (MGS, ScienCell 1952) and 1 x P/S. Primary mouse astrocytes were cultured on poly-L-lysine (ScienCell 0413) coated flasks in Astrocyte Medium (ScienCell 1801) supplemented with 2% FBS, 1x astrocyte growth supplement (AGS, ScienCell 1852) and 1 x P/S.

In vitro incubation with inactivated virus and endothelial supernatants

Acid/heat inactivated SARS-CoV-2 (B.1.1.7) (NIBSC 101027) of known titre was used for all experiments. For incubation with inactivated virus, cells were seeded into either 24 well plates or 6 well plates at 125,000 cells per cm^2 and allowed to adhere overnight. Virus dilutions were then prepared to give a ratio of 1 copy (MOI 1),

TABLE 3 Antibodies for immunofluorescent stain and confocal imaging.

Antibody target-fluorochrome	Company	Cat#	Host	Dilution Factor (for 200 µL per section)
CD45-PE	Invitrogen	12-0451-82	Rat	50
CD11b-AF647	BDBioscience	557686	Rat	200
NK1.1-AF488	BioLegend	108718	Mouse	100
CD3-FITC	Abcam	ab34722	Rat	50
GFAP	Invitrogen	41-9892-82	Mouse	100
NeuN	Merck	MAB377X	Mouse	100
CD68 unconjugated	Abcam	ab53444	Rat	200
Anti-rat AF488	Jackson Immunoresearch	712-546-153	Donkey	500
Iba1 unconjugated	Wako	019-19741	Rabbit	500
Anti-rabbit IgG-AF647	Invitrogen	A-31573	Donkey	500
Spike unconjugated	Invitrogen	703958	Human	100
Anti-human AF568	Fisher	A-21090	Goat	500

0.1 copies (MOI 0.1) or 0.01 copies (MOI 0.01) per cells plated in the culture medium. For bEnd.3 experiments, cells were incubated for 24 hours with inactivated virus, 20 µg/mL polyI:C (Merck PL530) or with untreated culture medium. For astrocyte and microglia experiments, cells were incubated for 2 hours with inactivated virus, polyI:C, untreated medium, or supernatant from bEnd.3 cells previously exposed for 24 hours to MOI 1 virus dilution. Supernatant from bEnd.3 cells was filtered with a 20 nm syringe filter directly prior to treating microglia and astrocytes to remove viral particles. After 2 hours, treatments were removed, cells were washed with 1X phosphate-buffered saline (PBS) (Capricorn Scientific CSR154) three times and then the normal culture medium was replaced. For each treatment condition (virus or supernatant) 6-7 individual well replicates were performed and for control conditions (poly:IC or untreated) 3-4 replicates were performed. After 24 hours, the supernatant from these cells was collected and cells were fixed with 4% paraformaldehyde (Sigma 16005).

ELISA of *in vitro* supernatants

Supernatants were collected into 1 mL cryovials and stored at 4° C for no longer than 1 week prior to cytokine levels being assessed using ELISA. Kits were purchased from Invitrogen for IL-6 (88-7064), CCL2 (88-7391), IFNγ (88-7314) and performed according to manufacturer's protocol.

Immunostaining of *in vitro* samples

Microglia were fixed with 4% paraformaldehyde and washed 3x with 1X PBS with calcium and magnesium (PBS +/+) (Capricorn Scientific CSR1576). Cells were then incubated for 1 hour with Dakoblock (Agilent X090930-2). Cells were then washed 1x with PBS and incubated with primary antibody (Iba1 Wako Chemicals 019-19741; CD45-PE Thermo Fisher 12-0451-83) diluted in antibody diluent (1X PBS +/+, 1% BSA, 10% donkey serum (Sigma D9663), 0.1% Triton-X (Sigma X100)) overnight at 4°C. Cells were then washed 3x with 1x PBS +/+ and incubated with secondary antibody (Donkey anti-rabbit AF657, Thermo Fisher A31573) and DAPI (Thermofisher P36962) in antibody diluent and incubated in the dark for 2 hours at room temperature. Cells were then washed 3x with PBS +/+.

TABLE 4 Confocal microscopy settings.

Microscope component	Parameters
Microscope	Leica DMi8 with Andor Dragonfly
Light source	7-line integrated laser engine equipped with: Solid state 405 smart diode laser at 100mW: set to 10% Solid state 488 smart diode laser at 50mW: set to 35% OBIS LS 561 smart OPSS laser at 50mW: set to 2.0% OBIS LX Solid state 637 smart diode laser at 140mW: set to 7.0%
Excitation/ emission optics	Dichroic mirror: Quad EM filter 405-488-561-640 Dual camera beam splitter: Dual camera dichroic 565nm long pass Emission filters: 450/50nm bandpass filter 525/50nm bandpass filter 600/50nm bandpass filter 700/75nm bandpass filter Spinning disk with 40 µm pinholes
Objective lenses	Leica objectives: 11506358 HC PL APO 40×/1.30 OIL CS2
Detector	Andor iXon Ultra 888 Ultra EMCCD Camera 1024 × 1024; 405: 500 ms exposure; 65 EM gain 488: 500 ms exposure; 65 EM gain 561: 30 ms exposure; 156 EM gain 637: 30 ms exposure; 156 EM gain Averaging: 1; Binning: 1; camera magnification 1x Nyquist Z sampling

10.3389/fimmu.2024.1440324

In vitro confocal microscopy and reactivation/ramification index quantitation

Microglia were imaged at 25x magnification on a Leica DMi8 on an Andor Dragonfly spinning disk confocal microscope. 16 images per well were taken and stitched into a tilescan image using Fusion imaging software. Tilescan images were then processed in Fiji/ImageJ by thresholding the PE/647 channel and gating for individual cells (excluding cell clusters) and then analysing particles between 500-1000 µm for solidity.

Statistical analyses

Prism software (version 9.4.1, GraphPad Software Inc.) was used for graph generation and statistical analysis. The Shapiro-Wilk normality test used to check the normality of the distribution. Data are expressed as mean ± S.E.M. The difference between two or more non-normally distributed groups was tested using Mann-Whitney U or Kruskal-Wallis tests, respectively. $P \leq 0.05$ was considered statistically significant.

Results

Low inoculum intranasal SARS-CoV-2 infection in human ACE2 transgenic C57BL/6 mice does not cause viral replication in the brain parenchyma

We established the mouse model by comparing intranasal infection with a low ($1x10^3$ PFU) and a high ($1x10^4$ PFU) inoculum of SARS-CoV-2, collecting serum, brain and lung tissues at day 5 post-infection (Figure 1A). At this stage, none

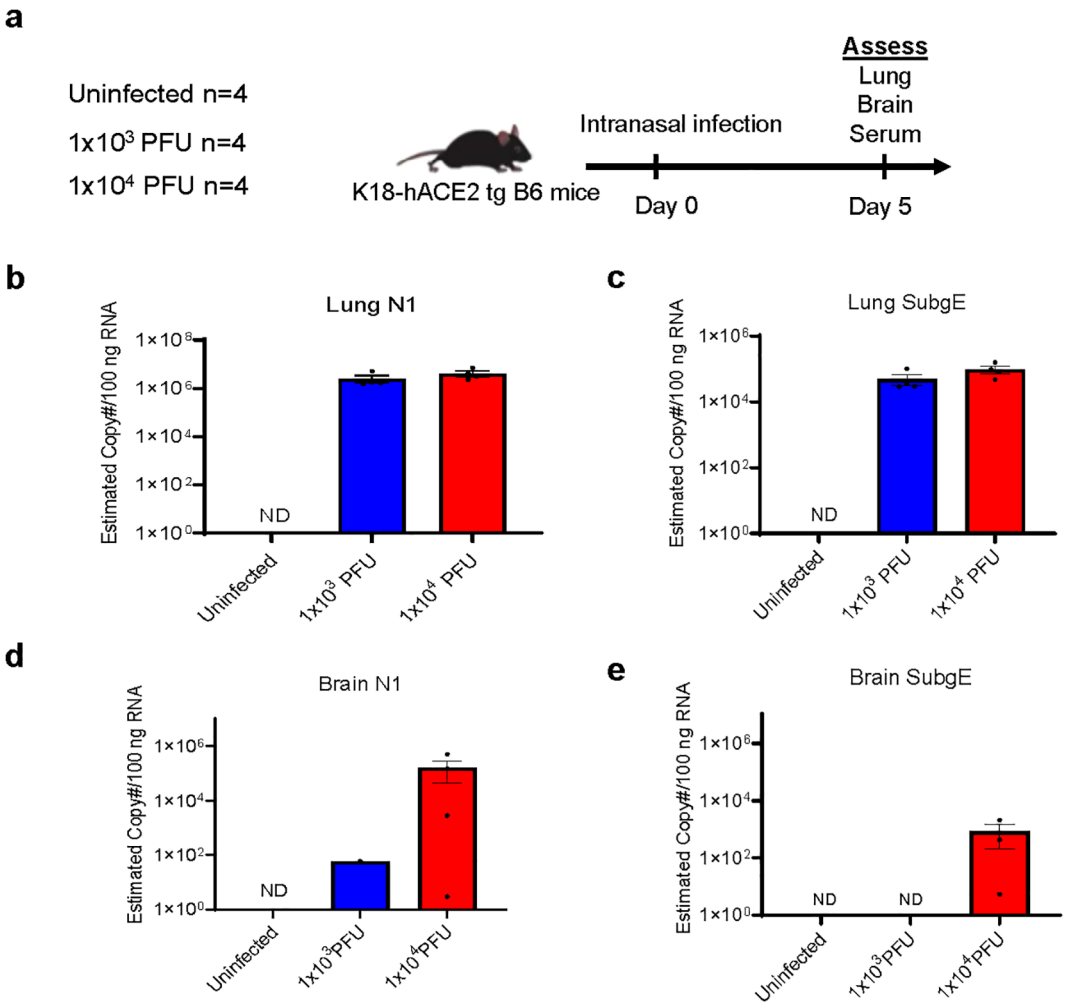

FIGURE 1
Low inoculum intranasal SARS-CoV-2 infection in human ACE2 transgenic C57BL/6 mice does not cause viral replication in the brain parenchyma. **(A)** Schema of K18 human-ACE2 transgenic C57B/6 mouse study randomised to no infection, 'low inoculum' infection at $1x10^3$ plaque-forming units (PFU) and 'high inoculum' infection at $1x10^4$ PFU, with endpoint at day 5 post-infection, showing one of two independent experiments, (n=4/group). **(B)** Real-time polymerase chain reaction (RT-QPCR) identifies SARS-CoV-2 N1 and **(C)** subgenomic E transcripts in lung homogenate confirming pulmonary infection and viral lytic replication at both inoculum of infection. **(D)** RT-QPCR of brain homogenate demonstrates that minimal SARS-CoV-2 N1 is present in the perfused brain parenchyma and there are no detectable SARS-CoV-2 subgenomic E transcripts **(E)** confirming the absence of lytic viral replication in the brain at low-dose infection. ND, not detected.

10.3389/fimmu.2024.1440324

of the mice showed weight loss (Supplementary Figure 1A). Both levels of infection caused pathology in the lung, with viral loads evidenced by qPCR of N1 with both low and high inocula (Figure 1B). There was also evidence of active viral replication in the lung, as defined by the surrogate readout of qPCR of subgenomic E which correlates with infectivity (18) (Figure 1C). SARS-CoV-2 N1 transcripts were detected in four out of four brains of mice that had received high inoculum of SARS-CoV-2 and in six of nine that received low inoculum (Figure 1D; first experiment displayed, n=4 group). However, whilst three of four high inoculum mice showed active viral transcription in the brain by the detection of subgenomic E, this was only detectable in two of nine low inoculum mouse brains (tissue from these two animals were not included in subsequent ex vivo experiments, Figure 1E; Supplementary Figures 1E–G).

H&E staining of lung and brain sections from infected mice were assessed for pathology and mononuclear cell clusters (Supplementary Figures 1B–D). The lungs of SARS-CoV-2 infected mice showed signs of pathology including oedema, haemorrhage, and fibrosis (Supplementary Figure 1B). Mononuclear cells were present with both inocula compared with uninfected mice (Supplementary Figure 1B. The brain tissue also had a few clusters of mononuclear cells in the frontal cortex with both inocula of SARS-CoV-2 (Supplementary Figures 1C, D).

Spike protein is present in the lungs, but not brains, of 1x10^3 PFU SARS-CoV-2 infected mice and there are differences in immune activation

Immunofluorescent staining and confocal microscopy of the lungs showed large amounts of viral spike protein with increased Iba1 expression (Figure 2A). The lungs also showed increases in CD45 and CD11b staining compared with uninfected animals (Figure 3A). Confocal microscopy of ex vivo brain sections from mice, following the low inoculum, demonstrated Iba-1 staining but, in contrast to lung tissue, showed no evidence of staining for SARS-CoV-2 spike protein (Figures 2B, 3B). These brains also showed no increases in numbers of CD3+ or NK1.1+ cells (Supplementary Figures 2A, B), or apoptotic cells (Supplementary Figure 2C).

Several inflammatory mediators are elevated in the lungs and brains of 1x10^3 PFU SARS-CoV-2 infected mice

In order to understand the mechanisms driving this apparent para-infectious neuropathology, we assessed transcription and protein levels of inflammatory mediators in brains and lung from the seven

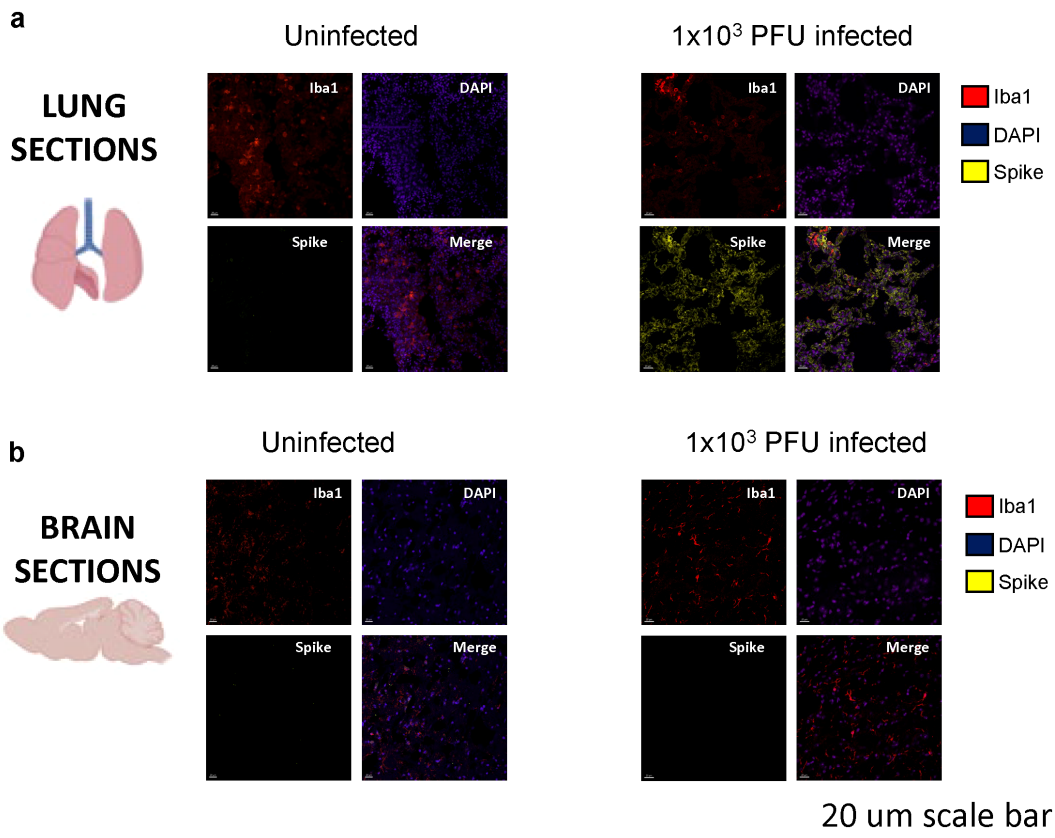

FIGURE 2
Spike protein is present in the lungs, but not in the brains of low-inoculum SARS-CoV-2 infected mice at day 5 post 1x10^3 PFU infection. **(A)** Confocal microscopy of low-inoculum infection in this model confirms the presence of both SARS-CoV-2 spike protein (yellow) and monocyte lineage cells (red) in the lungs. **(B)** Despite the absence of spike protein (yellow) in the brain in the low-inoculum infection model, there are consistent large areas of accumulation of Iba1+ microglia (red) of perfused brain parenchyma.

low-inoculum infected mice that showed no evidence of local viral replication in the brain. Our previous clinical study, comparing serum immune mediators from low vs. normal Glasgow coma scale score COVID-19 patients, demonstrated that six mediators of interest were increased in serum (7). Lung tissue from the mice revealed four of these, IL1-RA, IL-6, CCL2, and IL-12p40, to be upregulated with low-inoculum infection by QPCR (Figures 4A, B).

The brains from low inoculum infected mice showed increased transcripts of CCL4 and decreased levels of IL-1RA and IL-12p40 (Figures 4C, D; Supplementary Table 1). Although many brain cytokine proteins were not different between uninfected and low inoculum mice, CCL4, IFNγ and IL-17A were increased (Figures 4E, F; Supplementary Table 2). Consistent with an intra-cerebral local response, there were no increases in any of these cytokines in the mouse sera (Figures 4G, H).

Brains from low inoculum SARS-CoV-2 infected mice showed immune activation and increases in microglial reactivity despite the absence of active SARS-CoV-2 replication

Brains from low inoculum mice showed no detectable viral proteins (checked by spike staining) and no detectable viral transcription (checked using subgenomic E). However, these brains showed reactive microglia, with increased Iba1 expression (as measured by percentage area, fluorescence intensity and reactivation indices, Figures 5A–F). Clusters of GFAP+ astrocytes were found in the regions of high Iba1 expression in the brain, suggesting concomitant microgliosis and astrogliosis, as has been reported in human post-mortem samples (Supplementary Figures 3A, B). To ask whether parainfectious brain injury with potential blood-brain-barrier damage had taken place, the brain supernatant/serum albumin ratios were measured in uninfected mice and low inoculum infected animals (Supplementary Figure 3C). In humans post-COVID-19, NfL has been found to be raised, but there were no significant differences in the brain injury marker NfL, either by ELISA or Simoa (Supplementary Figure 3D) at this early time point (day 5 post infection) (7).

Viral effects on endothelial cells *in vitro* lead to pro-inflammatory cytokine production and subsequent microglia reactivation

We hypothesized that the cerebral vasculature is the most common route for SARS-CoV-2 infection interacting with neuroglial cells and causing local, not necessarily systemic, inflammation. To study the cascade of events in a controlled

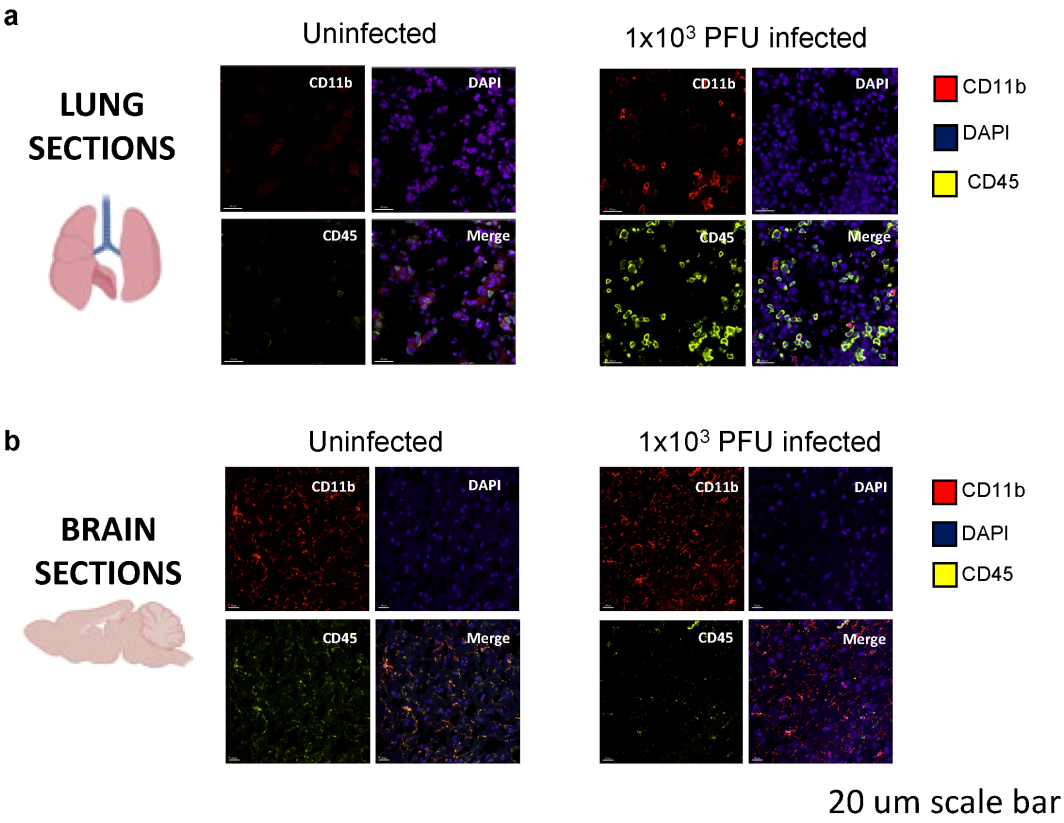

FIGURE 3
Immune activation is present in the lungs of SARS-CoV-2 infected mice at day 5 post 1x10^3 PFU infection. **(A)** Confocal microscopy of perfused organs in the low-inoculum SARS-CoV-2 infection model identifies the presence of CD45 positive leucocytes (yellow) and occasionally CD11b positive cells of macrophage/monocyte lineage (red), shown with DAPI (blue) in the lung. **(B)** No significant differences in CD45 and CD11b expression were found when comparing uninfected and infected brains.

environment, we exposed mouse endothelial cells (bEnd.3 cell line) to inactivated SARS-CoV-2 viral particles at three multiplicities of infection (MOI), collected and filtered the supernatant, and measured the cytokines present. The TLR3 agonist polyI:C served as a positive control (Figures 6A, B). The MOIs of 0.1 and 1 used to treat endothelial cells produced significant amounts of pro-inflammatory cytokines IL-6 and CCL2, so the MOI of 1 was chosen for the subsequent experiments as a way to mirror direct infection of brain endothelial cells, but not microglia and astrocytes (Figures 6C–E; Supplementary Figures 4A, B). Primary mouse microglia and astrocytes were exposed to the filtered supernatant from endothelial cells and their cytokine production and for microglia, their reactivation index was measured by Iba1+ morphology (Figures 6D, E; Supplementary Figures 4A, B). The supernatant from MOI=1 exposed endothelial cells resulted in the highest reactivation index indicating a pathway by which SARS-CoV-2 can indirectly affect brain cells and which is consistent with our *in vivo* data.

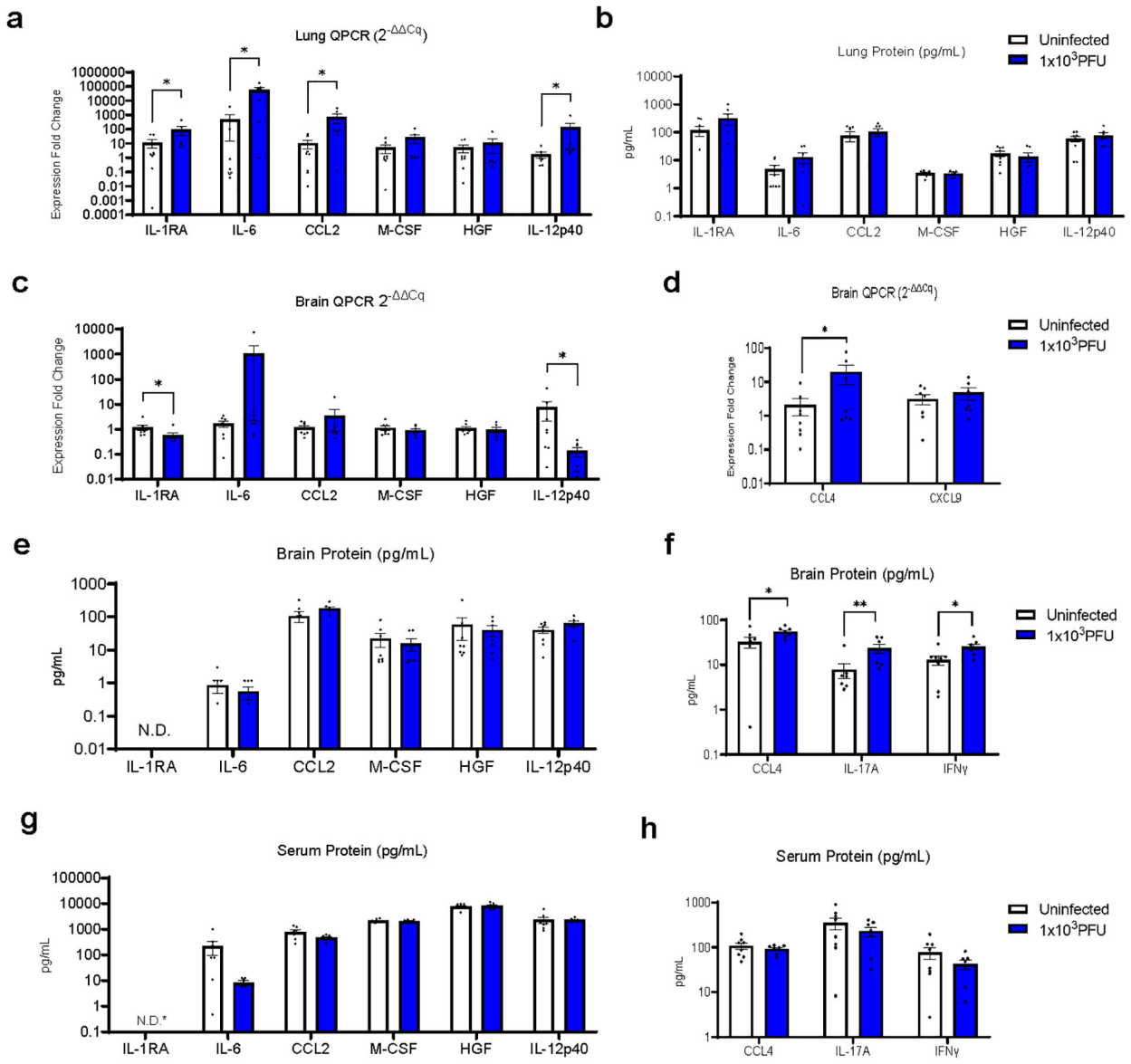

FIGURE 4
RT-QPCR of perfused lung parenchyma in the low-inoculum infection model (day 5 post 1x10^3 PFU infection) confirms upregulation of several inflammatory mediators. **(A)** RT-QPCR of six immune mediators of interest in perfused lung. **(B)** Luminex was used to check the same six immune mediators of interest in perfused lung. **(C–F)** In this low-inoculum infection model several pro-inflammatory mediators were found to be increased in the perfused brains, including **(D)** CCL4 by RT-QPCR and **(F)** IL-17A and IFNγ by Luminex. **(G, H)** In contrast, no statistically significant differences were seen in serum cytokine protein levels. *IL-RA undetectable by ELISA in all, but one uninfected serum sample (=3.5 pg/mL). (These data are from two independent experiments combined, n=7-8/group). *Pairwise comparisons by Mann-Whitney U test (*p<0.05, **p<0.01).*

Discussion

To better study the acute host response in SARS-CoV-2, and given that SARS-CoV-2 is rarely identified in the brain parenchyma in clinical samples, we developed a low-inoculum mouse model of COVID-19 which induced pulmonary infection in the absence of replication of virus in the brain. Following intranasal administration, by five days the mice had developed evidence of lung infection and immune cell infiltration (18), with production of inflammatory mediators, including CCL2, IL-6, IL-12p40 and IL-1RA; these cytokines were also elevated acutely in the serum of COVID-19 patients with low Glasgow coma scale scores (7). Despite the absence of viral replication in the brain parenchyma, there was some, albeit limited, production of inflammatory mediators in the brain, including CCL4, IFNγ and IL-17A. In addition, there was an increase in microglial Iba1 staining and microglia reactivation morphology. We had expected to also see increased numbers of CD45+ and CD11b+ cells, but believe that this was limited by the thin cryosections examined. In fact, we needed to examine thicker cryosections in order to quantify the microglia morphology (17). In future studies, flow cytometry would be an important way to quantify immune cell infiltration. Immune infiltrates and microgliosis were also observed in our previous mouse studies (19, 20). Parallel *in vitro* studies demonstrated that the filtered supernatant from brain endothelial cells exposed to SARS-CoV-2 virions, induced activation of microglia and production of CCL2. Our *in vitro* model using inactivated virus (due to limitations on CL3 work) delivered viral particles to endothelial cells and we hypothesize that this strongly stimulated them via innate PAMP pathways such as TLRs. Building on this, future studies could apply similar approaches to compare direct and indirect effects of vaccines and active virus on neuroglial cells. Active viruses would stimulate by DAMPs and PAMPs.

Our findings suggest that a primarily pulmonary inflammatory process is rapidly associated with parainfectious immune activation in the brain and the signature of an NK cell and/or T cell response which indicates a cascade of inflammation potentially amenable to treatment. Our mouse model is novel in using a low inoculum of SARS-CoV-2 virus for infection which does not induce lethal brain pathology, allowing us to study the immune activation in the brain in the absence of direct viral invasion. This is congruent with the majority of human autopsy results which show limited virus in the brain, but nevertheless demonstrate inflammation and microglia reactivity (21, 22). Human autopsy studies have studied this concept and found that exposure to lung-derived cytokines is association with microglia activation and that this was reduced by corticosteroid treatment (23). This may also reflect longer term effects, as a hamster model which examined neuropathology at 31 days post-SARS-CoV-2 infection found that Iba1 expression remained elevated (24). Studies of brain organoids have reported that Iba1+ microglia engulf post-synaptic material contributing to synapse elimination (25).

There have been reports of viral encephalitis and neuron degeneration and apoptosis observed in non-human primates (26, 27). Interestingly, in these studies the virus was present at low amounts in the brain and was found predominantly in the

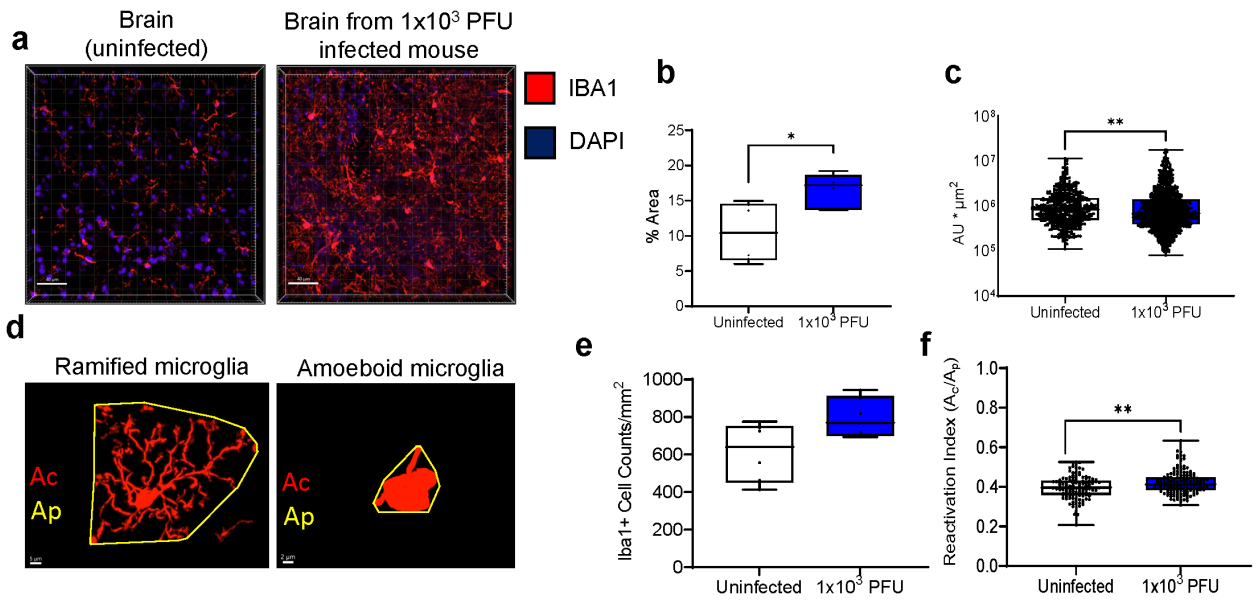

FIGURE 5
Low inoculum intranasal SARS-CoV-2 infection in mice results in increased pro-inflammatory cytokines in the lung and brain and causes increased microglia reactivity in the brain. **(A)** Confocal microscopy of 30 µm sections of frontal lobe brain parenchyma following low-inoculum infection reveals reactive microglia with increased expression of Iba1 (red) with nuclei stained by DAPI (purple, 3 images/mouse brain at 40X, n=2/group). **(B)** % area that was Iba1-positive, **(C)** Iba1+ cell counts, **(D)** Examples of microglia morphology Reactive Iba1+ microglia were quantified by **(E)** Iba1 fluorescence intensity, and **(F)** reactivation index between 0 and 1. Ac, cell area; Ap, projection area. *Pairwise comparisons by Mann-Whitney U test (*p< 0.05, **p<0.01).*

10.3389/fimmu.2024.1440324

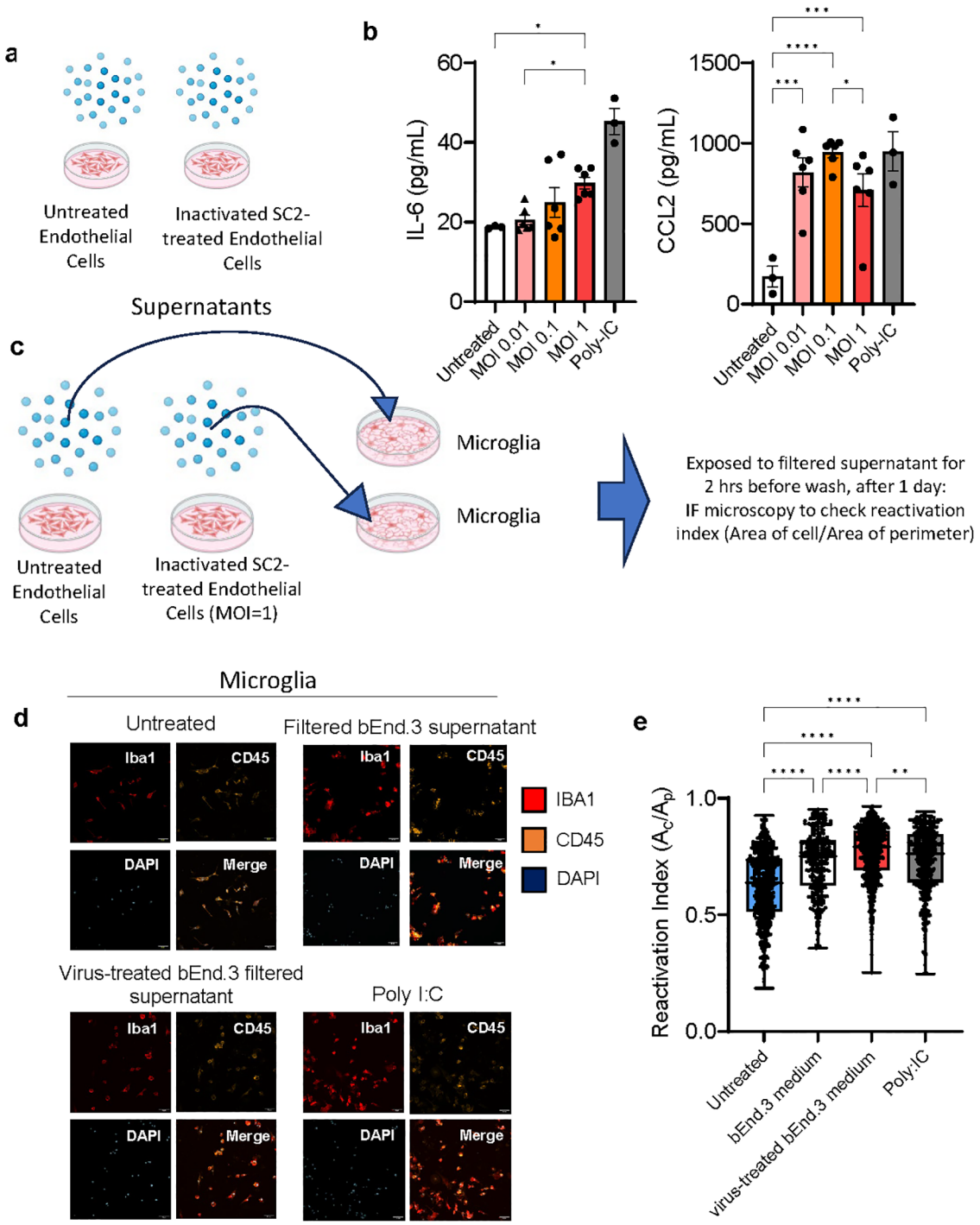

FIGURE 6
Viral effects on endothelial cells *in vitro* lead to pro-inflammatory cytokine production and subsequent microglia reactivation. **(A, B)** bEnd.3 cells were treated with heat and acid inactivated SARS-CoV-2 at a ratio of 0.01,0.1, or 1 virus copies per cell for 24 hours. At 24 hours concentrations of cytokines IL-6 and CCL2 were determined by ELISA and groups compared by ANOVA *p<0.05, **p<0.01, ***p<0.001, ****p<0.0001. **(C–E)** Primary mouse microglia were treated with 20 nm filtered supernatant taken from bEnd. 3 cells incubated with virus at an MOI of 1, for 2 hours, before being washed and culture medium replaced. At 24 hours cells were fixed and immunostained for Ibal and CD45 and imaged by confocal microscopy. 6-7 separate wells were cultured for each treatment condition and 3-4 for each control condition, with 16 images taken per well at 25x magnification. Dots represent individual cells. Groups compared by Kruskal-Wallis *p<0.05, **p<0.01, ***p<0.001, ****p<0.0001.

vasculature as visualized by co-localization with Von Willebrand Factor (27). Mimicking the clinical scenario, there was no correlation found between neurological markers with severity of respiratory disease. Another study reported increased CCL11 (eotaxin) in mouse serum and CSF that correlated with demyelination (28). That mouse model also lacked direct viral neural invasion by infecting mice that were intratracheally transfected with human ACE2. The demyelination was also observed after intraperitoneal administration of CCL11. Interestingly, clinical studies showed higher plasma levels of CCL11 in the patients who had brain fog (28). We did not observe elevated serum cytokines in our studies and this could be due to severity, timepoint, and/or technical differences. Our negative results in the serum are at least in part contributed to by heat-inactivation of experimental samples, which were part of safety protocols in the CL3 lab at the point when these experiments were conducted (29). Hamster studies have showed that COVID-19 leads to IL-1β and IL-6 expression within the hippocampus and medulla oblongata and is associated with decreased neurogenesis in the hippocampal dentate gyrus which leads to learning and memory deficits (30). This has also been shown in direct *in vitro* assays—with application of serum from COVID-19 patients with delirium with elevated IL-6 leading to decreased proliferation and increased apoptosis of a human hippocampal progenitor cell line (31). Our *in vitro* studies enabled us to isolate a potential mechanism by which SARS-CoV-2 indirectly affects brains cells—by studying endothelial cells which express ACE2 and can be directly infected by the virus (15), collecting their supernatants containing pro-inflammatory cytokines, and exposing microglia and astrocytes to them. Spike protein alone has previously been found to cause inflammation and associated cognitive deficits in animal models which is a common and important long-lasting symptom of COVID-19 in humans (32–34).

In conclusion, the low inoculum SARS-CoV-2 mouse model and parallel *in vitro* studies highlight an approach to study parainfectious effects on the brain and enables characterisation of the neuroglial cells themselves. The cytokine signature and microglia reactivity post infection indicate an acute local immune response including initial inflammation in the absence of active viral replication in the brain that could be amenable to targeted immunosuppression which can direct future studies.

Data availability statement

The raw data supporting the conclusions of this article will be made available by the authors, without undue reservation.

Ethics statement

The animal study was approved by an AWERB-approved protocol was followed for the mouse studies (University of Liverpool Animal Welfare and Ethical Review Body, UK Home Office Project Licence PP4715265. The study was conducted in accordance with the local legislation and institutional requirements.

Author contributions

CD: Formal analysis, Investigation, Writing – original draft, Conceptualization, Funding acquisition, Methodology, Visualization. CH: Formal analysis, Investigation, Methodology, Visualization, Writing – review & editing. SB: Formal analysis, Writing – review & editing. JJC: Methodology, Writing – review & editing. PS: Methodology, Writing – review & editing. KS: Methodology, Writing – review & editing. KT: Formal analysis, Writing – review & editing. EN: Writing – review & editing. RW: Writing – review & editing. AF: Writing – review & editing. HF: Writing – review & editing. YH: Writing – review & editing. GW: Writing – review & editing. CC: Writing – review & editing. ME: Writing – review & editing. MH: Formal analysis, Methodology, Visualization, Writing – review & editing. FE: Writing – review & editing. MG: Writing – review & editing. TS: Writing – review & editing. GB: Writing – review & editing. AK: Writing – review & editing. JC: Writing – review & editing. SI: Writing – review & editing. AV: Conceptualization, Investigation, Visualization, Writing – original draft, Writing – review & editing. JS: Funding acquisition, Investigation, Methodology, Project administration, Resources, Writing – review & editing, Supervision. LT: Investigation, Methodology, Writing – review & editing, Supervision. DM: Writing – review & editing, Conceptualization, Investigation, Supervision, Visualization. BM: Writing – original draft, Writing – review & editing, Conceptualization, Funding acquisition, Investigation, Methodology, Project administration, Resources, Supervision, Visualization.

Funding

The author(s) declare financial support was received for the research, authorship, and/or publication of this article. This research was funded by the National Institute for Health and Care Research (NIHR) (CO-CIN-01) and jointly by NIHR and UK Research and Innovation (CV220-169, MC_PC_19059). BDM is supported by the UKRI/MRC (MR/V03605X/1), the MRC/UKRI (MR/V007181/1), MRC (MR/T028750/1) and Wellcome (ISSF201902/3). BDM is also supported by the NIHR Health Protection Research Unit (HPRU) in Emerging and Zoonotic Infections at University of Liverpool in partnership with Public Health England (PHE), in collaboration with Liverpool School of Tropical Medicine and the University of Oxford [award 200907], NIHR HPRU in Respiratory Infections at Imperial College London with PHE [award 200927]. CD is supported by MRC (MC_PC_19044). We acknowledge the Liverpool Centre for Cell Imaging (CCI) for provision of imaging equipment (Dragonfly

confocal microscope) and excellent technical assistance (BBSRC grant number BB/R01390X/1). TS is supported by The Pandemic Institute and the NIHR Health Protection Research Unit (HPRU) in Emerging and Zoonotic Infections at University of Liverpool. DM and EN are supported by the NIHR Cambridge Biomedical Centre and by NIHR funding to the NIHR BioResource (RG94028 and RG85445), and by funding from Brain Research UK 201819-20.

Conflict of interest

The authors declare that the research was conducted in the absence of any commercial or financial relationships that could be construed as a potential conflict of interest.

Publisher's note

All claims expressed in this article are solely those of the authors and do not necessarily represent those of their affiliated organizations, or those of the publisher, the editors and the reviewers. Any product that may be evaluated in this article, or claim that may be made by its manufacturer, is not guaranteed or endorsed by the publisher.

Author disclaimer

The views expressed are those of the author(s) and not necessarily those of the UKRI, NHS, the NIHR or the Department of Health and Social Care.

Supplementary material

The Supplementary Material for this article can be found online at: https://www.frontiersin.org/articles/10.3389/fimmu.2024.1440324/full#supplementary-material

References

1. Grundmann A, Wu C-H, Hardwick M, Baillie JK, Openshaw PJM, Semple MG, et al. Fewer COVID-19 neurological complications with dexamethasone and remdesivir. *Ann Neurol.* (2023) 93-1:88–102. doi: 10.1002/ana.26536

2. Xu E, Xie Y, Al-Aly Z. Long-term neurologic outcomes of COVID-19. *Nat Med.* (2022), 1–10. doi: 10.1038/s41591-022-02001-z

3. Meinhardt J, Radke J, Dittmayer C, Franz J, Thomas C, Mothes R, et al. Olfactory transmucosal SARS-CoV-2 invasion as a port of central nervous system entry in individuals with COVID-19. *Nat Neurosci.* (2021) 24:168–75. doi: 10.1038/s41593-020-00758-5

4. Matschke J, Lütgehetmann M, Hagel C, Sperhake JP, Schröder AS, Edler C, et al. Neuropathology of patients with COVID-19 in Germany: a post-mortem case series. *Lancet Neurol.* (2020) 19:919–29. doi: 10.1016/S1474-4422(20)30308-2

5. Khan M, Yoo S-J, Clijsters M, Backaert W, Vanstapel A, Speleman K, et al. Visualizing in deceased COVID-19 patients how SARS-CoV-2 attacks the respiratory and olfactory mucosae but spares the olfactory bulb. *Cell.* (2021) 184:5932–5949.e15. doi: 10.1016/j.cell.2021.10.027

6. Dunai C, Collie C, Michael BD. Immune-mediated mechanisms of COVID-19 neuropathology. *Front Neurol.* (2022) 13. doi: 10.3389/fneur.2022.882905

7. Michael BD, Dunai C, Needham EJ, Tharmaratnam K, Williams R, Huang Y, et al. Para-infectious brain injury in COVID-19 persists at follow-up despite attenuated cytokine and autoantibody responses. *Nat Commun.* (2023) 14:8487. doi: 10.1038/s41467-023-42320-4

8. Needham EJ, Ren AL, Digby RJ, Norton EJ, Ebrahimi S, Outtrim JG, et al. Brain injury in COVID-19 is associated with dysregulated innate and adaptive immune responses. *Brain.* (2022), awac321. doi: 10.1093/brain/awac321

9. Frontera JA, Sabadia S, Lalchan R, Fang T, Flusty B, Millar-Vernetti P, et al. A prospective study of neurologic disorders in hospitalized patients with COVID-19 in New York City. *Neurology.* (2021) 96:e575–86. doi: 10.1212/WNL.0000000000010979

10. Thwaites RS, Sanchez Sevilla Uruchurtu A, Siggins MK, Liew F, Russell CD, et al. Inflammatory profiles across the spectrum of disease reveal a distinct role for GM-CSF in severe COVID-19. *Sci Immunol.* (2021) 6:eabg9873. doi: 10.1126/sciimmunol.abg9873

11. Leist SR, Dinnon KH, Schäfer A, Tse LV, Okuda K, Hou YJ, et al. A mouse-adapted SARS-CoV-2 induces acute lung injury and mortality in standard laboratory mice. *Cell.* (2020) 183:1070–1085.e12. doi: 10.1016/j.cell.2020.09.050

12. Carossino M, Montanaro P, O'Connell A, Kenney D, Gertje H, Grosz KA, et al. Fatal neuroinvasion and SARS-CoV-2 tropism in K18-hACE2 mice is partially independent on hACE2 expression. *Viruses.* (2021) 14(3):535. doi: 10.1101/2021.01.13.425144

13. Golden JW, Cline CR, Zeng X, Garrison AR, Carey BD, Mucker EM, et al. Human angiotensin-converting enzyme 2 transgenic mice infected with SARS-CoV-2 develop severe and fatal respiratory disease. *JCI Insight.* (2020) 5. doi: 10.1172/jci.insight.142032

14. Kumari P, Rothan HA, Natekar JP, Stone S, Pathak H, Strate PG, et al. Neuroinvasion and encephalitis following intranasal inoculation of SARS-CoV-2 in K18-hACE2 mice. *Viruses.* (2021) 13:132. doi: 10.3390/v13010132

15. Wenzel J, Lampe J, Müller-Fielitz H, Schuster R, Zille M, Müller K, et al. The SARS-CoV-2 main protease Mpro causes microvascular brain pathology by cleaving NEMO in brain endothelial cells. *Nat Neurosci.* (2021) 24:1522–33. doi: 10.1038/s41593-021-00926-1

16. Wittekindt M, Kaddatz H, Joost S, Staffeld A, Bitar Y, Kipp M, et al. Different methods for evaluating microglial activation using anti-ionized calcium-binding adaptor protein-1 immunohistochemistry in the cuprizone model. *Cells.* (2022) 11:1723. doi: 10.3390/cells11111723

17. Heindl S, Gesierich B, Benakis C, Llovera G, Duering M, Liesz A. Automated morphological analysis of microglia after stroke. *Front Cell Neurosci.* (2018) 12. doi: 10.3389/fncel.2018.00106

18. Santos Bravo M, Berengua C, Marín P, Esteban M, Rodriguez C, del Cuerpo M, et al. Viral culture confirmed SARS-CoV-2 subgenomic RNA value as a good surrogate marker of infectivity. *J Clin Microbiol.* (2022) 60:e01609–21. doi: 10.1128/JCM.01609-21

19. De Neck S, Penrice-Randal R, Clark JJ, Sharma P, Bentley EG, Kirby A, et al. The stereotypic response of the pulmonary vasculature to respiratory viral infections: findings in mouse models of SARS-CoV-2, influenza A and gammaherpesvirus infections. *Viruses.* (2023) 15:1637. doi: 10.3390/v15081637

20. Seehusen F, Clark JJ, Sharma P, Subramaniam K, Giuliani SW, Hughes GL, et al. Viral Neuroinvasion and Neurotropism without Neuronal Damage in the hACE2 Mouse Model of COVID-19. *Viruses.* (2021) 14(5):1020. doi: 10.1101/2021.04.16.440173

21. Thakur KT, Miller EH, Glendinning MD, Al-Dalahmah O, Banu MA, Boehme AK, et al. COVID-19 neuropathology at Columbia University Irving Medical Center/New York Presbyterian Hospital. *Brain.* (2021) 144:2696–708. doi: 10.1093/brain/awab148

22. Lee MH, Perl DP, Steiner J, Pasternack N, Li W, Maric D, et al. Neurovascular injury with complement activation and inflammation in COVID-19. *Brain J Neurol.* (2022) 145:2555–68. doi: 10.1093/brain/awac151

23. Grant RA, Poor TA, Sichizya L, Diaz E, Bailey JI, Soni S, et al. Prolonged exposure to lung-derived cytokines is associated with activation of microglia in patients with COVID-19. *JCI Insight.* (2024) 9:e178859. doi: 10.1172/jci.insight.178859

24. Frere JJ, Serafini RA, Pryce KD, Zazhytska M, Oishi K, Golynker I, et al. SARS-CoV-2 infection in hamsters and humans results in lasting and unique systemic perturbations after recovery. *Sci Transl Med.* (2022) 14:eabq3059. doi: 10.1126/scitranslmed.abq3059

25. Samudyata, Oliveira AO, Malwade S, Rufino de Sousa N, Goparaju SK, Gracias J, et al. SARS-CoV-2 promotes microglial synapse elimination in human brain organoids. *Mol Psychiatry.* (2022) 27:3939–50. doi: 10.1038/s41380-022-01786-2

26. Choudhary S, Kanevsky I, Yildiz S, Sellers RS, Swanson KA, Franks T, et al. Modeling SARS-CoV-2: comparative pathology in rhesus macaque and golden Syrian hamster models. *Toxicol Pathol*. (2022) 50(3):280–93. doi: 10.1177/01926233211072767

27. Rutkai I, Mayer MG, Hellmers LM, Ning B, Huang Z, Monjure CJ, et al. Neuropathology and virus in brain of SARS-CoV-2 infected non-human primates. *Nat Commun*. (2022) 13:1745. doi: 10.1038/s41467-022-29440-z

28. Fernández-Castañeda A, Lu P, Geraghty AC, Song E, Lee M-H, Wood J, et al. Mild respiratory COVID can cause multi-lineage neural cell and myelin dysregulation. *Cell*. (2022) 185:2452–2468.e16. doi: 10.1016/j.cell.2022.06.008

29. Xu E, Li T, Chen Q, Wang Z, Xu Y. Study on the effect and application value of heat-inactivated serum on the detection of thyroid function, tumor markers, and cytokines during the SARS-CoV-2 pandemic. *Front Med*. (2021) 8. doi: 10.3389/fmed.2021.742067

30. Soung AL, Vanderheiden A, Nordvig AS, Sissoko CA, Canoll P, Mariani MB, et al. COVID-19 induces CNS cytokine expression and loss of hippocampal neurogenesis. *Brain*. (2022), awac270. doi: 10.1093/brain/awac270

31. Borsini A, Merrick B, Edgeworth J, Mandal G, Srivastava DP, Vernon AC, et al. Neurogenesis is disrupted in human hippocampal progenitor cells upon exposure to serum samples from hospitalized COVID-19 patients with neurological symptoms. *Mol Psychiatry*. (2022), 1–13. doi: 10.1038/s41380-022-01741-1

32. Fontes-Dantas FL, Fernandes GG, Gutman EG, De Lima EV, Antonio LS, Hammerle MB, et al. SARS-CoV-2 Spike protein induces TLR4-mediated long-term cognitive dysfunction recapitulating post-COVID-19 syndrome in mice. *Cell Rep*. (2023) 42:112189. doi: 10.1016/j.celrep.2023.112189

33. Oh J, Cho W-H, Barcelon E, Kim KH, Hong J, Lee SJ. SARS-CoV-2 spike protein induces cognitive deficit and anxiety-like behavior in mouse via non-cell autonomous hippocampal neuronal death. *Sci Rep*. (2022) 12:5496. doi: 10.1038/s41598-022-09410-7

34. Wood GK, Sargent BF, Ahmad ZUA, Tharmaratnam K, Dunai C, Egbe FN. Post-hospitalisation COVID-19 cognitive deficits at one year are global and associated with elevated brain injury markers and grey matter volume reduction. *Nat Med*. (2024), 1–1.

Frontiers in Immunology

Explores novel approaches and diagnoses to treat immune disorders.

The official journal of the International Union of Immunological Societies (IUIS) and the most cited in its field, leading the way for research across basic, translational and clinical immunology.

Discover the latest Research Topics

See more →

Frontiers

Avenue du Tribunal-Fédéral 34
1005 Lausanne, Switzerland
frontiersin.org

Contact us

+41 (0)21 510 17 00
frontiersin.org/about/contact